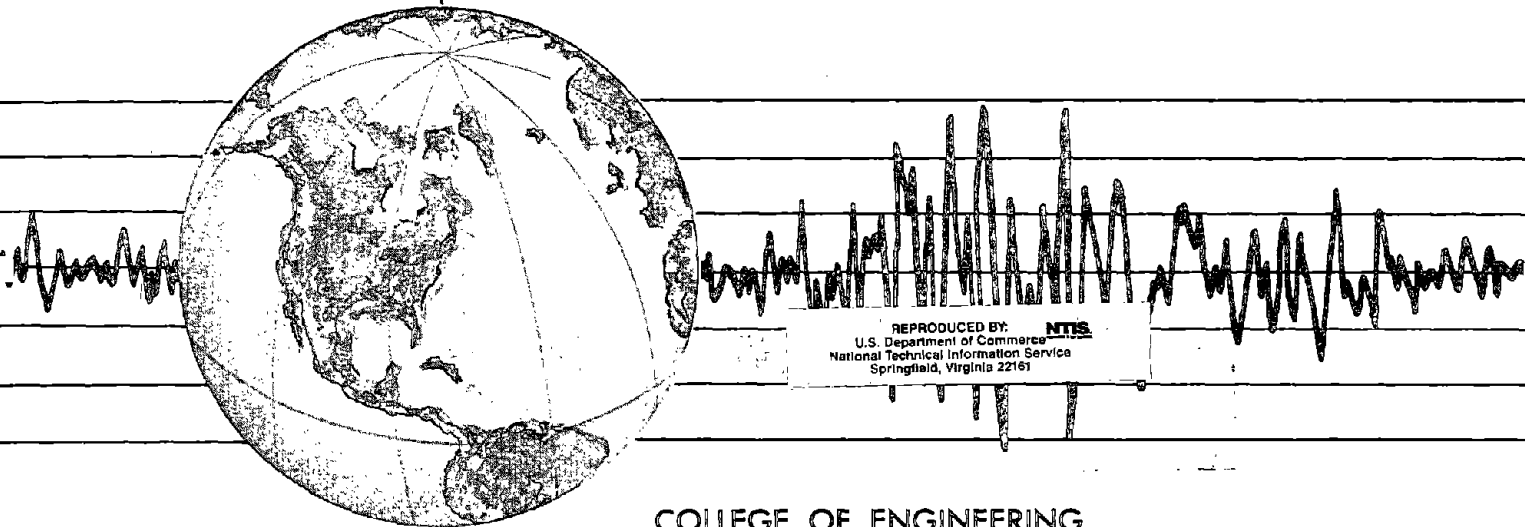EARTHQUAKE ENGINEERING RESEARCH CENTER

# EXPERIMENTS ON ECCENTRICALLY BRACED FRAMES WITH COMPOSITE FLOORS

by

JAMES M. RICLES

EGOR P. POPOV

COLLEGE OF ENGINEERING

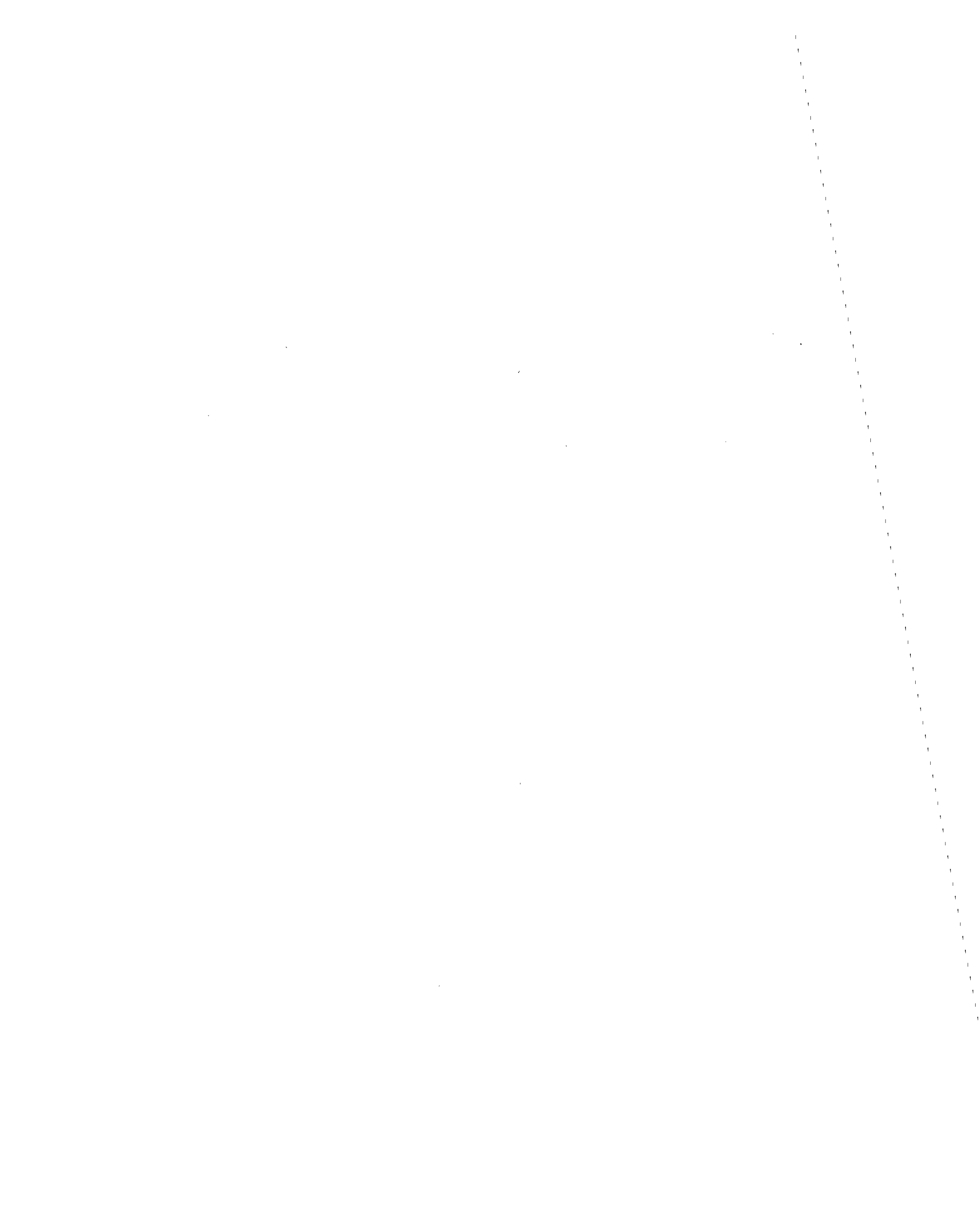UNIVERSITY OF CALIFORNIA · Berkeley, California

For sale by the National Technical Information Service, U.S. Department of Commerce, Springfield, Virginia 22161.

See back of report for up to date listing of EERC reports.

50272-101

| REPORT DOCUMENTATION PAGE | 1. REPORT NO. NSF/ENG-87033 | 2. | 3. Recipient's Accession No. PB88 173067/AS |
|---|---|---|---|
| 4. Title and Subtitle | | | 5. Report Date |
| Experiments on Eccentrically Braced Frames with Composite Floors | | | June 1987 |
| | | | 6. |
| 7. Author(s) | | | 8. Performing Organization Rept. No. |
| James M. Ricles and Egor P. Popov | | | UCB/EERC - 87/06 |
| 9. Performing Organization Name and Address | | | 10. Project/Task/Work Unit No. |
| Earthquake Engineering Research Center University of California 1301 South 46th Street Richmond, California 94804 | | | |
| | | | 11. Contract(C) or Grant(G) No. |
| | | | (C) |
| | | | (G) CEE82-8402268 ECE-8418487 |
| 12. Sponsoring Organization Name and Address | | | 13. Type of Report & Period Covered |
| National Science Foundation 1800 G. Street, N.W. Washington, D.C. 20550 | American Iron & Steel Institute 1000 16th Street, N.W. Washington, D.C. 20036 | | |
| | | | 14. |

15. Supplementary Notes

16. Abstract (Limit: 200 words)

The results of an experimental study on the cyclic behavior of short links in eccentrically braced steel frames (EBFs) with composite floors are presented. This study includes eight tests which were performed on two-thirds scale subassemblies consisting of floor beams of EBFs. Two of these specimens were bare steel, with the remaining six consisting of steel sections with a composite floor slab. The results of each test are analyzed to determine the increase in cyclic link capacity due to composite action, whether cyclic web buckling in composite links can be inhibited using bare steel link design criteria, and the extent of participation and damage of the concrete floor slab under extreme loading.

The report also deals with analysis of the interaction between the floor beam and slab in EBFs with composite floor systems. An analytical procedure is developed for determining the effective slab width and moment of inertia of composite floor beams in EBFs whereby orthotropic floor slab and beam flexural properties are taken into account. The accuracy and reliability of the method are indicated by analysis of several test specimens; additional analyses are reported to demonstrate the effects of orthotropic slab behavior and the beam spacing-to-span ratio.

17. Document Analysis    a. Descriptors

earthquake engineering
eccentrically braced frames
link

link capacity
web buckling
earthquake resistance

b. Identifiers/Open-Ended Terms

c. COSATI Field/Group

| 18. Availability Statement | 19. Security Class (This Report) Unclassified | 21. No. of Pages 325 |
|---|---|---|
| Release unlimited | 20. Security Class (This Page) Unclassified | |

(See ANSI-Z39.18)          See Instructions on Reverse

OPTIONAL FORM 272 (4-77)
(Formerly NTIS-35)
Department of Commerce

# EXPERIMENTS ON ECCENTRICALLY BRACED FRAMES
# WITH COMPOSITE FLOORS

by

James M. Ricles

and

Egor P. Popov

# EXPERIMENTS ON ECCENTRICALLY BRACED FRAMES

# WITH COMPOSITE FLOORS

## Abstract

An eccentrically braced steel frame is a structural system in which eccentricities are deliberately introduced into the bracing configuration. As a result, the axial forces in the braces are transferred among braces and to columns through shear and bending in a portion of the floor beam called the *link*. A link in an eccentrically braced steel frame acts as a ductile fuse. During overloading of the structure the links are designed to yield and dissipate large amounts of input energy while inhibiting brace buckling. In addition to possessing good ductility, an eccentrically braced steel frame also possesses a high elastic stiffness. As a result there is currently a growing interest with regards to its use in seismic design.

Past experimental research has assessed the performance of links and eccentrically braced steel frames under extreme cyclic loading. While these investigations have demonstrated the superiority of these structural systems and provided an adequate evaluation of the inelastic behavior of short links, they have not adequately addressed the issue of the effects of composite action on link performance due to concrete floor slabs. This important topic is treated in this report.

In the first part of this report the results of an experimental study are presented concerning the cyclic behavior of short links in eccentrically braced steel frames with composite floors. This study includes eight tests which were performed on two-thirds scale subassemblies consisting of floor beams of eccentrically braced steel frames. Two of these specimens were bare steel, with the remaining six consisting of steel sections with a composite floor slab. The observed behavior of each specimen is documented. The results of each test are then analyzed and compared in order to determine the increase in cyclic link capacity due to composite action, whether cyclic web buckling in composite links can be

inhibited using bare steel link design criteria, and the extent of participation and damage of the concrete floor slab under extreme loading.

The remaining part of this report deals with analysis of the interaction between the floor beam and slab in EBFs with composite floor systems. An analytical procedure is developed for determining the effective slab width and moment of inertia of composite floor beams in EBFs whereby orthotropic floor slab and beam flexural properties are taken into account. Analysis of several test specimens are reported in order to indicate the accuracy and reliability of the method. Additional analyses are also reported in order to demonstrate the effects of orthotropic slab behavior and the beam spacing-to-span ratio.

The results of the experimental study and floor slab-beam interaction analysis were used to establish constitutive relationships for finite element models. These finite element models were then used to perform cyclic static and seismic nonlinear analysis of eccentrically braced frames. The formulations for the finite element models and the nonlinear analysis results are discussed in a companion report entitled *Dynamic Analysis of Seismically Resistant Eccentrically Braced Frames*, which has been published as EERC Report No. 87/07.

## ACKNOWLEDGEMENTS

# TABLE OF CONTENTS

Preceding page blank

# CHAPTER 1

# INTRODUCTION

## 1.1. General

The design of earthquake resistant structures is a challenging task. The structural engineer must design a structure to resist seismically induced loads which are not clearly defined. Often, the seismic design loads are based on building codes or determined by a response spectra technique. Determining the seismic loads by one of these methods assumes that the building code or response spectra are representative of a major earthquake that would occur near the site of the structure. Choosing a representative earthquake is difficult, for each earthquake produces unique ground motions which affects the energy content at the various ground motion frequencies, in addition to the duration of strong shaking. Consequently, there is no assurance that the intensity of loads during an earthquake will not exceed the maximum intensity level which the structure was originally designed to resist.

Because of the uncertainties associated with estimating seismic induced forces on structures, a seismic design method has evolved based on a three tier philosophy. Firstly, under minor ground shaking which has a high probability of occurrence, the structure must not suffer any structural and non-structural damage. Hence, the structure must remain elastic during minor earthquakes and possess sufficient elastic stiffness to limit structural displacements and interstory drift. Secondly, during moderate earthquake activity which has a low probability of occurrence, the structure should not undergo any structural damage, although a limited amount of nonstructural damage is allowed. To meet these requirements, the structure can undergo minor inelastic activity in critical regions. Finally, under extreme ground shaking which has an extremely low probability of occurrence, the structure must not collapse resulting in loss of life. Inelastic structural behavior is allowed since it would not be economical to elastically resist such major earthquakes. Structural systems which

possess stable hysteretic loops and ductile behavior tend to perform well under extreme loading conditions during major earthquakes, for they are able to dissipate large amounts of energy input without collapsing.

## 1.2. Conventional Seismic Resistant Steel Structures

For medium and high rise buildings, structural steel has been used extensively due to its excellent strength and ductility properties. Two of the most commonly used structural steel systems in the past have been moment resisting frames (MRFs) and concentrically braced frames (CBFs).

Moment resisting frames can be designed to be ductile and dissipate large amounts of energy during earthquakes [1]. A typical configuration of such of system is shown in Fig. 1.1. The dissipation of energy is mainly obtained through inelastic action in the beam-column joints. Ductility of a moment resisting frame requires proportioning the beams and columns to meet the so-called strong column-weak beam design concept, with proper details for the beam-column joint. A properly designed moment resisting frame subjected to cyclic load is shown in Fig. 1.2, indicating the stable hysteretic behavior resulting in continued energy dissipation.

In the elastic range, moment resisting frames can often be laterally too flexible due to large flexural deformations of the beam. As a result, limiting the elastic interstory drift often controls the design of such systems. Consequently, a more costly design is required whereby larger beam sections are used. The moment that is transferred from beams to columns creates large shear forces in the beam-column panel zones [1,38]. In the inelastic range these panel zones can develop considerable distortion, resulting in a significant increase in the interstory drift. Furthermore, recent research [38] demonstrates that severe panel zone shear distortion can lead to distortion of the column flange at the beam-column connection, eventually causing a brittle fracture of the beam flange welds. Web doubler plates are often used in the beam-column panel zones to avoid these problems, thereby

adding to the expense of the design.

It is generally more economical to resist lateral loads and control deflections with bracing such as that used in concentric braced frames, Fig. 1.3. The braces in a concentric braced frame cause the structural system to act as a vertical truss which possesses an excellent lateral elastic stiffness. Concentrically braced frames are thereby able to control story drift and resist minor ground shaking. However, the use of this type of structural system is cautioned against where there exists a high probability of the occurrence of a major earthquake during the life of the structure. Popov and Black [2] have experimentally demonstrated that braces which repeatedly buckle under cyclic loading suffer a drastic decrease in their buckling strength and ability to dissipate energy, see Fig. 1.4. Such brace behavior affects the global behavior, as illustrated in Fig. 1.5 [39], where the concentrically braced frame's lateral load carrying capacity dramatically decreases with continued cyclic displacement. Unstable behavior could eventually develop leading to the collapse of the frame.

### 1.3. Eccentrically Braced Steel Frames

Since 1978 Popov and his associates at the University of California at Berkeley have conducted extensive research on a new type of structural system for earthquake resistant design. This new structural system is known as the eccentrically braced frame (EBF). EBF's have both properties of a high elastic lateral stiffness and good energy dissipation capacity, making its use advantageous for seismic resistant design. Some typical bracing configurations of EBFs are shown in Fig. 1.6. These types of framing configurations can be referred to as *K-braced frames, D-braced frames,* and *V-braced frames* ,respectively. Links of length $e$ are formed in these EBFs by arranging the braces as shown in Fig. 1.6. In EBFs, the axial forces in braces are transmitted through the adjoining links by bending and shear action.

The elastic lateral stiffness of an EBF is dependent upon the relative length of the links, $e$, to the bay width, $L$. For large values of $e/L$ the elastic lateral stiffness approaches

the stiffness of a moment resisting frame. By decreasing the $e/L$ ratio the elastic lateral stiffness increases and eventually approaches that of a concentrically braced frame. This behavior is demonstrated in Fig. 1.7 for two simple single story models.

Under severe seismic ground motion where inelastic behavior is expected, the links act as fuses for dissipating energy, as illustrated in Fig. 1.8. A link which undergoes inelastic activity and dissipates energy will be referred to as an active link. To ensure that an active link possesses sufficient ductility under cyclic loading and good energy dissipation capacity, the steel section forming the link must be checked to determine if web stiffeners are required to control cyclic web buckling [3,5,7]. The hysteretic behavior of a link designed where the web was reinforced with transverse stiffeners is shown in Fig. 1.9. This link was a bare steel specimen which yielded predominantly in the web due to shear. By observing the fact that the shear force reached a limiting value in the link following yielding and strain hardening, the maximum forces required to be developed in any adjoining brace of an EBF can be determined by statics. Therefore, the braces of an EBF can be prevented from buckling by designing them to resist the link's maximum shear force. This assures that an EBF will not have its energy dissipation capacity decreased due to cyclic buckling of the braces. This is difficult to guarantee for concentrically braced frames. The global hysteretic experimental response of a one-third size EBF is shown in Fig. 1.10, illustrating the stable hysteretic behavior. The performance of the EBF is superior compared to the concentrically braced steel frame's performance shown earlier in Fig. 1.5.

## 1.4. Bare Steel Link Behavior

A link is typically exposed to both high moments and shears in the elastic and inelastic states. The performance of an EBF during a major earthquake depends to a large extent on the inelastic behavior of the links. In a well designed EBF, except for the plastic hinges at the column bases, all the inelastic activity of the frame should be concentrated in the links. Representative examples of this condition are illustrated in Fig. 1.8 for the collapse

mechanism of a K-braced and V-braced EBF, respectively. Active links have been classified by previous researchers [7,18] into categories according to the type of hinge formed. Three type of hinges, shown in Fig. 1.11, can be identified in EBF:

1. Plastic hinges developing moment $M_p$ [Hinges (1)].

2. Plastic hinges developing moment larger than $M_p^*$ and less than $M_p$ which are simultaneously subjected to a relatively high shear force [Hinges (2)].

3. Plastic hinges with moments equal to or less than $M_p^*$ accompanied by web yielding in shear of $V_p$ [Hinges (3)].

The quantities $M_p^*$, $M_p$, and $V_p$ associated with the above hinges are defined as follows:

$$M_p = \sigma_y Z \tag{1.1}$$

$$M_p^* = \sigma_y(d-t_f)(b_f-t_w)t_f \tag{1.2}$$

$$V_p = \frac{\sigma_y}{\sqrt{3}}(d-t_f)t_w, \tag{1.3}$$

where

$M_p$ = plastic moment capacity of a steel section,

$M_p^*$ = plastic moment capacity of a steel section reduced by shear,

$V_p$ = plastic shear capacity of a steel section,

$\sigma_y$ = yield stress of steel,

$Z$ = plastic section modulus,

$d$, $t_f$, $t_w$, $b_f$ = depth, flange thickness, web thickness, and flange width of a steel section, respectively.

Fig. 1.12 shows a typical moment-shear $(M-V)$ interaction surface for a wide flange steel section. The function may be approximated by an expression developed by Neal [19]:

$$V \approx V_p \qquad (M \leq M_p^*) \tag{1.4}$$

$$\left[\frac{M-M_p^*}{M_p-M_p^*}\right]^2 + \left[\frac{V}{V_P}\right]^2 = 1 \qquad (M \geq M_p^*) \tag{1.5}$$

Considering the equilibrium of a link, Fig. 1.13, with moments $M_p^*$ and shear $V_p$ the maximum shear hinge length $b^*$ can be determined:

$$b^* = 2\frac{M_p^*}{V_P} \tag{1.6}$$

This force state at each end of the link corresponds to the balance point of the moment-shear interaction surface. Links with lengths shorter than $b^*$ develop shear yielding in the web. Such links are referred to as "shear links", and the hinges that form conform to type 3. A link with hinges of type 1 is called a "moment link", whereas a link with a hinge of type 2 is designated as an "intermediate link". Experimental studies [3] have indicated that shear links provide greater energy dissipation than links whose lengths are larger than $b^*$ where the hinges are of type 1 or 2.

Recent studies [7] indicated that no significant change in the link end moment capacity occurs even with large plastic shear deformation. It was concluded that in the strain-hardening range the cross-coupling effect between moment and shear was negligible. Therefore, a rectangular moment-shear yield surface was proposed, Fig. 1.14, where $M_p$ instead of $M_p^*$ is used to establish the maximum shear hinge length $b_{max}$:

$$b_{max} = 2\frac{M_p}{V_P} \tag{1.7}$$

If the link's length equals $b_{max}$ two moment hinges form at shear yield. In order to prevent excessive flange strain during strain hardening as a result of large moment hinge demand, it has been suggested to limit the end moment to $1.2M_p$ for a shear of $1.5V_p$, and the maximum recommended link length for a shear link has been limited to:

$$e \leq 1.6\frac{M_p}{V_p} \tag{1.8}$$

At Berkeley active links yielding primarily in shear in the web have been studied. Until further research is completed [41], it has been recommended not to exceed the link length given by Eq. (1.8).

The inelastic deformation of the link, $\gamma_p$, is related to the link's length $e$ and EBF configuration, as shown in Fig. 1.8. In shear links, most of $\gamma_p$ is due to inelastic shear strains in the web as a result of a large shear force. Large end moments develop in moment links, whereby inelastic axial strains develop in both of the flanges and the web which increase the link curvature at the link ends in agreement with ordinary beam theory. For long links no plastic shear deformations develop in the web. For a intermediate link, the inelastic deformation is due to both the shear and moment mechanisms.

Links are excellent energy dissipators under cyclic loading if the ultimate state of the link can be developed and maintained. To develop the link's full strength and deformation capacity, proper web stiffening is required, in addition to lateral bracing at both ends of the link. Furthermore, other frame members must be designed and detailed to be stronger than the links. Inadequate link energy dissipation capacity may result in collapse of an EBF under continued strong seismic forces. The ultimate state of shear links is reached when the ultimate shear force $V_{ult}$ has developed. Based on experimental studies [3,5,6,7,8] it has been determined by previous researchers that $V_{ult}$ for design purposes should be taken to be at least:

$$V_{ult} = 1.5V_p \tag{1.9}$$

The link end moments at the ultimate state are determined by statics considering the shear to be $V_{ult}$. For links adjacent to columns the link end moments are not equal, it has been found [7] that the link end moment at the column face approaches a maximum moment in excess of $M_p$.

Proper web stiffening of the link is accomplished by providing web stiffeners of uniform spacing. Early work by Hjelmstad [3] resulted in empirical equations relating the web stiffener spacing to the energy of the link:

$$\frac{a}{t_w} = 90 - 9 \ln\left[\frac{E_\Sigma^*}{E_e}\right] \tag{1.10}$$

$$\frac{a}{t_w} = 94 - 14 \ln\left[\frac{E^*}{E_e}\right] \tag{1.11}$$

where $a$, $t_w$, respectively, are the stiffener spacing and web thickness. $E_e$, $E^*$, and $E_\Sigma^*$, respectively, are the elastic energy stored by a link at yield, the energy absorbed during the largest prebuckling cycle, and the total energy dissipated prior to buckling.

Later it was proposed by Kasai [7] defining an allowable link deformation of a half cycle, $\gamma_b$, (see Fig. 1.15) as criterion for inhibiting link web buckling. Using the guidance of classical monotonic plastic plate buckling theory, an empirical relationship was developed relating $\gamma_b$ to the link panel zone dimensions and web thickness, reading:

$$\gamma_b = 8.7 \, K_s(\alpha)\left[\frac{1}{\beta}\right]^2 \tag{1.12}$$

where

$$\alpha = \frac{a}{b}$$

$$\beta = \frac{b}{t_w} = \frac{(d - 2t_f)}{t_w}$$

$$K_s(\alpha) = \begin{cases} 8.98 + \dfrac{5.60}{\alpha^2} & \text{for } \alpha \geq 1 \\[2ex] 5.60 + \dfrac{8.98}{\alpha^2} & \text{for } \alpha \leq 1 \,, \end{cases}$$

in which $a$, $b$, and $t_w$, respectively, are the web stiffener spacing, web panel zone height,

and web thickness. The terms $d$ and $t_f$, respectively, are the depth and flange thickness of the steel section.

Malley [5] has proposed design guidelines for sizing of the stiffeners, using criteria based on tension field action and modified elastic buckling solutions to account for the inelastic nature of shear link web buckling. Accordingly, design guidelines were provided requiring appropriate web stiffener strength and rigidity.

## 1.5. Composite Action of Links Under Monotonic and Cyclic Loading

For gravity loads, multistory steel frame buildings often are designed where the concrete floor slabs act compositely with the steel beams. Composite action results in an increased moment capacity of the members. This allows smaller sections to be used for the floor beams. Under gravity loads, a major portion of the beams' span length has the concrete slab acting in compression by the action of the positive moment developed in the floor beams. However, lateral loads applied to the structure due to an earthquake can cause cyclic reversal of moments in the composite beams, leading to cracks in the concrete slab under the action of negative moment. Cracking of the concrete slab has been found to decrease the strength of a composite beam under cyclic loading [22]. It is generally assumed in design that the concrete slab has no tensile strength, the negative moment capacity of a composite beam is thus equal only to that of the steel section and longitudinal slab reinforcement.

Composite action between a concrete slab and steel beam is achieved by using shear connectors to develop horizontal shear forces along the interface of the concrete and flange of the steel section. Internal forces acting at a section of a composite beam are shown in Fig. 1.16. From statics the total moment, $M$, at the section is equal to

$$M = M_{bm} + M_s + F \cdot z \qquad (1.13)$$

where $M_{bm}$ and $M_s$ are the moments in the steel section and concrete slab, respectively. The horizontal force $F$ is developed in the concrete slab and steel section through the

transfer of shear forces along the beam by the shear connectors. When no slip between the slab and beam occurs, $F$ has a maximum value of $F^*$. Under such conditions the strain in the slab, $\varepsilon_s$, and the steel beam, $\varepsilon_{bm}$, at the interface are equal, hence:

$$\varepsilon_s - \varepsilon_{bm} = 0 \qquad (1.14)$$

If applied loads to a composite beam cause connector deformation, slip between the slab and beam occurs, leading to partial composite action where the force $F$ is less than $F^*$. Under these conditions, $\varepsilon_s$ and $\varepsilon_{bm}$ are not equal and the strain profile appears as shown in Fig. 1.16. When the force $F$ is equal to zero, no composite action between the slab and beam develops. Since the curvatures for the two media are the same due to the weight of the slab acting on long spans, the total moment is equal to the sum of the steel section and the slab. That is:

$$M = M_{bm} + M_s \qquad (1.15)$$

This would be the case when no shear connectors are provided, or if the connector capacity has completely deteriorated under cyclic loading.

Since the critical aspect in composite design is the transfer of shear forces between the concrete slab and the steel section, it is essential that the shear connectors be given careful consideration. With the advances in cold formed metal decking systems through the 1950's, there has been an increased use of formed metal decking in the concrete floor slabs of steel framed buildings. Formed metal decking consists of ribs of height $h$, width $w$, with a cell between ribs as shown in Fig. 1.17. During construction the formed metal decking serves as a work platform and in-situ formwork for the concrete slab. As a finished floor, the metal decking serves as reinforcement for the concrete slab to resist floor loads applied between floor beams. To develop the composite action between the floor slab and the steel floor beam, the shear connectors are welded through the deck at the base of the rib, to the top flange of the steel section. Past research [9,13] has shown that the shear connector's rigidity and strength are affected not only by their size but also by the geometry of the deck

and the arrangement of the connectors within the ribs. Important facts related to this research are summarized below:

1. When the rib width to rib height ratio, $w/h$, becomes too small, the shear connector strength is reduced due to cracking and shearing of the concrete rib. A value of $w/h$ greater than 1.75 is recommended.

2. The shear connector length should extend as far as possible above the top of the rib into the solid portion of the slab.

3. Rotation of the rib with respect to the beam flange leads to cracking at the rib corners and precipitates the failure of the concrete by shearing of the ribs. To reduce rotation of the rib, the decking should be secured by welding the shear connectors directly through the decking to the beam. Furthermore, the shear connectors should not be too flexible.

The above have been incorporated into current building specifications for the design and construction of steel buildings in the U.S. [20].

The plastic positive moment capacity of composite beams under monotonic loading has been studied extensively [11,13,14,21,24,25]. Reasonable estimates for the plastic positive moment capacity under monotonic loading, $M_{ult}^+$, can be determined by considering only the compressive strength of the concrete slab above the ribs of the metal decking. Assuming full composite action, two cases need to be considered: Case 1 where the neutral axis is in the slab; and Case 2 where the neutral axis is in the steel section. The formulations for the two cases, respectively, are summarized in Figs. 1.18 and 1.19. Since incomplete shear connector capacity may exist, resulting in partial composite action, a third case needs to be considered assuming that the individual shear connector strength $q_u$ is known. The case of partial composite action is summarized in Fig. 1.20.

Few tests have been conducted on the behavior of composite beams subjected to cyclic loading. Humar conducted tests on composite beams with solid concrete slabs [22]. The results of his studies indicate that if longitudinal negative reinforcement is placed in the

slab and premature web buckling of the steel section is prevented then the steel-concrete composite sections exhibit stable hysteresis loops when subjected to cyclic loading. In these experiments, which were constructed with compact steel sections and longitudinal slab reinforcement, the maximum positive moment developed in the specimens ranged in value from $1.87M_p$ to $2.29M_p$, where $M_p$ is the plastic capacity of the steel section. Maximum negative moments ranged from $1.36M_p$ to $1.54M_p$. It therefore appears that some degree of composite action can be obtained under cyclic loading if longitudinal slab reinforcement is provided and beam web buckling is prevented. Tests on pushout specimens [23] examining the cyclic response of shear connectors indicate that the type of failure leading to the loss of composite action greatly influences the strength and ductility under cyclic loading. It was found that the cyclic shear strength of the connectors is approximately 17 to 29 percent lower, depending on the failure mode, than their monotonic strengths. Based on these findings, it is not likely that composite beams subjected to cyclic loading will develop their full monotonic strength. Therefore, the previous formulations for the positive monotonic moment capacity for composite beams, Figs. 1.18 to 1.20, need to be modified for cyclic loading. To estimate the maximum positive moment that would develop under cyclic loading, a reduced connector strength based on the cyclic shear strength could be used in the positive monotonic moment capacity formulation which considers partial composite action (Fig. 1.20). This procedure assumes that web buckling of the steel section does not occur and that the cyclic shear strength of the connectors is known.

Note that in the previous discussion the positive moment capacity of a composite beam is determined assuming the effective slab width, $b_{eff}$, is known. The effective slab width is an equivalent representation of longitudinal distributed stress distribution by a rectangular one. Research [24,25] had shown that the effective width for monotonic loading is influenced by many factors. The most important ones include: load distribution along the span, cross sectional properties of the composite beam, and boundary conditions. Experimental data has demonstrated that cracking of the concrete slab results in a decrease of the

effective width. Cyclic load test on composite beams in Japan [26] have indicated that the effective width decreases as the inelastic range of testing commences, and continues to decrease as the amplitude of the cyclic loading is increased. Based on the above observations, it appears that the degree of deterioration of the composite action is not only related to the loss of shear connector strength but also to the amount of slab cracking.

The previous formulation for positive moment capacity of composite beams, Figs. 1.18 to 1.20, also ignores the effect of vertical shear. As noted previously for bare steel links, the interaction of moment and shear is significant in that it affects the inelastic behavior of links. Limited published test results are available where the effect of cyclic load on moment-shear interaction of composite beams was studied. Tests involving vertical shear in continuous composite beams subjected to monotonic load [27] indicate that if longitudinal reinforcement is provided in the slab and has not yielded, then this reinforcement will carry a portion of the vertical shear. Once the longitudinal reinforcement yields, the steel section is forced to provide all the vertical shear resistance. This gives an indication that under severe cyclic loading, where the concrete slab cracks and yielding of longitudinal reinforcement takes place, the steel section in a composite beam is likely to provide most of the vertical shear resistance.

## 1.6. Effects of Composite Action on Link Behavior

Although the behavior of composite steel beam floor systems in moment resisting frames and concentrically braced frames has been studied and documented extensively for monotonic loading [9,10,11,12,13,14,16,21,24,25], as noted previously, less research has been performed involving cyclic loading on these types of frames as well as EBFs with composite floors [16,17,22,26]. All previous experimental research on EBFs in the U.S. has dealt with only bare steel frames, ignoring the effect of the concrete slab which serves as a floor system in steel frame buildings [3,4,5,6,7,8,18].

Recently, as part of the US-Japan Cooperative Earthquake Research Program [17],

tests were conducted in Tsukuba, Japan on an K-braced EBF with a composite floor system. The tests involved subjecting a full scale six-story, two by two bay steel structure with eccentric bracing to the Taft earthquake record scaled to 0.5 g maximum ground acceleration, and subsequent tests consisting of three cycles of sinusoidal ground acceleration. Details of the steel framing systems are shown in Figs. 1.21 and 1.22. The floor system consisted of formed metal decking with cast-in-place lightweight concrete which acted compositely with the girders and floor beams. The results of these tests indicated that the composite links performed well and were able to withstand a major earthquake with minor damage. Furthermore, the cracking and damage to the concrete slab was local and mostly in the region directly above the links which had experienced inelastic activity. The subsequent tests performed on the structure were an attempt to impose larger inelastic link deformations in order to study the strength, ductility, and failure mechanism of the EBF. However, failure occurred in a gusset plate which was used for the brace connection. This illustrates the important issue that both the braces and bracing details must be designed to resist the maximum possible forces that could develop in the composite links.

An examination of the test results [17] indicates that most of the inelastic activity occurred in links of the first and second floors. The maximum axial force of the first and second floor braces was 332 kips and 339 kips, respectively, during the response to the scaled Taft earthquake [17], with the maximum link deformation of the first floor equal to approximately 0.06 rad. Required axial brace forces, based on the plastic design of the EBF which ignores the contribution of the composite floors, were computed and found to be 336 kips for the first and second floor braces. It may appear that the design of braces can be based on the properties of only the bare steel frame, ignoring the effects of the composite floor slabs on the cyclic link capacity. However no general conclusions can be made, for the links were indeterminate and there were no direct measured link forces recorded during the Tsukuba tests. Instead, the links' shear forces were estimated from the vertical component of the axial forces in the braces. The link end moments are practically impossi-

ble to determine due to a lack of necessary data. Consequently, a precise description of the hysteretic behavior of the composite links is not available at present. Furthermore, the Tsukuba test program involved only one simulated earthquake and only links in a sole K-braced panel of an EBF. Composite links adjacent to columns in V-braced panels of an EBF were not a part of the tests.

Having reviewed the research on composite beams and the Tsukuba composite EBF, it appears that there is not sufficient experimental data on composite beams under cyclic loading to be able to predict precise cyclic behavior of composite short links. One could speculate, based on the monotonic load test results, that the composite links should initially have a greater positive moment capacity. However it is not clear, whether the composite action in a link will rapidly deteriorate or maintain its capacity under cyclic loading. Also, the effect of composite action on the moment-shear interaction behavior has not been well documented where conventional floor slabs are used, consisting of cold-formed metal decking with minimal longitudinal reinforcement for temperature effects.

In designing EBFs it is important to be able to assess the effects of composite action on the yield strength and ultimate strength of short links under cyclic loading. Using bare steel guidelines for EBFs with composite floor slabs does not preclude a possible failure of the braces, in the beams outside the link, and even columns if the composite links develop sufficient overstrength compared to bare steel links. These are pressing issues, since EBFs are usually constructed with concrete floor slabs. Furthermore, there is a need to assess whether the cyclic web buckling in composite links can be controlled using the criteria of previous studies based on bare steel links [3,7] in order that the ductility and energy dissipation capacity of composite links be maintained. Therefore, there is a need for additional experimental and analytical studies in order to be able to assess whether the design guidelines based on past research of bare steel links can assure their ductile performance in conventional composite floors.

It is also important to be able to estimate the beam capacity adjoining the link in order

to minimize yielding in this segment of the beam. Currently there is a lack of experimental data for estimating the degree of participation of the EBF floor slab in hysteretic response of the beam outside the link. The issue of whether the floor slab alone can restrain the ends of the link against lateral-torsional buckling under cyclic loading also has not been fully addressed in previous studies. It is also of importance to examine the extent of floor damage in an EBF during a simulated major earthquake in order to assess the possible necessary repair as well as the degree of damage to nonstructural components caused by floor uplift above the links.

There is also a need for nonlinear realistic dynamic analyses of EBFs subjected to strong seismic ground motions. While plastic design procedures have been proposed for EBF design [6,7,8], no thorough analyses of such frames under dynamic loading conditions have been made. The conclusions based on the studies of EBFs under pseudo-static loading including composite action based on the present study need to be assessed under dynamic loading conditions. To make such an appraisal of the seismic response of an EBF an accurate nonlinear analysis is required. This requires an accurate link element to model the links. Such an element must account for composite action. Since composite action can also develop in the floor beams outside the link, there is a great need for another element which can model these members. Besides including the effects of cyclic loading of composite beams, this additional element must also account for moment-axial load interaction.

### 1.7. Objectives

A considerable effort has been expended in order to satisfy the needs enumerated above. This was achieved by pursuing the following objectives:

(1) Experimentally investigate the cyclic behavior of short composite links and floor beams with a concrete slab cast on cold-formed metal decking.

(2) Assess whether cyclic web buckling of composite links is adequately controlled using the criteria for bare steel links.

(3) Experimentally investigate the participation and damage of the floor slab in EBFs subjected to cyclic load.

(4) Experimentally investigate the effectiveness of the floor slab in restraining the link from lateral-torsional buckling under cyclic loading.

(5) Develop an analytical procedure for predicting the degree of slab participation in the floor beam response for EBFs.

(6) Develop a practical stress resultant finite element for modeling links under random cyclic loading.

(7) Develop a practical stress resultant finite element for modeling the beams adjoining the link under random cyclic loading.

(8) Assess the analytical dynamic response of a plastically designed EBF to several strong ground motions.

## 1.8. Scope

This report is a summary of an experimental study of links and EBFs under simulated seismic conditions. Finite element formulations for cyclically loaded link and beam models as well as the nonlinear dynamic analysis of plastically designed EBFs are documented in a companion report [128].

After the introduction given in Chapter 1, Chapter 2 of this report describes the experimental program which involved the testing of bare steel links and links with composite floor slabs. The experimental behavior of each test specimen is described in Chapter 3. An analysis of the experimental results that includes an assessment of the effects of the composite floor systems in EBFs is presented in Chapter 4. In Chapter 5 the floor beam-slab interaction in EBFs with composite floor systems is analytically investigated and compared to experimental results.

# CHAPTER 2

# THE EXPERIMENTAL SYSTEM

## 2.1. General

The area of major interest in the experimental study was the links and floor system in the vicinity of the link. The design of the experimental system had the requirement that the test specimens simulate as accurately as possible the physical domain of the links in composite floor systems of EBF. In order to obtain realistic test results, the following two conditions had to be met:

(1)   Materials and members in the test setup had to closely resemble a typical EBF arrangement.

(2)   Boundary conditions and a collapse mechanism in the vicinity of the composite link and the link itself had to develop appropriate displacements and internal forces resembling the response of a prototype EBF floor system during a major earthquake.

In order to satisfy these conditions a subassembly of an EBF was designed, consisting of a concrete-metal deck floor system with steel floor beams. The Tsukuba Test Structure [17] was used as the prototype for a series of tests (Test I) involving links of a K-braced EBF. A second series (Test II) involved testing the links corresponding to a V-braced EBF. These framing schemes are shown in Fig. 1.8. In this manner the tests performed simulated both the interior and the exterior links of EBFs with composite floor systems. The specimens were made to a two-thirds scale of the Tsukuba prototype structure, where one floor slab was used in constructing the composite link specimens for Test I and II.

To directly determine the effects of a composite floor system on link performance, two bare steel links were also tested. A total of eight tests were performed: three composite link tests simulating links in a K-braced EBF; three composite link tests simulating links in a V-braced EBF; and two bare beam tests, where one test was performed involving the link of the

K-braced EBF simulation, and other test involving the link of the V-braced EBF simulation. Of the three composite link tests for each EBF simulation, two were exterior links. The other composite links were on the interior of the floor slab. The test specimens are identified in Table 2.1. The nomenclature given in column 1 will be adopted for identifying the various test specimens and will be referred to throughout this report. In column 6 of the table the cyclic link deformation history is briefly described for each specimen. To meet the objectives of the experimental program the link deformation history of each specimen had to be selected in such a manner that general conclusions could be drawn concerning the response of composite links during major earthquakes.

## 2.2. Experimental Setup

The experimental setup for studying the link behavior was based on the kinematics of the collapse mechanism for a K-braced EBF, Fig. 2.1(a), and a V-braced EBF, Fig. 2.2(a).

The plastic deformation angle $\gamma_p$ in the links of the K-braced EBF mechanism with uniform plastic story drift $\Theta_p$ can be determined from the kinematics of deformation, and is:

$$\gamma_p = \frac{\Theta_p L}{e} \tag{2.1}$$

The subassembly shown in Fig. 2.1(b) can simulate the inelastic behavior of the link by controlling the displacements $\delta$. The displacements $\delta$ include both the elastic and plastic components. Since large deformations can be imposed on a link, approximating the plastic displacement $\delta_p$ of the K-braced EBF by $\delta$ of the subassembly is reasonable. The ensuing link deformation $\gamma$ therefore includes elastic and plastic components of deformation. In this arrangement the effects of axial force in the link are not considered, and $P_A$ and $P_B$ correspond only to the vertical components of the brace forces in an EBF.

The plastic deformation angle $\gamma_p$ in the links of the V-braced EBF shown in Fig. 2.2 (a) is the same as that given by Eq. 2.1. As shown in Fig. 2.2(b), by controlling the angle $\Theta$ of the subassembly the inelastic behavior of links in a V-braced EBF can be simulated. Since

these links will also be subjected to large deformations, approximating the plastic displacement $\delta_p$ by $\delta$ of the subassembly is reasonable. Along the length $L_c$ of the subassembly, the moment of inertia, $Ic$, of the test beam has been increased relative to the moment of inertia of the remaining part of the beam, $I_b$. This has been done to simulate the rotational constraint of the exterior column. In this manner a larger elastic moment is attracted to the end of the link that is usually restrained by the column. Numerous elastic analyses of V-braced EBFs have shown that the end moments in a link are unequal, and the link end moment at the column face is larger than the moment at the other end of a link. Note that in the experimental simulation the axial force effects are not considered. The force $P_B$ represents the vertical component of the brace force, while $P_A$ corresponds to the axial force developed in the exterior column. Research recently completed at Berkeley [7] examined the effect of axial force in bare steel links.

The displacements $\delta$ and the angle $\Theta$ of the subassemblies were developed by controlled displacements at the ends of each link. These displacements of the link were imposed by the two hydraulic jacks generating forces $P_A$ and $P_B$. The moment and shear forces that are caused by the applied forces in the subassemblies are shown in Fig. 2.3. The encircled areas on the diagrams in the vicinity of the links are of primary interest.

The composite deck including links was constructed by casting a concrete slab on formed metal deck which had been placed over three parallel test beams A, B, and C as shown in Fig. 2.4. These beams were spaced seven feet on center. The ribs of the decking were oriented perpendicular to the test beams. Beams A and C at the edge of the slab simulated conditions for exterior EBFs, while beam B in the middle of the slab simulated an interior EBF similar to that in the Tsukuba tests [17]. The experimental set-ups for the two types of tests are shown in Fig. 2.5. By locating the beam supports, the test frame, and hydraulic jacks according to Figs. 2.4 and 2.5, only one test beam containing the link either for the K-braced or V-braced EBF subassembly was required. The extent of slab damage from testing a link, as in the Tsukuba test [17], was expected to be rather local. Therefore all six composite link tests could

be performed using one slab supported by three test beams. Figure 2.6 shows the location of the links for the K-braced and V-braced subassemblies.

For each test beam the support was provided by 2.5 in. diameter shear pins passing through the web of the test beam and secured to shear tabs on the test frame as shown in Fig. 2.7(a). The other end of each test beam was supported by a pinned column which also had a 2.5 in. diameter shear pin at the bottom and a 3 in. diameter shear pin at the top, as shown in Fig. 2.7(b). Each pinned column was attached to a test beam by placing the 3 in. diameter pin through attachment plates which had been welded to the bottom flange of the test beam. The pins prevented the development of end moment in the test beams and thereby complied with the required boundary conditions shown in Figs. 2.1(b) and 2.2(b). With 3 in. diameter pins at both ends, each hydraulic jack was connected to the hydraulic jack support and an attachment plate welded to a test beam at the end of the link, as shown in Fig. 2.7(c). The test frame, pin-column supports, and hydraulic jack support were attached to the laboratory tie-down floor slab by post tensioning rods as shown in Figs. 2.7(b) and 2.7(c).

## 2.3. Design of Test Specimens

**Selection of Link Beam** - At the time that the specimens were designed the new design guidelines [7] had not yet evolved. Consequently, the design of the links was based on the earlier criteria [3,5,18], and the Tsukuba design. The links in the bottom floor beams of the Tsukuba test structure were of particular interest since it was already known that most of the inelastic activity was concentrated there. The first floor beam section size of the Tsukuba structure was a W18 x 40 with a link length of 28 in. This link length is less than $b^*$ and satisfies the current criteria [7], and therefore the prototype link can be considered to be a shear link. Since a two-thirds scale factor was adopted in these test, in order to simulate the prototype behavior, the test specimens must have elastic and plastic section properties for shear and moment scaled in correct proportion. Therefore the link length, and the elastic and plastic section properties of the specimens were scaled as follows:

Link Length, $\quad \dfrac{e_{model}}{e_{prototype}} = \dfrac{2}{3}$ (2.2)

Shear, $\qquad \dfrac{V_{model}}{V_{prototype}} = \left(\dfrac{2}{3}\right)^2$ (2.3)

Moment, $\qquad \dfrac{M_{model}}{M_{prototype}} = \left(\dfrac{2}{3}\right)^3$ (2.4)

A W12 x 19 section with a link length of 19 in. was found to have the best overall correlation to two-thirds scale of the W18 x 40 prototype link. The link length of 19 in. satisfies the criterion for a shear link based on $b^*$ as well as on Eq. 1.8. A comparison between the prototype link beam and a W12 x 19 is given in Table 2.2. In this table, $A_w$ and $S$, respectively, are the area of the web and the elastic section modulus. All other section properties were defined previously in Chapter 1. The composite plastic moment capacity $M_{ult}^+$ is based on the effective slab width $b_{eff}$ for an interior composite beam defined by AISC [20]. The choice of the slab thickness for the model will be discussed later.

**Test Beam Details** - The details of the test beam and links are shown in Fig. 2.8. As noted earlier, the reinforced beam was used to simulate the column restraint of the link in a V-braced EBF. This was constructed by welding WT6 x 9.5 sections to the top and bottom flanges of the W12 x 19. The moment of inertia $I_c$ of the simulated column restraint member was 5.9 times greater than the W12 x 19 test beam. This enabled an elastic moment $M_A$ to develop at the link end adjoining the column restraint which was three times greater than the moment $M_B$ developed at the other end of the link. In an EBF, the elastic distribution of moments in a link adjacent to a column has typical values of $M_A/M_B$ ranging from 2.5 to 6.

The length of the link was selected as being equal to $b^*$ for a W12 x 19. The spacing of the web stiffeners in the link was based on the criteria developed by Hjelmstad [3], such that the ratio of stiffener spacing $a$ to web thickness $t_w$, $a/t_w$, was 25.0 for all specimens, except Specimen A2 where $a/t_w$ was 12.5 . All web stiffeners in the link were 0.25 in. thick, satisfying the strength criterion given in [5]. However, the criterion for stiffener rigidity was

relaxed. In the link the stiffeners were placed on only one side of the web and were welded to the web and the top and bottom flanges of the beam.

As shown in Fig. 1.21, in the Tsukuba test structure large gusset plates were used outside the link for attaching the braces to the floor beams. Consequently, the moment capacity of the floor beam was increased in the regions of the gusset plates, and yielding of the flanges in these areas was inhibited. To prevent flange yielding from developing outside the link in the test beam adjacent to the hydraulic jack attachments, cover plates were welded to the top and bottom flanges of the beam at these locations. The length of the cover plates was based on preventing yielding in the flanges outside the link from occurring at a shear force of $1.5V_p$ in the link. The moments for causing flange yielding of the composite section were determined using the AISC effective slab width [20]. Doubler plates were placed on the beam web above the jack attachment plates to prevent web distortion and yielding due to the concentrated jack forces.

**Floor Slab Details** - The floor slab thickness, metal decking, slab reinforcement, and shear connector size were selected such as to simulate as accurately as possible a two-thirds scale model of the prototype, as well as to conform to the AISC Specification [20]. The thickness of the floor slab was selected to be 4.5 in. A standard 20 gage cold formed metal deck with a two inch rib height was used. Details of the decking are shown in Fig. 2.9. The floor slab was constructed using a lightweight concrete which had a 28 day design strength of 4000 psi. Welded mesh reinforcing consisting of $0.045in.^2$ of cold drawn wire spaced at 6 in. on centers both ways was employed. This provided for a 0.3 percent transverse and longitudinal reinforcement per linear foot of concrete. This mesh provided the required minimum temperature reinforcement. The selected concrete slab-metal decking system [28] for the model correctly simulated the prototype Tsukuba floor system. The rib geometry of the model deck permitted the development of the full capacity of two shear connectors since they could be placed in the same rib [20], just as it was done in the prototype. The shear connectors used were 3.5 in. long and were 0.5 in. in diameter. Except along a segment of beam B, these

shear connectors were welded through the metal decking to the top flange of all test beams. Fig. 2.10 shows the metal decking, shear connectors, and reinforcement in place before casting of the concrete slab.

A plan of the shear connector layout for the test beams is shown in Fig. 2.11. The metal decking over a major part of the span for beam B was placed to form a gap over the floor beam, as shown in Fig. 2.12. Sheet metal was fitted between the ribs of the gap, thereby enclosing the gap. This made it possible to place concrete in the gap above the floor beam. This also permitted placement of additional shear connectors in the vicinity of the link simulating the interior K-braced EBF subassembly (Specimen B1). This detail was a two-thirds replica of the slab and decking detail used above the links in the Tsukuba test. All of the remaining links in the model had the conventional U.S. decking detail where the metal deck is placed continuously over the top flange of steel beams. An elevation of the deck rib layout with respect to the links is shown in Fig. 2.13. A vertical plate was welded to the top WT6 x 9.5 section of each test beam at the end of the link, as shown in Fig. 2.8, in order to simulate the effect of a column flange which the concrete slab would butt up against during the testing of the V-braced EBF subassemblies.

**Lateral Bracing** - In all tests, except for Specimen C2 and Specimen D2, both ends of the links were laterally braced from one side by W10 x 15 transverse beams as shown in Fig. 2.14. Shear connections consisting of three bolts placed through the web of transverse beams and attached to the stiffeners of the floor beams were used. Specimen D2, simulating a bare steel link in a V-braced EBF, had a transverse beam only at the end of the link attached to the simulated column. This transverse beam represented an edge framing member. An exterior composite link in Specimen C2 was not braced by transverse beams. Instead, W12 x 19 transverse stub beams six inches long were placed on each side of the link web, and shear connectors were used to anchor the top flange of the stub beams to the concrete slab as shown in Fig. 2.15. Only the end of the link in a subassembly that would normally be attached to the diagonal bracing in a V-braced EBF had this detail. The other end of the link in the

subassembly adjacent to the simulated column restraint was braced by only the floor slab. The same stub beam detail was used in the Tsukuba test structure to laterally brace the composite floor beams at locations away from the links. The purpose of using the stub beam at the end of the link of Specimen C2 was to examine its effectiveness to lateral brace the link where large moments and inelastic activity develop. All bare steel specimens as well as simulated columns had lateral bracing at intermediate points outside the link as well as at the ends of the test beams.

## 2.4. Material and Section Properties

All test beams were fabricated from the same heat of ASTM A36 steel. The material properties of the steel were determined from uniaxial tension tests using ASTM procedures [30] and are presented in Table 2.3, where E = Young's modulus, $\epsilon_{sh}$ = strain at onset of strain hardening, $\epsilon_u$ = strain corresponding to ultimate stress, $\Delta_{\%}$ = percent of elongation at fracture, $\sigma_y$ = yield stress, $\sigma_u$ = ultimate stress. The lightweight concrete batch design consisted of a water-cement ratio of 0.54 and a 6.5 in. slump. As noted previously, the design strength at 28 days was 4000 psi. The maximum aggregate size was 0.5 in. The concrete was placed, then moist cured for seven days under wet burlap covered by a plastic sheet. The compressive strength, splitting tensile strength, and flexural strength were determined for the concrete using ASTM procedures [31,32,33]. These strengths were obtained over the period of time covering the composite link test program. The results of these strength tests are summarized in Figs. 2.16, 2.17, and 2.18 indicating the increase in strength with time. Young's modulus was determined from six by twelve inch cylinders 28 days after casting the concrete slab. Test cylinders were cured in fog room as well as in the test specimen conditions. The results are summarized in Table 2.4. The measured cross-sectional areas of the slab reinforcement and their mechanical properties are given in Table 2.5. The cold drawn wires of the mesh reinforcement did not have a well defined yield stress and exhibited low toughness.

Calculated plastic capacities for the test beams are given in Table 2.6. These quantities

are based on the actual material strengths and using the average of the measured cross-sectional dimensions of the test specimens (see Table 2.7). The first row of Table 2.6 is based on different yield strengths for the flange and web of the test beams. In the second row, the average value of the above stresses were used. Since $M_p$, $V_p$, $M_p^*$, $M_u^{int}$, and $M_u^{ext}$ have a direct relationship to the web and flange stresses developed in the steel section, it is more accurate to use values given in the first row. Therefore, unless otherwise noted, all future references to the plastic capacities refer to the values given in the first row of Table 2.6. The positive bending moment capacity $M_u^{int}$ for the interior composite test beams, and the exterior composite test beams, $M_u^{ext}$, assume full composite action between the concrete floor slab and steel section. An appropriate method given in Figs. 1.18 or 1.19 was used to calculate $M_u^{int}$ and $M_u^{ext}$. Per AISC [20] an effective slab width of one quarter of the beam span was used for interior beams. As recommended by the AISC [20], for the exterior beams the effective slab width was taken to be one twelfth of the span length plus the exterior slab overhang and the beam flange width. The contribution of the slab temperature reinforcement was ignored. A concrete compressive strength of 4200 psi was used, which was the average concrete strength during the period of the composite link tests.

### 2.5. Floor Slab Properties

The moment-curvature relationship, $M-\phi$, of the slab was determined by testing 2 by 4 ft. size slab specimens under monotonic loading. A total of four tests were performed, enabling the $M-\phi$ relationship to be established for positive and negative moments having parallel as well as perpendicular ribs to the direction of bending as shown in Fig. 2.19. The curvature was determined by measuring the strain on both sides of the slab specimens using clip gages. For Slabs 3 and 4 this curvature represented an average curvature between ribs.

The $M-\phi$ relationships are shown in Fig. 2.20, and the effective elastic stiffnesses $EI$, the cracking moments $M_{cr}$, and the ultimate moment capacities $M_u$ are summarized in Table 2.8. From Fig. 2.20 it is evident that the elastic stiffness of Slabs 1 and 2 is significantly

greater then that of Slabs 3 and 4. This signifies that the slab exhibits orthotropic behavior. The average of the elastic stiffnesses for Slabs 1 and 2, $EI_y$, compared to the average for Slabs 3 and 4, $EI_x$, is 3.25.

$M_{cr}$ and $M_u$ is also greater when the ribs are effectively engaged in resisting moment as in Slabs 1 and 2. A slab, when called upon to resist the total applied moment where the ribs are not effectively engaged in resisting moment, as in Slabs 3 and 4, has a tendency to crack between ribs.

## 2.6. Instrumentation

The methods of measuring specimen displacements are shown in Figs. 2.21 and 2.22. The instrumentation support frame may be seen in Figs. 2.7 and 2.13. The link displacements were monitored by arranging two linear potentiometers at each end of the link for obtaining the vertical movement and twisting of the beam cross-section (Fig. 2.21). Pairs of LVDTs (linear variable differential transformers) were used to measure the rotation and longitudinal movement of the steel section at each end of the link.

Strain gages were placed on the test beam flanges to measure strains in and outside the link to monitor yielding. The location of the strain gages is shown in Fig. 2.23. The links were whitewashed to aid in observing the yield pattern and progress of yielding. Slip gages were used in the composite link tests to measure the relative slip between the floor beam and concrete slab, as well as the relative slip between the concrete slab and metal decking. The strain gages were placed as shown in Fig. 2.24 at locations at the link and at selected locations outside the link. A typical slip gage consisted of an LVDT measuring the movement of a tab attached to the underside of the concrete floor slab as shown in Fig. 2.22. An LVDT was either attached to the floor beam to measure slip between the steel section and the concrete slab, or on the metal decking to measure slip between the metal decking and the concrete slab.

The longitudinal strains were measured on the concrete slab top surface and on the slab underside using arrays of 12-in. clip and strain gages. The location of the arrays of clip gages

pertaining to the reported results are shown in Figs. 2.25 and 2.26. The clip gages are shown in place on the top surface and underside of the slab in Fig. 2.27. The clip gages on the underside of the floor slab were mounted onto brass inserts which had been cast into the ribs of the concrete slab. The clip gages on the top surface of the floor slab were mounted onto small metal pads which had been epoxied to the concrete surface. Arrays of 12-in. clip gages were used both in the vicinity of the link and along the test beam. The strain gages were used on the top and bottom surfaces of the slab only at locations away from the vicinity of the link where excessive cracking of the slab surface was not to be anticipated.

The vertical displacement of the slab top surface in the vicinity of the link was monitored in Specimen A1 using an array of linear potentiometers placed above the slab's top surface, see Fig. 2.28. The location of the linear potentiometers to measure the vertical slab movement is shown in Fig. 2.29.

The forces in the hydraulic jacks were measured using calibrated load cells. The shear connection tabs on the test frame and the floor supports for the pin-ended columns were instrumented and calibrated in order to monitor the support reactions of all the beams supporting the slab. With these forces and reactions known, moment and shear forces in the test beam could be determined from static equilibrium.

## 2.7. Test Procedure

All instrumentation was connected to a multi-channel scanner system, which at a command would read all the instruments and record the information onto a Data General Nova computer system for future data reduction. The displacements at the ends of a link were used to control the link deformation $\gamma$. All tests were performed using displacement control for predetermined displacement histories for each end of a link. The hydraulic jacks were manually operated to impose the required displacement history. As indicated in Fig. 2.5, the forces applied by the hydraulic jacks are labeled as Jack $P_A$ and $P_B$.

The link end displacement histories $\Delta_A$ and $\Delta_B$ corresponding to applied forces $P_A$ and

$P_B$, respectively, for the eight tests are shown in Figs. 2.30 to 2.37. With the exception of Specimens A1 and C1, the imposed displacement histories for the link deformation were symmetric. Generally the amplitude of the cycles was progressively increased and the test was terminated when either web tearing occurred or link deformation reached a value of 0.1 rad. The end displacements for Specimens A1 and C1 were more random. Specimen A1 was subjected to large unsymmetric pulses at the beginning of the test, whereas Specimen C1 was subjected to link deformations that simulated the Taft Earthquake with a peak ground acceleration of 0.5g, with both specimens being subjected to several subsequent symmetric cycles.

For Specimen C1 the imposed link deformations were based on the estimates of $\Theta_p$ (Fig. 2.1 (a)) corresponding to the first story lateral displacement history of the Tsukuba test structure [17]. These displacements were recorded while subjecting the test structure to the Taft Earthquake with a peak ground acceleration of 0.5 g. Thus with $\Theta_p$ established, the value of $\gamma_p$ followed from Eq. 2.1. The calculated record of $\gamma_p$ is given later (see Fig. 3.26 (b)). The maximum value of $\gamma_p$ was found to be 0.06 rad. during the Taft Earthquake simulation. As noted previously, since the link deformations are large, the plastic link deformation $\gamma_p$ can be approximated by the total link deformation $\gamma$. Additional cycles with amplitudes of $\gamma_p$ equal to 0.06, 0.08, and 0.10 rad. were imposed after the conclusion of the Taft Earthquake simulation.

# CHAPTER 3

# EXPERIMENTAL BEHAVIOR

## 3.1. General

In this chapter the behavior of the links and floor system are discussed. Each of the eight tests is presented individually. The bare steel specimens are presented first followed by the composite specimens. A summary and a list of conclusions based on observations of the experimental behavior are given at the end of the chapter.

To facilitate the presentation, the nomenclature and sign convention shown in Fig. 3.1 will be adopted. Reference will be made to the shear force, $V$, end moments $M_A$ and $M_B$, and angular deformation $\gamma$ between the ends of a link. End A is located at the north end of the link while end B is located at the south end. For the links of the V-braced EBF subassembly the end A of the link is adjacent to the simulated column restraint. A positive value of a link deformation occurs when the end A displaces downwards relative to the end B.

The location of the composite links and slab edges were previously identified in Fig. 2.6.

## 3.2. Bare Steel Specimen Behavior

**Test Specimen D1** - Specimen D1 simulated a link in a bare steel K-braced EBF. The cyclic displacement program in Section 2.7 was used to impose symmetric cycles of link deformations. Figs. 3.2 and 3.3 illustrate the $V$-$\gamma$ and $M$-$\gamma$ relationships for the link.

Yielding of Specimen D1 occurred in the web of all panels of the link during the initial part of Cycle 1 as evidenced by fine cracks in the white wash. At link yielding the stiffness of the link decreased dramatically as shown in the $V$-$\gamma$ and $M$-$\gamma$ relationships. The link shear force at yielding was 85.3 kips, which is eight percent below the theoretical value of $V_p$ listed in Table 2.6. As the link deformation increased to 0.02 rad., strain hardening developed resulting in an increase in the shear force after yielding. Minor flange yielding also occurred

at both ends of the link. It was anticipated that the link end moments $M_A$ and $M_B$ would be equal since the test beam was to be displaced in an antisymmetric configuration with respect to the center of the link, see Fig. 2.3(a). However these end moments were found not to be equal with $M_A$ being $1.35M_B$. It was determined that small differences in the jack forces are amplified into a large difference in link end moments. This is due to the fact that the distance between jacks is relatively small compared to the total span length of the test beam. The same should be true in EBF.

As can be seen from the hysteretic diagrams, a reversal of link deformation dissipates a large amount of energy. Strain hardening during the later half of Cycle 1 resulted in a link shear force that was three percent greater than the maximum link shear force developed in the first half of Cycle 1 at a $\gamma = 0.02$ rad. Due to the significant amount of strain hardening in subsequent cycles, as a result of cyclic deformation coupled with increased amplitudes of $\gamma$, the link shear force continued to increase till web buckling. Furthermore, with increasing $\gamma$ the web yielding in the link continued and developed uniformly in the link as shown in Fig. 3.4(a).

At a $\gamma$ of -0.06 rad. during Cycle 4 minor distortions occurred in the compression flanges at both ends of the link as shown in Fig. 3.4(b). The flange distortion at the end A of the link, on the right in Fig. 3.4(b), was more pronounced. The moment $M_A$ was equal to $1.09M_p$. The flange distortion however did not inhibit the link from developing larger forces as can be seen from the $V$-$\gamma$ and $M$-$\gamma$ hysteretic loops. The link deformed shape resembled a parallelo-gram.

When the link was subjected to a $\gamma$ of 0.08 rad. in Cycle 6 slight web buckling was observed in the link center panel. The link shear force was 117.5 kips, representing a 38 percent increase over the shear force at initial web yielding. During this cycle $M_A$ reached a moment of $1.11M_p$ and $M_B$ a moment of $0.79M_p$. A reversal of the imposed link deformation caused a more pronounced web buckling, where the link exhibited the cyclically symmetric buckling mode depicted in Fig. 3.5. This phenomenon continued in subsequent cycles. At a $\gamma$

of 0.08 rad. in Cycle 7 both the web stiffeners and the flanges of the link center panel began to yield and deform. A photograph of the link at this instant is shown in Fig. 3.4(c). The maximum shear force and end moments of the link during Cycle 7 were less than the corresponding forces in Cycle 6.

Subsequent cycles of link deformation resulted in deterioration in the link capacity. However, the hysteretic behavior of the link remained stable and continued to dissipate energy. As the direction of $\gamma$ was reversed, tension field action in the link resulted in recovery of link capacity. During Cycle 8, the link web stiffeners and flanges of the middle panel deformed considerably and developed a flexure type deformation mode. Figure 3.5(d) shows this phenomenon during Cycle 8 at a $\gamma$ of -0.10 rad.

Near a $\gamma$ of -0.02 rad. in Cycle 9 web tearing occurred in the link center panel. This tearing originated at a web stiffener weld. Then as $\gamma$ was increased to -0.10 rad. the link's capacity deteriorated rapidly, and the test was terminated. An examination of the test beam indicated that no yielding had occurred outside the link.

**Test Specimen D2** - Specimen D2 involved the testing of link in a V-braced EBF. Lateral bracing of the link was provided only at the link end A adjacent to the simulated column restraint. Symmetric cycles of link deformation were imposed by the displacement program given in Section 2.7. Figs. 3.6 and 3.7 illustrate the $V$-$\gamma$ and $M$-$\gamma$ hysteretic loops for this link.

During Cycle 1 the link developed web yielding in all panels, as shown in Fig. 3.8(a). The corresponding link shear force was 81.4 kips, which was equal to $0.87V_p$. The link end moment $M_A$ was equal to $3.5M_B$, indicating that larger elastic link end moments developed at the simulated column. As the link deformation was increased, strain hardening resulted in the increase of the link's forces. At the peak link deformation of Cycle 1, where $\gamma$ was equal to 0.02 rad., minor flange yielding developed at end A of the link . Due to strain hardening during the subsequent cycles the link progressively developed greater shear and end moments. The inelastically deformed shape of the link resembled a parallelogram.

During Cycles 3 and 4, which had $\gamma$ amplitudes of 0.04 and 0.06 rad., respectively, the moment $M_A$ remained constant after reaching a moment of $1.1M_p$, while $M_B$ continued to increase till a moment of $0.70M_p$ was reached at the end of each half cycle. At the peak $\gamma$ of Cycles 3 and 4, $M_A$ was equal to $1.7M_B$. At the peak $\gamma$ of 0.06 rad. in both half cycles of Cycle 5, $M_A$ remained equal to $1.7M_B$. However, $M_A$ had increased to a moment of $1.16M_p$. At the same time full flange yielding developed at end A of the link accompanied with minor distortion of the compression flange as shown in Fig. 3.8(b).

The maximum link forces for Specimen D2 developed during Cycle 6 at a $\gamma$ of 0.08 rad. At that instant $V$ was equal to 117.7 kips and moments $M_A$ and $M_B$ were equal to $0.71M_p$ and $1.16M_p$, respectively. Since initial web yielding the link shear had increased by 44 percent due to strain hardening, and the moments $M_A$ and $M_B$ had increased by 94 percent and 24 percent, respectively. On reversing the link deformation during Cycle 6 web buckling occurred near a $\gamma$ of -0.08 rad.

In the subsequent cycles of link deformation the link web buckling modes developed as shown in Fig. 3.5. In Cycle 7 at a $\gamma$ of -0.08 rad. the web stiffeners of the center panel of the link as well as the compression flanges near the ends of the link began to show signs of distortion and yielding, as illustrated in Fig. 3.8(c). The maximum link forces developed during this cycle were less than those for Cycle 6, indicating that the link capacity was deteriorating. However, the $V$-$\gamma$ and $M$-$\gamma$ hysteresis loops indicate that the hysteretic behavior remained stable and the link continued to dissipate energy. The link end moments did not equalize as evident from the $M$-$\gamma$ response.

While imposing a $\gamma$ of 0.10 rad. during Cycle 8, the link's flanges at the center panel buckled, developing a deformed shape shown in Fig. 3.8(d). The $V$-$\gamma$ hysteretic loops show signs of tension field action occurring in the link during Cycles 8 and 9. In the first half of Cycle 9 web tearing developed in the link center panel along the weld of a web stiffener. As a result, the link capacity deteriorated rapidly and the test was then terminated. No signs of yielding were visible in the test beam outside the link.

### 3.3. Composite Specimen Behavior

**Test Specimen A1** - A link in an exterior K-braced EBF with composite floors was simulated by Specimen A1. The displacement history shown in Section 2.7 was used, imposing initially a series of unsymmetric pulses of link deformations in order to develop an early web buckling in the link. The subsequent cycles of link deformation were cyclically symmetric and began with small amplitudes of $\gamma=0.2$ rad., and were progressively increased to $\gamma=0.10$ rad. in increments of 0.02 rad. Although the sequence of these cycles was not the same as the deformation history of Specimen D1, they were similar. Each cycle of deformation began by displacing the end A downwards relative to the end B of the link. The $V$-$\gamma$ and $M$-$\gamma$ hysteretic loops for the link are shown in Figs. 3.9 and 3.10.

Yielding in all link web panels occurred during the first half of Cycle 1. The maximum link shear force during this cycle was 88.1 kips representing only a four percent increase compared to the corresponding bare steel link, Specimen D1. In this cycle $M_B$ had reached a moment of $0.82M_p$ while $M_A$ a moment of $0.60M_p$. Therefore, $M_B$ was equal to $1.36M_A$ when web yielding occurred, being nearly identical to the ratio of link end moments at initial web yielding of Specimen D1. With increased link deformation in Cycle 1, cracking of the concrete rib above the link occurred at end A, and along the link the deck separated from the concrete slab. Above the end B of the link cracks appeared on the slab surface in the transverse direction with respect to the longitudinal axis of the test beam. When a $\gamma$ of 0.08 rad. had been imposed on the link the maximum deformation for the first half of Cycle 1 was reached. The link end moment $M_B$ was equal to $M_p$, while $M_A$ was $0.70M_p$. Consequently $M_B$ was equal to $1.43M_A$. A photograph of the link during Cycle 1 at a $\gamma$ of 0.08 rad. is shown in Fig. 3.11(a) where uniform yielding of all web panels can be seen. The deformed link had a shape of a parallelogram.

In the next half of Cycle 1 a $\gamma$ of -0.06 rad. was imposed on the link. When this deformation was reached moments $M_A$ and $M_B$ were both equal to $M_p$. Minor flange yielding was noticed at both ends of the link. However the rib above the end B of the link had cracked,

and the earlier deck separation as well as the transverse slab surface cracks above the link had intensified.

The first half of Cycle 2 subjected the link to a $\gamma$ of 0.10 rad. The rib cracking at end A caused end B of the link to become stiffer than end A, and thereby develop greater moment. The link end moment $M_B$ was equal to $1.29M_p$, which was 2.4 times greater than $M_A$. Consequently, additional flange yielding developed at end B of the link. This value of $M_B$ was the largest link end moment developed during the test. Furthermore, the link shear force and slab damage became greater than that during the previous cycle. Although the floor cracking became more pronounced, the damage to the floor remained localized in the vicinity of the link. The last half of Cycle 2 subjected the link to a $\gamma$ of -0.08 rad. This caused web buckling to occur in the center panel of the link at a deformation of approximately -0.06 rad. As $\gamma$ reached -0.08 rad., a minor deformation of the link web stiffeners was observed together with some buckling of the compression flanges at both ends of the link as shown in Fig. 3.11(b). Moments $M_A$ and $M_B$ both were equal to $1.07M_p$ and the link shear was 127.2 kips. This link shear force was the maximum achieved during the test and represents a 44 percent increase over that at initial web yielding. This shear is eight percent greater than the maximum value for Specimen D1.

As noted previously, all subsequent cycles following Cycle 2 were cyclically symmetric. In Cycles 3 and 4, which had maximum amplitudes of $\gamma$ of 0.02 and 0.04 rad., respectively, the previously buckled web and the compression flanges of the link became partially straightened out by the action of the link. During this process strain hardening of the link continued. However since the plastic deformations were smaller than those that had occurred in Cycles 1 and 2, the link forces remained smaller. No further slab damage was observed, but the earlier one had a pronounced effect on the ratio of moments $M_A$ and $M_B$. At the peak link deformation of Cycles 3 and 4 end B developed a negative moment $M_B$ that was 2.5 times that of $M_A$. For a positive moment, $M_B$ eventually reached $0.85M_A$ at the peak of link deformations during Cycles 3 and 4. Evidently, the stiffnesses at the link ends were influenced by

rib cracking and composite action.

At a $\gamma$ of -0.06 rad. in Cycle 5 the web buckling of the link center panel and compression flanges at the ends of the link intensified to the level of first web buckling, see Fig. 3.11(c). Also, yielding developed in the link web stiffeners. The slab damage in the vicinity of the link became more intense. For this displacement the moments $M_A$ and $M_B$ were equal.

On increasing $\gamma$ to $\pm 0.08$ rad. in Cycle 6 the link's previously buckled web and compression flange became more pronounced as shown in Fig. 3.11(d). The cyclic web buckling modes illustrated in Fig. 3.5 continued to develop during these cycles. The flanges of the link's middle panel showed signs of distress as the link began to assume a localized deformation mode. Furthermore, deterioration of the link capacity was detected, for the maximum shear force developed during Cycle 6 was less than that of the previous cycle. Damage to the slab and rib above end A of the link had increased, resulting in end B becoming stiffer than end A. As a result, $M_B$ developed a moment equal to $1.5M_A$ at $\gamma=\pm 0.08$ rad.

During Cycle 7 tension field action in the link is evident from the $V$-$\gamma$ hysteretic loops. In this cycle the link capacity continued to deteriorate. However the hysteretic behavior remained stable and the link continued to dissipate energy. After reaching a $\gamma$ of 0.10 rad. in Cycle 7 the link deformation was reversed until a $\gamma$ of -0.04 rad., and the test was then terminated.

The major damage suffered by the floor system during the test remained in the vicinity of the link and only minor cracking developed in the floor slab away from the area of the link. Figure 3.12 shows rib cracking, deck separation, and transverse slab surface cracks after the completion of the test. An examination of the test beam indicated that yielding had not occurred outside the link during the test.

**Test Specimen A2** - Specimen A2 simulated a link in an exterior V-braced EBF with composite floor slabs. The spacing of the link web stiffeners was one-half of that in the other specimens. The displacement history imposed symmetric cycles of link deformation as given in Section 2.7. The $V$-$\gamma$ and $M$-$\gamma$ hysteretic loops for the link are shown in Figs. 3.13 and

3.14. Each cycle began by displacing end A downwards relative to end B of the link. As in previous tests, end A was located adjacent to the simulated column restraint.

During Cycle 1 yielding developed in all the link web panels, as shown Fig. 3.15(a). The initial shear yield force for the link was 87.0 kips, representing a seven percent increase compared to that of the corresponding bare steel link, Specimen D2. Moment $M_A$ was $0.90M_p$ while $M_B$ was $0.49M_p$. Hence at web yielding $M_A$ was equal to $1.84M_B$. Additional link deformations caused strain hardening of the link. At a $\gamma$ of 0.02 rad. a transverse crack appeared in the slab above end B of the link. Reversal of $\gamma$ to complete Cycle 1 resulted in minor cracking of the rib above the end B as the link deformation approached -0.02 rad. Moment $M_A$ had become equal to $1.1M_B$, indicating that the slab had increased the link and the floor beam stiffnesses outside the link at end B. This occurred as a positive moment developed along this portion of the test beam.

During Cycles 2 and 3, where the amplitudes of both cycles were equal to a $\gamma$ of 0.04 rad. the floor slab above the link suffered further damage. Separation between the deck and the concrete slab had occurred as a longitudinal crack developed in the slab above the link. The cracks in the rib above end B of the link became more extensive as end B was displaced downwards during the second half of Cycle 2. At a $\gamma$ of 0.04 rad. in Cycle 3 a crack protruded outwards from end A of the link along the north edge of the slab. It was discovered that the shear connectors at end A of the link had pulled out of the concrete slab as end A was displaced downwards relative to end B, see Fig. 3.17(b). Simultaneously, flange yielding developed at the end A of the link. As shown in Fig. 3.16(a), the crack in the rib opened as end B was displaced downwards relative to end A. As a result, slightly less positive moment developed at end B in the second half of Cycle 3 compared to the maximum values of moment $M_B$ developed in Cycles 1 and 2, as shown in the $M$-$V$ hysteresis loops of Fig. 3.14(b). Furthermore, at end B the negative moments were larger in magnitude compared to the positive moments. Because the moment $M_A$ did not deteriorate but rather kept increasing in each subsequent half cycle, the link shear force also continued to increase.

The slab damage became more intense during Cycles 4 through 6 but remained in the vicinity above the link. The distribution of link end moments $M_A$ and $M_B$ during the peak deformation of these cycles continued to resemble that of Cycle 3 as shown in the $M$-$\gamma$ hysteresis loops. At a $\gamma$ of 0.08 rad. in Cycle 7 the link web stiffeners developed yielding as minor compression flange buckling occurred at both ends of the link, as shown in Fig. 3.15(c). The corresponding moments $M_A$ and $M_B$ were equal to $1.11M_p$ and $0.96M_p$, respectively.

The compression flange buckling did not prevent the link end moments from becoming larger with increasing number of cycles. Consequently, a larger shear force developed in the link with each new cycle. After completing Cycle 8, which imposed a $\gamma$ of $\pm0.10$ rad., the test was terminated. Web buckling did not occur in the link because of the closely spaced web stiffeners. Throughout the test the link deformed into the shape of a parallelogram as shown in Fig. 3.15. The maximum shear force developed in the link during the test was 133.2 kips, representing a 53 percent increase from the initial web yielding. The maximum link end moment occurred at the simulated column restraint where $M_A$ reached $1.35M_p$, the corresponding moment for $M_B$ was $0.77M_p$. The maximum moment developed during the test at end B was $0.98M_p$. The $M$-$\gamma$ hysteretic loops indicate, as does the above observations, that the link end moments did not equalize during the test. The test beam was found not to develop yielding outside the link. The damage condition to the slab at the conclusion of the test is shown in Figs. 3.16 and 3.17, indicating that the damage to the floor slab was confined to the vicinity of the link and is remarkably mild considering the amount of deformation imposed on the link.

**Test Specimen B1** - Specimen B1 involved the simulation of a link in an interior K-braced EBF with a composite floor slab. As in the Tsukuba prototype, the metal decking provided a gap along the top flange of the test beam creating space for additional shear connectors. The displacement history as given in Section 2.7 was used to impose symmetric cycles of link deformation. Each cycle began by displacing end A downwards relative to end B of the link. Illustrated in Figs. 3.18 and 3.19 are the $V$-$\gamma$ and $M$-$\gamma$ hysteretic loops for the link.

During the first half of Cycle 1 at a link shear force of 100.1 kips all web panels of the

link developed yielding, see Fig. 3.20 (a). This shear force represented a 17 percent increase over that for the bare steel link, Specimen D1. The link end moments $M_A$ and $M_B$ were equal to $0.97M_p$ and $0.63M_p$, respectively. Therefore at initial web yielding $M_A$ was equal to $1.54M_B$. Continuing the link deformation to 0.02 rad. caused strain hardening in addition to a longitudinal surface crack in the floor slab above the link. Strain hardening during the reversal of $\gamma$ to complete Cycle 1 resulted in a further increase in the link shear force. At a $\gamma$ of -0.02 rad. of Cycle 1 the moment $M_A$ was equal to $1.18M_B$.

During Cycles 2 through 4 the metal deck separated from the concrete along the link. The longitudinal surface crack became more extensive, and a large transverse crack developed in the floor slab above end B of the link which indicated that the rib had cracked. The link shear force continued to increase in each successive half cycle, and as in previous tests the deformed link shape resembled a parallelogram. The positive moment developed at end A during Cycles 3 and 4 was less than the maximum positive moment obtained at end A in Cycles 1 and 2. The slab damage caused the distribution of link end moments to change. At $\pm 0.06$ rad. in Cycle 4, $M_A$ was $0.83M_B$ when $M_A$ developed a positive moment of $0.84M_p$, and $1.25M_B$ when $M_A$ developed a negative moment of $M_p$. Flange yielding occurred at end A in the link during the second half of Cycle 4 at a $\gamma$ approximately equal to -0.05 rad., when $M_A$ was equal to $1.10M_p$ and $M_B$ was equal to $0.90M_p$. During Cycle 4 at a $\gamma$ of -0.06 rad. the concrete in the deck gap above the link flange cracked and pushed out the fitted sheet metal between the ribs, as shown in Fig. 3.20(b).

During Cycle 5 at a $\gamma$ of -0.07 rad. web buckling occurred in the center panel of the link when the link shear force was 125.9 kips. At the same time, compression flange buckling developed at end A of the link where $M_A$ was $1.10M_p$ and $M_B$ was $0.90M_p$.

The cyclic web buckling phenomenon illustrated earlier in Fig. 3.5 developed during Cycle 6, as well as in each subsequent cycle of link deformation. In the first half of Cycle 6 at a $\gamma$ of 0.07 rad. the flanges and web stiffeners of the link center web panel began to distort. At a $\gamma$ of -0.07 rad. in the second half of Cycle 6 the link developed a shear force of 129.2

kips. This was the maximum shear force developed by the link, and represented a 29 percent increase from the shear at initial web yielding. The maximum link shear force of Specimen B1 was ten percent greater than the maximum shear force developed in the corresponding bare steel link, Specimen D1. A photograph of the link is shown in Fig. 3.20(c), indicating the distortion of the flanges and web stiffeners in the center panel which developed during Cycle 6.

During Cycles 7 and 8 the flange distortion, web buckling, and web stiffener deformation in the link became more pronounced. In Cycle 7 at a $\gamma$ of 0.08 rad. the compression flange at end B of the link also developed buckling, as shown in Fig. 3.20(d). The corresponding moment $M_B$ was $1.07M_p$. The link maximum shear forces in Cycles 7 and 8 were less than that in Cycle 6. The maximum negative link end moments for Cycles 7 and 8 decreased as the corresponding positive moments at the other end of the link increased. The maximum link end moment for the test developed at end A during Cycle 8 at a $\gamma$ of 0.10 rad., when $M_A$ reached a moment of $1.15M_p$. The corresponding moment $M_B$ was $0.78M_p$. During Cycle 8, upon unloading and proceeding to load in the opposite direction web tearing occurred in the link center panel along a web stiffener. The link capacity rapidly deteriorated with increasing deformation. The test was terminated at a $\gamma$ of -0.06 rad. before completing the second half of Cycle 8.

An examination of the major floor slab after the test indicated that the floor damage remained concentrated in the vicinity of the link. Fig. 3.21 shows the damaged floor area above the link. The test beam showed no signs of yielding outside the link.

**Test Specimen B2** - Specimen B2 simulated a link in an interior V-braced EBF with a composite floor slab. The $V$-$\gamma$ and $M$-$\gamma$ hysteresis loops are shown in Figs. 3.22 and 3.23. A series of symmetric deformation cycles were imposed to the link using the displacement program described in Section 2.7. As in other specimens, each cycle of deformation began by imposing a downwards displacement to end A relative to end B. The end A of the link was adjacent to the simulated column restraint.

During the first half of Cycle 1 all of the link's web panels yielded, as shown in Fig.

3.24(a). The shear force at yield was 94.7 kips, which was 16 percent greater than the corresponding value for the bare steel link, Specimen D2. At the onset of web yielding the link end moment $M_A$ at the simulated column restraint was approximately equal to $M_p$. This value of $M_A$ was 2.09 times that of $M_B$. Continued link deformation to a $\gamma$ of 0.02 rad. caused strain hardening of the link. Upon reversing the link deformation, the slab contributed to the stiffening of the test beam, for now moment $M_B$ was greater than $M_A$. On the slab surface longitudinal cracks appeared above the link.

In Cycle 2 greater plastic deformation developed in the link then in Cycle 1, and more cracks appeared on the floor surface above the link. The $M$-$\gamma$ hysteretic loops indicate that moment redistribution had occurred in the link during the second half of Cycle 2. Initially the moment $M_A$ reached $1.1M_p$ following link yielding, then decreased as moment $M_B$ continued to increase. This phenomenon is shown in the $M$-$\gamma$ hysteretic loops for Cycle 2 and all cycles subsequent to Cycle 2. At end B the slab appeared to increase the stiffness of the test beam when a positive moment developed, for the redistribution of link end moments $M_A$ and $M_B$ became more pronounced in the $M$-$\gamma$ relationships to the extent that $M_B$ eventually exceeded $M_A$. Under the conditions when end B developed a negative moment, $M_B$ is shown to never exceed $M_A$ through moment redistribution. An examination of the $V$-$\gamma$ hysteretic loops indicates that evidently $M_B$ must have increased at a faster rate than $M_A$ decreased, since the link shear force continued to increase in each cycle following web yielding.

During the cycles of link deformation following Cycle 2 the slab continued to suffer damage, mainly in the vicinity of the link. This damage consisted of separation between the metal deck and the concrete slab above the link, and horizontal cracking along the north edge of the slab at end A of the link. Furthermore, longitudinal cracks appeared on the slab surface along the link, with transverse cracks occurring at end B of the link. The cracks or the slab's north edge indicated that the shear connectors at end A of the link were beginning to pull out of the concrete slab.

At a link deformation of 0.08 rad. during Cycle 6 web buckling occurred in the center

panel of the link. Some minor buckling also developed in the compression flange at end A of the link. This occurred at a link shear force of 128.4 kips with a moment of $M_A$ equal to $1.14M_p$.

The shear force in the link continued to increase, reaching a value of 130.7 kips at a $\gamma$ of -0.08 rad. in the later half of Cycle 6. This was the maximum link shear force attained by Specimen B2 representing a 38 percent increase since initial web yielding. Compared to the corresponding bare steel link, Specimen D2, the maximum shear force of Specimen B2 was 11 percent greater. The maximum link end moment $M_B$ had also developed during the latter half of Cycle 6, where $M_B$ reached a value of 1.23 $M_p$. As the maximum shear force and moment $M_B$ developed in Specimen B2, the flange and web stiffeners of the center panel of the link developed severe distortion, as shown in Fig. 3.24(c). During the transition from the first to the second half of Cycle 6 the web buckling in the link followed the same cyclic mode as illustrated in Fig. 3.5. This buckling became more pronounced with each cycle of link deformation. At the conclusion of Cycle 6 the concrete slab had begun to spall on contacting the vertical plate representing a column flange at the simulated column restraint.

Smaller link shear forces were developed at the peak values of $\gamma$ in the subsequent cycles, indicating that the link capacity was deteriorating. Beginning with Cycle 7 tension field action in the link is evident from the $V$-$\gamma$ hysteretic loops, where the lost capacity is partially regained as $\gamma$ is reversed. During the first half of Cycle 8 at a link deformation of 0.10 rad. the metal decking buckled between ribs above the link. At the same time the shear connectors completely pulled out of the concrete slab at end A of the link. Figure 3.24(d) shows a photograph when the link deformation was 0.10 rad., illustrating the severe deformation of the flanges and a web stiffener in the link center panel. Near the end of Cycle 8 web tearing developed in the center panel of the link at the weld of a web stiffener, resulting in a rapid decrease of the load carrying capacity of the link. The test was terminated after reaching a $\gamma$ of -0.10 rad. An examination of the floor damage after the completion of the test, Fig. 3.25, indicated that the major floor damage consisting of concrete spalling and major cracks had

remained in an area that was above the link. The cracking of the floor slab outside of the link area was minor. No yielding of the beam outside of the link was detected.

**Test Specimen C1** - Specimen C1 involved the investigation of a link in an exterior K-braced EBF with composite floors. The displacement program given in Section 2.7 was used to impose a series of link deformations which simulated the response to the first 14.5 seconds of the Taft earthquake which had been scaled to a maximum ground acceleration of 0.5 g. In addition, tests identified as Test 1, 2, and 3 were then conducted which involved imposing three successive symmetric cycles of link deformation having amplitudes of 0.06, 0.08 and 0.10 rad., respectively. The measured floor displacements, Fig. 3.26(a), of the Tsukuba test results [17] and the estimated link deformation history, Fig. 3.26(b), will be used to facilitate the discussion. The link $V$-$\gamma$ hysteretic loops for the simulated scaled Taft earthquake are shown in Fig. 3.27. These results are combined with the hysteretic loops of Test 1, 2, and 3 in Fig. 3.28. The corresponding $M$-$\gamma$ hysteretic loops are shown in Fig. 3.29. The link deformation history for the scaled Taft earthquake was started by displacing end A downwards relative to end B of the link.

Yielding developed in all of the web panels of the link at pt. B in Fig. 3.26. The link shear force was 86.9 kips, which was two percent greater than that in the corresponding bare steel link, Specimen D1. The photograph shown in Fig. 3.30(a), indicating the web yielding in the link, was taken shortly after pt. B was reached. At the onset of web yielding, moment $M_A$ was $0.81M_p$ which was 1.41 times greater than moment $M_B$. Approximately midway through the Taft earthquake, pt. D, a $\gamma$ of 0.044 rad. was imposed on the link. Fig. 3.30(b) shows the link at that time, indicating a more developed yielding in the web. This link deformation resulted in cracking of the floor slab and separation of the metal deck from the concrete slab above the link. The ribs of the slab also cracked near both ends of the link. The floor slab cracks extended in a transverse direction along the surface with respect to the longitudinal axis of the link. When pt. F was reached in the link deformation history, imposing a $\gamma$ of -0.027 rad., the floor damage had become more extensive. Fig. 3.30(c) shows the floor damage with

fully developed yielding in the link at pt. G in the deformation history. The link deformation at this time was -0.027 rad.

The slab damage resulted in a change in the initial distribution of the link's end moments. Near the end of the simulated Taft earthquake the negative moment at end B approached $1.9M_A$. At a positive moment at end B, $M_B$ approached $1.2M_A$. An examination of the $M$-$\gamma$ hysteretic loops reveals that the inelastic stiffness at end A and magnitude of $M_A$ had decreased when it became positive.

The two largest successive peaks of link deformation during the scaled Taft earthquake occurred at pts. J and K which had a $\gamma$ of 0.06 and -0.04 rad., respectively. As a result of these sequence of deformations the maximum shear in the link developed during the scaled Taft earthquake. The maximum shear in the link was 111.3 kips, which was 28 percent greater then the link shear force at initial web yielding. The corresponding link moment $M_B$ was $1.13M_p$, which caused flange yielding at end B of the link. Figure 3.30(d) shows the link at the deformation of 0.06 rad. The extensive web yielding can be judged by noting that most of the white wash scaled off.

Upon unloading from pt. K the link response simulation to the first 14.5 seconds of the scaled Taft earthquake was complete. An examination of the $V$-$\gamma$ hysteresis loops in Fig. 3.27 reveals that the link displayed stable hysteretic behavior and good energy dissipation. Increasing plastic deformation resulted in continuing strain hardening. The link maintained parallelogram shapes while undergoing cyclic deformation. Figures 3.31(a) and (b) show the rib damage, mainly at the left end A of the link, and the transverse slab cracks above the link. Overall, during the scaled Taft record the link performed very well with the major floor damage confined to an area above the link.

Imposing greater $\gamma$s in Tests 1, 2, and 3 resulted in a more extensive slab cracking of the ribs and deck separation above the link. An examination of the $M$-$\gamma$ hysteretic loops indicates that in each subsequent cycle of increased link deformation, the negative end moment of the link decreased near the termination of each half cycle as a result of the slab damage. How-

ever, the corresponding positive end moment continued to increase at such a rate that the link shear force continued to strain harden.

At a $\gamma$ of -0.06 rad. in Test 1 the link compression flange buckled at end A, see Fig. 3.32(a). At this point moment $M_A$ reached $1.15M_p$. During the first half of Test 2 at a $\gamma$ of 0.08 rad., web buckling developed in the center panel of the link, and the compression flange buckled at end B when $M_B$ reached $1.21M_p$. The flange and web stiffeners in the link center panel began to distort during the second half of Test 2 as shown in Fig. 3.32(b). Also the center panel began to show significant local deformation. The cyclic web buckling pattern depicted in Fig. 3.5 developed during the remaining cycles of the test as the buckling became more pronounced. As a result of continued strain hardening coupled with tension field action in the link, the link maximum shear and end moment developed during the last half of Test 3 at a $\gamma$ of -0.10 rad. The maximum shear was 118 kips, representing a 35 percent increase from the initial web yielding. The link maximum end moment developed at end A, where $M_A$ was $1.38M_p$. Fig. 3.32(c) shows the link at a $\gamma$ of -0.10 rad. when the link maximum shear and end moment had developed.

Test 3 was terminated upon completing the current half cycle. Photographs shown in Figs. 3.33(a) and (b) were taken after the completion of Test 3. The floor damage is shown to have occurred mostly in an area above the link and consists of rib cracking, separation of the metal deck from the concrete slab, and transverse surface cracks. A comparison with Figs. 3.31(a) and (b) indicates that increased floor damage of Specimen C1 occurred during the severe cycles of link deformation which followed the scaled Taft earthquake simulation. During the testing of Specimen C1 there was no evidence of yielding of the beam outside of the link.

**Test Specimen C2** - Specimen C2 simulated a link in an exterior V-braced EBF with composite floors. No lateral bracing by transverse beams was provided at either end of the link. Using the displacement program given in Section 2.7, an initial symmetric pulse of link deformation with an amplitude of 0.06 rad. was applied followed by symmetric cycles of link

deformation which were similar to those for Specimen D2. The $V$-$\gamma$ and $M$-$\gamma$ hysteretic loops are shown in Figs. 3.34 and 3.35. Each cycle of link deformation was initiated by displacing end A of the link downwards with respect to end B of the link. As noted previously, end A of the link was adjacent to the simulated column restraint.

During the initial pulse of $\gamma$ in Cycle 1 web yielding occurred in the link as shown in Fig. 3.36(a). The shear force at this initial web yielding was 85.9 kips, which represents a six percent increase over that for the corresponding bare steel link, Specimen D2. Moment $M_A$ was $0.77M_p$, which was 1.27 times greater than moment $M_B$. Continued link deformation resulted in the development of transverse cracks in the slab above the link. In addition, separation of the metal decking from the concrete slab along the slab's exterior edge parallel to the link had occurred. Typically, the link's shear force increased with strain hardening. Unloading and reversing the link deformation to complete Cycle 1 resulted in further floor damage in the ribs above end B.

At the peak link deformation in all subsequent cycles the link end moments maintained the same relative ratios. For a negative $M_B$, $M_A$ was equal; for a positive $M_B$ it was approximately equal to $1.33M_B$. This distribution of end moments was a result of rib cracking at end B of the link in Cycle 1. As end B was displaced downwards the crack in the rib would open as shown in Fig. 3.36(b). A reversal of the link deformation would close the crack in the rib. Thus, the stiffness at end B of the link increased when a negative moment was imposed which closed the crack. During plastic deformation the link maintained a deformed parallelogram shape and continued to strain hardening. However, the shear force which developed in the link did not exceed the maximum value developed in Cycle 1 until the imposed $\gamma$ became equal to the maximum link deformation developed in Cycle 1. This occurred in Cycle 5. Also, the damage to the floor slab did not become more extensive until $\gamma$ reached or exceeded the maximum link deformation in Cycle 1. Buckling of the compression flange at end A in the link occurred during Cycle 6 at a $\gamma$ of 0.06 rad. The corresponding moment $M_A$ was $1.08M_p$.

During the first half of Cycle 7 with $\gamma$ equal to 0.08 rad. web buckling occurred in the link center panel as the web stiffeners began to deform, as shown in Fig. 3.36(c). Upon unloading and proceeding to a $\gamma$ of -0.08 rad., the flanges of the center panel of the link also began to deform. The cyclic web buckling mode illustrated in Fig. 3.5 developed during Cycle 7 as well as in all subsequent cycles as the buckling became more pronounced. The forces in the link were less at a $\gamma$ of -0.08 rad. in the second half of Cycle 7 compared to the first half when $\gamma$ was equal to 0.08 rad. This indicated that the link capacity was deteriorating. Hence the shear force at the instant of web buckling was the largest shear ever developed in the link. This shear force was 120 kips, representing a 40 percent increase from the initial web yielding and a two percent greater value than the maximum link shear force for Specimen D2. At the instant of web buckling, the maximum end moment had also developed in the link. This occurred at end A where $M_A$ had reached a moment of $1.14M_p$, the corresponding moment $M_B$ was equal to $0.79M_p$.

During Cycle 8 the flanges in the link center panel began to severely deform at the peak $\gamma$ of 0.08 rad. During the last half of Cycle 8 tension field action becomes quite noticeable in the $V$-$\gamma$ hysteretic loops. As shown in Fig. 3.37(a) the floor developed concrete spalling at the face of the simulated column face where the slab was abutting against a vertical plate.

In an attempt to impose a $\gamma$ of -0.10 rad. during the second half of Cycle 9, web tearing occurred along a web stiffener of the link center panel at a $\gamma$ of -0.07 rad. Continued link deformation resulted in the capacity of the link deteriorating rapidly. With no lateral bracing provided by transverse beams, there was significant twisting of the link cross section causing lateral movement. This was an indication of the onset of lateral-torsional buckling. Hence, the test was immediately terminated to avoid damaging the hydraulic jacks. The maximum link deformation developed in the second half of Cycle 9 was -0.09 rad. Figure 3.36(d) shows the link at the end of the test. An examination of the floor slab indicated that the major floor damage had remained in the vicinity of the link, as shown in Fig. 3.37. The link appeared to isolate itself from the remaining part of the floor slab because of the rib cracking at end B and

spalling of the concrete floor slab. No yielding was found in the test beam outside of link.

## 3.4. Summary and Conclusions

The results of the tests indicate that composite links designed as short bare steel links will yield predominantly in shear. Therefore, energy dissipation occurs primarily through web yielding. Following initial yielding the links continued to strain harden to at least the point of web buckling thereby enabling the links to develop larger shear forces than at the initial yield. As a result, the link end moments eventually exceed $M_p$. By comparing the performance of the composite links with those of bare steel, it was found that the shear yield strength and ultimate shear capacity of short links subjected to cyclic deformation is augmented by composite action. Composite action appears to have a greater affect on the links of interior EBF where the average shear yield strength and shear capacity is noticeable greater than for the bare steel links.

Composite floor systems increase the stiffness of the beams. The degree of increase in stiffness depends on the extent of floor slab damage. The floor damage generally consisted of a separation of the metal deck from the concrete slab, spalling and cracking of the concrete slab, as well as slippage and failure of the shear connectors. This major floor damage became more intense as the link deformations increased, however the floor damage remained in an area that was in close vicinity of the link. Rib cracking near the ends of the link appeared to be the major influence on the relative rotational stiffness of the link ends. If cracks became closed, the rotational stiffness at that particular end of the link would increase compared to that of a case when the cracks were open. As a result of floor damage from cyclic action the ratio of the link end moments $M_A$ and $M_B$ would not remain constant.

The end moments of the bare steel link in the K-braced EBF subassembly were found not to be equal due to sensitivity in the values of the end moments resulting from the closely spaced jacks relative to the test beam span length. These end moments, however, were closer to being equal then the elastic link end moments in composite specimens and the bare steel

link specimen which represented links in a V-braced EBF. It was found that larger elastic link end moments developed at the simulated column restraint in the links of the V-braced than in the K-braced EBF subassemblies. An equalization of these end moments by moment redistribution during plastic deformation did not occur in the bare steel links of the V-braced EBF subassembly and the composite links of the exterior V-braced EBF subassemblies. However, the composite link of the interior V-braced EBF subassembly showed a greater degree of moment redistribution of the link end moments. With cover plates on the steel test beam, moment yielding did not develop outside the link.

Several of the specimens had different histories of link deformation. However, the accumulated angular deformation from the last point of zero shear to the point of web buckling, $\gamma_b$, was approximately equal for all specimens. Therefore, it appears that $\gamma_b$ is related to the hysteretic deformation of the cycle in which web buckling occurred. The value of $\gamma_b$ was found not to be significantly affected by composite action.

Web buckling in the link generally resulted in deterioration of the link load carrying capacity when subsequent link deformations exceeded $\gamma_b$. On the contrary, flange buckling at the ends of a link did not inhibit the link from developing greater forces. These phenomena were noted for both bare steel as well as for composite link specimens. By comparing the $V$-$\gamma$ hysteretic loops for Specimen A2 with those for the other specimens having fewer stiffeners, it is apparent that by prolonging or preventing link web buckling results in the ability of a link to strain harden and more effectively to dissipate additional energy. For the link with a larger number of stiffeners a greater shear force could be developed.

Web stiffeners were found to play an important role in the post buckling behavior of the links. A decrease in the stiffener rigidity caused by their buckling still allowed the link to dissipate energy in a stable manner even after the web buckled. However, within one to two cycles after web buckling the stiffeners became so severely deformed that the tension field could not be developed. This caused an extensive damage to the metal decking and concrete slab. If for such cases the web stiffeners were made stiffer, the performance of the link after

web buckling would have been improved by maintaining stiffer boundaries around the buckled web.

Severe cyclic web buckling coupled with buckling of the flanges and web stiffeners caused a deterioration in the panel strength. The effect of web tearing was found to be catastrophic for the capacity of the link. A link which had developed web tearing was found to possess a low resistance to lateral buckling in a case where no lateral bracing was provided.

Based on the observed experimental behavior of the specimens, the following conclusions can be made:

(1) Composite links initially designed as bare steel short links yield in shear and dissipate energy primarily through web yielding.

(2) Composite action results in an increase in the shear yield strength and ultimate capacity of links under cyclic loading. The interior links of EBFs with composite floor systems benefit more from the composite action and attain greater yield and ultimate shear strengths than comparable links in exterior EBFs.

(3) The relative magnitudes of the link end moments is affected by composite action, which in turn is affected by the damage to the floor slab. Under cyclic loading the major floor damage occurs in a local area of the slab above a link. Failure of the shear connectors takes place mainly at the link with shear connectors pulling out of the concrete. The floor damage causes changes in the relative rotational stiffnesses of the ends of the link. Therefore the distribution of the initial elastic link end moments is not maintained.

(4) Strain hardening following the initial shear yielding of the link causes the link's maximum end moments to exceed $M_p$. Larger link end moments are developed in composite links than in bare steel links.

(5) Flange buckling at the ends of a link does not have a significant effect on the shear and moment capacity of a link.

(6) The amount of link deformation to cause web buckling is independent of the previous link deformation history. Web buckling occurs when the link deformation exceeds a

specific value of link deformation $\gamma_b$. For cyclic loading this deformation is measured from the point of zero shear to the shear at web buckling corresponding to the half cycle in which web buckling occurred. A diagonal tension field forms in a link panel where web buckling occurs. If the web stiffeners do not possess sufficient stiffness, the tension field action can lead to a severe deformation of the web stiffeners and flanges.

(7)   To avoid unsatisfactory post buckling link behavior, the web stiffeners should be designed to have both adequate strength and stiffness.

(8)   If an early pulse of link deformation leads to web buckling adverse effects do not develop as long as in subsequent cycles the link deformations do not exceed $\gamma_b$. In situations where the cyclic link deformations exceed $\gamma_b$ the link strength rapidly deteriorates.

# CHAPTER 4

# ANALYSIS OF EXPERIMENTAL RESULTS

## 4.1. General

In Chapter 3, observations of the hysteretic behavior of each of the eight specimens were discussed. Based on these observations general conclusions were made. In Chapter 4 a detailed evaluation of the experimental behavior will be performed by analyzing the measured data for each of the eight specimens. In order to draw general conclusions on the effects of composite action in EBF, results of the analysis of each specimen will be compared. Topics which will be examined will include the elastic state, yield state, and the inelastic state of the link, along with the participation of the floor slab.

## 4.2. Elastic Link Behavior

During the initial elastic response of each specimen, data were gathered which enabled the initial elastic link stiffness to be determined. For purposes of comparing the initial elastic stiffness of different specimens, a pseudo-elastic link stiffness, $K^*$, was computed for each specimen:

$$K^* = \frac{V}{v} \tag{4.1}$$

where $V$ is the link shear corresponding to the relative elastic vertical end displacement, $v$, between the ends of the link. The computed values for $K^*$ are summarized in Tables 4.1 and 4.2 for the links of the K-braced and V-braced EBF subassemblies. In these tables $K^*_{D1}$ and $K^*_{D2}$, respectively, represent the value of $K^*$ for Specimens D1 and D2. Accurate values of $K^*$ were difficult to compute due to the small displacements associated with the initial elastic response. Basing the computations of $K^*$ on data from the X-Y recorders giving continuous response curves during each test provided greater accuracy than using the discrete data from

the scanner system.

It can be noted from Table 4.1 that $K^*$ for the composite link for the interior K-braced EBF subassembly (Specimen B1) is greater than $K^*$ for the composite links of the exterior K-braced EBF subassembly (Specimens A1 and C1). Specimen B1 has a 51 percent greater value for $K^*$ compared to the corresponding bare steel link (Specimen D1), while Specimens A1 and C1 have a value of $K^*$ that is 24 percent greater. Likewise, Table 4.2 shows that $K^*$ for the composite link for the interior V-braced EBF subassembly (Specimen B2) is greater than $K^*$ of the composite links for the exterior V-braced EBF subassemblies (Specimens A2 and C2). Specimen B2 has a 17 percent greater value for $K^*$ than the corresponding bare steel link (Specimen D2), while Specimens A2 and C2 have an average value of $K^*$ that is only about 6 percent greater than the corresponding bare steel link. Based on the results for $K^*$, it is evident that links with composite action have a greater initial elastic stiffness compared to bare steel links. Furthermore, the composite links of the interior EBF subassemblies have a greater $K^*$ than those for the exterior EBF subassemblies.

The $V$-$\gamma$ hysteretic loops for each composite link test, excluding Specimen C1, were superimposed on the $V$-$\gamma$ hysteretic loops for the corresponding bare steel link, as shown in Figs. 4.1 through 4.3. An examination of these results confirms that the composite links have a greater initial elastic stiffness compared to the bare steel links. However, after imposing cyclic deformations to each of the composite links, their elastic stiffness appears to deteriorate to the level of the corresponding bare steel link. This is a consequence of damage to the floor slab during the cyclic link deformation.

## 4.3. Link Yield Limit State

For each link specimen the shear force $V_y$ and the largest of the two end moments $M_y$ at initial yield are given in Table 4.3. In column 4 of this table $V_y$ of each composite link has been normalized with respect to the corresponding shear yield strength $V_y^{Bare}$ of a bare steel link. Table 4.3 indicates that the composite links have a greater $V_y$ than the corresponding

bare steel links, ranging in values from 2 to 17 percent. The composite links of Specimens B1 and B2 show the greatest increase in $V_y$, being 17 and 16 percent above the corresponding bare steel links.

To predict the yield limit state and inelastic behavior of links without the presence of axial load, it is essential to know the form of the $M$-$V$ interaction surface. This interaction surface for bare steel links has been studied in the past, both experimentally and analytically. Accordingly, in the present study the values of $V_y$ and $M_y$ for the eight links were normalized by $V_p$ and $M_p$ of the bare steel link (see Table 2.6) and along with the results for previous tests of bare steel links [3,6,7] are plotted on the $M$-$V$ diagram shown in Fig. 4.4. In this figure theoretical solutions by Hodge [43], Leth [44], and Neal [19] are also shown.

An examination of Fig. 4.4 indicates that the present tests appear to have a yield limit state that is similar to the majority of the previous tests. The present experimental data on bare steel specimen are in good agreement with Leth's solution. The same conclusion was reached for the previous tests [7]. Leth's solution also provides a better estimate of the $M$-$V$ yield state for the composite links compared to the solutions of Hodge and Neal.

## 4.4. Postyield Link Behavior

After shear yielding had developed in the web, the stiffness of the link would decrease as inelastic deformation continued. The majority of the inelastic link deformation is due to the inelastic shear strains developed in the web. This results in a shear mechanism where each link assumes the shape of a parallelogram. Figures 4.1 to 4.3 indicate that in the first complete inelastic cycle of link deformation the composite links sustain a greater shear yield force relative to the corresponding bare steel specimens. For Specimens B1 and B2 this phenomenon is more pronounced compared to the other composite specimens. With each subsequent cycle the shear force at the onset of yielding of the composite links comes closer to the shear force at the onset of yielding of the corresponding bare steel links.

In all specimens strain hardening developed in the link during plastic deformation follow-

ing shear yielding. Consequently, the link shear force of each specimen continued to increase after initial yielding. The influence of the effect of cyclic application of the loads and strain hardening on the change in the link shear force was examined for each specimen. This was done by determining the maximum shear force $V_i^{max}$ for each consecutive half cycle and the cumulative relative displacement ductility $\Sigma\mu_{v_i}$ for the link. $\Sigma\mu_{v_i}$ was obtained by summing a link's relative displacement ductility $\mu_{v_i}$ for each half cycle, where $\mu_{v_i}$ is defined as:

$$\mu_{v_i} = \begin{cases} \dfrac{\Delta v_i}{v_y} & (\Delta v_i \geq v_y) \\[2mm] 0 & (\Delta v_i < v_y) \end{cases} \qquad (4.2)$$

Here $\Delta v_i$ = maximum relative displacement between the ends of a link during half cycle $i$ as shown in Fig. 4.5, and $v_y$ = relative displacement between ends of the link at initial yield. $\Sigma\mu_{v_i}$ therefore is representative of the plastic deformation accumulated by a link.

The result of plotting $V_i^{max}$ against $\Sigma\mu_{v_i}$ for the links is shown in Figs. 4.6 to 4.11. These results indicate that $V_i^{max}$ increases by strain hardening until shortly after web buckling occurs. Thereafter $V_i^{max}$ begins to decrease for all specimens, excluding Specimens A2 and C1. As was noted previously, web buckling did not occur in Specimen A2 because of the closely spaced web stiffeners. For Specimen C1, $V_i^{max}$ continued to increase slightly after web buckling.

A summary of the maximum shear forces $V_{max}$ developed in the links is given in Table 4.4. As shown in column 3 of this table, cyclic strain hardening resulted in maximum shears ranging from $1.29V_y$ to $1.44V_y$ for links exhibiting web buckling. Because web buckling did not develop in Specimen A2, a larger shear force of $1.53V_y$ could develop. The average of the composite link maximum shear force was $1.36V_y$ for the links of the K-braced EBF subassemblies (Specimens A1, B1, and C1), and was $1.39V_y$ for the composite links of the V-braced EBF subassemblies, excluding Specimen A2 (e.g. Specimens B2 and C2). These average

values are very close to the increases in the shear force relative to $V_y$ for the corresponding bare steel specimens, where $V_{max}$ was $1.38V_y$ and $1.44V_y$, respectively, for the link in the K-braced EBF subassembly (Specimen D1) and the V-braced EBF subassembly (Specimen D2).

A direct comparison between the $V_{max}$ of the composite links and the maximum shear force $V_{max}^{Bare}$ of the corresponding bare steel links is shown in column 4 of Table 4.4. This comparison, excluding Specimen A2, indicates that the interior composite links (Specimens B1 and B2) have the largest increase in $V_{max}$ relative to $V_{max}^{Bare}$, where $V_{max}$ is equal to $1.10V_{max}^{Bare}$ for Specimen B1 and $1.11V_{max}^{Bare}$ for Specimen B2. Specimen A2, a composite exterior link of a V-brace EBF subassembly, shows a 13 percent increase in $V_{max}$ relative to $V_{max}^{Bare}$, due mainly to the fact that web buckling did not occur in Specimen A2. The exterior composite link of the other V-braced EBF subassembly (Specimen C2) developed web buckling and as a result shows no apparent increase in $V_{max}$ relative to $V_{max}^{Bare}$. However, the exterior composite links of the K-braced subassemblies (Specimens A1 and C1) had an average increase of five percent in $V_{max}$ relative to $V_{max}^{Bare}$.

Strain hardening of the links is a combination of kinematic and isotropic hardening. This is evident from the $V$-$\gamma$ hysteretic loops shown in Figs. 4.1 to 4.3, where during the elastic response the height of the hysteretic loops increases in each subsequent cycle before yielding occurs. For Specimens D1 and B1, which had nearly the same link deformation history, the isotropic hardening of the $V$-$\gamma$ hysteretic loops was examined by determining the increase in shear yield strength as a result of cyclic link deformation. For a given current half cycle the shear force at the onset of yielding was determined by the procedure shown in Fig. 4.12, which involved drawing a line parallel to the elastic curve and a line parallel to the stiffness of the fully plastic link. The point of intersection of these lines, pt. B, was used as the state where the onset of yielding occurred for the current half cycle. The shear force $\Delta V_y$ required to unload from the previous yield state, pt. A, to pt. B was then determined as shown in Fig. 4.12. For the first half cycle $\Delta V_y$ was set equal to twice the initial shear yield strength. The

plastic link deformation of the current half cycle, $\gamma_p$, was taken to be from pt. B to the peak of the current half cycle, pt. C. $\Delta V_y$ and $\gamma_p$ were then normalized with respect to the shear force $V_{y_0}$ and link deformation $\gamma_{y_0}$ at initial yielding of the first half cycle. The normalized value of $\Delta V_y$ was then plotted against the accumulated normalized values of $\gamma_p$ from the previous half cycles. This process was repeated for each of the half cycles for the complete deformation histories of Specimens B1 and D1. These results are shown in Fig. 4.13.

The onset of yielding shown in Fig. 4.13 progressively occurs at greater values of $\Delta V_y$ of successive half cycles, illustrating isotropic hardening behavior of the link in shear. It appears that the composite link (Specimen B1) has less isotropic hardening then the bare steel link (Specimen D1). However, as shown in Fig. 4.1(b), Specimen B1 has a greater stiffness than that of Specimen D1 when the link is fully plastic. This phenomenon is also true for the other composite links as shown in Figs. 4.1 to 4.3.

Comparisons between the $M$-$\gamma$ hysteretic behavior for link end moments of Specimens B1 and B2 and their corresponding bare steel links, Specimens D1 and D2, are shown in Fig. 4.14. The nomenclature and positive sign convention for the link and moments was shown previously in Fig. 3.1. Figure 4.14 shows that during the first cycle of link deformation, the composite links develop greater magnitudes of elastic stiffness and positive moments compared to the corresponding bare steel links. The deterioration of the elastic stiffness at the end of the links is shown to occur during subsequent cycles as a result of slab damage in the vicinity of the link. Figure 4.14 also shows that the $M$-$\gamma$ hysteretic loops are slightly pinched in advanced cycles of testing when positive moments develop, leading to an increase in stiffness following closing of the cracks in the floor slab at $\gamma = 0$. Consequently, the composite links developed greater ultimate positive end moments than the corresponding bare steel links.

For Specimen B2 the increase in the inelastic stiffness under positive moment compared to the corresponding bare steel link is more substantial than that for Specimen B1 and its corresponding bare steel link. The pinching of the $M$-$\gamma$ hysteretic loops is not however very severe, particularly when comparing it with the cyclic response of a long composite floor beam

[22] shown in Fig. 4.15. The pinching of the $M$-$\gamma$ hysteretic loops does not occur when the ends of the links are subjected to a negative moment since the inelastic stiffnesses of the composite links remain essentially constant. This hysteretic behavior was typical for all composite links except for Specimen B2 at the simulated column restraint. In Specimen B2 at the simulated column restraint the moment $M_A$ was found to redistribute to end B of the link, as previously shown in Fig. 3.23.

The maximum positive and negative link end moments for all specimens pertaining to links in the K-braced EBF subassemblies are summarized in columns 2 and 3 of Table 4.5. These moments represent the largest magnitude of positive and negative link end moments which must be resisted by the combined flexural strength of the brace and floor beam outside the link in a K-braced EBF. An examination of columns 4 and 5 in Table 13 indicates that the maximum end moments of all links in the K-braced EBF subassemblies exceed the moment capacity of a bare steel section, $M_p$. Also, the maximum link end moment of the composite links are greater than that of the corresponding bare steel link (Specimen D1). The increase in the maximum end moment of the composite links relative to that of the corresponding bare steel link ranges from less than one percent (Specimen A1) to 25 percent (Specimen C1). Columns 6 and 7 of Table 4.5 indicate that the magnitudes of the maximum link end moments were less then the monotonic positive moment capacity of the links based on full composite action, $M_{ult}^+$. The composite links developed only $0.58 M_{ult}^-$ to $0.75 M_{ult}^+$ maximum end moment, indicating that it is necessary to account for the reduction of the shear connector's monotonic shear strength and the effects of slab damage when dealing with cyclic behavior.

Table 4.6 summarizes the maximum positive and negative link end moment for both ends of the links pertaining to the V-braced EBF subassemblies. The values of $M_A^{max}$ in columns 2 and 3 of this table represent the largest magnitudes of positive and negative link end moment which must be resisted by the columns of a V-braced EBF. Values of $M_B^{max}$ in columns 4 and 5 represent the largest magnitudes of positive and negative link end moment that must be

resisted by the combined flexural strength of the brace and link beam outside the link of a V-braced EBF. An examination of columns 6 through 9 in Table 4.6 indicates that the values of $M_A^{max}$ are greater than the values of $M_B^{max}$ for all links for except Specimen B2. For the links which exclude Specimen B2, the values of $M_A^{max}$ exceed $M_p$ with $M_B^{max}$ at most approximately equal to $M_p$. Consequently, the equalization of end moments did not occur in the links of these specimens. For Specimen B2, the effect of composite action lead to a greater amount of redistribution of the link end moments resulting in an equalization of end moments, where the value of $M_B^{max}$ for a positive moment was equal to $1.23M_p$. The values of $M_A^{max}$ and $M_B^{max}$ of the composite links are larger in most specimens than those for the bare steel link, Specimen D2. Excluding Specimen A2, the interior composite link (Specimen B2) developed the largest (14 percent) increase in $M_A^{max}$ relative to the bare steel link. Specimen C2, an exterior composite link, did not develop an increase in $M_A^{max}$ compared to the bare steel link. Because web buckling did not occur in Specimen A2 the increase in $M_A^{max}$ was the largest of all the composite links (25 percent) relative to the bare steel link. However, an increase of 38 percent in $M_B^{max}$ by Specimen A2 relative to the bare steel link was smaller than the increase of the other composite links given in Table 4.6. Specimen B2 developed as much as a 48 percent increase and Specimen C2 a 42 percent increase in $M_B^{max}$ relative to the bare steel link. Columns 10 through 13 of Table 4.6 show that the magnitudes of $M_A^{max}$ and $M_B^{max}$ had a range from $0.42M_{ult}^+$ to $0.74M_{ult}^+$ and therefore did not reach $M_{ult}^+$. Thus, full composite action was not maintained in the links.

The above findings with regard to the differences in the post yield behavior of composite links and bare steel links, as well as the elastic and yield limit states, should have an influence on the response of an EBF. It is essential that these findings be considered in the formulation of a cyclically loaded link model in order to achieve accurate nonlinear analysis of EBFs.

### 4.5. Jack Forces

As noted in Chapter 1, it is important to design the braces in an EBF to remain elastic under extreme loading conditions and not to buckle. This will maintain the strength and energy dissipation capacity of the links and an EBF. Indicated in Fig. 4.16 are the measured jack forces $P_A$ and $P_B$ for each specimen when the initial web yielding, $P_y$, of a link had occurred, and when the maximum jack forces, $P_{max}$, were applied to the specimen. $P_A$ and $P_B$ for the K-braced subassembly are related to the axial brace forces in K-braced EBFs. The jack forces $(P_B)$ for the V-braced subassemblies are related to the axial forces in the braces, and forces $(P_A)$ are related to those in the columns. It is apparent from Fig. 4.16 that the composite specimens developed larger values of $P_y$ and $P_{max}$ compared to the those in the steel specimens (Specimens D1 and D2). Furthermore, in all cases the forces $P_A$ were larger than $P_B$. This was more pronounced in the V-braced simulated subassemblies.

In Table 4.7 the values of $P_{max}$ for the K-braced EBF subassemblies are compared to $P_{max}^{Bare}$ of Specimen D1. The values of $P_{max}$ used in developing this table are the largest ones for $P_A$ and $P_B$. The values of $P_{max}$ relative to $P_{max}^{Bare}$ are greater when the jacks are in tension because this results in pulling down of the end of the link, causing a positive moment resulting in compressive stresses in the slab. This assertion is substantiated by the results in Table 4.7. However, the difference in $P_{max}$ between the compression and tension jack forces is rather small. This difference is only about one percent for Specimens A1 and B1, and 10 percent for Specimen C1. The composite interior link of Specimen B1 developed the largest increase of $P_{max}$ relative to the bare steel link (14 percent). As can be seen from columns 2 and 3 of Table 4.7, the exterior composite links in the K-braced subassemblies developed at most an 11 percent increase in $P_{max}$ relative to the bare steel link.

In Table 4.8, $P_{max}$ is compared to $P_{max}^{Bare}$ of Specimen D2 for both ends of the link in the V-braced subassemblies. As in the previous case, slightly larger values of $P_{max}$ relative to $P_{max}^{Bare}$ develop in the V-braced EBF subassemblies when the jacks are in tension. The largest

tensile jack forces $P_{max}$ developed in Specimen A2 relative to the bare steel link (17 percent at $\cdot$ end A and 12 percent at end B). This was primarily due to the fact that no web buckling occurred in Specimen A2. In another exterior composite link, Specimen C2, web buckling in the link had occurred and as a consequence $P_{max}$ was equal to $1.01P_{max}^{Bare}$ at end A and $1.07P_{max}^{Bare}$ at end B. Of the links exhibiting some web buckling, the interior composite link Specimen B2 developed the largest values of $P_{max}$, where at end A $P_{max}$ was equal to $1.08P_{max}^{Bare}$ and at end B $1.11P_{max}^{Bare}$. Thus, relative to the bare steel link this specimen showed a larger increase in the jack forces at end B of the link compared to end A. Specimen A2 developed the opposite effect where the lack of web buckling resulted in a larger increase in $P_{max}$ occurring at end A.

Hence, it can be concluded that the composite specimens develop larger jack forces than the corresponding bare steel counterparts in both the K-braced and V-braced EBF subassemblies. Excluding Specimen A2, the interior composite links develop the largest increase in the jack forces relative to the bare steel links. The average increase in the jack forces relative to the corresponding values of $P_{max}^{Bare}$ for each specimen (column 4 in Table 4.7 and column 6 in Table 4.8) are very consistent with the increase in $V_{max}$ relative to $V_{max}^{Bare}$ of the link (column 4 of Table 4.4). However, the increase in $P_{max}$ is slightly greater than $V_{max}$ relative to the bare steel link due to the floor slab transferring some of the applied load to adjacent floor beams. This phenomenon will be elaborated on later in this chapter.

## 4.6. Energy Dissipation

The effects of composite action, load history, and web buckling of the link on the energy dissipation process are of major importance in designs of EBFs. Therefore, the energy dissipation characteristics were calculated for all specimens. The calculations of the energy dissipation for each specimen were based on the load-displacement hysteretic loops for both jacks, therefore the results represent the energy dissipated by the entire specimen and not just that of the link. However based on the observations of the experimental behavior described in

Chapter 3, it appears that most of the energy is dissipated by the link through web yielding. The two energy quantities determined for each specimen were: $E_N$, the energy dissipated during each half cycle which has been normalized by the energy that would have been dissipated during the same half cycle by an elastic-perfectly plastic system having the same yield strength and going through the same inelastic displacement; and $E_\Sigma$, the accumulated energy dissipated by the specimen. The cumulative relative displacement ductility $\Sigma\mu_{v_i}$ of the link was used as an independent variable for plotting the energy dissipation history of each specimen.

The results of plotting $E_\Sigma$ against $\Sigma\mu_{v_i}$ are shown in Figs. 4.17 and 4.18 for the various specimens. From these results the dissipation of energy by specimens with nearly identical link deformation histories (Specimens B1 and D1 in addition to Specimens B2 and D2) is approximately 10 percent greater in the composite specimens compared to the bare steel specimens for the same value of $\Sigma\mu_{v_i}$. Specimen C1, subjected initially to a link deformation history which simulated the link deformation during a scaled record of the Taft earthquake, dissipated considerably less energy than other specimens with the same amount of $\Sigma\mu_{v_i}$. Unlike the other specimens, during the initial deformation history of Specimen C1 the link was not subjected to a sequence of cyclicly symmetric half cycles where each successive cycle had considerable amounts of plastic deformation. Instead, for Specimen C1 cycles of elastic deformation and minute plastic deformation along with a few cycles of large plastic deformation were developed in the link at various stages of the test. Consequently, Specimen C1 did not dissipate as much energy as the other specimen for the same amount of plastic deformation. Therefore it is apparent that the energy dissipation process of a link is related to its deformation history.

The normalized energy dissipated per half cycle, $E_N$, is plotted against $\Sigma\mu_{v_i}$ in Figs. 4.19 to 4.24 for examining the effect of web buckling on the energy dissipation capacity of links. In these figures the decrease of energy dissipation capacity of links is shown to occur after the development of web buckling. In Fig. 4.22 Specimen A2 shows no deterioration in its energy dissipation capacity because of the fact that web buckling did not occur, while the energy dis-

sipation capacity of Specimen D2 deteriorates after web buckling had occurred. An examination of the results for Specimen A1, Fig. 4.19, and for Specimen C2, Fig. 4.24, indicates that an early pulse of link deformation affects only the energy dissipation capacity in cycles subsequent to web buckling. Specimen A1 does not maintain the same level of $E_N$ in the cycles following web buckling whereas Specimen C2 is able to maintain the same level of $E_N$ following the initial pulse because web buckling did not occur in the link.

## 4.7. Prediction of Web Buckling

It was noted in Chapter 1 that two previous studies on bare steel links pursued systematic efforts for inhibiting web buckling. The first one of these by Hjelmstad [3] empirically related web buckling to energy dissipation and energy absorption for a given stiffener spacing and web thickness. This was expressed by two relations:

$$\frac{a}{t_w} = 90 - 9 \ln\left[\frac{E_\Sigma^*}{E_e}\right] \tag{1.10}$$

$$\frac{a}{t_w} = 94 - 14 \ln\left[\frac{E^*}{E_e}\right] \tag{1.11}$$

The definition of the terms in these equations is given in Chapter 1. Excluding Specimen A2 from consideration, and using the stiffener spacing $a$ and web thickness $t_w$ of the link for all other specimens, Eqs. 1.10 and 1.11 result in predicting web buckling when either one of the following two criteria is met:

$$\frac{E_\Sigma^*}{E_e} = 1369 \tag{4.3}$$

$$\frac{E^*}{E_e} = 138 \tag{4.4}$$

The values of $E_\Sigma^*/E_e$ and $E^*/E_e$ for the specimens were determined at web buckling and are summarized in Table 4.9. By comparing the results given in Table 4.9 with the criteria of

Eqs. 4.3 and 4.4 it appears that neither one of the relationships is sufficiently accurate for predicting web buckling of the bare steel links as well as the composite links. Furthermore, in this table a comparison of Specimen A1 with Specimen C1 indicates that $E_\Sigma^*/E_e$ at web buckling does not have the same value for two specimens which have similar web stiffeners and link properties but significantly different link deformation histories. Therefore, since different link deformation histories are likely to be produced by different earthquakes, the use of Eq. 1.10 does not appear to be appropriate for predicting web buckling.

In a more recent second study on web buckling noted in Chapter 1, a different criterion was developed [7] which defines an allowable link deformation $\gamma_b$ for a half cycle for inhibiting web buckling as

$$\gamma_b = 8.7 \, K_s(\alpha) \left[ \frac{1}{\beta} \right]^2 \qquad (1.12)$$

The definition of the above terms can be found in Chapter 1.

Using the averaged measured dimensions of the steel sections of the specimens summarized in Table 2.7, the value of $\gamma_b$ based on Eq. 1.12 was found to be 0.15 radians. This value of $\gamma_b$ defines the instant when web buckling is likely to occur. The measured values of $\gamma_b$ at web buckling for the specimen are given in Table 4.10. These results show reasonable agreement with the predicted value of 0.15 rad. for both the bare steel and composite links. Therefore, this criterion appears to be sufficiently accurate for predicting web buckling in links. It is also convenient for use, since the value of $\gamma_b$ can be readily determined for any given link. Kasai [7] has extended the criterion by recasting Eq. 1.12 into a form which relates the link beam depth $d$, web thickness $t_w$, and web stiffener spacing $a$ to the angle of maximum link deformation $\gamma_u$ defined in Fig. 4.25. This result appears as:

$$\frac{a}{t_w} + \frac{1}{5} \frac{d}{t_w} = C_B = \begin{cases} 56, & \text{for } \gamma_u = 0.03 \\ 38, & \text{for } \gamma_u = 0.06 \\ 29, & \text{for } \gamma_u = 0.09 \end{cases} \qquad (4.5)$$

where for other values of $\gamma_u$, $C_B$ can be linearly interpolated. This makes this criterion

attractive for design purposes since the current seismic design philosophy in codes [58,66] is related to $\gamma_u$.

## 4.8. Floor Slab Participation

**Vertical Slab Displacement** - By imposing deformation to the steel link, deformations and forces are developed in the floor slab. An isometric view and contours of measured vertical displacements of the floor slab for Specimen A1 are shown in Figs. 4.26 to 4.28 at a link deformation of 0.01 rad. during Cycle 1 and at a link deformation of 0.06 rad. during Cycle 5. For Cycle 1 the floor slab in Fig. 4.26 appears to deform as a plate subjected to biaxial moment, developing curvature along the x and y axes as a result of the displacement in the vertical direction along the z axis. The largest magnitude of the vertical floor slab displacement, $w_{max}$, occurs along the floor beam outside the link due to the elastic curvature of the floor beam. Figure 4.27 shows the relative vertical displacement, $\Delta_r$, between the the maximum and minimum contours to be 0.28 in. for Cycle 1, which is equal to 1.65 times the relative vertical displacement between the ends of the link. As link yielding and slab damage develop in Cycle 5, the locations of the maximum and minimum vertical displacement contours remain outside the link, as shown in Fig. 4.29. The value of $\Delta_r$ corresponding to these contours is 0.90 in., which is equal to 1.47 times the relative vertical displacement between the ends of the link. It is apparent that even after the floor beam develops a shear mechanism during Cycle 5 that elastic curvature persists in the floor beam outside the link, as shown in Fig. 4.28. The consequences of developing a larger magnitude of vertical displacement in the floor slab increases a possibility of nonstructural damage outside the link.

**Outrigger Effect** - The fact that the floor slab was found to develop curvature along both the x and y axes suggests that perhaps some of the applied load was transferred to the adjoining floor beams. This can be referred to as the outrigger effect. The load which is transferred to the adjacent floor beams develops reactions in the test frame's shear tabs and the supports of the pinned columns (see Fig. 2.5) supporting these beams. Having anticipated this

phenomenon, all of the test frame's shear tabs and supports of the pinned columns were instru-
mented with calibrated load cells in order to measure the load resisted by all floor beams. The
measured reactions of all the floor beams during testing of Specimens A1 and B1, respectively,
are shown in Figs. 4.30 and 4.31. These particular specimens were selected for discussion
because they represent the tests in which the adjacent floor beams developed the largest reac-
tions. These results indicate that the load transferred by the slab to the adjacent floor beams is
less than 10 percent of the load transferred to the supports of the floor beam to which the load
was applied.

By treating the floor system as a beam on an elastic foundation [46,47], the outrigger
effect can be approximated. The stiffness, $k$, of the elastic foundation is a function of the
spacing of the floor beams, $b$, the slab flexural rigidity, $(EI)_y$, and the boundary conditions
along the edges of the slab at the adjacent floor beams, as shown in Fig. 4.32(a). Several ana-
lyses were performed to determine the load transferred to the exterior floor beams from the
interior floor beam of the K-braced EBF subassembly (Specimen B1). In each analysis a
different beam spacing $b$ was used. The interior beam was idealized as shown in Fig. 4.32(b).
Concentrated forces $P$ were applied at each end of the link acting in opposite directions to
simulate the jack forces. The flexural rigidity $EI$ for the floor beam was determined by using
the average of the measured properties given in Tables 2.3 and 2.7. For an assumed value for
beam spacing the stiffness $k$ of the elastic foundation was determined as shown in Fig. 4.32(a).
The flexural rigidity $(EI)_y$ for the floor slab was based on the average of the measured proper-
ties perpendicular to the ribs as given in Table 2.8.

The results of the analyses are shown in Fig. 4.33, where they have been normalized into
a dimensionless form. In this figure $\beta$ is defined as:

$$\beta = \left[ \frac{k}{4EI} \right]^{0.25}$$

(4.6)

In Fig. 4.33 the range in which the experimental conditions exists are noted. The lower bound
solution assumes that in calculating the foundation stiffness $k$ the floor slab is pinned at the

exterior floor beams while the upper bound solution assumes that the floor slab is fixed against rotation by the torsional stiffness of the exterior floor beams. The range of the measured reactions of the exterior floor beams for Specimen B1 is also noted in Fig. 4.33. The predicted amount of load transferred to the exterior floor beams appears to agree reasonably well with the measured experimental data. If the adjacent floor beams had been spaced closer the force transferred to such beams would have been greater. Using the dimensionless curve of Fig. 4.33 and assuming the lower bound solution, it was determined that by decreasing the existing floor beam spacing to 42 in., i.e., by a factor of two, the load transferred to the exterior floor beams would increase by a factor of about seven. By applying in the same manner the upper bound solution, the load transferred to the exterior floor beams would be increased approximately by a factor of 4.5 (see pts. C and D in Fig. 4.33).

**Link Axial Deformation** - Fig. 4.34 shows axial link deformations $\Delta_a$ plotted against relative end displacements of the link, $v$, for Specimens B1, C2, and D1. Similar data are plotted in Fig. 4.35 for Specimens A1 and B2. These diagrams show that the links appear to elongate in the early stages of link deformation. The link elongations for all of these specimens were about the same. For example, the interior composite link of the K-braced EBF subassembly (Specimen B1) developed a maximum elongation of 0.05 in., the exterior composite link of the same subassembly (Specimen C2) a 0.07 in. maximum elongation, and the bare steel link (Specimen D1) a 0.08 in. elongation. The exterior composite link of the K-braced EBF subassembly (Specimen A1) and the interior composite link of the V-braced EBF subassembly (Specimen B2) both had a maximum link elongation of 0.08 in.

A sudden shortening of the links occurs in advanced stages of the link deformation history. This is due to flange buckling of the middle panel of the link being induced by the tension field action after the development of web buckling. The bare steel link (Specimen D1) during the final excursion had a maximum link shortening of 0.55 in. With the concrete slab attached to the top beam flange of Specimen B1, the axial shortening of the link during the final excursion was only 0.09 in. The axial shortening of the link for Specimen C2 was simi-

lar to that of Specimen D1, and had the maximum link shortening of 0.50 in. Apparently Specimen C2 did not benefit from the attached concrete floor slab because the link was located at a corner of the floor slab. Specimens A1 and B2 had a maximum link shortening of 0.13 in. and 0.37 in., respectively, during their final excursions. As a result of the link being closer to an edge of the floor slab these specimens were not as restrained as Specimen B1, consequently they developed a greater link shortening than Specimen B1.

The above results indicate that both the bare steel and composite links develop about the same axial elongation. However, the length of the link decreases after flange buckling occurs in the link due to tension field action. The floor slab partially restrains the link against axial shortening, where the composite links of the K-braced EBF subassemblies (Specimens A1 and B1) were more restrained by the floor slab than the links of the V-braced EBF subassemblies (Specimens B2 and C2), and therefore developed less shortening.

**Concrete Floor Slab Damage** - The measured longitudinal strains $\epsilon_x$ give an indication of the damage to the concrete of the floor slab. These strains were measured on the top surface of the floor slab using an array of clip gages shown previously in Figs. 2.25 and 2.26. The strain data corresponding to points 1 through 7 in Fig. 4.36 are plotted for Specimen A1 along transverse sections in Figs. 4.37 to 4.40. In a similar manner, the strain data corresponding to points 1 through 6 in Fig. 4.41 have been plotted for Specimen B1 in Figs. 4.42 to 4.45, while the strain data corresponding to points 1 through 6 in Fig. 4.46 have been plotted for Specimen B2 in Figs. 4.47 to 4.50. These specimens are selected for discussion since they were affected the most by composite action. Similar data are plotted along longitudinal sections in Figs. 4.51 to 4.53 for $\epsilon_x$ directly above the floor beam and at a distance of 24 in. from the beam's centerline.

An examination of strains along the transverse sections shows that their maximum magnitudes generally occur directly above or in the vicinity of the floor beam where the loads are applied. The strain $\epsilon_x$ decays with distance from a floor beam. From the longitudinal sections it can be seen that larger strains develop in the slab above or near the link at locations where

major transverse cracking and spalling of the concrete floor slab occurs.

As the magnitude of link deformation is increased, the magnitude of $\epsilon_x$ appears to increase more near the ends of the links than at other locations. Large strains along the longitudinal sections at 24 in. from the floor beam occurred mostly near the ends of the link, and were due to the combined effect of large link deformations and extension of the transverse cracks from the link area. In Specimens A1 and B1, both belonging to K-braced subassemblies, the floor damage appears to have a greater tendency to attenuate in a transverse direction from the link along cracks in the floor slab. In Specimen B2, belonging to a V-braced EBF subassembly, a tendency for the floor slab damage to attenuate perpendicular to the link remains, however $\epsilon_x$ outside the link above the floor beam has a tendency to increase.

The slip $\delta_f$ between the steel beam and concrete slab for Specimens B1 and A1 is shown in Figs. 4.54 and 4.55. These figures indicate that inside the link slip between the steel beam and concrete slab occurs during the first cycle and increases in magnitude with continued cyclic link deformation. The slip $\delta_f$ is seen to be considerably more inside the link compared to outside the link. In Specimen B1 the measured slip $\delta_f$ outside the link at a distance of 18 in. and 53 in. from the end of the link were 5 and 30 times, respectively, less then $\delta_f$ in the link. For Specimen A1, $\delta_f$ measured at a distance of 18 in. outside the link is 30 times less then the maximum $\delta_f$ measured in the link. The slip between the steel beam and the floor slab results in a reduction of shear transferred by the shear connectors between the two media, leading to a loss in composite action. The deterioration of full composite action occurs primarily in the link.

**Effective Slab Width** - The effective width $b_{eff}$ of the slab was calculated based on the stress distribution, and also the stiffness of the floor beam outside the link based on measured experimental data. The purpose of calculating $b_{eff}$ was to examine its variation along the test beam, and to compare $b_{eff}$ as defined above with the AISC Specification [20].

The effective slab width based on stress distribution, $b_{eff}^\sigma$, was calculated for the specimens using the available measured data for longitudinal strain $\epsilon_x$. Since it has been found by

previous researchers [48,49] that for cyclic loading conditions the determination of stress from cyclic strain is difficult, $b_{\it eff}^{\sigma}$ was determined only for the first cycle. The concrete stresses were determined from the measured compressive strains using the Hognestad stress-strain relationship for concrete [50]. Then $b_{\it eff}^{\sigma}$ was calculated using the following definition:

$$b_{\it eff}^{\sigma} = \frac{\int \sigma_x(y)\,dy}{\sigma_x(y)_{\max}}$$ (4.7)

where for beam spacing $b$ the limits of integration should not exceed $\pm 0.5b$.

The calculated results for $b_{\it eff}^{\sigma}$ are shown in Figs. 4.56 and 4.57 along with $b_{\it eff}$ based on the AISC Specification. It is apparent from the experimental results that the value of $b_{\it eff}^{\sigma}$ for the composite specimens varies along the beam, and it is a minimum at the link. Furthermore, $b_{\it eff}^{\sigma}$ is smaller at the exterior beams (Specimens A1 and C2) compared to the interior beams (Specimens B1 and B2). The indicated values for $b_{\it eff}^{\sigma}$ represent the upper bound values. Subsequent cycling of a link would likely reduce these values because of the deterioration in the composite action due to slip between the steel beam and the concrete slab as well as cracking of the slab.

Comparing the above results with the AISC Specification shows that outside the link $b_{\it eff}$ is smaller than $b_{\it eff}^{\sigma}$. The variation in $b_{\it eff}$ along the floor beam is also not accounted for by the the AISC Specification. For an interior composite floor beam $b_{\it eff}$ based on the AISC Specification shows a reasonable agreement with the experimental results for $b_{\it eff}^{\sigma}$ at the end of the link. There is less such agreement for the exterior composite floor beams. Nevertheless, the AISC Specification provides a reasonable lower bound for $b_{\it eff}$ for the exterior composite floor beams. Due to the effects of cyclic degregation, the effective width given by the AISC Specification may not agree well with the experimental results from subsequent cycles. This assertion however requires further experimental verification.

The effective slab width $b_{\it eff}^{\theta}$ based on the floor beam stiffness was determined from the rotational stiffness of the floor beam outside the link. The rotations $\Theta^{*}$ and the vertical

displacement $\Delta$ measured at end of a link were used to calculate the rotation $\Theta_{ch}$ from the chord of a floor beam outside the link as shown in Fig. 4.58. Values of moment $M$ and rotation $\Theta_{ch}$ based on the experimental data are plotted on $M$-$\Theta_{ch}$ diagrams in Figs. 4.59 to 4.64. These results show that the beam stiffness outside the link does not experience a significant reduction in stiffness under cyclic action of the link. Furthermore, the cyclic $M$-$\Theta_{ch}$ behavior closely fits a bilinear relationship where the beam stiffness outside the link is greater when subjected to a positive moment than a negative moment.

A linear regression analysis was performed on the $M$-$\Theta_{ch}$ results for each composite specimen in order to establish a bilinear relationship between $M$ and $\Theta_{ch}$. Then using an elastic solution for a simply supported beam subjected to an end moment, the rotational stiffness provides an expression for an estimation of the effective moment of inertia, $I_{eff}$. On this basis:

$$I_{eff} = \frac{ML^*}{3E\Theta_{ch}} \tag{4.8}$$

where $E$ and $L^*$, respectively, are the elastic modulus of the steel beam and the span length of the floor beam between the support and the link, as shown in Fig. 4.58. The effective slab width $b_{eff}^{\Theta}$ was then determined based on the computed values of $I_{eff}$.

The calculated values for $I_{eff}$ in a nondimensionalized form are shown plotted in Fig. 4.65, where $I_{eff}^+$ represents $I_{eff}$ for a positive moment and $I_{eff}^-$ represents $I_{eff}$ for a negative moment. $I$ is the moment of inertia of the steel beam given in Table 2.7. Linear regression analyses were performed on these results to establish the average values for $I_{eff}$ for the exterior and interior composite floor beams. Figure 4.65 indicates the ensuing linear relationships, where $I_{eff}^+$ is equal to $1.37I_{eff}^-$ for the exterior composite floor beams and equal to $2.03I_{eff}^-$ for the interior composite floor beams. It was found that the average value of $I_{eff}^-$ for both the interior and the exterior composite floor beams, respectively, was equal to $1.28I$. Therefore, $I_{eff}^+$ is equal to $1.75I$ for the exterior and $2.60I$ for the interior composite floor beams. The ensuing values for $b_{eff}^{\Theta}$ for positive and negative moment are given in Table 4.11, where $b_{eff}^{\Theta}$

for positive moment is equal to 5.9 in. for the exterior and 17.4 in. for the interior composite floor beams, and is 2.2 in. for both the interior and exterior composite floor beams when subjected to a negative moment.

Comparing the effective width based on beam stiffness with that based on stress distribution, shown in Figs. 4.56 and 4.57, it is apparent that $b_{\it eff}^{\theta}$ is significantly smaller than $b_{\it eff}^{\sigma}$. The AISC Specification substantially overestimates $b_{\it eff}$ for beam stiffness, as indicated in these figures as well as in Table 4.11.

### 4.9. Effectiveness of Floor Slab as Lateral Bracing

It is important to have steel beams adequately braced against lateral movement to prevent lateral-torsional buckling. Otherwise the capacity and ductility of the link can be greatly jeopardized. Lateral-torsional buckling of bare steel beams has been studied extensively in the past, both experimentally and analytically [52,53,54,55]. Less research has been conducted on the lateral-torsional buckling of composite beams [56,57]. Such buckling of composite beams can occur if the applied bending moment causes compression in the bottom flange. Such a bending moment will be referred to as a negative bending moment. The buckling configuration for a composite beam subjected to a negative bending moment is shown in Fig. 4.66. The current SEAOC code for the design of ductile EBFs [58] requires that the top and bottom flanges of the steel beam in an EBF be laterally braced at both ends of a link. The bracing is required to have the strength and stiffness to resist 1.5 percent of the beam flange strength, computed as yield stress times flange area, with a total lateral displacement of less than 0.10 in. Nevertheless, the question remains whether the floor slab alone can provide the necessary restraint thereby avoiding the use of transverse lateral bracing.

To answer this question the twist $\phi_A$ and $\phi_B$ of the steel beam at ends A and B of a link were measured and studied. Figures 4.67 to 4.69 shows the lateral twist developed at each end of the links for bare steel beam Specimens D1 and D2 and also for the composite link of Specimen C2. Specimen D1 had its cross section laterally braced by transverse beams at both

ends of the link. Specimen D2 had its cross section laterally braced, but only at the link end A which was adjacent to the simulated column restraint. Specimen C2 had only the support of the floor slab without the benefit of any transverse beams for lateral bracing. The above figures show that a greater amount of the cross section twist develops in Specimens D2 and C2 compared to that in Specimen D1. Unlike Specimen D1, both link ends in Specimens C2 and D2 developed a drift from the initial position. The twist at both ends of the link for Specimen C2 is approximately two times the twist of Specimen D1 at a link deformation of 0.06 radians, and 1.40 times that of Specimen D1 at a link deformation of 0.08 radians. This indicates that the floor slab alone is not as effective as transverse beams placed at the ends of a link.

For Specimen C2 a ratio $F_N$ was computed for the link end B. The ratio $F_N$ is defined as the flange force $F_T$ relative to the beam flange strength $F_{flg}$. That is:

$$F_N = \frac{F_T}{F_{flg}} = \frac{F_T}{b_f t_f \sigma_{yf}}$$ 

(4.9)

where $b_f$, $t_f$, and $\sigma_{yf}$, respectively, are the flange width, flange thickness, and flange yield stress. The force $F_T$ is determined by calculating the flange forces that resist the torque induced by the applied load $P_B$ causing a lateral movement $\Delta_L$ of the steel section at end B of the link, as shown in Fig. 4.66(b). Only the cases where end B developed a negative moment were considered. Therefore:

$$F_N = \frac{d_b P_B \sin\alpha + \Delta_L P_B \cos\alpha}{d_b b_f t_f \sigma_{yf}}$$

(4.10)

A plot of $P_B$ versus $F_N$ is shown in Fig. 4.70. As $P_B$ increases, the cross section develops a greater amount of twist, resulting in a greater amount of $\Delta_L$. Consequently, a larger magnitude of the force $F_T$ develops in the flanges, resulting in larger ratios of $F_N$. In Fig. 4.70 the ratio $F_N$ is shown to exceed 0.015, the SEAOC limit, and approach the value of 0.04 at the peak of each excursion of the cyclic link deformation history. The values of $\Delta_L$ were plotted also against $P_B$ as shown in Fig. 4.71. These results indicate that the floor slab will restrain the flange from developing an amount of $\Delta_L$ which exceeds the SEAOC limit of

0.10 inches by no more than 10 percent.

The above results give an indication that by limiting $\Delta_L$ the floor slab does provide some restraint to the steel beam. However, as was found by comparing the twist of the cross sections at the link ends for braced and unbraced steel sections, the slab is not as effective as the transverse beams in laterally bracing the link ends. Furthermore, the ratio $F_N$ exceeds the recommended SEAOC limit of 0.015. Using the maximum values of the ratio $F_N$ shown in Fig. 4.70 for designing the lateral bracing for composite links would be conservative, since less force is required to prevent lateral-torsional buckling then to restore the cross section to a stable configuration. In order to provide general design guidelines, additional experiments are necessary which specifically address the lateral-torsional buckling of composite links.

## 4.10. Conclusions

Based on the analysis of the experimental behavior of the bare steel and composite links the following conclusions can be established:

(1) Composite links have a greater initial elastic stiffness than bare steel links. The composite links in the K-braced EBF subassemblies developed larger initial elastic stiffness than the composite links in the V-braced EBF subassemblies, with the interior composite links having a greater initial elastic stiffness than the exterior composite links.

(2) Composite links have a greater shear yield strength than bare steel links, with the interior composite links in the EBF subassemblies having the largest shear yield strength. The yield limit state for the composite links may be considered to be bounded by $V_p$ and $M_p$ as for the bare steel links.

(3) After the initial shear yielding, the links exhibit a combined isotropic and kinematic strain hardening. The isotropic hardening in composite links is less than that observed for the bare steel links. However the stiffness of a fully plastic composite link is greater than that of the corresponding bare steel link.

(4) The interior composite links of EBF subassemblies have a greater shear capacity than

bare steel links.

(5) Most of the floor slab damage occurs in the vicinity of a link and the slip between the steel beam and the concrete floor slab occurs largely at the link. The concrete strain in the floor slab was found to be greatest in the vicinity of the link, increasing during cyclic deformation as a result of cracking in the concrete. The composite action deteriorated in the link under cyclic loading, and the positive moment capacity based on full composite action generally was not developed. However, the end moments developed in the composite links were larger than in bare steel links.

(6) With the same link deformation history the energy dissipation of a composite link is greater than that of a bare steel link. The amount of energy dissipated by a link depends on the link deformation history.

(7) Link web buckling results in the deterioration of the link's energy dissipation capacity. Web buckling is reasonably well predicted by the plastic plate shear buckling theory [7].

(8) Composite links develop less axial shortening than bare steel links. Composite links located away from the edges of the floor slab are better axially restrained by the floor slab and consequently develop less axial shortening.

(9) The beam stiffness of the composite floor beam outside the link do not show significant deterioration under cyclic loading. The composite beam stiffness under positive moment is greater than that under negative moment, which in turn is greater than that of the bare steel beam.

(10) Due to the elastic curvature of the floor beam outside the link, the maximum vertical displacement of the floor slab occurs outside of the link above a floor beam.

(11) The outrigger effect depends on the beam spacing, mechanical properties of the floor slab, and the torsional rigidity of the floor beams. The outrigger effect for the specimens used in these test was found to be minimal.

(12) The effective slab width based on experimentally determined stress distribution is a

minimum at the link and increases along the floor beam outside the link. The calculated effective slab width to provide an equivalent composite beam stiffness is less than the calculated effective slab width based on stress distribution. For the initial cycles before major slab damage occurs the AISC Specification [20] provides a reasonable estimate of the effective slab width. However, the AISC Specification effective slab width for determining the stiffness of the composite floor beams outside the link results in excessive stiffness.

(13)    The floor slab is not as effective as transverse beams in providing lateral bracing at the ends of a link for preventing lateral-torsional buckling of the beam.

# CHAPTER 5

# ANALYSIS OF COMPOSITE FLOOR SYSTEMS IN EBFs

## 5.1. General

In order to assess the effect of the floor slab on the behavior of the floor beam in EBFs, analyses were performed on composite floor systems of these structural systems. Both an interior and an exterior floor beam were analyzed. Consideration was given to the orthotropic behavior of the floor slab and spacing of the adjacent floor beams, requiring several analysis. The analyses of the EBF floor systems required applying concentrated forces to the models to simulate vertical components of axial brace forces. Additional load patterns were also considered in order to determine the effect of spatial distribution of the loads applied to the floor system. In these analyses the effective slab widths based on the obtained stress distribution were determined. In addition, the effective moments of inertia of the composite floor beams outside the link were also found. These values were then compared to the experimental results and the AISC Specification [20]. The information on internal forces in the floor beams and floor slabs made it possible to evaluate the contributions of each to the composite floor system.

To analyze the floor system, the floor slab was described using an orthotropic elastic plane stress theory combined with an orthotropic thin elastic plate theory. The first one of these theories was incorporated into the analysis by deriving a differential equation in terms of a stress function for a plane orthotropic material. The second theory was included into the analysis by considering a differential equation expressed in terms of transverse displacements describing the equilibrium of an orthotropic plate. The effect of in-plane forces on the floor slab behavior were considered not to have a significant effect on the stability of the floor system, and therefore were neglected in the equilibrium equation. The floor system's steel beams were described by an elastic beam theory.

Solutions of the differential equations describing the behavior of the floor system were

78

obtained by enforcing equilibrium and compatibility conditions between the floor beam and slab together with the appropriate boundary conditions. The stresses in the middle surface of the floor slab were determined from a stress function while the internal forces in the floor slab and the floor beam were found using transverse displacements.

## 5.2. Plane Stress Theory for an Orthotropic Material

The differential equation in terms of a stress function for an orthotropic material in the state of plane stress can be derived by considering the compatibility equation of a thin membrane in the x-y plane (Eq. 5.1), Hooke's law for an orthotropic material (Eqs. 5.2), and the momentum balance equations for static equilibrium (Eqs. 5.3), leading to the following relations [60,61,68]. That is:

$$\frac{\partial^2 \epsilon_x}{\partial y^2} + \frac{\partial^2 \epsilon_y}{\partial x^2} = 2 \frac{\partial^2 \epsilon_{xy}}{\partial x \, \partial y} \tag{5.1}$$

$$\epsilon_x = \frac{\sigma_x}{E_x} - \nu_y \frac{\sigma_y}{E_y} \tag{5.2a}$$

$$\epsilon_y = \frac{\sigma_y}{E_y} - \nu_x \frac{\sigma_x}{E_x} \tag{5.2b}$$

$$\frac{\partial \sigma_x}{\partial x} + \frac{\partial \sigma_{xy}}{\partial y} + X = 0 \tag{5.3a}$$

$$\frac{\partial \sigma_y}{\partial y} + \frac{\partial \sigma_{xy}}{\partial x} + Y = 0 \tag{5.3b}$$

In the above set of equations $\epsilon$, $\sigma$, $\nu$, and $E$, respectively, represent strain, stress, Poisson's ratio, and the elastic modulus. A single subscript $x$ or $y$ indicates the direction in which the given quantity is acting. Double subscripts represent shear strain and shear stress (e.g. $2\epsilon_{xy}$ and $\sigma_{xy}$) in the x-y plane. The terms $X$ and $Y$ in the momentum balance equations represent, respectively, the body forces in the x and y-direction. The above compatibility equation is applicable only for small deformations [61].

By noting that:

$$2\epsilon_{xy} = \frac{\sigma_{xy}}{G_{xy}}$$ (5.4)

where

$$G_{xy} \approx \frac{\sqrt{E_x E_y}}{2\left(1 + \sqrt{v_x v_y}\right)}$$

and substituting Eqs. 5.2 and 5.4 into Eq. 5.1, one obtains:

$$\frac{\partial^2}{\partial y^2}\left[\frac{\sigma_x}{E_x} - v_y \frac{\sigma_y}{E_y}\right] + \frac{\partial^2}{\partial x^2}\left[\frac{\sigma_y}{E_y} - v_x \frac{\sigma_x}{E_x}\right] = \frac{1}{G_{xy}}\frac{\partial^2 \sigma_{xy}}{\partial x \partial y}$$ (5.5)

Using Eqs. 5.3 (a) and 5.3 (b) for constant body forces, it can be shown [61]:

$$\frac{\partial^2 \sigma_x}{\partial x^2} + \frac{\partial^2 \sigma_y}{\partial y^2} = -2\frac{\partial^2 \sigma_{xy}}{\partial x \partial y}$$ (5.6)

Therefore Eq. 5.5 can be written as:

$$\frac{1}{E_x}\left[\left(\frac{E_x}{E_y}\right)^{0.5}\frac{\partial^2 \sigma_x}{\partial x^2} + \frac{\partial^2 \sigma_x}{\partial y^2} + \frac{E_x}{E_y}\frac{\partial^2 \sigma_y}{\partial x^2} + \left(\frac{E_x}{E_y}\right)^{0.5}\frac{\partial^2 \sigma_y}{\partial y^2}\right] +$$

$$\frac{1}{E_x}\left[\left(\frac{v_x v_y E_x}{E_y}\right)^{0.5}\left(\frac{\partial^2 \sigma_x}{\partial x^2} + \frac{\partial^2 \sigma_y}{\partial y^2}\right) - v_x\frac{\partial^2 \sigma_x}{\partial x^2} - v_y\frac{E_x}{E_y}\frac{\partial^2 \sigma_y}{\partial y^2}\right] = 0$$ (5.7)

Applying Betti's reciprocal theorem to a plane stress element results in the following:

$$\sigma_{y_1} \epsilon_{y_2} = \sigma_{x_2} \epsilon_{x_1}$$ (5.8)

where $\sigma_{y_1}$, $\epsilon_{y_2}$ and $\sigma_{x_2}$, $\epsilon_{x_1}$ are stresses and strains corresponding to the two loading conditions shown in Fig. 5.1. Substituting Hooke's Law Eqs. 5.2 into Eq. 5.8 leads to the following relation:

$$v_x E_y = v_y E_x$$ (5.9)

Substitution of Eq. 5.9 into Eq. 5.7 leads to the following simplified result:

$$\left(\frac{E_x}{E_y}\right)^{0.5} \frac{\partial^2 \sigma_x}{\partial x^2} + \frac{\partial^2 \sigma_x}{\partial y^2} + \frac{E_x}{E_y} \frac{\partial^2 \sigma_y}{\partial x^2} + \left(\frac{E_x}{E_y}\right)^{0.5} \frac{\partial^2 \sigma_y}{\partial y^2} = 0 \qquad (5.10)$$

The Airy's stress function $\phi(x,y)$ satisfying the momentum balance equations with constant body forces defines stresses as follows:

$$\sigma_x = \frac{\partial^2 \phi}{\partial y^2} \qquad (5.11a)$$

$$\sigma_y = \frac{\partial^2 \phi}{\partial x^2} \qquad (5.11b)$$

$$\sigma_{xy} = -\frac{\partial^2 \phi}{\partial x \partial y} \qquad (5.11c)$$

On substituting these relations into Eq. 5.10 the following differential equation for an orthotropic material in the state of plane stress is obtained:

$$\frac{E_x}{E_y} \frac{\partial^4 \phi}{\partial x^4} + 2 \left(\frac{E_x}{E_y}\right)^{0.5} \frac{\partial^4 \phi}{\partial x^2 \partial y^2} + \frac{\partial^4 \phi}{\partial y^4} = 0 \qquad (5.12)$$

## 5.3. Orthotropic Plate Theory

The governoring differential equation for an orthotropic plate is readily available in the literature [62,63], and is often referred to as the Huber equation. It reads as follows:

$$D_x \frac{\partial^4 w}{\partial x^4} + 2H \frac{\partial^4 w}{\partial x^2 \partial y^2} + D_y \frac{\partial^4 w}{\partial y^4} = q_z(x,y) \qquad (5.13)$$

where $H$ is called Huber's constant, and

$w$ = transverse displacement in the z-direction,

$D_x$ = the flexural rigidity of the orthotropic plate associated with the x-direction,

$D_y$ = the flexural rigidity of the orthotropic plate associated with the y-direction,

$2H = D_x \nu_y + D_y \nu_x + 4D_{xy}$,

$q_z(x,y)$ = distributed transverse surface load.

Assuming that Huber's hypothesis for reinforced concrete slabs holds [68], the torsional rigidity $D_{xy}$ can be approximated as:

$$4D_{xy} = 2(1 - \sqrt{v_x v_y})\sqrt{D_x D_y} \tag{5.14}$$

Since by using Betti's reciprocal theorem it can be shown that:

$$v_x D_y = v_y D_x \tag{5.15}$$

the Huber's constant can be written as:

$$2H = 2\sqrt{D_x D_y} \tag{5.16}$$

Taking advantage of this fact, the Huber equation can be rewritten in the following form:

$$\frac{D_x}{D_y}\frac{\partial^4 w}{\partial x^4} + 2\left(\frac{D_x}{D_y}\right)^{0.5}\frac{\partial^4 w}{\partial x^2 \partial y^2} + \frac{\partial^4 w}{\partial y^4} = \frac{q_z(x,y)}{D_y} \tag{5.17}$$

Once the displacement field is known which satisfies the Huber equation and the appropriate boundary conditions, the internal forces of the orthotropic plate can be determined using the following relations [62]:

$$m_x = -D_x\left[\frac{\partial^2 w}{\partial x^2} + v_y\frac{\partial^2 w}{\partial y^2}\right] \tag{5.18a}$$

$$m_y = -D_y\left[\frac{\partial^2 w}{\partial y^2} + v_x\frac{\partial^2 w}{\partial x^2}\right] \tag{5.18b}$$

$$m_{xy} = -(1 - \sqrt{v_x v_y})\sqrt{D_x D_y}\frac{\partial^2 w}{\partial x \partial y} \tag{5.18c}$$

$$q_x = -D_x\frac{\partial^3 w}{\partial x^3} - \sqrt{D_x D_y}\frac{\partial^3 w}{\partial y^2 \partial x} \tag{5.18d}$$

$$q_y = -D_y\frac{\partial^3 w}{\partial y^3} - \sqrt{D_x D_y}\frac{\partial^3 w}{\partial x^2 \partial y} \tag{5.18e}$$

where $m_x$, $m_y$, $m_{xy}$, respectively, are the moment associated with the x-direction, the moment associated with the y-direction, and the twisting moment associated with the x and y-directions in the floor slab. The quantities $q_x$ and $q_y$, respectively, are the transverse shear forces associated with the x-direction and y-direction.

## 5.4. Composite Beam Models

Solutions of the governoring differential equations (Eqs. 5.12 and 5.17) were sought which would be suitable for the boundary conditions of composite floor beams to be analyzed. K-braced EBFs which had composite interior and exterior floor beams were of particular interest. The appropriate boundary conditions for these two cases are shown in Figs. 5.2 and 5.3. In both cases the floor beam and slab are simply supported at both ends and correspond with the experimental setup described in Chapter 2. However, there are some differences between the models and the experimental setup. For the interior beam model the floor slab extends laterally in both directions to infinity, and in one direction for the exterior model, as shown in Figs. 5.2 and 5.3. Moreover, the floor beam parallel to the exterior beam was not included in the exterior floor beam analysis in order not to exceed the number of possible boundary conditions which could be satisfied by the selected solution. Further, in order to simplify the problem the overhanging portion of the floor slab for the exterior floor beam analysis was not included in the model. Finally, for both models the floor slab at both ends were assumed to be simply supported.

It is believed that the above boundary conditions for the models should lead to reasonable results, since the floor slab in EBFs is wide in relation to the beam span length. Furthermore, because of the dominate effect caused by the applied concentrated forces at both ends of the link, the attenuation of deformations and internal forces in the floor slab should be localized. This phenomenon was verified both analytically and experimentally.

## 5.5. Solution Procedure

Being guided by the Levy method and a known rigorous solution for biharmonic equations [62], solutions involving a series of harmonics with unknown coefficients were used to solve the governoring differential equations, Eqs. 5.12 and 5.17. The harmonic functions were taken as:

$$\phi(x,y) = \sum_{n=1}^{\infty} \left[ A_{n_1} e^{-\alpha_n \xi y} + A_{n_2} e^{\alpha_n \xi y} + A_{n_3} y e^{-\alpha_n \xi y} + A_{n_4} y e^{\alpha_n \xi y} \right] \sin \alpha_n x \qquad (5.19)$$

$$w(x,y) = \sum_{n=1}^{\infty} \left[ \frac{2 q_o L^4}{(n \pi)^5 D_y} (1 - \cos n \pi) + B_{n_1} e^{-\alpha_n \lambda y} + B_{n_2} e^{\alpha_n \lambda y} + \right.$$

$$\left. B_{n_3} \lambda y e^{-\alpha_n \lambda y} + B_{n_4} \lambda y e^{\alpha_n \lambda y} \right] \sin \alpha_n x \qquad (5.20)$$

in which

$$\alpha_n = \frac{n \pi}{L}$$

$$\xi^4 = \frac{E_x}{E_y}$$

$$\lambda^4 = \frac{D_x}{D_y}$$

In the solution of the Huber equation for the transverse displacements (Eq. 5.20) it was assumed that a uniform surface gravity load of magnitude $q_o$ acts on the floor slab.

The sine series used in Eqs. 5.19 and 5.20 satisfy the four boundary conditions at the simple supports where $x=0$ and $x=L$. However on noting Eq. 5.11c it can be seen that the shear stress $\sigma_{xy}$ in the plane of the floor slab does not vanish at the ends of the floor slab and thereby violates a boundary condition. Fortunately, previous research [64] has shown that even without satisfying this boundary condition the solution based on Eq. 5.19 leads to reasonable results which agree with experimental measurements of deflection and strain.

### 5.5.1. Solution for Interior Composite Beam Model

For the interior floor beam model the remaining boundary conditions shown in Fig. 5.2 were applied to Eqs. 5.19 and 5.20 to solve for the unknown coefficients. Since a plane of symmetry exists around $y=0$, only the region in the positive y-direction need be considered. Further since at $y=\infty$ the solution must be bounded,

$$A_{n_2} = A_{n_4} = 0 \qquad\qquad\qquad (5.21a)$$

$$B_{n_2} = B_{n_4} = 0 \qquad\qquad\qquad (5.21b)$$

Using Eq. 5.2b together with Eqs. 5.11a and 5.11b one obtains:

$$v = \int \epsilon_y \, dy$$

$$= \int \left[ \frac{1}{E_y} \frac{\partial^2 \phi}{\partial x^2} - \frac{v_x}{E_x} \frac{\partial^2 \phi}{\partial y^2} \right] dy \qquad\qquad (5.22)$$

Then applying the condition that $v=0$ at $y=0$, a relationship between the unknown coefficients $A_{n_1}$ and $A_{n_3}$, is established:

$$A_{n_1} = -A_{n_3} \frac{\Lambda}{\alpha_n \xi} \qquad\qquad\qquad (5.23)$$

where

$$\Lambda = \frac{1 - \xi^2 v_x}{1 + \xi^2 v_x}$$

Substituting these relations into Eq. 5.19, one obtains the required stress function:

$$\phi(x,y) = \sum_{n=1}^{\infty} A_{n_3} \left[ -\frac{\Lambda}{\alpha_n \xi} + y \right] e^{-\alpha_n \xi y} \sin\alpha_n x \qquad\qquad (5.24)$$

Since the edge floor beams are at distances $b$ away from the interior floor beam, the vertical displacement $w$ was set equal to zero at $y=b$. This is an approximation as these beams are not completely rigid. However, since only the behavior of the slab in the proximity of the link is of interest such an approximation appears to be satisfactory. Enforcing this condition in Eq. 5.20 results in the following relationship between the unknown coefficients $B_{n_1}$ and $B_{n_3}$:

$$B_{n_1} = -\left[ B_{n_3} \lambda b + q_n e^{\alpha_n \lambda b} \right] \qquad\qquad (5.25)$$

Upon substituting $B_{n_1}$ into Eq. 5.20, the expression for the transverse displacement reads:

$$w(x,y) = \sum_{i=1}^{\infty} \left[ q_n \left( 1 - e^{-\alpha_n \lambda(y-b)} \right) + B_{n_3} \lambda(y-b) e^{-\alpha_n \lambda y} \right] \sin\alpha_n x \qquad\qquad (5.26)$$

where

$$q_n = \frac{2q_oL^4}{(n\pi)^5 D_y}(1 - \cos n\pi)$$

To impose the equilibrium conditions between the floor beam and the slab, reference is made to Fig. 5.4 which shows the free body diagram of an element of length $dx$ at the interior floor beam-slab juncture. Consideration of vertical equilibrium and moment equilibrium of the free body and using the middle surface of the floor slab as a reference plane, results in the following relationships:

$$\frac{\partial Q_s}{\partial x} + \frac{\partial Q_b}{\partial x} + p(x) - 2S = 0 \tag{5.27}$$

$$\frac{\partial M_s}{\partial x} + \frac{\partial M_b}{\partial x} - Q_s - Q_b + h\frac{\partial F}{\partial x} = 0 \tag{5.28}$$

In Eq. 5.28 the higher order terms have been ignored. Differentiating Eq. 5.28 with respect to $x$ and combining the result with Eq. 5.27 leads to the following:

$$\frac{\partial^2 M_b}{\partial x^2} + \frac{\partial^2 M_s}{\partial x^2} + p(x) - 2S = -h\frac{\partial^2 F}{\partial x^2} \tag{5.29}$$

where

$$\frac{\partial^2 M_b}{\partial x^2} = -EI\frac{\partial^4 w}{\partial x^4}$$

$$\frac{\partial^2 M_s}{\partial x^2} = -D_x\left[\frac{\partial^4 w}{\partial x^4} + v_y\frac{\partial^4 w}{\partial x^2\partial y^2}\right]$$

$$S = \frac{\partial m_y}{\partial y} + \frac{\partial m_{xy}}{\partial x} + \frac{\partial m_{yx}}{\partial x}$$

$$= -D_y\left[\frac{\partial^3 w}{\partial y^3} + v_x\frac{\partial^3 w}{\partial x^2\partial y}\right] - 2\sqrt{D_xD_y}(1 - \sqrt{v_xv_y})\frac{\partial^3 w}{\partial x^2\partial y}$$

$$\frac{\partial^2 F}{\partial x^2} = \frac{\partial^2}{\partial x^2}2t\int_0^\infty \sigma_x dy$$

and,

$p(x)$ = distributed transverse load acting directly on the interior floor beam,

$EI$ = flexural rigidity of the floor beam,

$S$ = transverse shear force per unit length acting on the y-face of the floor slab.

$t$ = thickness of floor slab,

The distributed transverse load $p(x)$ acting directly on the interior floor beam must be expressed in terms of a Fourier series, considering only the harmonics associated with $\sin\alpha_n x$, i.e.,

$$p(x) = \sum_{n=1}^{\infty} p_n \sin\alpha_n x \qquad (5.30)$$

where

$$p_n = \frac{2}{L}\int_0^L p(x)\sin\alpha_n x \ dx \qquad (5.31)$$

A concentrated force of $P$ applied at a distance $a$ from a support, as shown in Fig. 5.5, can be expressed as a Fourier series by using a Dirac delta function, i.e.,

$$P(x) = P\delta(x - a) \qquad (5.32)$$

where $\delta(x - a)$ = the Dirac delta function for a unit concentrated force applied at a positive distance $a$ from the origin of the x-axis. Upon employing this in Eq. 5.31 the amplitude of each harmonic is determined, where for the $n^{th}$ harmonic:

$$p_n = \frac{2P}{L}\sin\alpha_n a$$

By substituting Eqs. 5.11a, 5.24, and 5.26 into Eq. 5.29, the equilibrium condition at the beam-slab interface, where $y=0$, leads to a relationship between the unknown coefficients $A_{n_3}$ and $B_{n_3}$, reading:

$$B_{n_3}\left[\alpha_n^4 b\lambda(D_x + EI) - D_x\nu_y\alpha_n^3\lambda^2(2 + \alpha_n\lambda b) + \right.$$

$$\left. 2D_y\alpha_n^2\lambda^3(3 + \alpha_n\lambda b) - \Gamma\alpha_n^2\lambda(1 + \alpha_n\lambda b)\right] -$$

$$q_n\left[\alpha_n^4(D_x + EI)\left(1 - e^{\alpha_n\lambda b}\right) + D_x\nu_y\alpha_n^4\lambda^2 e^{\alpha_n\lambda b} - \right.$$

$$2D_y\alpha_n^3\lambda^3e^{\alpha_n\lambda b} + 2\Gamma\alpha_n^3\lambda e^{\alpha_n\lambda b}\Big] + p_n$$

$$= -A_{n_3}\Big[2th\,\alpha_n^2(\Lambda + 1)\Big] \tag{5.33}$$

where

$$\Gamma = D_y\nu_x + 2\sqrt{D_xD_y}(1 - \sqrt{\nu_y\nu_x})$$

The condition of compatibility between the floor beam and the slab at the interior beam-slab juncture was enforced assuming that plane sections remain plane, and that slip does not occur between the two media. Therefore, the strain profile through the depth of the composite floor beam is as shown in Fig. 5.6. As a result, the strain in the bottom flange of the floor beam, $\epsilon_b$, can be written in terms of the strain, $\epsilon_m$, at the middle surface of the floor slab in the x-direction, where:

$$\epsilon_m = -\left[\frac{0.5t + d_b - NA}{NA}\right]\epsilon_b$$

$$= \Psi\epsilon_b \tag{5.34}$$

in which NA is the location of the neutral axis in the floor beam, referenced from the bottom flange. By simple beam theory $\epsilon_b$ is equal to:

$$\epsilon_b = \frac{1}{E}\left[\frac{M_bd_b}{2I} + \frac{F}{A}\right] \tag{5.35}$$

and,

$$M_b = -EI\frac{\partial^2w}{\partial x^2} \tag{5.36}$$

The axial force in the interior floor beam, $F$, is equal to the corresponding stress $\sigma_x$ integrated over the slab's cross section. That is:

$$F = 2t\int_0^\infty \sigma_x dy \tag{5.37}$$

where $\sigma_x$ is determined by differentiating the stress function per Eq. 5.11a. In Eq. 5.35 $A$ represents the cross-sectional area of the floor beam. Since $\epsilon_m$ is equivalent to $\epsilon_x$, using Eq.

5.2a together with Eqs. 5.11a, and 5.11b establishes a relationship for $\epsilon_m$ in terms of the stress function $\phi(x,y)$. Then upon substituting Eqs. 5.35, 5.36, and 5.37 into Eq. 5.34 one obtains the following:

$$\frac{1}{E_x}\frac{\partial^2\phi}{\partial y^2} - \frac{v_y}{E_y}\frac{\partial^2\phi}{\partial x^2} = \frac{\Psi}{E}\left[\frac{2t}{A}\int_0^\infty\frac{\partial^2\phi}{\partial y^2}dy - \frac{Ed_b}{2}\frac{\partial^2 w}{\partial x^2}\right]$$

(5.38)

A second expression relating the coefficients $A_{n_j}$ and $B_{n_j}$ evolves by substituting the expressions for the stress function (Eq. 5.24) and transverse displacement (Eq. 5.26) into Eq. 5.38, reading:

$$B_{n_j}\left[-\alpha_n^2\frac{d_b}{2}\lambda b\,\Psi\right] + q_n\alpha_n^2\frac{d_b}{2}\Psi\left(1 - e^{\alpha_n\lambda b}\right)$$

$$= A_{n_j}\left[\frac{2t\Psi}{AE}\left(1 + \Lambda\right) - \Lambda\alpha_n\xi\left(\frac{1}{E_x} + \frac{v_y}{E_y\xi^2}\right) - \frac{2\alpha_n\xi}{E_x}\right]$$

(5.39)

The unknown coefficients $A_{n_j}$ and $B_{n_j}$ can be determined for each harmonic from Eqs. 5.33 and 5.39. The results can then be summed to obtain a solution for the stress function and the transverse displacement per Eqs. 5.24 and 5.26.

Note that in Eq. 5.39 the value of $\Psi$ is unknown until the location of the neutral axis is established. In this investigation an iterative technique was employed by first assuming a location for the neutral axis, leading to initial solutions for the stress function and transverse displacement. The location of the neutral axis was then calculated based on the initial solutions, given as:

$$NA = \frac{\epsilon_b}{\epsilon_b - \epsilon_t}d_b$$

(5.40)

in which $\epsilon_t$ is the strain at the top flange of the floor beam where:

$$\epsilon_t = \frac{1}{E}\left[\frac{F}{A} - \frac{M_b d_b}{2I}\right]$$

If the new location for the neutral axis showed a significant change compared to the assumed

value, then the solutions for the stress function and transverse displacement were recomputed using the new location of the neutral axis. The location of the neutral axis was then again computed and checked with the previous value. This process was repeated until the location of the neutral axis was within a specified tolerance.

The number of harmonics used in the analyses was determined by beginning with a few, and then increasing this number until no significant change occurred in the final results.

It should be pointed out that in solving the governoring differential equations, the condition of zero slope in the y-direction of the interior floor slab above the floor beam was not enforced. That is:

$$\left[ \frac{\partial w}{\partial y} \right]_{y=0} \neq 0 \qquad (5.41)$$

This implies that there is a discontinuity in the slope of the interior floor slab above the floor beam, as shown in Fig. 5.7(a). In experiments it was observed that similar cracks have appeared in the floor slab directly above the link of the floor beam, extending along the beam in the x-direction. This crack developed at about the same time when the initial yielding occurred in the link. Therefore, in the floor slab of an interior EBF the above condition is likely to develop to some degree, and it is believed that the obtained analyses should give reasonable results. These results indicate that the slope of the floor slab in the y-direction above the interior floor beam was small in comparison to the slope in the x-direction for typical span-width ratios of $b/L = 0.40$ to $1.0$. Furthermore, a comparison with solutions where the slope in the y-direction was zero showed no significant difference in the results for the same ratios of $b/L$.

### 5.5.2. Solution for Exterior Composite Beam Model

The boundary conditions for an exterior composite floor beam were shown previously in Fig. 5.3. Since the floor slab is assumed to extend to infinity in the positive y-direction and the solution must be bounded, the following must hold:

$$A_{n_2}^{'} = A_{n_4} = 0 \tag{5.42a}$$

$$B_{n_2} = B_{n_4} = 0 \tag{5.42b}$$

With all of the simple support end conditions being satisfied by Eqs. 5.19 and 5.20, except for the shear stress being equal to zero, the remaining four available boundary conditions in Fig. 5.3 were applied to these equations to solve for the unknown coefficients. These four boundary conditions are sufficient for the solution of Eqs. 5.19 and 5.20.

One of these available four boundary conditions shown in Fig. 5.3 states that $\sigma_y = 0$ at $y = 0$. Therefore,

$$A_{n_1} = 0 \tag{5.43}$$

and the stress function for the exterior floor beam can be written as:

$$\phi(x,y) = \sum_{n=1}^{\infty} A_{n_3} y e^{-\alpha_n \xi y} \sin\alpha_n x \tag{5.44}$$

Enforcing the second boundary condition $m_y = 0$ at $y = 0$ results in the following relationship between the unknown coefficients $B_{n_1}$ and $B_{n_3}$:

$$B_{n_3} = B_{n_1}\left[\frac{\alpha_n}{2} - \frac{v_x \alpha_n}{2\lambda^2}\right] - q_n \frac{v_x \alpha_n}{2\lambda^2} \tag{5.45}$$

where

$$q_n = \frac{2q_o L^4}{(n\pi)^5 D_y}(1 - \cos n\pi)$$

Therefore, the transverse displacement field $w(x,y)$ can be rewritten as:

$$w(x,y) = \sum_{n=1}^{\infty} \left[ q_n\left(1 - \frac{v_x \alpha_n}{2\lambda} y e^{-\alpha_n \lambda y}\right) + \right.$$

$$\left. B_{n_1}\left(1 + \left(\alpha_n - \frac{v_x \alpha_n}{\lambda^2}\right)\frac{\lambda y}{2}\right)e^{-\alpha_n \lambda y} \right]\sin\alpha_n x \tag{5.46}$$

The equilibrium conditions between the floor slab and the exterior floor beam are formu-

lated on the basis of the free body diagram shown in Fig. 5.8. Since the floor slab is only to one side of the exterior floor beam, the transverse shear $S$ and the torsional moment $m_{xy}$ act on the beam as shown in the figure. Using the middle surface of the floor slab as a reference, the vertical equilibrium and moment equilibrium for an element are:

$$\frac{\partial Q_s}{\partial x} + \frac{\partial Q_b}{\partial x} + p(x) - S = 0 \tag{5.47}$$

$$\frac{\partial M_s}{\partial x} + \frac{\partial M_b}{\partial x} + \frac{\partial m_{xy}}{\partial y} - Q_s - Q_b + h\frac{\partial F}{\partial x} = 0 \tag{5.48}$$

In Eq. 5.48 the higher order terms have been neglected. Differentiating Eq. 5.48 with respect to $x$ and combining the result with Eq. 5.47 leads to the following relationship:

$$\frac{\partial^2 M_b}{\partial x^2} + \frac{\partial^2 M_s}{\partial x^2} + \frac{\partial^2 m_{xy}}{\partial x \partial y} + p(x) - S = -h\frac{\partial^2 F}{\partial x^2} \tag{5.49}$$

where for the exterior composite floor beam model:

$$\frac{\partial^2 F}{\partial x^2} = \frac{\partial^2}{\partial x^2} t \int_0^\infty \sigma_x dy$$

$$\frac{\partial^2 m_{xy}}{\partial x \partial y} = -(1 - \sqrt{v_x v_y})\sqrt{D_x D_y}\frac{\partial^4 w}{\partial x^2 \partial y^2} \tag{5.50}$$

The remaining terms in Eq. 5.49 were defined previously for the interior composite floor beam model, Eq. 5.29. By imposing the equilibrium requirements at the beam-slab interface, the following relationships between the unknown coefficients $A_{n_1}$ and $B_{n_1}$ apply:

$$B_{n_1}\left[D_y \alpha_n^2 \lambda^2 \left(3\Omega\alpha_n \lambda - \alpha_n \lambda + v_x \alpha_n^2 - 2\Omega v_x \alpha_n\right) - \alpha_n^4\left(D_x + EI\right) + \right.$$

$$\left. \Gamma\alpha_n^2\lambda\left(\alpha_n - \Omega\right) + 0.5\alpha_n^4 v_x\left(\Gamma - D_y v_x\right)\right] +$$

$$q_n\left[\Xi\alpha_n^2\lambda\left(2D_x v_y \alpha_n \lambda - 3D_y \lambda^2 + \Gamma\right) - \alpha_n^4\left(D_x + EI\right) + 0.5\alpha_n^4 v_x\left(\Gamma - D_y v_x\right)\right] + p_n$$

$$= -A_{n_1}\left[\alpha_n^2 ht\right] \tag{5.51}$$

where

$$\Xi = \frac{\nu_x \alpha_n}{2\lambda^2},$$

$$\Omega = \frac{\alpha_n}{2} - \Xi,$$

$$\Gamma = D_y \nu_x + 2\sqrt{D_x D_y}(1 - \sqrt{\nu_y \nu_x}).$$

The compatibility condition between the exterior floor beam and slab is the same as for the interior composite floor beam model, and Eqs. 5.34 to 5.36 apply here as well, however, the axial force in the exterior floor beam $F$ should be defined as

$$F = t\int_0^\infty \sigma_x dy \qquad (5.52)$$

On following the same procedure that was used in deriving Eq. 5.38, using Eq. 5.52 for the exterior floor one has

$$\frac{1}{E_x}\frac{\partial^2 \phi}{\partial y^2} - \frac{\nu_y}{E_y}\frac{\partial^2 \phi}{\partial x^2} = \frac{\Psi}{E}\left[\frac{t}{A}\int_0^\infty \frac{\partial^2 \phi}{\partial y^2}dy - \frac{Ed_b}{2}\frac{\partial^2 w}{\partial x^2}\right] \qquad (5.53)$$

Upon substituting Eqs. 5.44 and 5.46 into the above equation a second relationship between the unknown coefficients $A_{n_3}$ and $B_{n_1}$ is obtained, reading:

$$B_{n_1}\left[\Psi\alpha_n^2 \frac{d_b}{2}\right] + q_n \Psi\alpha_n^2 \frac{d_b}{2} = A_{n_3}\left[\frac{\Psi t}{AE} - \frac{2\alpha_n \xi}{E_x}\right] \qquad (5.54)$$

The two unknown coefficients $B_{n_1}$ and $A_{n_3}$ were determined by the same iterative procedure that was used for the interior composite floor beam model, except that in the present case $B_{n_1}$ and $A_{n_3}$ were determined using Eqs. 5.51 and 5.54.

## 5.6. Analysis of Composite Floor Slabs

Solutions were obtained for the interior and exterior composite floor beam models by programming on a computer the relevant equations for the two unknown coefficients, and then summing the required number of harmonics. During the iterative process the convergence to a

solution was considered to be satisfactory when the change in the location of the neutral axis between cycles changed by less than 0.01 in. It was found that the number of harmonics, $N_{max}$, needed to obtain an accurate solution depended on the type of loading. Two concentrated loads simulating the vertical components of axial brace forces in an EBF required the largest number of $N_{max}$. For such cases $N_{max}$ was 31.

Altogether, three sets of analyses were performed for both the interior and the exterior composite floor beam models. The first set of these analyses involved modeling the beams use in the experiments. The properties of these beams were based on measured values, Tables 2.3 and 2.7. The orthotropic properties of the floor slab in the models were based on the average of the measured values obtained from the small slab tests listed in Table 2.8. The average values of $D_x$ and $D_y$, respectively, were equal to 2806 k–in$^2$/in and 9109 k–in$^2$/in. Therefore, the extent of slab orthotropy was taken to be

$$\lambda^4 = \frac{D_x}{D_y} \approx \frac{1}{3.25} \tag{5.55}$$

For consistency it was also assumed that

$$\xi^4 = \frac{E_x}{E_y} \approx \frac{1}{3.25} \tag{5.56}$$

The average measured value of 3332 ksi was used for the elastic modulus $E_y$ for the specimen cured conditions listed in Table 2.4. For the floor slab in the x-direction an effective slab thickness $t$ was used which provided the required flexural rigidity $D_x$. The effective slab thickness was based on the following relation [68]:

$$D_x = \frac{E_x t^3}{12(1 - v_x v_y)} \tag{5.57}$$

The value for $v_x$ was calculated using Eq. 5.15, with $v_y$ assumed to be 0.20. $E_x$ followed from Eq. 5.56 knowing $E_y$. Based on these material properties, the effective slab thickness was determined to be 3.2 in.

The second set of analyses was the same as the first set except that an isotropic floor slab was assumed. The slab properties associated with the y-direction of the orthotropic slab in the first set of analyses were used in both directions. The elastic modulus and the flexural rigidity were therefore equal to 3332 ksi and 9109 k–in$^2$/in, with $v_x$ and $v_y$ assumed to be 0.20. The floor slab's thickness was determined by Eq. 5.57 and was again found to be approximately 3.2 in.

The third set of analyses involved modeling a composite floor system consisting of a W18 x 40 steel beam and an orthotropic slab. The floor beam corresponded to the Tsukuba prototype first floor beam [17]. The orthotropic plate parameters $\xi$ and $\lambda$ as well as the moduli $E_x$ and $E_y$ were taken to be the same as in the first set of analyses. An effective slab thickness $t$ equal to 4.8 in. was used. This was determined by scaling the value of $t$ used in the previous analyses by a three halves factor. The flexural rigidities $D_x$ and $D_y$ were obtained from Eqs. 5.57 and 5.55, with a $v_y$ of 0.20 and $v_x$ found from Eq. 5.9. As a result, the values for $D_x$ and $D_y$, respectively, were equal to 9566 k–in$^2$/in and 31090 k–in$^2$/in.

In each set of analyses the spacing of the adjacent floor beams relative to their length was varied for the interior floor beam model, whereas for the exterior floor beam model only the length of the beam was varied. Concentrated forces at the ends of the link were applied to the models in each set of analyses to simulate the loading conditions of the floor beams in EBFs. Additional load cases for the first two sets of analyses were analyzed, which included gravity load, a line load applied to the floor beam, and a concentrated load applied at midspan of the beam.

## 5.7. Results of Analysis of Composite Floor Slabs

### 5.7.1. Verification of Formulations

An exterior composite link in the K-braced EBF subassembly was analyzed using the exterior floor beam model by applying at each end of the link concentrated forces to cause initial link yielding. The floor beam modeled was similar to Specimen A1 tested in the

experiments. The resulting vertical displacements of the floor system are shown in Figs. 5.9 and 5.10. These results correspond to a link deformation $\gamma$ of approximately 0.006 rad. Measured values of floor deflections were not available at this deformation, however, Figs. 4.26 and 4.27 show the earliest recorded values for Specimen A1, which were measured at a $\gamma$ of 0.01 rad. A comparison between the results of analysis and measured values indicates that both have a similar displacement pattern with maximum displacements occurring beyond the ends of the link. In Fig. 4.27 the measured relative displacement between the maximum and minimum transverse displacement contours, $\Delta_r$, is 0.28 in., while the calculated result in Fig. 5.10 indicates a displacement of 0.16 in. This discrepancy is to be expected since at a $\gamma$ of 0.01 rad. yielding of Specimen A1 had already occurred, whereas the model was assumed to remain elastic. By linear extrapolation to a $\gamma$ of 0.007 rad. the value of $\Delta_r$ at yielding of Specimen A1 was estimated to be approximately 0.20 in. This compares reasonably well with the model results.

Plots of calculated stresses $\sigma_x$ in the floor slab are shown in Figs. 5.11 and 5.12. These results indicate that the largest stress $\sigma_x$ develops near the ends of the link at the concentrated forces. It was interesting to note that initial cracking of the floor slab in Specimen A1 had developed near these locations.

In Fig. 5.13 the calculated strains $\epsilon_x$ at the top of the floor slab are compared with the measured values for Specimen A1 during Cycle 1 at a $\gamma$ of -0.02 rad. In general, the calculated quantities agree reasonably well with measured ones. The analysis correctly predicts larger values of $\epsilon_x$ in sections that are closer to the link. The location of the neutral axis along the beam, referenced from the bottom beam flange, is shown in Fig. 5.14. The analysis shows that the location of the neutral axis varies along the span, reaching a minimum at the link. This result agrees with the experimental findings.

Analytically determined vertical displacements of the floor slab for the interior floor beam are shown in Figs. 5.15 and 5.16. These displacements are for equally applied forces of 110 kips at the ends of the link. No vertical displacements of the floor slab were made for the

corresponding test specimen (Specimen B1). However, the results appear to be reasonable. The calculated $\Delta_r$ of 0.14 in. for this interior floor beam model is 88 percent of that which developed in the exterior floor beam model. The calculated stresses $\sigma_x$ for this case are shown in Figs. 5.17 and 5.18. Their trend is similar to those for the exterior beam, and as before the largest magnitudes of stress develop at the ends of the link.

In Fig. 5.19 the strains $\epsilon_x$ on top of the slab for the interior floor beam model are compared to the measured values for Specimen B1 during Cycle 1 at a $\gamma$ of -0.02 rad. The calculated results shown in Fig. 5.19 compare reasonably well with the measured values. In all cases larger values of $\epsilon_x$ develop in sections that are closer to the end of the link. Based on the analytical and experimental results shown in Fig. 5.20, the location of the neutral axis before yielding occurs compares very favorably.

## 5.7.2. Effective Slab Width

From the analyses the effective slab width $b_{eff}^\sigma$ was determined based on results for stress distribution. In calculations, the stress $\sigma_x$ at the middle surface of the slab was used resulting in the following expression for a section at x:

$$b_{eff}^\sigma = \frac{\int \sigma_x(y)\,dy}{\left[\sigma_x(y)\right]_{y=0}} \tag{5.58}$$

For consistency with the adopted analytical model, the limits of integration for the exterior composite floor beam model are from zero to $\infty$, while for the interior composite floor beam model these limits are $\pm\infty$. However in designing a composite beam, consideration must be given to the adjacent floor beams sharing the applied vertical load. Therefore, $b_{eff}^\sigma$ should not exceed the width of $b$ for an interior composite beam and $0.5b$ plus an exterior overhang for an exterior composite beam.

Analytical and experimental results for $b_{eff}^\sigma$ are shown in Figs. 5.21 and 5.22 for the exterior and interior composite floor beams (Specimens A1 and B1). The effective slab width

according to the AISC Specification is also shown in these figures. The recommended maximum values of $b_{eff}^{\sigma}$ limited by the spacing of the adjacent beams are also indicated. In order to be consistent with the analytical model, the contribution of the overhang was removed when determining $b_{eff}^{\sigma}$ for the exterior beam, Specimen A1. Both theoretical analyses show that $b_{eff}^{\sigma}$ are minimum at the links. The overall comparisons given in Figs. 5.21 and 5.22 show that the analytical and experimental results develop the same trend. The recommended values of $b_{eff}^{\sigma}$ by the AISC Specification differ from those indicated by the analytical results. Compared to the AISC Specification, the analysis results indicate a smaller value of $b_{eff}^{\sigma}$ in the link.

The effect of slab orthotropy as well as loading conditions were studied by analyzing interior composite floor beam models with orthotropic and isotropic floor slabs for different loading conditions. The floor beam was a W12 x 19 section while the slab had a 3.2 in. effective thickness. The loading conditions included the effect of EBF brace force simulation, a concentrated load at midspan, a uniform load $p(x)$ applied directly to the floor beam over half of the span length, and a uniform dead load acting on the floor slab. The variation of $b_{eff}^{\sigma}$ for these cases is shown in Figs. 5.23 to 5.26. These results indicate that $b_{eff}^{\sigma}$ varies for different load conditions and the degree of slab orthotropy. In a study simulating the loading conditions in the test specimen (Fig. 5.23), a minimum $b_{eff}^{\sigma}$ occurs at the link. However, for the case involving a uniform dead load (Fig. 5.26), $b_{eff}^{\sigma}$ has a maximum value in the region of large moment. In all cases somewhat larger values of $b_{eff}^{\sigma}$ occur for orthotropic slabs compared to the isotropic ones.

The variation of $b_{eff}^{\sigma}$ for an interior composite beam as a function of $b/L$ is shown in Fig. 5.27. These results are from three sets of analyses and include $b_{eff}^{\sigma}$ at the end of the link, and at one-quarter of the length $L^{*}$ from the support. As shown in Fig. 5.27, $L^{*}$ is the distance between a link and a support. The different analyses are identified in the figure by their floor slab and beam sizes. In figure 5.27 $b_{eff}^{\sigma}$ has been normalized with respect to the beam

spacing $b$, and its upper limit has been set to $b$. These results show that in all cases $b_{eff}^{\sigma}$ decreases with larger ratios of $b/L$. The value of $b_{eff}^{\sigma}$ is less at the end of the link compared to that outside the link. Orthotropic slabs, where $D_y$ is greater then $D_x$, have greater effective widths compared to the corresponding isotropic floor slabs. Therefore it appears that by increasing the floor slab flexural rigidity in the direction of the adjacent floor beam relative to the flexural rigidity in the longitudinal direction of the floor beam has the same effect as decreasing the beam spacing of floor beams with an isotropic floor slab. At the ends of a link $b_{eff}^{\sigma}$ by analysis is greater for the prototype floor beam (W18 x 40 section with a t=4.8 in.) than for the test specimens (W12 x 19 section with a t=3.2 in.). Analyses shows that at the ends of a link $b_{eff}^{\sigma}$ is less than by the AISC Specification [20]. The degree of overestimation of $b_{eff}^{\sigma}$ by the AISC Specification at the end of the link increases for the smaller ratios of $b/L$. Towards the supports the AISC Specification predicts a smaller value of $b_{eff}^{\sigma}$ compared to the analysis results.

The variation of $b_{eff}^{\sigma}$ for an exterior composite beam as a function of beam span $L$ is shown in Fig. 5.28 for three sets of analyses. These results show that $b_{eff}^{\sigma}$ decreases as the span length decreases. Furthermore, $b_{eff}^{\sigma}$ is less at the end of a link compared to that outside a link. As for the interior composite beam, the exterior beams with isotropic floor slabs appear to have smaller values of $b_{eff}^{\sigma}$ compared to the corresponding composite beams with orthotropic floor slabs. The AISC Specification predicts a larger $b_{eff}^{\sigma}$ at the end of a link compared to the analyses. Towards the supports, $b_{eff}^{\sigma}$ from the analyses is greater then that given by the AISC Specification.

## 5.7.3. Effective Moment of Inertia

An effective moment of inertia $I_{eff}$ of the composite beam was determined analytically from the rotation of the beam outside the link. First the beam rotation $\Theta_{ch}$ from the chord

was determined, see Fig. 4.58. This rotation was then equated to an elastic solution for end rotation of a simply supported beam subjected to an end moment. On this basis:

$$I_{eff} = \frac{ML^*}{3E\,\Theta_{ch}}$$

(5.59)

where $M$ is the moment at the end of a composite beam of length $L^*$.

The variation of $I_{eff}$ for the interior composite beam as a function of $b/L$ is shown in Fig. 5.29. In this figure $I_{eff}$ has been normalized with respect to the moment of inertia of a bare beam, $I$. The results show a similar trend as that for the $b_{eff}^{\sigma}$, where $I_{eff}$ increases as the ratio of $b/L$ decreases. However, $I_{eff}$ for the composite beams with an isotropic floor slab are greater than those for the orthotropic floor slabs. The average experimental value for $I_{eff}$ is shown to be somewhat greater then the analysis results. The AISC Specification [20] gives a greater value for the effective slab width than the analytical prediction if calculations are based on the span length $L$. However, a better agreement is achieved if the AISC effective slab width is based on the length $L^*$ outside the link. Nevertheless, $I_{eff}$ is overestimated by the AISC Specification compared to the results of the orthotropic analyses, where this difference becomes more pronounced for smaller ratios of $b/L$.

A similar graph as above of the variation of $I_{eff}$ for the exterior composite beam is presented in Fig. 5.30. As in the analysis of the interior composite beams, the computed results shown in Fig. 5.30 indicate that values of $b_{eff}^{\sigma}$ are greater for isotropic floor slabs than those for the orthotropic ones. Furthermore, $I_{eff}$ decreases as the span length $L^*$ decreases. The average experimental value of $I_{eff}$ for the exterior specimens agrees reasonably well with the results of the analysis. For this case the AISC Code provides better agreement than before, particularly if the length $L^*$ is used.

### 5.7.4. Distribution of Internal Forces

Axial force, moment and shear forces for the slab and beam were determined along the beam using the analysis results for transverse displacements and the stress function. This was

carried out for both for the interior and exterior K-braced EBF subassemblies. In this study concentrated forces of equal magnitude were applied at the ends of the links. The axial force, $F$, was determined using either Eq. 5.37 or 5.52, depending on whether the beam was interior or exterior. The moment $M_b$ in the beam was found first using Eq. 5.36. The floor slab moment $M_s$ was then obtained by subtracting $M_b$ and the force couple $F \cdot h$ from the total moment $M$ which was determined from statics. The shear force $Q_b$ in the beam was found by considering the moment equilibrium of a free-body of the member shown in Fig. 5.31. Whence on suppressing the higher order terms,

$$Q_b = \frac{\partial M_b}{\partial x} + \frac{d_b}{2} \frac{\partial F}{\partial x} \qquad (5.60)$$

where

$$\frac{\partial M_b}{\partial x} = -EI \frac{\partial^3 w}{\partial x^3}$$

$$\frac{\partial F}{\partial x} = \begin{cases} 2t \dfrac{\partial}{\partial x} \displaystyle\int_0^\infty \dfrac{\partial^2 \phi}{\partial y^2} dy & \text{(Interior Beam)} \\[4mm] t \dfrac{\partial}{\partial x} \displaystyle\int_o^\infty \dfrac{\partial^2 \phi}{\partial y^2} dy & \text{(Exterior Beam)} \end{cases}$$

The shear force $Q_s$ resisted by the slab was determined by subtracting $Q_b$ from the total shear force $V$ obtained from statics.

The internal distribution of forces along the beam are plotted in Figs. 5.32 to 5.37. The analysis results for both the interior and exterior composite beams show that the axial force varies along the span, reaching a maximum just beyond the link ends. As can be seen from Figs. 5.33 and 5.36, the contribution of the floor slab in resisting the shear appears to be greater in the link region than outside the link. The contribution of $M_s$ to the total moment $M$ is small relative to both the beam moment $M_b$ and the force couple $F \cdot h$.

A summary of the internal force distribution in the steel section and the floor slab at the end of the link is given in Fig. 5.38. In the link, where the maximum shear force develops,

the steel section resists 88 percent of the total shear force for the interior composite beam and 92 percent of the total shear for the exterior composite beam. At the ends of the link where the maximum moment develops, 56 percent of the total moment for the interior composite beam and 67 percent of the total moment for the exterior composite beam is resisted by the steel section. The maximum axial force developed outside the link for the interior composite beam was 22 percent of-the yield force $F_Y$ of a A36 steel W12 x 19 section. As a result, the force couple at the ends of the composite link accounted for approximately 43 percent of the total moment. Inside the link the maximum value of $F$ was $0.15F_Y$ for the interior composite beam. The exterior composite steel beam develops a maximum $F$ of $0.17F_Y$ outside the link and $0.11F_Y$ in the link. Consequently, the force couple at the end of the link accounted for approximately 32 percent of the total moment. It can be noted that $M_s$ does not offer much of a contribution to the total moment in neither the interior nor exterior composite beam. $M_s$ is approximately one percent of the total moment developed at the ends of the links. Hence, the force couple developed by composite action is the main contributor to the increase in the total moment.

## 5.8. Conclusions

Based on the analyses of the interior and exterior composite floor beams, the following conclusions can be noted:

(1)  Compared with experimental data the analyses were able to predict reasonably well the transverse displacements, longitudinal strain in the floor slab, and variation in the location of the neutral axis along the beam during the initial cycles of loading.

(2)  The effective slab width based on stress distribution depends on beam spacing, loading conditions, beam span, and orthotropic properties of the slab.

(3)  The effective slab width based on stress distribution for composite beams in EBFs varies along the span of the floor beam, where it is a minimum at the ends of the links. This conclusion is corroborated by experimental results.

102

(4)  The use of the effective slab width based on the AISC Specification [20] results in an overestimation of the effective moment of inertia of the composite beam stiffness outside the link. The effective slab width determined using the AISC Specification is greater in the link region compared to the analytical results, outside the link the situation is reversed.

(5)  The floor slab and beam both contribute to the resistance of the applied loads. The force couple provides the largest contribution to the increase in the composite section's capacity. The elastic shear force resisted by the floor slab at the link is from 8 to 12 percent of the total shear force. Floor slabs above an interior link offer larger contributions to the applied shear than the exterior links.

# BIBLIOGRAPHY

[1]     Krawinkler, H., Bertero, V.V., and Popov, E.P., "Inelastic Behavior of Steel Beam to Column Subassemblages," *EERC Report No. 71-7,* Earthquake Engineering Research Center, University of California, Berkeley, CA, Oct. 1971.

[2]     Popov, E.P. and Black, R., "Steel Struts Under Severe Cyclic Loadings," *Journal of the Structural Division,* ASCE, Vol. 107, No. ST9, Sept. 1981.

[3]     Hjelmstad, K.D. and Popov, E.P., "Seismic Behavior of Active Beam Links in Eccentrically Braced Frames," *EERC Report No. 83-15,* Earthquake Engineering Research Center, University of California, Berkeley, CA, July 1983.

[4]     Kasai, K., "A Plastic Design Method of Eccentrically Braced Frames," CE 299 Report Submitted to University of California, Berkeley, SESM.

[5]     Malley, J.O. and Popov, E.P., "Design Considerations for Shear Links in Eccentric Braced Frames," *EERC Report No. 83-24,* Earthquake Engineering Research Center, University of California, Berkeley, CA, November 1983.

[6]     Roeder, C.W. and Popov, E.P., "Inelastic Behavior of Eccentric Braced Steel Frames Under Cyclic Loadings," *EERC Report No. 77-18,* Earthquake Engineering Research Center, University of California, Berkeley, CA, August 1977.

[7]     Kasai, K. and Popov, E.P.,"A Study of Seismically Resistant Ecccentrically Braced Steel Frame Systems," *EERC Report No. 86-01,* Earthquake Engineering Research Center, University of California, Berkeley, CA, January 1986.

[8]     Manheim, D., "On The Design of Eccentrically Braced Frames," Thesis presented to the University of California, Berkeley, in partial fulfillment for the degree of Doctor of Engineering, 1982.

[9]     Fisher, J., "Design of Composite Beams With Formed Metal Deck," *AISC Engineering Journal,* Vol. 7, No. 3, July 1970.

[10]    Grant, J., Fisher, J., and Slutter, R.O., "Composite Beams With Formed Steel Deck," *AISC Engineering Journal,* Vol. 14, No. 1, 1st Quarter, 1977.

[11]     Slutter, R., Driscoll, G., "Flexural Strength of Steel-Concrete Composite Beams," *Journal of the Structural Division, ASCE*, Vol. 91, No. ST2, April, 1965.

[12]     Ollgaord, J.G., Slutter, R.G., and Fisher, J.W., "Shear Strength of Stud Connectors in Lightweight and Normal-Weight Concrete," *Engineering Journal of the American Institute of Steel Construction*, Vol. 8, No. 2, 1971.

[13]     Robinson, H., "Tests on Composite Beams With Cellular Deck," *Journal of the Structural Division, ASCE*, Vol. 93, No. ST4, August 1967.

[14]     Robinson, H., "Composite Beam Incorporating Cellular Steel Decking," *Journal of the Structural Division, ASCE*, Vol. 95, No. ST3, March 1979.

[15]     Robinson, H., "Preliminary Investigation of a Composite Beam With a Ribbed Slab formed by Cellular Steel Decking," *Engineering Dept. Report No. 35*, McMaster University, October 1961.

[16]     Iyengar, H.S.,"State of the Art Report on Composite or Mixed Steel-Concrete Construction for Buildings," Structural Specification Liaison Committee, ASCE, 1977.

[17]     Goel, S.C., Foutch, D.A., "Preliminary Studies and Test Results of Eccentrically Braced Full-Size Steel Structure," U.S.-Japan Cooperative Earthquake Research Program Sixteenth Joint Meeting, May 15-18, Washington D.C., 1984.

[18]     Popov, E.P., Malley, J.O., "Design of Links and Beam-to-Column Connections for Eccentrically Braced Steel Frames," *EERC Report No. 83-03*, Earthquake Engineering Research Center, University of California, Berkeley, CA, January, 1983.

[19]     Neal, B.G.,"Effect of Shear Force on the Fully Plastic Moment of an I-Beam," *Journal of Mechanical Engineering Science*, Vol. 3(3), 1961.

[20]     Specification for the Design, Fabrication and Erection of Structural Steel for Buildings, 8th ed., American Institute of Steel Construction, New York, 1980.

[21]     Siess, C.P., Viest, I.M., and Newmark, N.M., "Small-Scale Tests of Shear Connectors and Composite T-Beams," *Bulletin No. 396*, Experimental Station, University of Illinois, Urbana, Illinois, 1952.

[22] Humar, J.L., "Composite Beams Under Cyclic Loading," *Journal of the Structural Division, ASCE,* Vol. 105, No. ST10, October, 1979.

[23] Hawkins, N.M., Mitchell, D., "Seismic Response of Composite Shear Connections," *Journal of Structural Engineering, ASCE,* Vol. 110, No. 9, September, 1984.

[24] Moffat, K.R., "An Analytical Study of the Longitudinal Bending Behavior of Composite Box Girder Bridges Having Incomplete Interaction," *CESLIC Report CB1,* Civil Engineering Structures Laboratory, Imperial College of Science and Technology, London, England, 1976.

[25] Moffat, K.R., "Shear Lag in Steel Box Girder Bridges," *The Structural Engineer,* London, England, Vol. 53, October, 1975.

[26] Kato, B., Aoyama, H., Okada, T., Uchida, N., "Composite Steel and Concrete Beams in the Building Structure in Japan," Regional Conference on Planning and Design of Tall Buildings, August 28-30, 1973, Tokyo, Japan.

[27] Johnson, R.P., Willmington, R.T., "Vertical Shear in Continuous Composite Beams," *Proceedings,* Institution of Civil Engineers, 1972.

[28] H.H. Robertson Company, *Technical Data Book,* Pittsburgh, Pennsylvania.

[29] "Embedment Properties of Head Studs," TRW Nelson Division, Ohio, January, 1983.

[30] American Society for Testing and Materials, Standard Methods of Tension Testing of Metallic Materials, ASTM Designation E8-79, Philadelphia, 1980.

[31] American Society for Testing and Materials, Standard Methods for Compressive Strength of Cylindrical Concrete Specimens, ASTM Designation C39-72, Philadelphia, 1980.

[32] American Society for Testing and Materials, Standard Method for Splitting Tensile Strength of Cylindrical Concrete Specimens, ASTM Designation C496-71, Philadelphia, 1980.

[33] American Society for Testing and Materials, Standard Method for Flexural Strength of Concrete, ASTM Designation C78-75, Philadelphia, 1980.

[34] American Society for Testing and Materials, Standard Method for Unit Weight of Structural Lightweight Concrete, ASTM Designation C567-71, Philadelphia, 1980.

[35] Kasai, K., Popov, E.P., "General Behavior of WF Steel Shear Link Beams," *Journal of Structural Engineering, ASCE,* Vol. 112, No. 2, February 1986.

[36] Kasai, K., Popov, E.P., "Cyclic Web Buckling Control for Shear Link Beams," *Journal of Structural Engineering, ASCE,* Vol. 112, No. 3, March 1986.

[37] Wakabayashi, M., "Inelastic Behavior of Full-Scale Steel Frames with and without Bracings," *Bulletin of the Disaster Prevention Research Institute,* Vol. 24, Part 1, Kyoto University, Kyoto, Japan, March 1974.

[38] Popov, E.P., Amin, N.R., Louie, J.J.C., and Stephen, R.M., "Cyclic Behavior of Large Beam-Column Assemblies", *Earthquake Spectra,* Vol. 1, No. 2, Feb. 1985, pp. 3-38.

[39] Maison, B.F.and Popov, E.P., "Cyclic Response prediction for Braced Steel Frames", *Journal of the Structural Division,* ASCE, 106, No. ST7, Proc. Paper 15534, 1401-1416, July 1980.

[40] Nigam, N.C., "Inelastic Interactions in the Dynamic Response of Structures," Earthquake Engineering Laboratory, California Institute of Technology, Pasadena, CA 1967.

[41] Engelhardt, M.D., Thesis to be presented to the University of California, Berkeley in Partial Fulfillment for the Degree of Doctor of Philosophy in 1988.

[42] Boutros, M.K., Goel, S.C., "Analytical Modelling of Braced Steel Structures," *Report No. UMCE 85-7,* Department of Civil Engineering, University of Michigan, Ann Arbor, Michigan, August 1985.

[43]    Hodge, P.G., "Plastic Analysis of Structure," McGraw-Hill Book Company, Inc., New York, 1959.

[44]    Leth, C.F., "Effect of Shear Stresses on the Carrying Capacity of I-Beams," *Technical Report No. A-11-107*, Brown University, 1954.

[45]    ASCE-WRC, "Plastic Design in Steel", *ASCE Manual 41*, 2nd Edition, Welding Research Council and American Society of Civil Engineers, New York, 1971.

[46]    Timoshenko, S.P., "Strength of Materials," Part II, Second Edition, D. Van Nostrand Company Inc., New York, August 1941.

[47]    Roark, R.J., Young, W.C., "Formulas for Stress and Strain," Fifth Edition, McGraw-Hill Book Company, New York, 1975.

[48]    Karsan, I.D., Jirsa, J.O., "Behavior of Concrete under Compressive Loadings," *Journal of Structural Division, ASCE*, Vol. 95, ST12, December 1969.

[49]    Sinha, B.P., Gerstle, K.H., and Tulin, L.G., "Stress-Strain Relationships for Concrete under Cyclic Loading," *Journal ACI*, Vol. 61, No. 2, February 1964.

[50]    Hognestad, E., "A Study of Combined Bending and Axial Load in Reinforced Concrete Members," *Bulletin Series No. 399*, University of Illinois Engineering Experimental Station, November 1951.

[51]    Salmon, C.G., Johnson, J.E., "Steel Structures - Design and Behavior," Harper and Row Publishers, New York, New York, 1971.

[52]    Bleich, F., "Strength of Metal Structures," 1st Edition, McGraw-Hill Book Company, Inc., New York, 1952.

[53]    Timoshenko, S.P., Gere, J.M., "Theory of Elastic Stability," McGraw-Hill Book Co., New York, New York, 1969.

[54]    Hechtman, R.A., Hattrup, J.S., Styer, E.F., and Tiedemann, J.L., "Lateral Buckling of Rolled Steel Beams," *Proceedings, ASCE*, Vol. 81, Paper 797, 1955.

108

[55] Gaylord, E.H., Gaylord, C.N., "Design of Steel Structures," McGraw-Hill Book Co., New York, New York, 1972.

[56] Johnson, R.P., Van Dolen, K., and Kemp, A.R., "Ultimate Strength of Continuous Composite Beams," *Proceedings, Conference on Structural Steelwork*, British Constructional Steelwork Association, November 1967.

[57] Hamada, S., Longworth, J., "Buckling of Composite Beams in Negative Bending," *Journal of the Structural Division, ASCE*, Vol. 100, No. ST11, November, 1974.

[58] SEAOC Tentative Lateral Force Requirements, Seismology Committee, Structural Engineers Association of California, Sacramento/San Francisco/Los Angeles, California, 1985

[59] Kusuda, T., and Thurlimann, B., "Strength of Wide-Flange Beams Under Combined Influence of Moment, Shear, and Axial Force", *Report No. 248.1*, Fritz Engineering Laboratory, Lehigh University, Bethlehem, Pennsylvania, 1958.

[60] Fung, Y.C., "Foundations of Solid Mechanics," Prentice-Hall, Inc., Englewood Cliffs, N.J., 1965.

[61] Timoshenko, S.P., "Theory of Elasticity," Third Edition, McGraw-Hill Book Company, Inc., New York, 1970.

[62] Szilard, R., "Theory and Analysis of Plates," Prentice-Hall Inc., Englewood Cliffs, N.J., 1974.

[63] Timoshenko, S.P., "Theory of Plates and Shells," Second Edition, McGraw-Hill Book Company, New York, 1959.

[64] Allen, D.N., Severn, R.T., "Composite Action Between Beams and Slabs under Transverse Load," *The Structural Engineer*, Vol. 39, No. 5, May 1961.

[65] Popov, E.P., "Introduction to Mechanics of Solids," Prentice-Hall, Englewood Cliffs, N.J., 1968.

[66]    NEHRP (National Earthquake Hazards Reduction Program), *Recommended Provisions for the Development of Seismic Regulations for New Buildings*, Building Seismic Safety Council, Federal Emergency Management Agency, Washington, D.C., 1985.

[67]    Girkmann, K., "Flächentragwerke," Springer-Verlag, Austria, 1946 (in German).

[68]    Troitsky, M.S., "Orthotropic Bridges -- Theory and Design," James F. Lincoln Arc Welding Foundation, Cleveland, Ohio, August 1967.

[69]    Plantema, F.J., "Sandwich Construction: The Bending and Bucking of Sandwich Beams, Plates, and Shells," John Wiley and Sons, Inc., New York, 1966.

[70]    Giberson, M.F., "Two Nonlinear Beams with Definitions of Ductility," *Journal of the Structural Division, ASCE*, Vol. 95, No. ST2, February 1969.

[71]    Clough, R.W., Benuska, K.L., and Lin, T.Y., "FHA Study of Seismic Design Criteria for High-Rise Buildings," *HUDTS-3*, Federal Housing Administration, Washington, D.C. August 1966.

[72]    Yang, M.S., "Seismic Behavior of an Eccentrically X-Braced Steel Structure," *EERC Report 82-14*, Earthquake Engineering Research Center, University of California, Berkeley, CA, September 1982.

[73]    Neal, G.G., "The Effect of Shear and Normal Force on the Fully Plastic Moment of a Beam of Rectangular Cross Section," *Journal of Applied Mechanics*, Vol. 28, No. 2, 1961.

[74]    Bathe, K.J., and Wilson, E.L., "Numerical Methods in Finite Element Analysis," Prentice-Hall, Englewood Cliffs, N.J., 1976.

[75]    Mroz, Z., "An Attempt to Describe the Behavior of Metals under Cyclic Loads using a More General Workhardening Model," *Acta Mechanica*, Vol. 7, 1969.

110

[76] Mroz, Z., "On the Description of Anisotropic Workhardening," *Journal Mech. Phys. Solids,* Vol. 15, Pergammon Press, Ltd., Great Britain, 1967.

[77] Naghdi, A., "Plasticity," Office of Naval Research, Pergammon Books, 1960.

[78] Porter, F.L., and Powell, G.H., "Static and Dynamic Analysis of Inelastic Frame Structures," *EERC Report No. 71-3,* Earthquake Engineering Research Center, University of California, Berkeley, CA, June 1971.

[79] Chen, P.F., and Powell, G.H., "Generalized Plastic Hinge Concepts for 3D Beam-Column Elements," *EERC Report No. 82-20,* Earthquake Engineering Research Center, University of California, Berkeley, CA, November 1982.

[80] Ziegler, H., "A Modification of Prager's Hardening Rule," *Quarterly of Applied Mathematics,* Vol. 17, No. 55, 1959.

[81] Riahi, A., Row, D., and Powell, G.H., "Three Dimensional Inelastic Frame Elements for the ANSR-I Program," *EERC Report No. 78-06,* Earthquake Engineering Research Center, University of California, Berkeley, CA, 1978.

[82] Nigam, N.C., "Yielding in Framed Structures under Dynamic Loads," *Journal of Engineering Mechanics Division, ASCE,* Vol. 96, No. EM5, October, 1970.

[83] Argyris, J.H., "Finite Element Analysis of Two and Three-Dimensional Elasto-Plastic Frames -- The Natural Approach," *Computer Methods in Applied Mechanics and Engineering,* Vol. 35, 1982.

[84] Wen, R.K., "Dynamic Analysis of Inelastic Space Frames," *Journal of Engineering Mechanics Division, ASCE,* Vol. 96, No. EM5, 1970.

[85] Orbison, J.G., "Nonlinear Static Analysis of Three-Dimensional Steel Frames," Dissertation Submitted in Partial Fulfillment of the Degree of Doctor of Philosophy, Cornell University, Ithaca, New York, May 1982.

[86]   Row, D.G., Powell, G.H., and Mondkar, D.P., "2D Beam Column Element (Type 5 - Parallel Element Theory) for the ANSR-II Program," *EERC Report No. 79-30*, Earthquake Engineering Research Center, University of California, Berkeley, CA, 1979.

[87]   Uzgider, E.U., "Inelastic Response of Space Frames to Dynamic Loads," *Computers and Structures*, Vol. 11, 1980.

[88]   Hilmy, S.I., "Adaptive Nonlinear Dynamic Analysis of Three-Dimensional Steel Framed Structures with Interactive Computer Graphics," *Report No. 84-8*, Department of Structural Engineering, Cornell University, Ithaca, New York, June 1984.

[89]   Powell, G.H., "DRAIN-2D User's Guide," *EERC Report No. 73-22*, Earthquake Engineering Research Center, University of California, Berkeley, CA, 1973.

[90]   Bergan, P., "Solution Algorithms for Nonlinear Structural Problems," *Proceedings, International Conference on Engineering Applications of the Finite Element Methods*, Hovik, Norway, May 1979.

[91]   Mattheis, H. and Strang, G., "The Solution of Nonlinear Finite Element Equations," *International Journal of Numerical Methods in Engineering*, Vol. 14, 1979.

[92]   Powell, G., and Simmons, J., "Improved Iteration Strategy for Nonlinear Structures," *International Journal of Numerical Methods in Engineering*, Vol. 17, 1981.

[93]   Riks, E., "An Incremental Approach to the Solution of Snapping and Buckling Problems," *International Journal of Solids and Structures*, Vol. 15, 1979.

[94]   Mondkar, D.P., and Powell, G.H., "ANSR-I General Purpose Computer Program for Analysis of Non-Linear Structural Response", *EERC Report No. 75-37*, Earthquake Engineering Research Center, University of California, Berkeley, CA, 1975.

[95]   Bathe, K.J., "Finite Element Procedures in Engineering Analysis," Prentice-Hall, Englewood Cliffs, N.J., 1982.

112

[96]    UCB, Uniform Building Code, International Conference of Building Officials, Whittier, California, 1982.

[97]    Newmark, N.M., and Hall, W.J., "Earthquake Spectra and Design", EERI (Earthquake Engineering Research Institute), Berkeley, CA.

[98]    Zienkiewicz, O.C.,"The Finite Element Method," 3rd Edition, McGraw-Hill Book Company, Inc., 1977.

[99]    Clough, R.W., and Penzien, J., *Dynamics of Structures*, McGraw-Hill Book Company, Inc., New York, 1975.

[100]   Collatz, L., "The Numerical Treatment of Differential Equations," Springer-Verlag, New York, New York, 1966.

[101]   Houbolt, J.C., "A Recurrence Matrix Solution for the Dynamic Response of Elastic Aircraft," *Journal of Aeronautic Science*, Vol. 17, 1950.

[102]   Wilson, E.L., Farhoomad, I., and Bathe, K.J., "Nonlinear Dynamic Analysis of Complex Structures," *International Journal of Earthquake Engineering and Structural Dynamics*, Vol. 1, 1973.

[103]   Newmark, N.M., "A Method of Computing for Structural Dynamics," *Journal of Engineering Mechanics Division, ASCE*, Vol. 85, 1959.

[104]   Hilber, H.M., Hughes, T.J.R., and Taylor, R.L., "Improved Numerical Dissipation of Time Integration Algorithms in Structural Dynamics," *Earthquake Engineering and Structural Dynamics*, Vol. 5, 1977.

[105]   Hughes, T.J.R., Caughey, T.K., and Liu, W.K., "Finite Element Methods for Nonlinear Elastodynamics which Conserve Energy," *Journal of Applied Mechanics*, Vol. 45, 1978.

[106]   Nickell, R.E., "On the Stability of Approximation Operators in problems of Structural Dynamics," *International Journal of Solids and Structures*, Vol. 7, 1971.

[107] Goudreau, G.L., and Taylor, R.L., "Evaluation of Numerical Integration Methods in Elastodynamics," *Computer Methods in Applied Mechanics and Engineering,* Vol. 2, 1972.

[108] Warburton, G.B., and Soni, S.R., "Errors in Response Calculations for Non-Classically Damped Structures," *Earthquake Engineering and Structural Dynamics,* Vol. 5, 1977.

[109] Shing, P.B., and Mahin, S.A., "Elimination of Spurious Higher-Mode Response in Pseudodynamic Tests," *to be published in Earthquake Engineering and Structural Dynamics in 1987.*

[110] Meirovitch, L, "Analytical Methods in Vibrations," Macmillan, New York, 1967.

[111] Saiidi, M., and Sozen, M.A., "Simple Nonlinear Seismic Analysis of Reinforced Concrete Structures," *Journal of the Structural Division, ASCE,* Vol. 107, No. ST5, May 1981.

[112] Shibata, A., and Sozen, M., "Substitute - Structure Method for Seismic Design in Reinforced Concrete," *Journal of the Structural Division, ASCE,* Vol. 102, No. ST1, January 1976.

[113] Tansirikongkol, V., and Pecknold, D.A., "Approximate Model Analysis of Bilinear MDF Systems Subjected to Earthquake Motions," *Civil Engineering Studies, Structural Research Series, No. 449,* University of Illinois, Urbana, August 1978.

[114] Mahin, S.A., and Lin, J., "Construction of Inelastic Response Spectra for Single Degree of Freedom Systems," *EERC Report No. 83-17,* Earthquake Engineering Research Center, University of California, Berkeley, CA, 1983.

]115] Galambos, T.V., "Deformation and Energy Absorption Capacity of Steel Structures in the Inelastic Range," *AISC Bulletin No. 8,* New York, New York, 1968.

[116] Hurty, W.C., Rubinstein, M.F., "Dynamics of Structures," Prentice-Hall, Inc.,

114

Englewood cliffs, N.J., 1964.

[117]  Leger, P., Wilson, E.L., and Clough, R.W., "The Use of Load Dependent Vectors for Dynamic and Earthquake Analyses," *EERC Report No. 86-04*, Earthquake Engineering Research Center, University of California, Berkeley, CA, 1986.

[118]  Golafshani, A., and Powell, G.H., "DRAIN-2D2: A Computer Program for Inelastic Seismic Response of Structures," Ph.D., Dissertation, University of California, Berkeley, 1974.

[119]  Popov, E.P., Kasai, K., and Engelhardt, M.D., "Advances in Design of Eccentrically Braced Frames," *Proceedings, Pacific Structural Steel Conference*, New Zealand, August 1986.

[120]  Kasai, K., and Popov, E.P., "On Seismic Design of Eccentrically Braced Steel Frames," *Proceedings 8WCEE*, San Francisco, California, Vol. 5, July 21-28, 1984, pp.387-394.

[121]  Paulay, T., "Deterministic Seismic Design Procedures for Reinforced Concrete Buildings," *Engineering Structures*, Vol. 5, No. 1, January 1983.

[122]  Standards Association of New Zealand, "Code of Practice for the Design of Concrete Structures," Draft, New Zealand Standard NZS 3101, Parts 1 and 2, 1982.

[123]  Jennings, P.C., Housher, G.W., and Tsai, N.C., "Simulated Earthquake Motions," California Institute of Technology, Pasadena, California, 1968.

[124]  AISC, "Specifications for the Design, Fabrication and Erection of Structural Steel for Buildings with Commentary," *Manual of Steel Construction*, 8th Edition, American Institute of Steel Construction, 1980.

[125]  Mahin, S.A., and Bertero, V.V., "An Evaluation of Inelastic Seismic Design Spectra," *Journal of the Structural Division, ASCE*, Vol. 107, No. ST9, September 1981.

[126]   ANSI, "American National Standard Minimum Design Loads for Buildings and other Structures," ANSI A58.1-1982, New York, New York, 1982.

[127]   Popov, E.P., and Engelhardt, M.D., "Seismic Eccentrically Braced Frames," *to be published in Journal of Construction Steel Research*, United Kingdom, 1987.

[128]   Ricles, J.M., and Popov, E.P., "Dynamic Analysis of Seismically Resistant Eccentrically Braced Frames," *EERC Report No. 87-07*, Earthquake Engineering Research Center, University of California, Berkeley, CA, 1987.

116

# TABLES

| SPECIMEN NO. | EBF TYPE | PANEL ZONE | | | LINK DEFORMATION HISTORY |
|---|---|---|---|---|---|
| | | NUMBER PANELS | a (in) | $\dfrac{a}{t_w}$ | |
| [1] | [2] | [3] | [4] | [5] | [6] |
| A1 | Composite, Exterior K-braced | 3 | 6.33 | 25.0 | Random Pulses + Cyclic Sym. |
| A2 | Composite, Exterior V-braced | 6 | 3.17 | 12.5 | Cyclically Symmetric |
| B1 | Composite, Interior K-braced | 3 | 6.33 | 25.0 | Cyclically Symmetric |
| B2 | Composite, Interior V-braced | 3 | 6.33 | 25.0 | Cyclically Symmetric |
| C1 | Composite, Exterior K-braced | 3 | 6.33 | 25.0 | Taft E.Q. + Cyclic Sym. |
| C2 | Composite, Exterior V-braced | 3 | 6.33 | 25.0 | Sym. Pulse + Cyclic Sym. |
| D1 | Bare Steel, K-braced | 3 | 6.33 | 25.0 | Cyclically Symmetric |
| D2 | Bare Steel, K-braced | 3 | 6.33 | 25.0 | Cyclically Symmetric |

Table 2.1  Specimen Indentification and Link Deformation History.

| Section | $\dfrac{b_f}{2t_f}$ | $\dfrac{d}{t_w}$ | $A_w$ (in$^2$) | $S$ (in$^3$) | $Z$ (in$^3$) | $e$ (in) | $M_{int}^+$ (k-in) |
|---|---|---|---|---|---|---|---|
| [1] | [2] | [3] | [4] | [5] | [6] | [7] | [8] |
| (a) W18x40 | 5.7 | 56.8 | 5.31 | 68.4 | 78.4 | 28 | 9751 |
| (b) $\frac{2}{3}$ Scale Model | 5.7 | 56.8 | 2.36 | 20.3 | 23.2 | 18.7 | 2889 |
| (c) W12x19 | 5.7 | 51.7 | 2.69 | 21.3 | 24.7 | 19 | 3119 |

Table 2.2  Section Properties for (a) Prototype, (b) Two Thirds Scale Model of Prototype, and (c) Specimen.

| Coupon Location [1] | E (ksi) [2] | $\varepsilon_{sh}$ (in/in) [3] | $\varepsilon_u$ (in/in) [4] | $\Delta_\%$ (%) [5] | $\sigma_y$ (ksi) [6] | $\sigma_u$ (ksi) [7] |
|---|---|---|---|---|---|---|
| Web | 28734 | 0.036 | 0.175 | 20.1 | 54.3 | 66.4 |
| Flange | 28831 | 0.032 | 0.247 | 25.8 | 45.1 | 62.1 |

Table 2.3  Steel Section Material Properties.

| Cylinder [1] | Curing Condition [2] | Young's Modulus (ksi) [3] |
|---|---|---|
| 1 | specimen | 3346 |
| 2 | specimen | 3317 |
| 3 | fog room | 3694 |
| 4 | fog room | 3510 |

Table 2.4  Young's Modulus of Concrete at 28 Days.

| Coupon [1] | E (ksi) [2] | $\varepsilon_u$ (in/in) [3] | $\Delta_\%$ (%) [4] | $\sigma_u$ (ksi) [5] | Area (in$^2$) [6] |
|---|---|---|---|---|---|
| 1 | 29914 | 0.0135 | 6.9 | 102.5 | 0.0452 |
| 2 | 27345 | 0.0167 | 7.6 | 97.7 | 0.0452 |
| 3 | 28035 | 0.0167 | 6.9 | 98.2 | 0.0452 |

Table 2.5  Material Properties and Cross Sectional Area of Wire Reinforcement.

| $\sigma$ (ksi) | | $V_p$ | $M_p^*$ | $M_p$ | $M_u^{int}$ | $M_u^{ext}$ | $b^*$ |
|---|---|---|---|---|---|---|---|
| Web [1] | Flange [2] | (kips) [3] | (k-in) [4] | (k-in) [5] | (k-in) [6] | (k-in) [7] | (in) [8] |
| 54.3 | 45.1 | 93.2 | 700 | 1192 | 2259 | 2185 | 15.0 |
| 49.7 (average) | | 85.3 | 772 | 1231 | 2272 | 2194 | 18.1 |

Table 2.6  Plastic Section Properties of Specimen.

| Section [1] | $b_f$ (in) [2] | $t_f$ (in) [3] | d (in) [4] | $t_w$ (in) [5] | I (in⁴) [6] | Z (in⁴) [7] | A (in²) [8] | $A_{web}$ (in²) [9] |
|---|---|---|---|---|---|---|---|---|
| Specimen | 4.0 | 0.354 | 12.06 | 0.254 | 128.1 | 24.8 | 5.72 | 2.88 |
| W12x19 | 4.005 | 0.350 | 12.16 | 0.235 | 130.0 | 24.7 | 5.57 | 2.69 |

Table 2.7 Steel Section Properties.

| Specimen [ 1 ] | Setup [ 2 ] | EI (k−in²/in) [ 3 ] | $M_{cr}$ (k−in/ft) [ 4 ] | $M_u$ (k−in/ft) [ 5 ] |
|---|---|---|---|---|
| Slab 1 | Positive Moment, Perpendicular to Rib | 8909 | 32.8 | 32.8 |
| Slab 2 | Negative Moment, Perpendicular to Rib | 9309 | 11.8 | 38.6 |
| Slab 3 | Positive Moment, Parallel to Rib | 2712 | 2.3 | 5.5 |
| Slab 4 | Negative Moment, Parallel to Rib | 2900 | 7.8 | 11.9 |

Table 2.8 Properties of Floor Slab.

| Specimen [1] | Elastic Stiffness - $K^*$ (kip/in) [2] | Normalized Elastic Stiffness - $\dfrac{K^*}{K^*_{D1}}$ [3] |
| --- | --- | --- |
| A1 | 706 | 1.24 |
| B1 | 859 | 1.51 |
| C1 | 707 | 1.24 |
| D1 | 569 | 1.0 |

Table 4.1  Pseudo-Elastic Link Stiffness, Links in K-Braced EBF Subassemblies.

| Specimen [1] | Elastic Stiffness - $K^*$ (kip/in) [2] | Normalized Elastic Stiffness - $\dfrac{K^*}{K^*_{D2}}$ [3] |
| --- | --- | --- |
| A2 | 747 | 1.07 |
| B2 | 812 | 1.17 |
| C2 | 744 | 1.06 |
| D2 | 698 | 1.0 |

Table 4.2  Pseudo-Elastic Link Stiffness, Links in V-Braced EBF Subassemblies.

| Specimen [1] | $V_y$ (kips) [2] | $M_y$ (kip-in) [3] | $\dfrac{V_y}{V_y^{Bare}}$ [4] | $\dfrac{V_y}{V_p}$ [5] | $\dfrac{M_y}{M_p}$ [6] |
|---|---|---|---|---|---|
| A1 | 88.1 | 975 | 1.03 | 0.94 | 0.82 |
| A2 | 87.0 | 1021 | 1.07 | 0.93 | 0.86 |
| B1 | 100.1 | 1154 | 1.17 | 1.07 | 0.97 |
| B2 | 94.7 | 1182 | 1.16 | 1.01 | 0.99 |
| C1 | 86.9 | 965 | 1.02 | 0.93 | 0.81 |
| C2 | 85.9 | 914 | 1.06 | 0.92 | 0.77 |
| D1 | 85.3 | 1170 | 1.0 | 0.92 | 0.98 |
| D2 | 81.4 | 1111 | 1.0 | 0.87 | 0.93 |

Table 4.3 Forces in Links at Initial Web Yielding.

| Specimen [1] | $V_{max}$ (kips) [2] | $\dfrac{V_{max}}{V_y}$ [3] | $\dfrac{V_{max}}{V_{max}^{Bare}}$ [4] |
|---|---|---|---|
| A1 | 127.2 | 1.44 | 1.08 |
| A2 | 133.2 | 1.53 | 1.13 |
| B1 | 129.2 | 1.29 | 1.10 |
| B2 | 130.7 | 1.38 | 1.11 |
| C1 | 118.0 | 1.36 | 1.01 |
| C2 | 120.0 | 1.40 | 1.02 |
| D1 | 117.5 | 1.38 | 1.0 |
| D2 | 117.7 | 1.44 | 1.0 |

Table 4.4 Maximum Shear Force Developed in Links.

| Specimen [1] | $M_{max}^+$ (kip-in) [2] | $M_{max}^-$ (kip-in) [3] | $\dfrac{M_{max}^+}{M_p}$ [4] | $\dfrac{M_{max}^-}{M_p}$ [5] | $\dfrac{M_{max}^+}{M_{ult}^+}$ [6] | $\dfrac{M_{max}^-}{M_{ult}^+}$ [7] |
|---|---|---|---|---|---|---|
| A1 | 1333 | 1534 | 1.12 | 1.29 | 0.61 | 0.70 |
| B1 | 1369 | 1315 | 1.15 | 1.10 | 0.61 | 0.58 |
| C1 | 1644 | 1425 | 1.38 | 1.19 | 0.75 | 0.65 |
| D1 | 1323 | 1274 | 1.11 | 1.07 | 0.61 | 0.58 |

Table 4.5  Maximum End Moments Developed in Links, K-Braced EBF.

| Specimen [1] | $M_A^{+max}$ (kip-in) [2] | $M_A^{-max}$ (kip-in) [3] | $M_B^{+max}$ (kip-in) [4] | $M_B^{-max}$ (kip-in) [5] | $\dfrac{M_A^{+max}}{M_p}$ [6] | $\dfrac{M_A^{-max}}{M_p}$ [7] | $\dfrac{M_B^{+max}}{M_p}$ [8] | $\dfrac{M_B^{-max}}{M_p}$ [9] | $\dfrac{M_A^{+max}}{M_{ult}^+}$ [10] | $\dfrac{M_A^{-max}}{M_{ult}^+}$ [11] | $\dfrac{M_B^{+max}}{M_{ult}^+}$ [12] | $\dfrac{M_B^{-max}}{M_{ult}^+}$ [13] |
|---|---|---|---|---|---|---|---|---|---|---|---|---|
| A2 | 1417 | 1609 | 918 | 1167 | 1.19 | 1.35 | 0.77 | 0.98 | 0.65 | 0.74 | 0.42 | 0.53 |
| B2 | 1500 | 1466 | 1466 | 1140 | 1.26 | 1.23 | 1.23 | 0.96 | 0.66 | 0.65 | 0.65 | 0.50 |
| C2 | 1358 | 1274 | 966 | 1200 | 1.14 | 1.07 | 0.81 | 1.01 | 0.62 | 0.58 | 0.44 | 0.55 |
| D2 | 1377 | 1295 | 986 | 842 | 1.16 | 1.08 | 0.83 | 0.71 | 0.64 | 0.59 | 0.44 | 0.37 |

Table 4.6  Maximum End Moments Developed in Links, V-Braced EBF.

| Specimen [1] | Compression $\left(\dfrac{P^{max}}{P^{Bare}_{max}}\right)$ [2] | Tension $\left(\dfrac{P^{max}}{P^{Bare}_{max}}\right)$ [3] | $\left(\dfrac{P^{max}}{P^{Bare}_{max}}\right)_{AVG}$ [4] |
|---|---|---|---|
| A1 | 1.09 | 1.10 | 1.09 |
| B1 | 1.13 | 1.14 | 1.14 |
| C1 | 1.01 | 1.11 | 1.06 |
| D1 | 1.0 | 1.0 | 1.0 |

Table 4.7    Maximum Jack Forces of Specimens Relative to Bare Steel Specimen, K-Braced EBF Subassemblies.

| Specimen [1] | Compression | | Tension | | $\left(\dfrac{P^{max}}{P^{Bare}_{max}}\right)_{AVG}$ [6] |
|---|---|---|---|---|---|
| | End A $\left(\dfrac{P^{max}}{P^{Bare}_{max}}\right)$ [2] | End B $\left(\dfrac{P^{max}}{P^{Bare}_{max}}\right)$ [3] | End A $\left(\dfrac{P^{max}}{P^{Bare}_{max}}\right)$ [4] | End B $\left(\dfrac{P^{max}}{P^{Bare}_{max}}\right)$ [5] | |
| A2 | 1.15 | 1.11 | 1.17 | 1.12 | 1.14 |
| B2 | 1.07 | 1.11 | 1.08 | 1.11 | 1.09 |
| C2 | 0.99 | 1.01 | 1.01 | 1.07 | 1.02 |
| D2 | 1.0 | 1.0 | 1.0 | 1.0 | 1.0 |

Table 4.8    Maximum Jack Forces of Specimens Relative to Bare Steel Specimen, V-Braced EBF Subassemblies.

| Specimen [1] | $\dfrac{E_\Sigma^*}{E_e}$ [2] | $\dfrac{E^*}{E_e}$ [3] |
|---|---|---|
| A1 | 132.5 | 44.9 |
| B1 | 213.5 | 43.2 |
| B2 | 264.9 | 43.2 |
| C1 | 363.4 | 41.8 |
| C2 | 304.4 | 39.5 |
| D1 | 177.4 | 32.4 |
| D2 | 264.0 | 48.9 |

| Specimen [1] | $\gamma_b$ (radians) [2] |
|---|---|
| A1 | 0.150 |
| B1 | 0.129 |
| B2 | 0.133 |
| C1 | 0.131 |
| C2 | 0.130 |
| D1 | 0.138 |
| D2 | 0.145 |

Table 4.9 Energy Dissipated at Web Buckling.

Table 4.10 Measured Link Deformation $\gamma_b$ at Web Buckling.

| Specimen [1] | Positive Moment | | Negative Moment | | AISC $b_{eff}$ (in) [6] |
|---|---|---|---|---|---|
| | $\dfrac{I_{eff}^+}{I}$ [2] | $b_{eff}^\theta$ (in) [3] | $\dfrac{I_{eff}^-}{I}$ [4] | $b_{eff}^\theta$ (in) [5] | |
| Exterior Beam | 1.75 | 5.9 | 1.28 | 2.2 | 20 |
| Interior Beam | 2.57 | 17.4 | 1.28 | 2.2 | 48 |

Table 4.11 Effective Moment of Inertia and Slab Width for Composite Test Beam Outside the Link.

# FIGURES
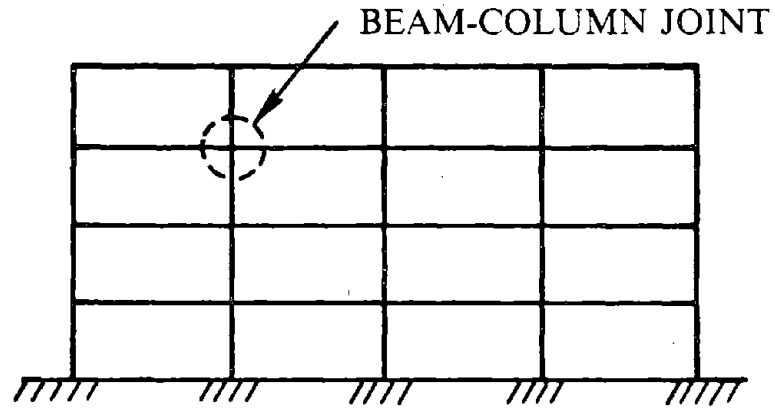
Fig. 1.1    A Typical Moment Resisting Frame [7].
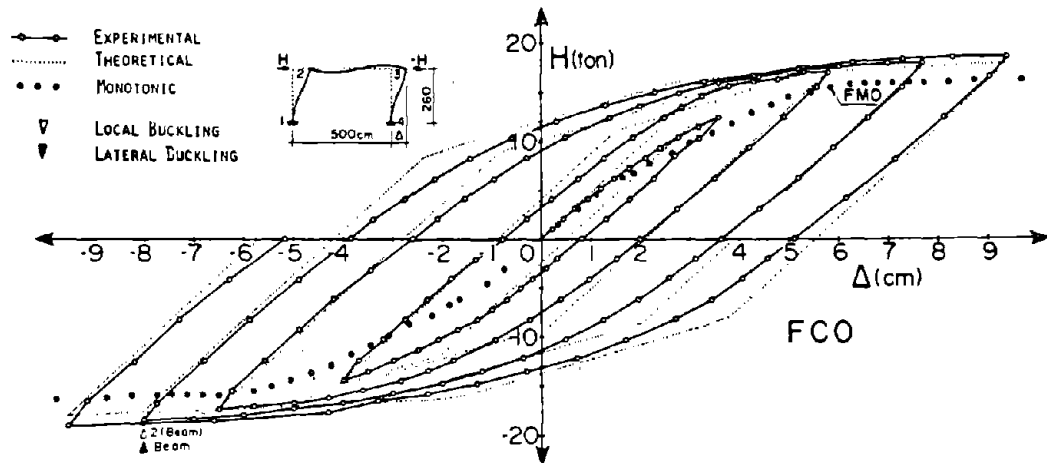


Fig. 1.2    One-Story Moment Resisting Frame Subjected
to Severe Cyclic Loading [37].
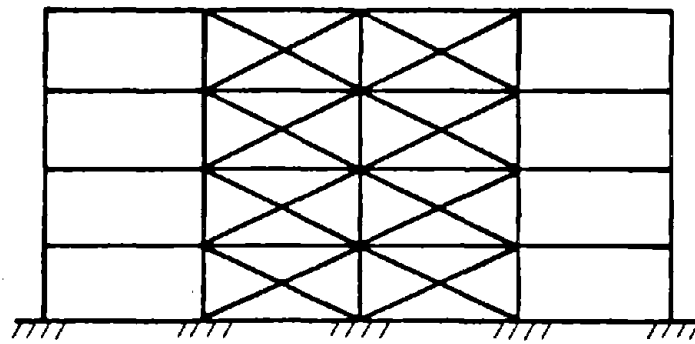
(a)
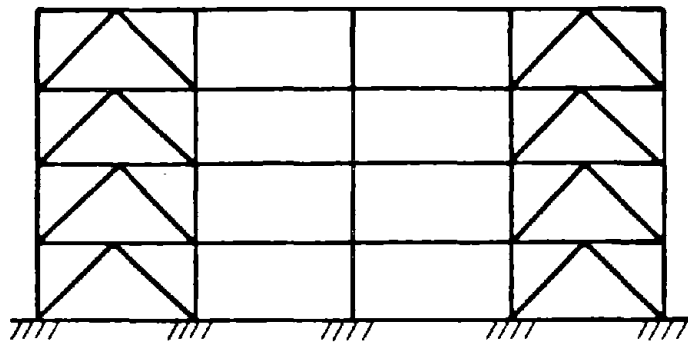


(b)

Fig. 1.3    Typical Arrangements for Concentrically Braced Frames [7].
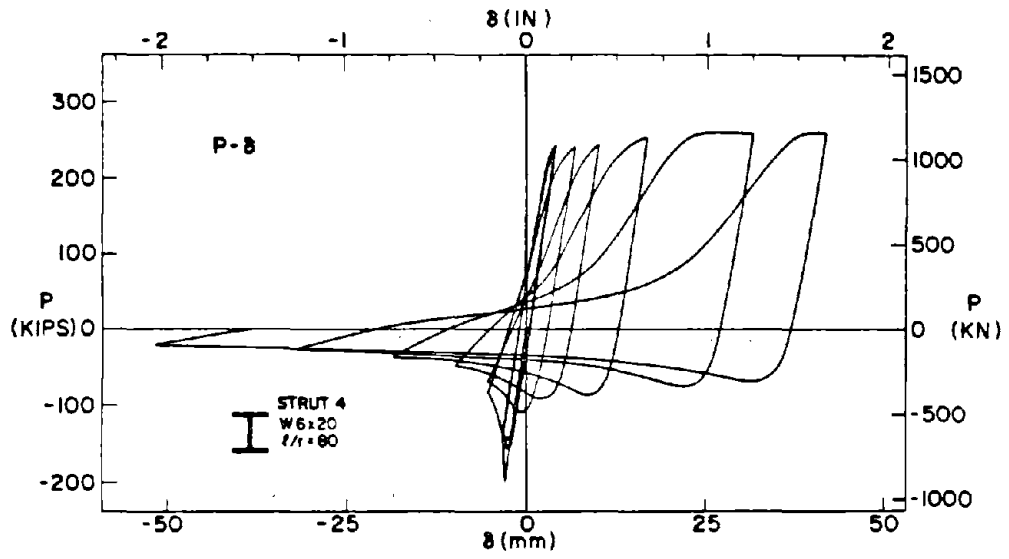
Fig. 1.4    Hysteretic Loops for Axial Force vs. Axial Displacement
of a Pin-Ended Brace Strut [2].
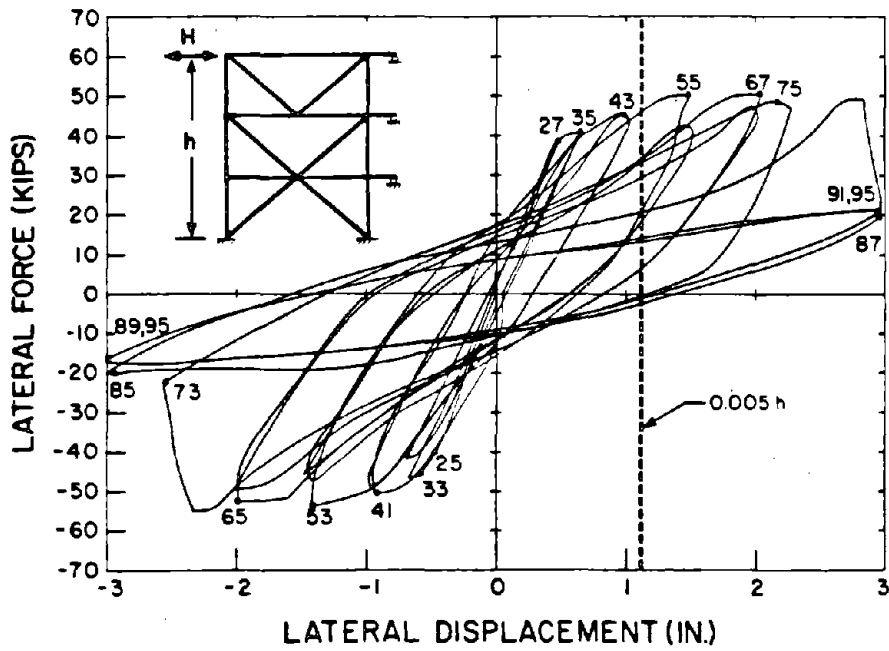


Fig. 1.5    Hysteretic Loops for One-Third Size Concentric K-Braced Frame [39].
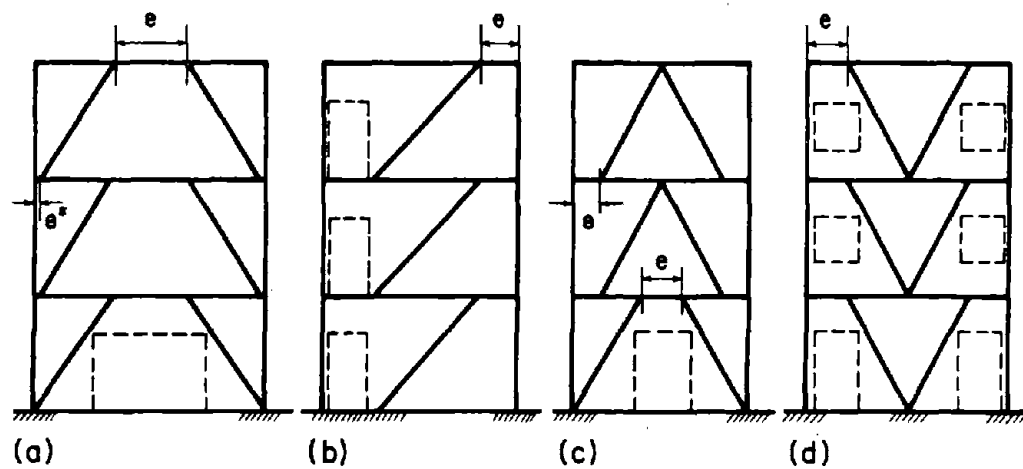
Fig. 1.6    Eccentric Braced Frame With Alternative Arrangement of Braces [5].
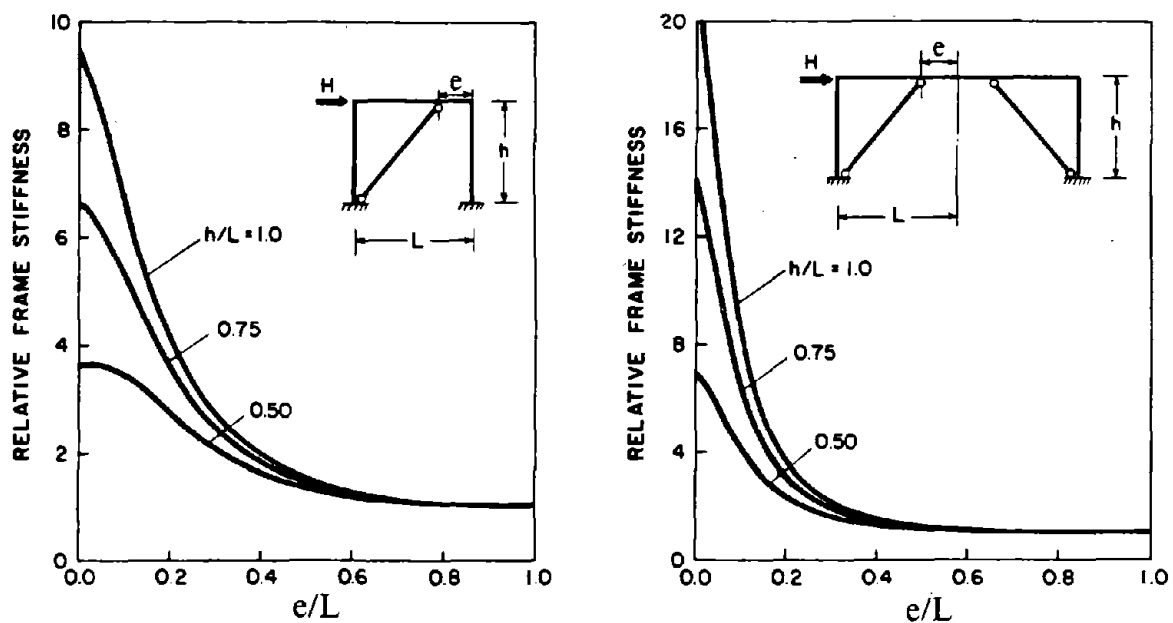


Fig. 1.7    Variation of Elastic Lateral Stiffness With e/L [3].

132



$$\gamma_p = \frac{L}{e}\Theta_p$$

LINK

e

$\Theta_p$

L

(a) K-Brace

$$\gamma_p = \frac{L}{2e}\Theta_p$$

LINK

e

LINK

$\Theta_p$

L/2    L/2
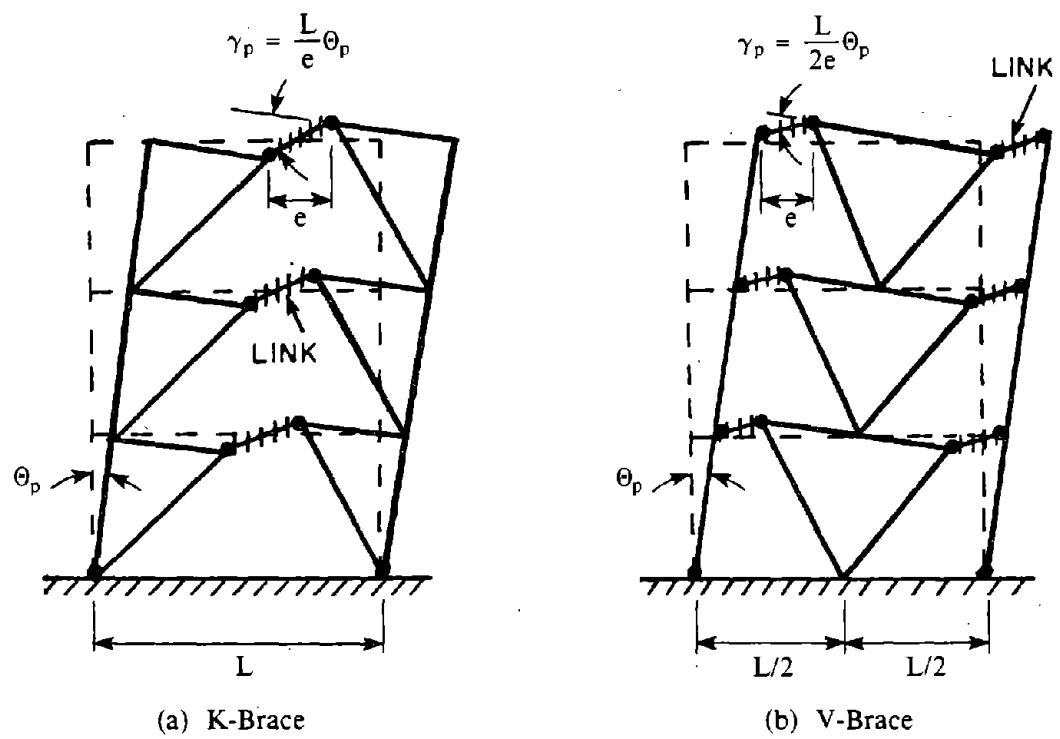
(b) V-Brace

Fig. 1.8    Collapse Mechanism for K-Braced and V-Braced EBFs.
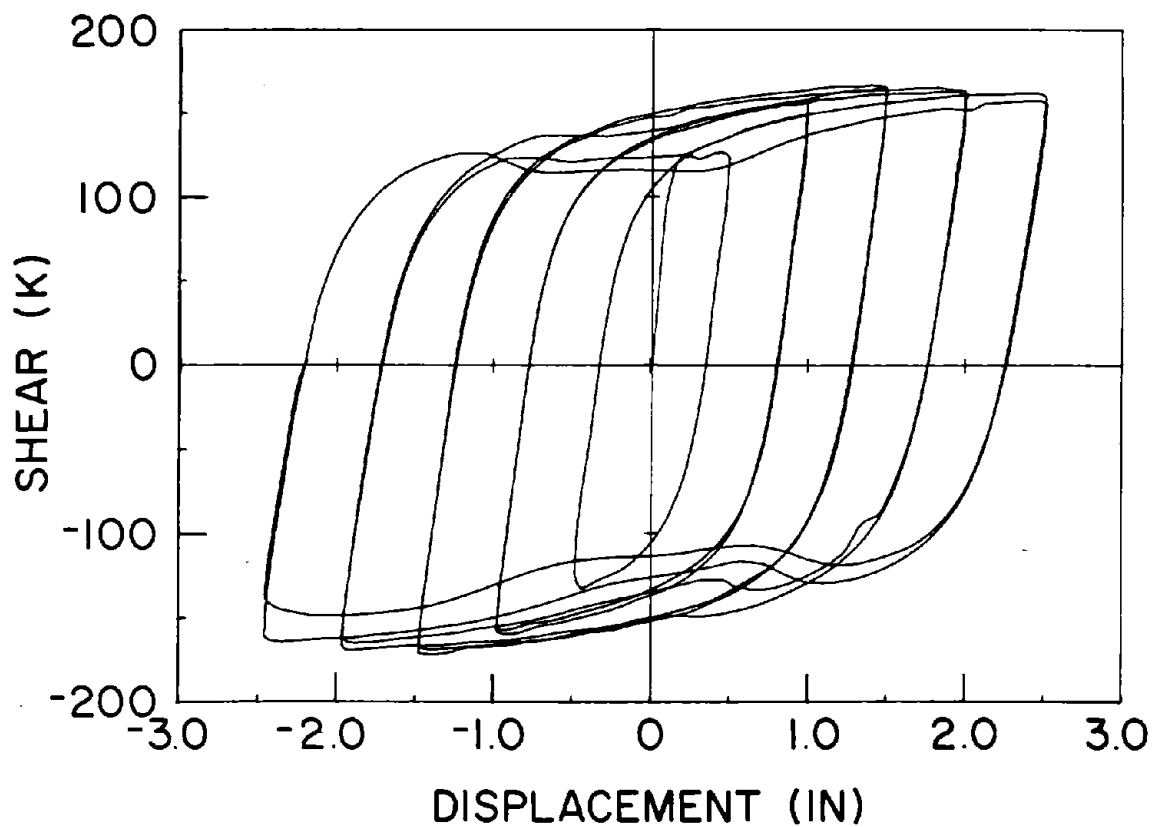
(a) Applied Shear vs. Relative End Displacement
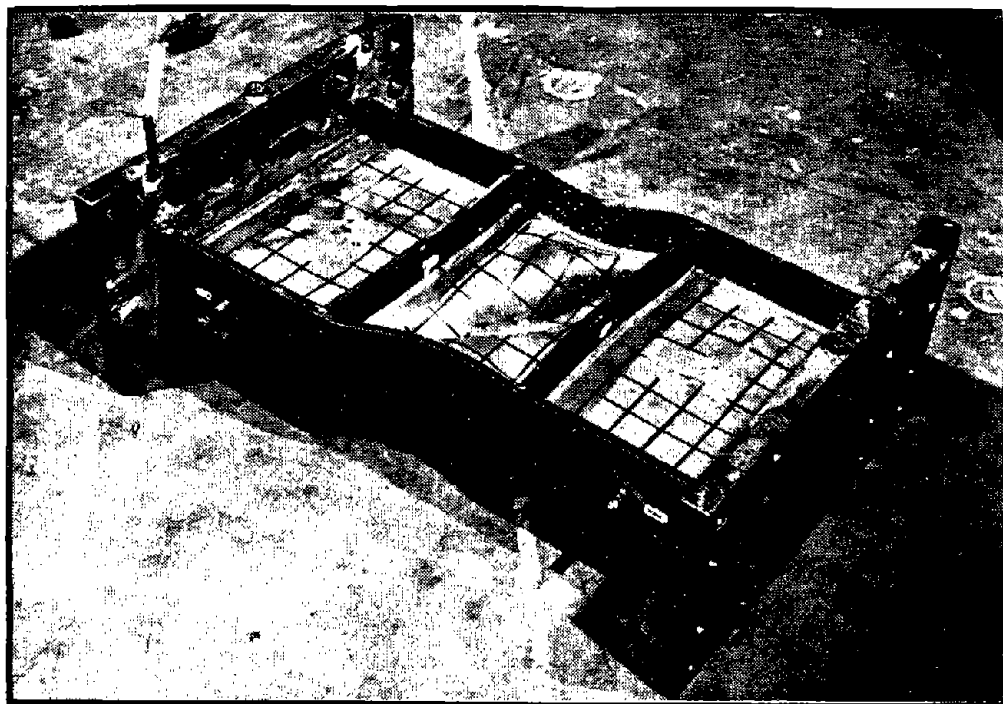
(b) Specimen 9 After Failure

Fig. 1.9    Hysteretic Behavior of an Active Link [3].

134
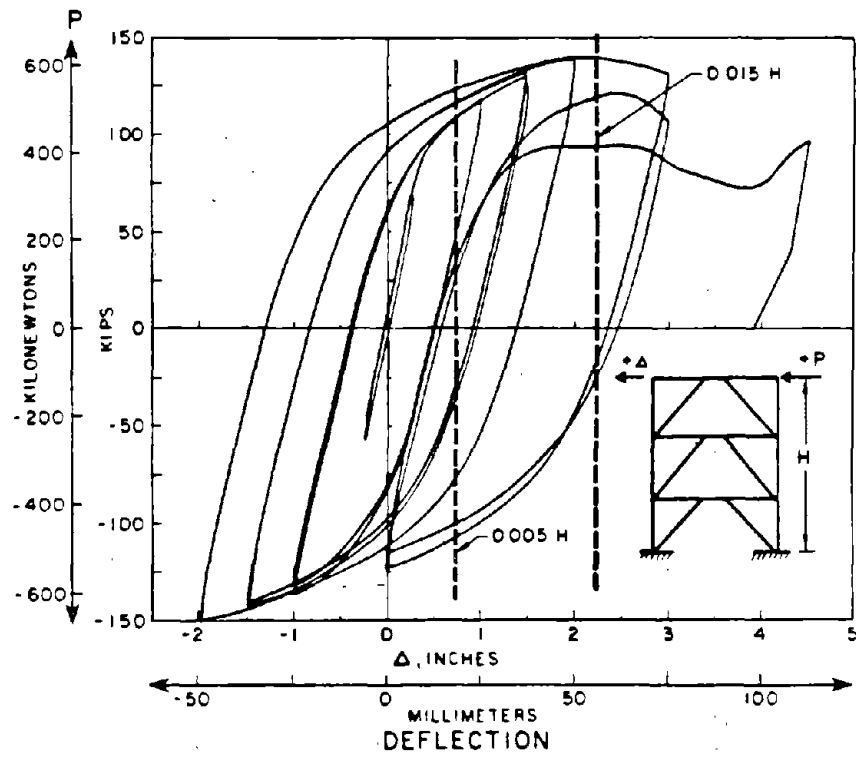


Fig. 1.10    Hysteretic Loops for One-Third Size EBF [8].
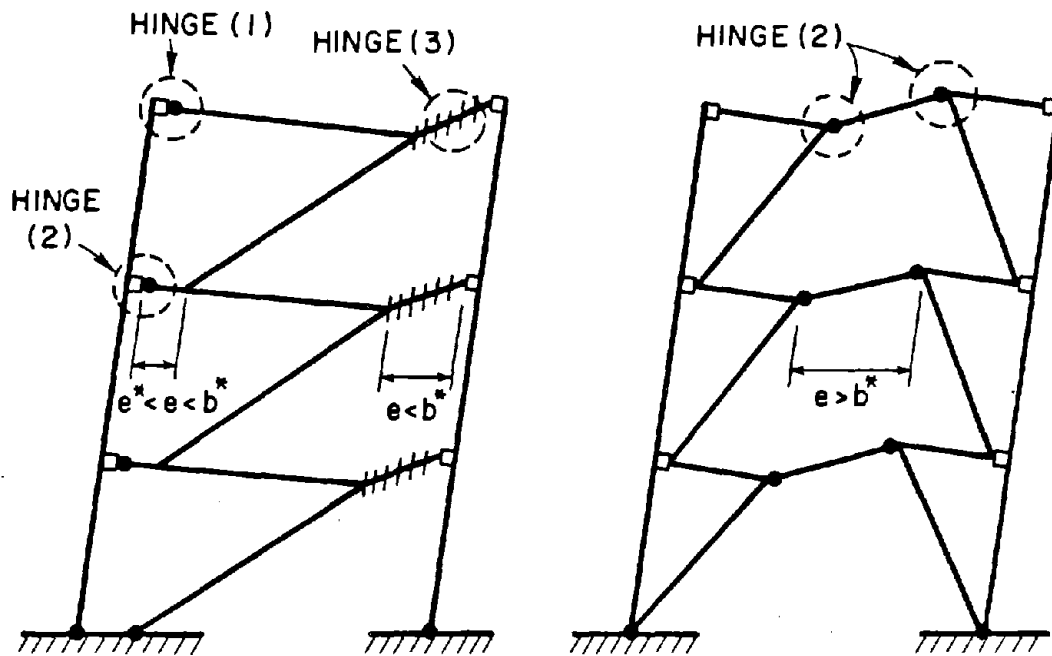
Fig. 1.11      Energy Dissipation Mechanisms of EBFs [7].
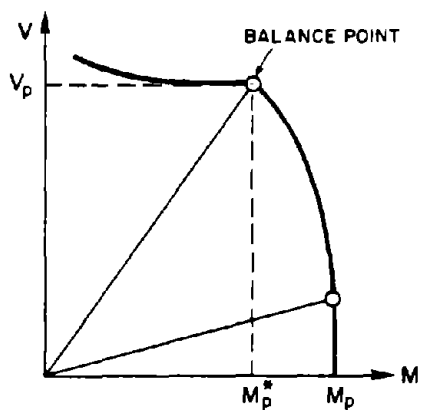


Fig. 1.12      Moment-Shear Interaction Diagram for Wide Flange Steel Sections [5].
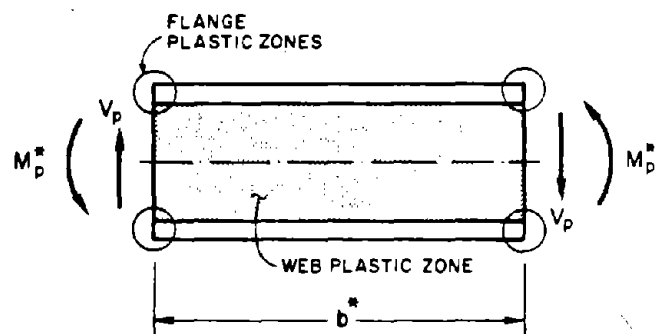


Fig. 1.13      Free Body Diagram of an Active Link.

136
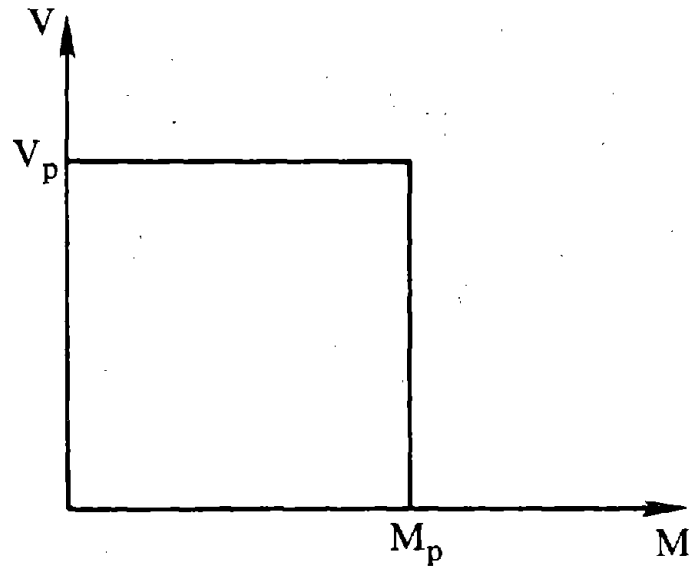


Fig. 1.14    Rectangular Moment-Shear Interaction Surface for Shear Links, After Kasai [7].
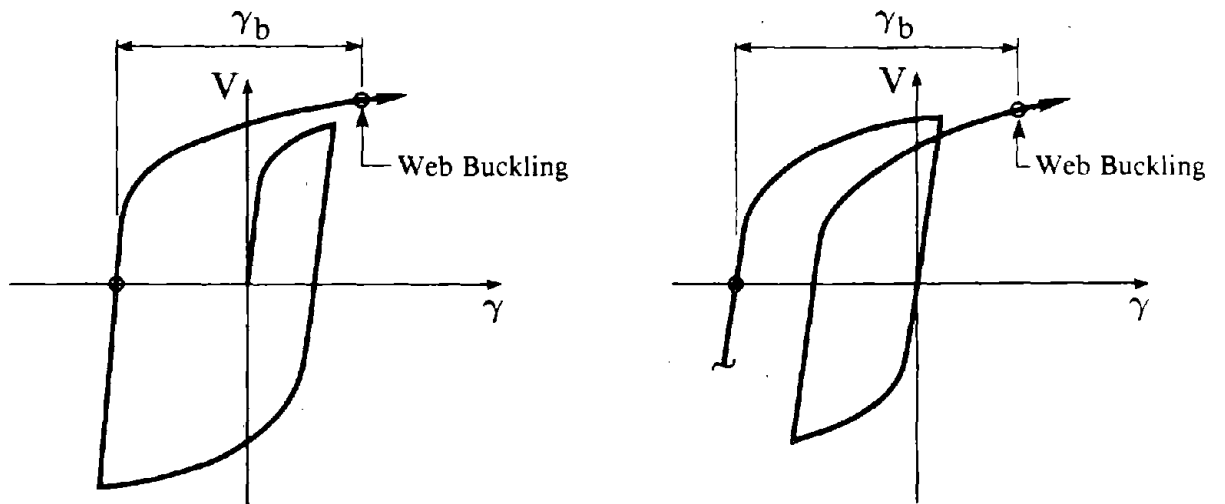


Fig. 1.15    Shear vs. Link Deformation Angle [7].
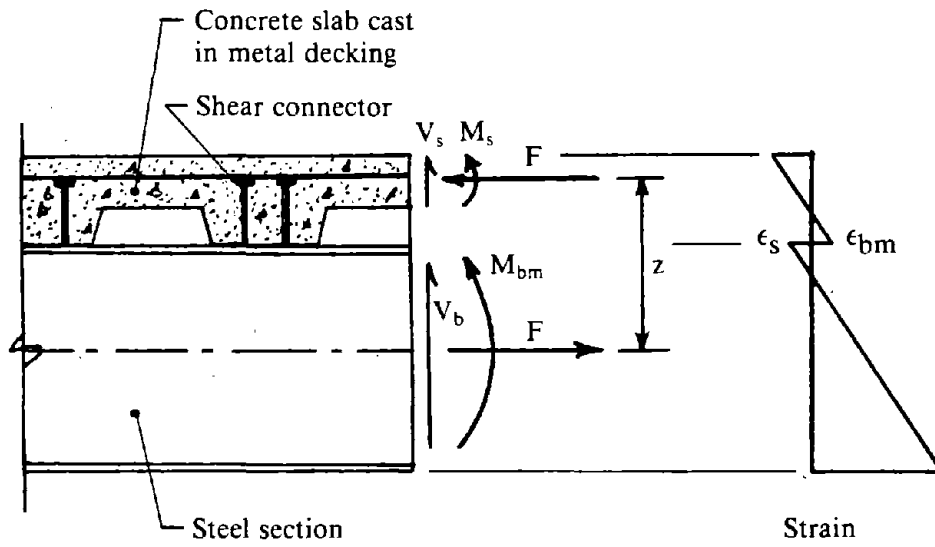
Fig. 1.16    Internal Forces Acting at a Section of a Composite Beam.
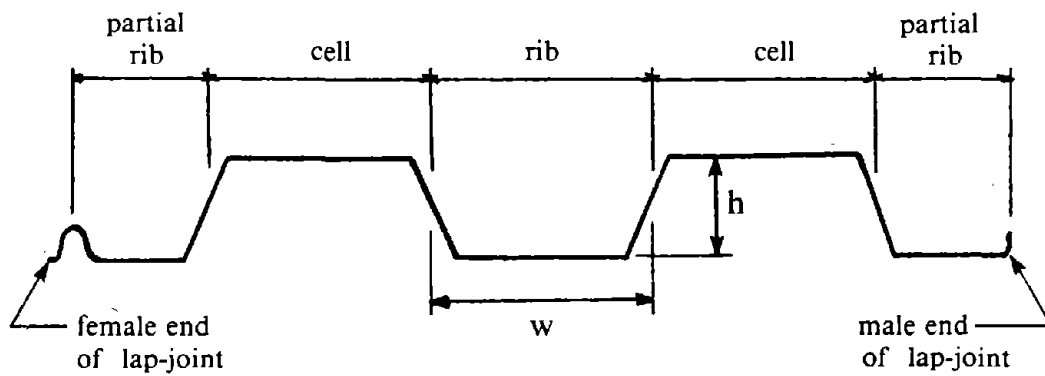


Fig. 1.17    Typical Metal Decking Used in Composite Construction.

Section
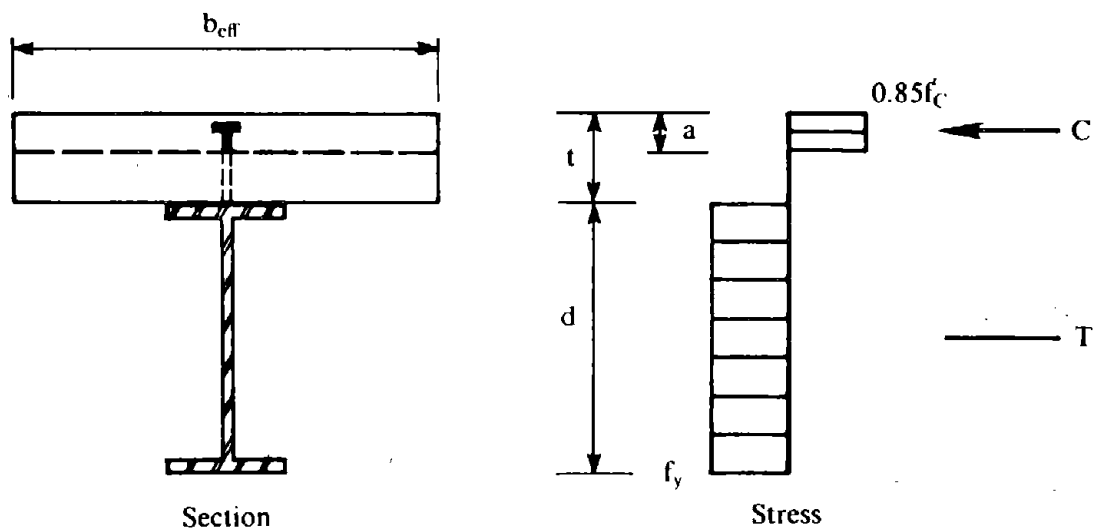
Stress

(1) ● **From stress field**

$$C = 0.85f'_C ab_{eff}$$

$$T = A_s f_y$$

(2) ● **From equilibrium**

$$a = \frac{A_s f_y}{0.85f'_C b_{eff}}$$

(3) ● **Since**

$$e = \frac{d}{2} + t - \frac{a}{2}$$

(4) ● **Hence**

$$M^+_{ult} = T \cdot e = A_s f_y \left[ \frac{d}{2} + t - \frac{a}{2} \right]$$

Fig. 1.18    Plastic Positive Moment Capacity For Full Composite
Action, Case 1:  Neutral Axis in Slab [11].

**Section**
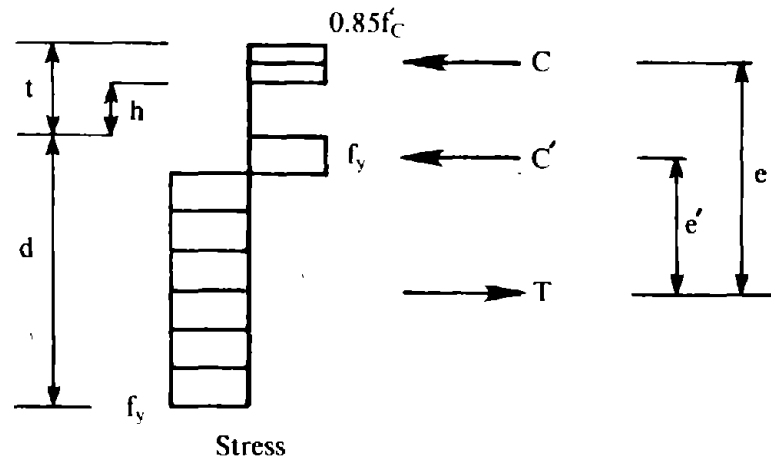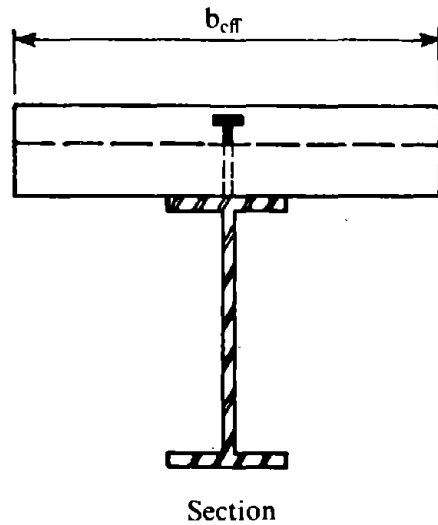
**Stress**

(1) ● **From stress field**

$$C = 0.85f'_C b_{eff}(t - h)$$

(2) ● **From equilibrium**

$$A_s f_y = T + C'$$

$$T = C + C'$$

thus, $$C' = \frac{A_s f_y - 0.85f'_C b_{eff}(t - h)}{2}$$

(3) ● **Determine e and e', knowing T and C'**

(4) ● **Hence**

$$M^+_{ult} = C \cdot e + C' \cdot e'$$

$$= 0.85f'_C b_{eff}(t - h)(e - \frac{e'}{2}) + A_s f_y \frac{e'}{2}$$

Fig. 1.19    Plastic Positive Moment Capacity For Full Composite
Action, Case 2: Neutral Axis in Steel Section [11].
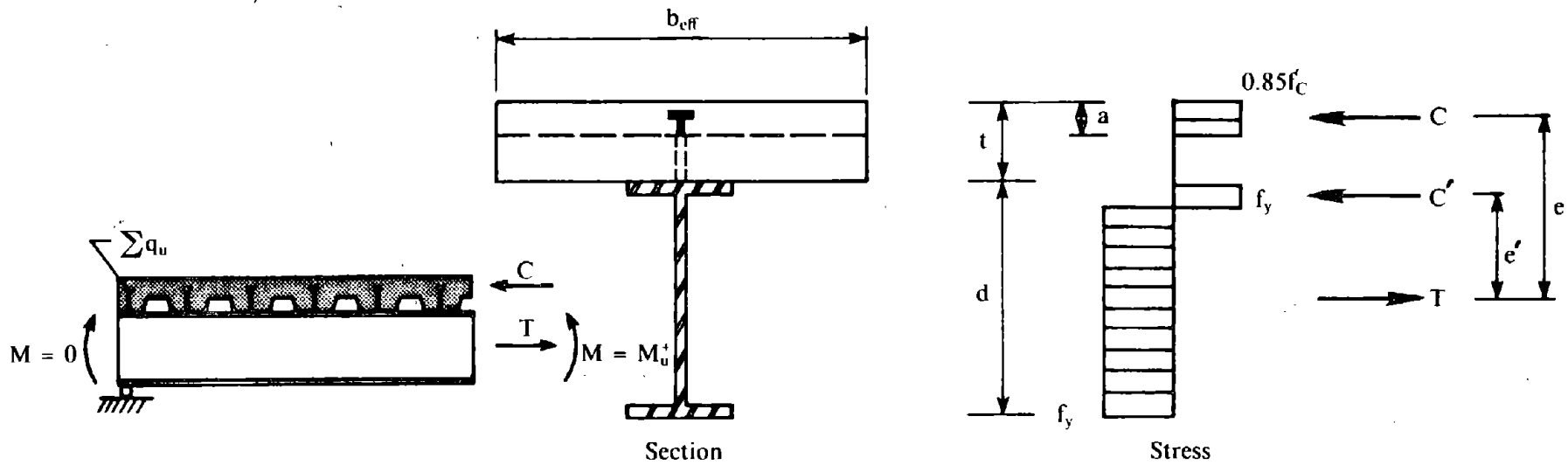
**(1)** ● **From connector strength**

$$C = \sum q_u$$

**(2)** ● **From stress field**

$$a = \frac{\sum q_u}{0.85 f_C' b_{cff}}$$

**(3)** ● **From equilibrium**

$$C' = T - C = \frac{A_s f_y - \sum q_u}{2}$$

**(4)** ● **Determine e and e', knowing T and C'**

**(5)** ● **Hence**

$$M_{ult}^+ = C \cdot e + C' \cdot e'$$

$$= (e - \frac{e'}{2})\sum q_u + A_s f_y \frac{e'}{2}$$

Fig. 1.20    Plastic Positive Moment Capacity for Partial Composite Action [11].

141
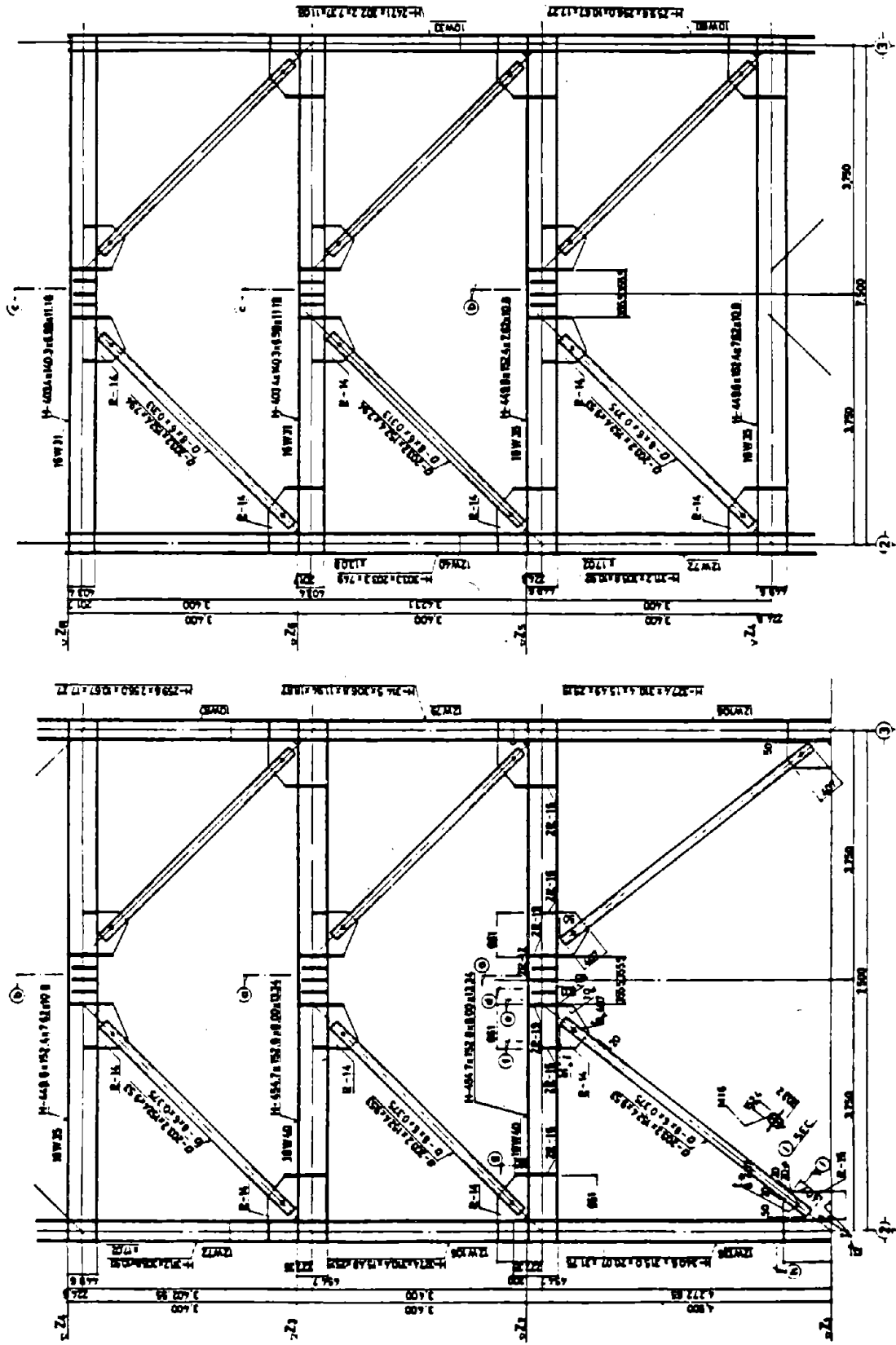


Fig. 1.21    Tsukuba EBF Test Structure [17].

142
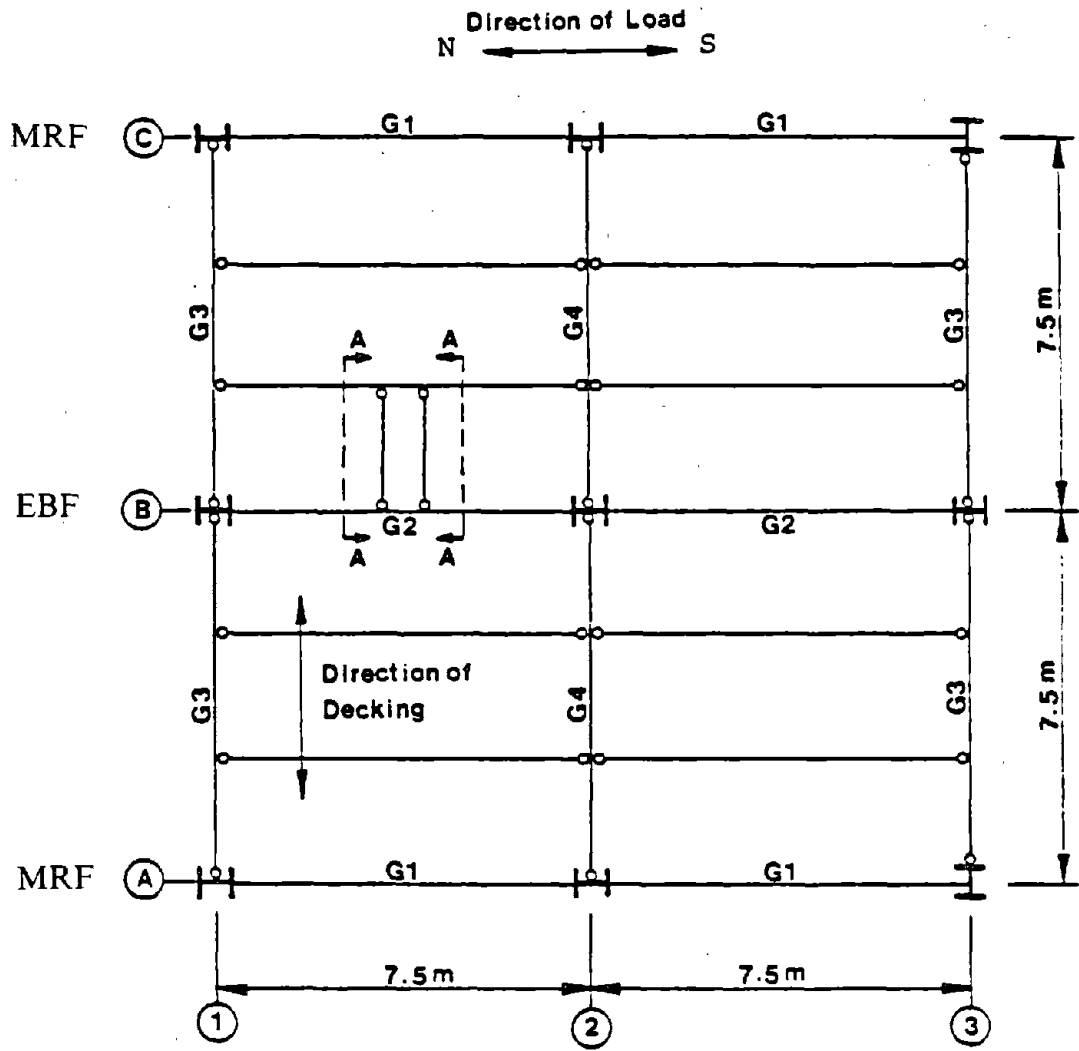


Fig. 1.22     Typical Floor Plan of Tsukuba Test Structure [17].
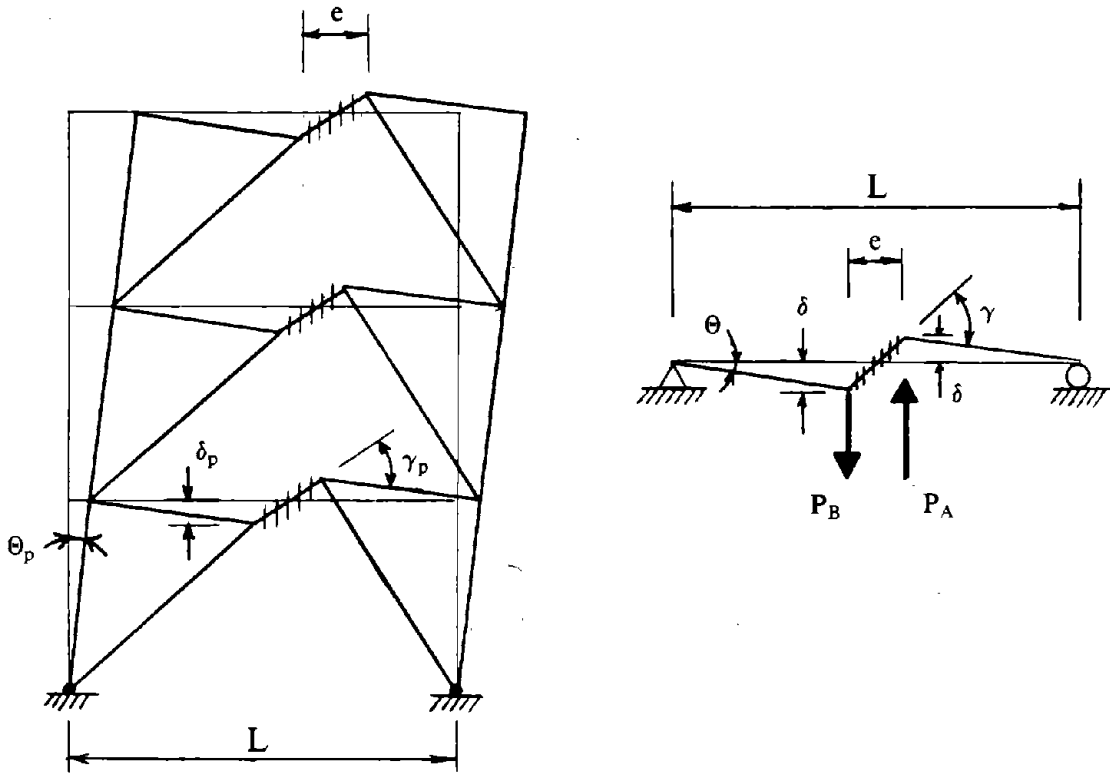
Fig. 2.1    Collapse Mechanism for (a) K-Braced EBF and (b) Experimental Simulation.
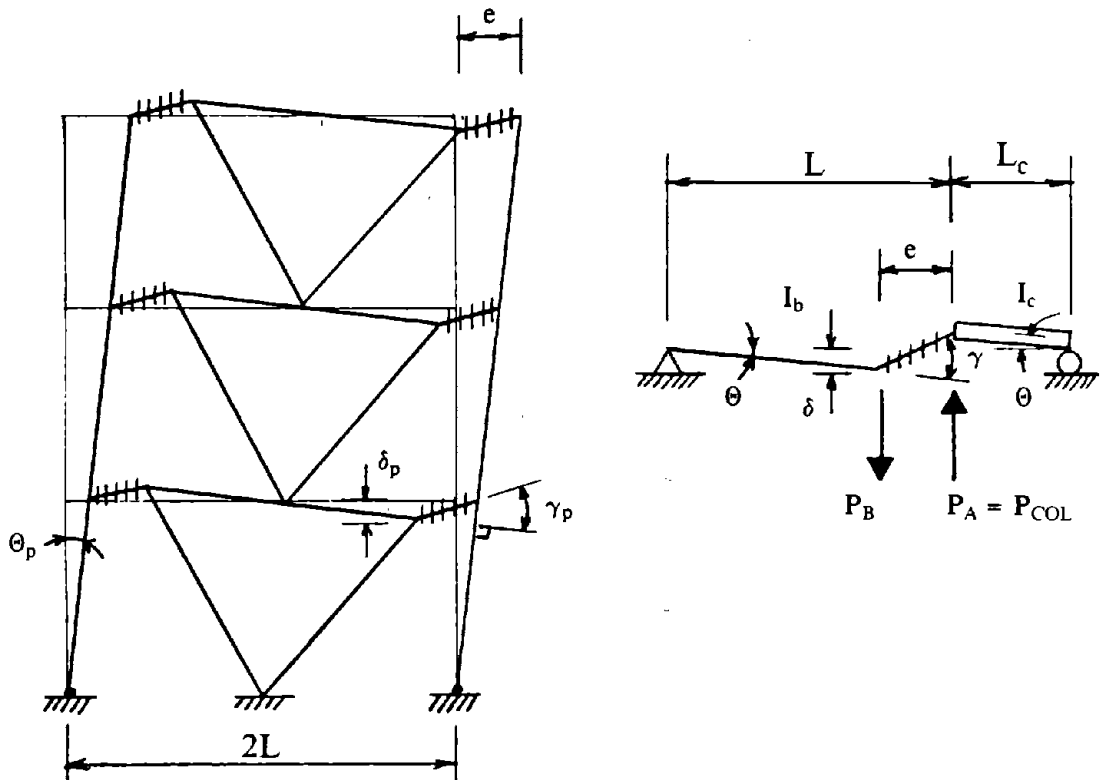


Fig. 2.2    Collapse Mechanism for (a) V-Braced EBF and (b) Experimental Simulation.
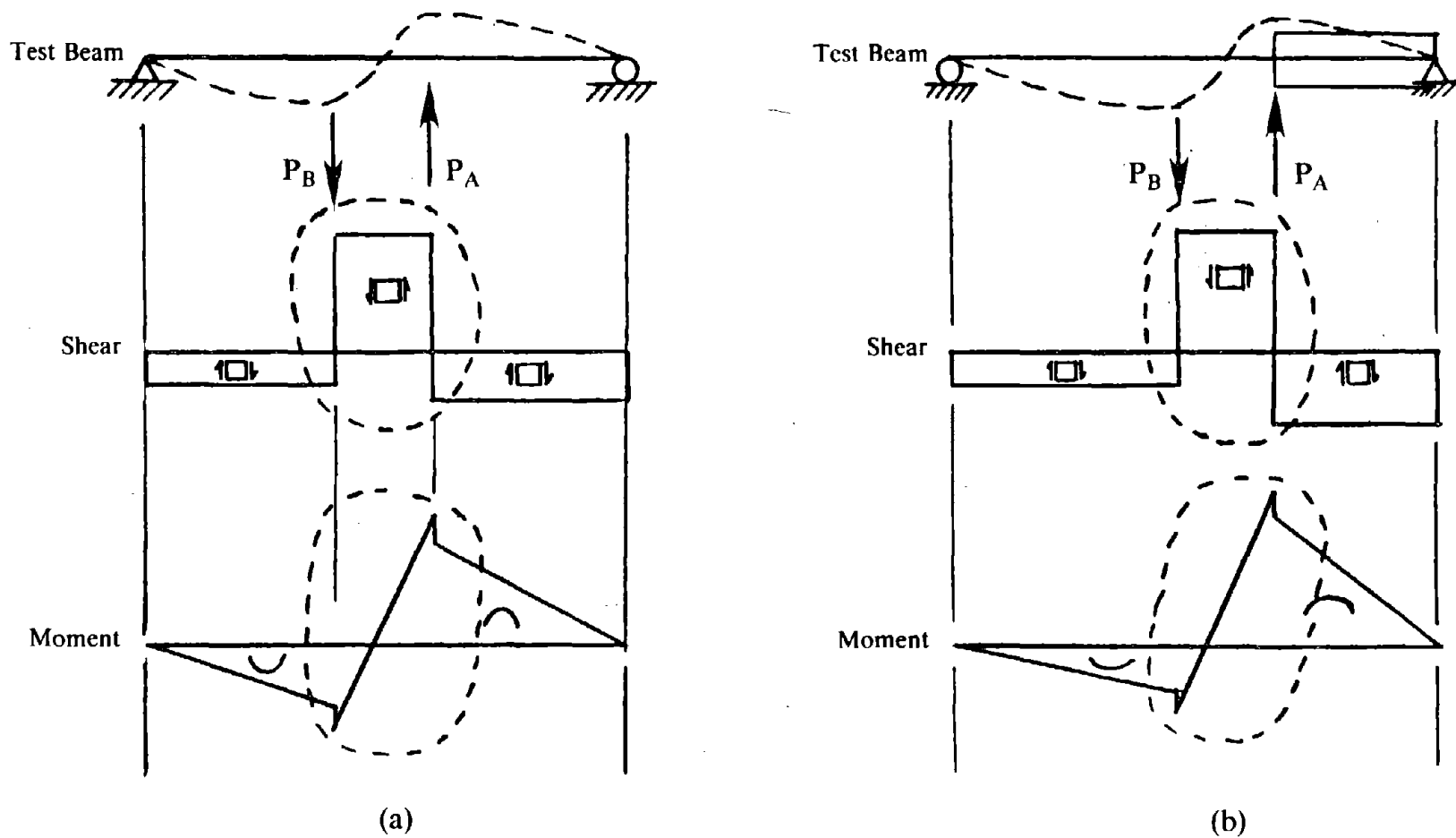
Fig. 2.3    Idealized Shear and Moment Diagrams of Test Beam for (a) K-Braced EBF and (b) V-Braced EBF Subassemblies.
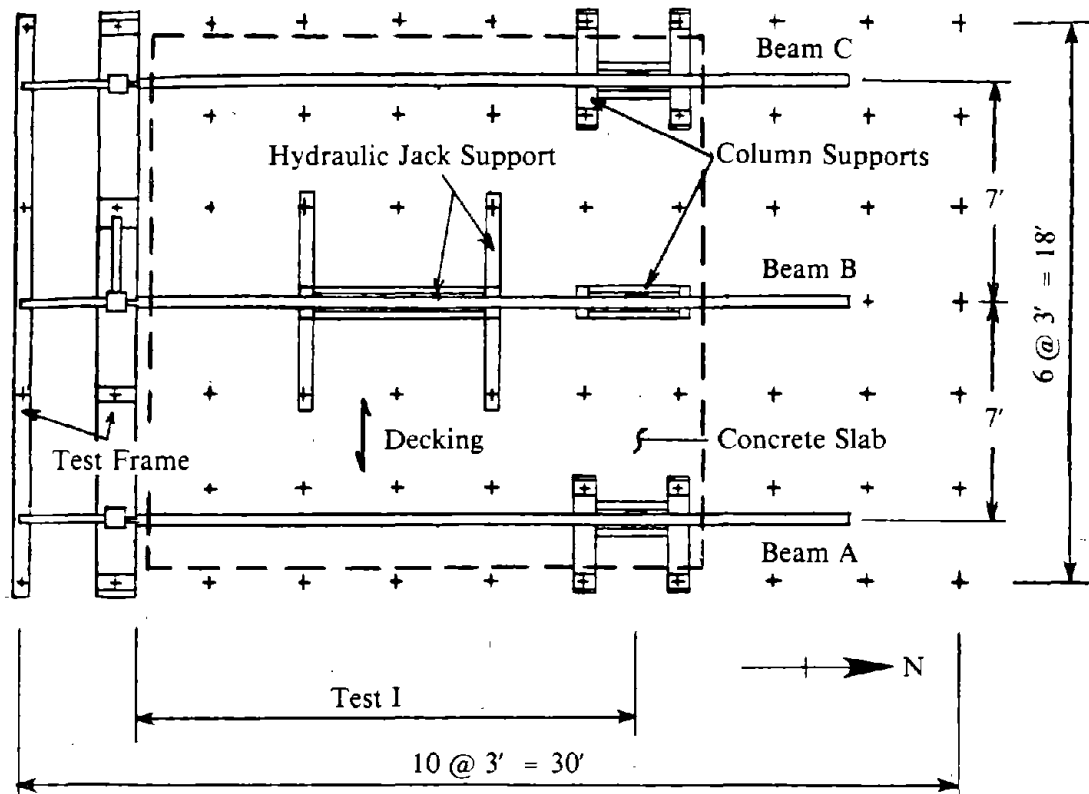
(a) Plan View - Test I
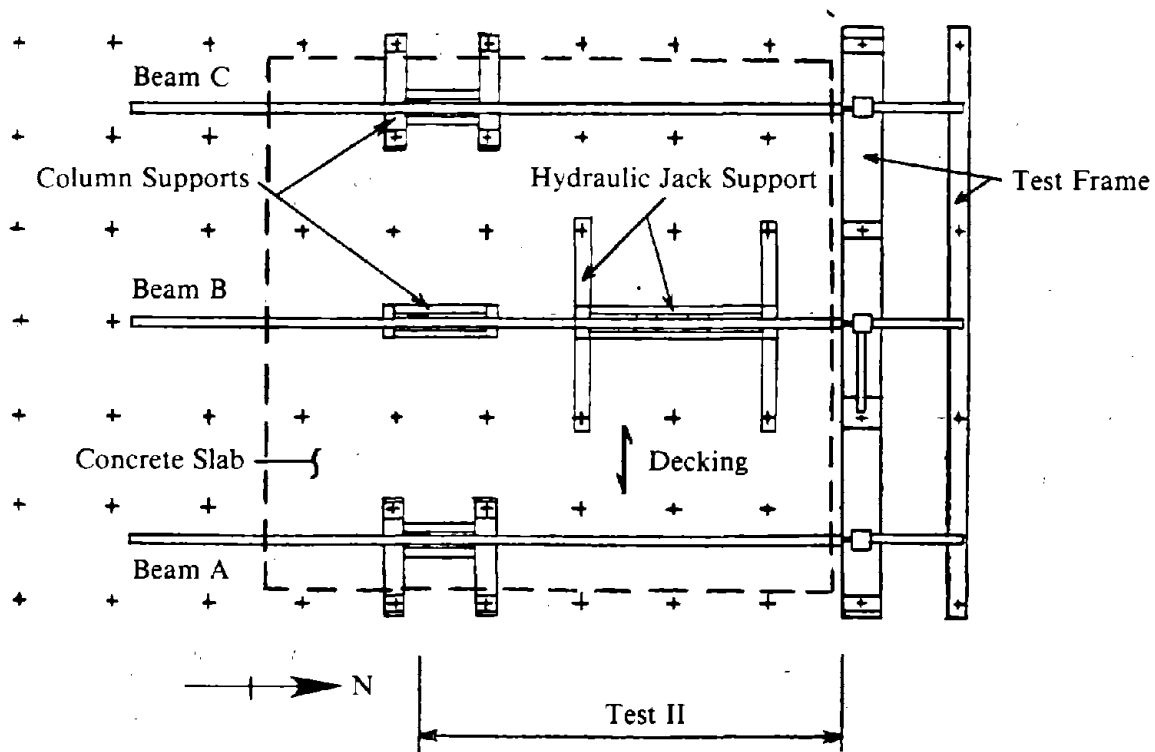


(b) Plan View - Test II

Fig. 2.4    Arrangement of Apparatus on Laboratory Floor for Testing of Links.
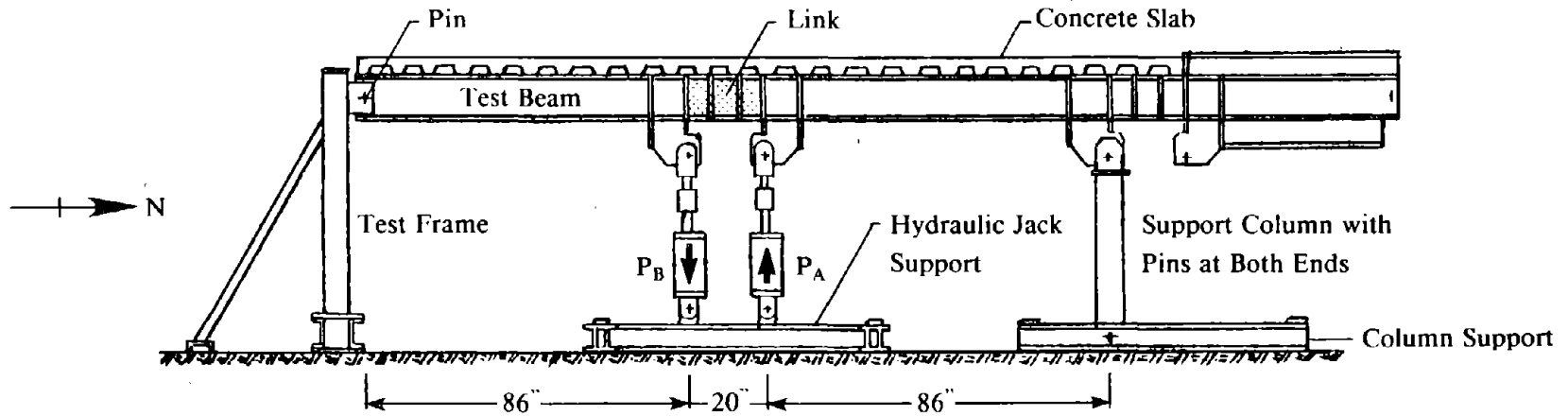
(a) K-Braced EBF Subassembly, Test Series I
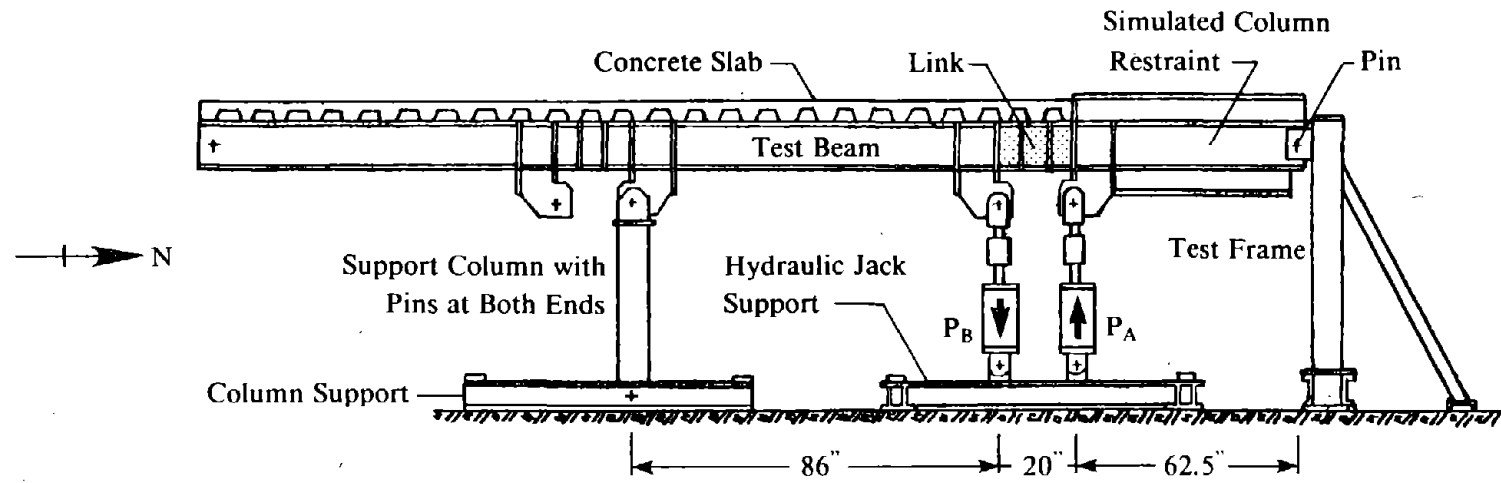
(b) V-Braced EBF Subassembly, Test Series II

Fig. 2.5    Test Setup for Testing of Links.
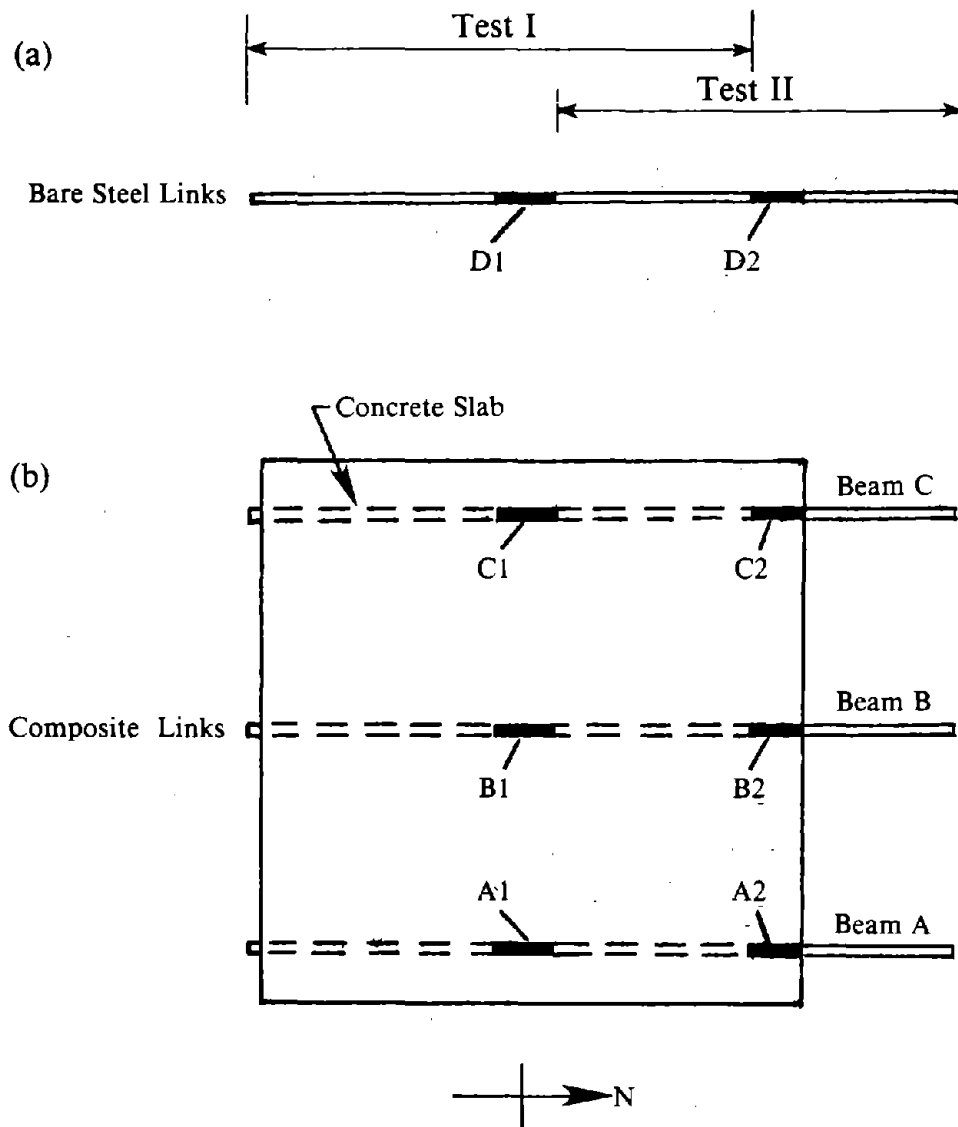
Fig. 2.6    Location of (a) Bare Steel and (b) Composite Links.

148
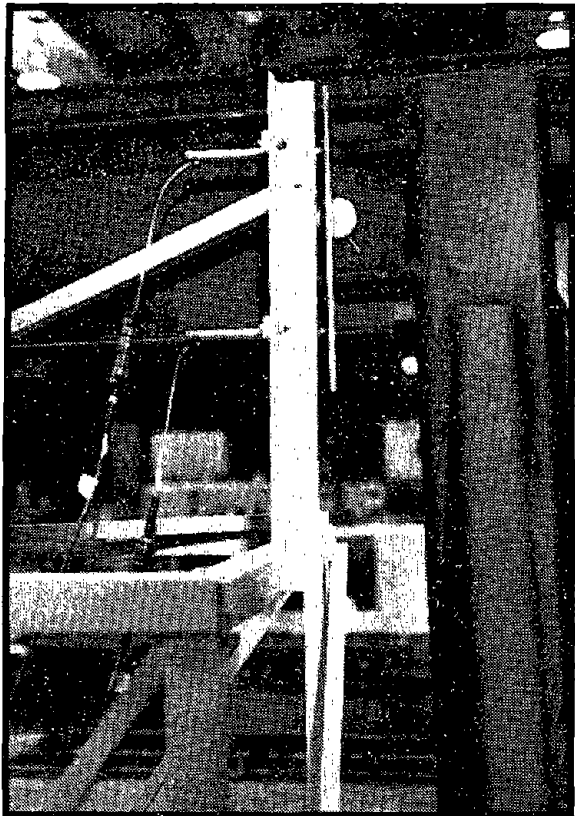


(a) Pinned Shear Tab Connection to
Test Frame
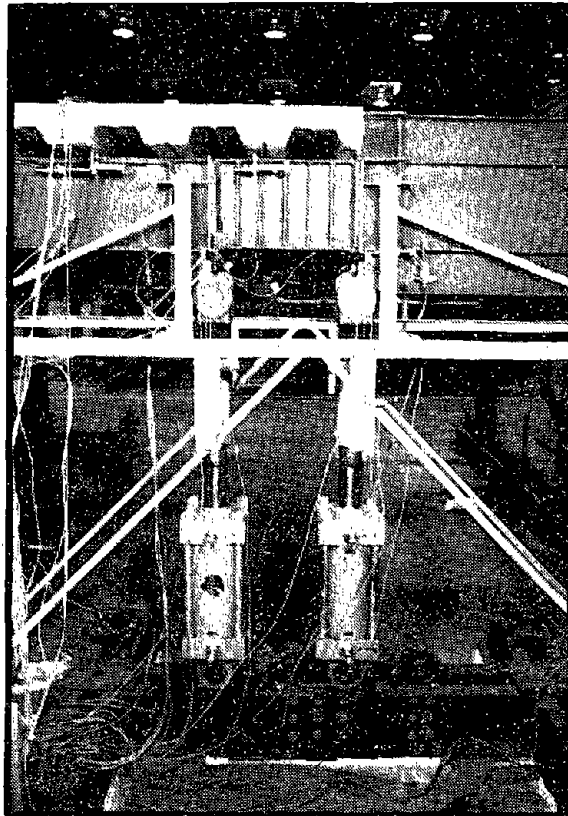


(c) Hydraulic Jacks
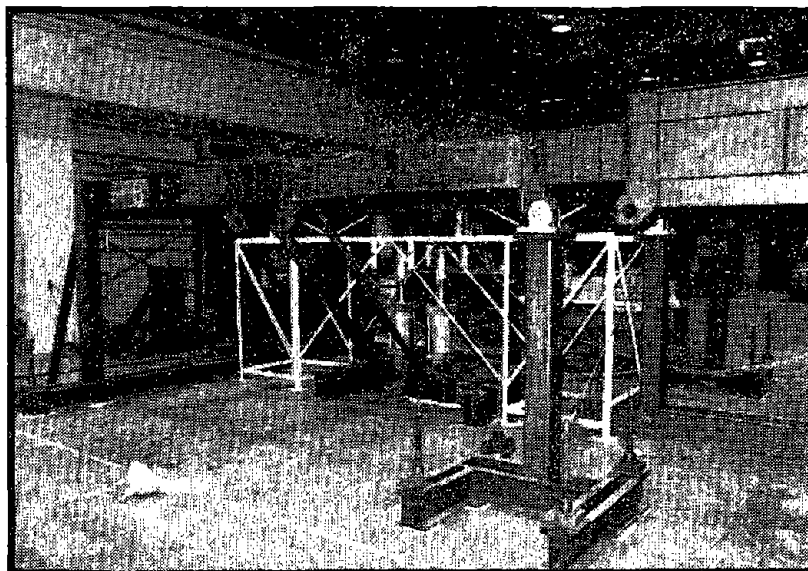


(b) Pinned Ended Support Column

Fig. 2.7     Beam Support and Hydraulic Jacks.
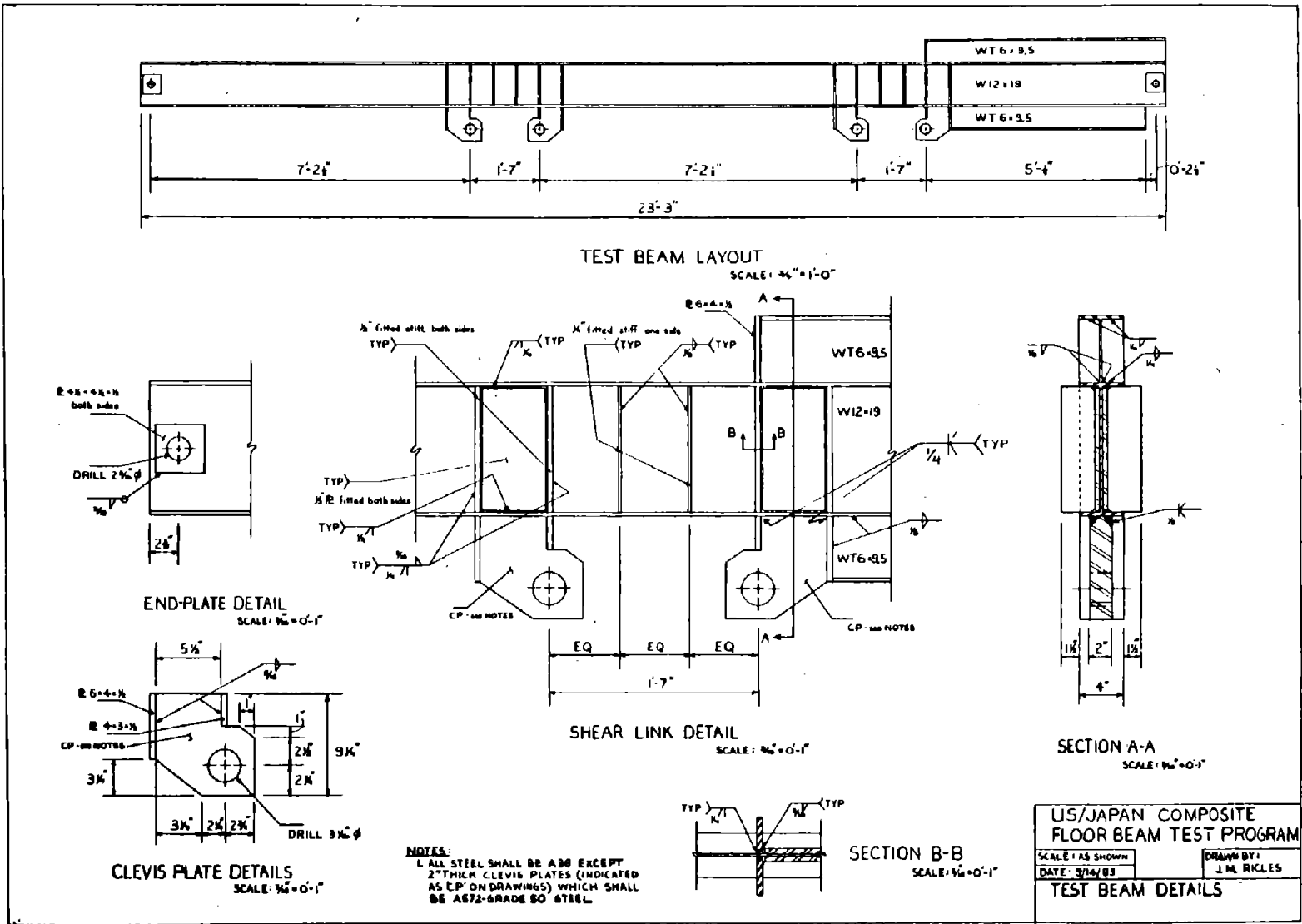
Fig. 2.8    Test Beam Details.
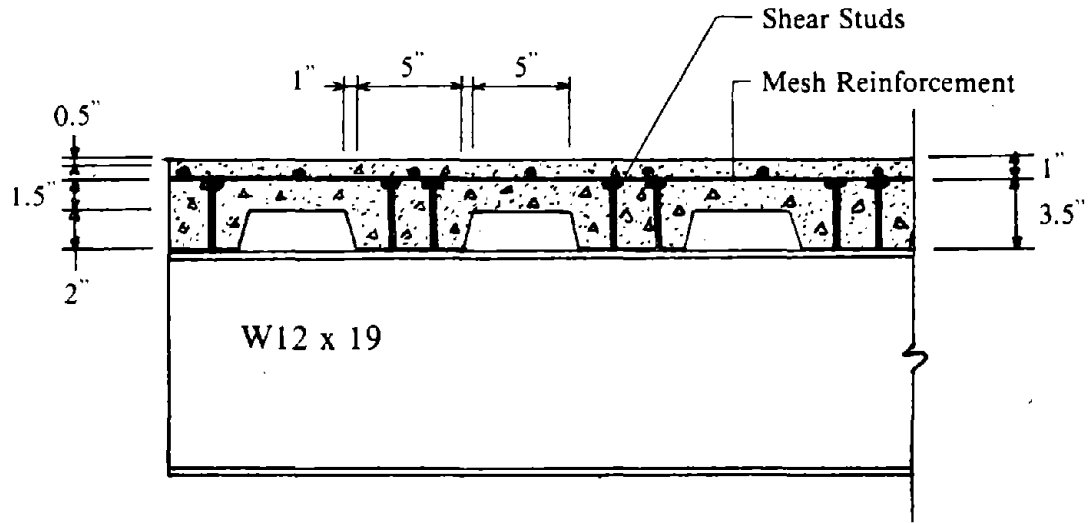
Fig. 2.9      Longitudinal Section Through Ribbed Concrete Floor Slab.

(a)
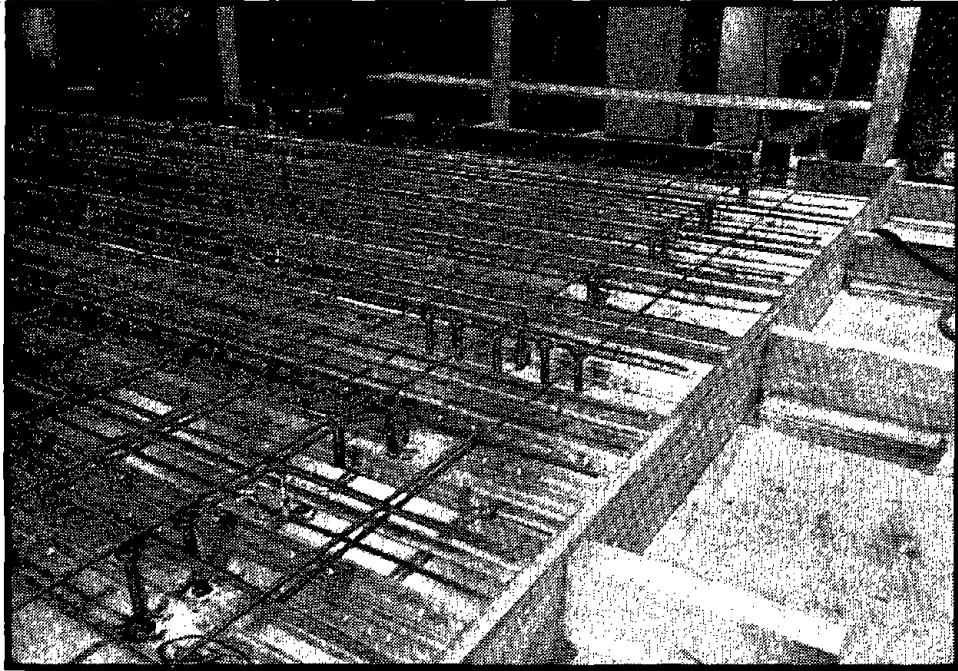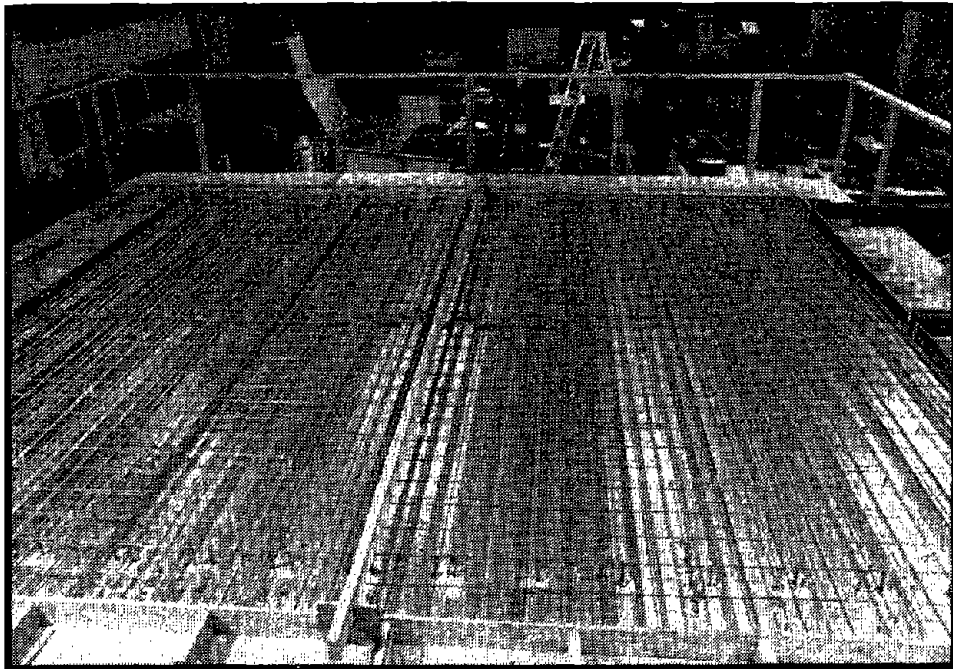
(b)

Fig. 2.10    Floor Slab Before Casting Concrete.
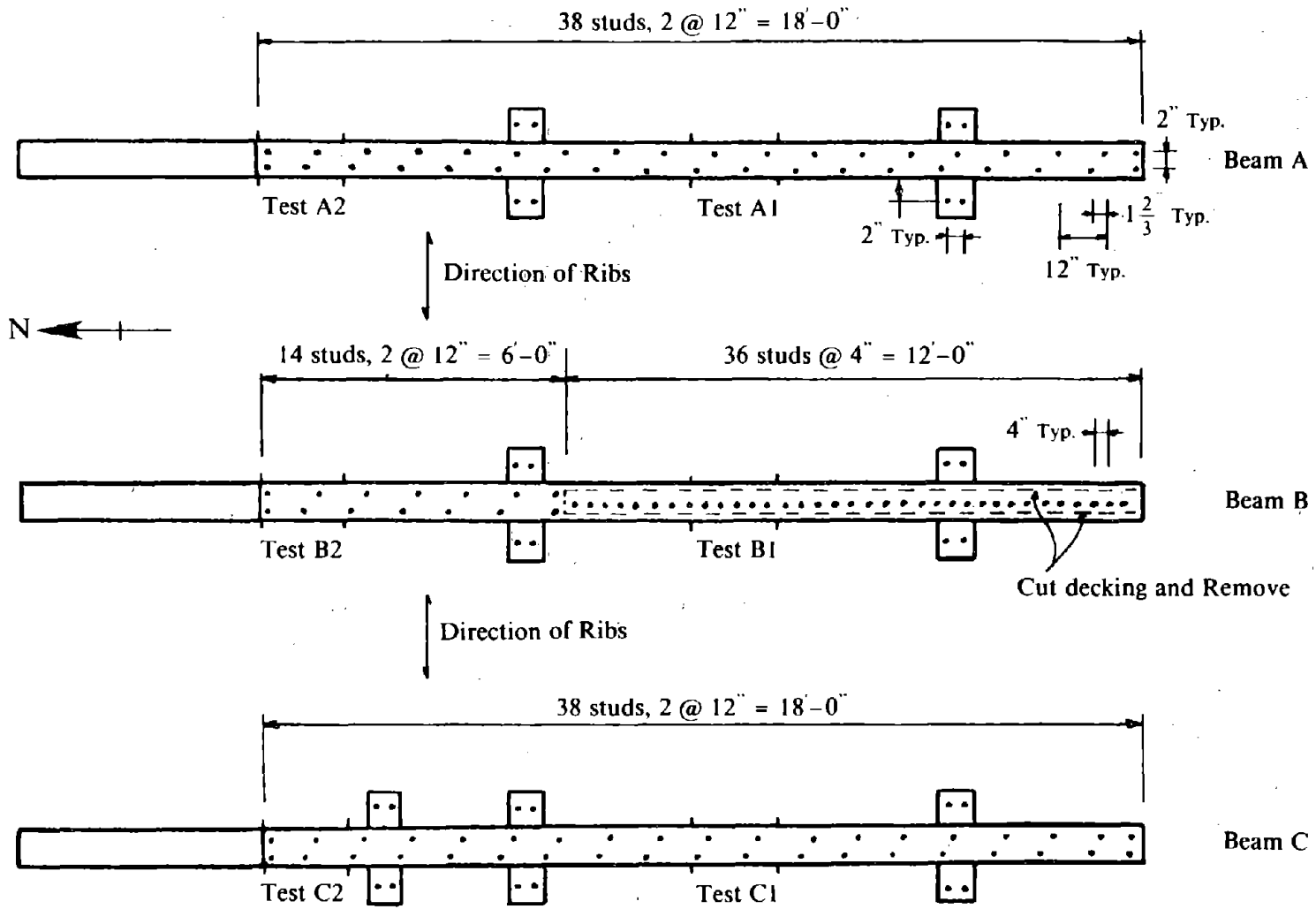
Fig. 2.11    Shear Connector Layouts.
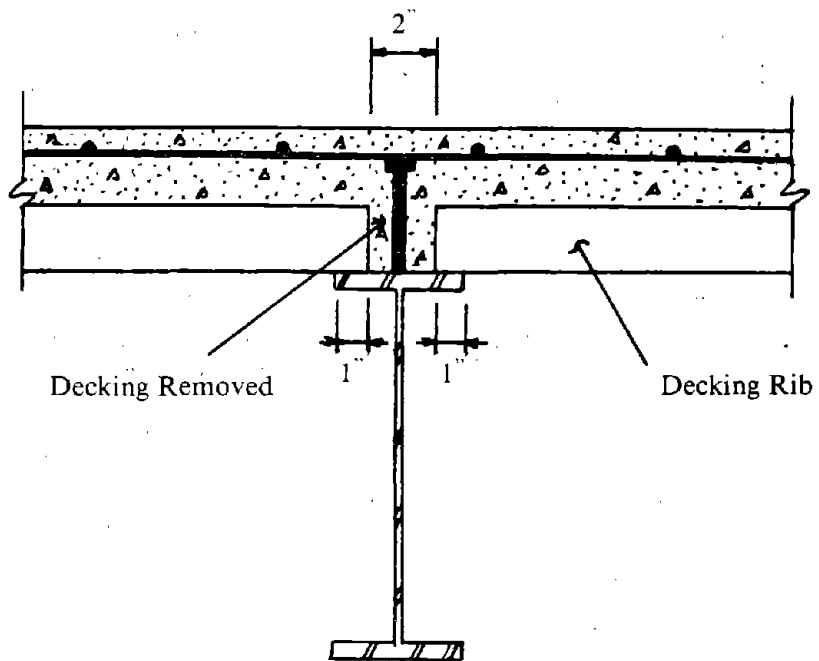
(a)  Transverse Section Through Concrete Floor Slab

(b)  General View

Fig. 2.12      Decking Detail for Specimen B1.
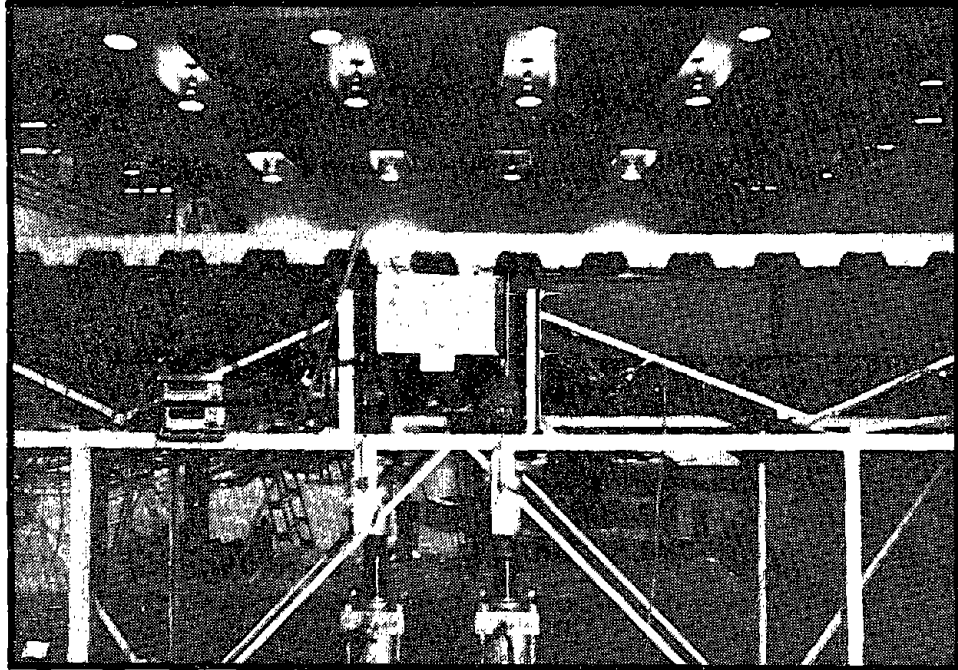
154



(a) K-Braced EBF Subassembly
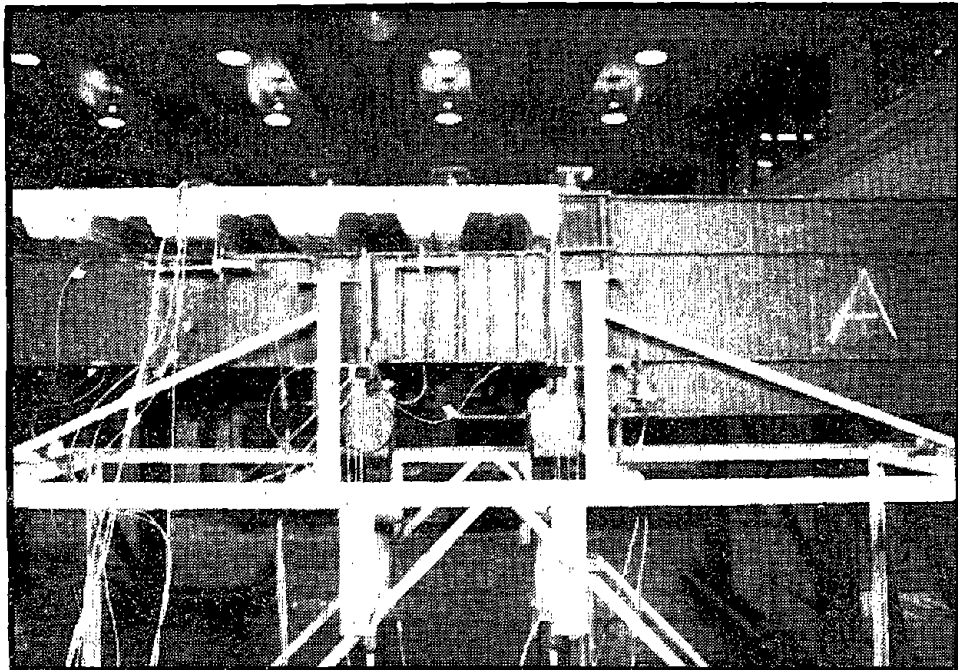
(b) V-Braced EBF Subassembly

Fig. 2.13    Deck Rib Locations Over Links.
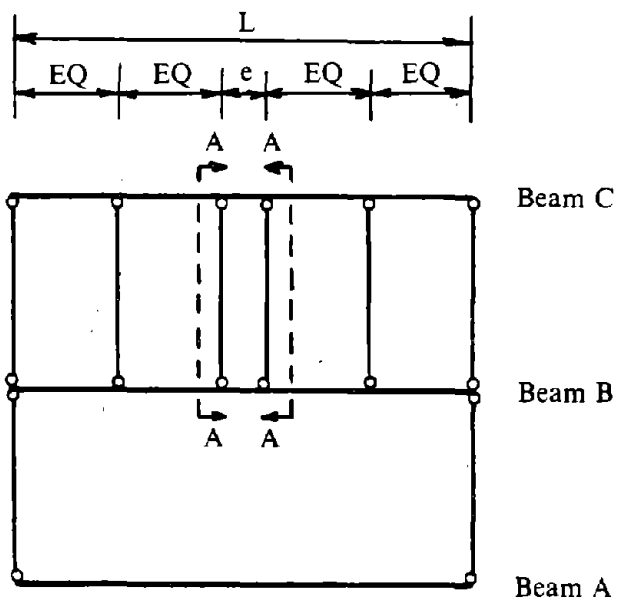
(a) Plan of Lateral Bracing for Beam B or C
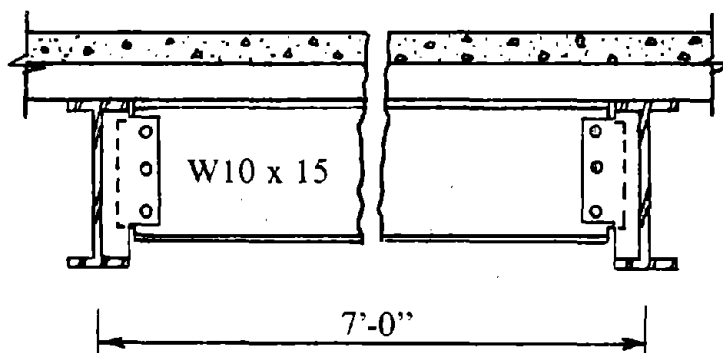
(b) Section A-A

Fig. 2.14    Lateral Bracing of Typical Test Beam.
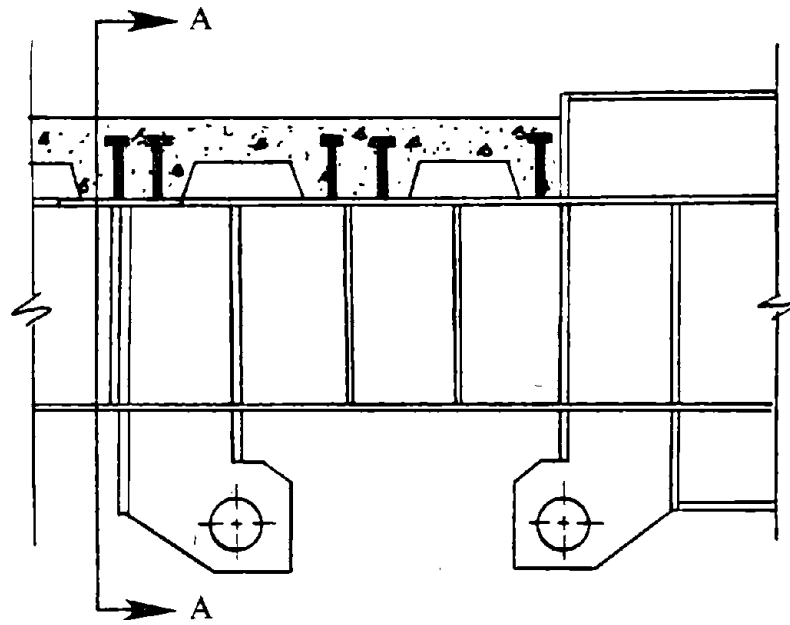
(a)
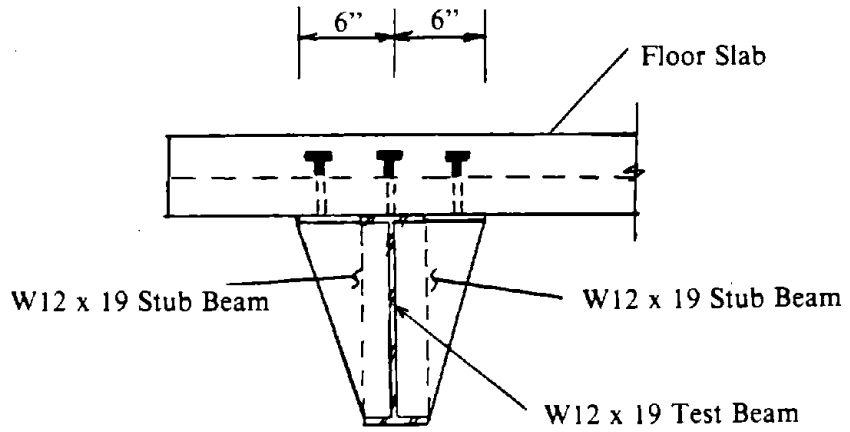


SECTION A-A

(b)

Fig. 2.15    Specimen C2 Lateral Bracing Stub Beam Detail at End of Link.
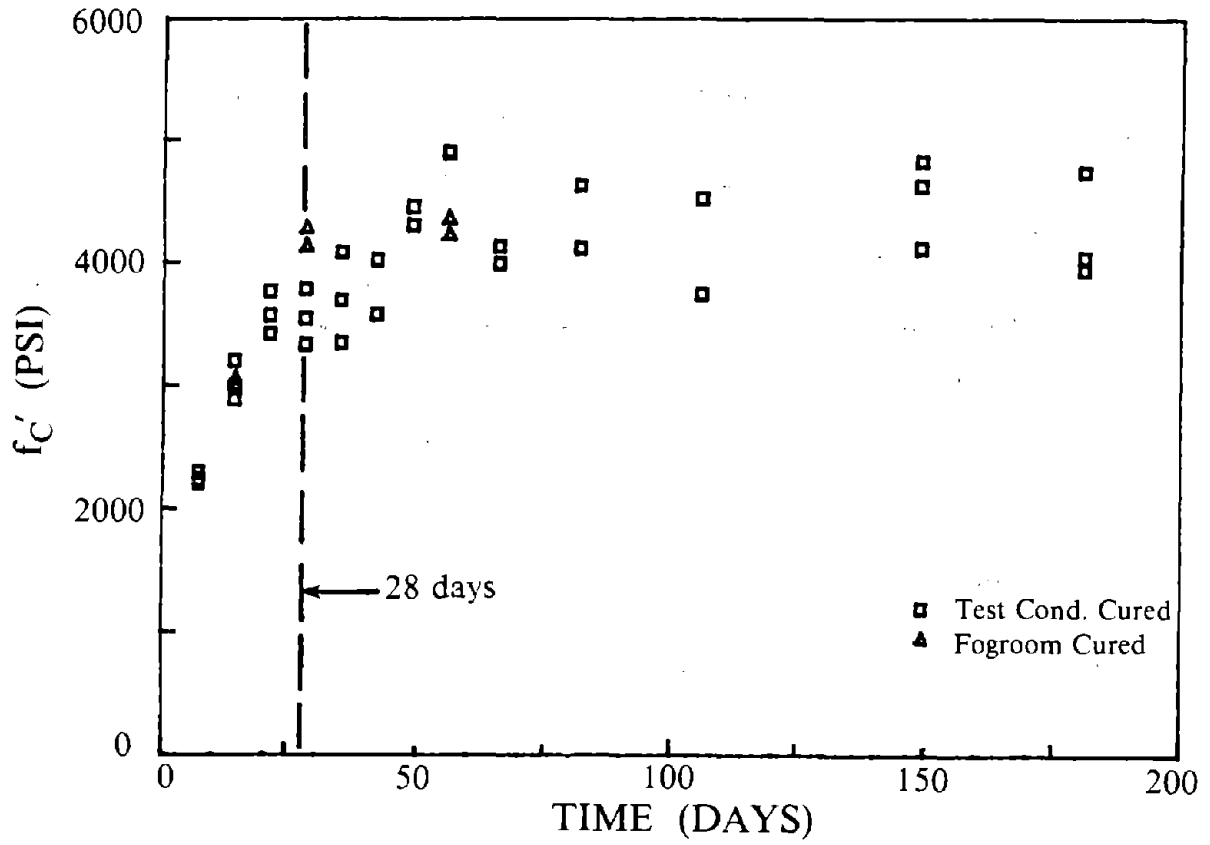
Fig. 2.16      Concrete Compressive Strength.
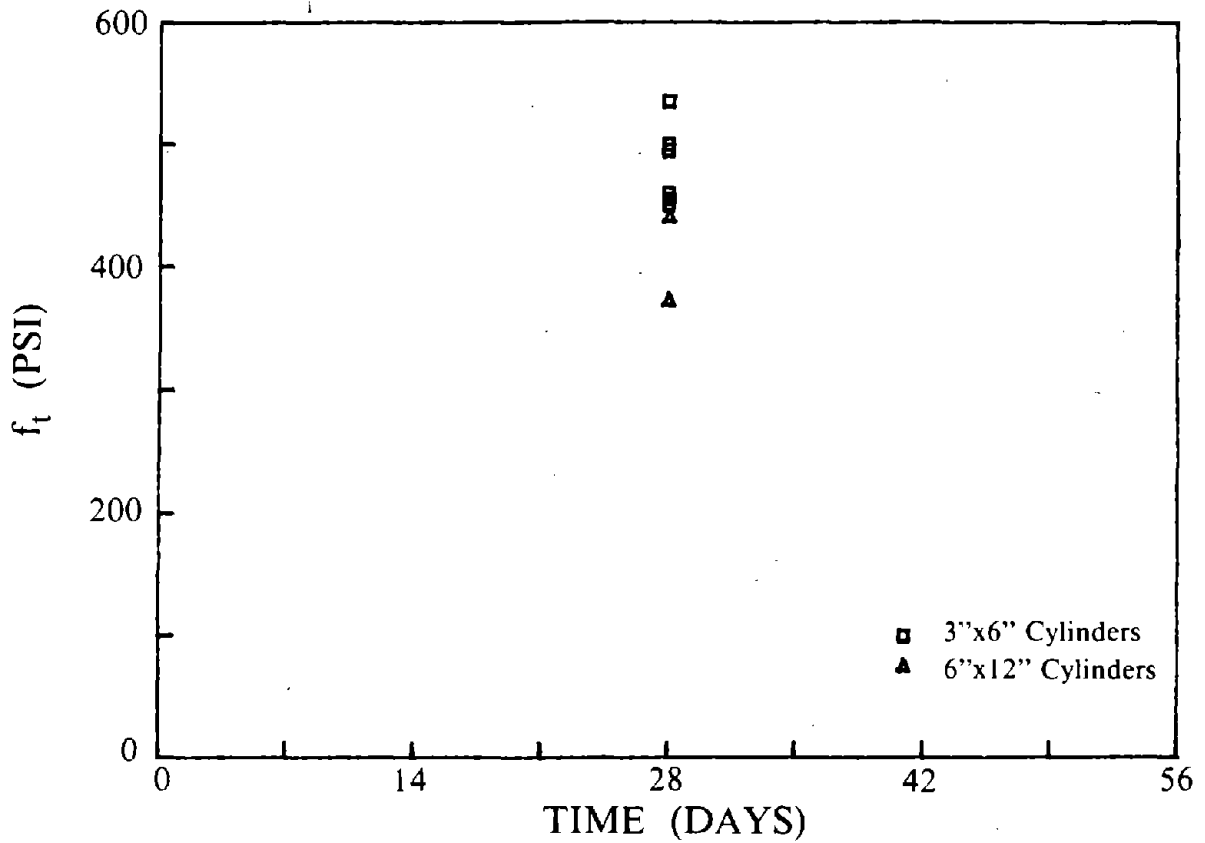


Fig. 2.17      Concrete Tensile Strength.
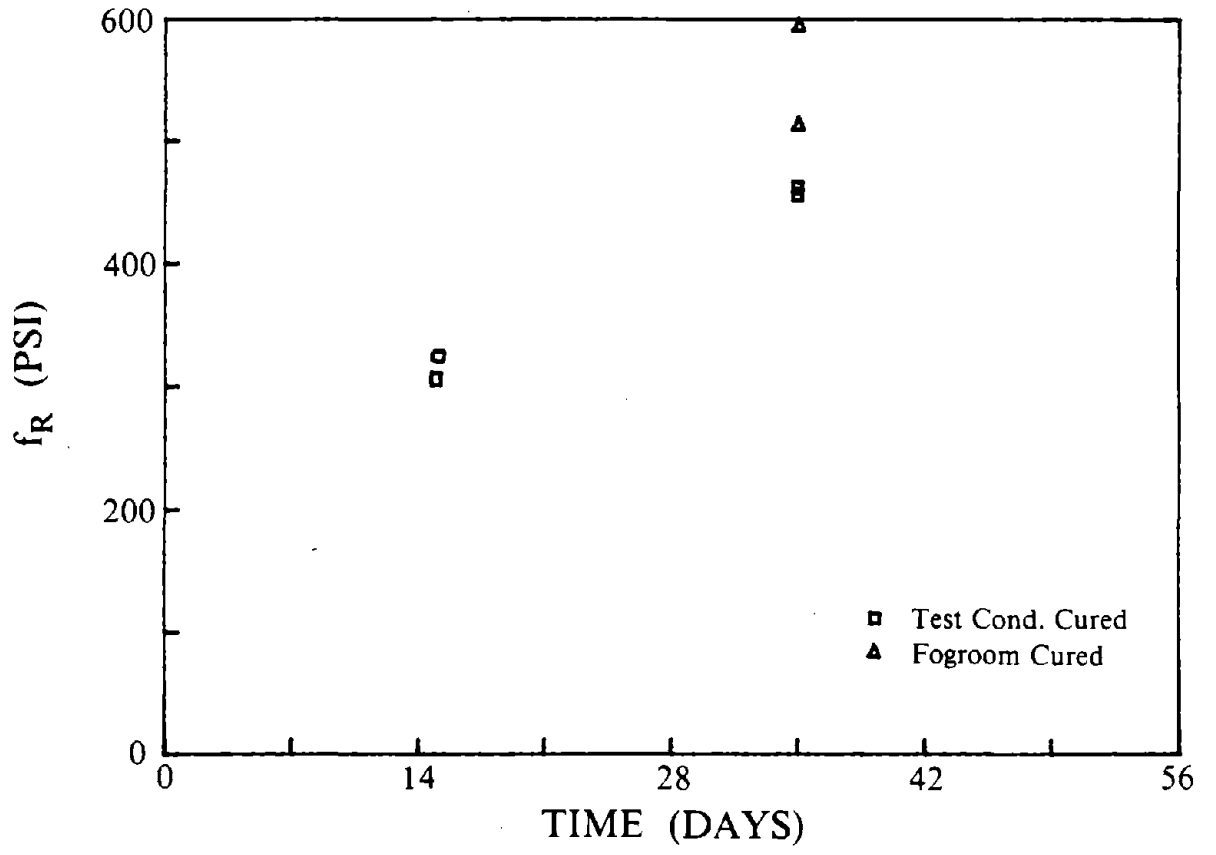
Fig. 2.18        Concrete Modulus of Rupture.
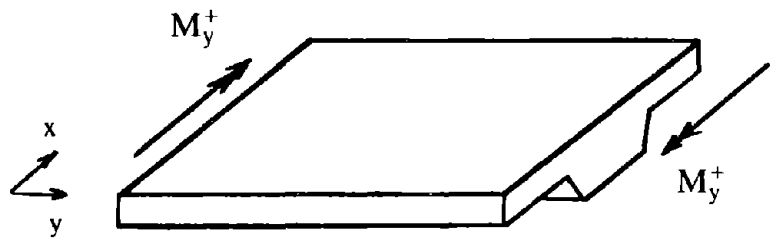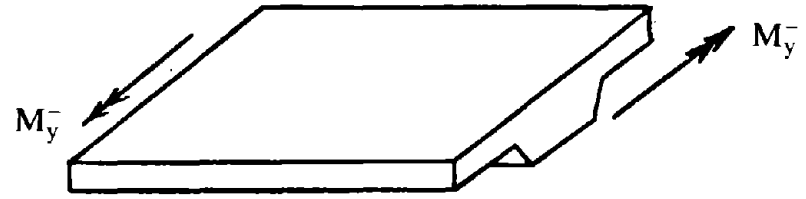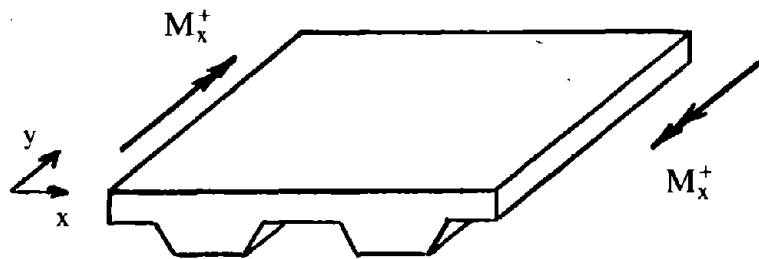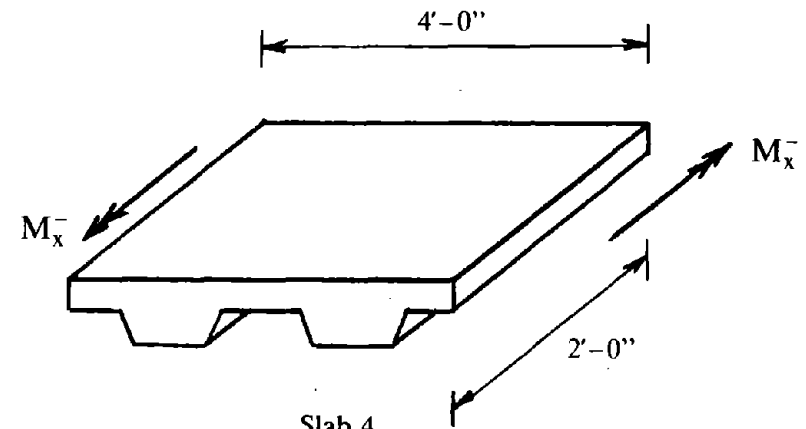
Fig. 2.19    Slab Test Specimens.
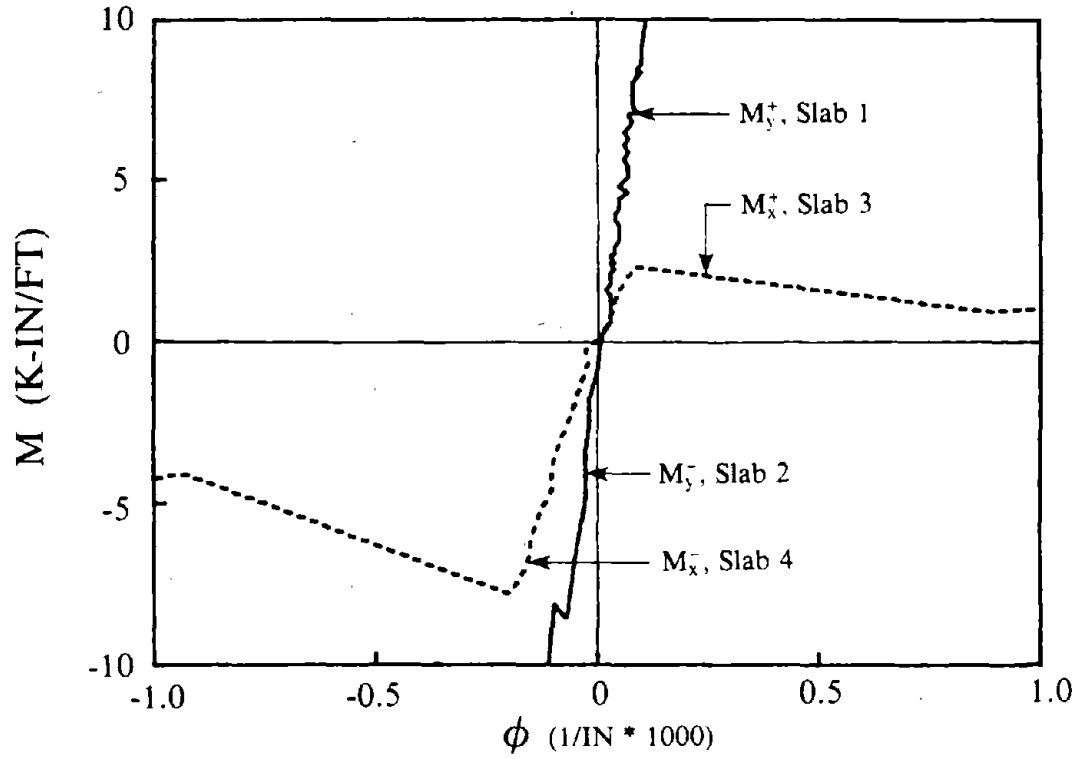
(a)  Small Curvature Regime
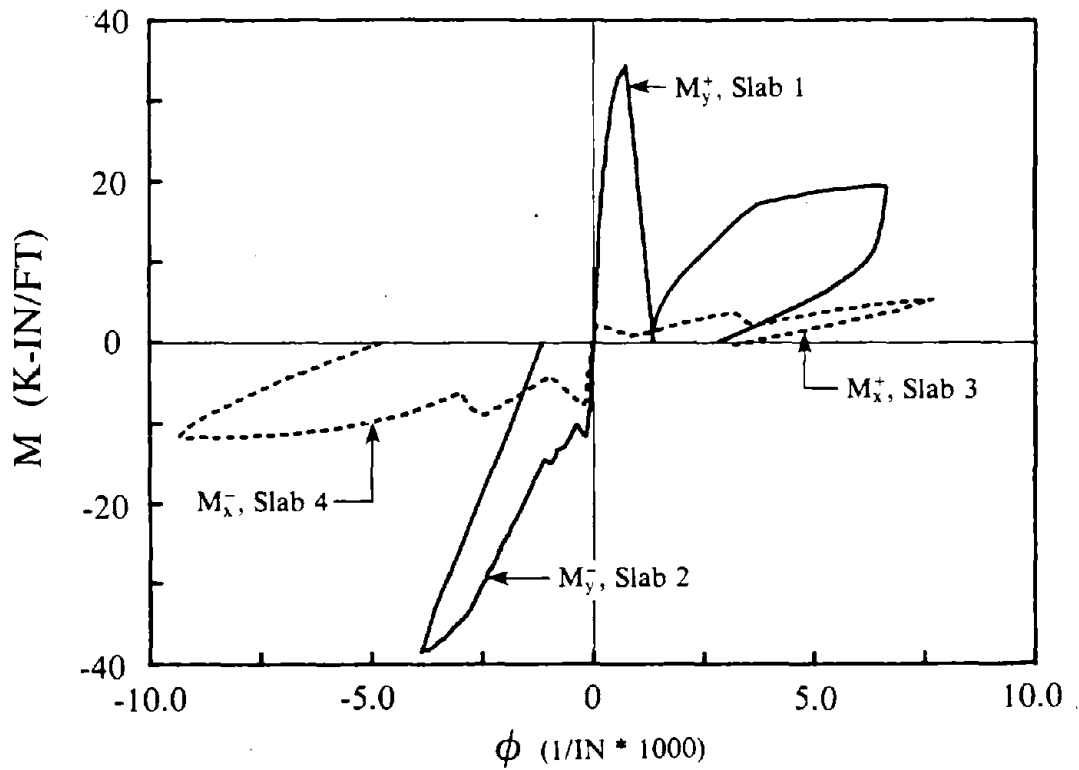
(b)  Large Curvature Regime

Fig. 2.20        Moment-Curvature Relationship of Floor Slab.
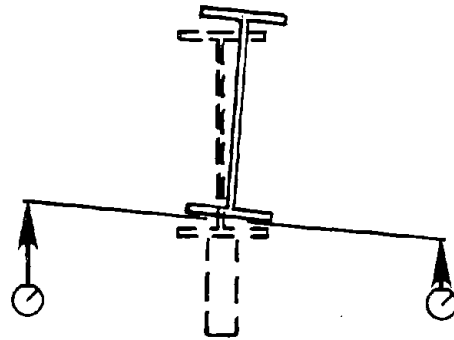
(a) Instrumentation for Vertical Displacement and Twist
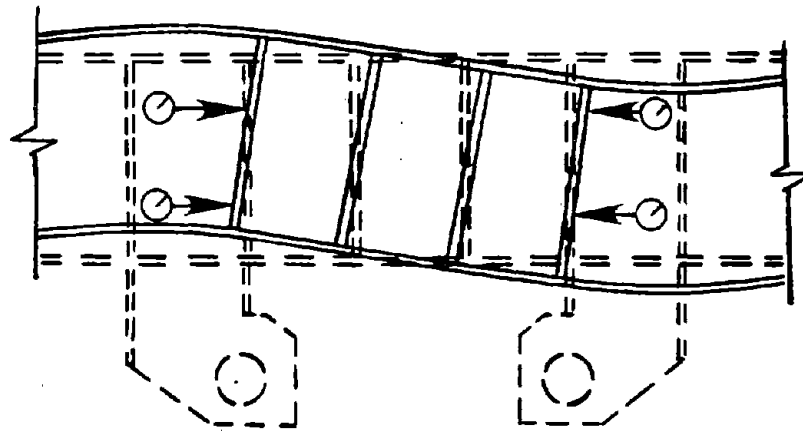


(b) Instrumentation for Horizontal Displacement and Rotation

Fig. 2.21    Measuring Movement of the Steel Section.

162
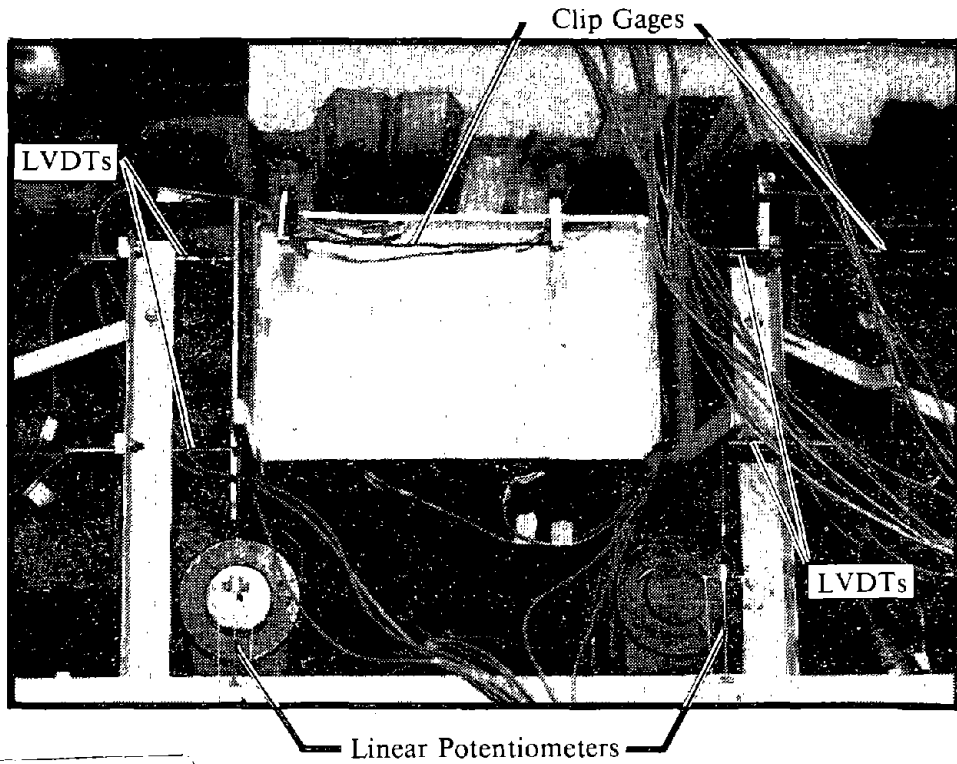


(a)
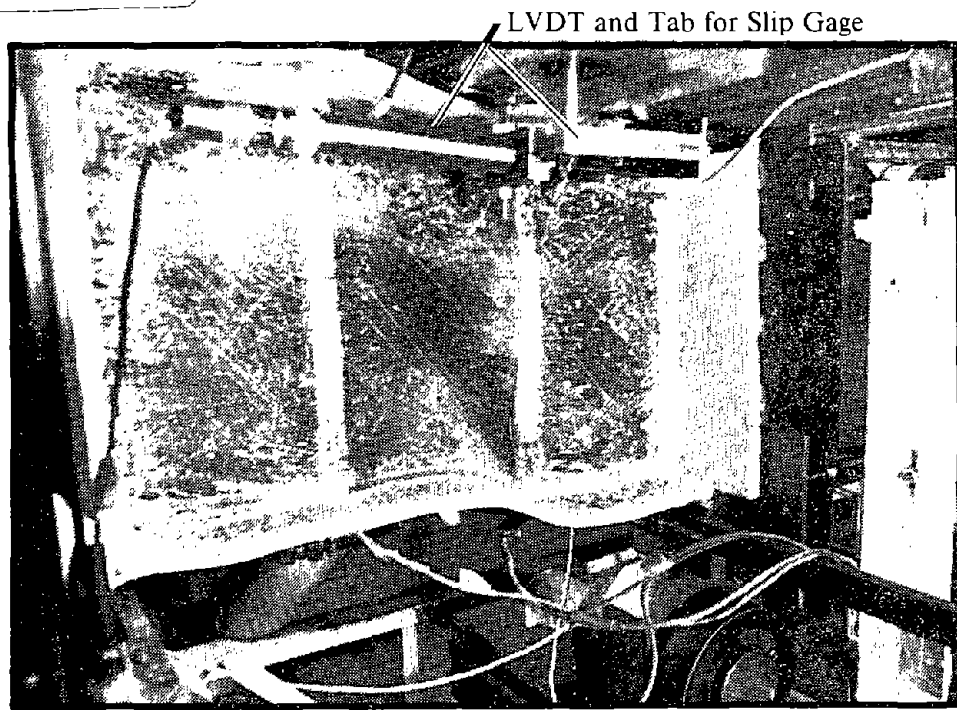
(b)

Fig. 2.22      Instrumentation of Link Specimens.
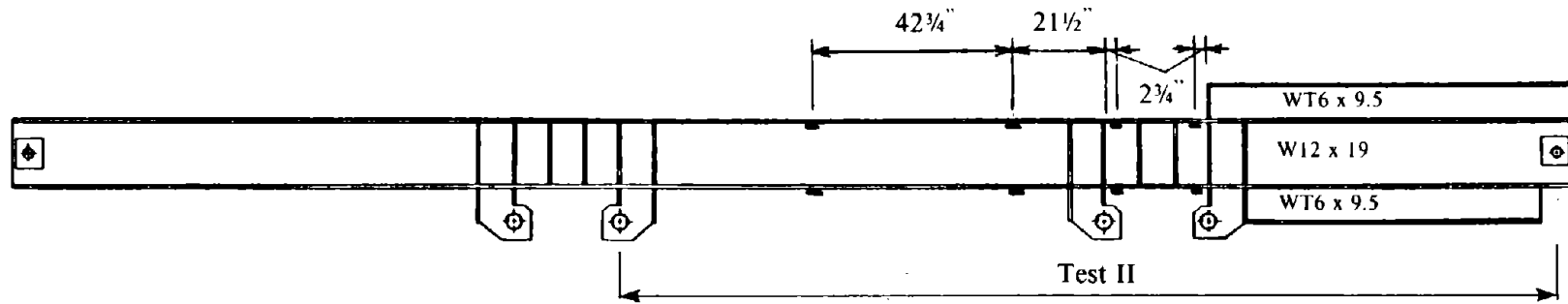
(a) V-Braced EBF Subassembly
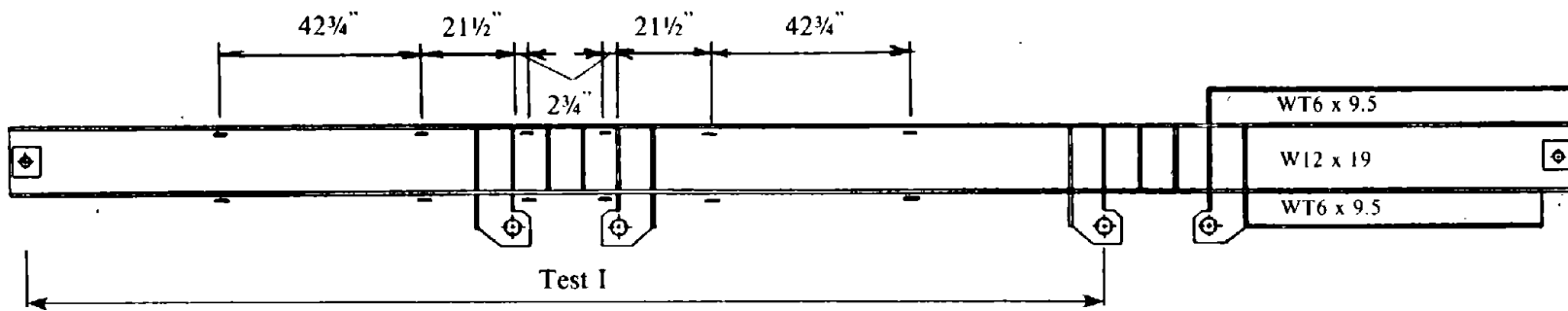
(b) K-Braced EBF Subassembly

Fig. 2.23     Strain Gage Locations for Test Beam.
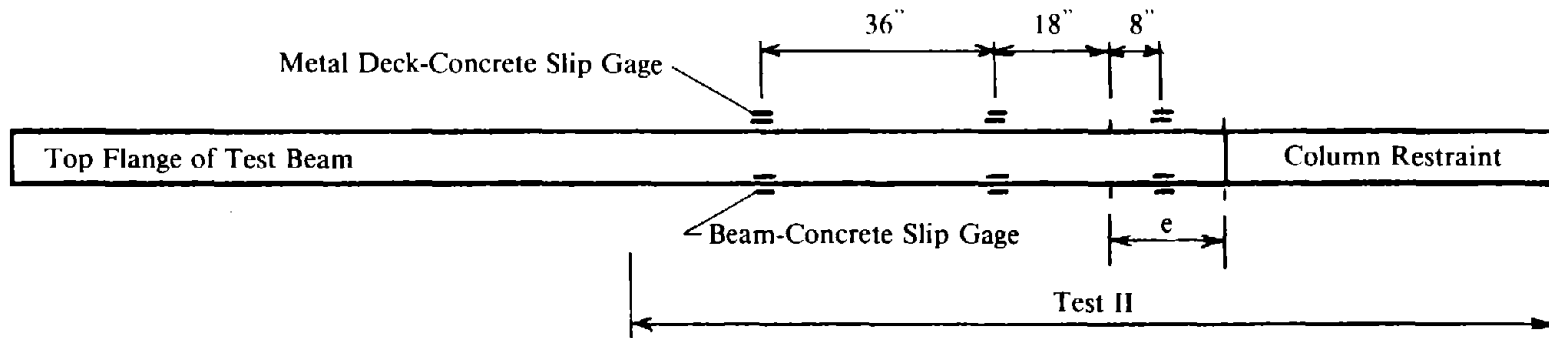
(a) V-Braced EBF Subassembly
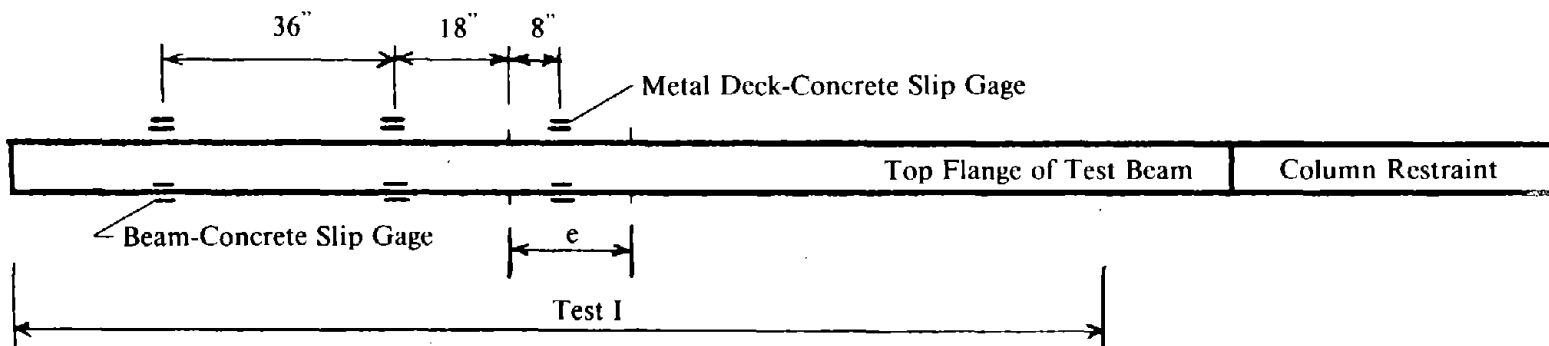
(b) K-Braced EBF Subassembly

Fig. 2.24    Plan of Slip Gage Locations for Test Beam.
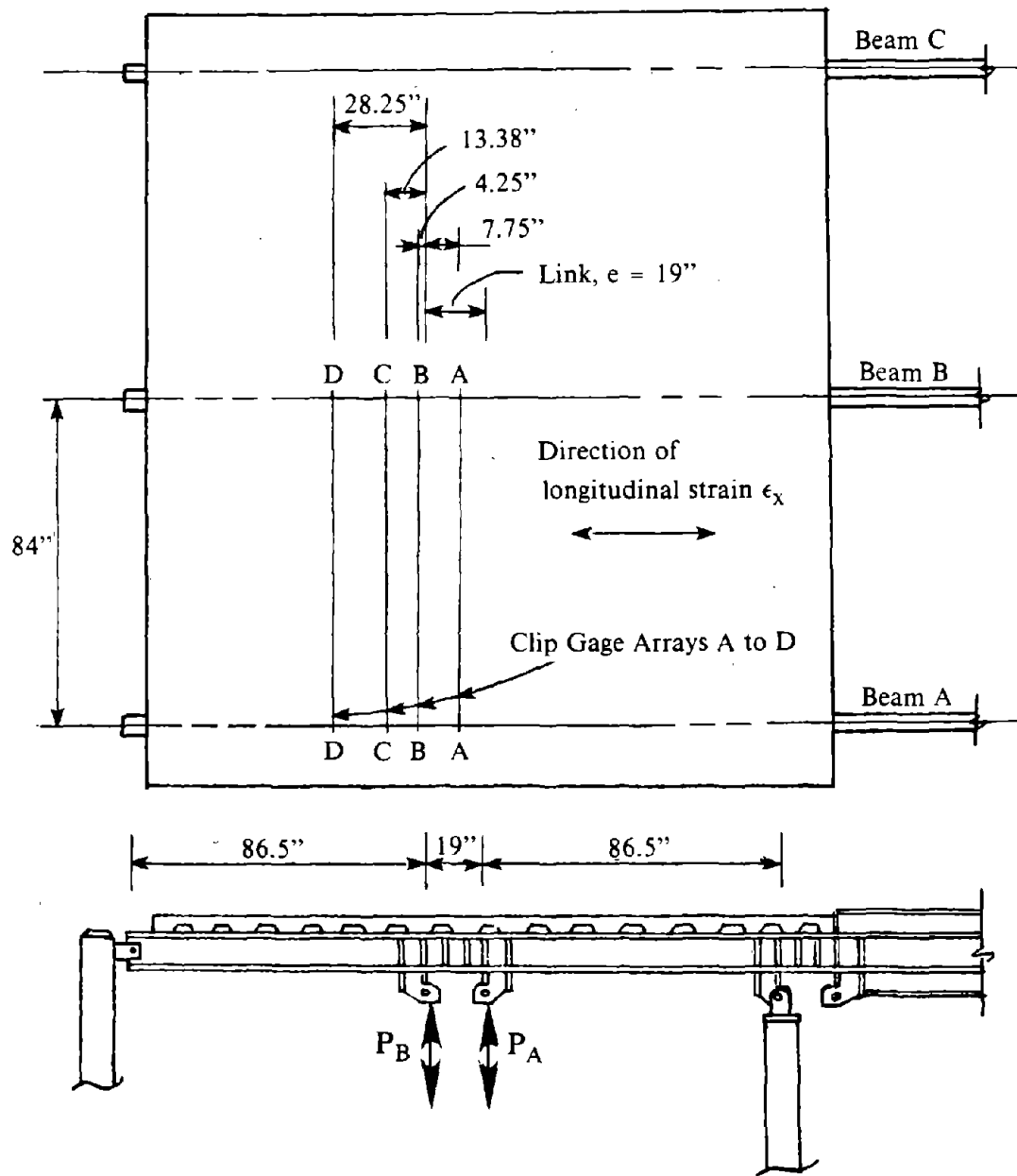
Fig. 2.25     Clip Gage Locations for Specimens A1 and B1.
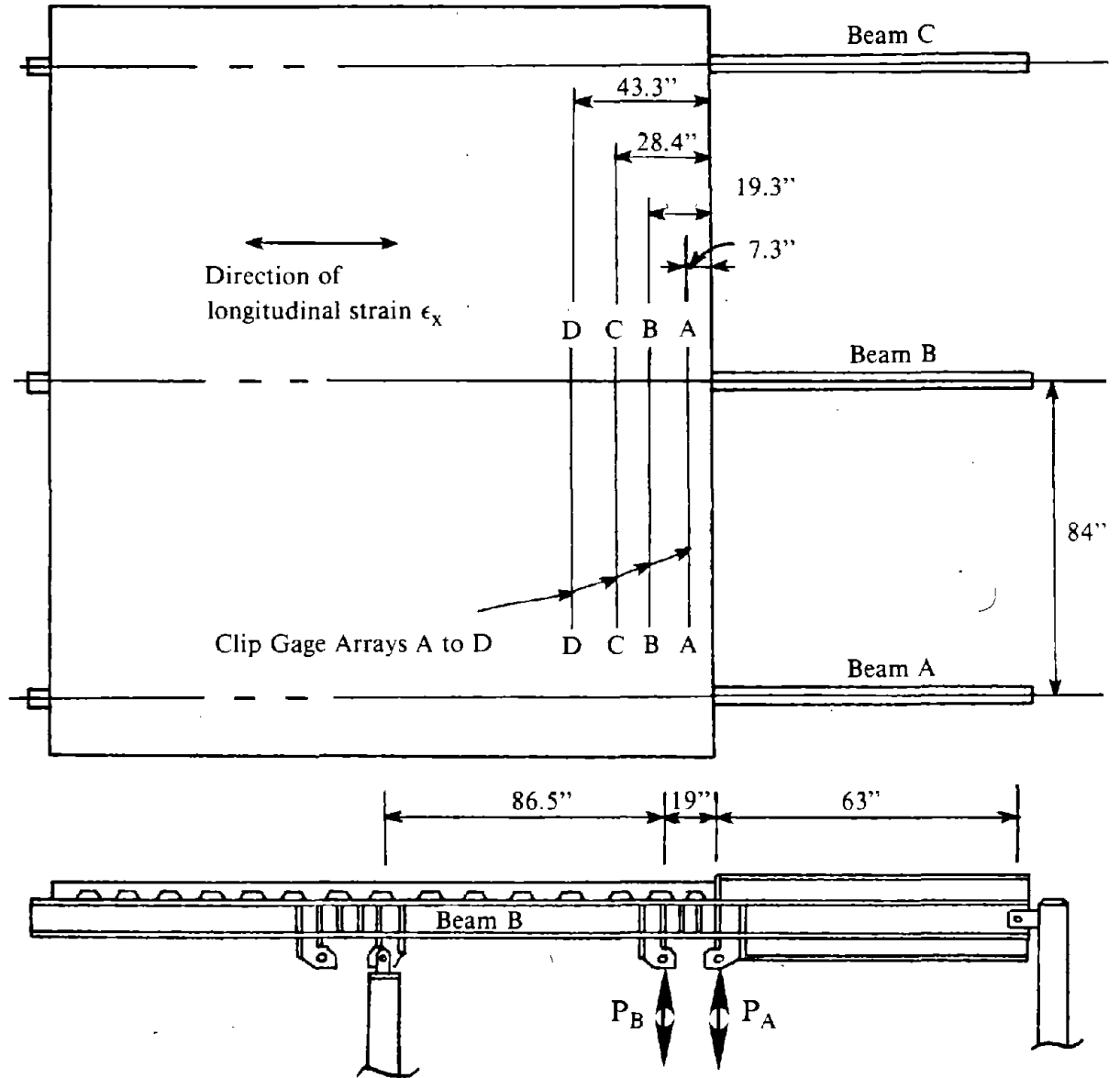
Fig. 2.26    Clip Gage Locations for Specimen B2.
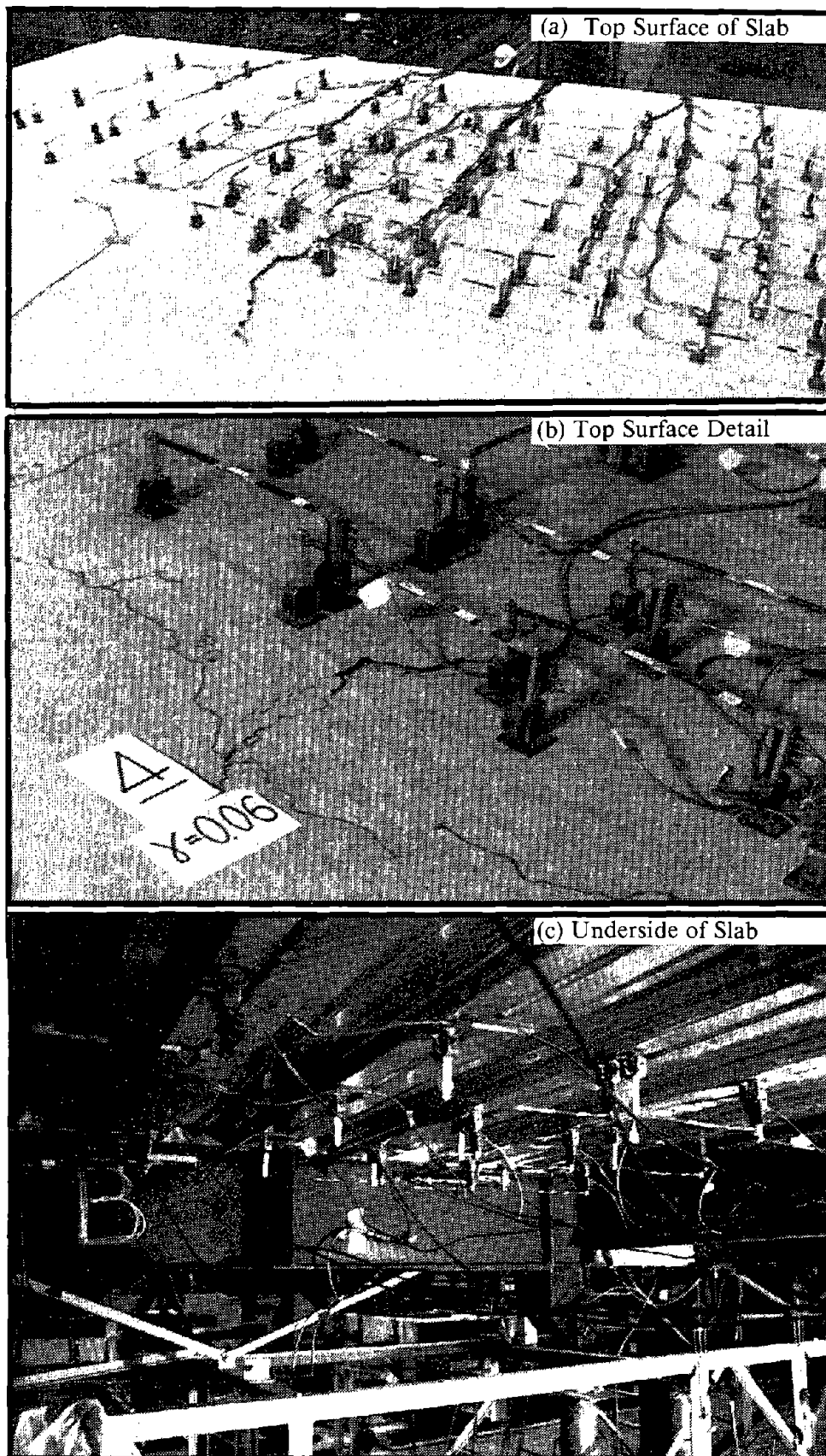
Fig. 2.27    Clip Gages to Measure Longitudinal Strain on Floor Slab Surfaces.

(b)  Arrays of Linear Potentiometers Placed Above Link

(a)  Linear Potentiometer to Measure Movement

Fig. 2.28      Measurement of Vertical Slab Displacement Above Link for Specimen A1.
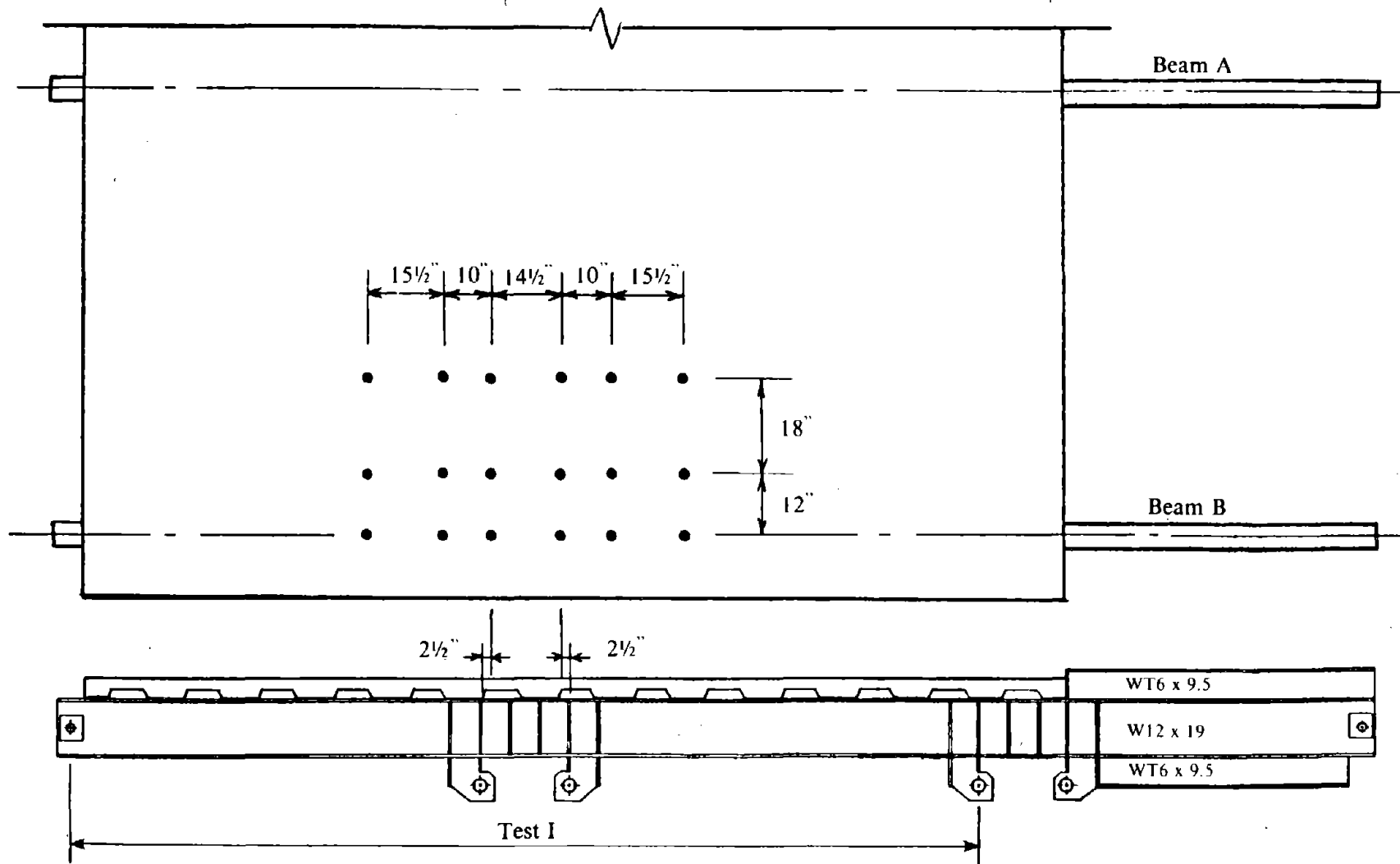
Fig. 2.29      Linear Potentiometer Locations for Measuring Vertical
Displacement of Floor Slab, Specimen A1.

$\Delta_A$ (IN)



LOAD STEP

$\Delta_B$ (IN)



LOAD STEP
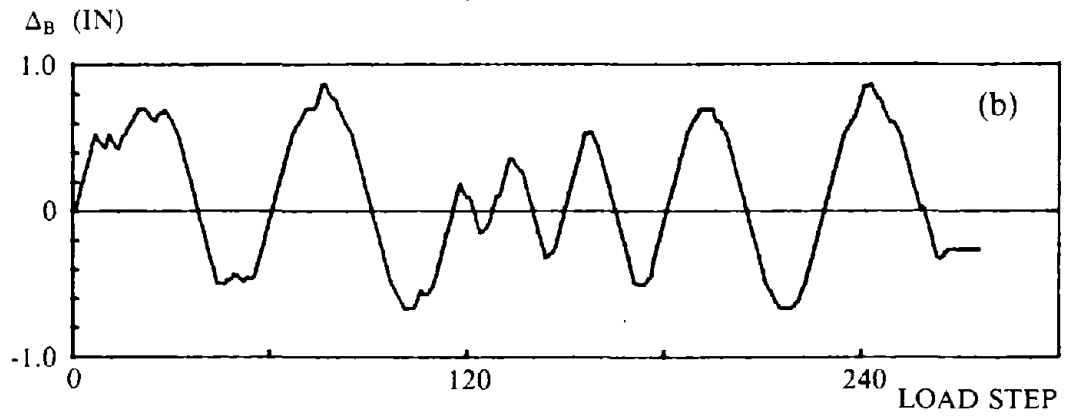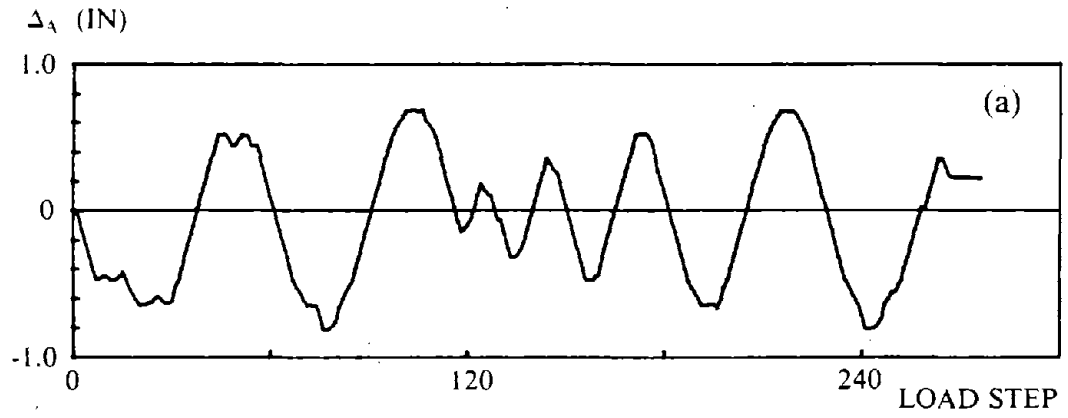
Fig. 2.30    Specimen A1 Displacement History.

$\Delta_A$ (IN)



LOAD STEP

$\Delta_B$ (IN)



LOAD STEP
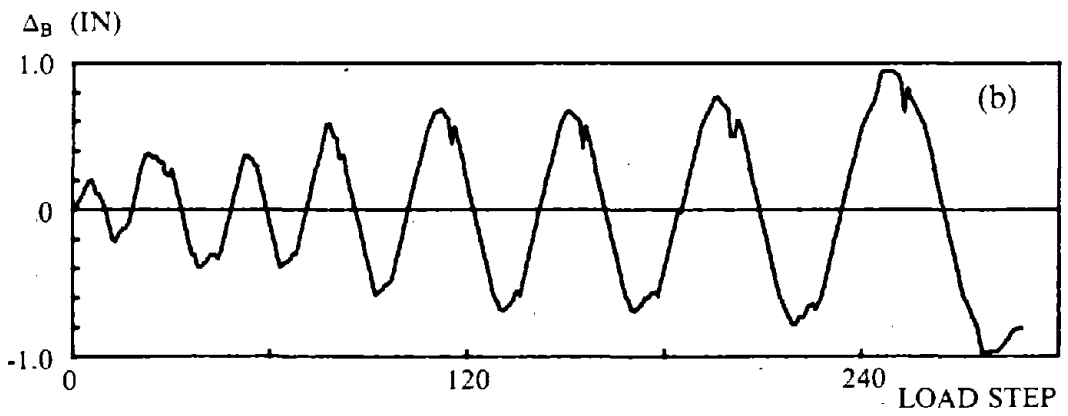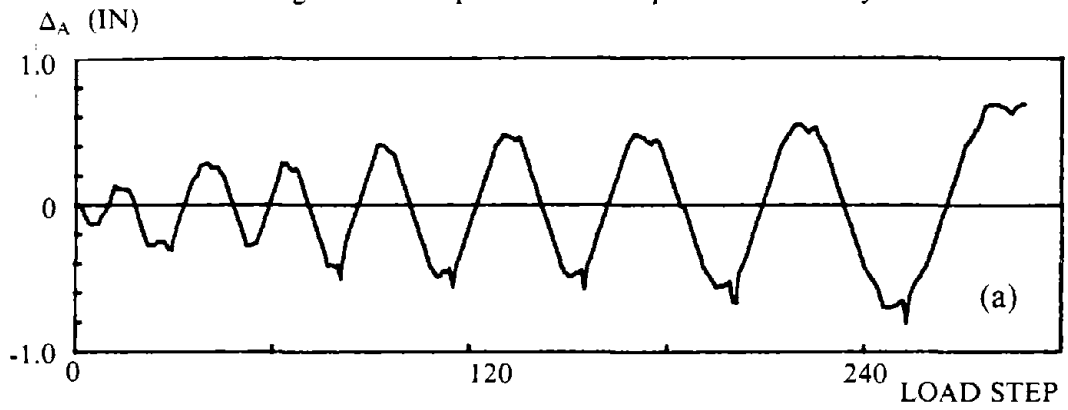
Fig. 2.31    Specimen A2 Displacement History.
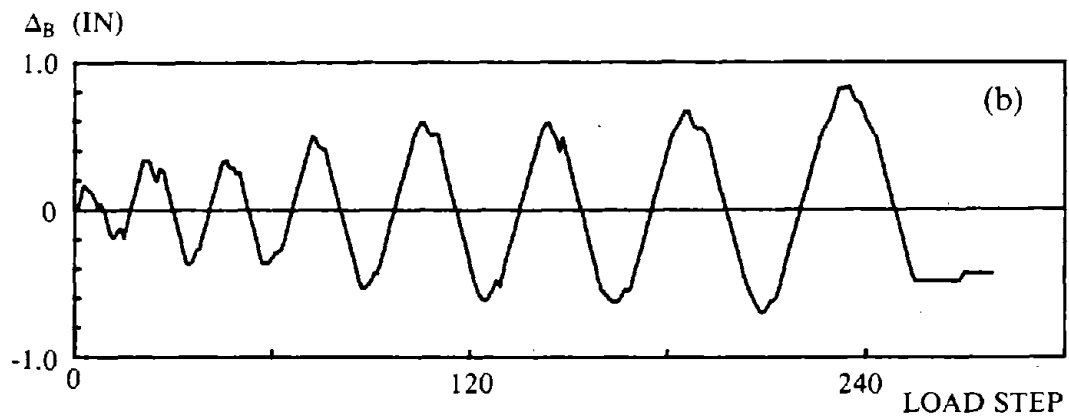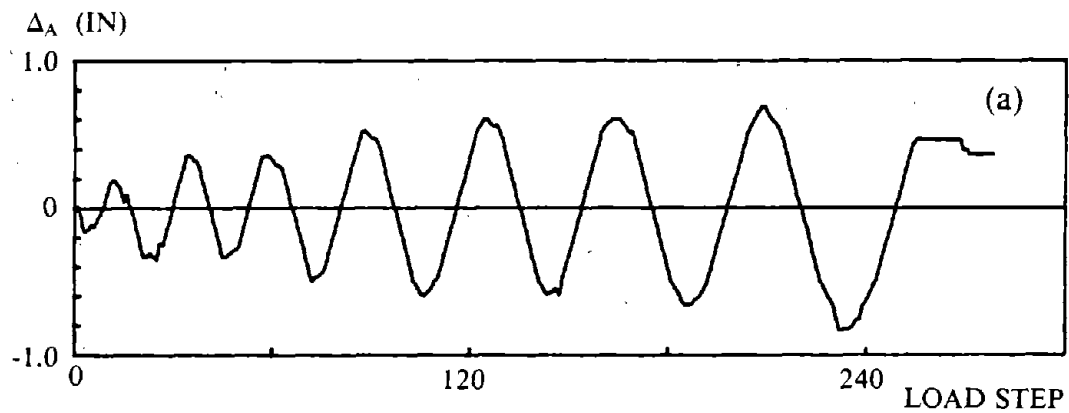
Fig. 2.32     Specimen B1 Displacement History.
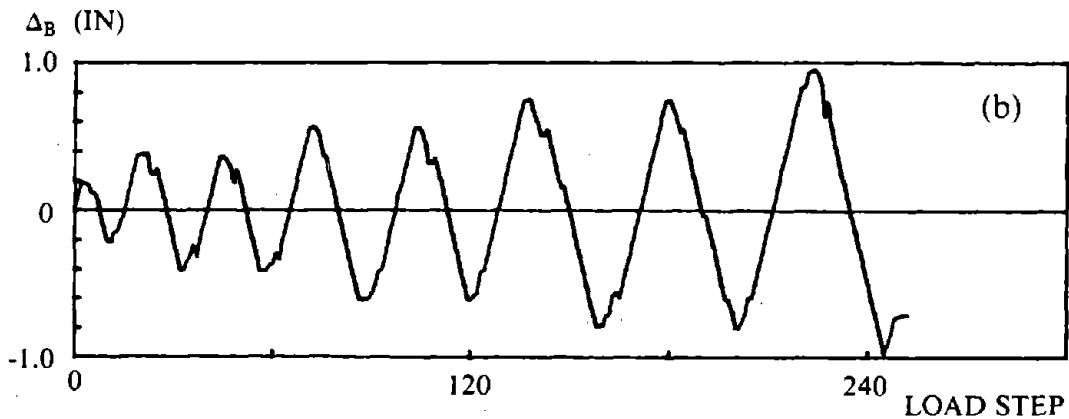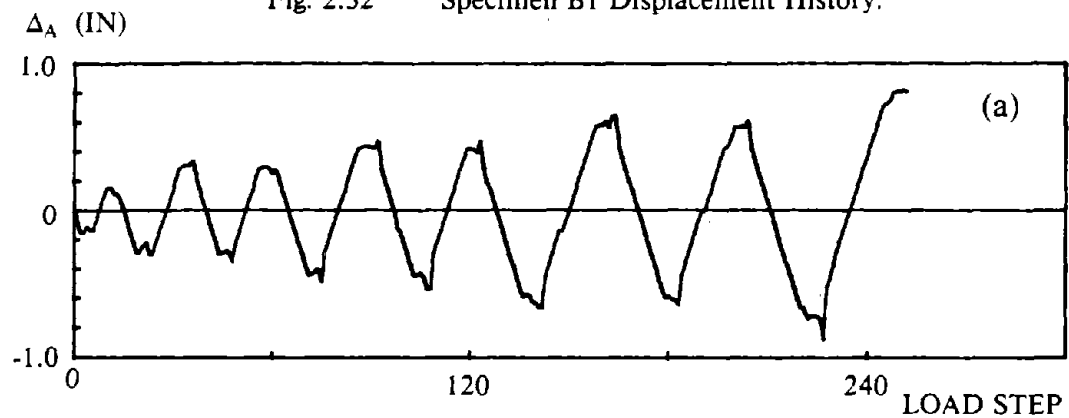


Fig. 2.33     Specimen B2 Displacement History.

172

$\Delta_A$ (IN)



(a)

LOAD STEP

$\Delta_B$ (IN)



(b)

LOAD STEP
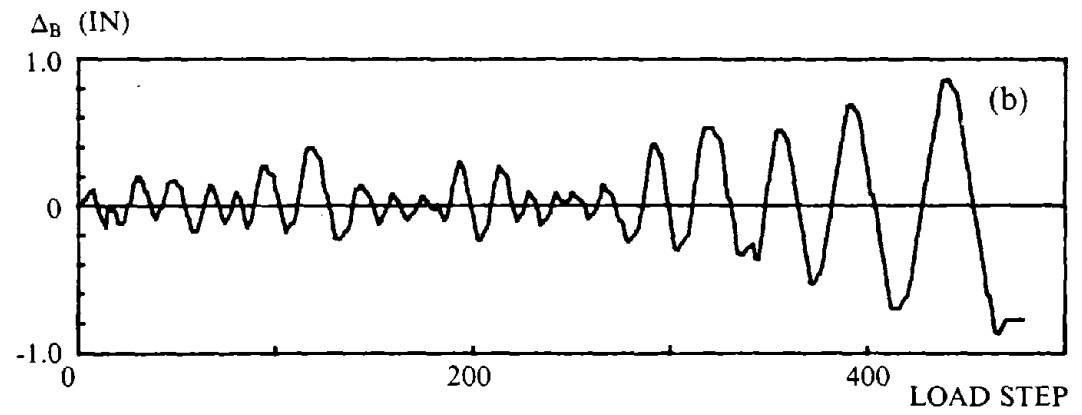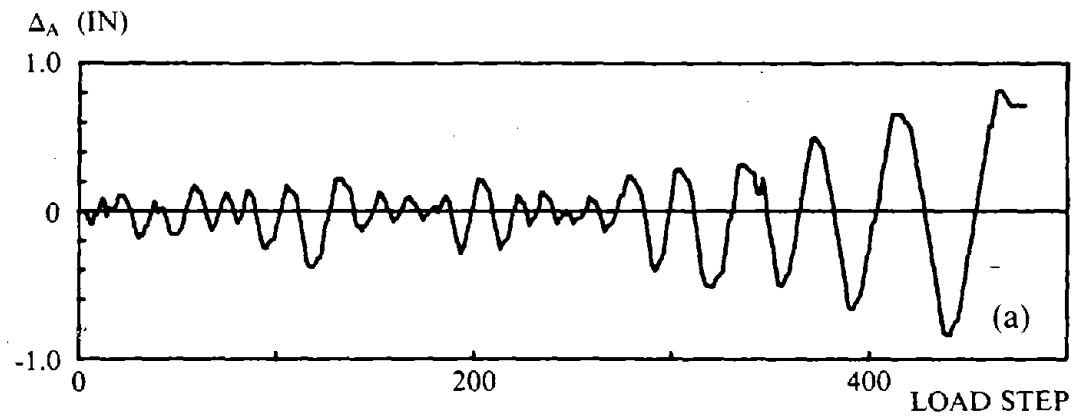
Fig. 2.34    Specimen C1 Displacement History.

$\Delta_A$ (IN)



(a)

LOAD STEP

$\Delta_B$ (IN)



(b)

LOAD STEP
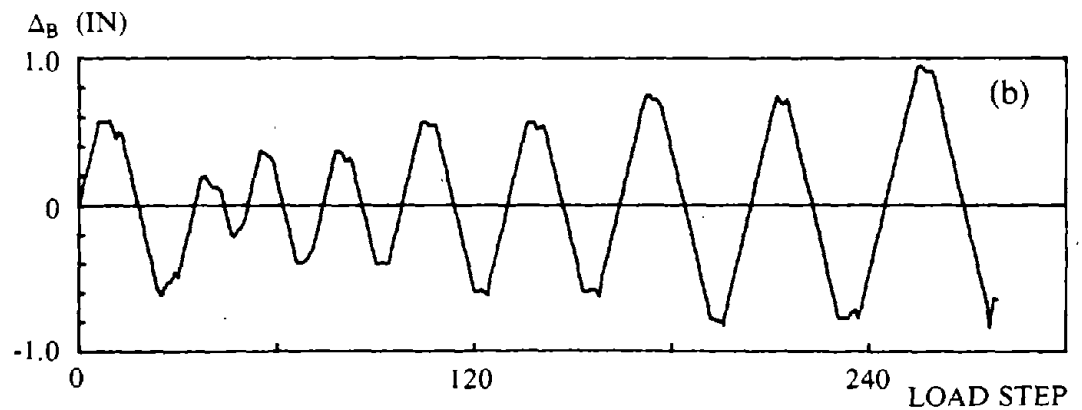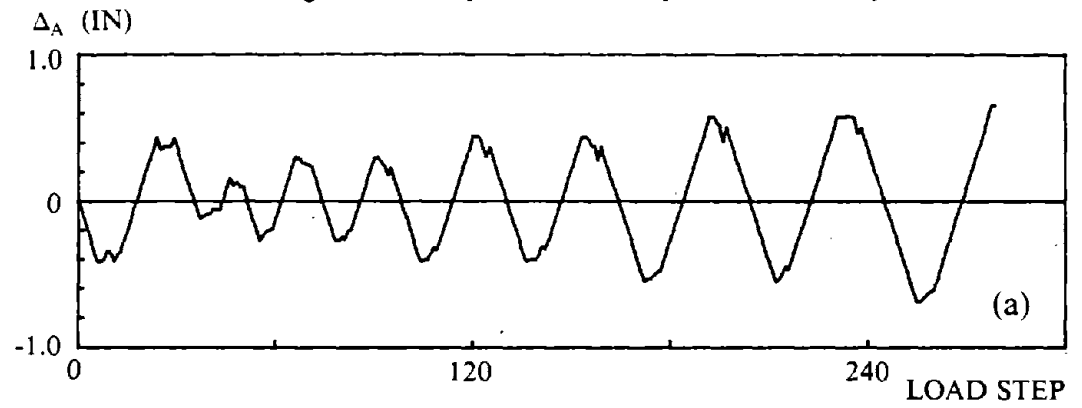
Fig. 2.35    Specimen C2 Displacement History.

$\Delta_A$ (IN)
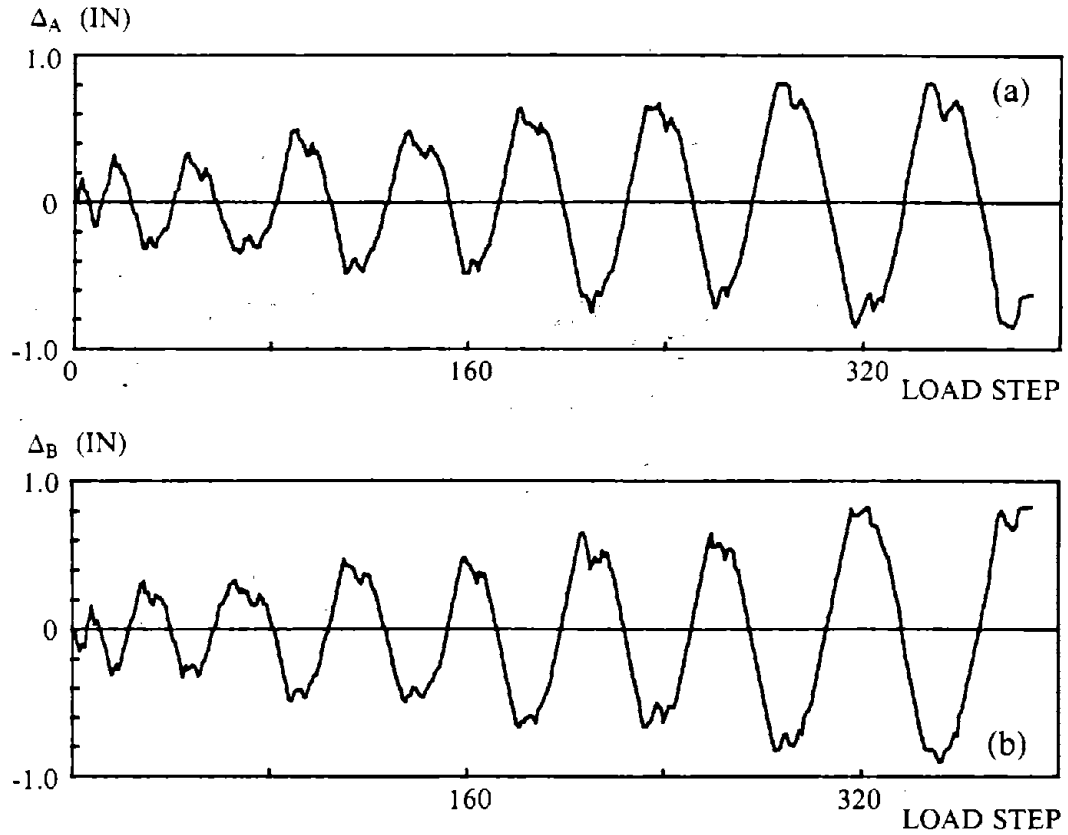


Fig. 2.36    Specimen D1 Displacement History.
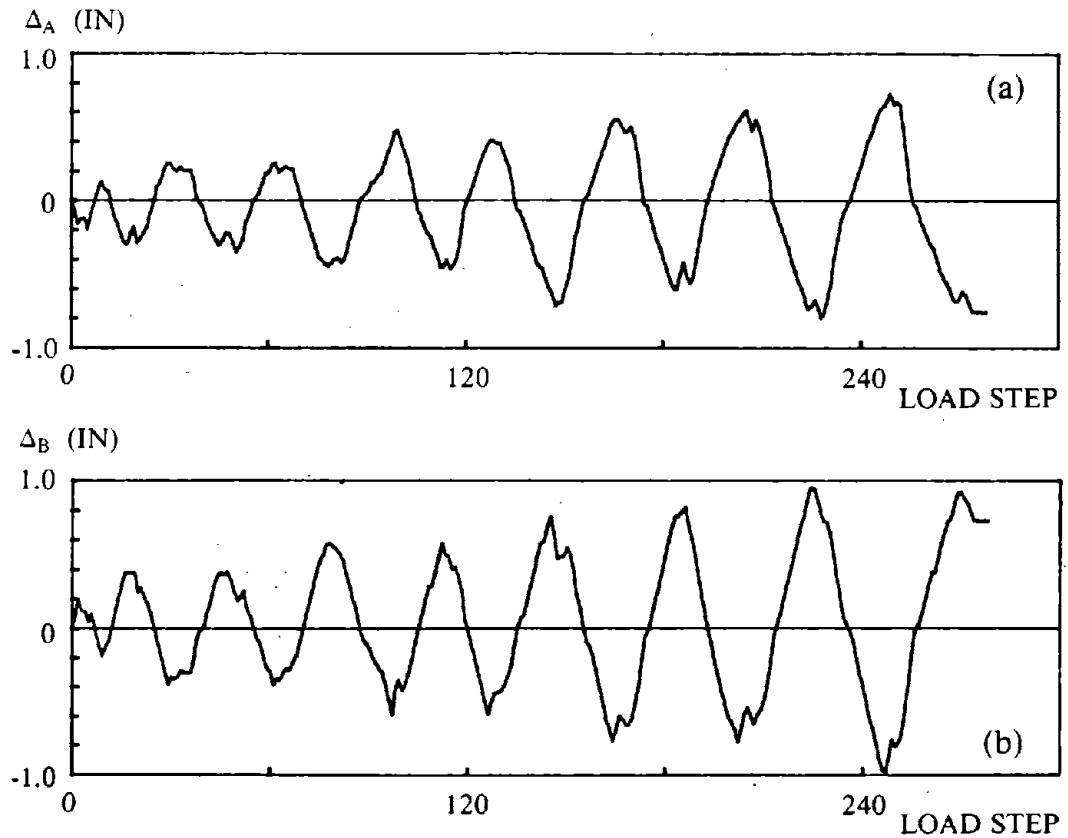


Fig. 2.37    Specimen D2 Displacement History.

(a) K-Braced EBF Subassembly         (b) V-Braced EBF Subassembly
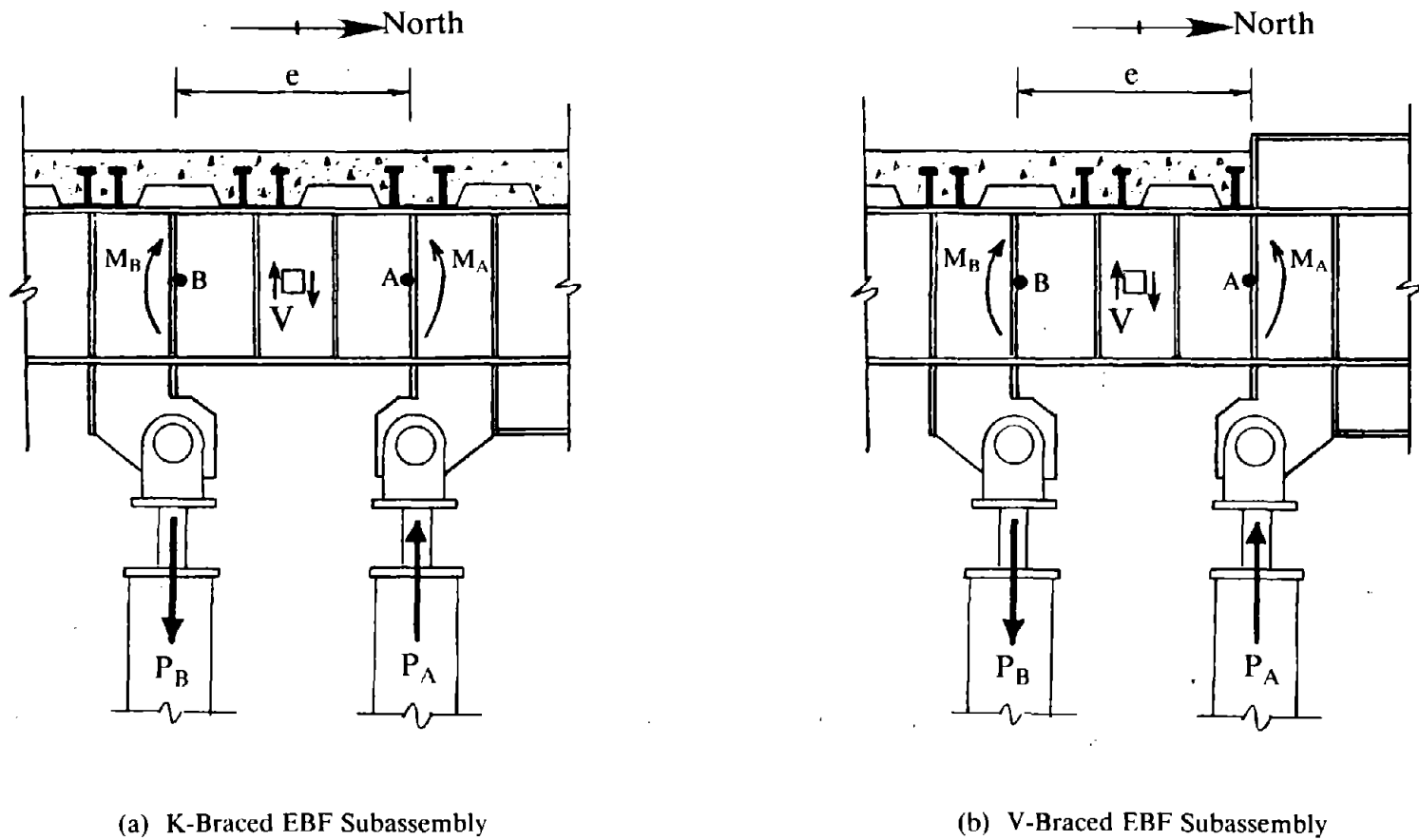
Fig. 3.1     Nomenclature and Positive Sign Convention For Link Forces.
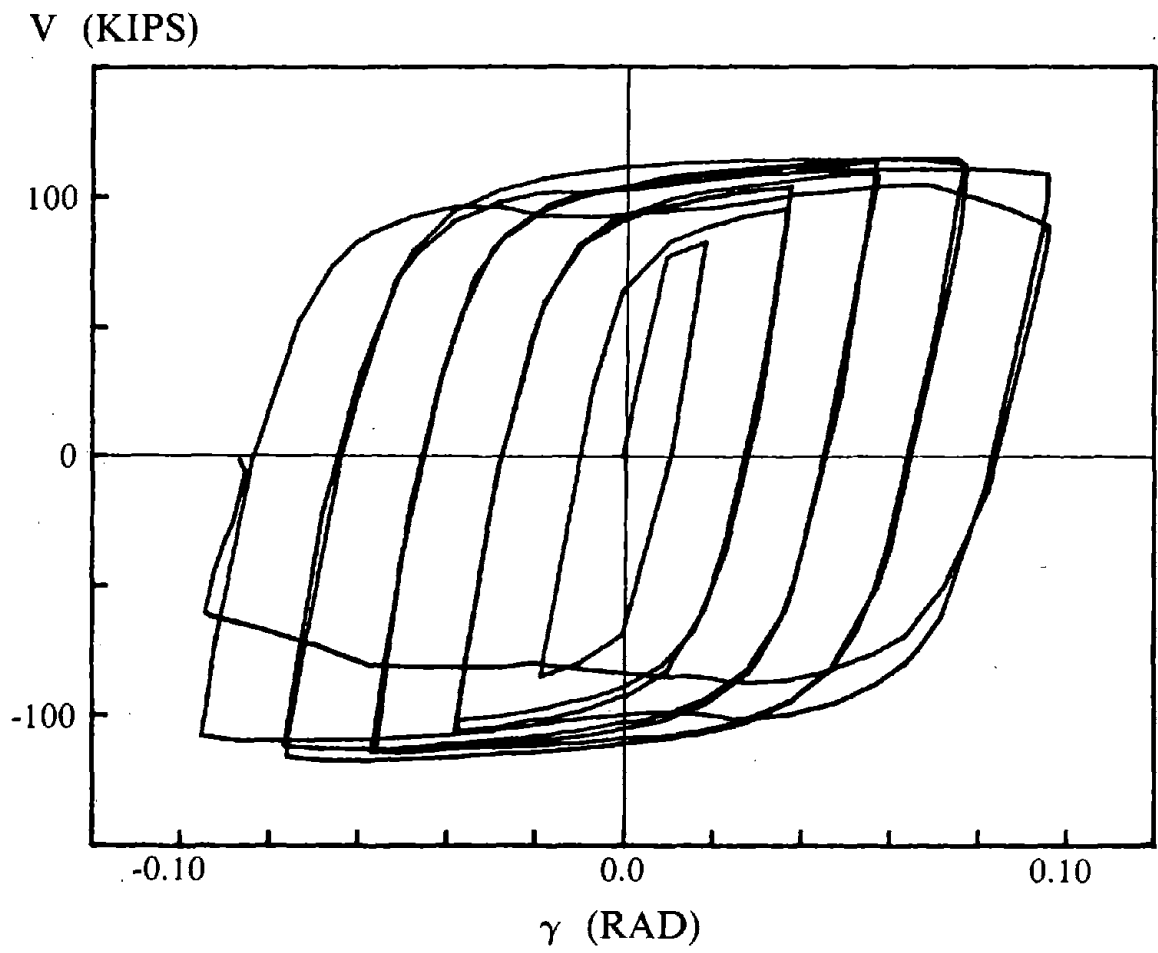
Fig. 3.2    Shear-Deformation Relationship for Link, Specimen D1.

M_A (K-IN)

(a)

1200

0

-1200

-0.10          0.0          0.10

γ (RAD)

-M_B (K-IN)

(b)

1200

0

-1200

-0.10          0.0          0.10

γ (RAD)
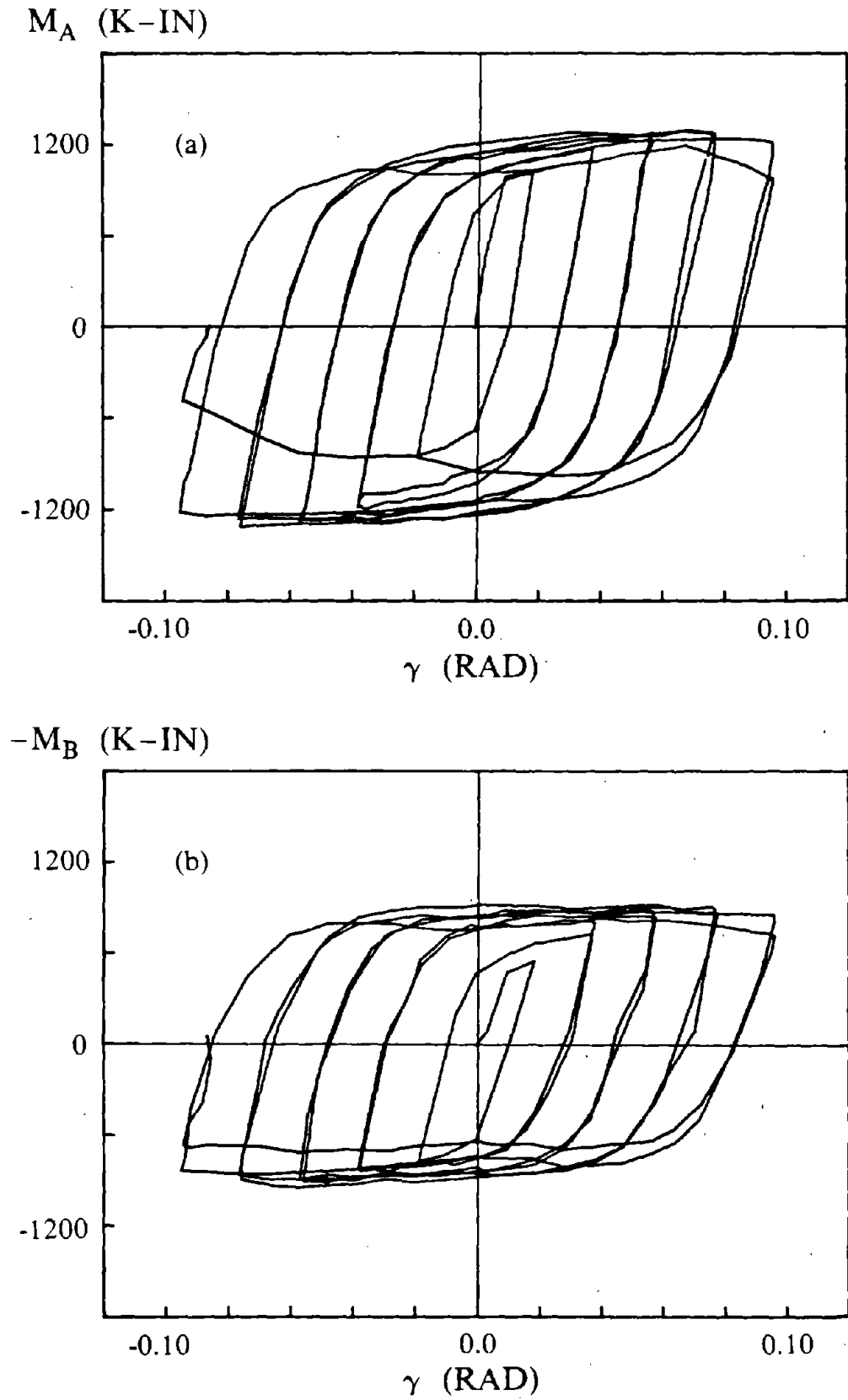
Fig. 3.3    Moment-Deformation Relationships for Link, Specimen D1.

177



(a) Cycle 2, at $\gamma = 0.04$ rad.
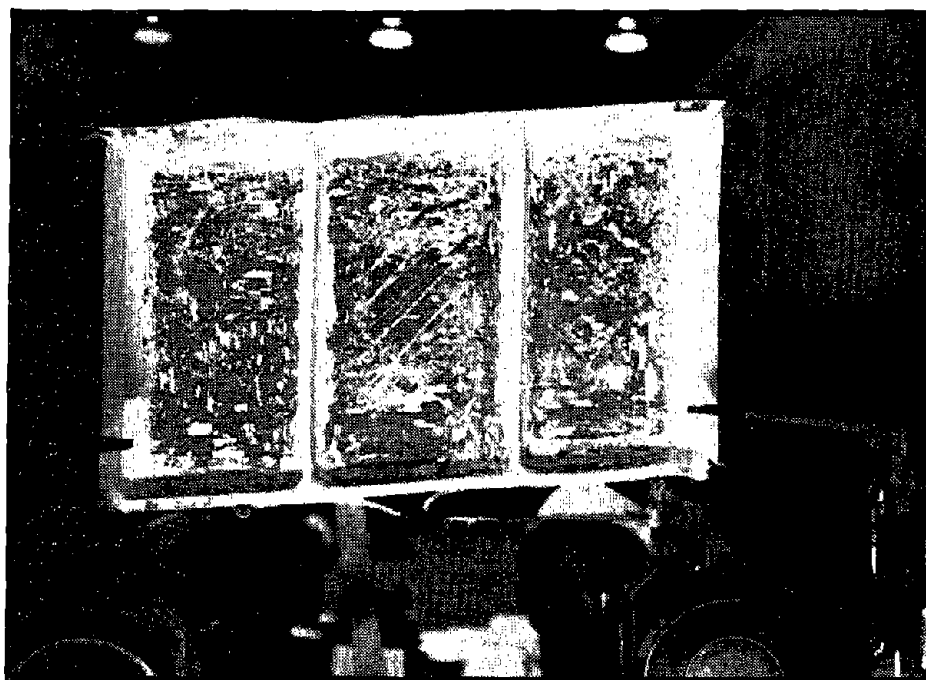
(b) Cycle 4, at $\gamma = -0.06$ rad.

Fig. 3.4    Photos of Specimen D1 During Test.

178
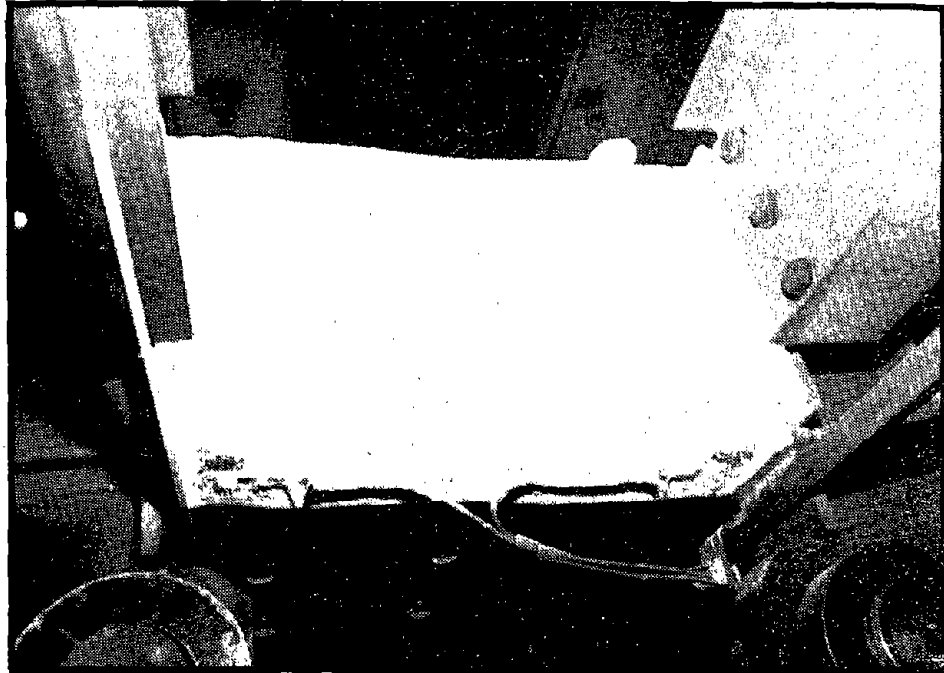


(c) Cycle 7, at $\gamma = 0.08$ rad.
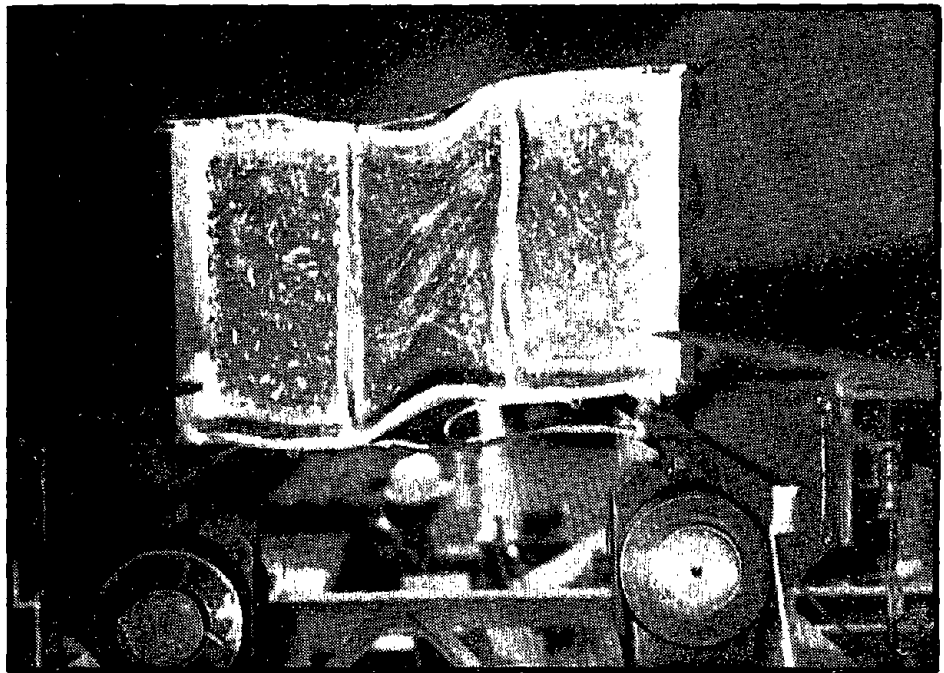
(d) Cycle 8, at $\gamma = -0.10$ rad.

Fig. 3.4     Photos of Specimen D1 During Test.
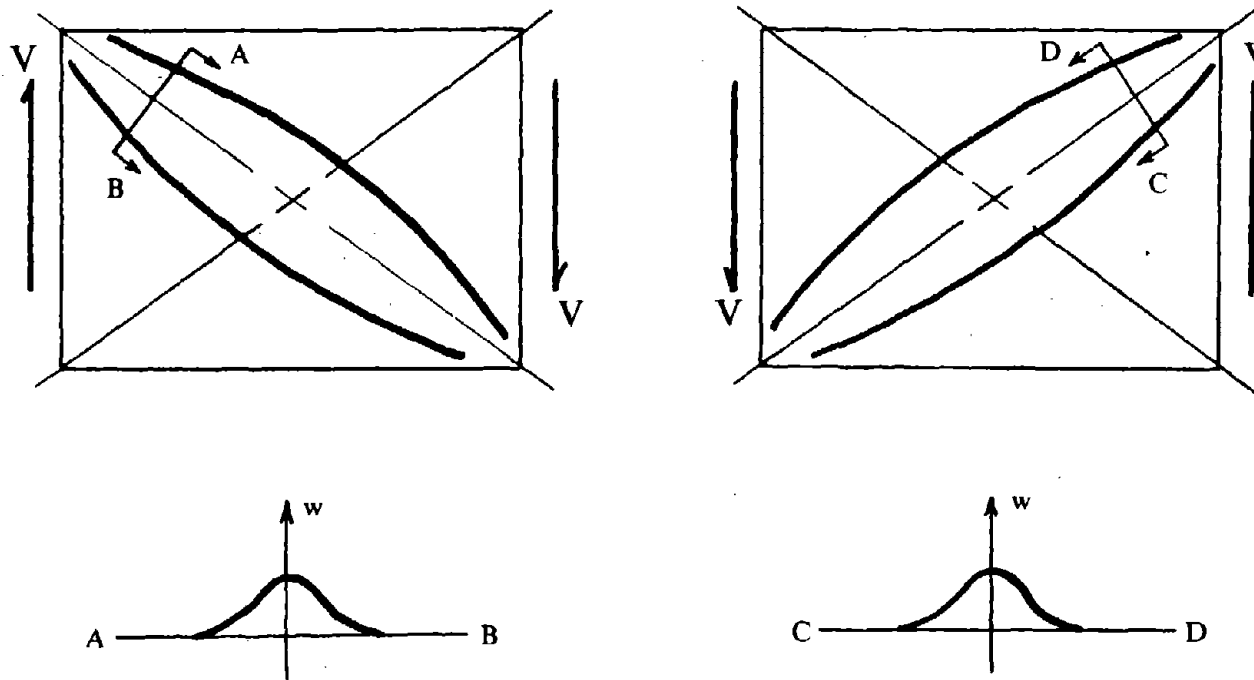
Fig. 3.5    Cyclic Symmetric Mode of Link Web Buckling.
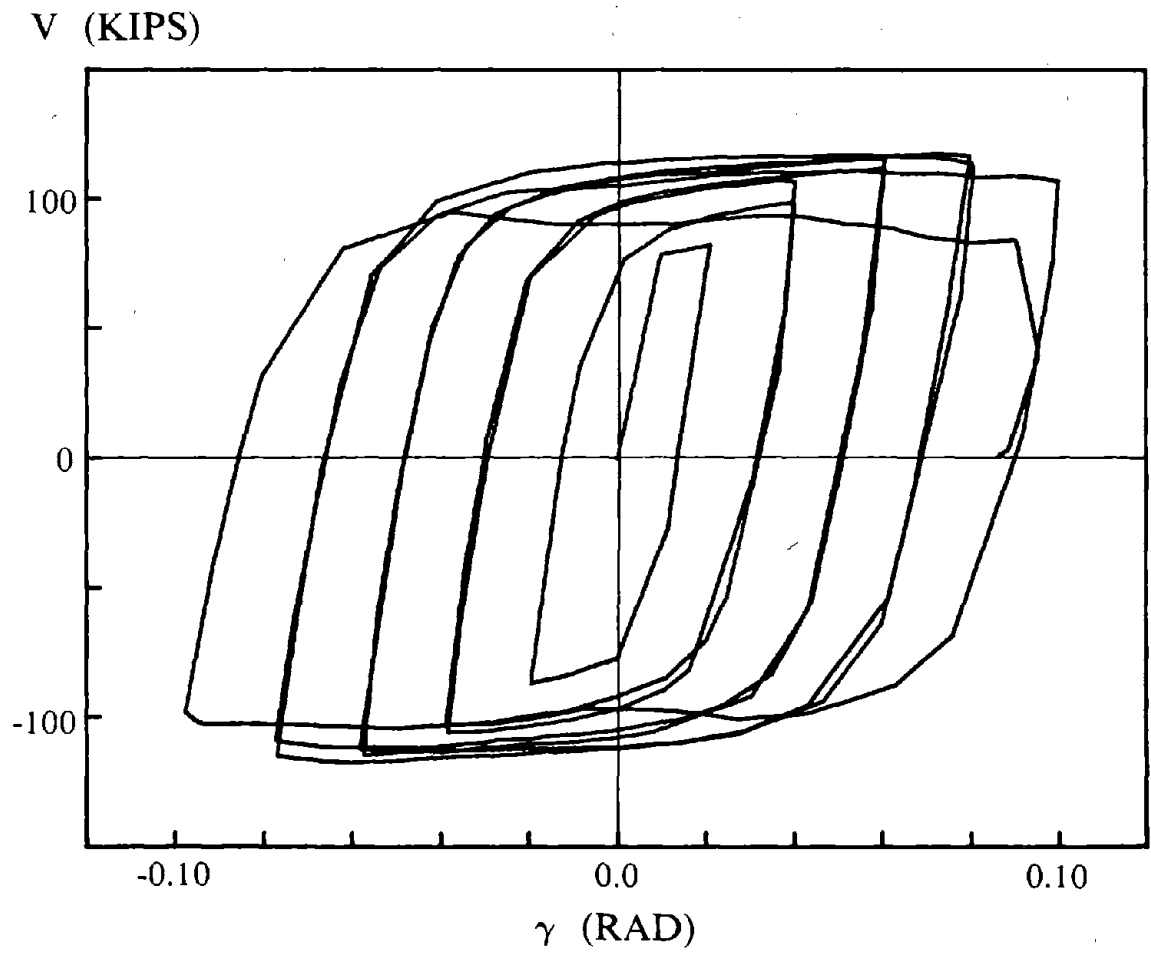
Fig. 3.6    Shear-Deformation Relationship for Link, Specimen D2.
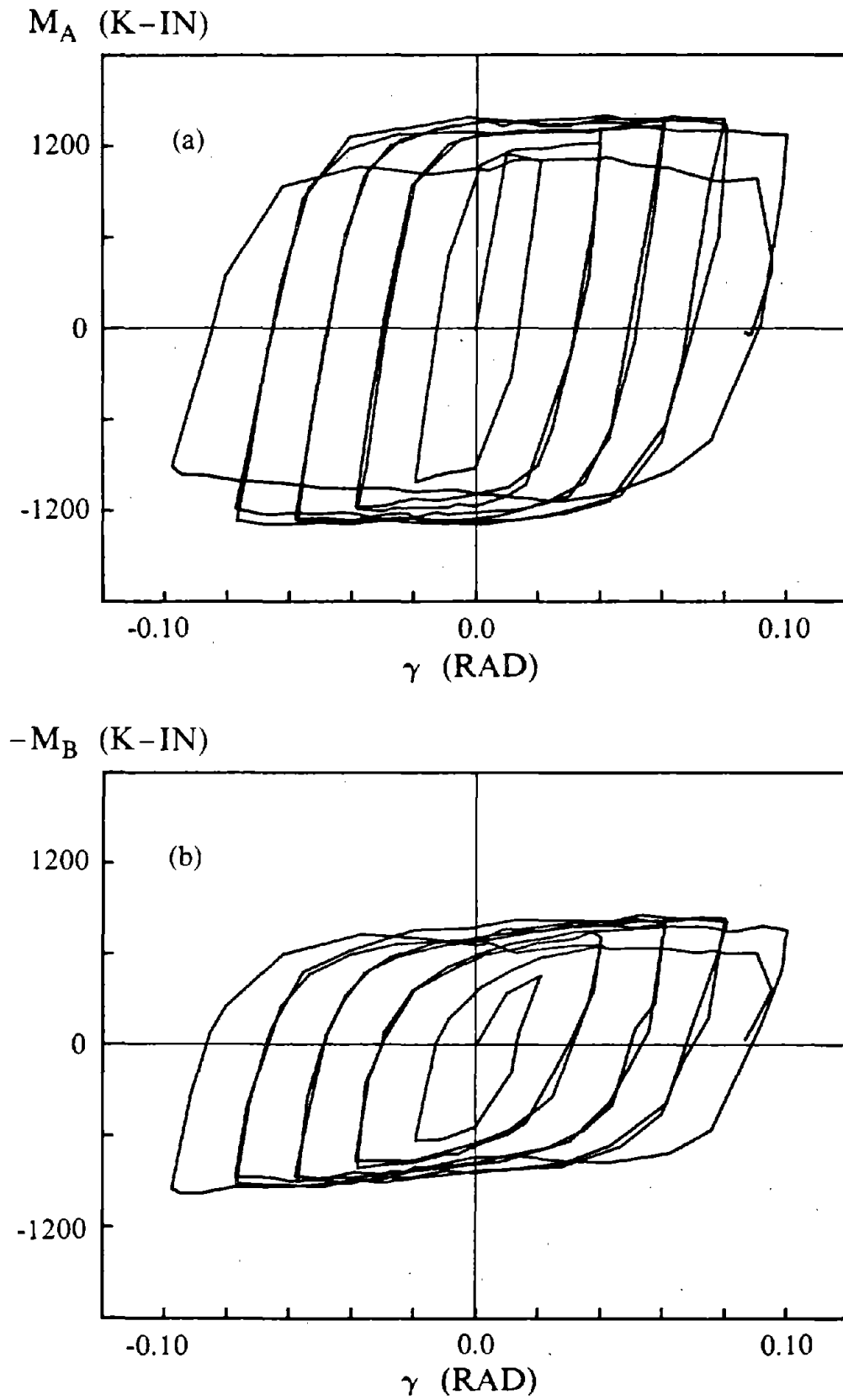
$M_A$ (K-IN)



(a)

1200

0

-1200

-0.10          0.0          0.10

$\gamma$ (RAD)

$-M_B$ (K-IN)



(b)

1200

0

-1200

-0.10          0.0          0.10

$\gamma$ (RAD)

Fig. 3.7     Moment-Deformation Relationships for Link, Specimen D2.

182
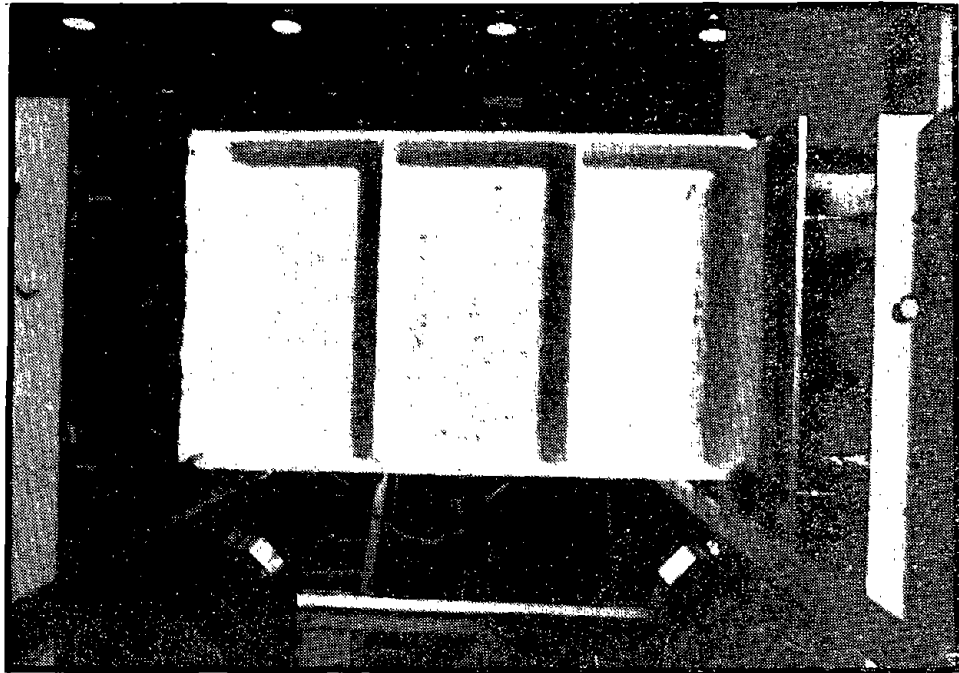


(a) Cycle 1, at $\gamma = 0.02$ rad.

(b) Cycle 5, at $\gamma = -0.06$ rad.

Fig. 3.8     Photos of Specimen D2 During Test.
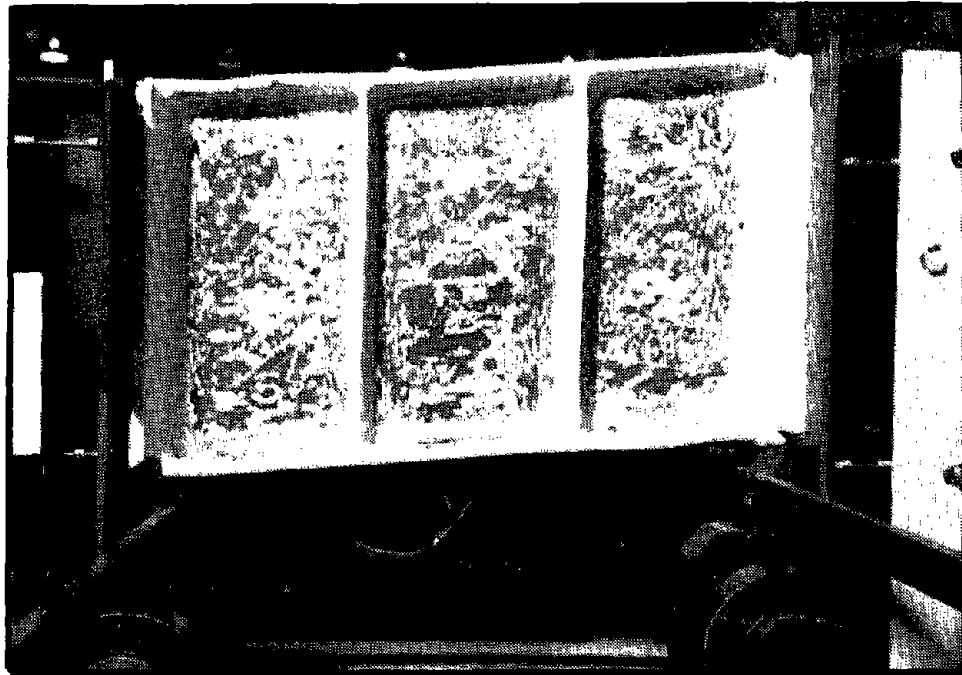
(c) Cycle 7, at $\gamma = -0.08$ rad.
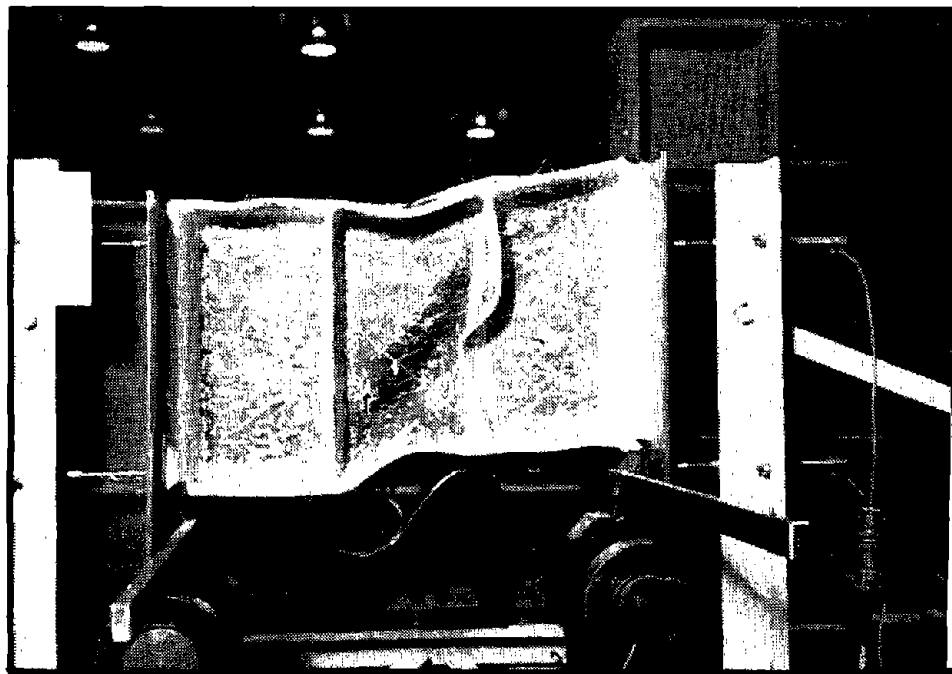
(d) Cycle 8, at $\gamma = -0.10$ rad.

Fig. 3.8    Photos of Specimen D2 During Test.
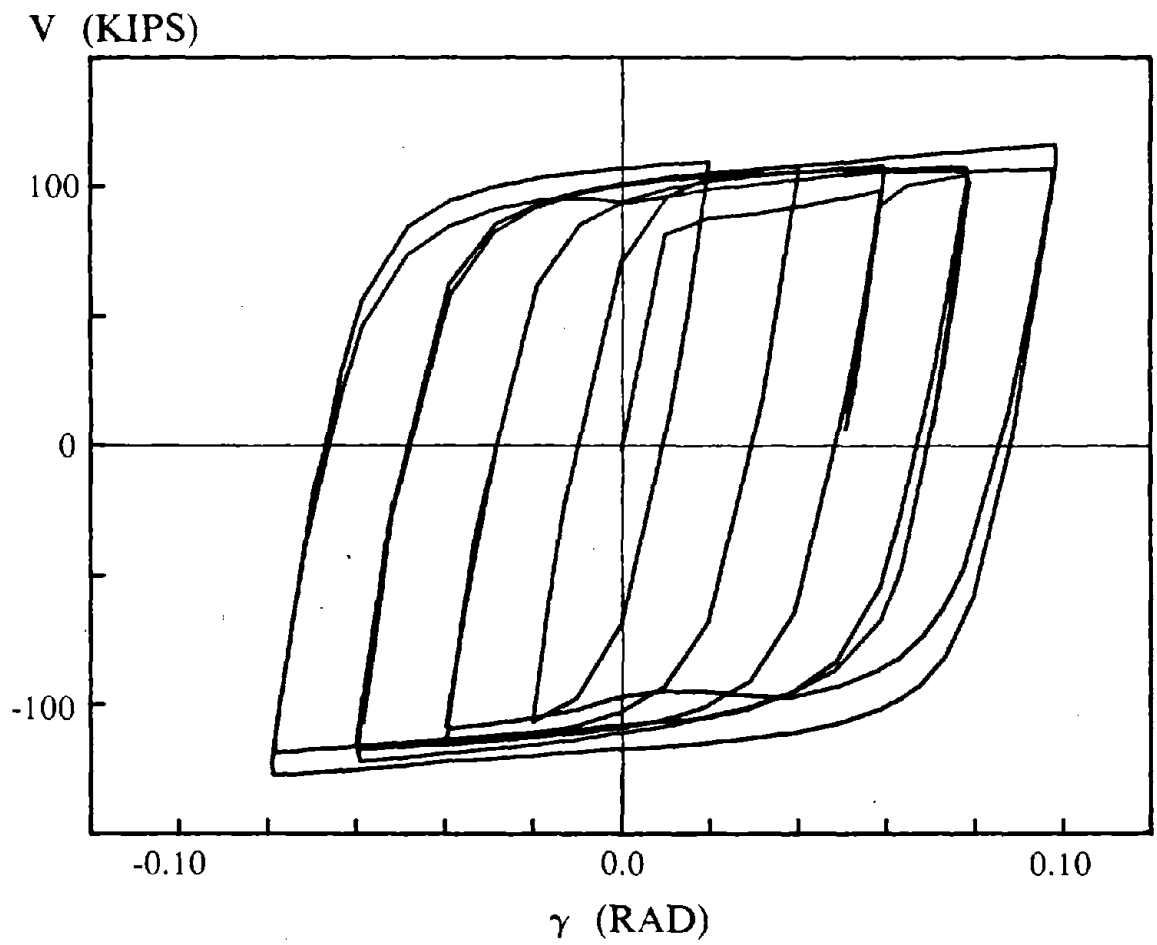
Fig. 3.9    Shear-Deformation Relationship for Link, Specimen A1.
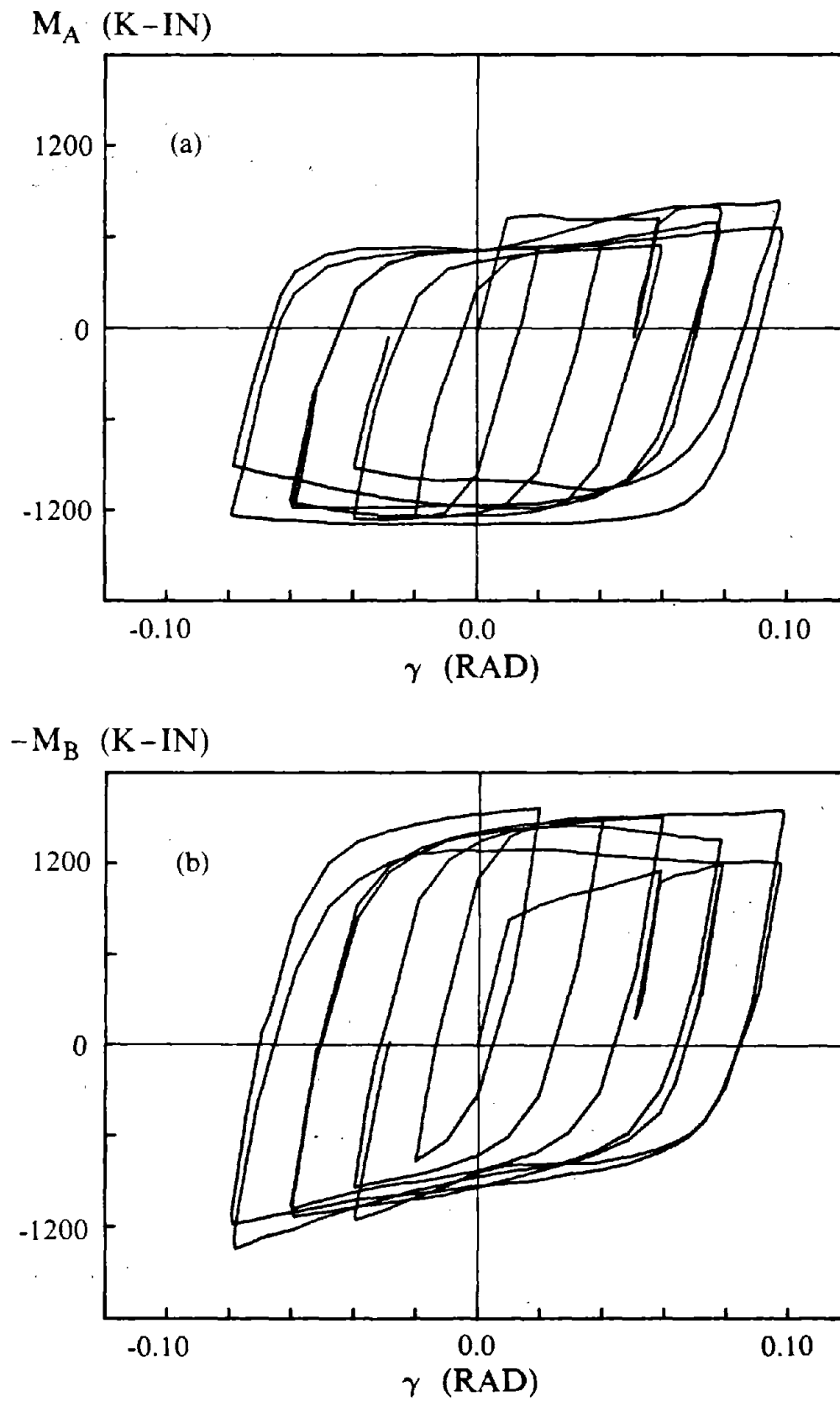
Fig. 3.10    Moment-Deformation Relationships for Link, Specimen A1.
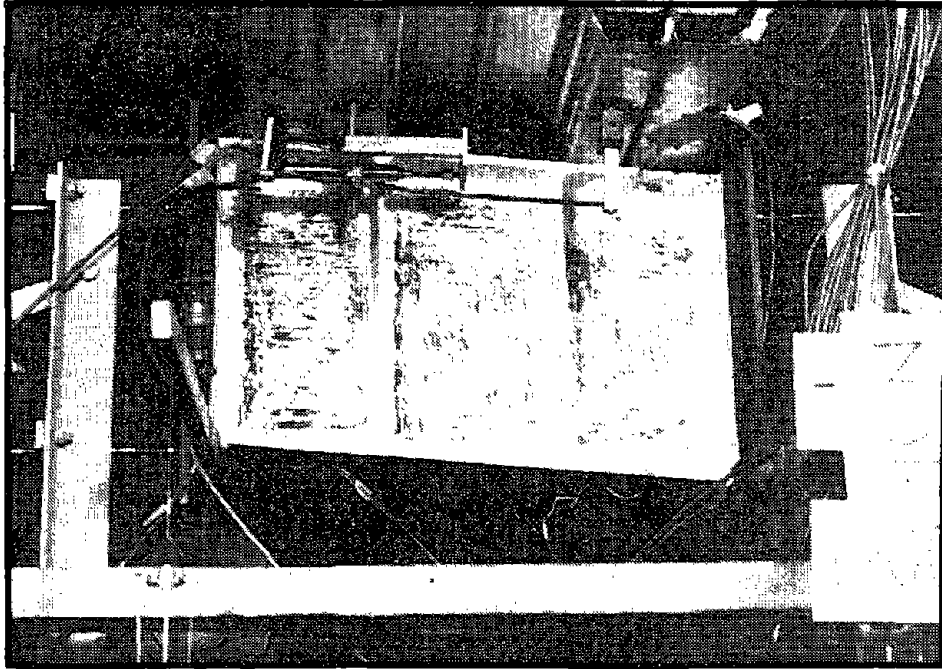
(a) Cycle 1, at $\gamma = 0.08$ rad.
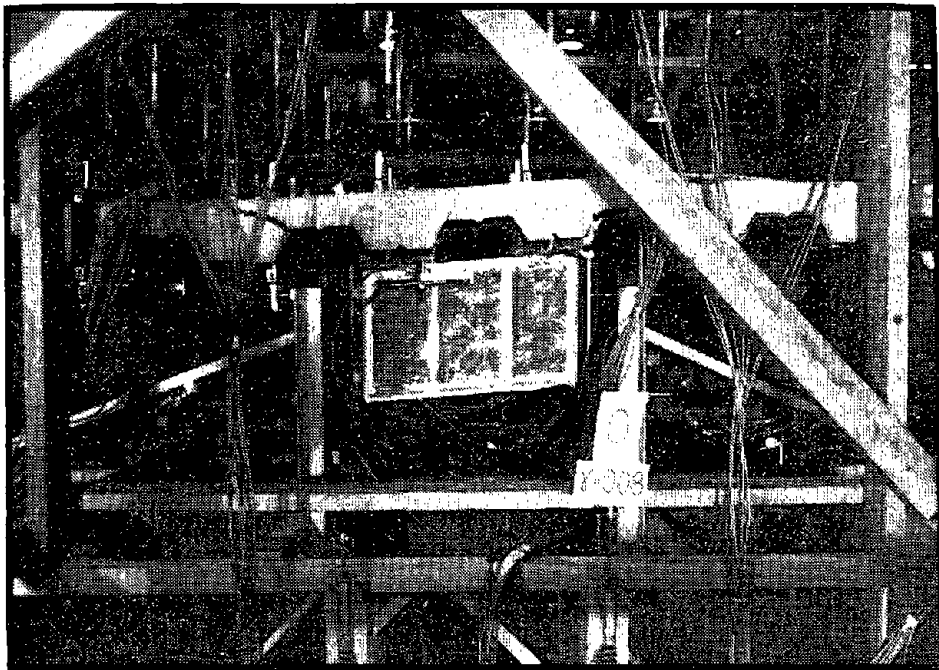


(b) Cycle 2, at $\gamma = -0.08$ rad.

Fig. 3.11    Photos of Specimen A1 During Test.
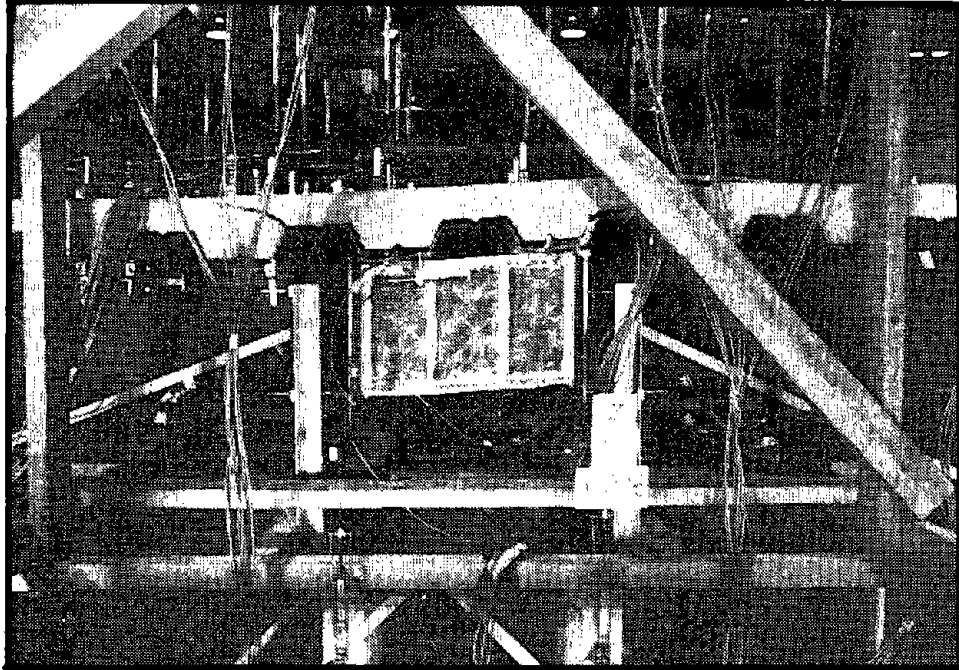
(c) Cycle 5, at $\gamma = -0.06$ rad.
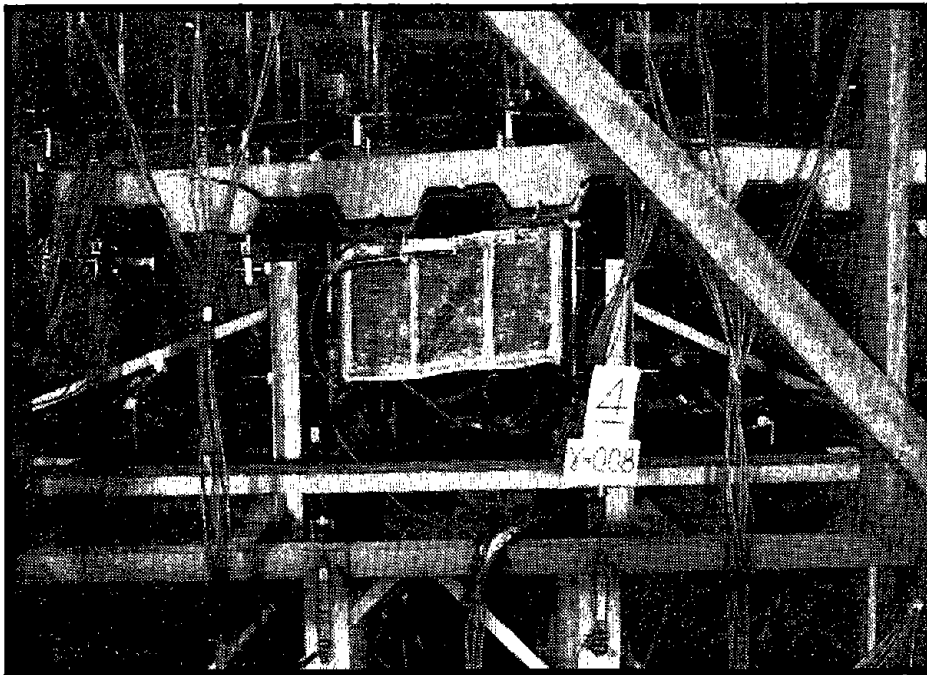
(d) Cycle 6, at $\gamma = -0.08$ rad.

Fig. 3.11      Photos of Specimen A1 During Test.

188
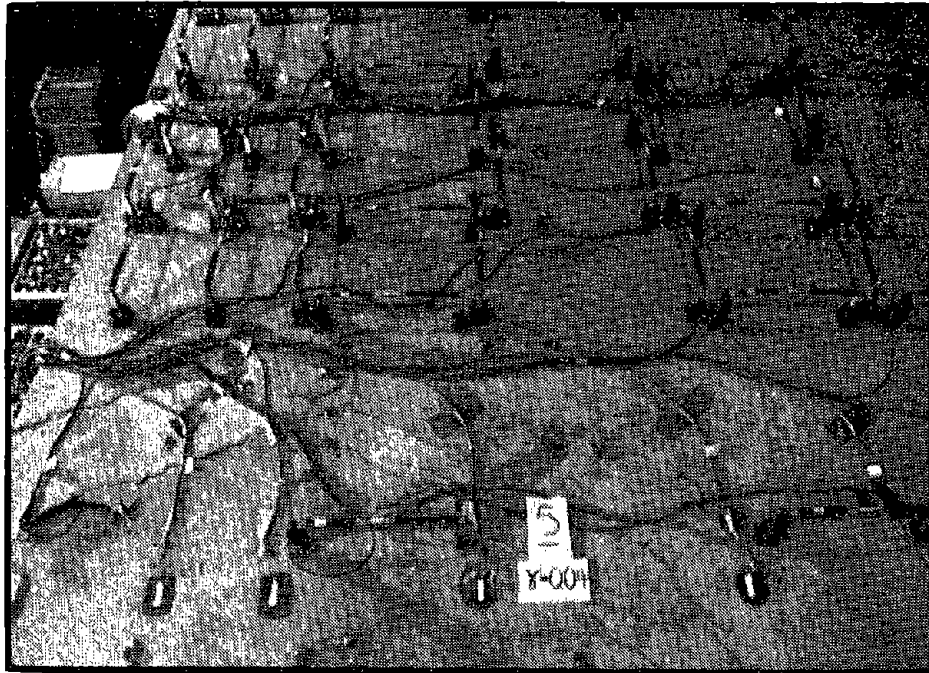
(a)  Floor Slab in Vicinity of Link
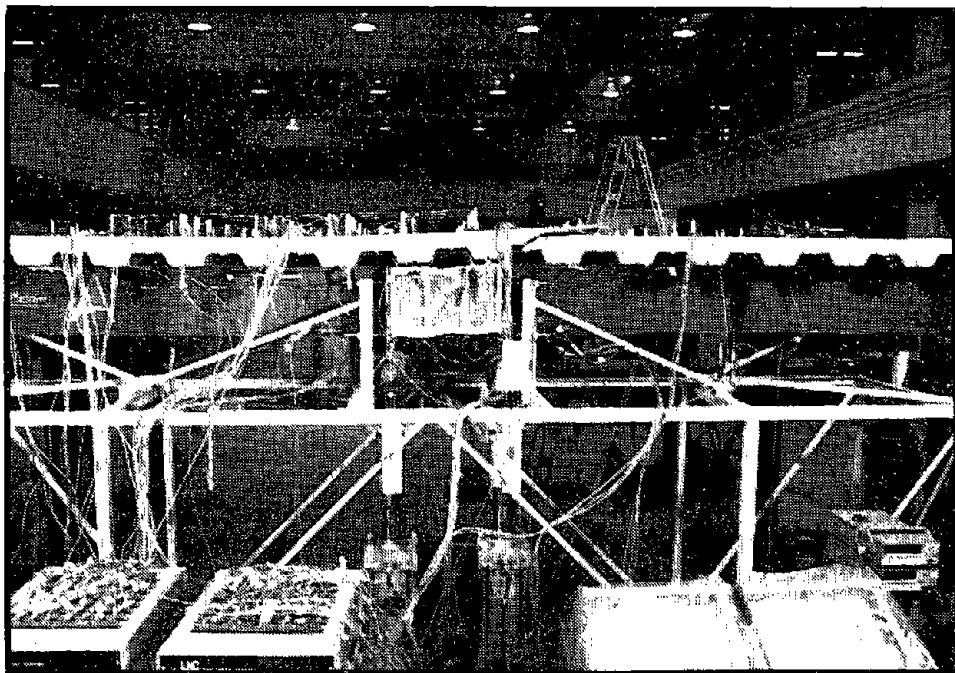


(b)  General View of Test Beam

Fig. 3.12     Photos of Floor Damage After Completion of Test, Specimen A1.
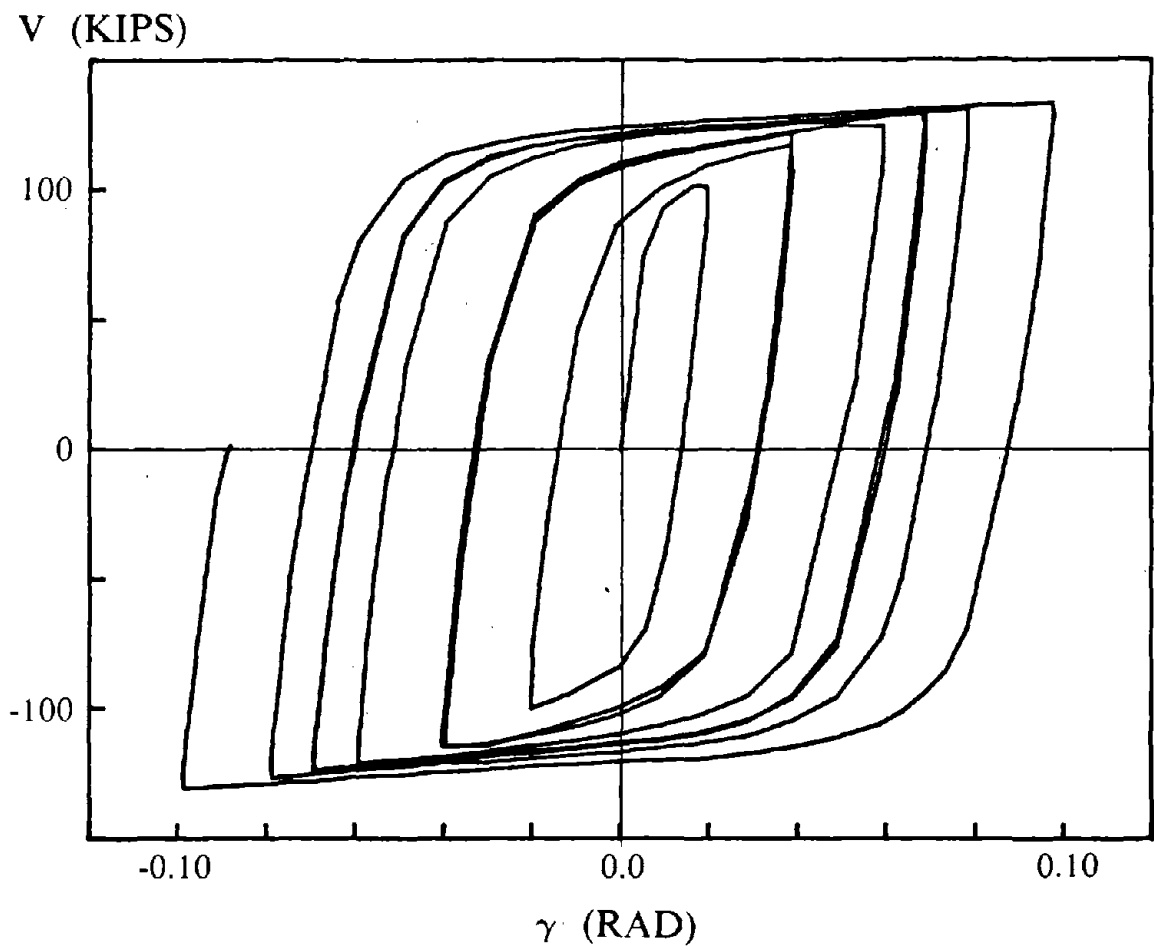
Fig. 3.13    Shear-Deformation Relationship for Link, Specimen A2.

$M_A$ (K-IN)
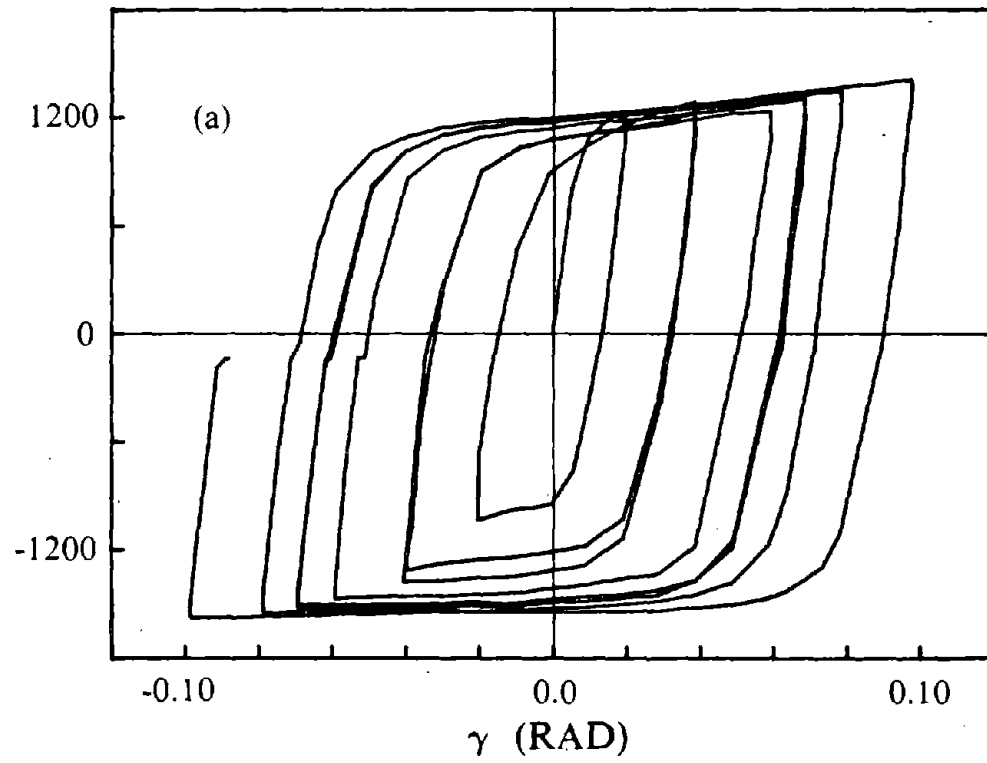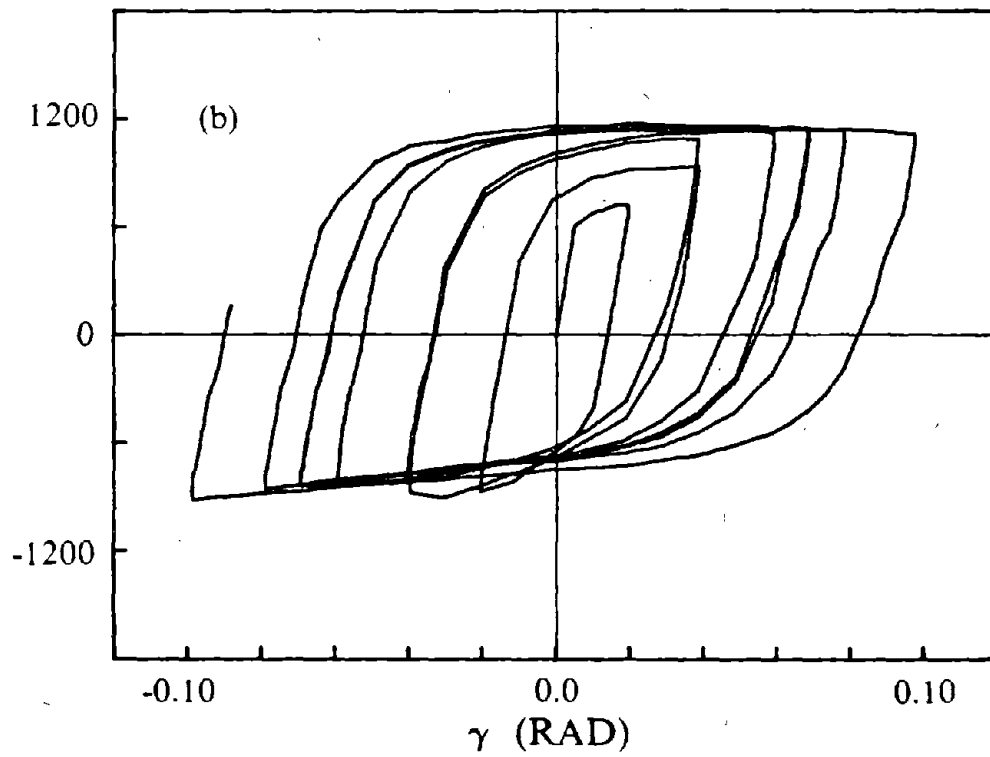
(a)

1200

0

-1200

-0.10          0.0          0.10

$\gamma$ (RAD)

$-M_B$ (K-IN)

(b)

1200

0

-1200

-0.10          0.0          0.10

$\gamma$ (RAD)

Fig. 3.14    Moment-Deformation Relationships for Link, Specimen A2.
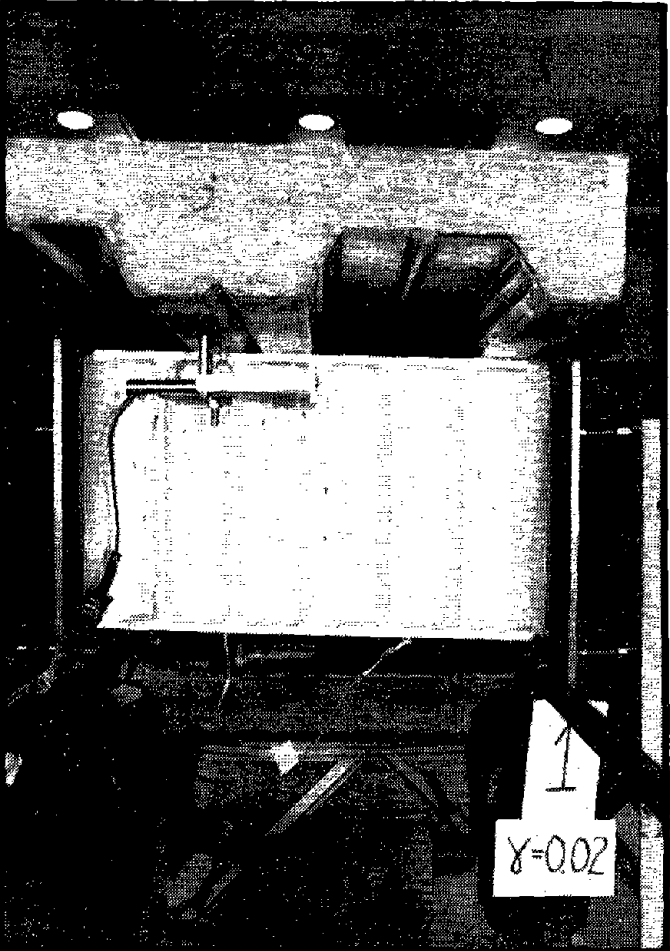
(a) Cycle 1, at $\gamma$ = 0.02 rad.
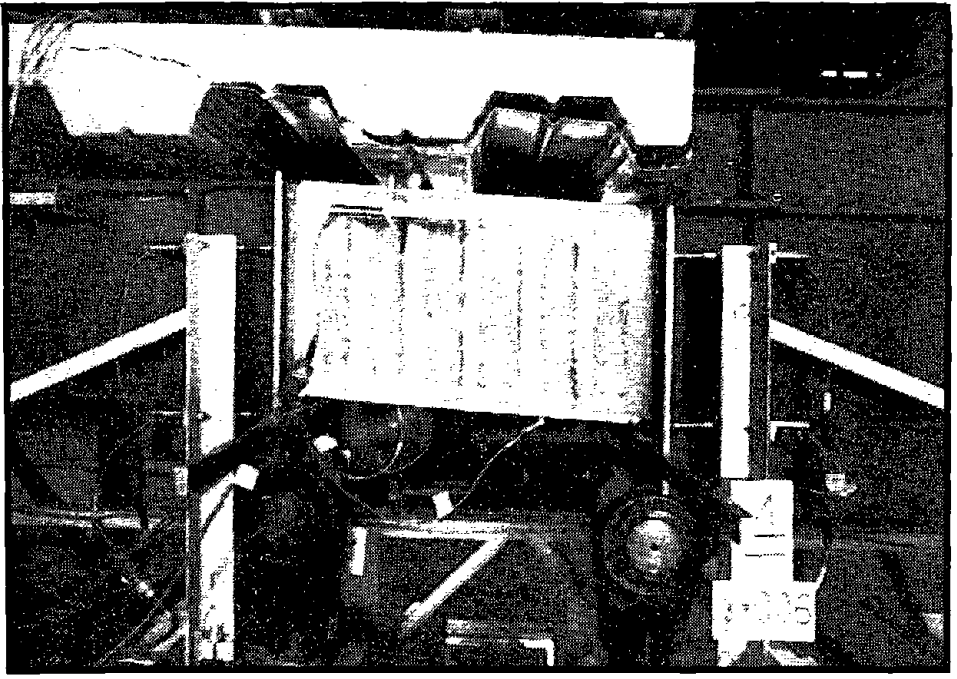


(b) Cycle 4, at $\gamma$ = 0.06 rad.

Fig. 3.15    Photos of Specimen A2 During Test.

192
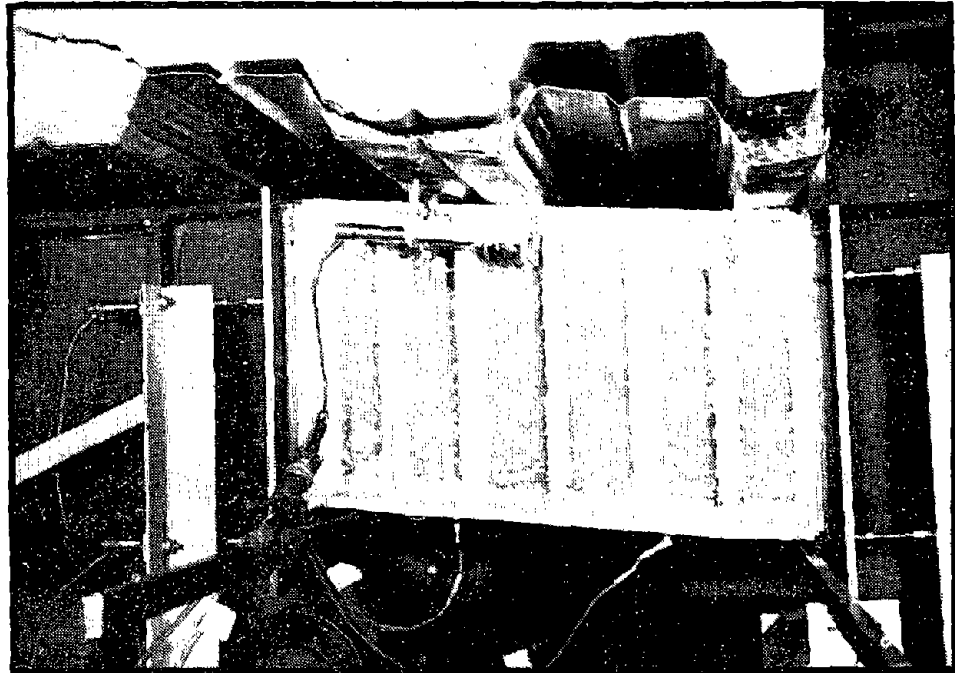


(c) Cycle 7, at $\gamma$ = 0.08 rad.
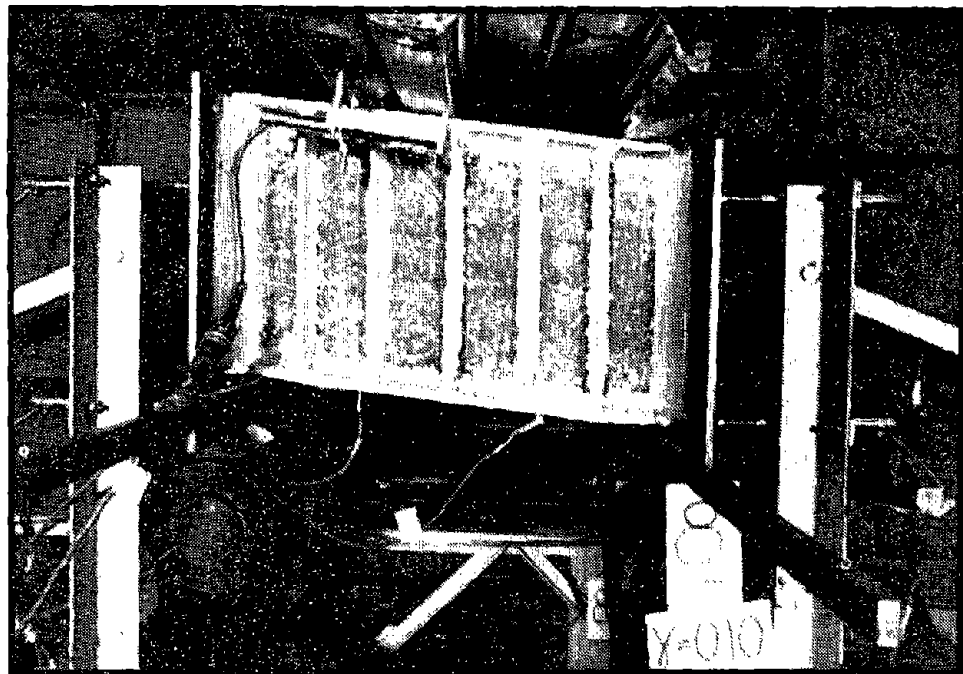
(d) Cycle 8, at $\gamma$ = 0.10 rad.

Fig. 3.15    Photos of Specimen A2 During Test.
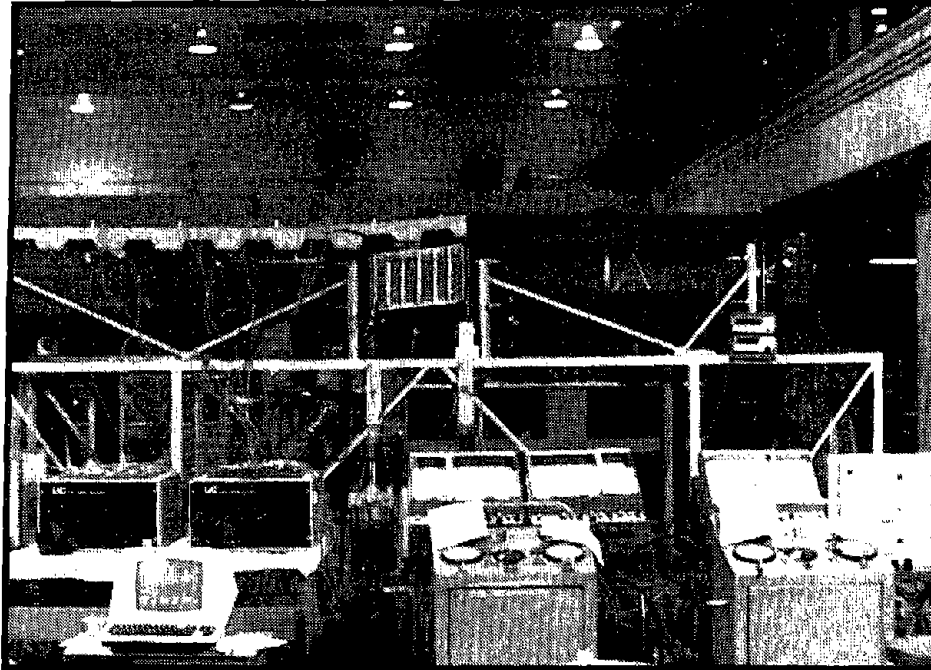
(a) Rib Cracking and Deck Separation Above Link,
Positive Moment at End B of Link
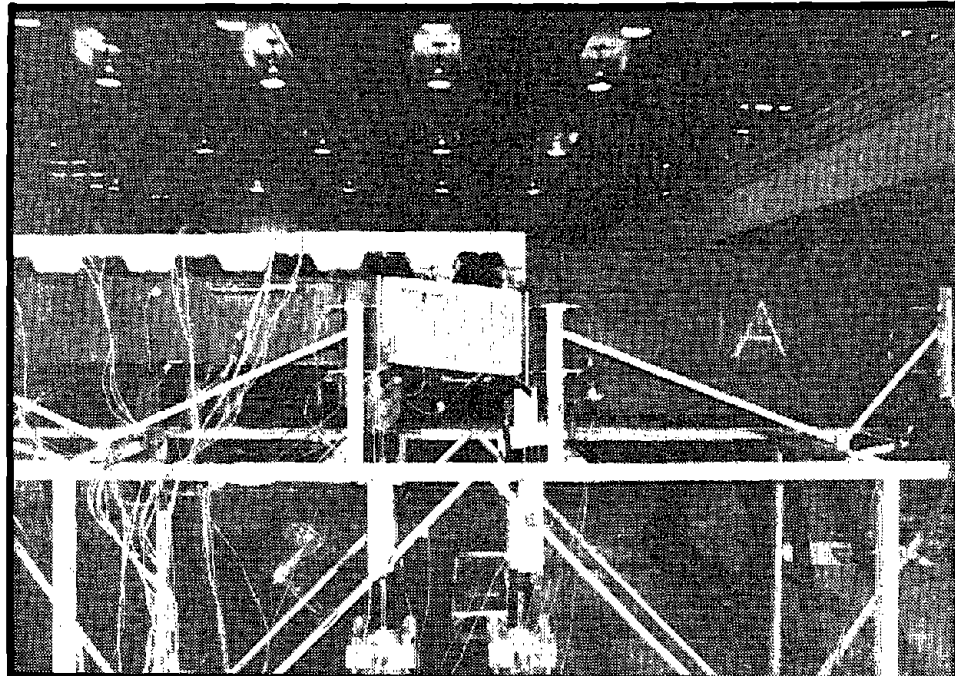
(b) Rib Cracking and Deck Separation Above Link,
Negative Moment at End B of Link

Fig. 3.16    Photos of Floor Damage During Cycle 8 With $\gamma = \pm 0.10$ rad.,
Specimen A2
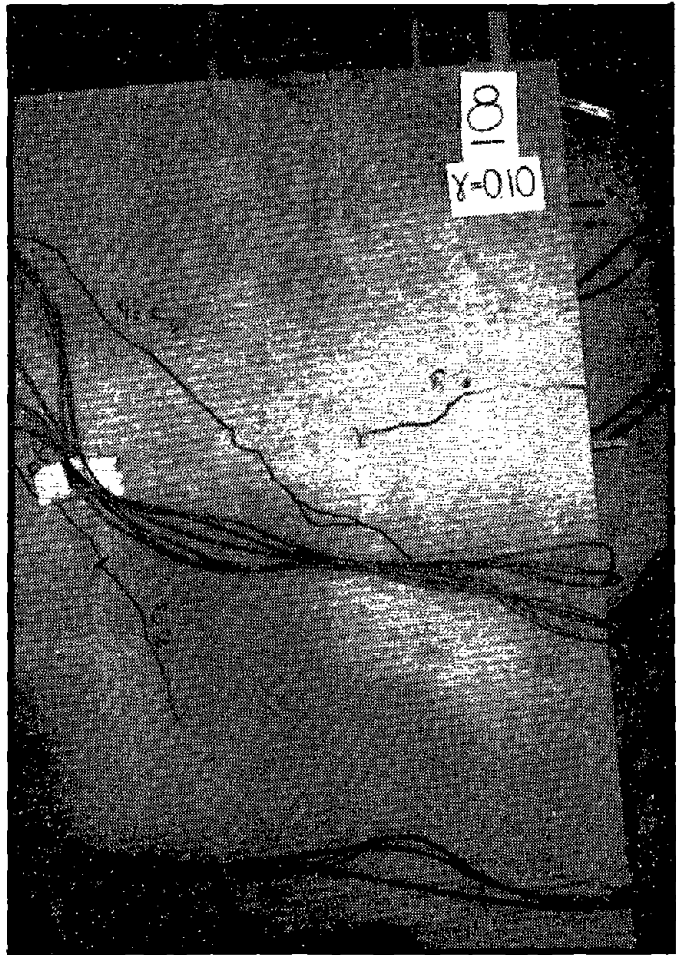
(a) Floor Slab Above Link
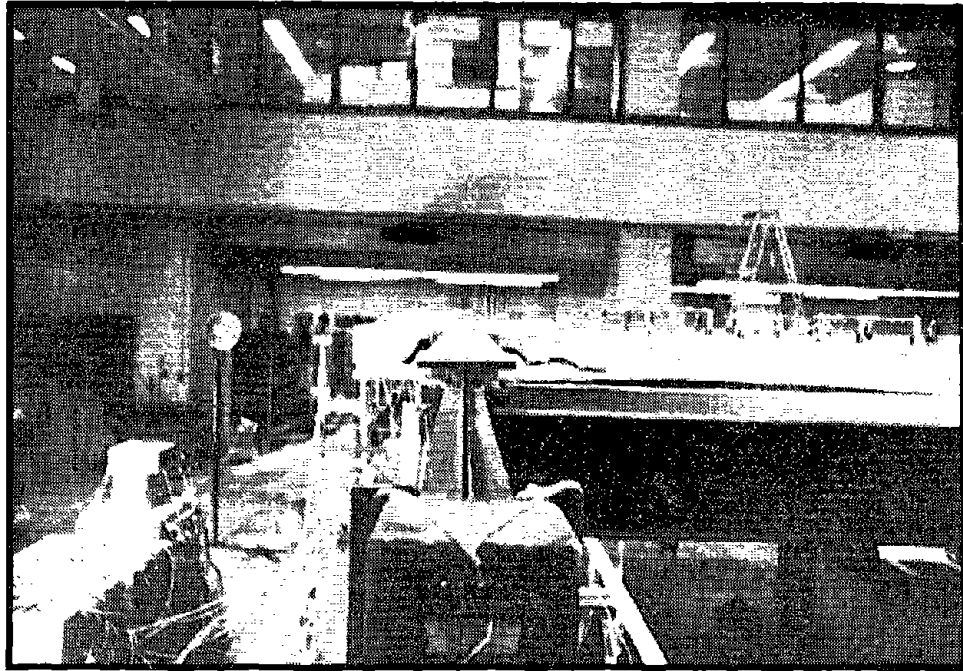
(b) North Edge of Floor Slab

Fig. 3.17    Photos of Floor Damage After Completion of Test, Specimen A2.
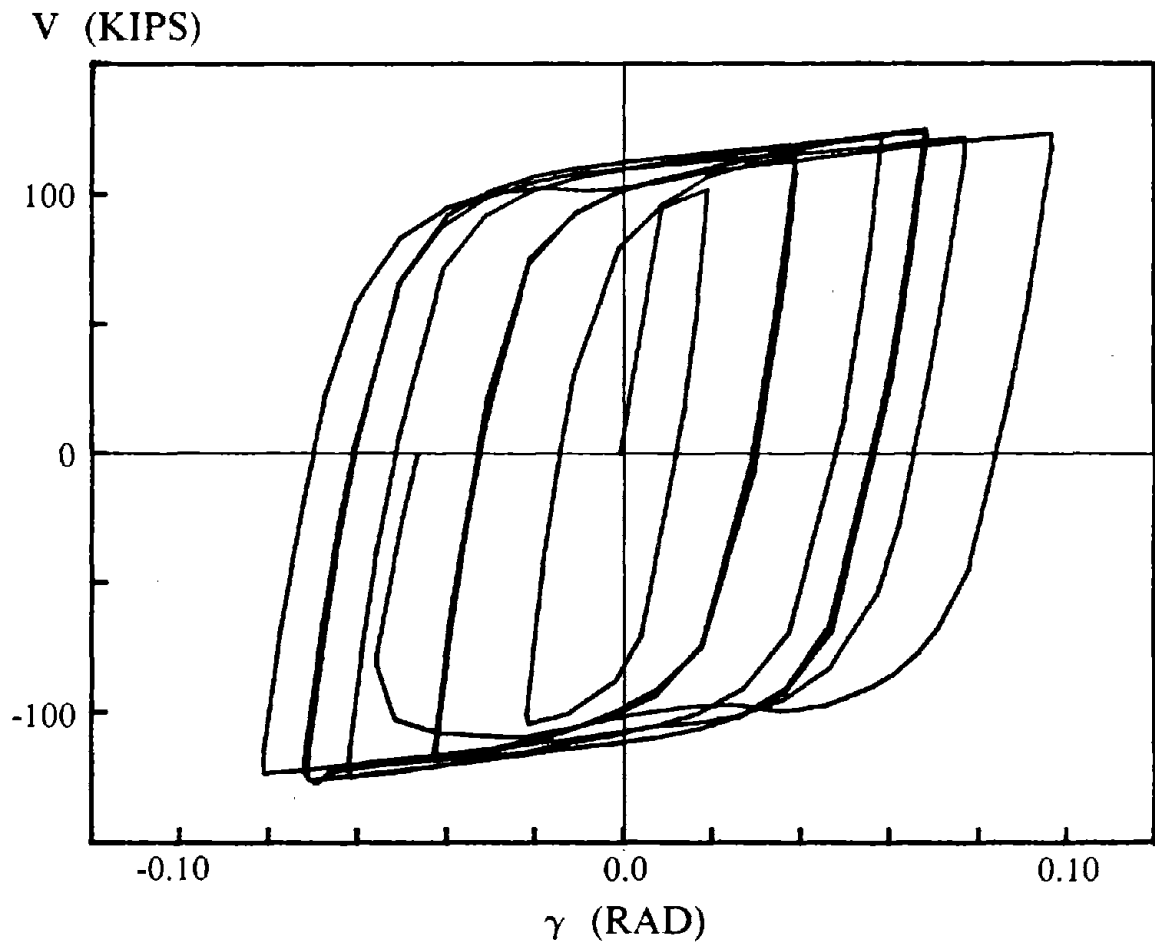
Fig. 3.18    Shear-Deformation Relationship for Link, Specimen B1.

$M_A$ (K-IN)
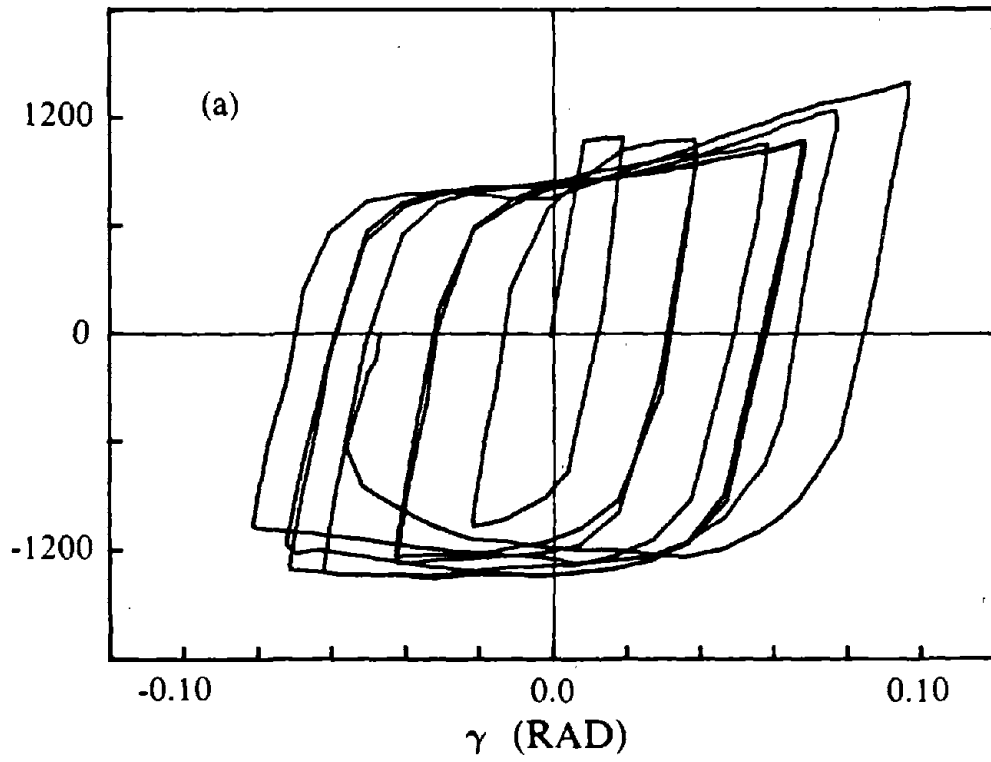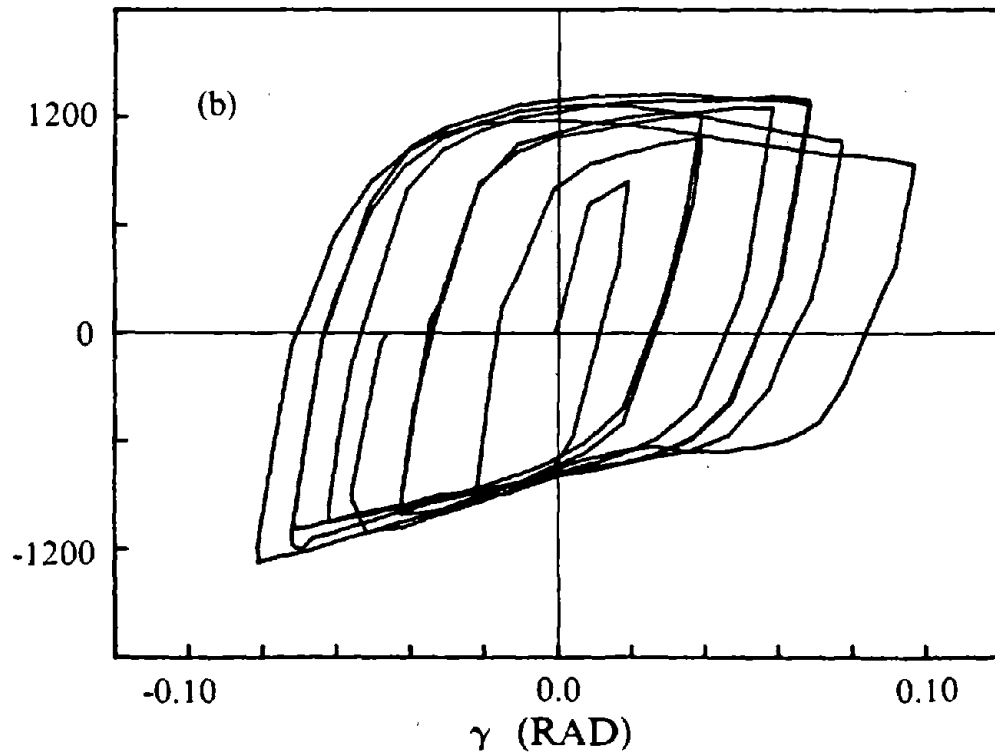
(a)

1200

0.0

-1200

$\gamma$ (RAD)

-0.10          0.0          0.10

$-M_B$ (K-IN)

(b)

1200

0.0

-1200

$\gamma$ (RAD)

-0.10          0.0          0.10

Fig. 3.19    Moment-Deformation Relationships for Link, Specimen B1.
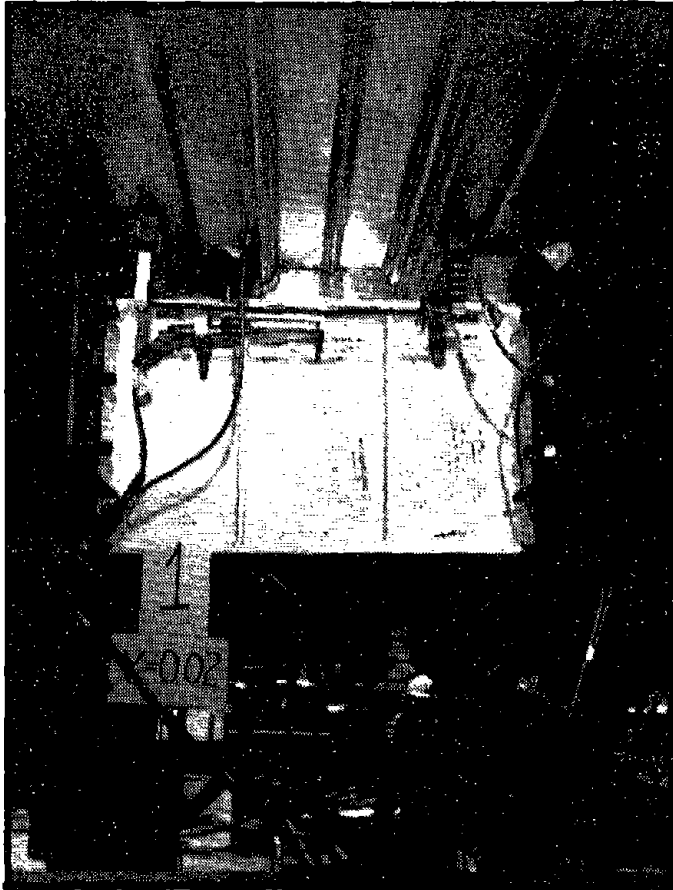
(b) Cycle 4, at $\gamma = -0.06$ rad.

(a) Cycle 1, at $\gamma = 0.02$ rad.

Fig. 3.20    Photos of Specimen B1 During Test.

198
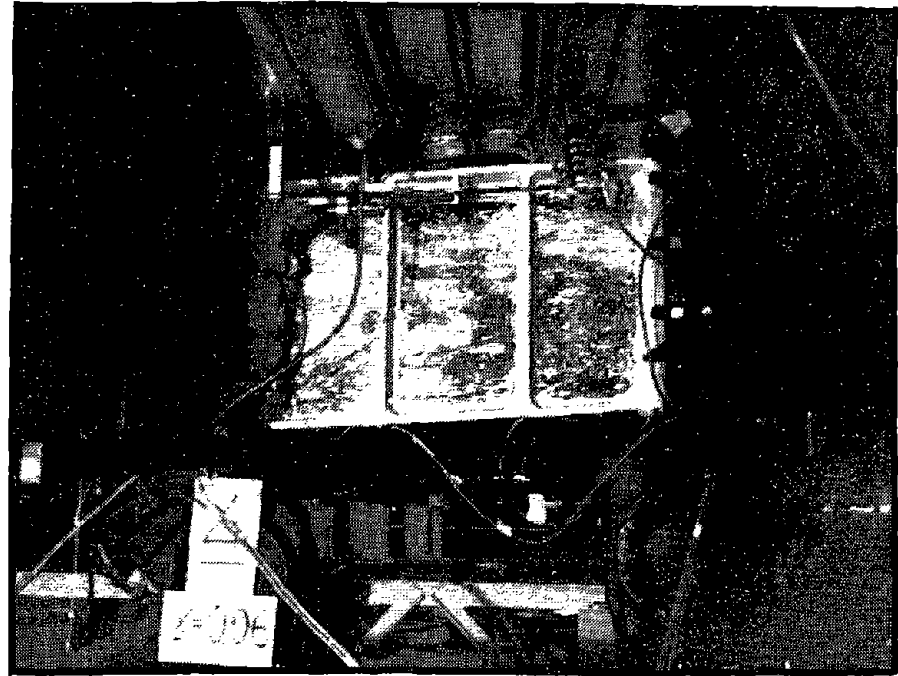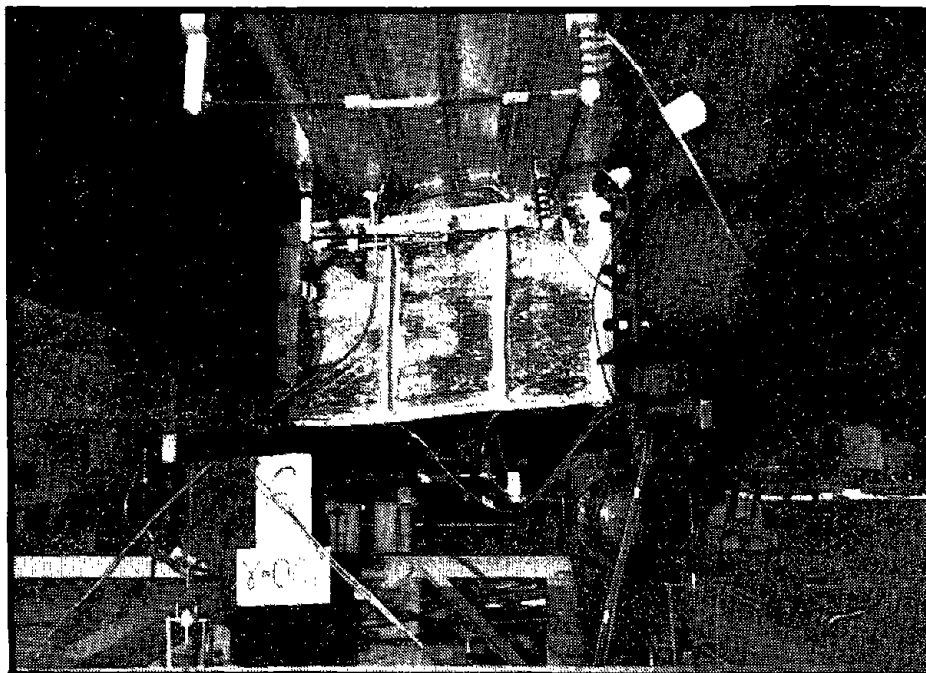


(c)  Cycle 6, at $\gamma$ = -0.07 rad.
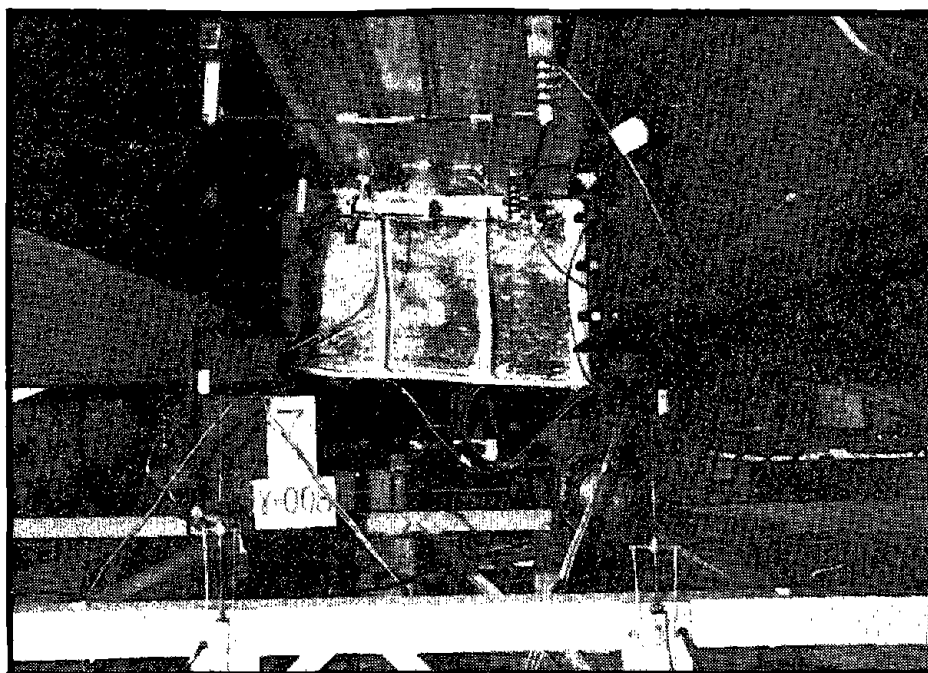
(d)  Cycle 7, at $\gamma$ = 0.08 rad.

Fig. 3.20    Photos of Specimen B1 During Test.
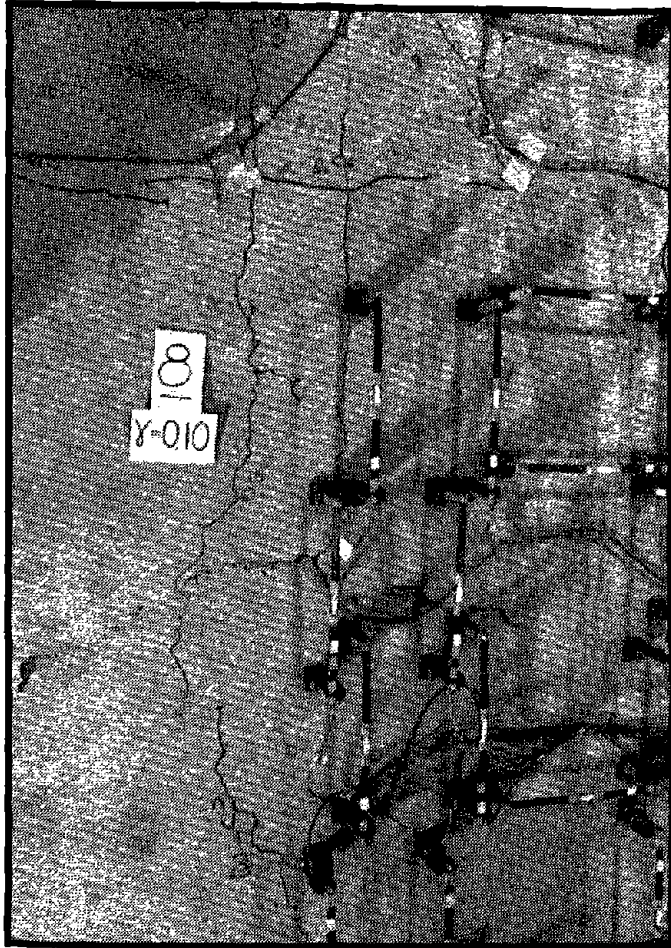
(a) Floor Slab Above Link
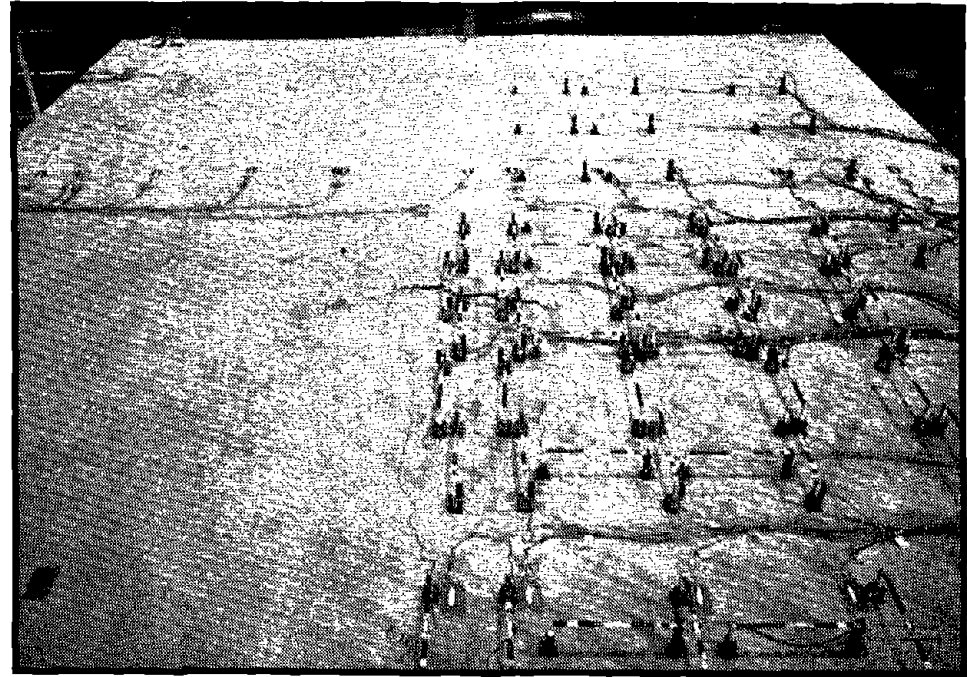
(b) General View of Floor Slab

Fig. 3.21　Photos of Floor Damage During Cycle 8 With $\gamma = 0.10$ rad., Specimen B1.

V (KIPS)
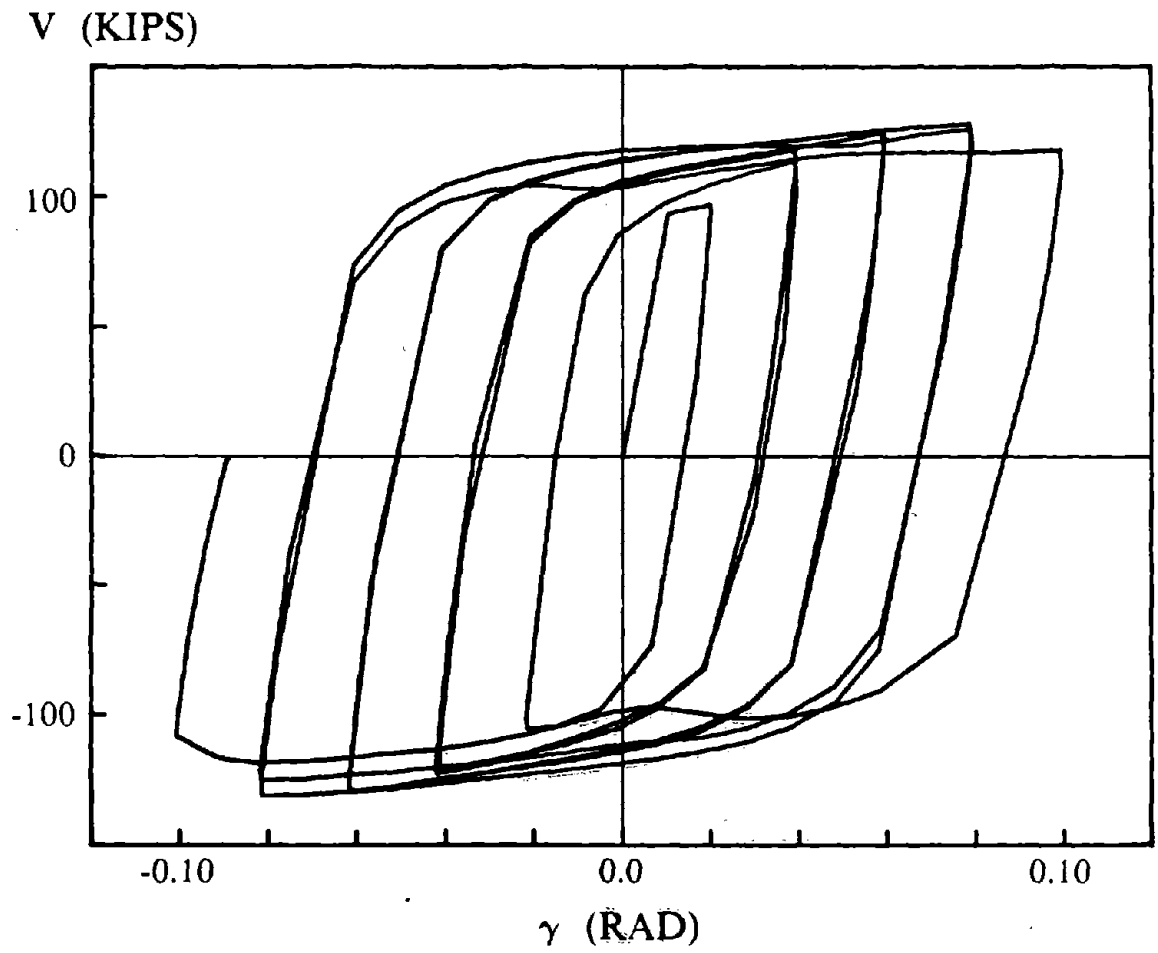


Fig. 3.22    Shear-Deformation Relationship for Link, Specimen B2.
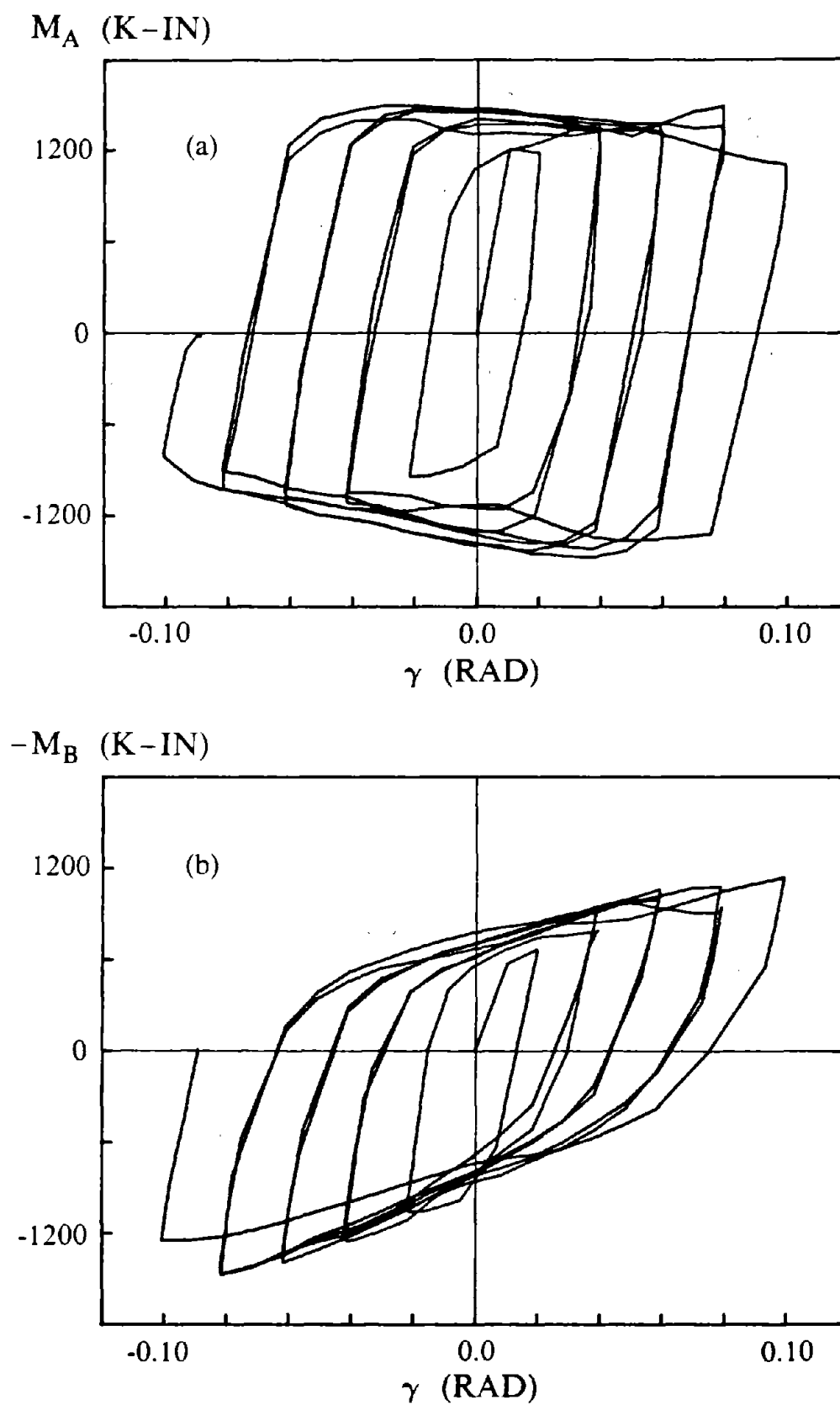
Fig. 3.23    Moment-Deformation Relationships for Link, Specimen B2.
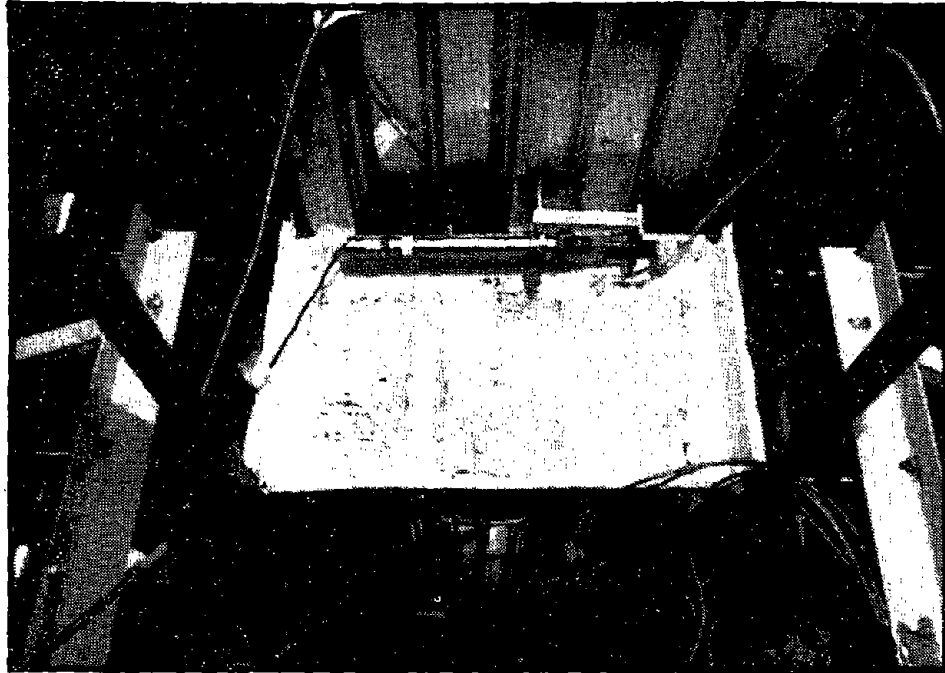
(a) Cycle 1, at $\gamma = 0.02$ rad.
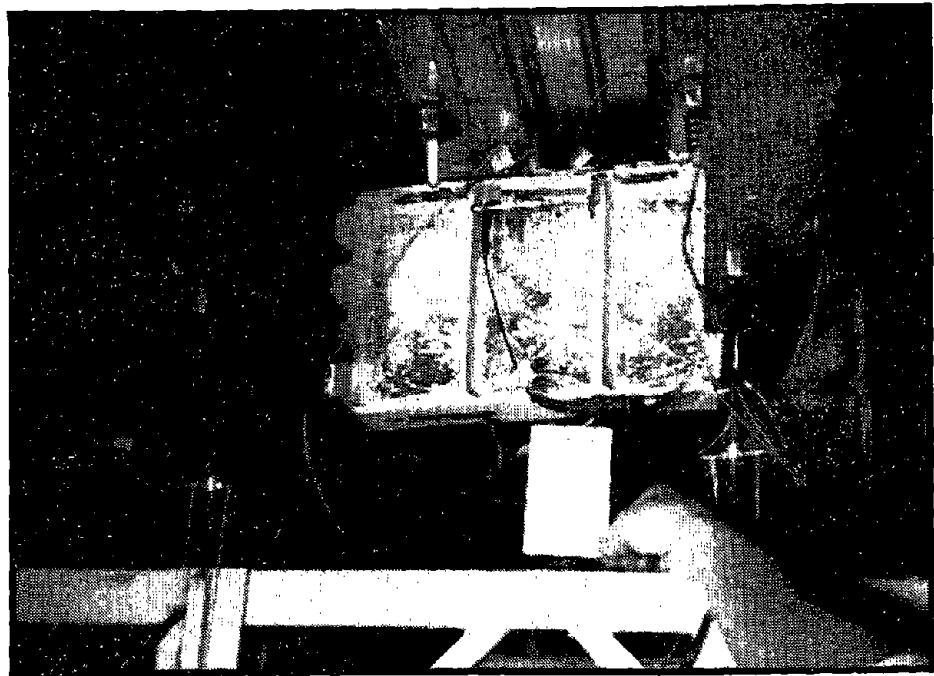
(b) Cycle 4, at $\gamma = -0.06$ rad.

Fig. 3.24    Photos of Specimen B2 During Test.
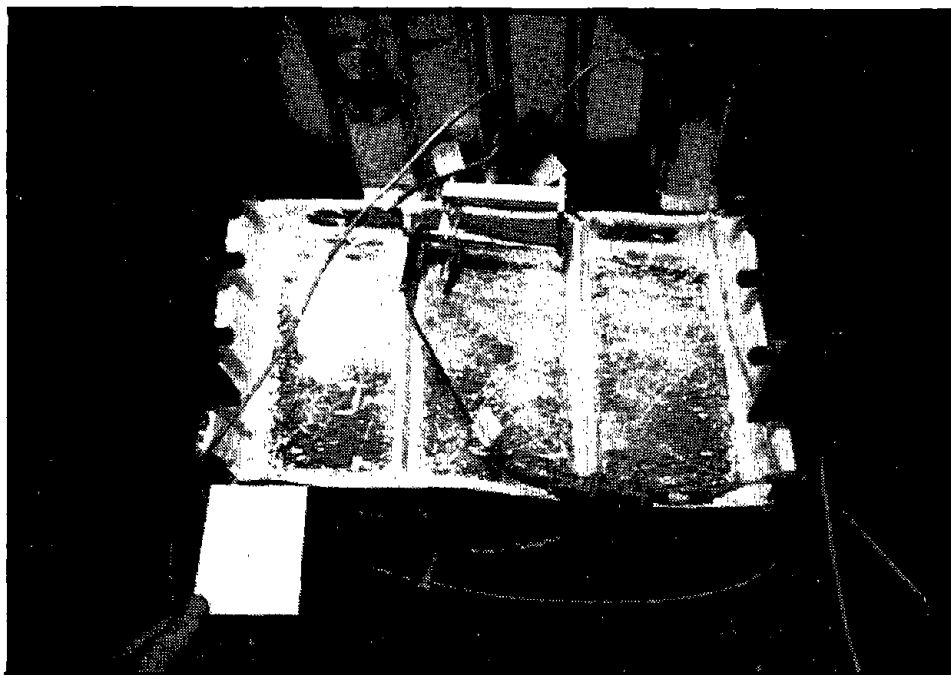
(c) Cycle 7, at $\gamma = 0.08$ rad.
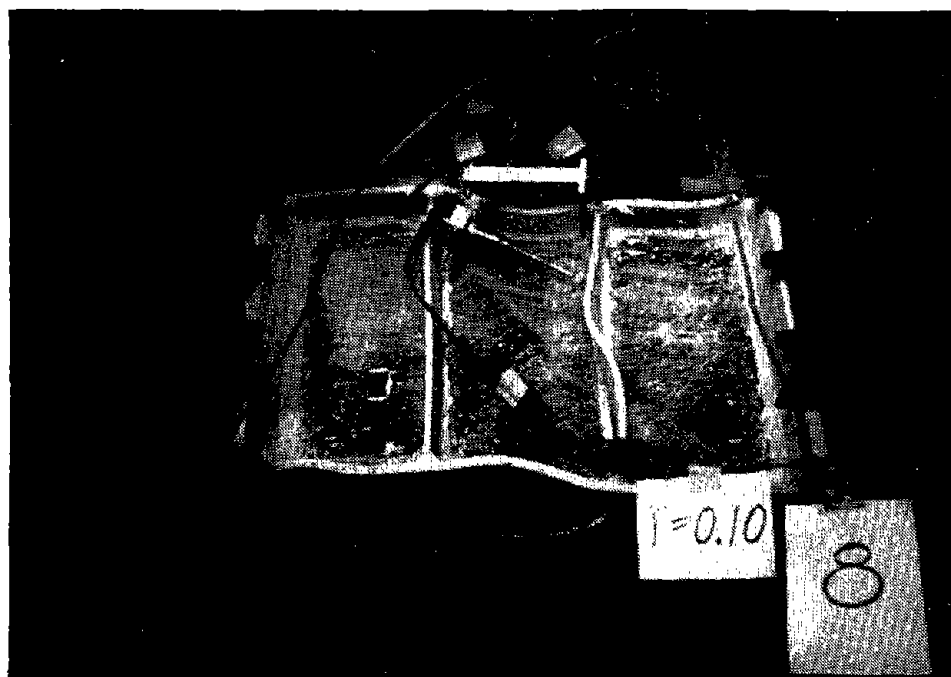
(d) Cycle 8, at $\gamma = 0.10$ rad.

Fig. 3.24    Photos of Specimen B2 During Test.

(a) Floor Slab Above Link

(b) Deformation of Link and Metal Deck

(c) General View of Floor Slab
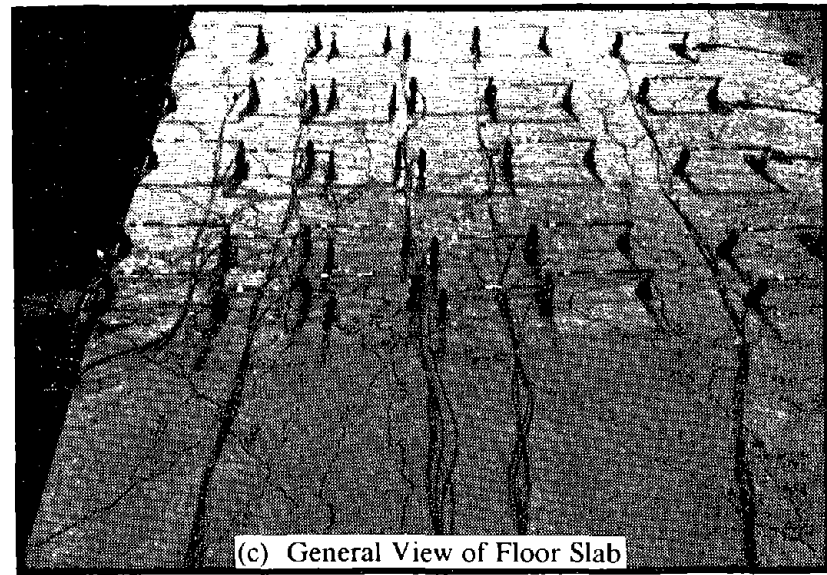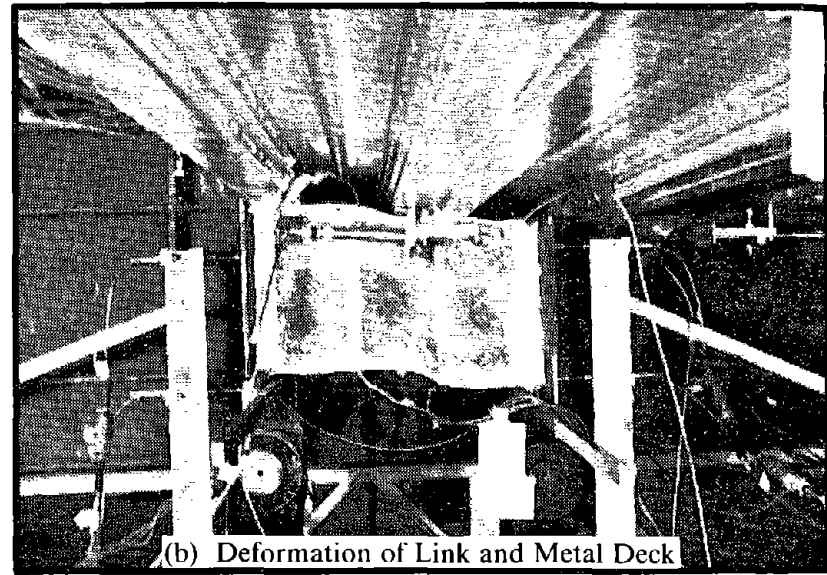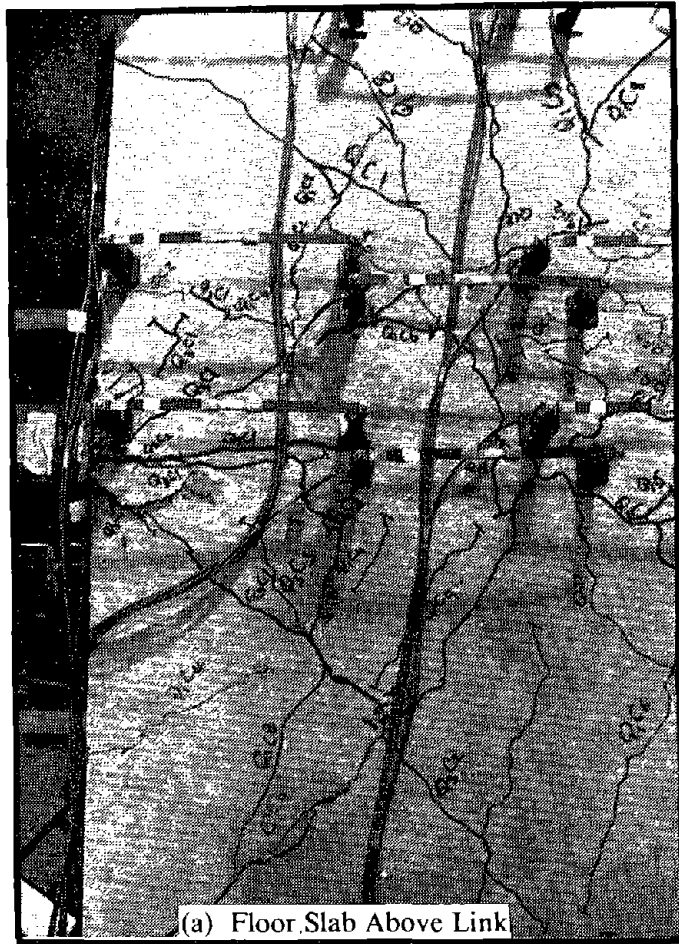
Fig. 3.25    Photos of Floor Slab Damage After Test, Specimen B2.
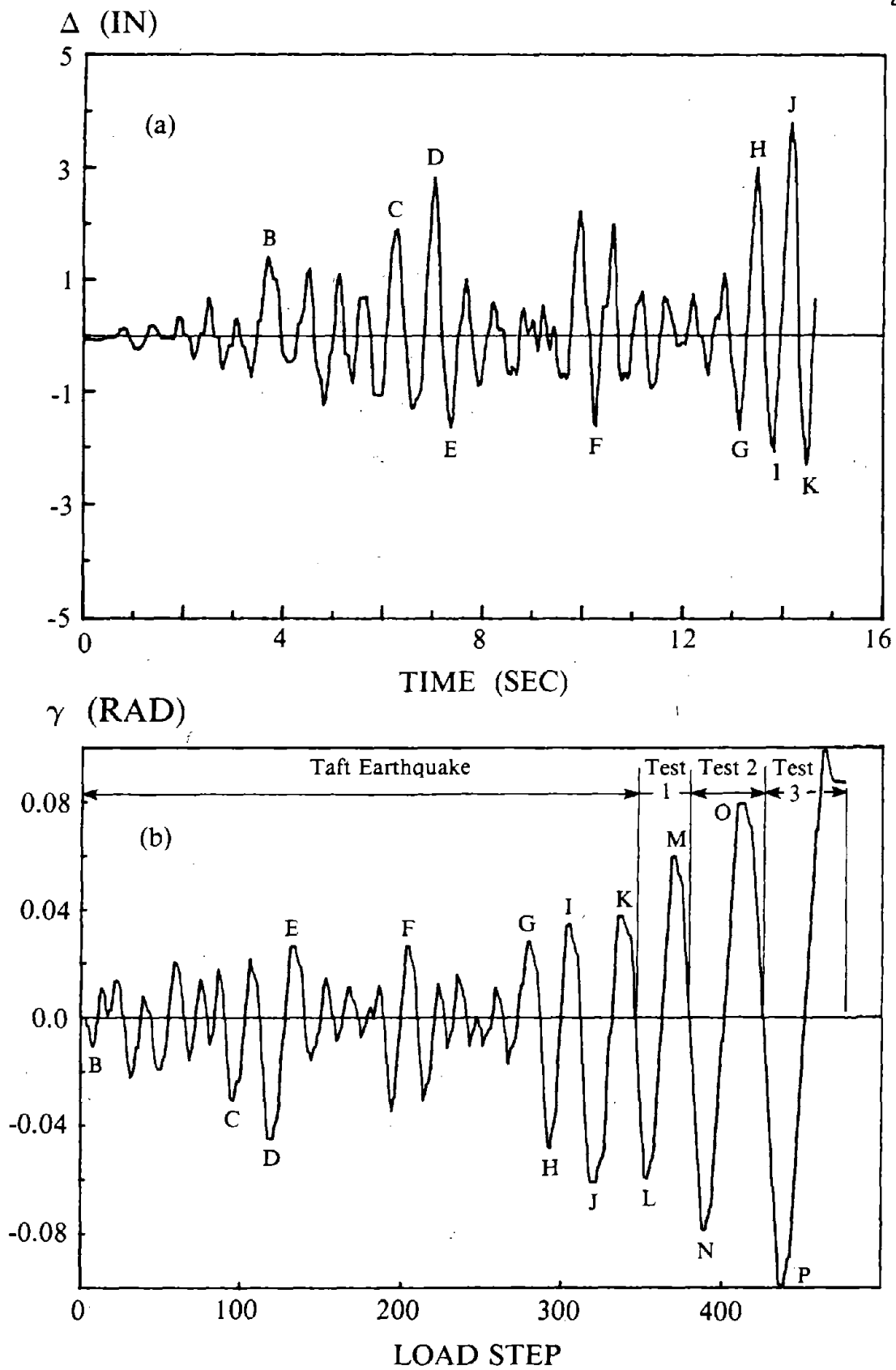
Fig. 3.26    Histories for (a) Tsukuba First Floor Displacement and
(b) Simulated Link Deformation for Specimen C1.

V (KIPS)
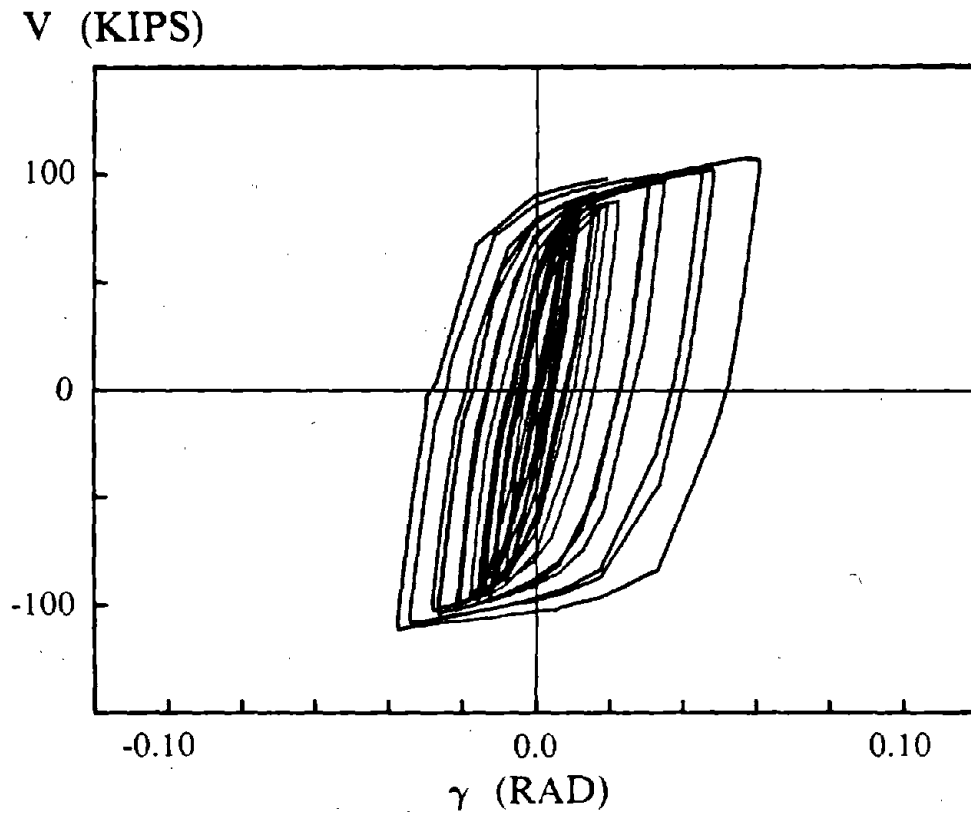


Fig. 3.27    Shear-Deformation Relationship of Link During Scaled Taft Earthquake, Specimen C1.

V (KIPS)
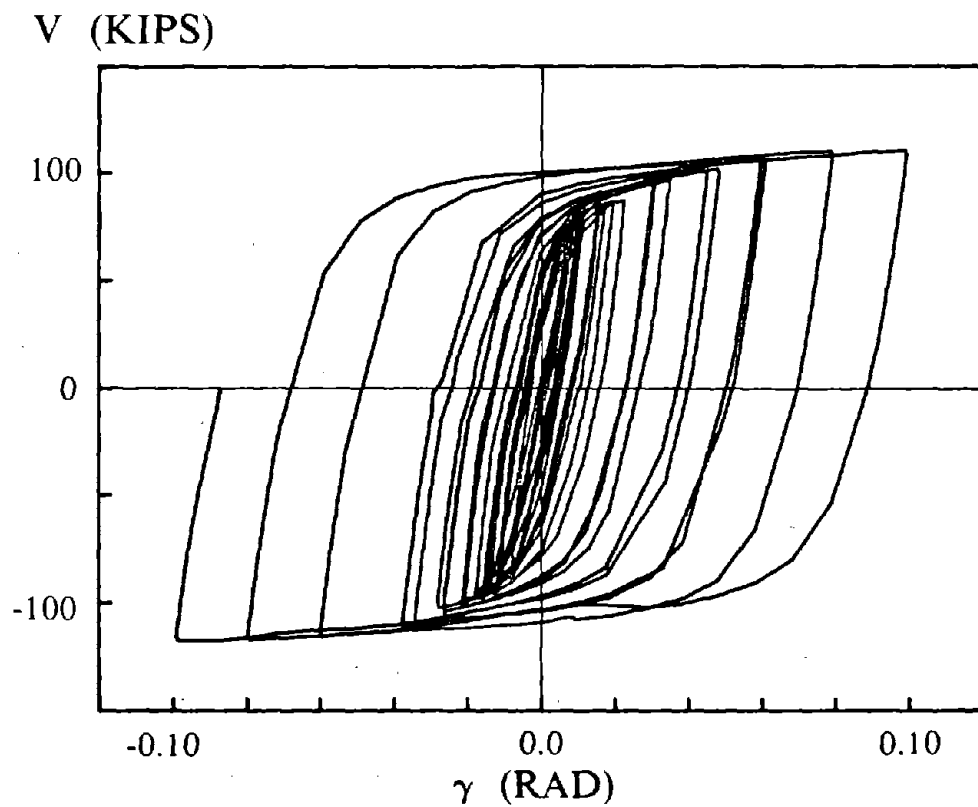


Fig 3.28    Shear-Deformation Relationship for Complete Test of Link, Specimen C1.

$M_A$ (K–IN)

(a)

1200

0

Test 3

Test 2

Test 1

–1200

-0.10          0.0          0.10

$\gamma$ (RAD)

$-M_B$ (K–IN)

(b)

1200

0

Test 1

Test 2

Test 3

–1200

-0.10          0.0          0.10

$\gamma$ (RAD)
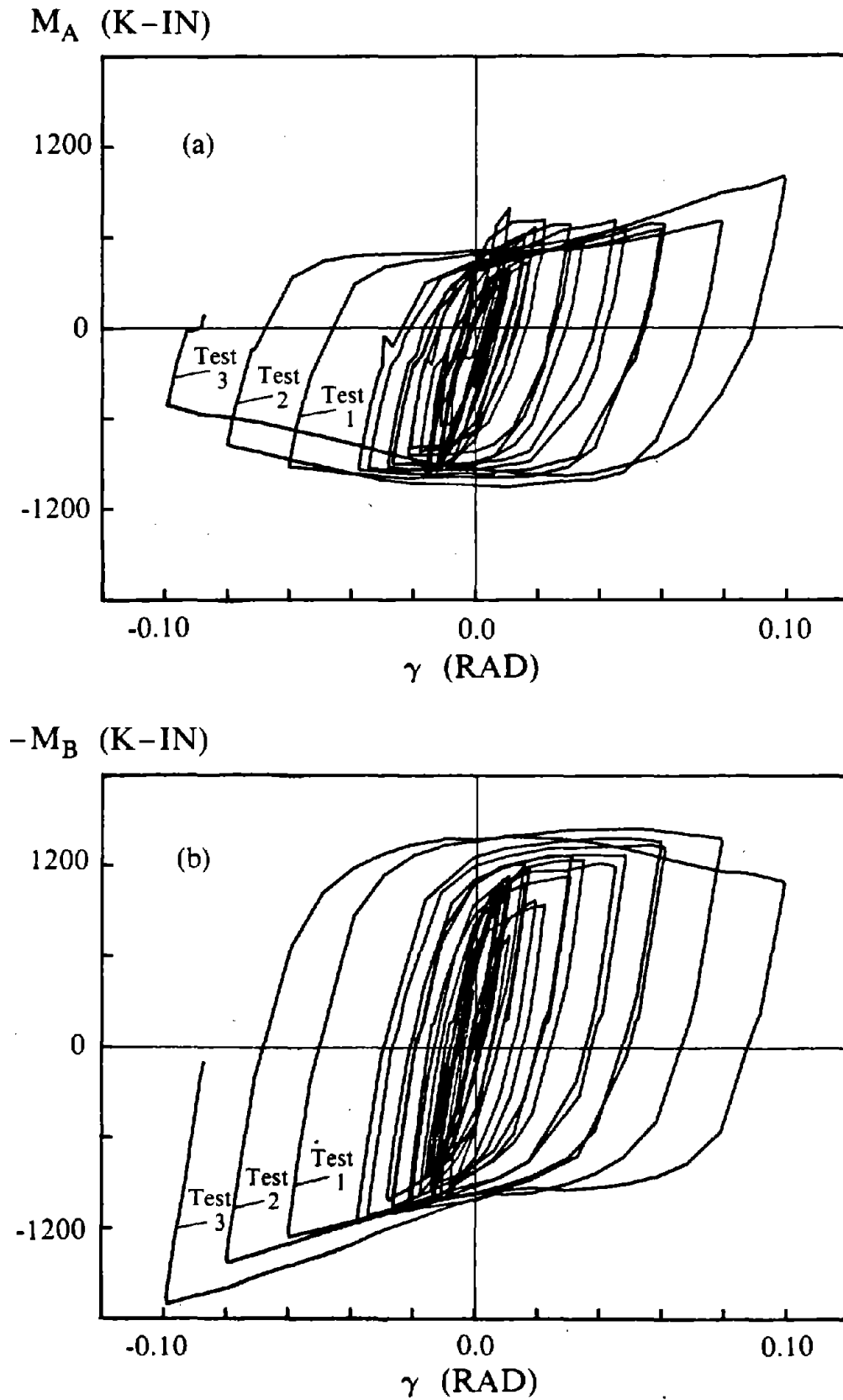
Fig. 3.29   Moment-Deformation Relationships for Complete Test of Link, Specimen C1.
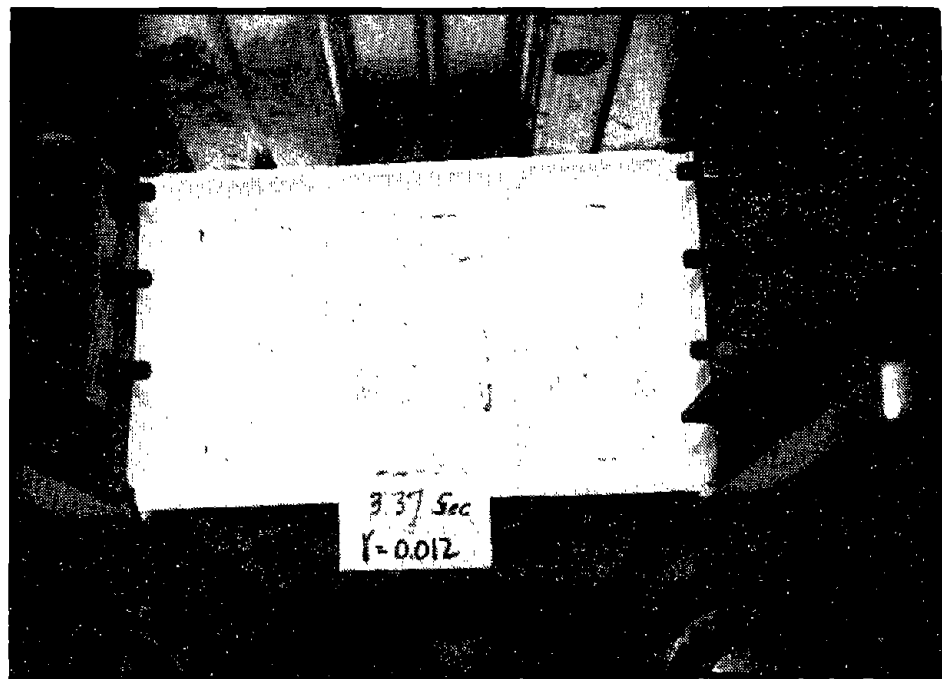
(a)    At t = 3.37 seconds, $\gamma$ = -0.012 rad.
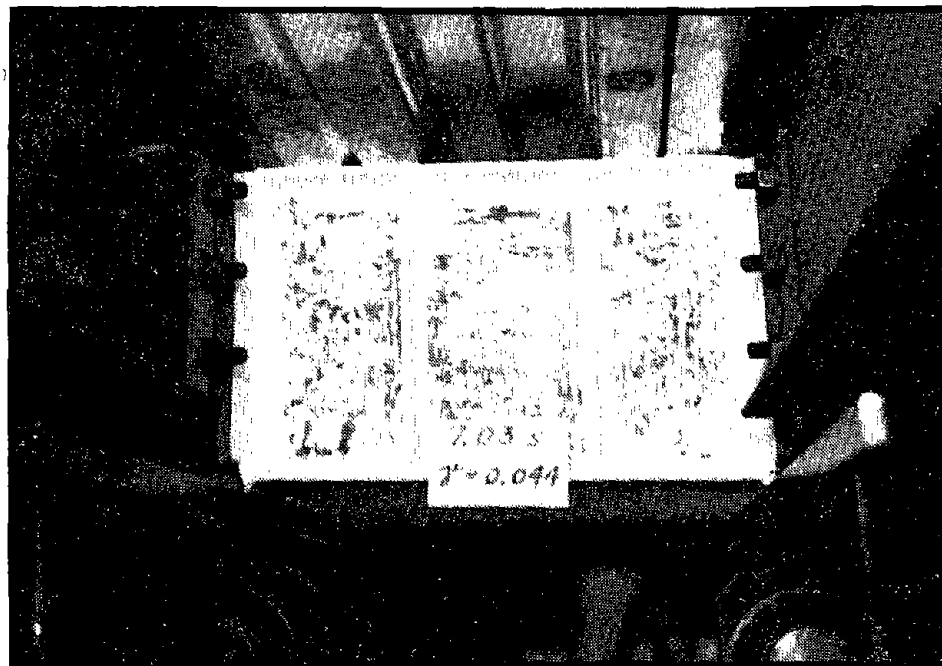


(b)    At t = 7.03 seconds, $\gamma$ = 0.044 rad.

Fig. 3.30    Photos of Link During Scaled Taft Earthquake Simulation, Specimen C1.
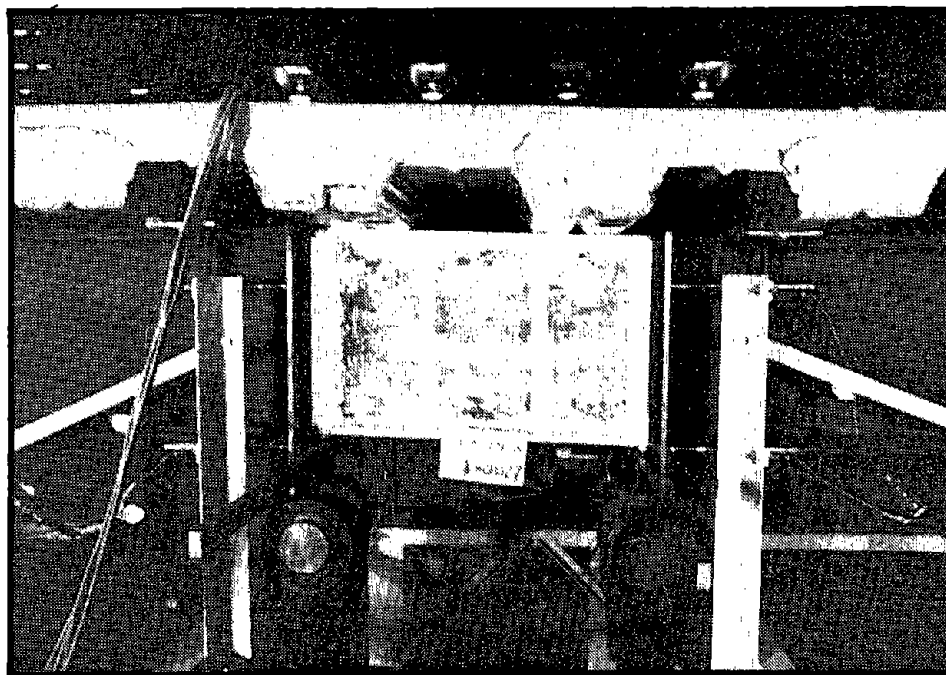
(c)    At t = 13.14 seconds, γ = -0.027 rad.
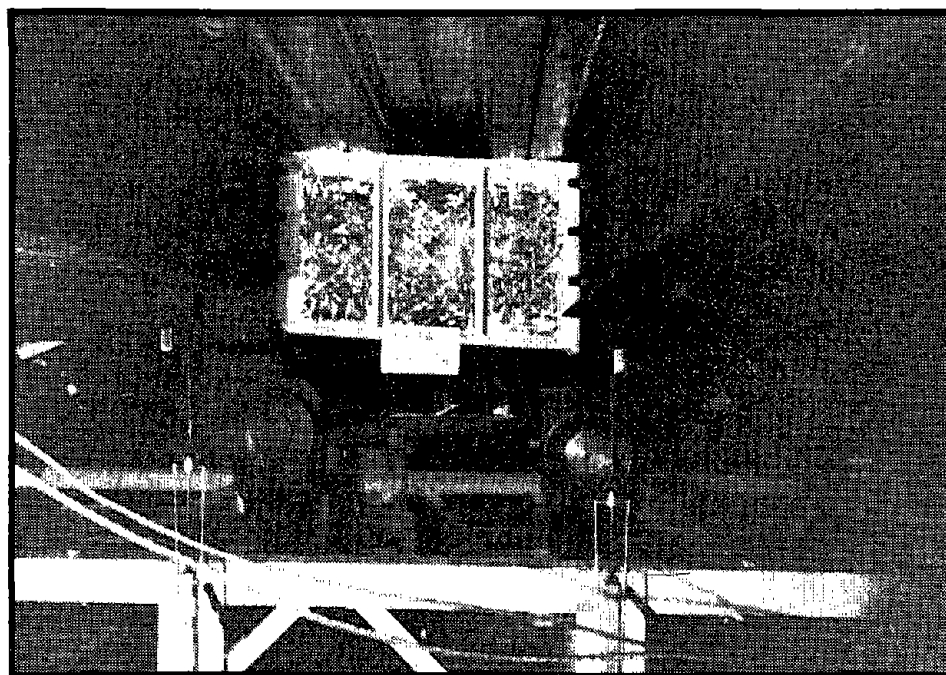
(d)    At t = 14.16 seconds, γ = -0.06 rad.

Fig. 3.30    Photos of Link During Scaled Taft Earthquake Simulation, Specimen C1.
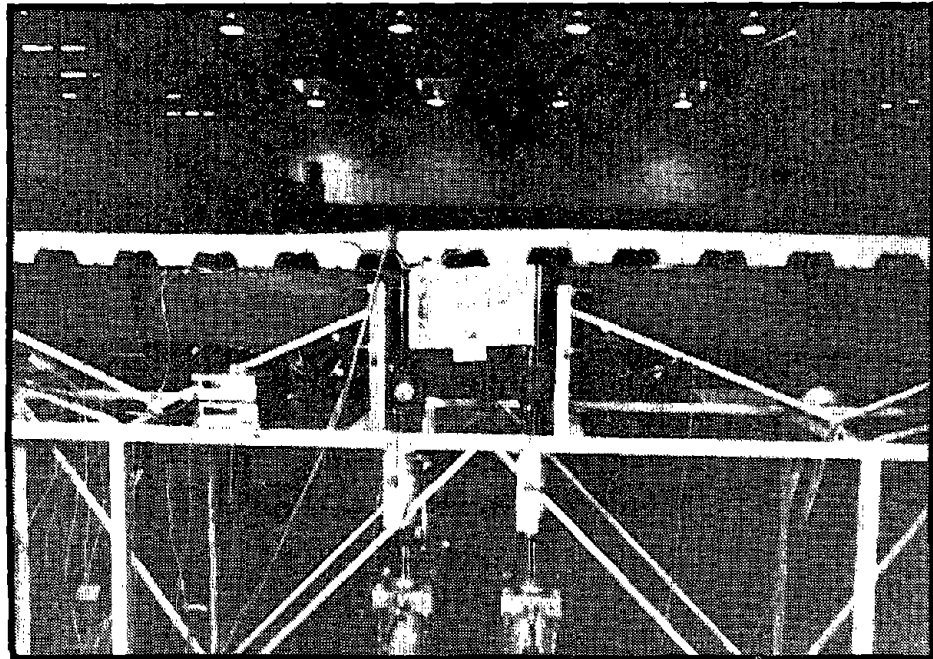
(a) General View of Test Beam and Floor Slab
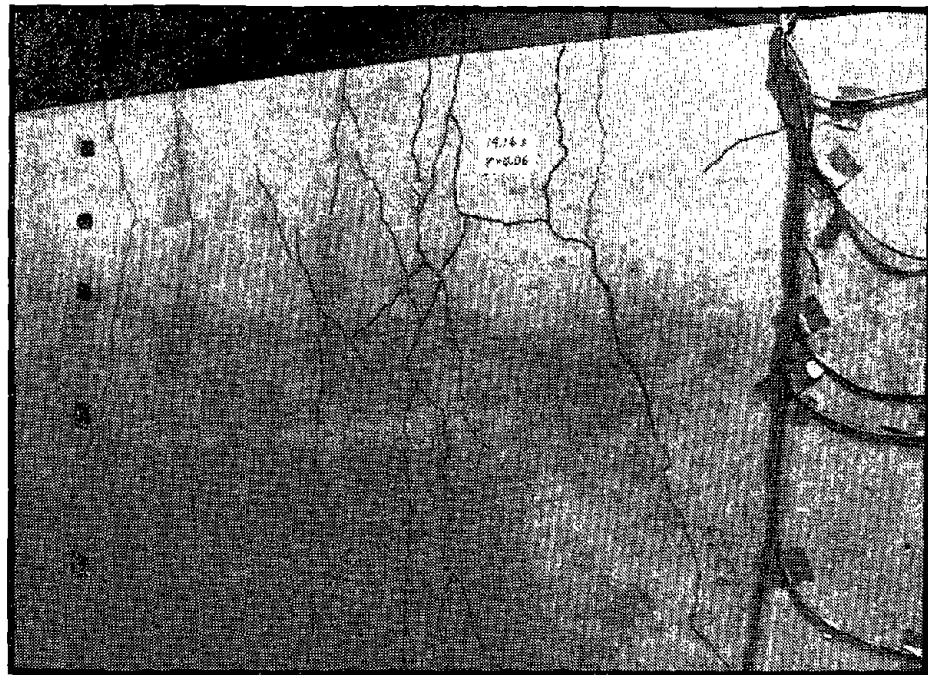
(b) Floor Slab Above the Link

Fig. 3.31    Photos of Floor Damage at the End of Scaled Taft Earthquake Simulation,
Specimen C1.

(a)  Test 1, at $\gamma$ = -0.06 rad.

(b)  Test 2, at $\gamma$ = -0.08 rad.

(c)  Test 3, at $\gamma$ = -0.10 rad.
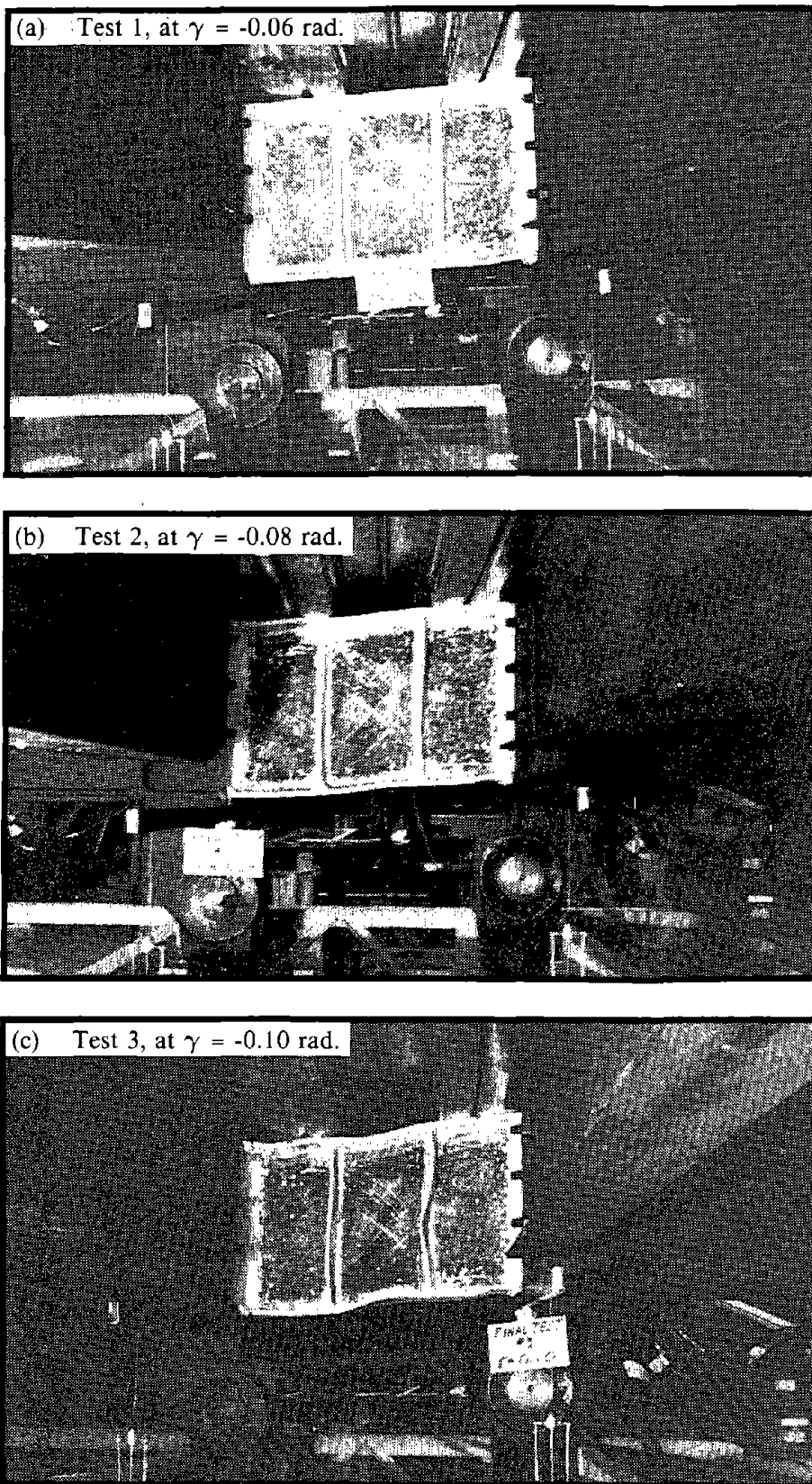
Fig. 3.32    Photos of Specimen C1 During Tests 1, 2, and 3.
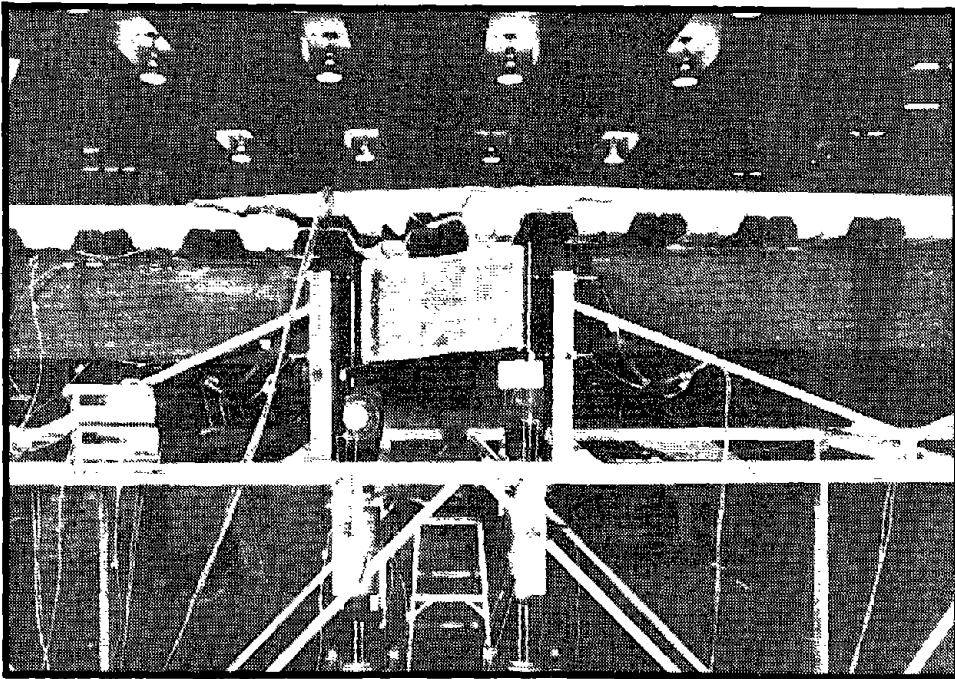
(a) General View of Test Beam and Floor Slab
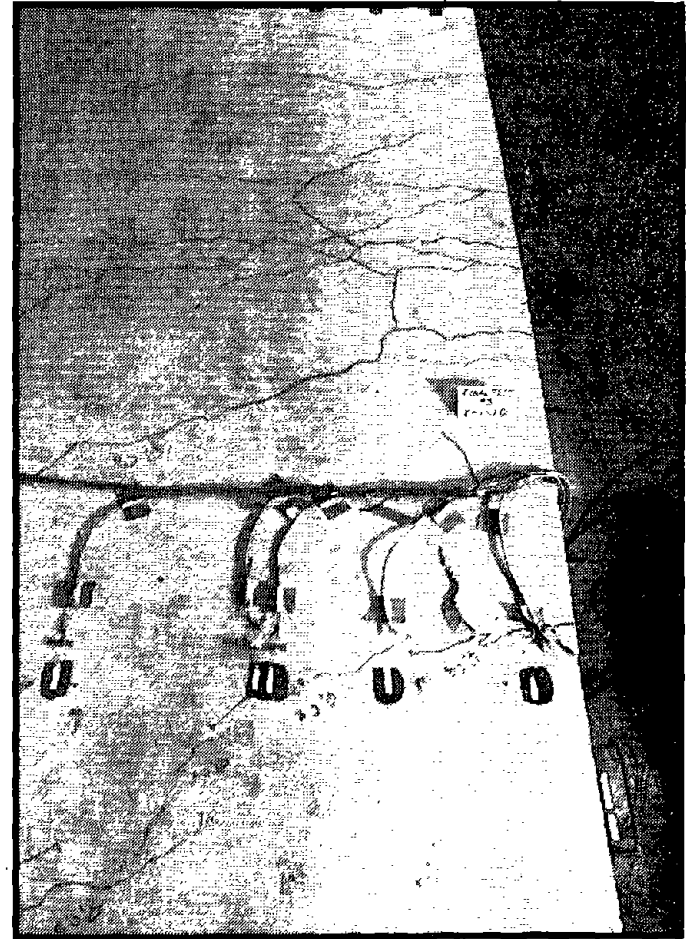
(b) Floor Slab Above the Link

Fig. 3.33    Photos of Floor Damage at the End of Test 3, Specimen Cl.
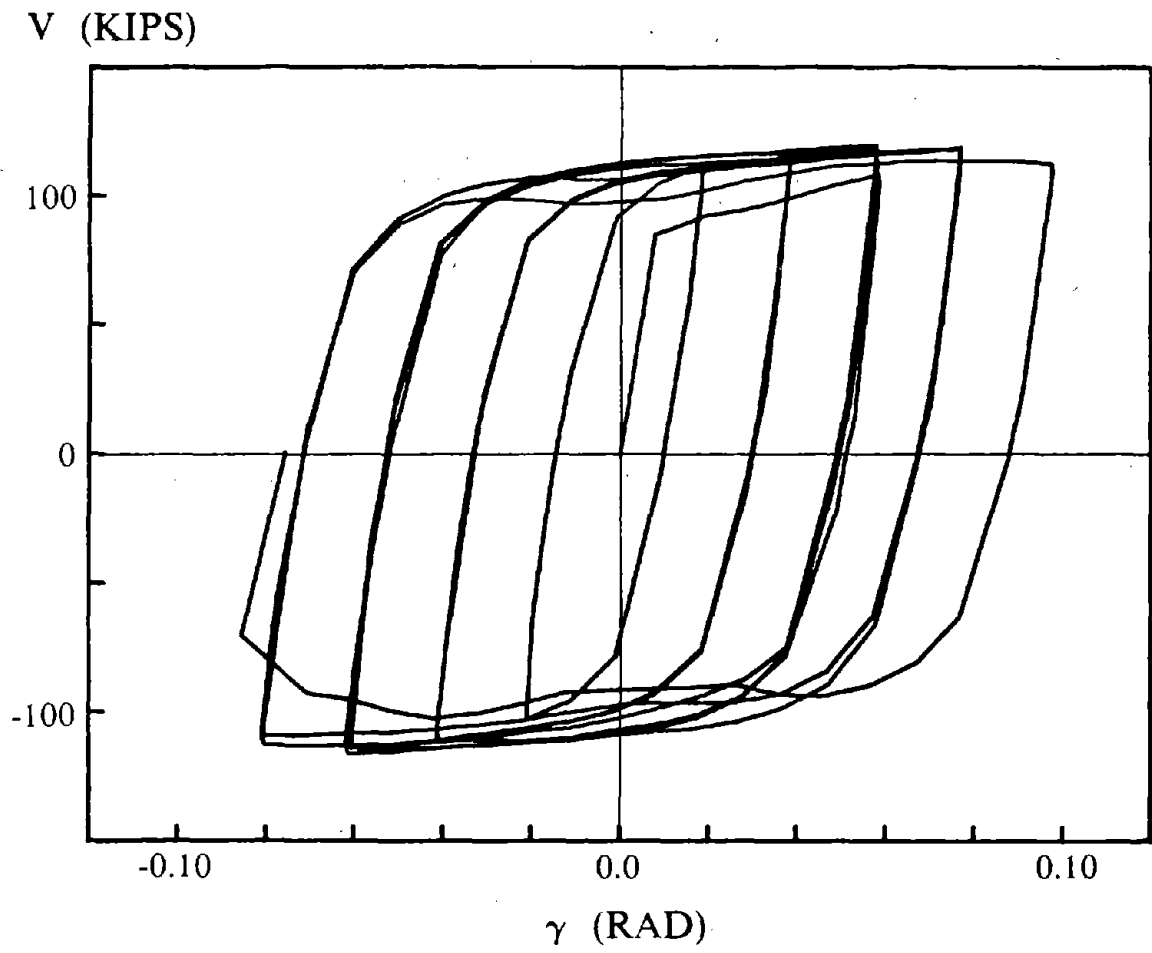
Fig. 3.34    Shear-Deformation Relationship for Link, Specimen C2.

$M_A$ (K-IN)



(a)

1200

0

-1200

-0.10          0.0          0.10

$\gamma$ (RAD)

$-M_B$ (K-IN)



(b)

1200

0

-1200

-0.10          0.0          0.10

$\gamma$ (RAD)
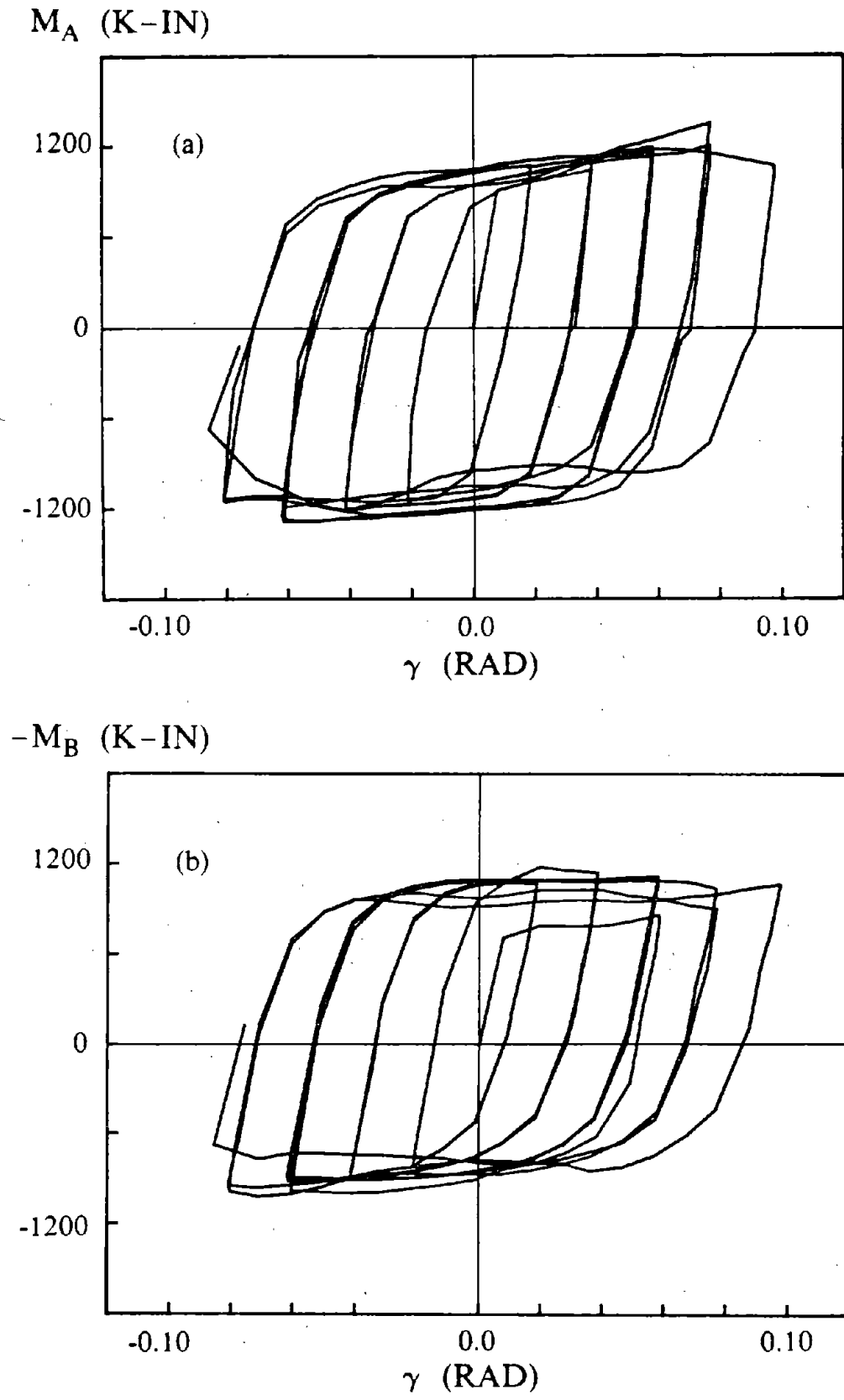
Fig. 3.35    Moment-Deformation Relationships for Link. Specimen C2.
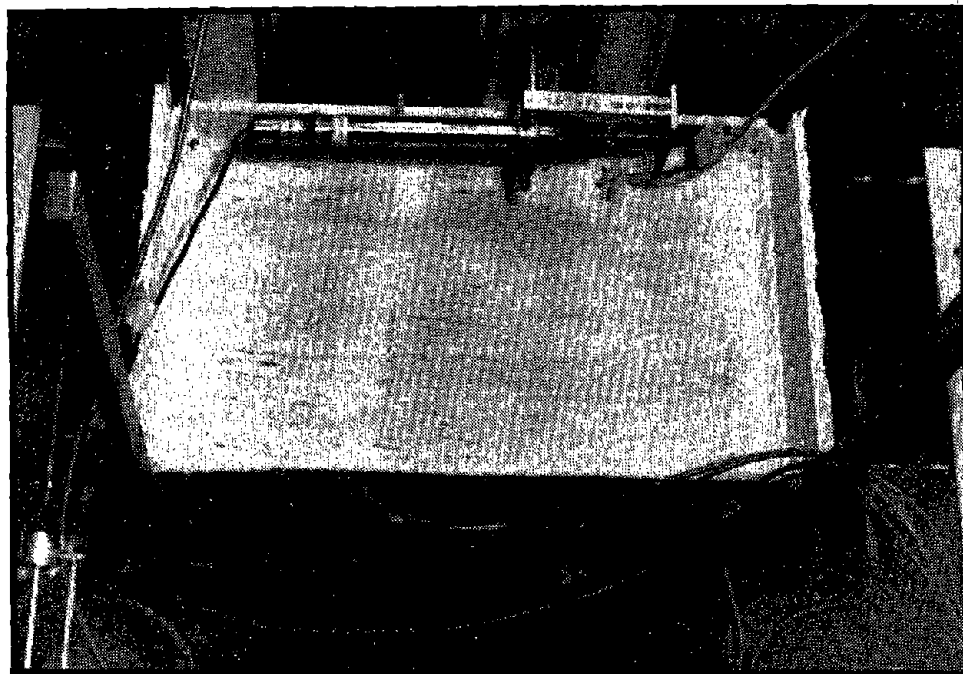
(a)     Cycle 1, at $\gamma$ = 0.02 rad.
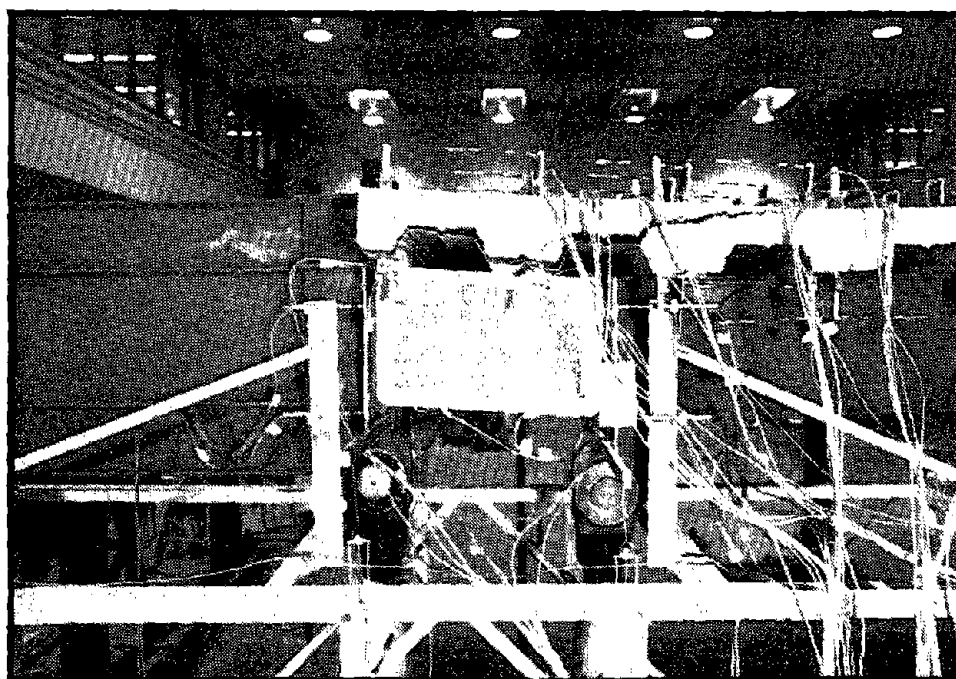
(b)     Cycle 5, at $\gamma$ = -0.06 rad.

Fig. 3.36     Photos of Specimen C2 During Test.

216
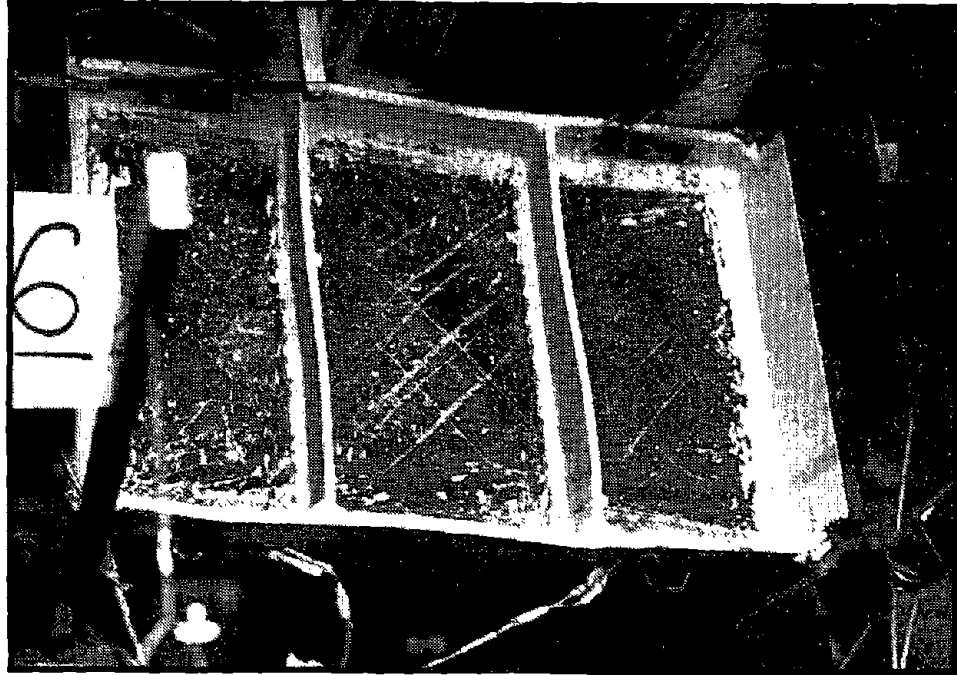


(c)    Cycle 7, at $\gamma = 0.08$ rad.
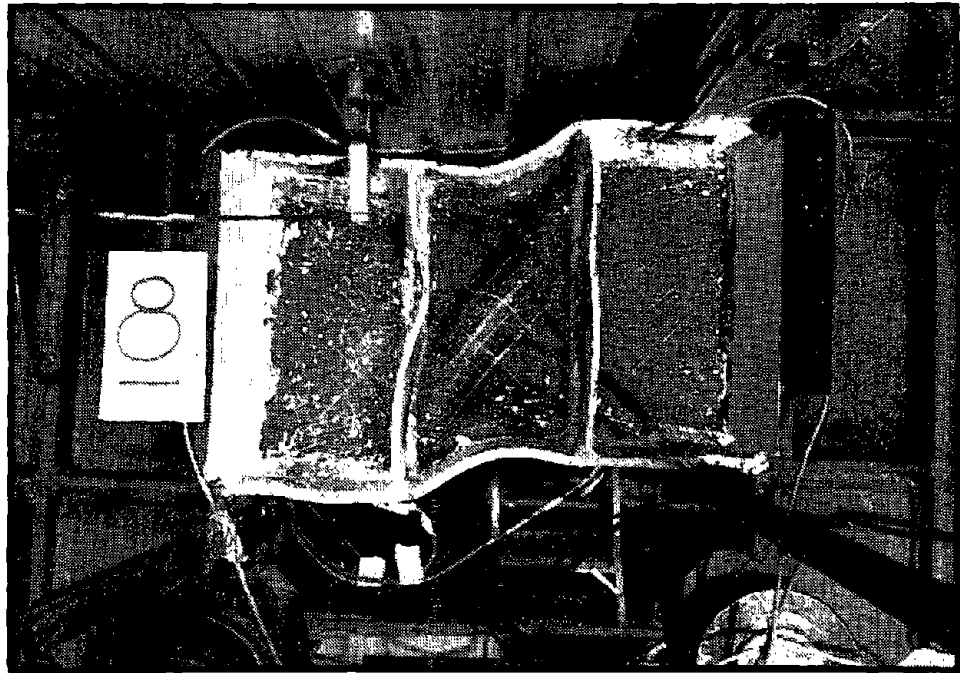
(d)    Cycle 9, at $\gamma = -0.09$ rad.

Fig. 3.36    Photos of Specimen C2 During Test.
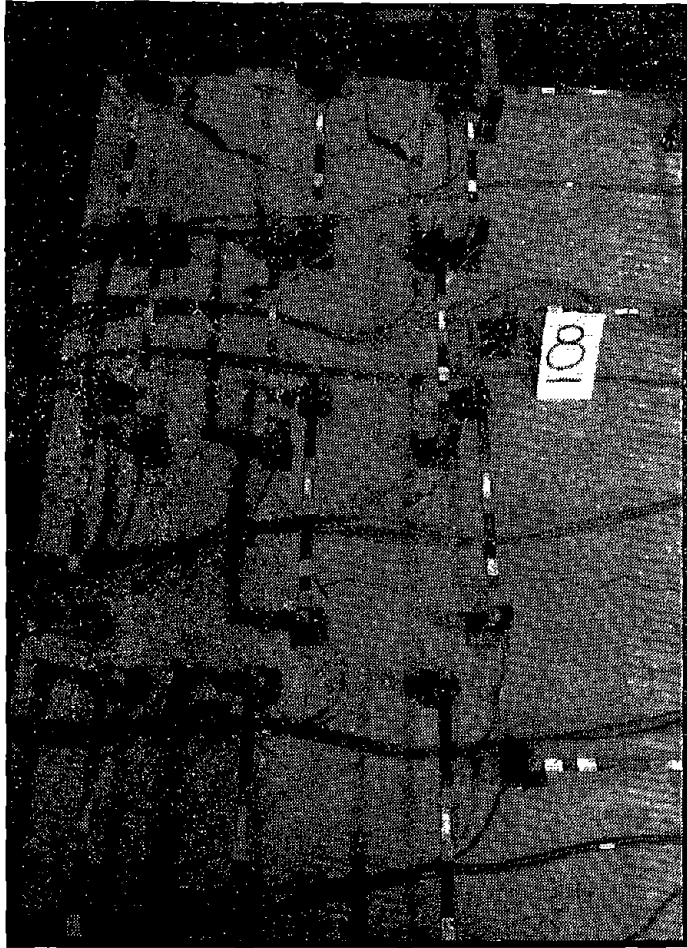
(a) Floor Slab Above the Link
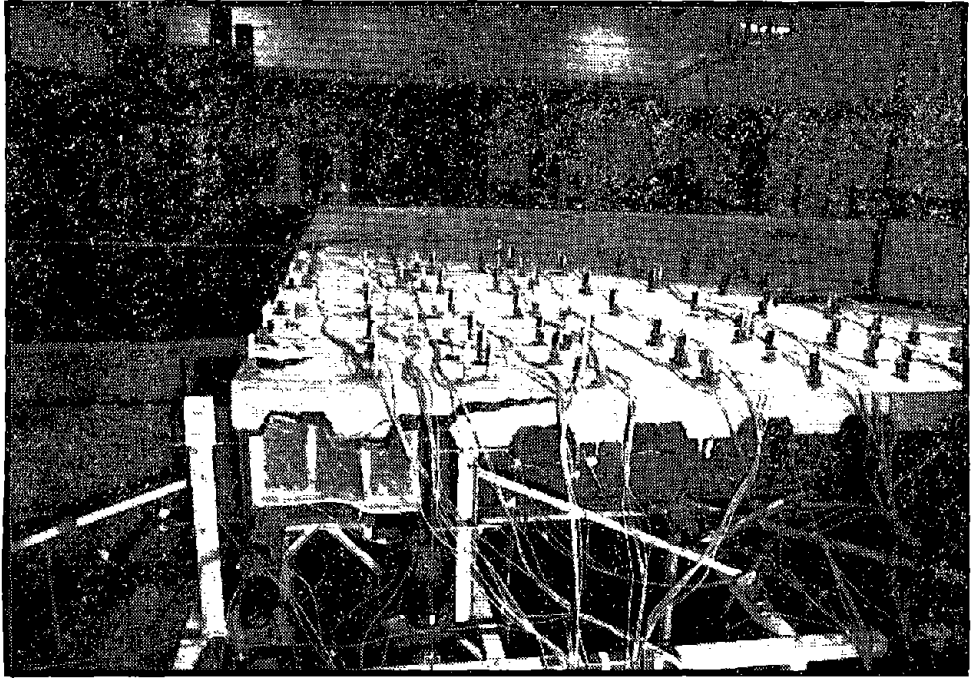


(b) General View of Floor Slab

Fig. 3.37    Photos of Floor Damage After Completion of Test, Specimen C2.

V (KIPS)
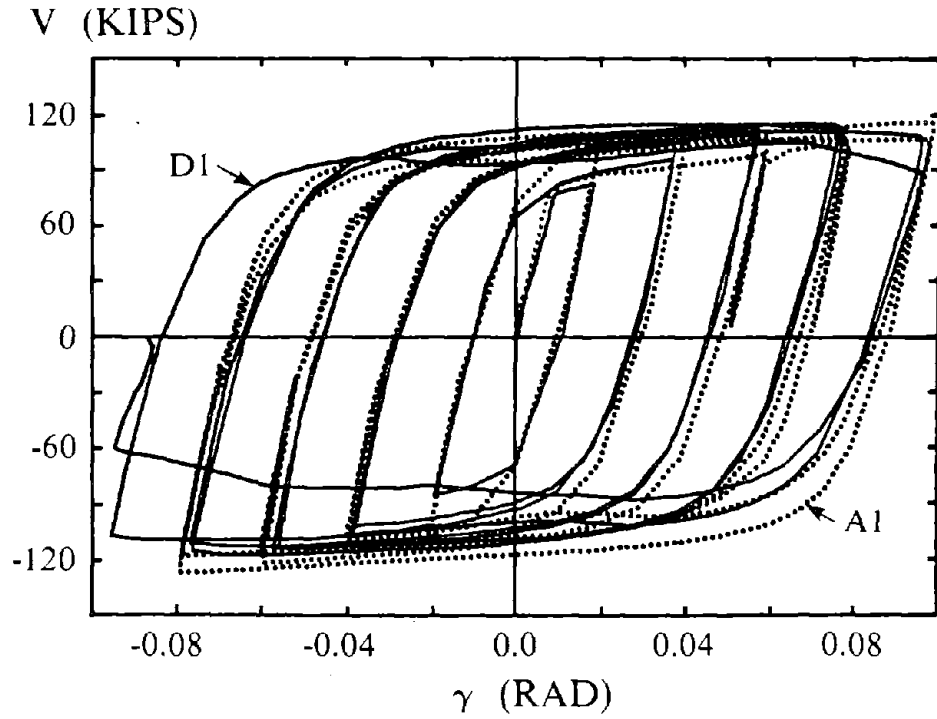


(a) Specimens A1 and D1

V (KIPS)
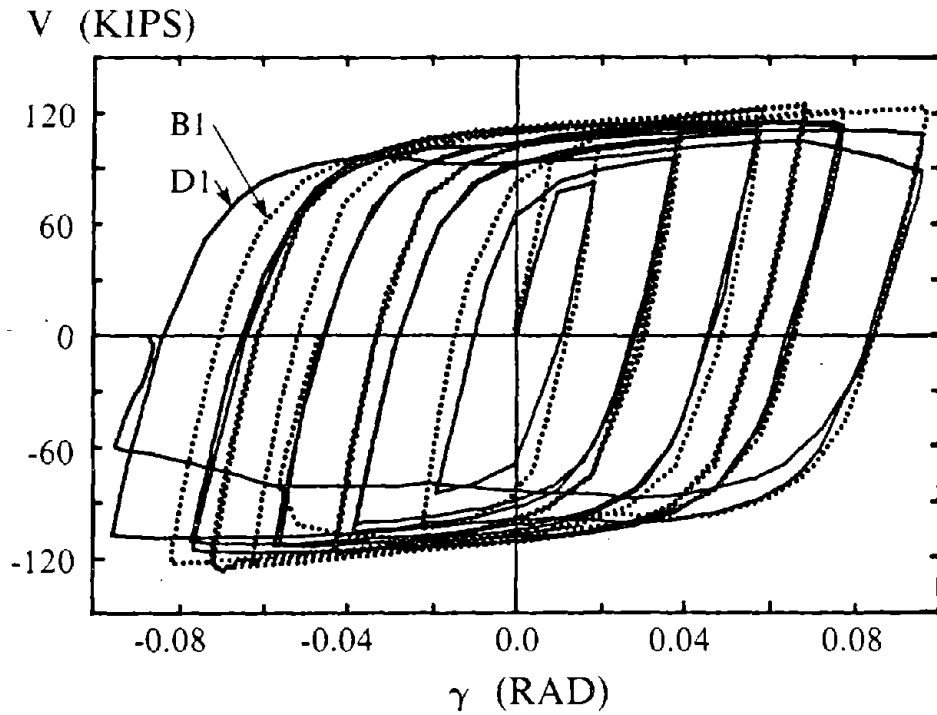


(b) Specimens B1 and D1

Fig. 4.1    Shear-Deformation Relationship, Comparing Composite Links and Bare Steel
Link (Specimen D1) of K-Braced EBF Subassembly.
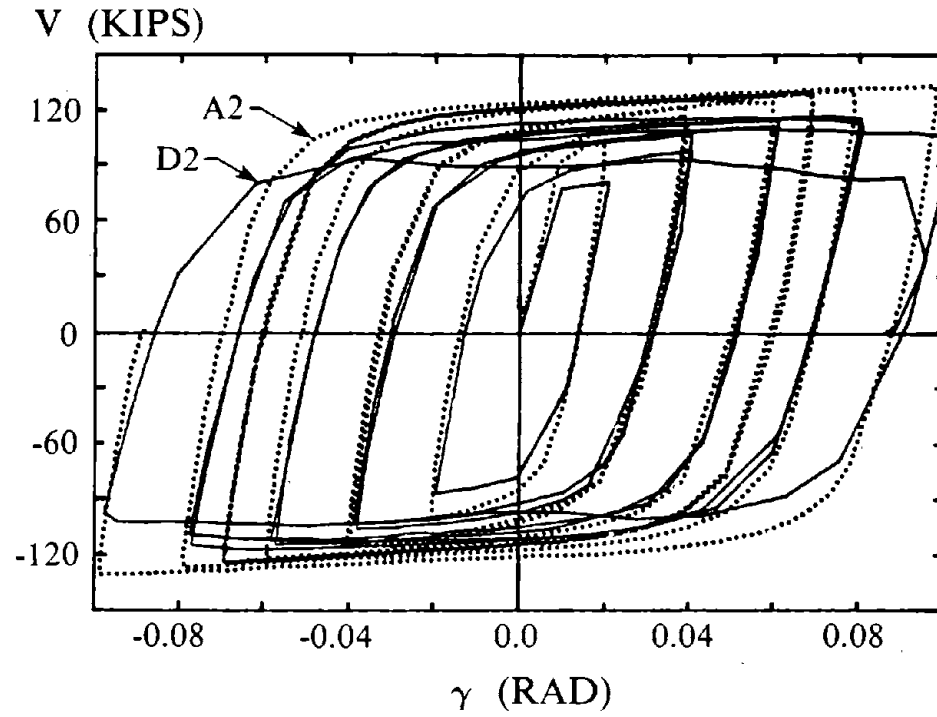
(a) Specimens A2 and D2
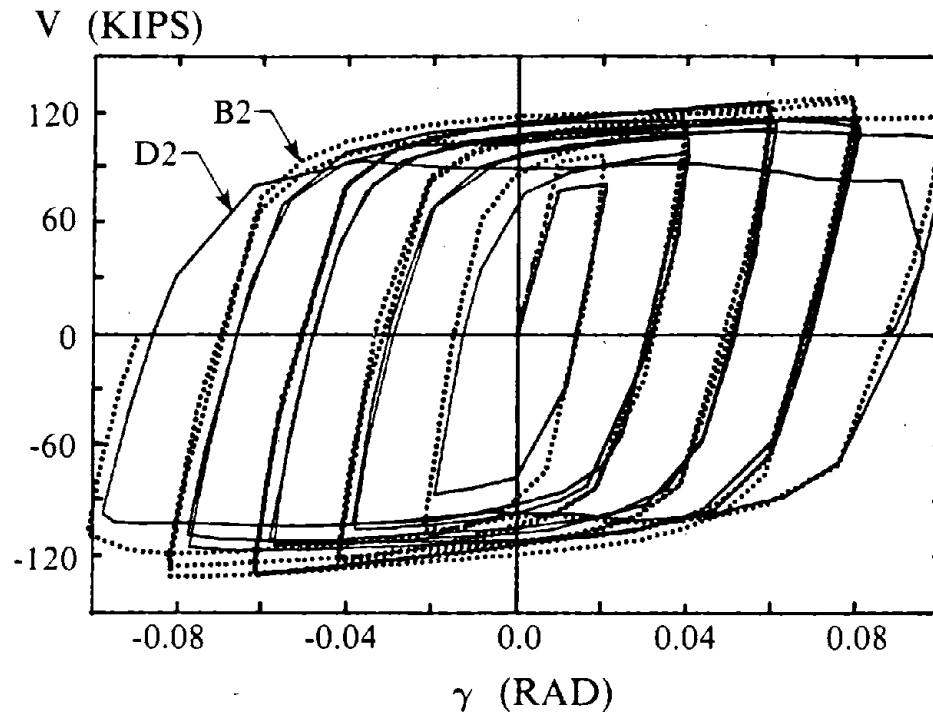


(b) Specimens B2 and D2

Fig. 4.2    Shear-Deformation Relationship, Comparing Composite Links and Bare Steel
Link (Specimen D2) of V-Braced EBF Subassembly.

V (KIPS)



Specimens C2 and D2
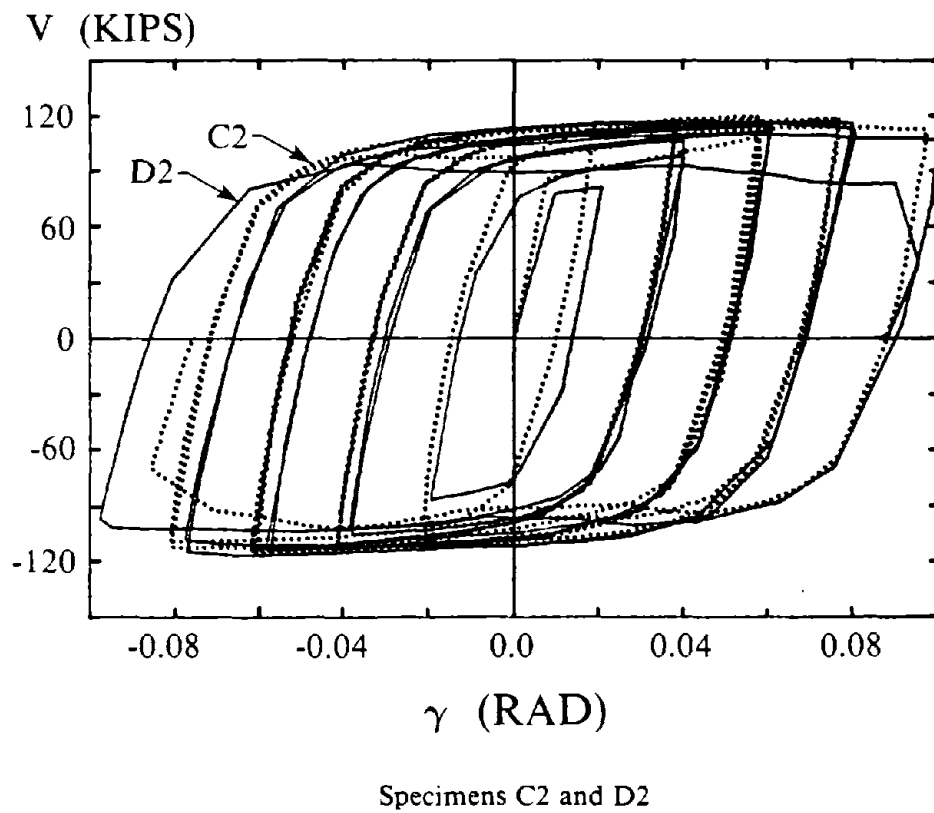
Fig. 4.3    Shear-Deformation Relationship, Comparing Composite Links and Bare Steel
Link (Specimen D2) of V-Braced EBF Subassembly.
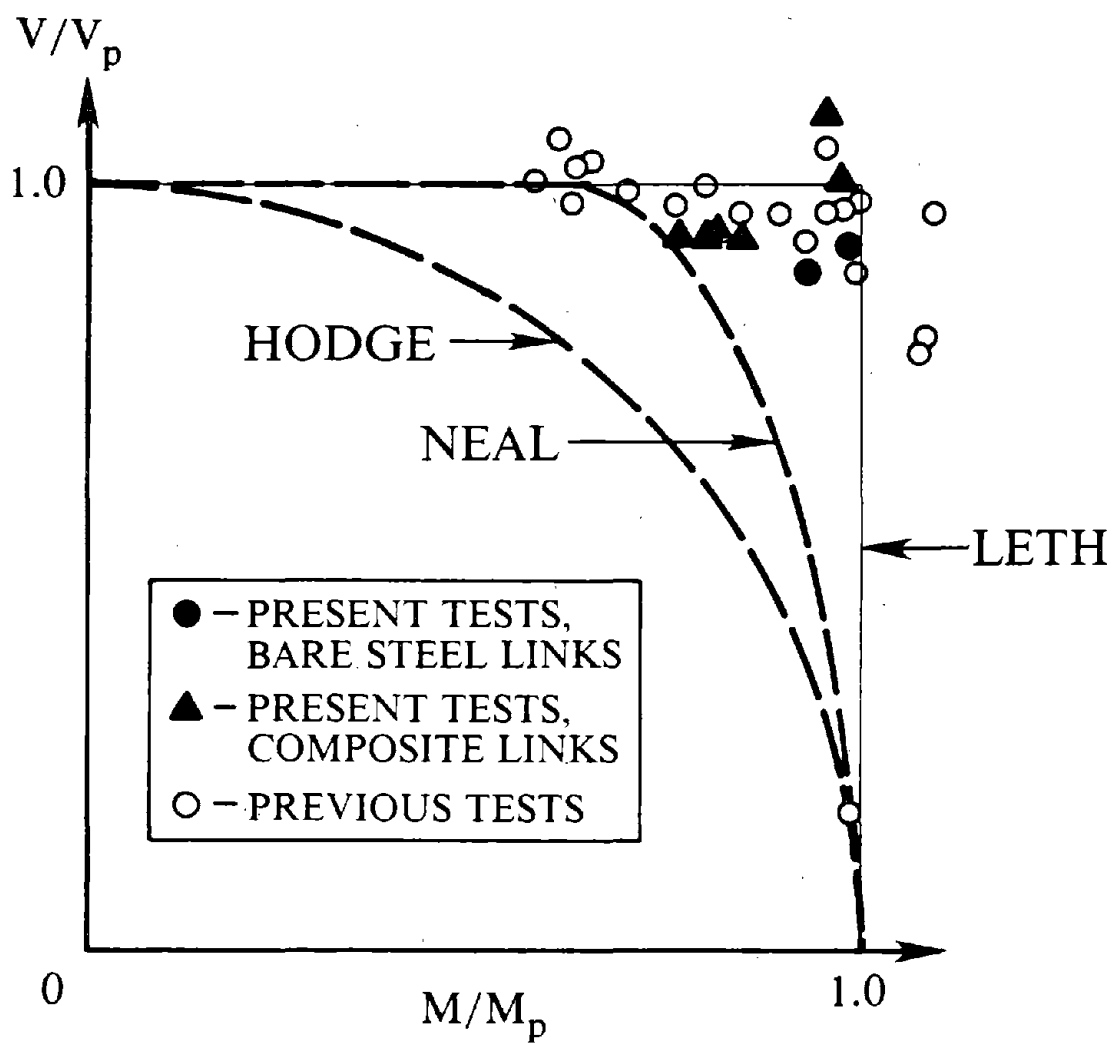
Fig. 4.4    Test Results at First Yield in Normalized Moment-Shear Space.
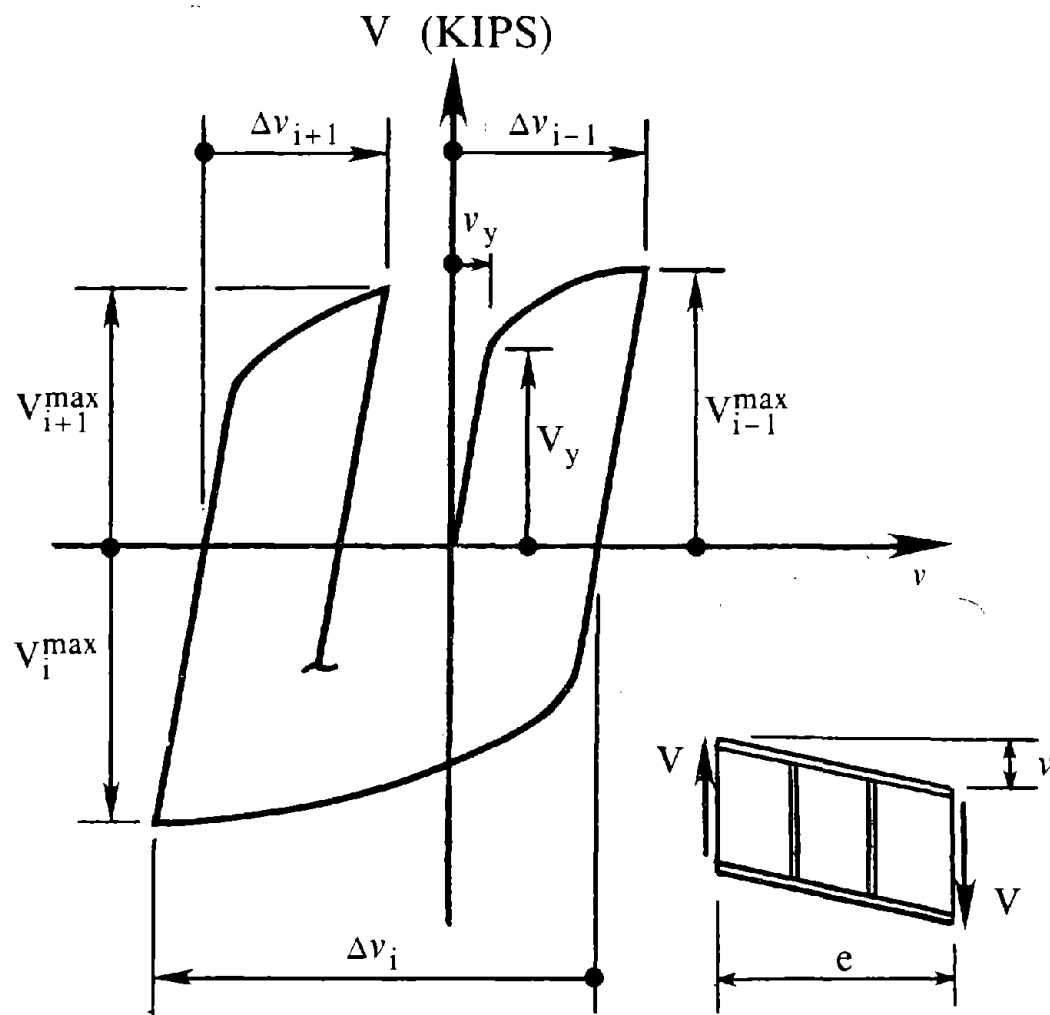
Fig. 4.5    Defining Half Cycle Relative Displacement Between Link Ends,
as Shown for Half Cycles i-1, i, and i+1.

V (KIPS)
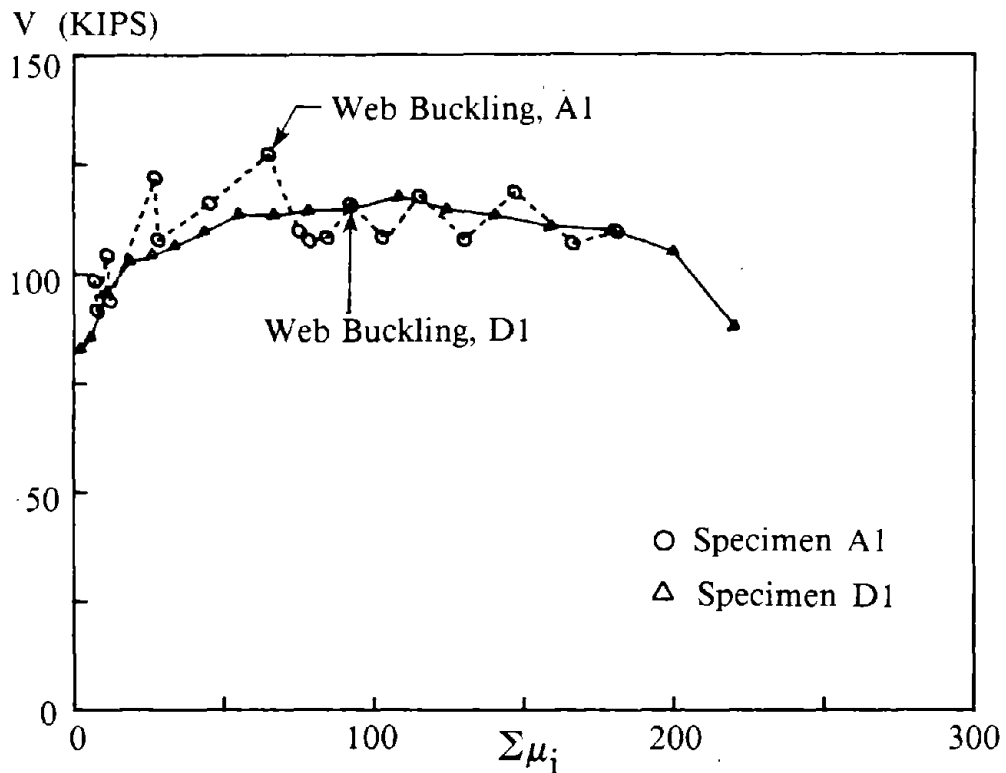


Fig. 4.6    Link Maximum Shear Force-Cumulative Ductility Relationship for
Successive Half Cycles, Specimens A1 and D1.

V (KIPS)



Fig. 4.7    Link Maximum Shear Force-Cumulative Ductility Relationship for
Successive Half Cycles, Specimens B1 and D1.

V (KIPS)

Web Buckling, D1    Web Buckling, C1

O   Specimen C1

△   Specimen D1

$\Sigma \mu_i$

Fig. 4.8    Link Maximum Shear Force-Cumulative Ductility Relationship for
Successive Half Cycles, Specimens C1 and D1.

V (KIPS)

Web Buckling, D2

O   Specimen A2

△   Specimen D2

$\Sigma \mu_i$
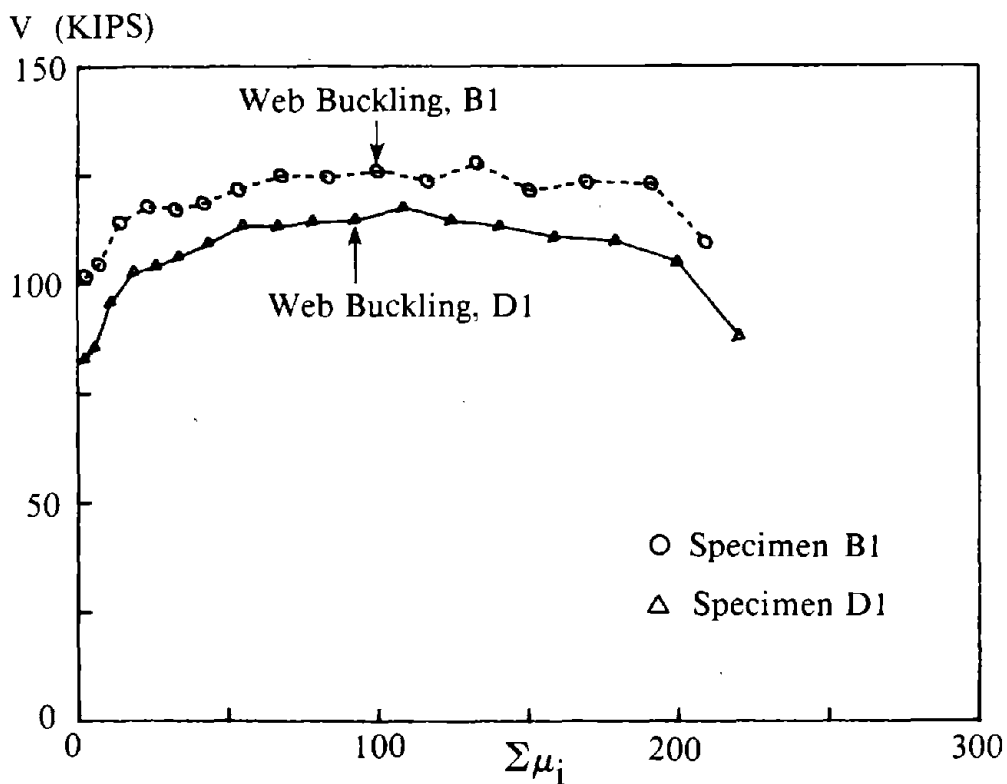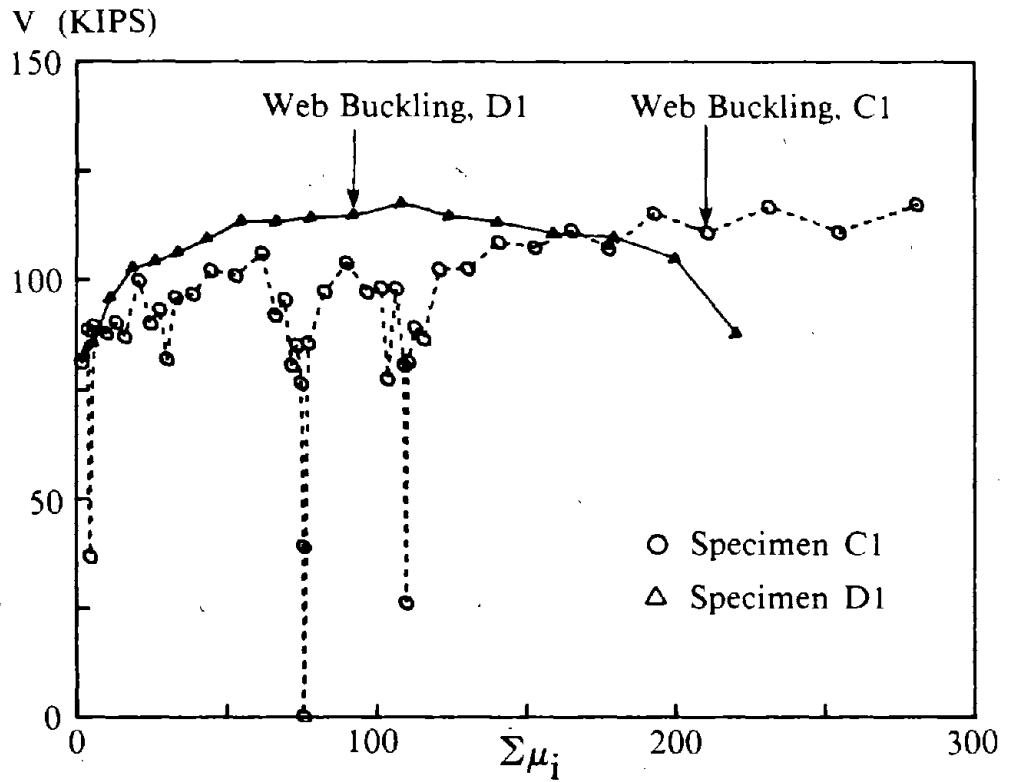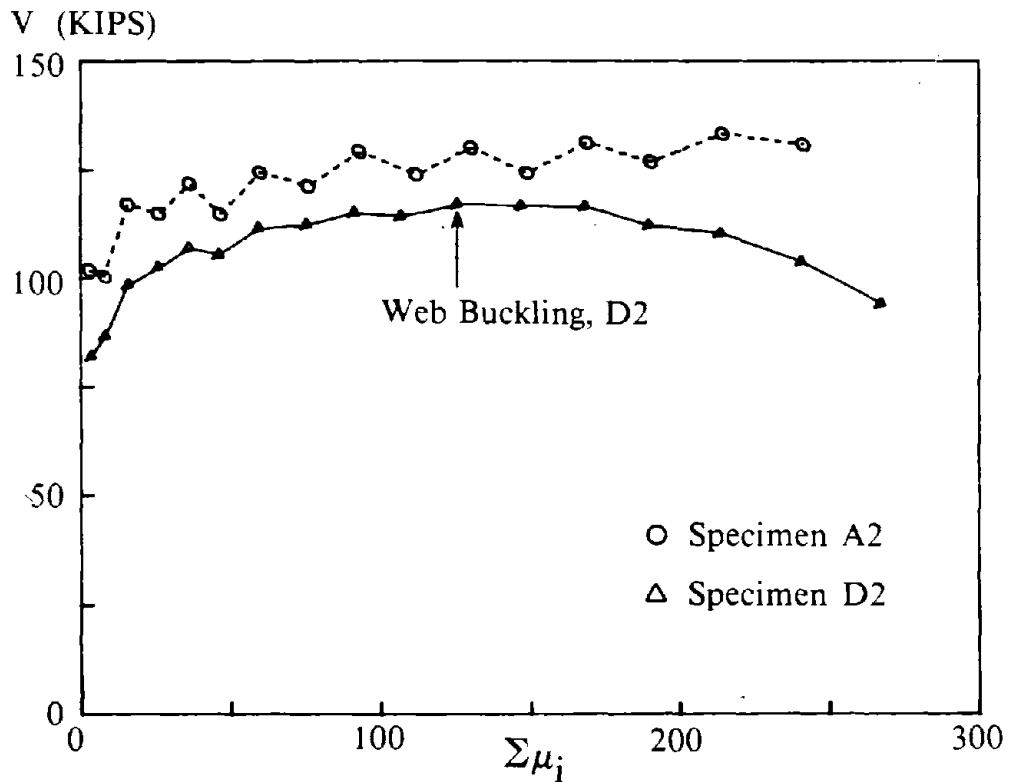
Fig. 4.9    Link Maximum Shear Force-Cumulative Ductility Relationship for
Successive Half Cycles, Specimens A2 and D2.

Fig. 4.10    Link Maximum Shear Force-Cumulative Ductility Relationship for
            Successive Half Cycles, Specimens B2 and D2.
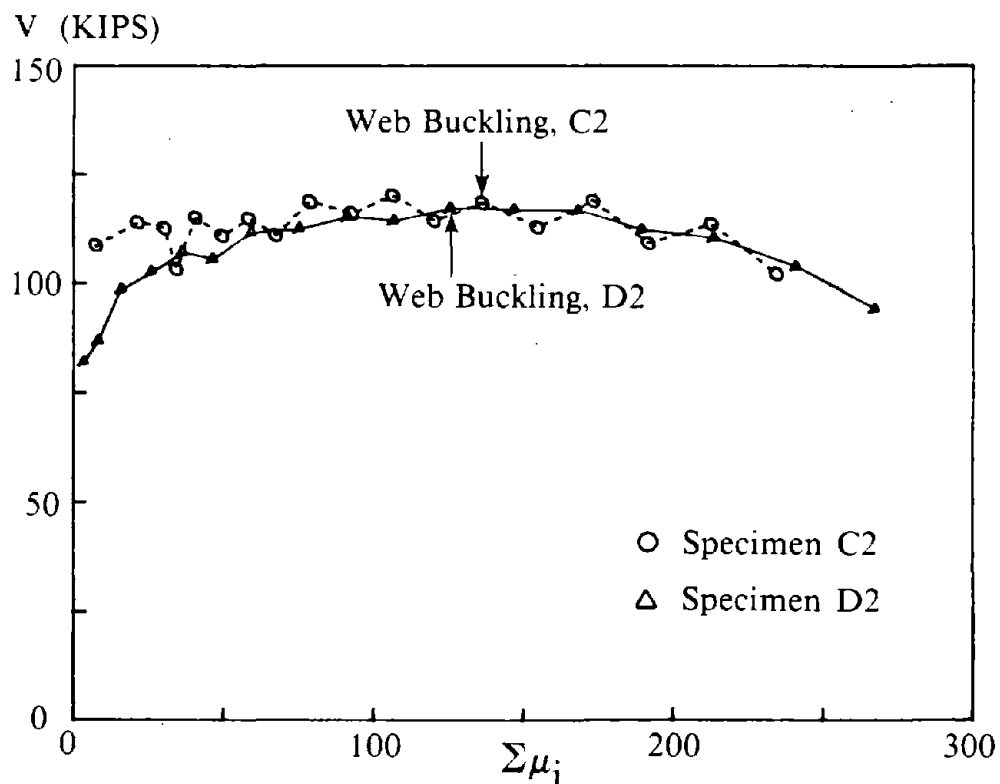


Fig. 4.11    Link Maximum Shear Force-Cumulative Ductility Relationship for
            Successive Half Cycles, Specimens C2 and D2.
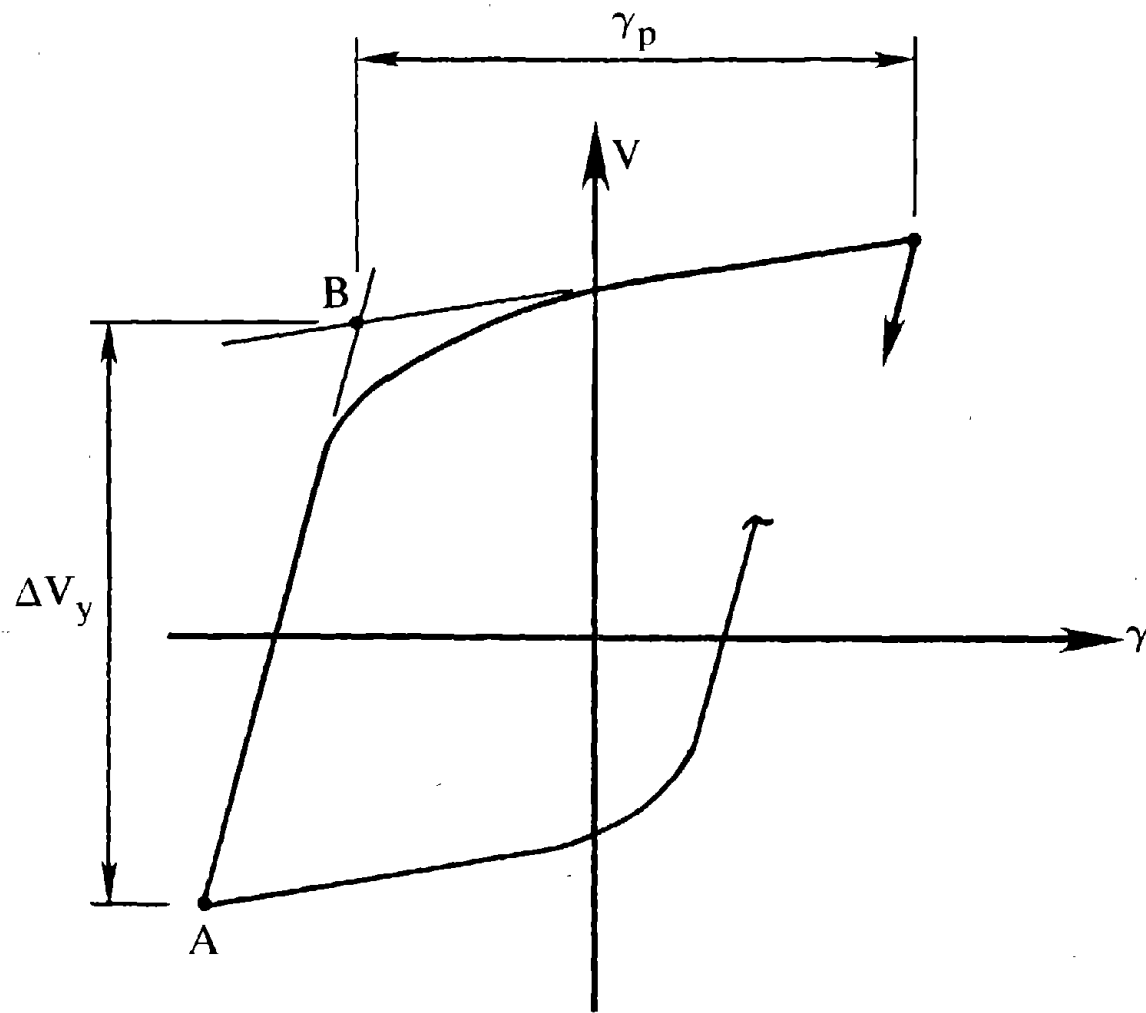
Fig. 4.12     Means of Determining Parameters for Isotropic Shear Hardening.

$$\frac{\Delta V_{yi}}{V_{y0}}$$
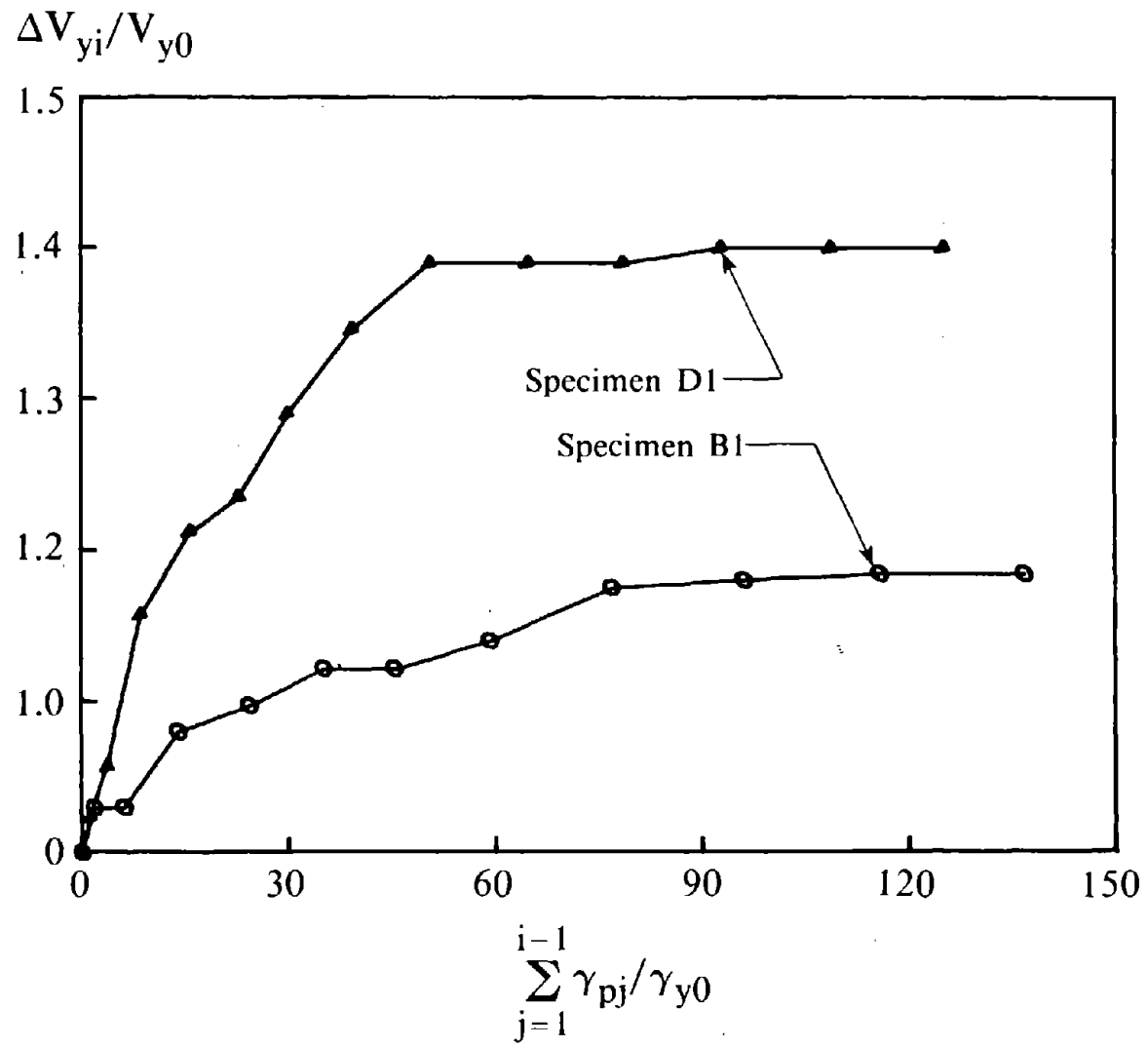
Fig. 4.13    Isotropic Hardening of Cyclic Shear Force in Links, Specimens B1 and D1.

$M_A$ (K-IN)

1000

D1

B1

0

-1000

-0.08   -0.04   0.0   0.04   0.08

$\gamma$ (RAD)
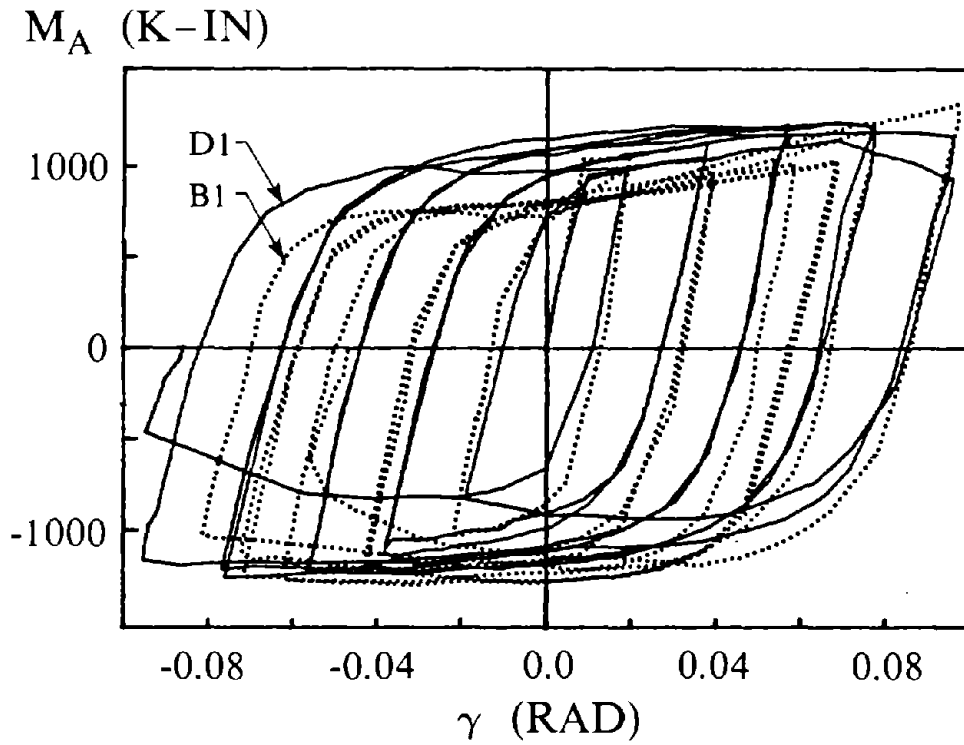
(a)  At Link End A, Specimens B1 and D1

$-M_B$ (K-IN)

1000

D2

B2

0

-1000

-0.08   -0.04   0.0   0.04   0.08

$\gamma$ (RAD)
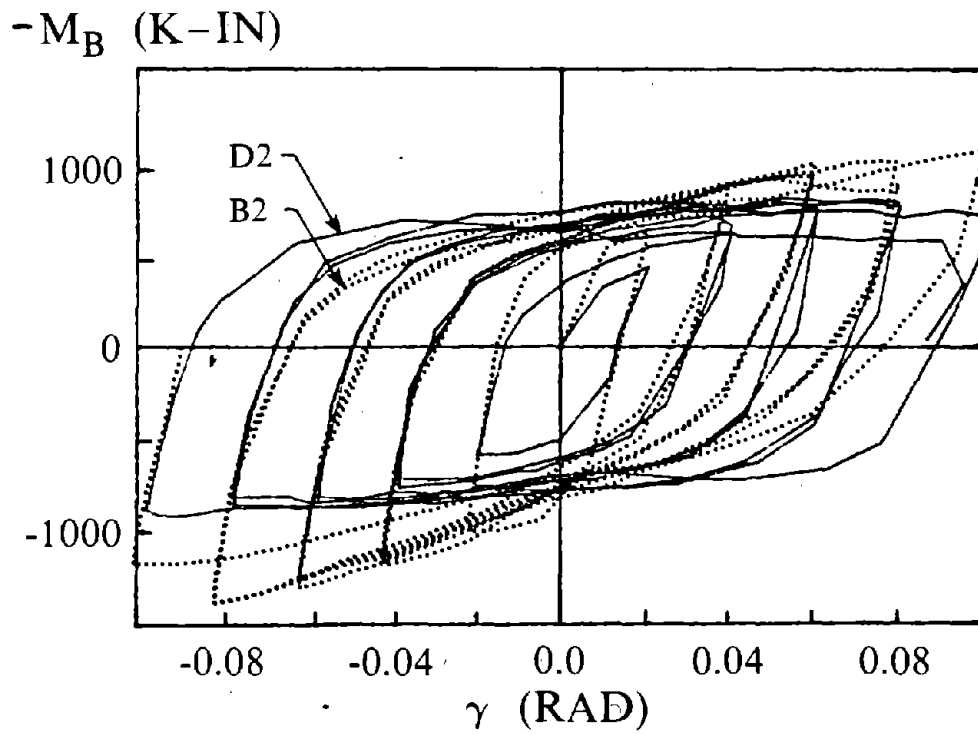
(b)  At Link End B, Specimens B2 and D2

Fig. 4.14   Moment-Deformation Relationship, Comparing Composite and Bare Steel Links.
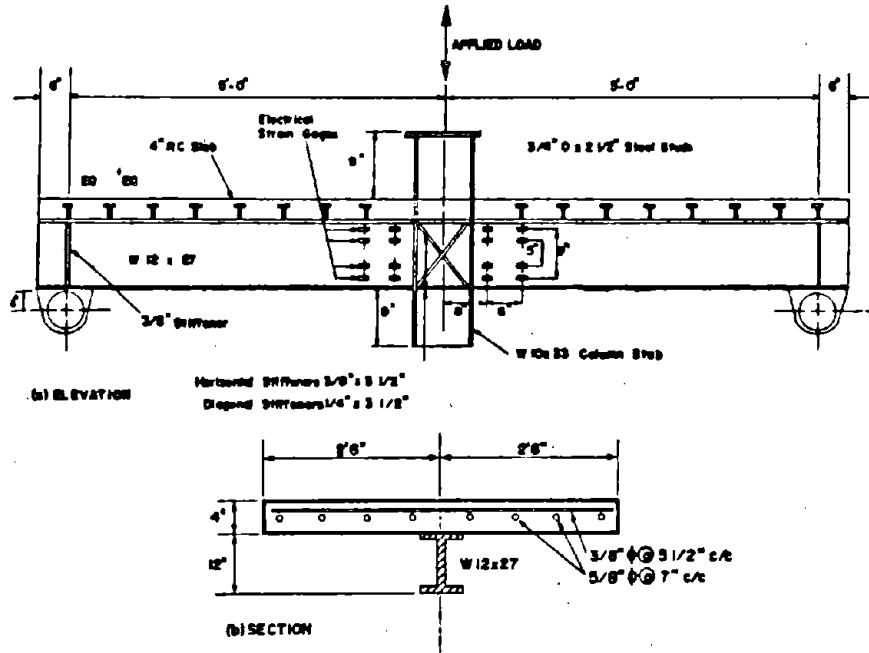
(a) Details of Test Specimen
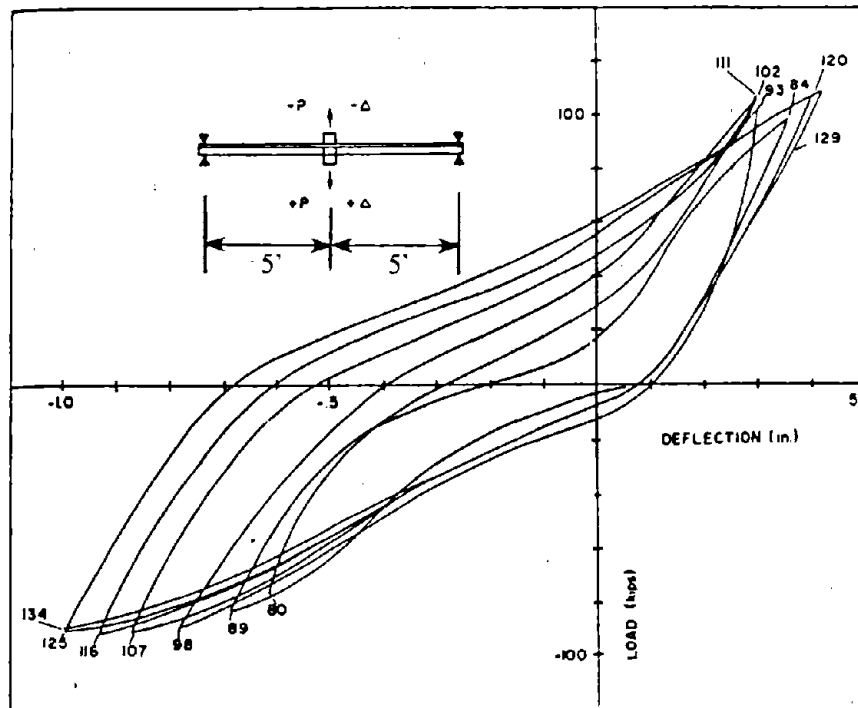
(b) Load-Deflection Hysteretic Behavior

Fig. 4.15    Cyclic Response of a Composite Steel Beam of Longer Length
Indicating Significant Pinching in Hysteresis Loops [22].
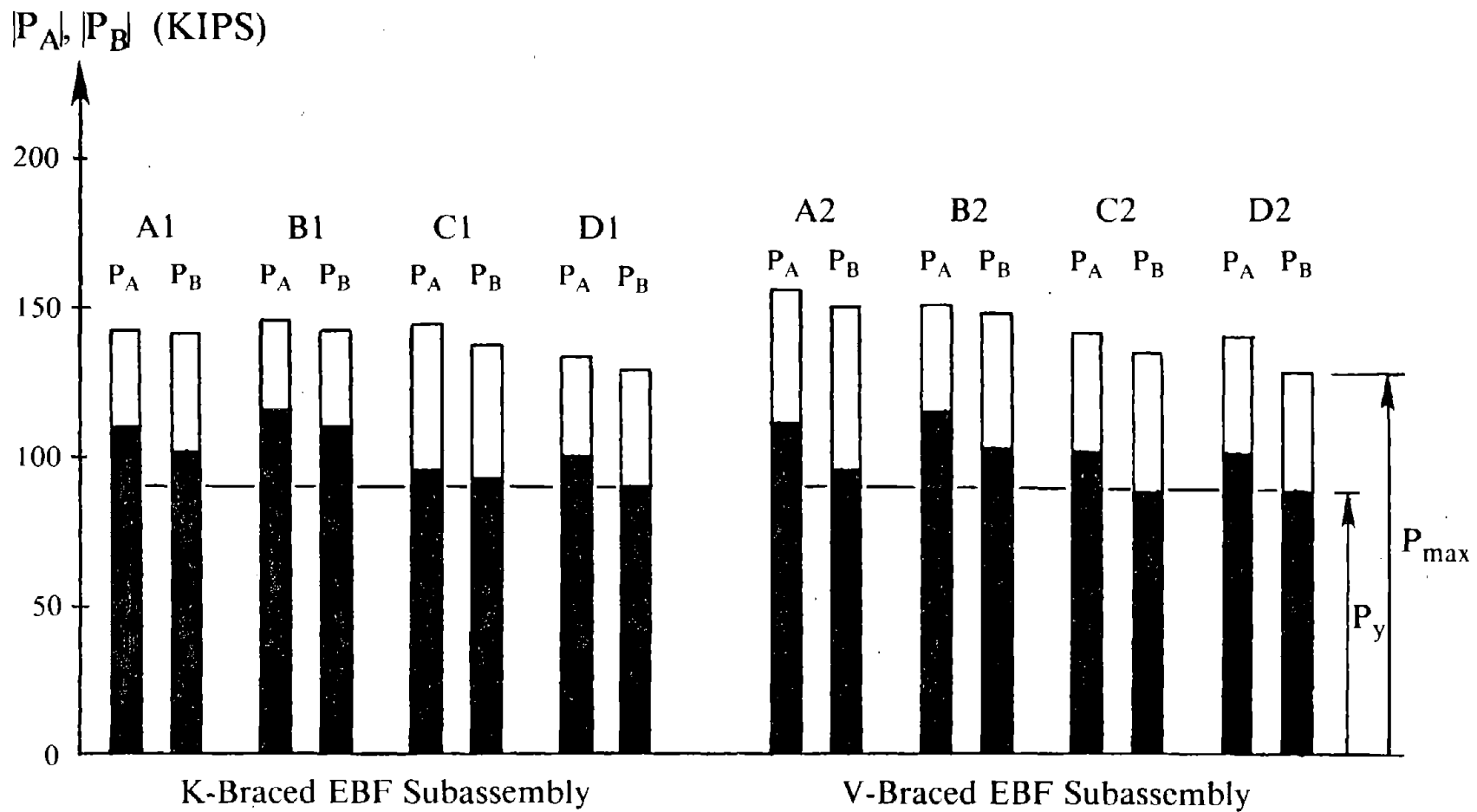
Fig. 4.16    Magnitude of Jack Forces for Specimens at Initial Yield and Ultimate State.
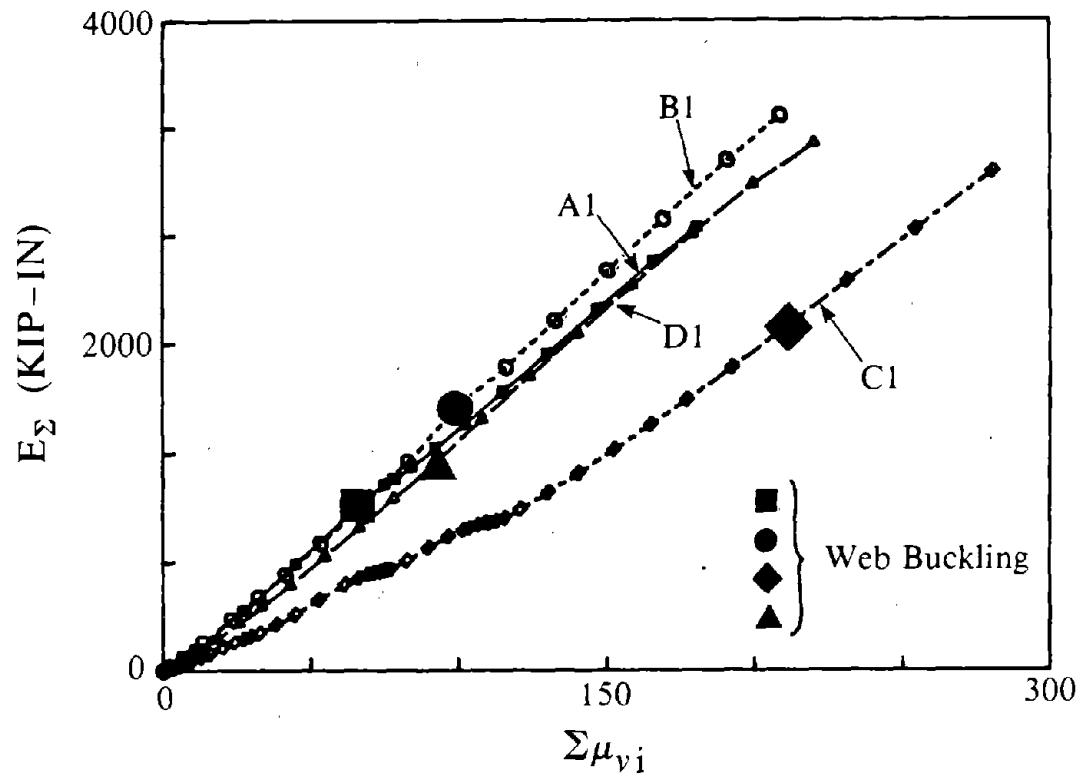
Fig. 4.17    Energy Dissipation of Specimens, K-Braced EBF Subassembly.
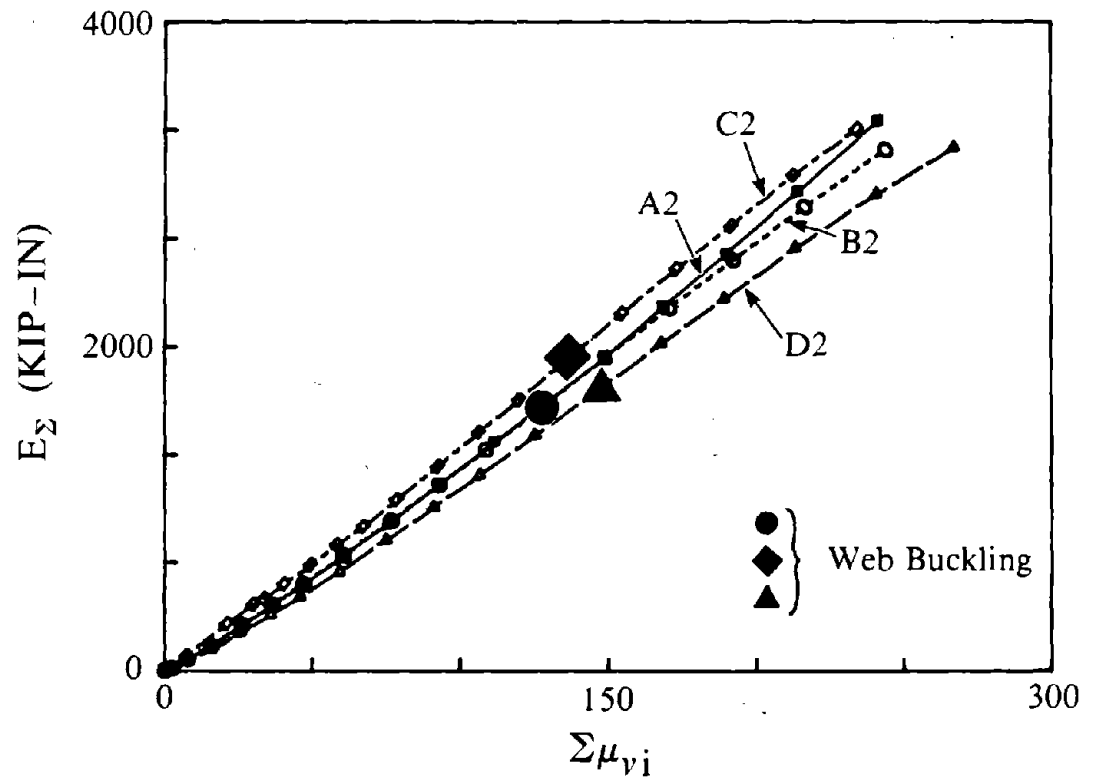


Fig. 4.18    Energy Dissipation of Specimens, V-Braced EBF Subassembly.
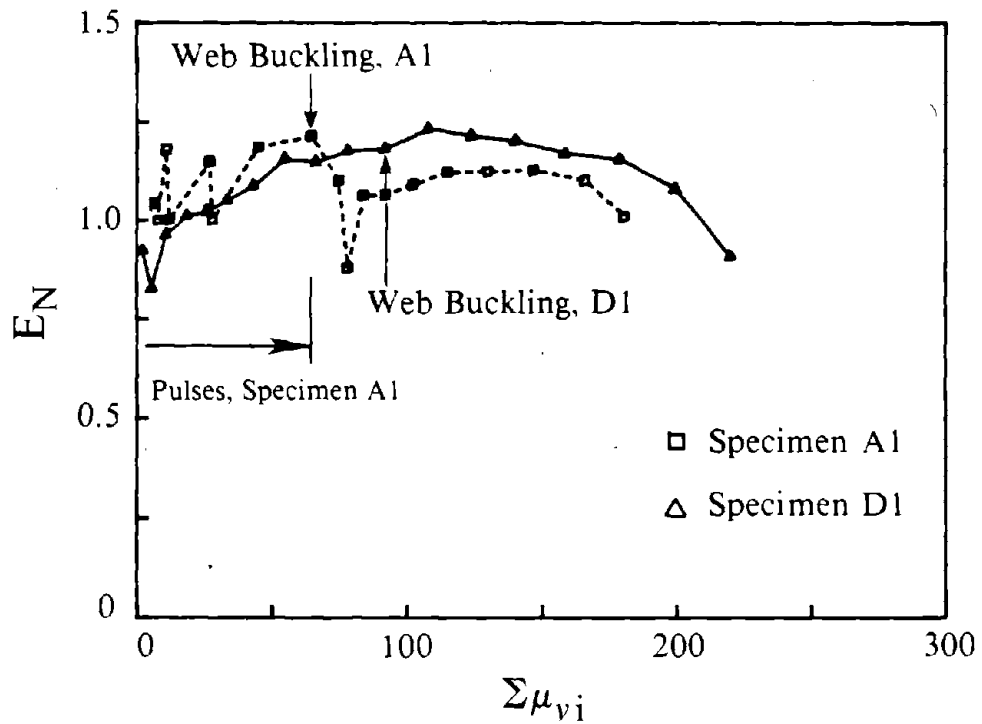
Fig. 4.19      Normalized Dissipated Energy-Cumulative Link Ductility Relationship for Successive Half Cycles, Specimens A1 and D1.
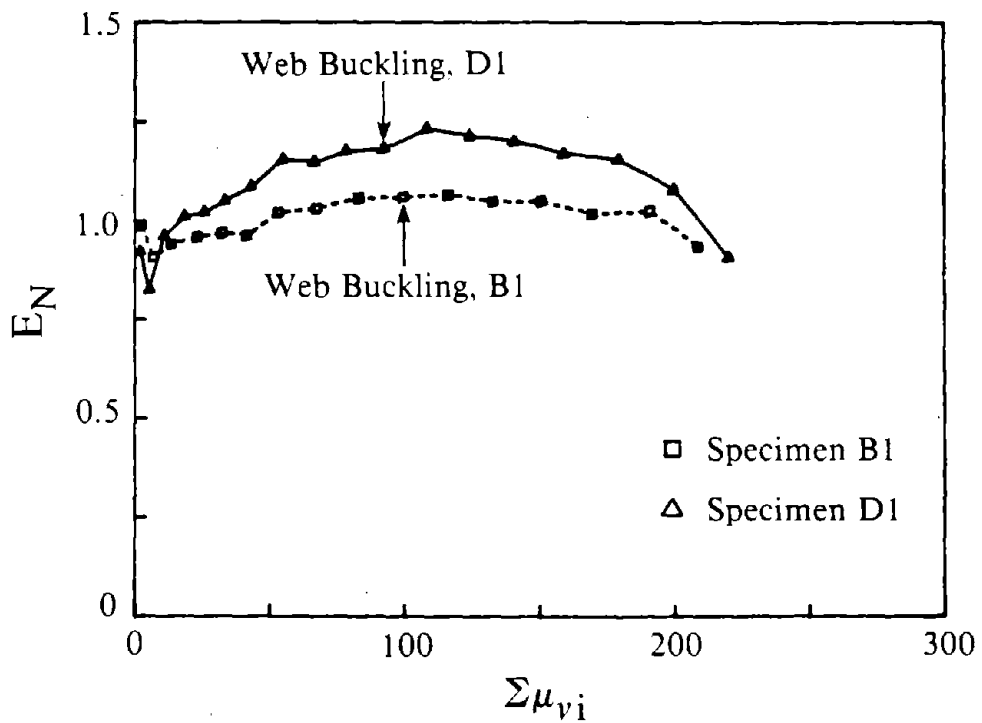


Fig. 4.20      Normalized Dissipated Energy-Cumulative Link Ductility Relationship for Successive Half Cycles, Specimens B1 and D1.
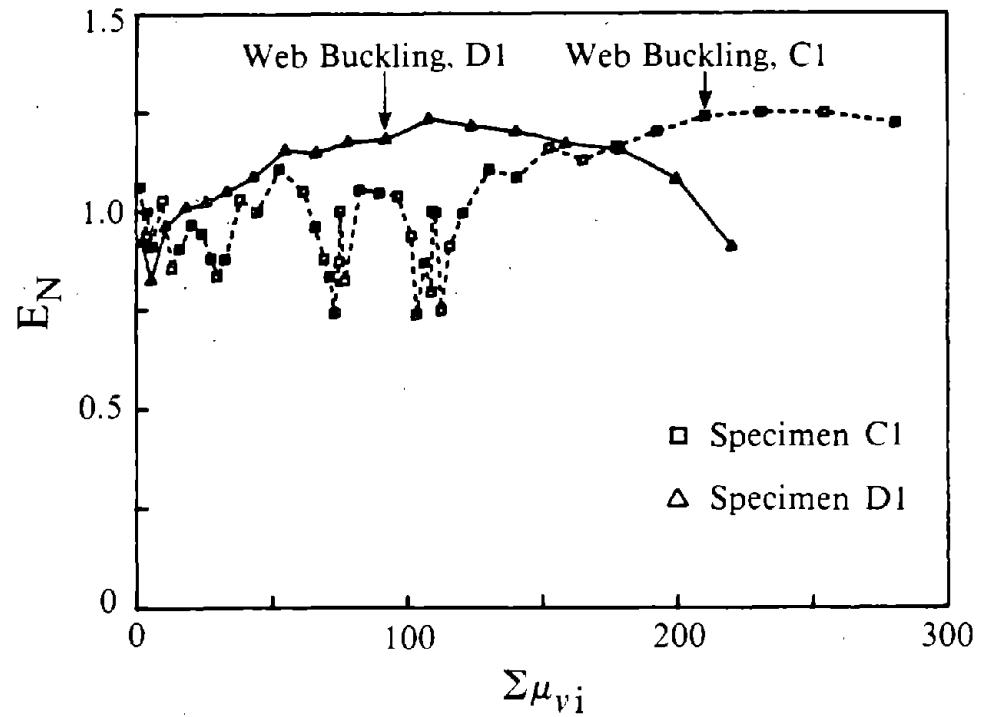
Fig. 4.21    Normalized Dissipated Energy-Cumulative Link Ductility Relationship for Successive Half Cycles, Specimens C1 and D1.
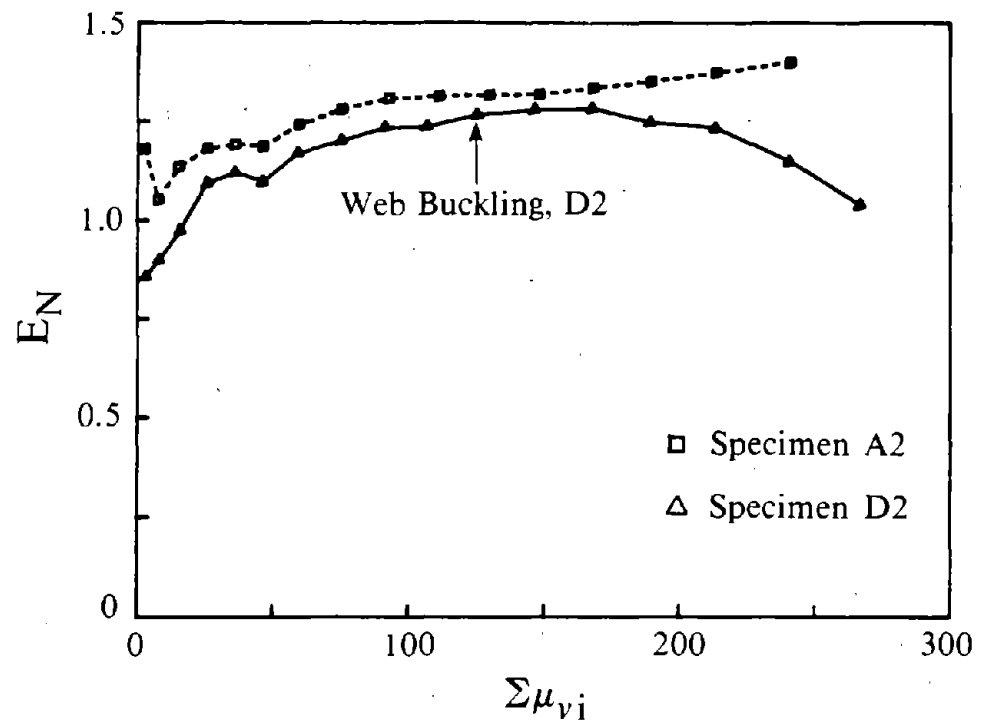


Fig. 4.22 .   Normalized Dissipated Energy-Cumulative Link Ductility Relationship for Successive Half Cycles, Specimens A2 and D2.
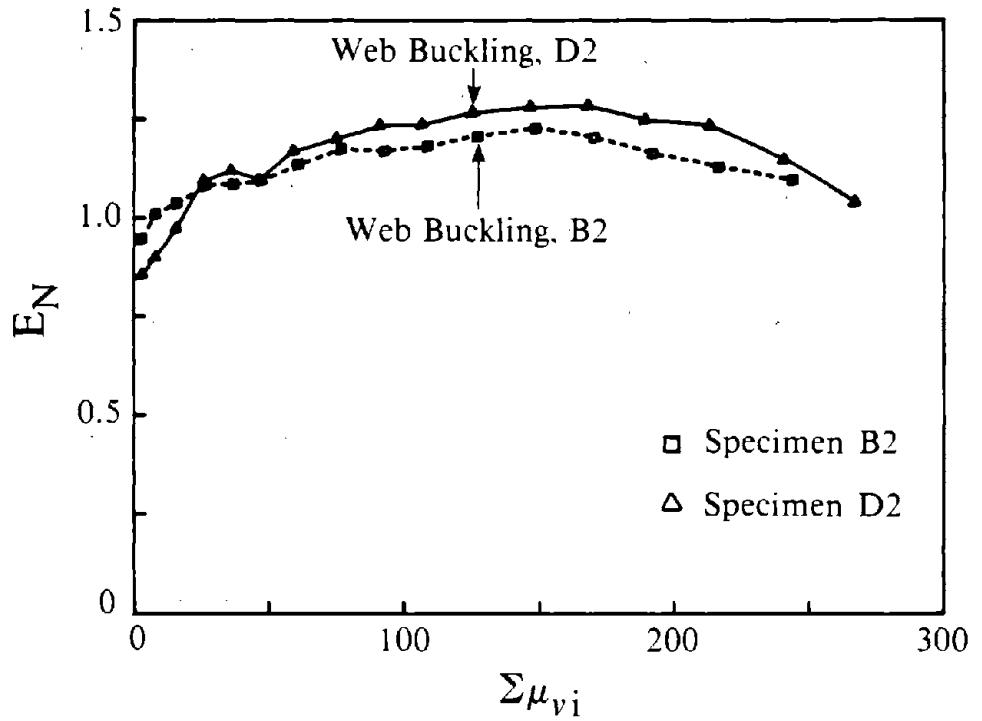
Fig. 4.23    Normalized Dissipated Energy-Cumulative Link Ductility Relationship
for Successive Half Cycles, Specimens B2 and D2.
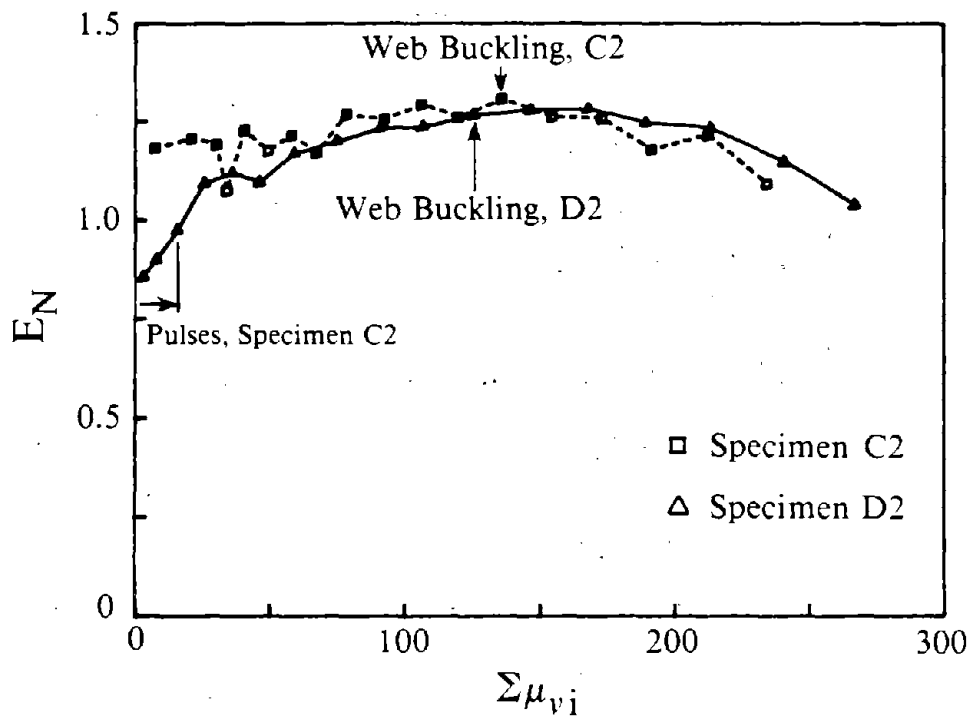


Fig. 4.24    Normalized Dissipated Energy-Cumulative Link Ductility Relationship
for Successive Half Cycles, Specimens C2 and D2.
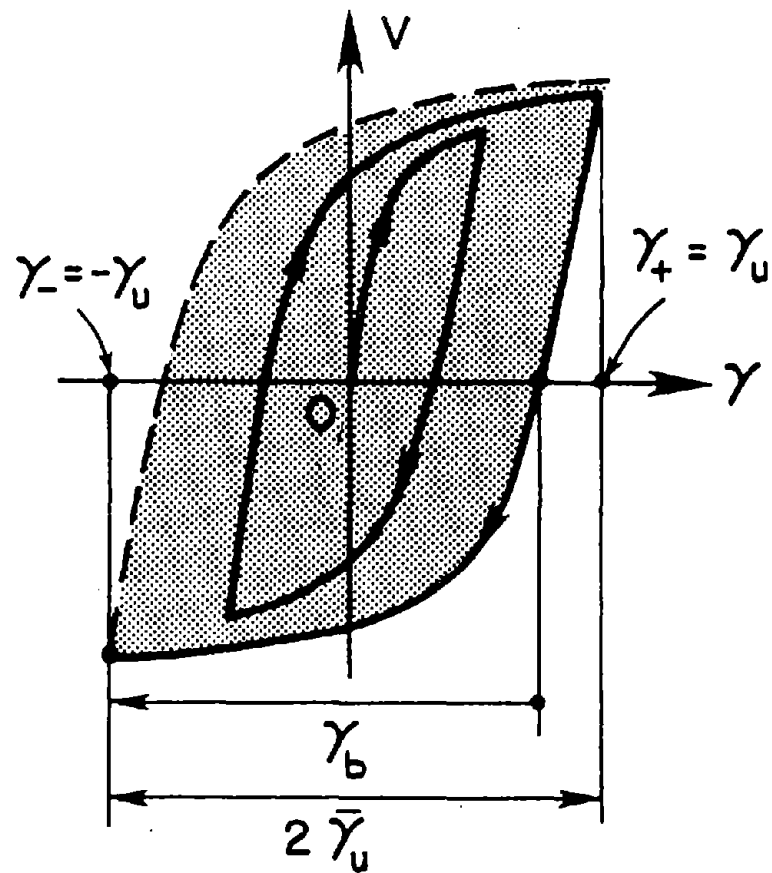
Fig. 4.25    Defining Maximum Link Deformation $\gamma_u$ [7].
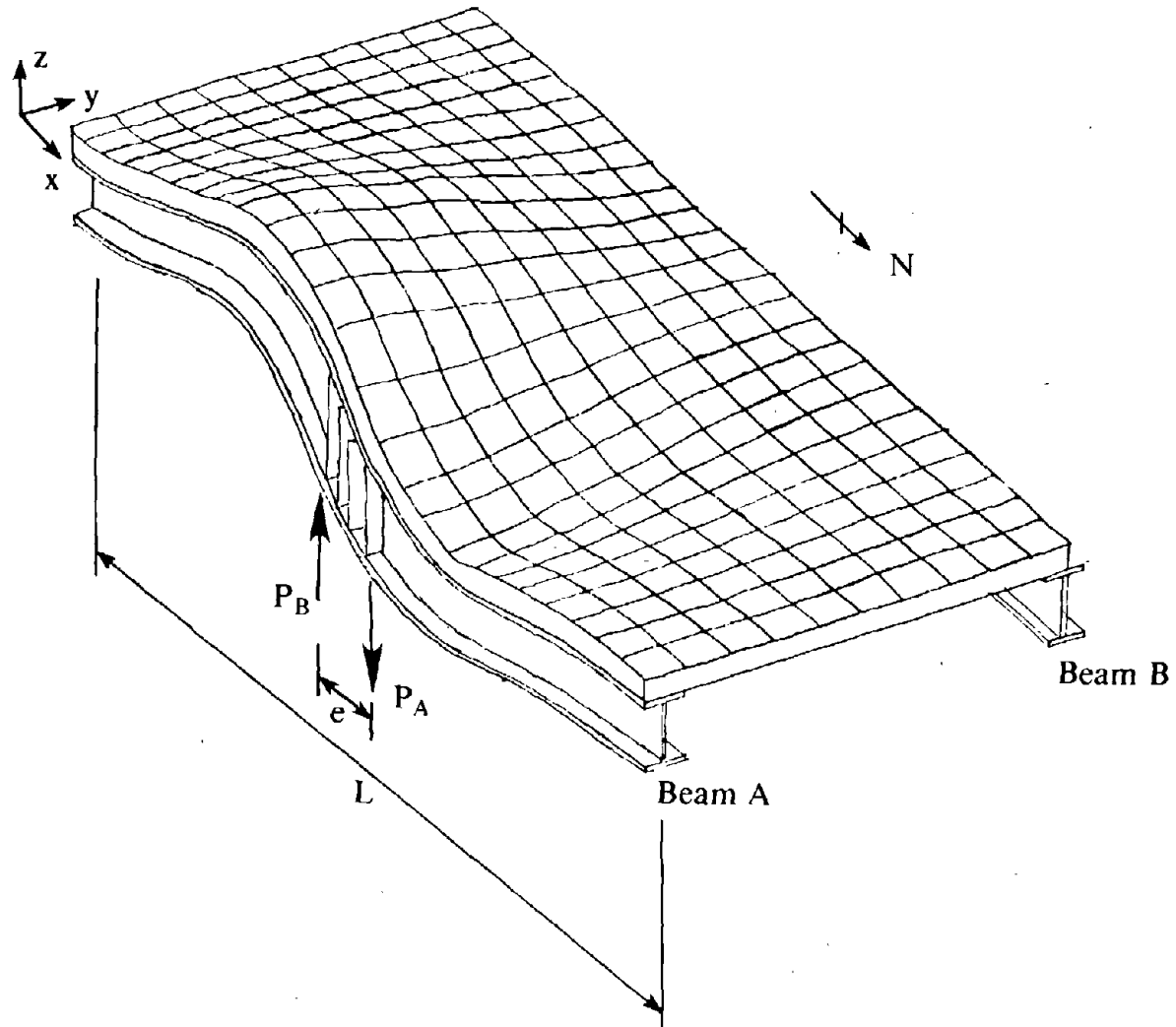
Fig. 4.26     Exaggerated Displaced Shape of Floor Slab During Cycle 1 at $\gamma = 0.01$ rad., Specimen A1.
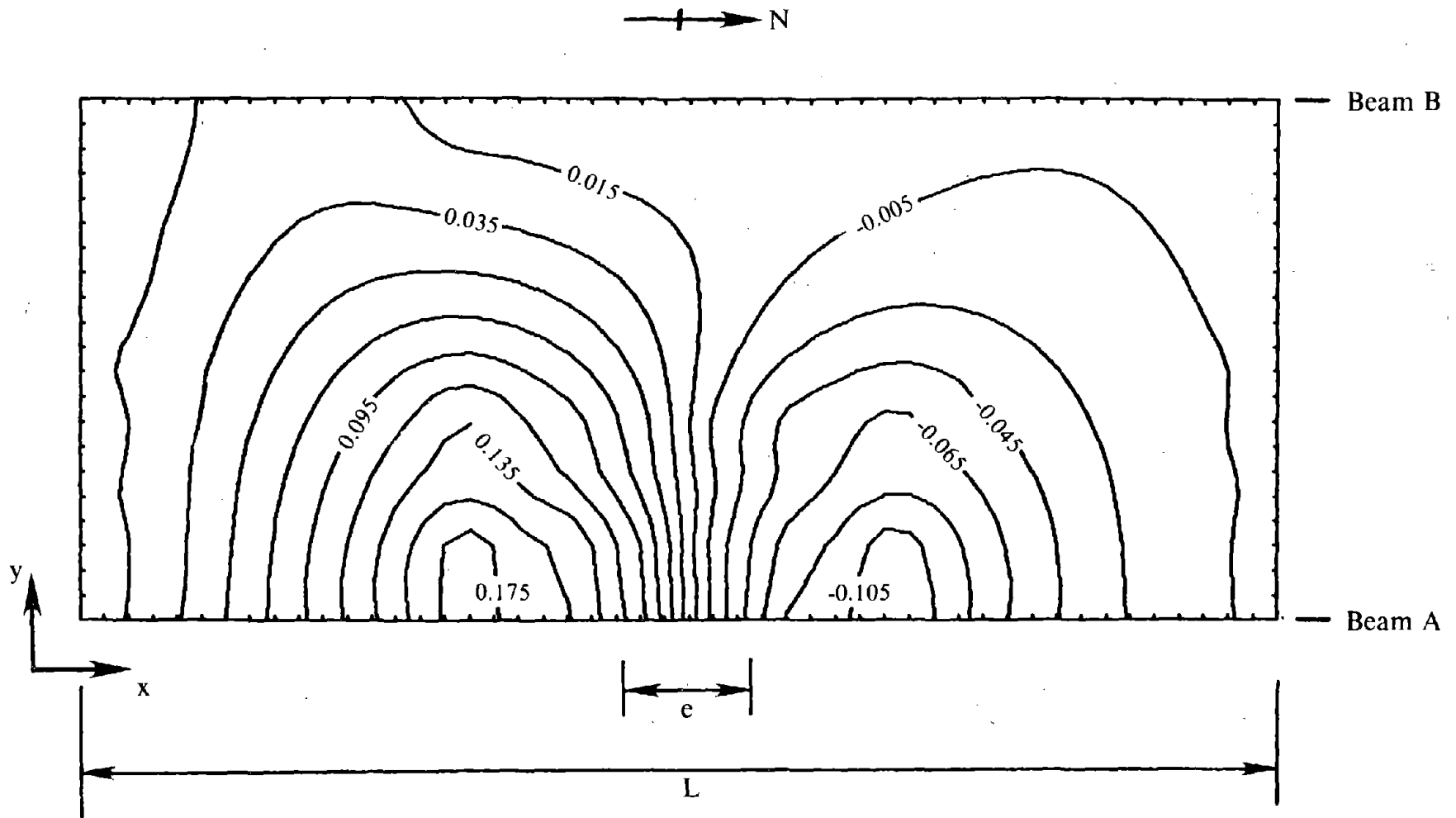
Fig. 4.27    Vertical Displacement Contours for Floor Slab During Cycle 1 at $\gamma = 0.01$ rad, Specimen A1.
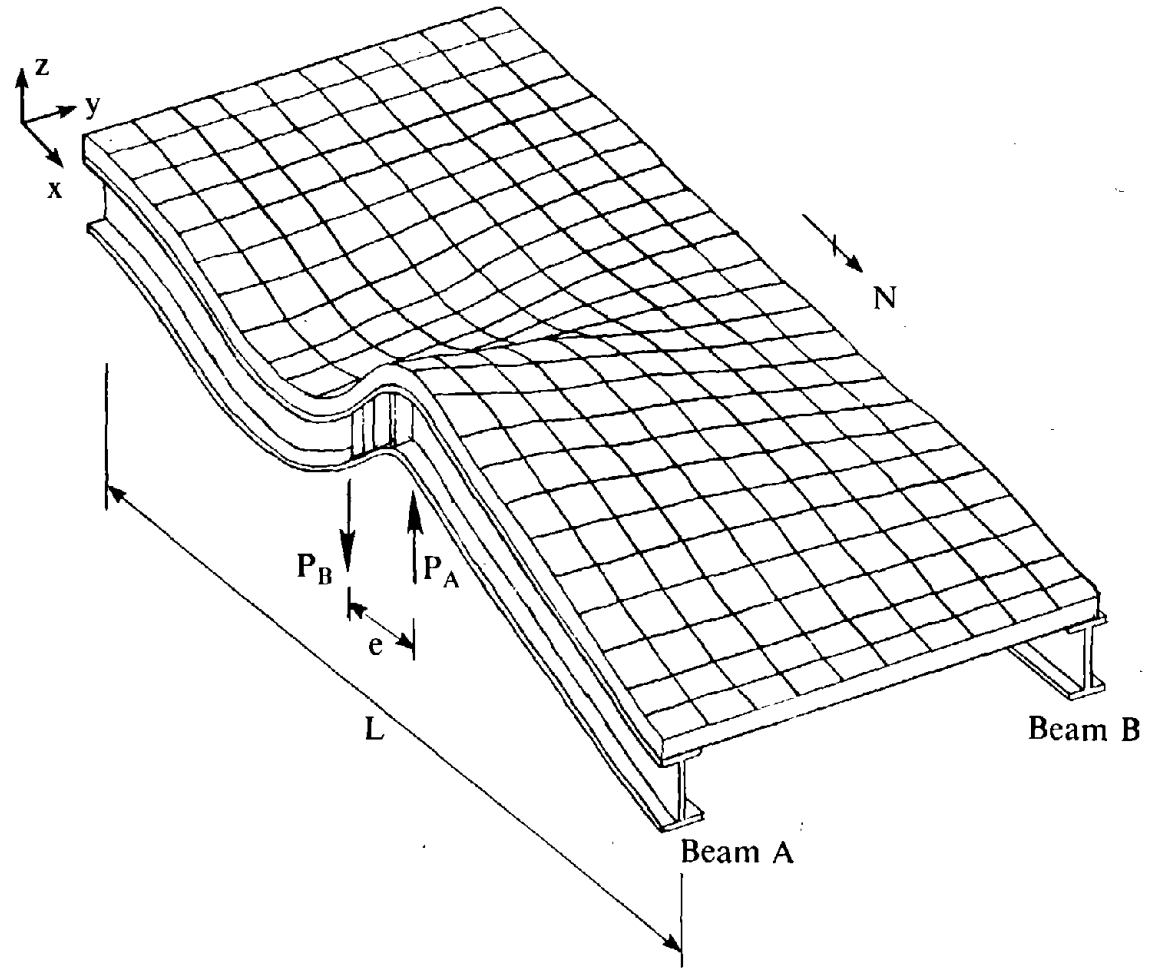
Fig. 4.28    Exaggerated Displaced Shape of Floor Slab During Cycle 5 at $\gamma$ = -0.06 rad., Specimen A1.
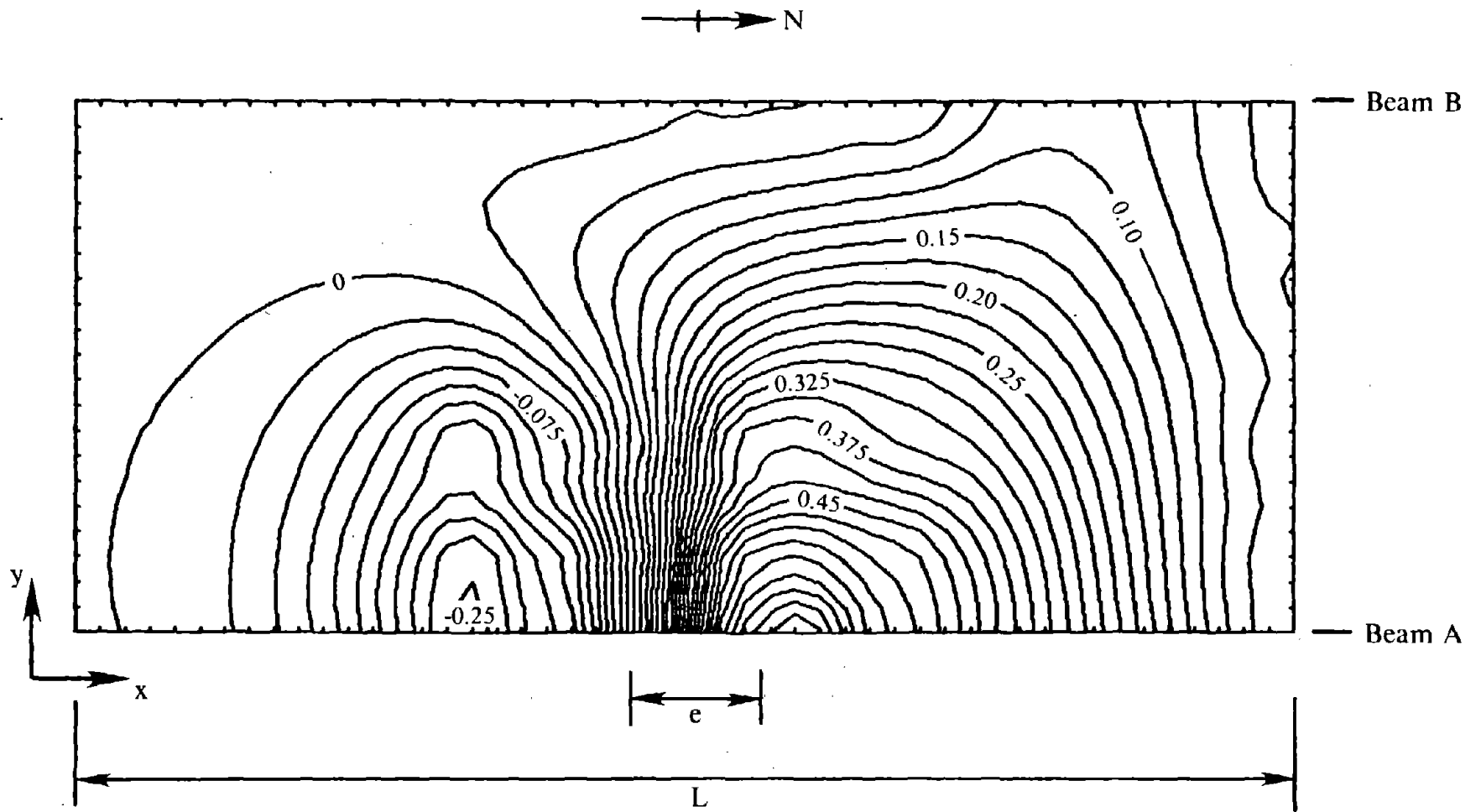
Fig. 4.29    Vertical Displacement Contours for Floor Slab During Cycle 5 at $\gamma$ = -0.06 rad, Specimen A1.

(a) Shear Tabs

(b) Supports for Pinned Columns
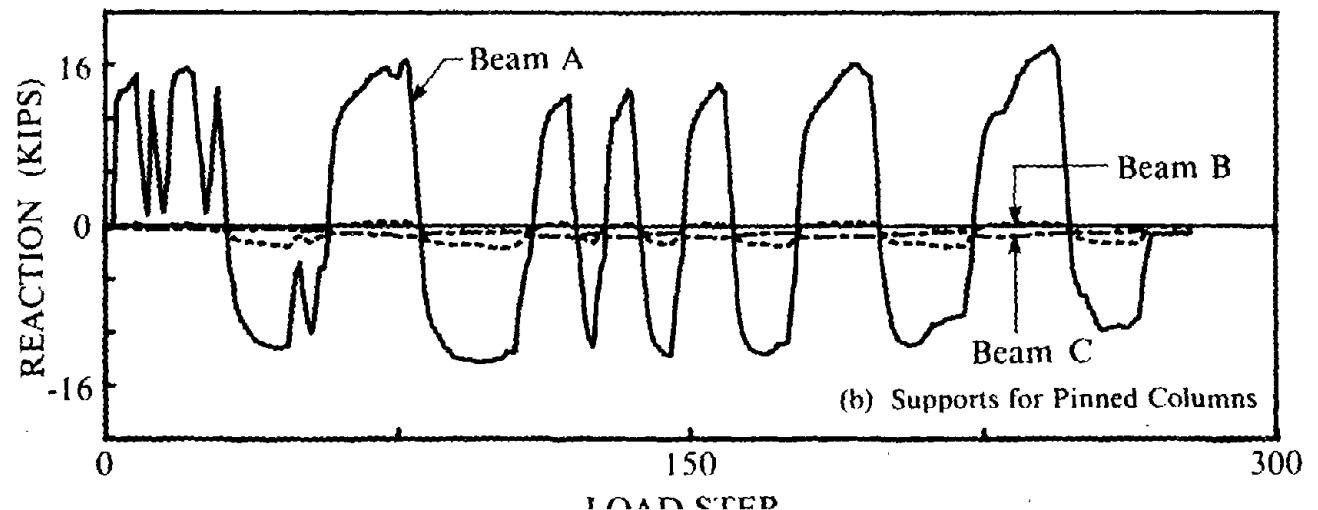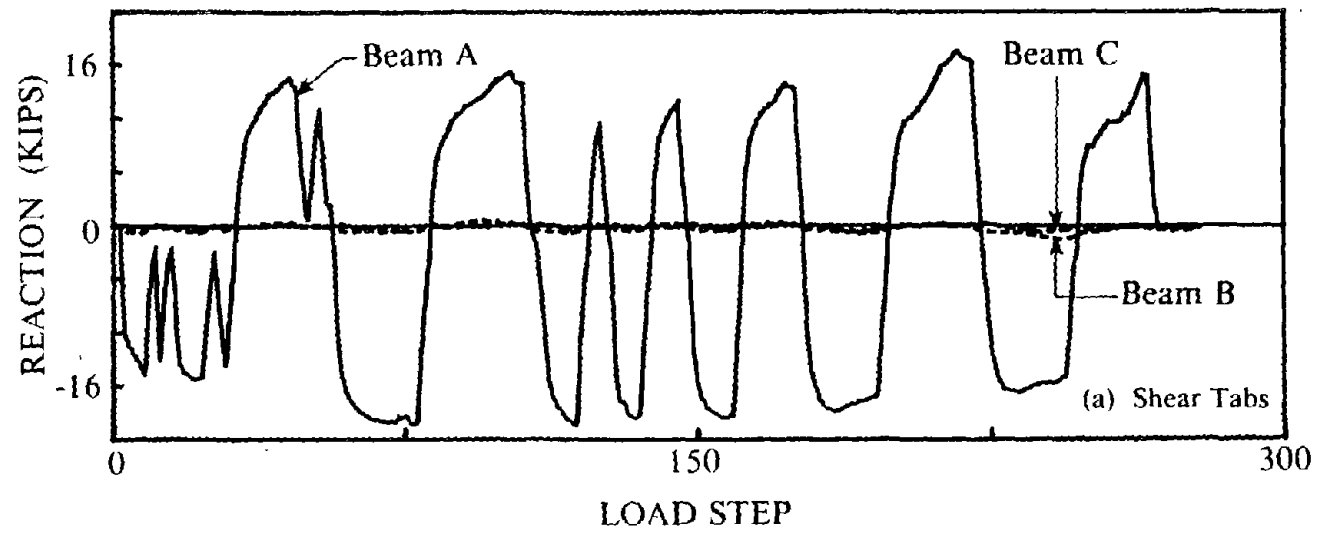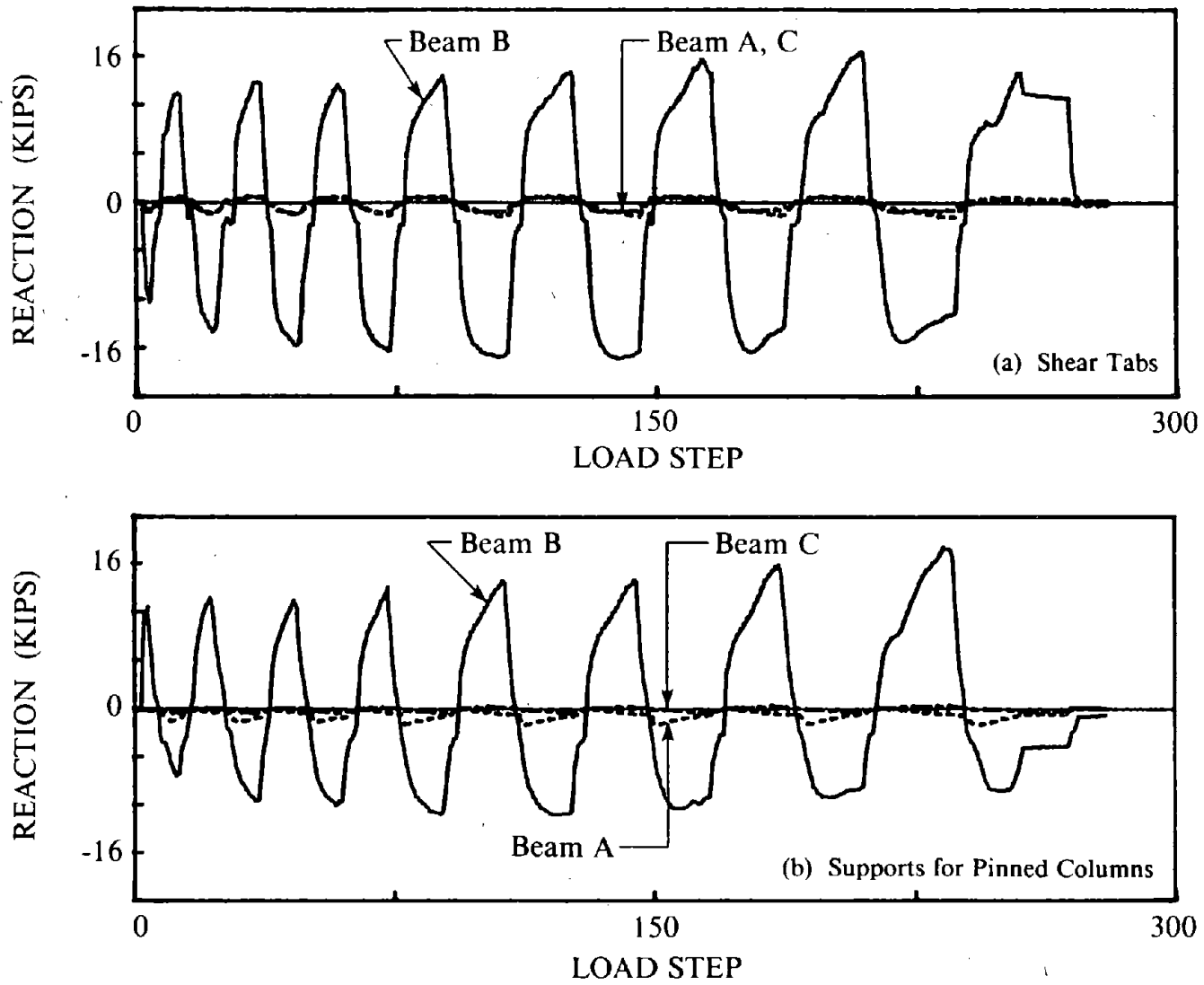
Fig. 4.31    Measured Reactions at Ends of Floor Beams During Test of Specimen B1.
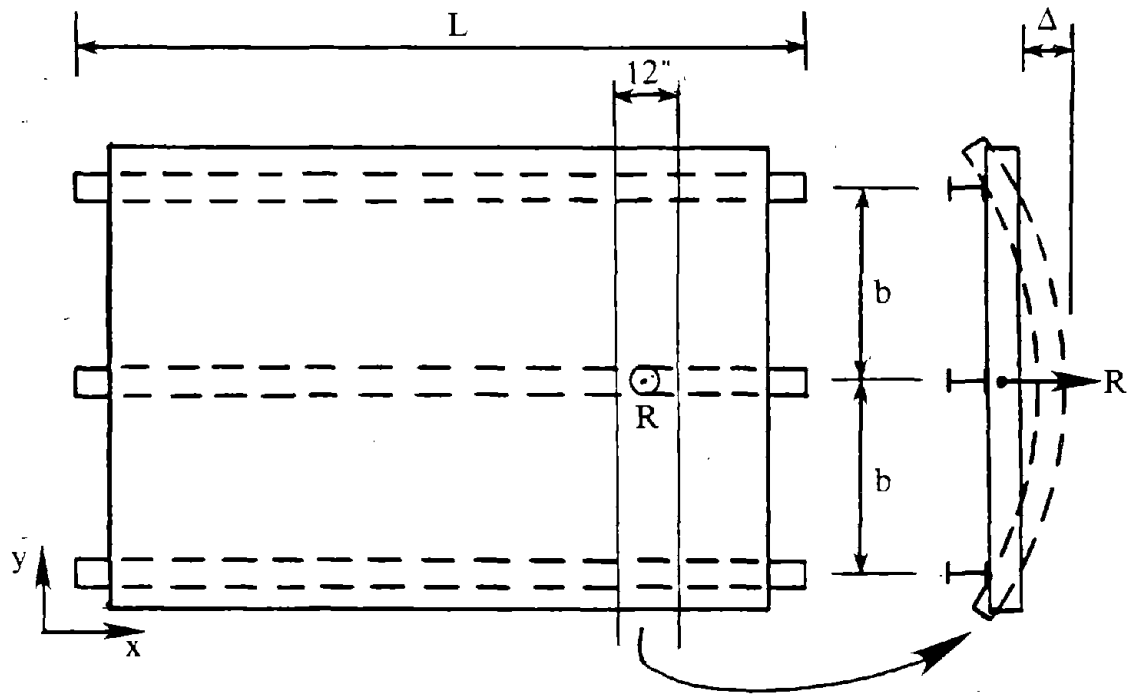
$$k = \frac{R}{\Delta} = \frac{48(EI)_y}{(2b)^3} \quad [k/in/ft]$$

(a) Determination of Foundation Stiffness, Assuming
Strip of Floor Slab is Pinned at Exterior Floor Beams
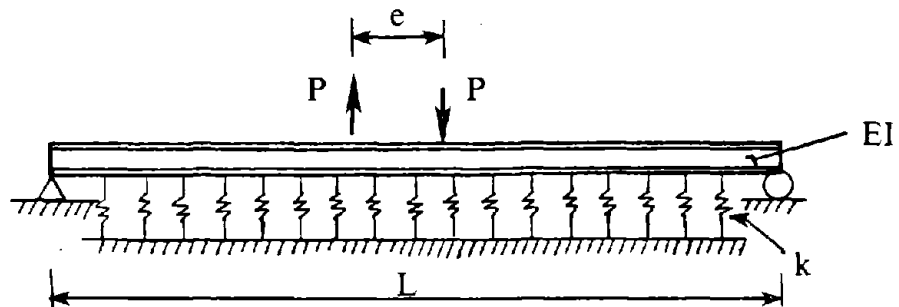


(b) Model for Interior Beam on an Elastic Foundation

Fig. 4.32    Analysis of Interior Beam on an Elastic Foundation.
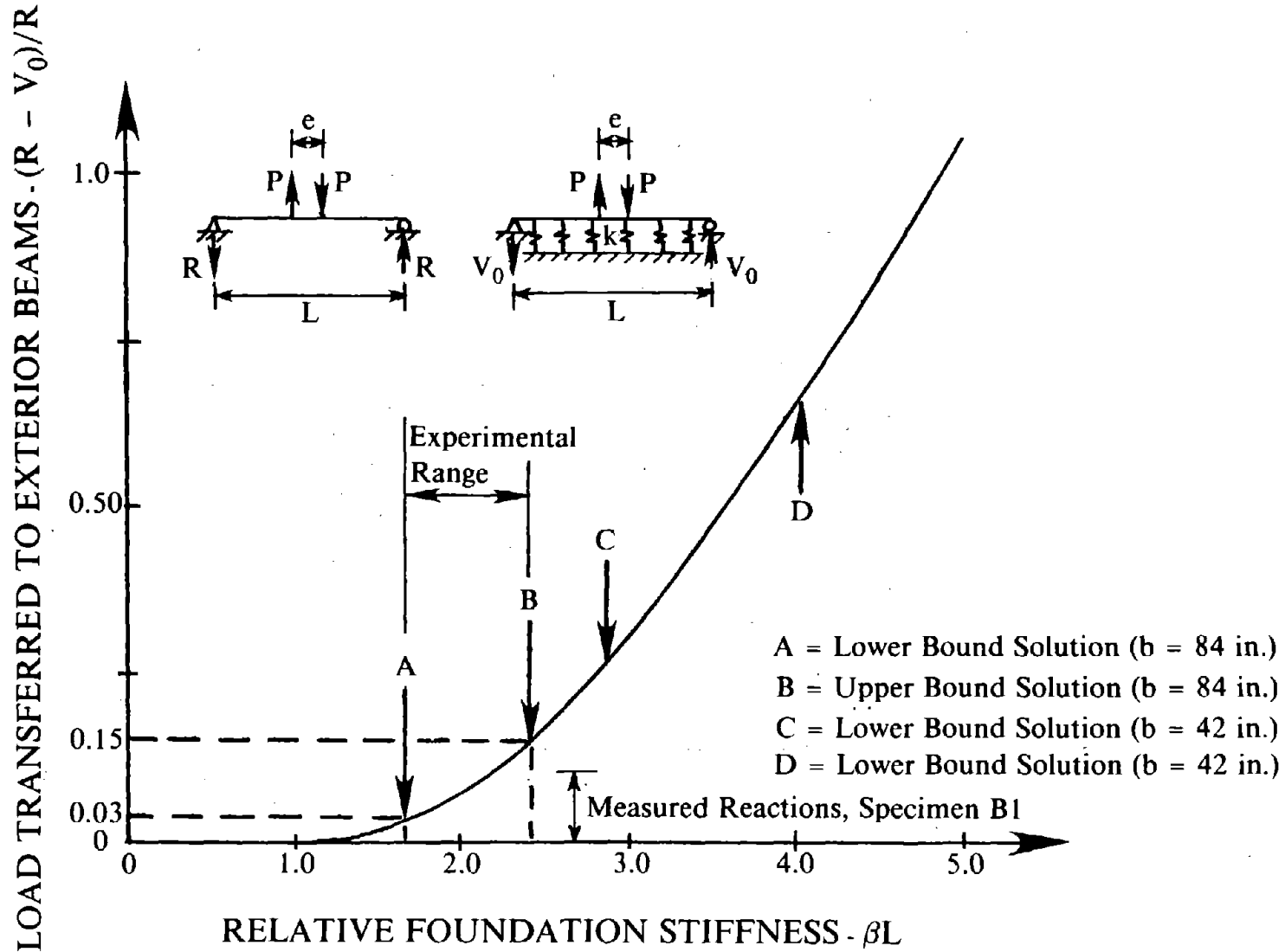
Fig. 4.33    Variation of Load Transfer to Adjacent Beams With Increase in Floor Slab Stiffness.
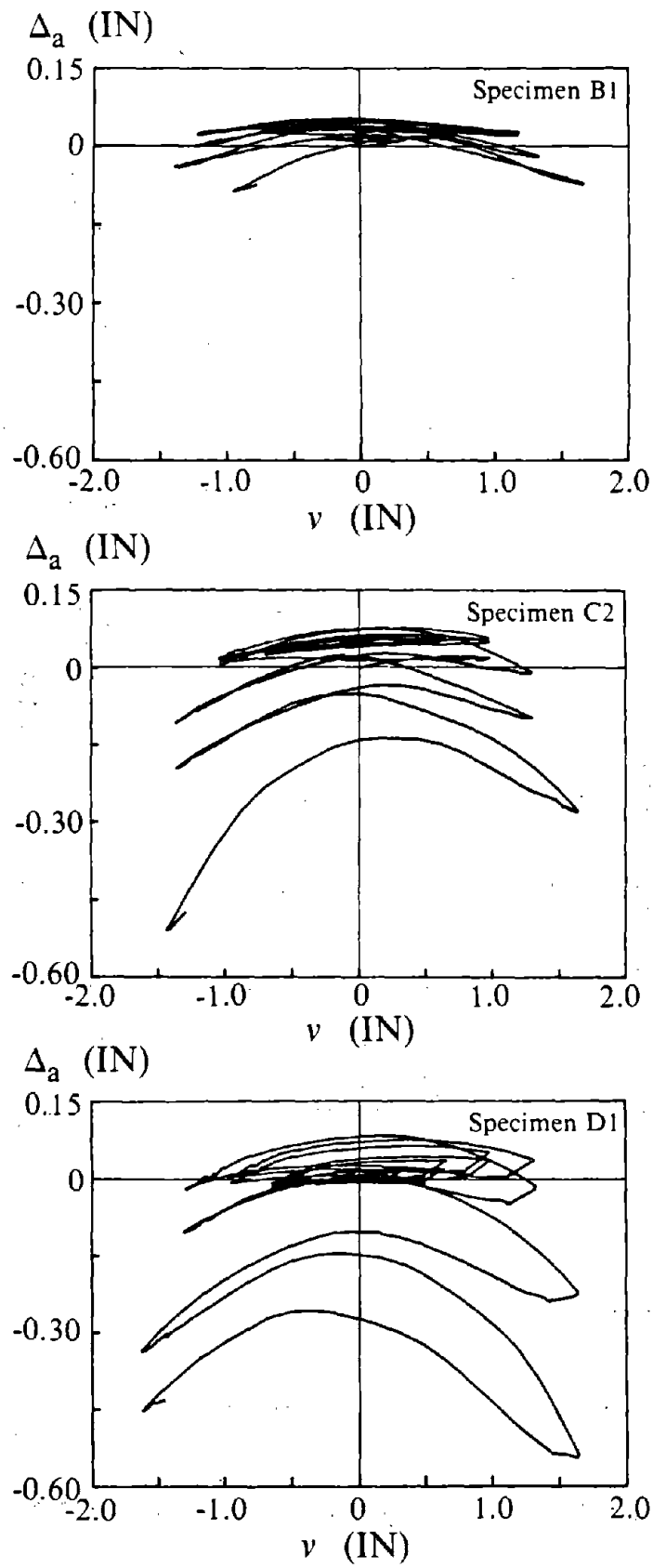
Fig. 4.34      Axial Deformation-Relative Displacement Relationship
for Links; Specimens B1, C2 and D1.

$\Delta_a$ (IN)



$v$ (IN)

$\Delta_a$ (IN)



$v$ (IN)
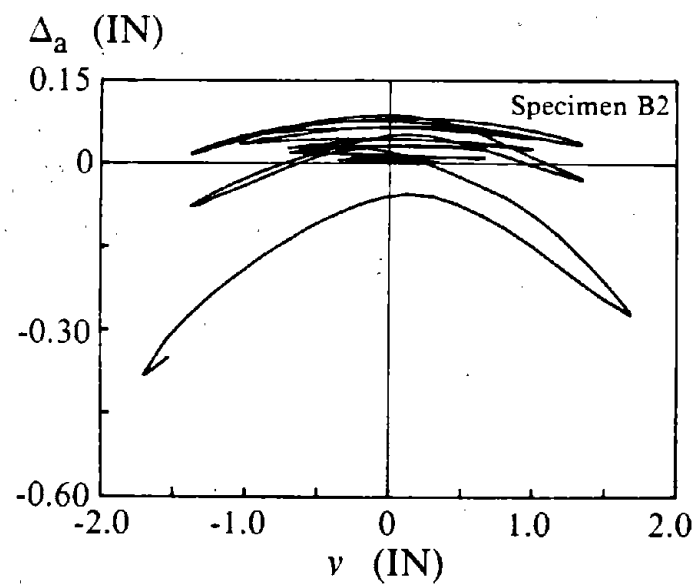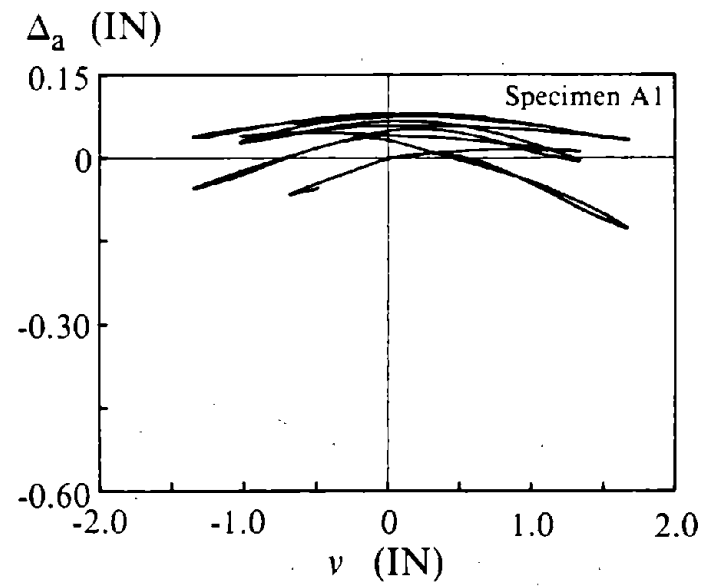
Fig. 4.35    Axial Deformation-Relative Displacement Relationship
for Links; Specimens A1 and B2.
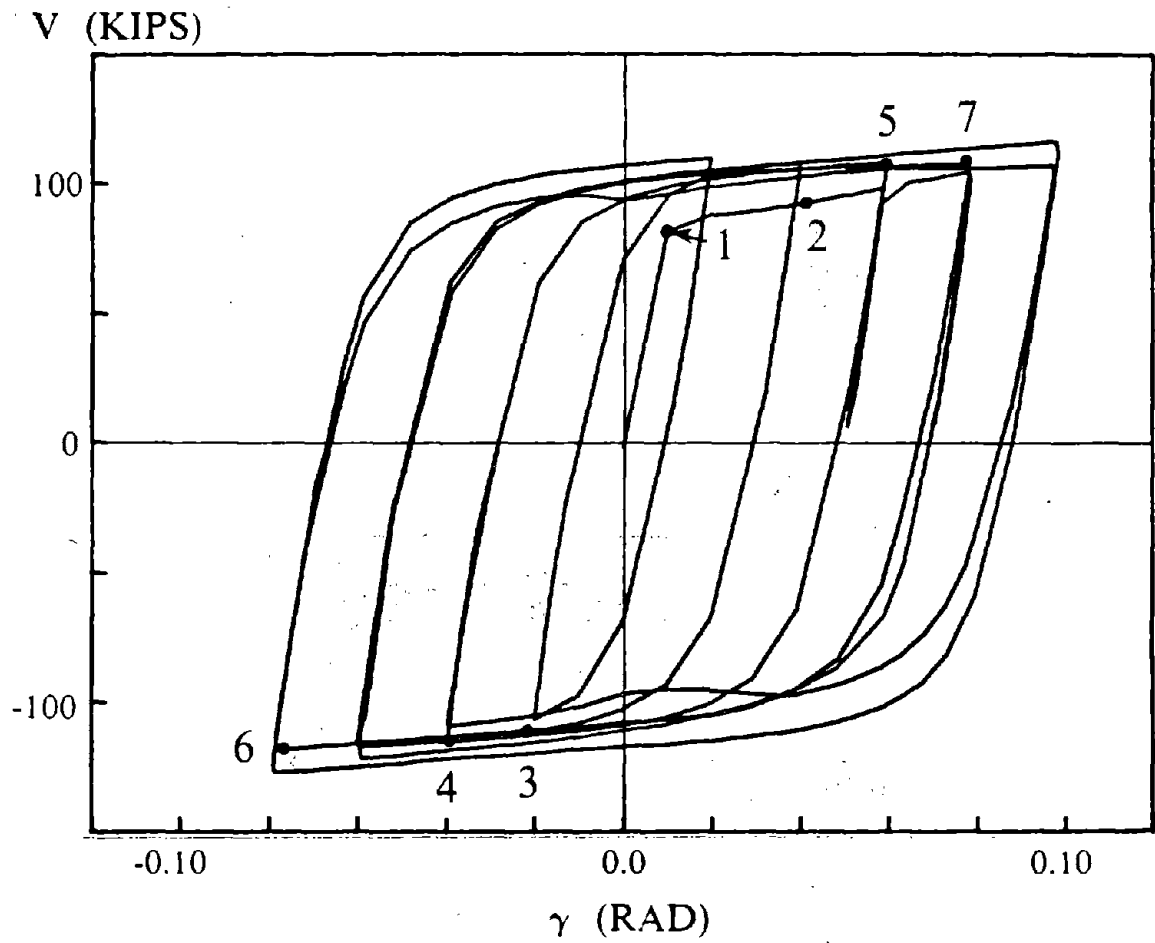
Fig. 4.36    Points 1 Through 7 At Which Strain Data for Specimen A1 are Plotted
in Figs. 4.37 to 4.40.
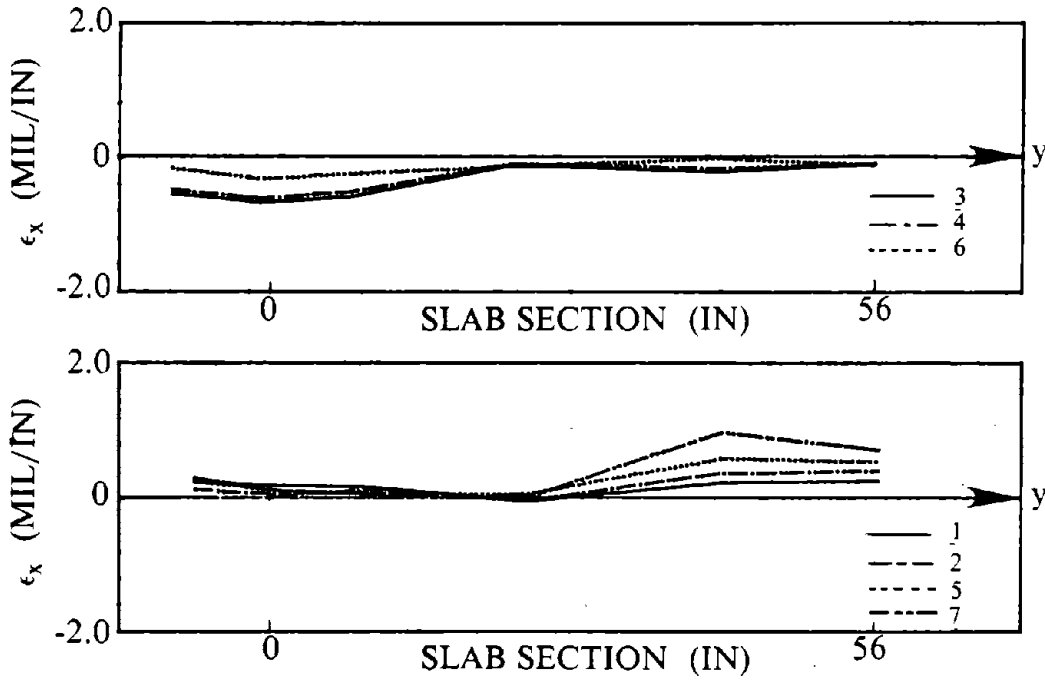
Fig. 4.37     Longitudinal Strain $\epsilon_x$ on Top Surface of Floor Slab at
a Transverse Section in the Link (Array A), Specimen A1.
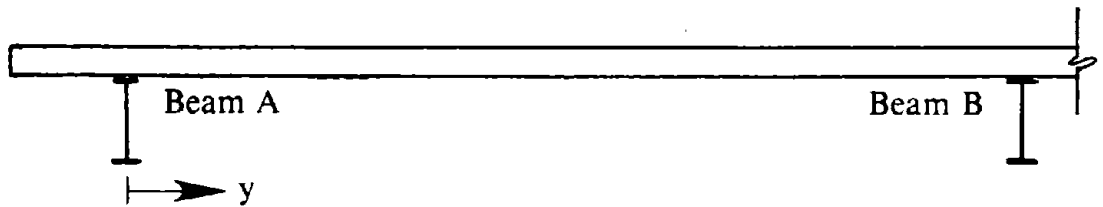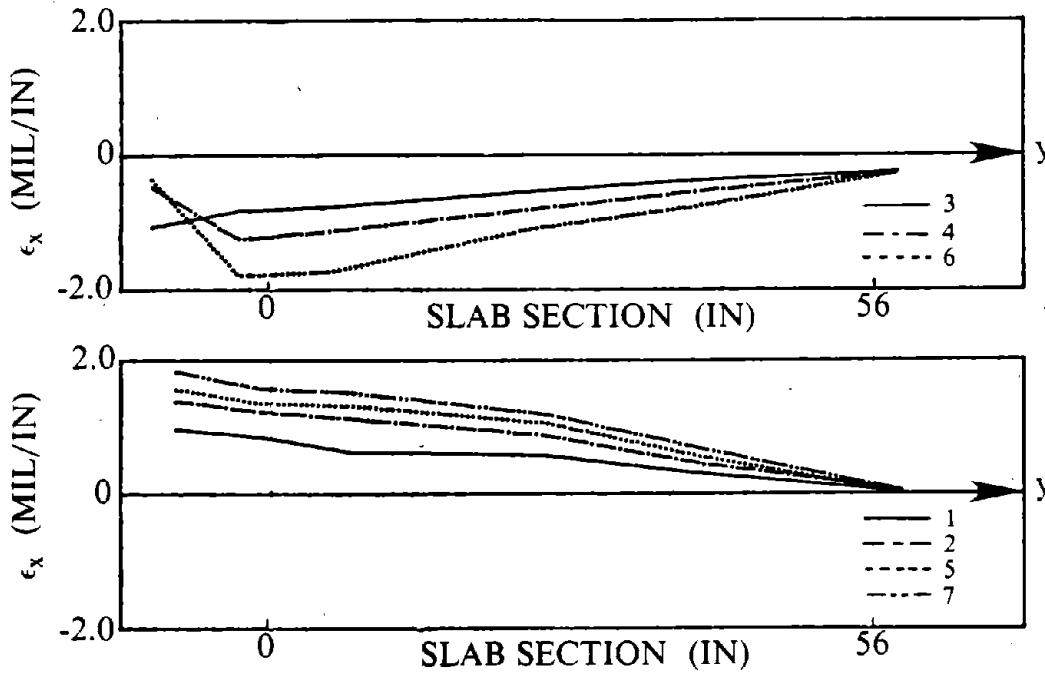


Fig. 4.38     Longitudinal Strain $\epsilon_x$ on Top Surface of Floor Slab at
a Transverse Section 4.3 in. From End of Link (Array B), Specimen A1.
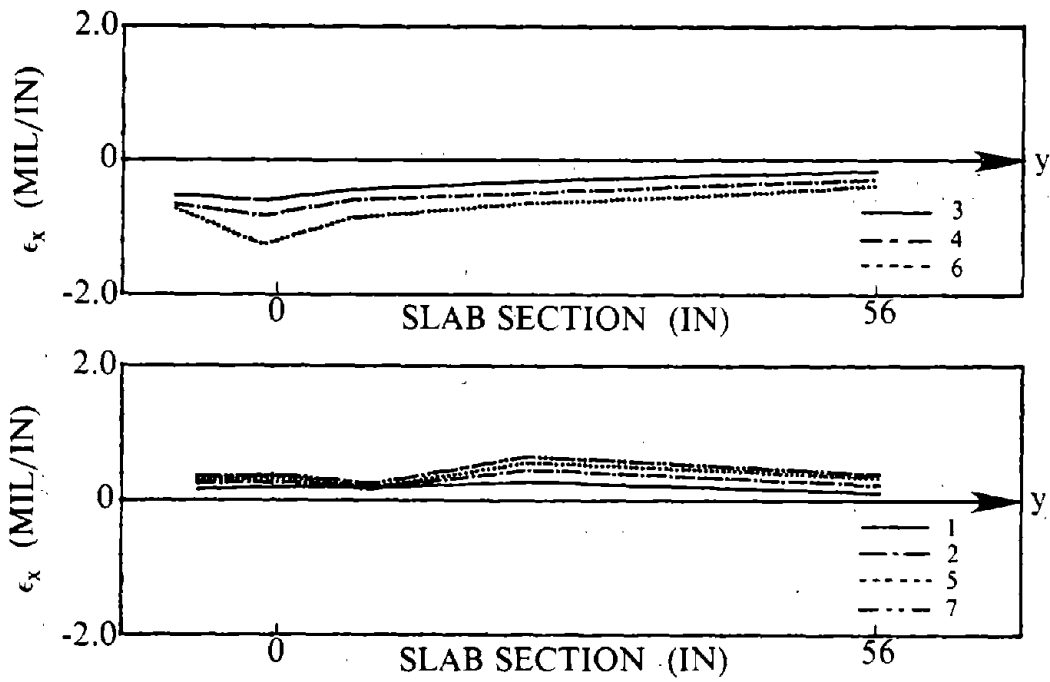
Fig. 4.39    Longitudinal Strain $\epsilon_x$ on Top Surface of Floor Slab at
a Transverse Section 13.4 in. From End of Link (Array C), Specimen A1.
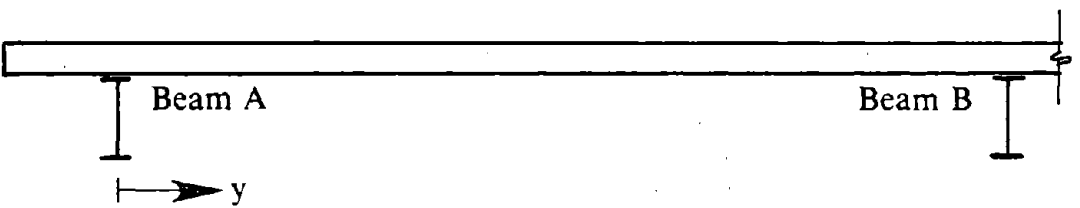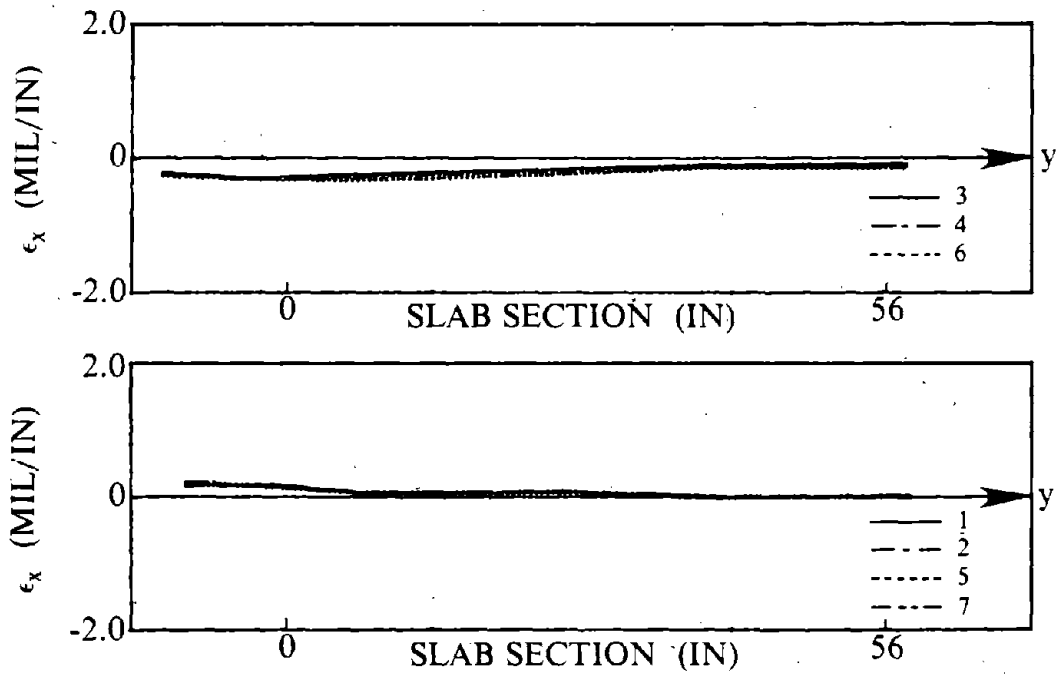


Fig. 4.40    Longitudinal Strain $\epsilon_x$ on Top Surface of Floor Slab at
a Transverse Section 28.3 in. From End of Link (Array D), Specimen A1.
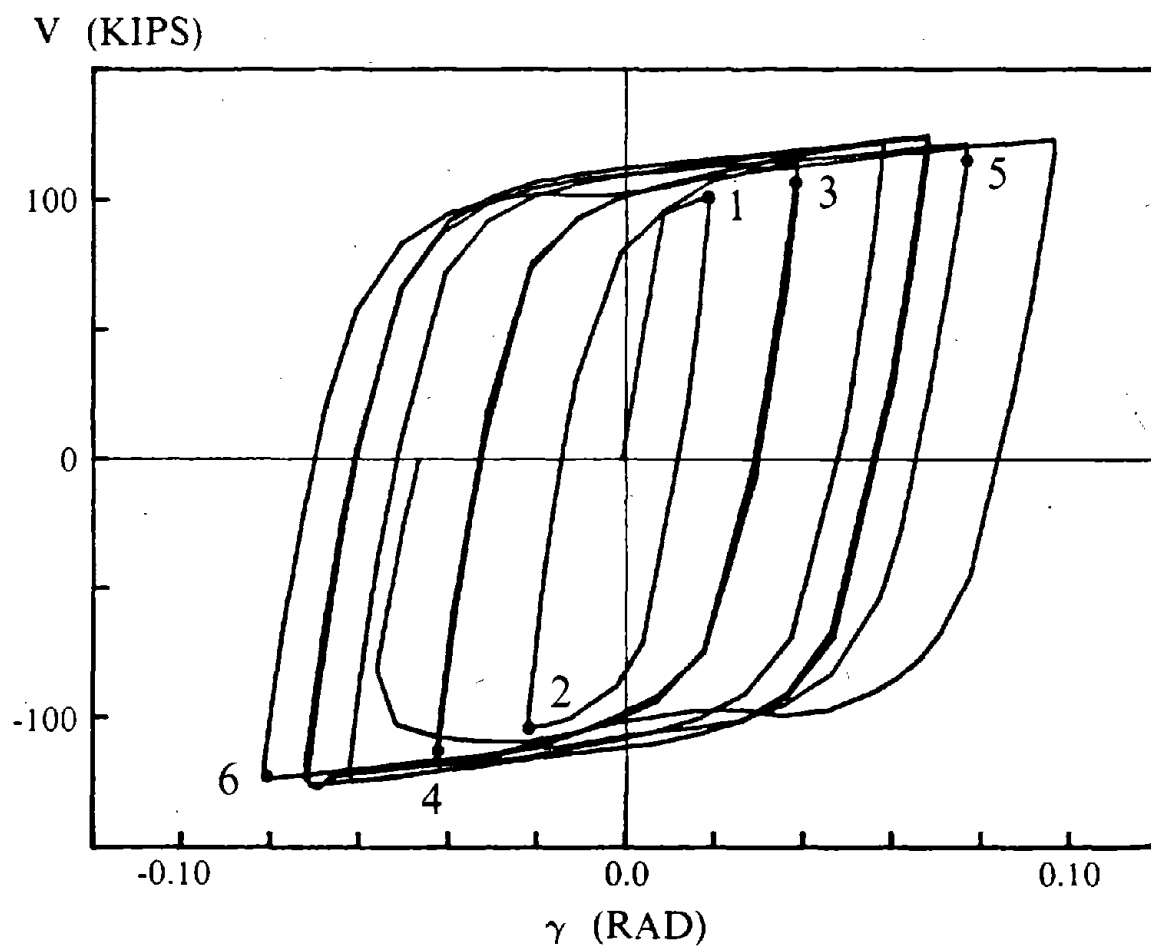
Fig. 4.41    Points 1 Through 6 At Which Strain Data for Specimen B1 are Plotted
in Figs. 4.42 to 4.45.

250
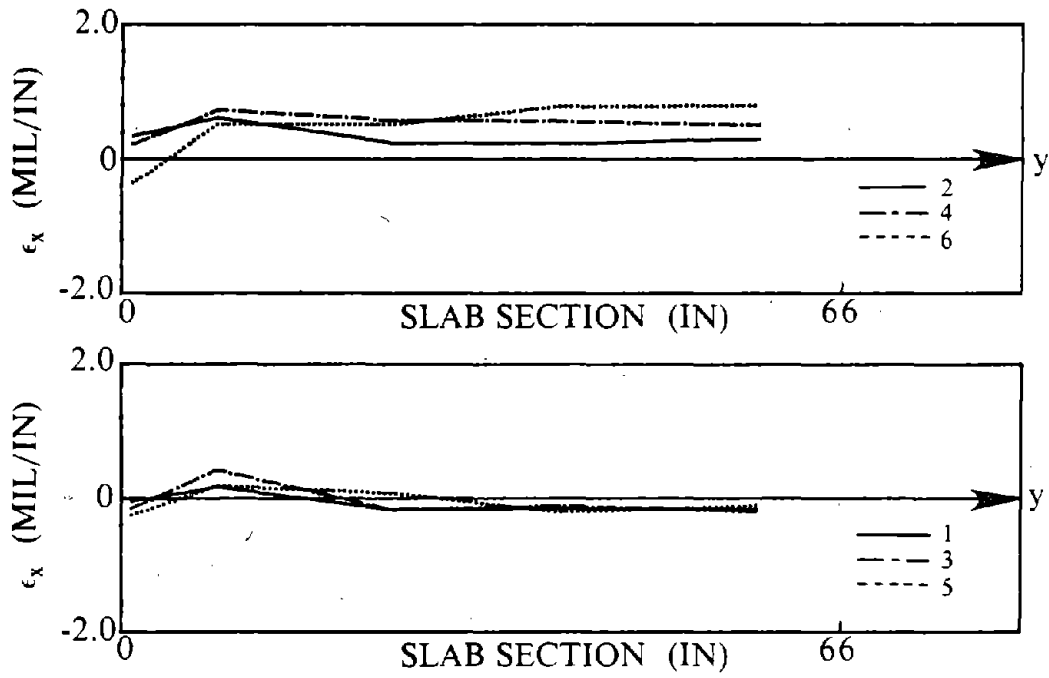


Fig. 4.42　　Longitudinal Strain $\epsilon_x$ on Top Surface of Floor Slab at a Transverse Section in the Link (Array A), Specimen B1.
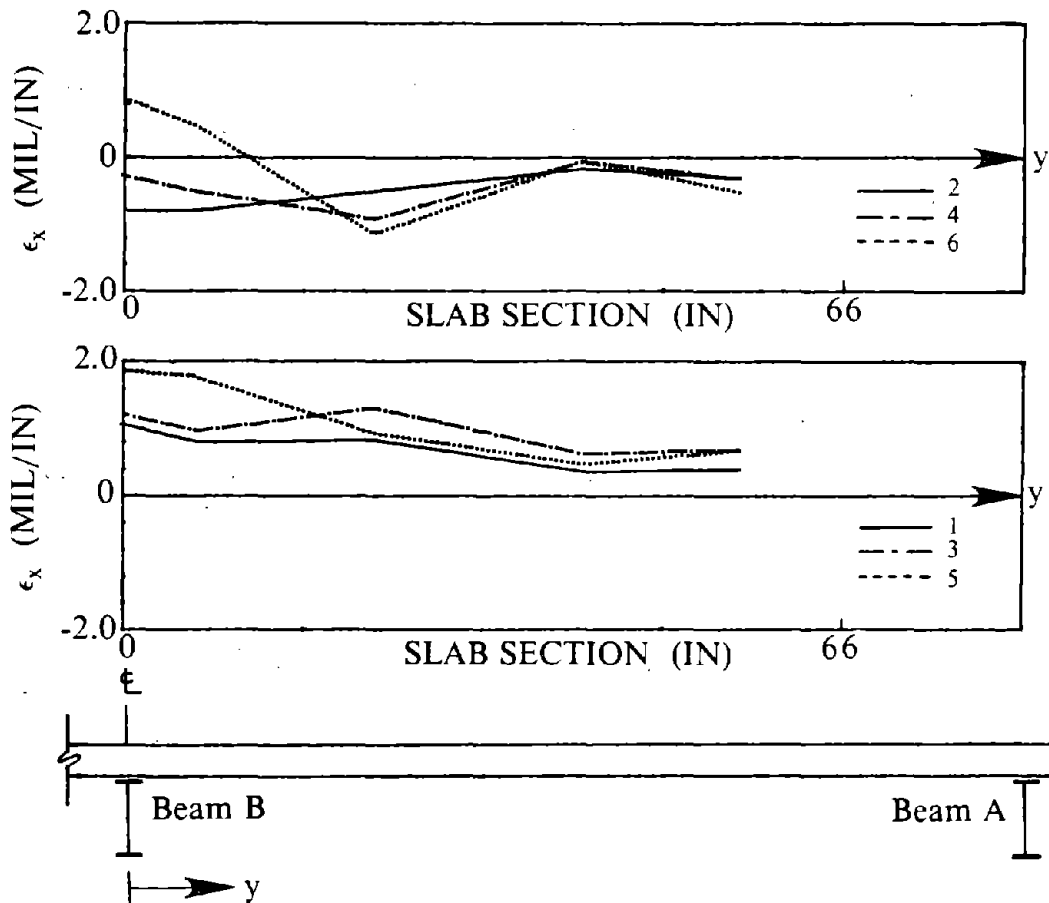


Fig. 4.43　　Longitudinal Strain $\epsilon_x$ on Top Surface of Floor Slab at a Transverse Section 4.3 in. From End of Link (Array B), Specimen B1.
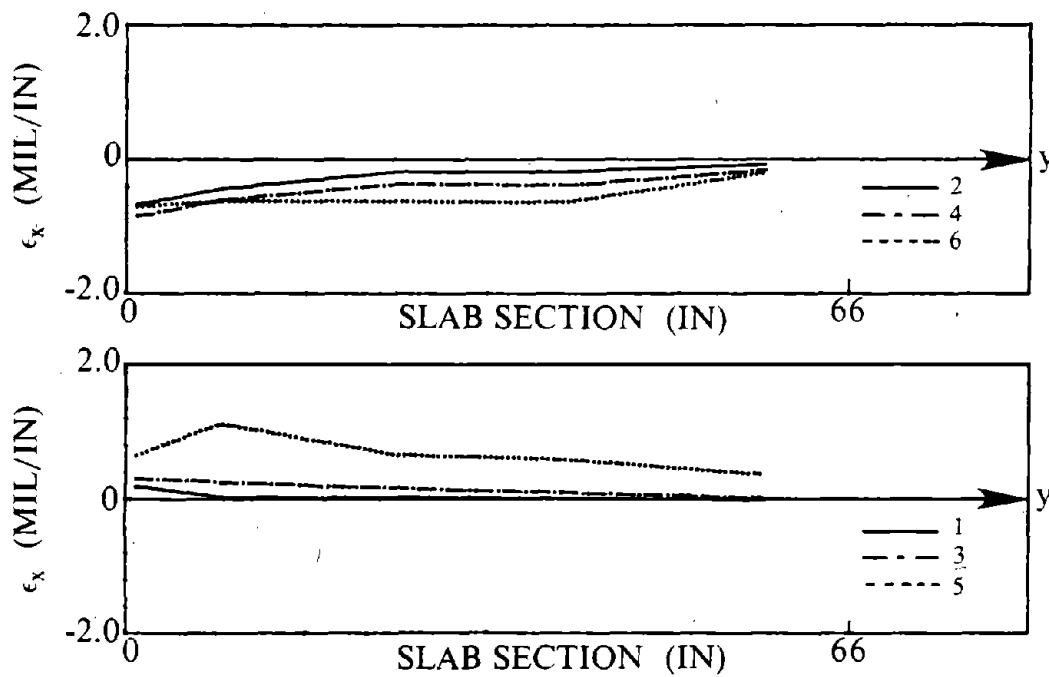
Fig. 4.44    Longitudinal Strain $\epsilon_x$ on Top Surface of Floor Slab at
a Transverse Section 13.4 in. From End of Link (Array C), Specimen B1.
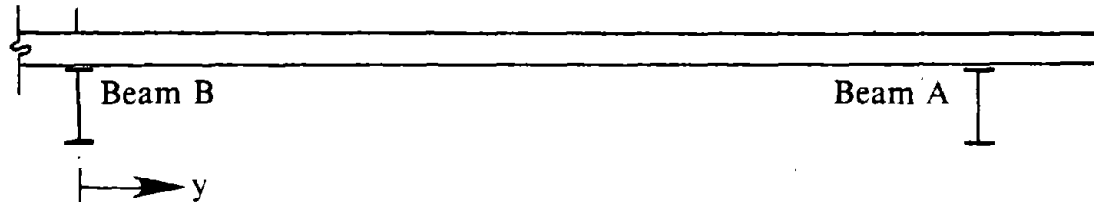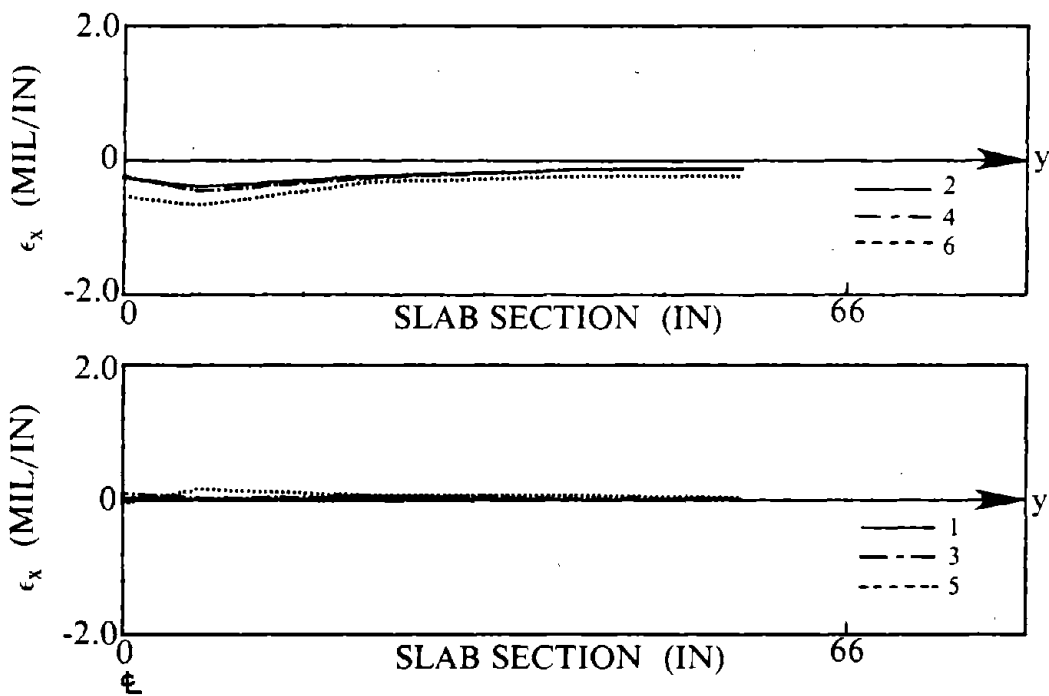
Fig. 4.45    Longitudinal Strain $\epsilon_x$ on Top Surface of Floor Slab at
a Transverse Section 28.3 in. From End of Link (Array D), Specimen B1.
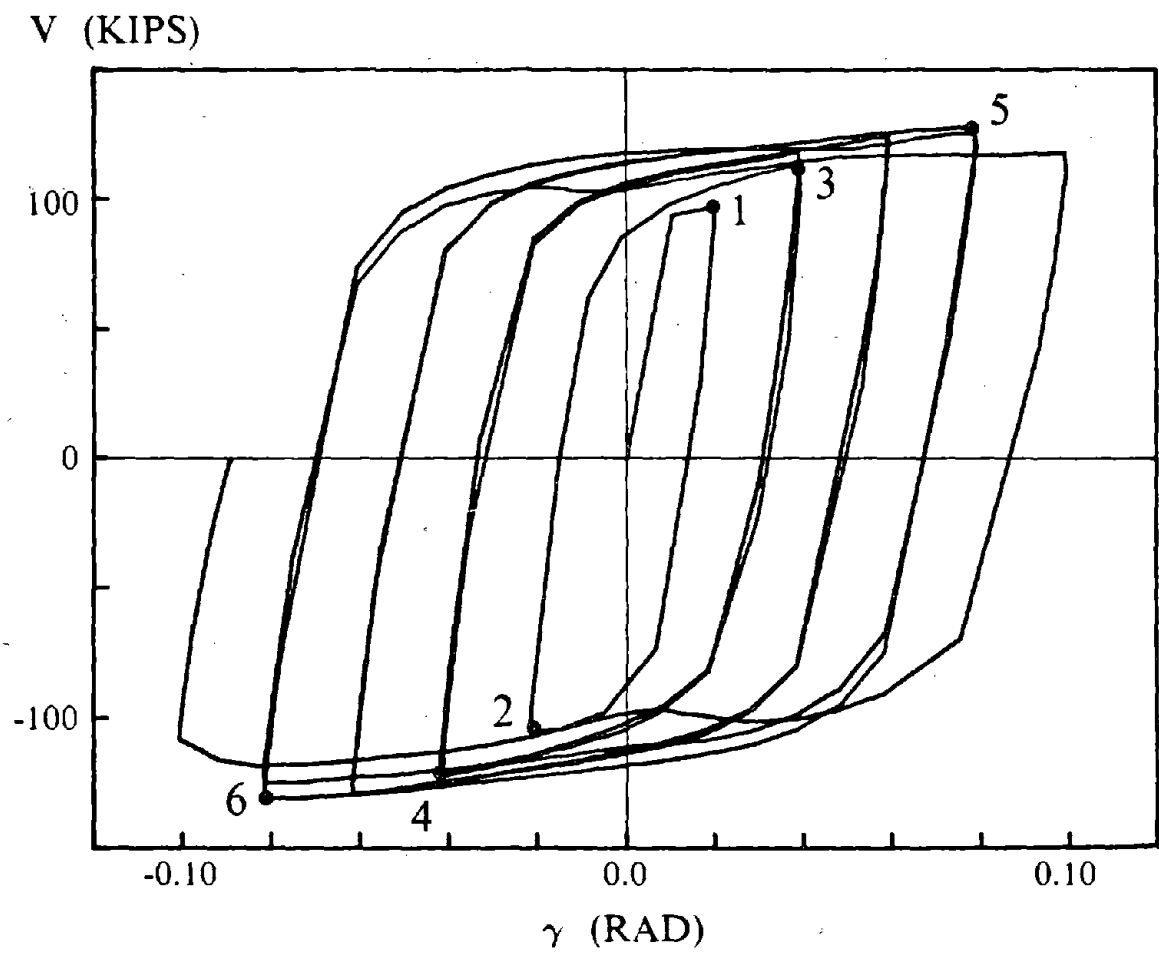
Fig. 4.46    Points 1 Through 6 At Which Strain Data for Specimen B2 are Plotted in Figs. 4.47 to 4.50.
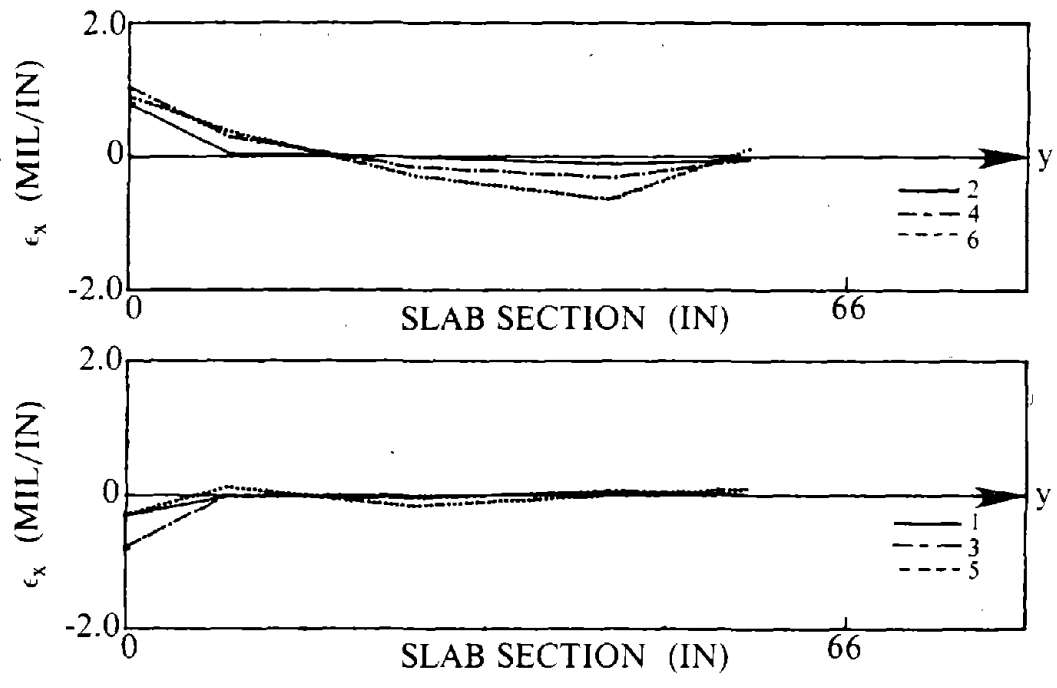
Fig. 4.47    Longitudinal Strain $\epsilon_x$ on Top Surface of Floor Slab at
a Transverse Section in the Link (Array A), Specimen B2.
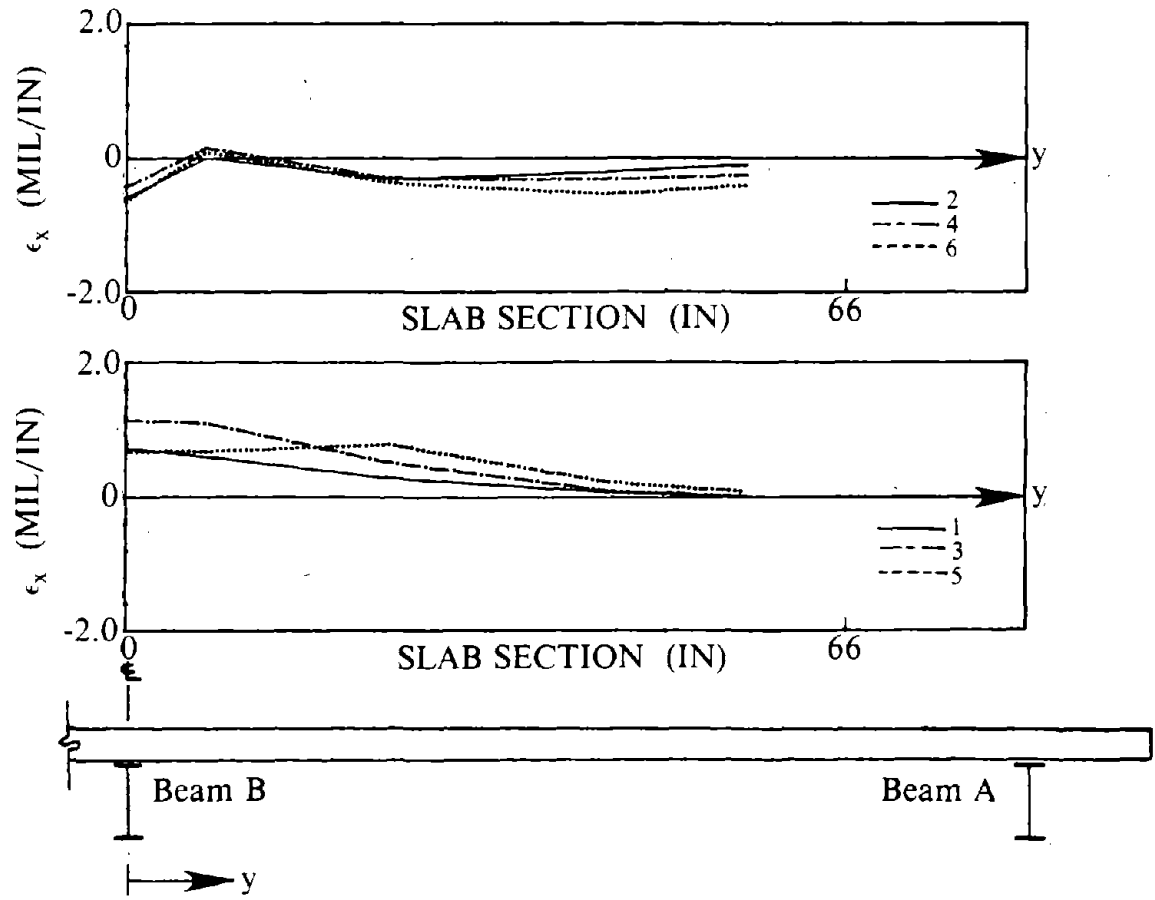


Fig. 4.48    Longitudinal Strain $\epsilon_x$ on Top Surface of Floor Slab at
a Transverse Section 0.3 in. From End of Link (Array B), Specimen B2.
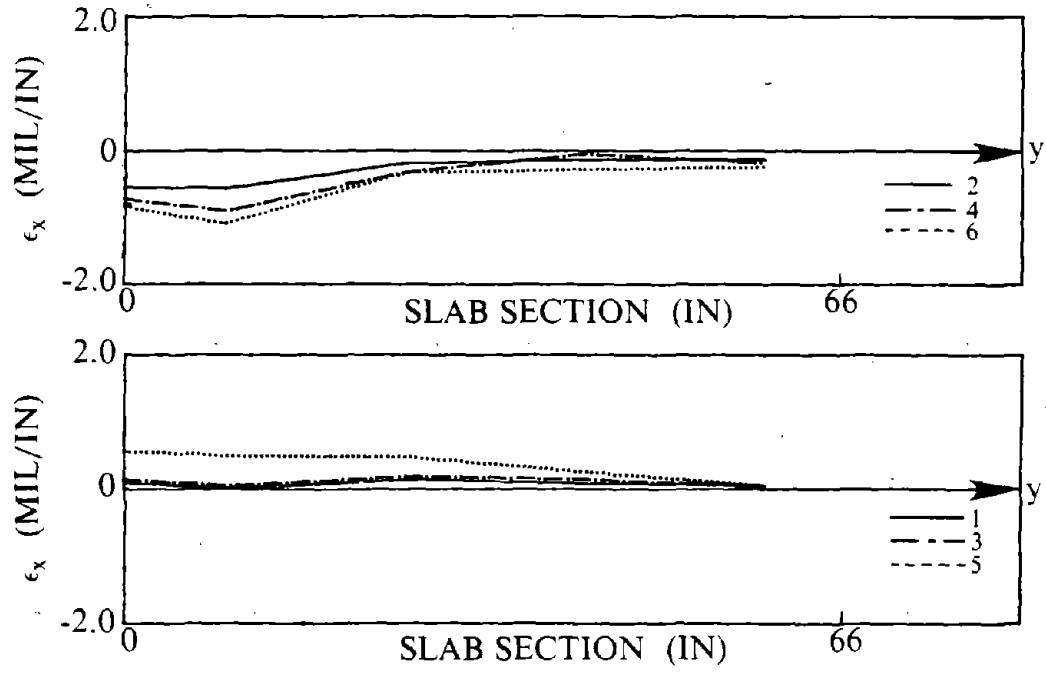
Fig. 4.49    Longitudinal Strain $\epsilon_x$ on Top Surface of Floor Slab at
a Transverse Section 9.4 in. From End of Link (Array C), Specimen B2.
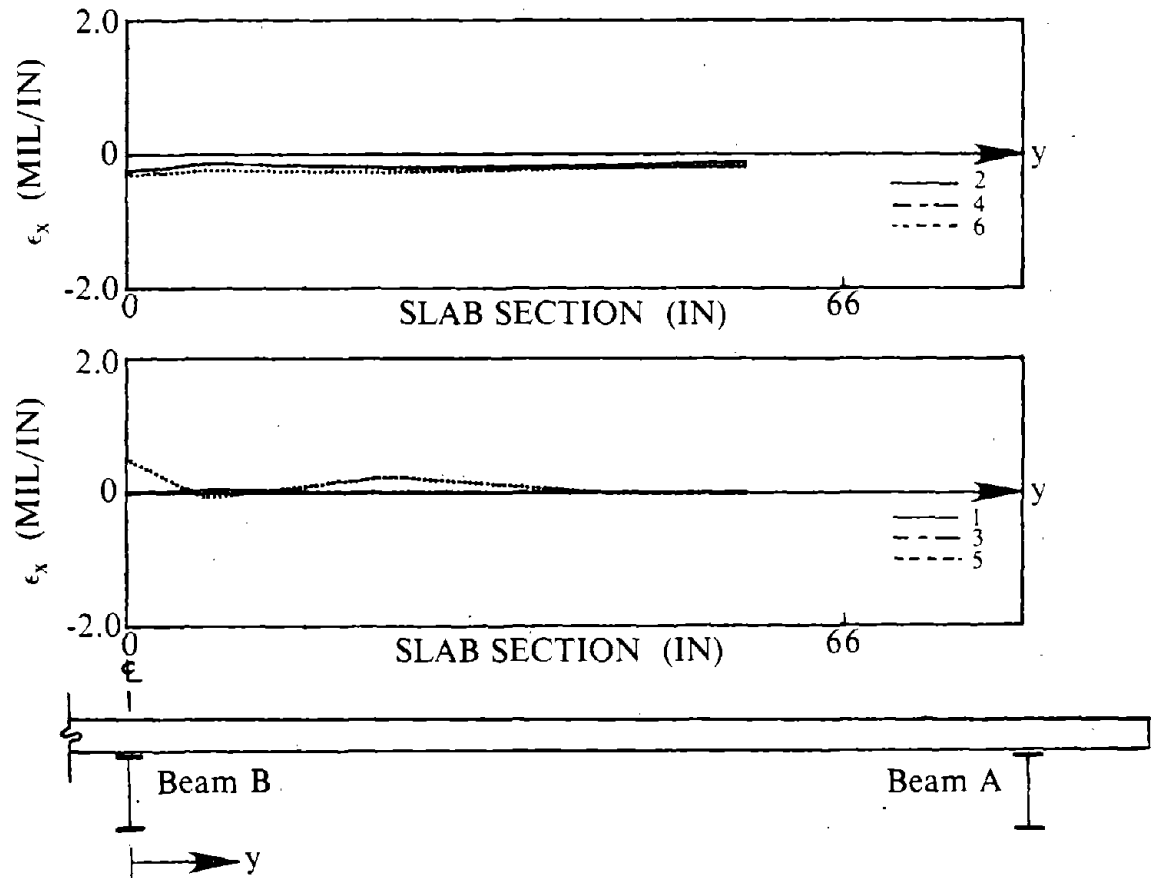


Fig. 4.50    Longitudinal Strain $\epsilon_x$ on Top Surface of Floor Slab at
a Transverse Section 24.3 in. From End of Link (Array D), Specimen B2.
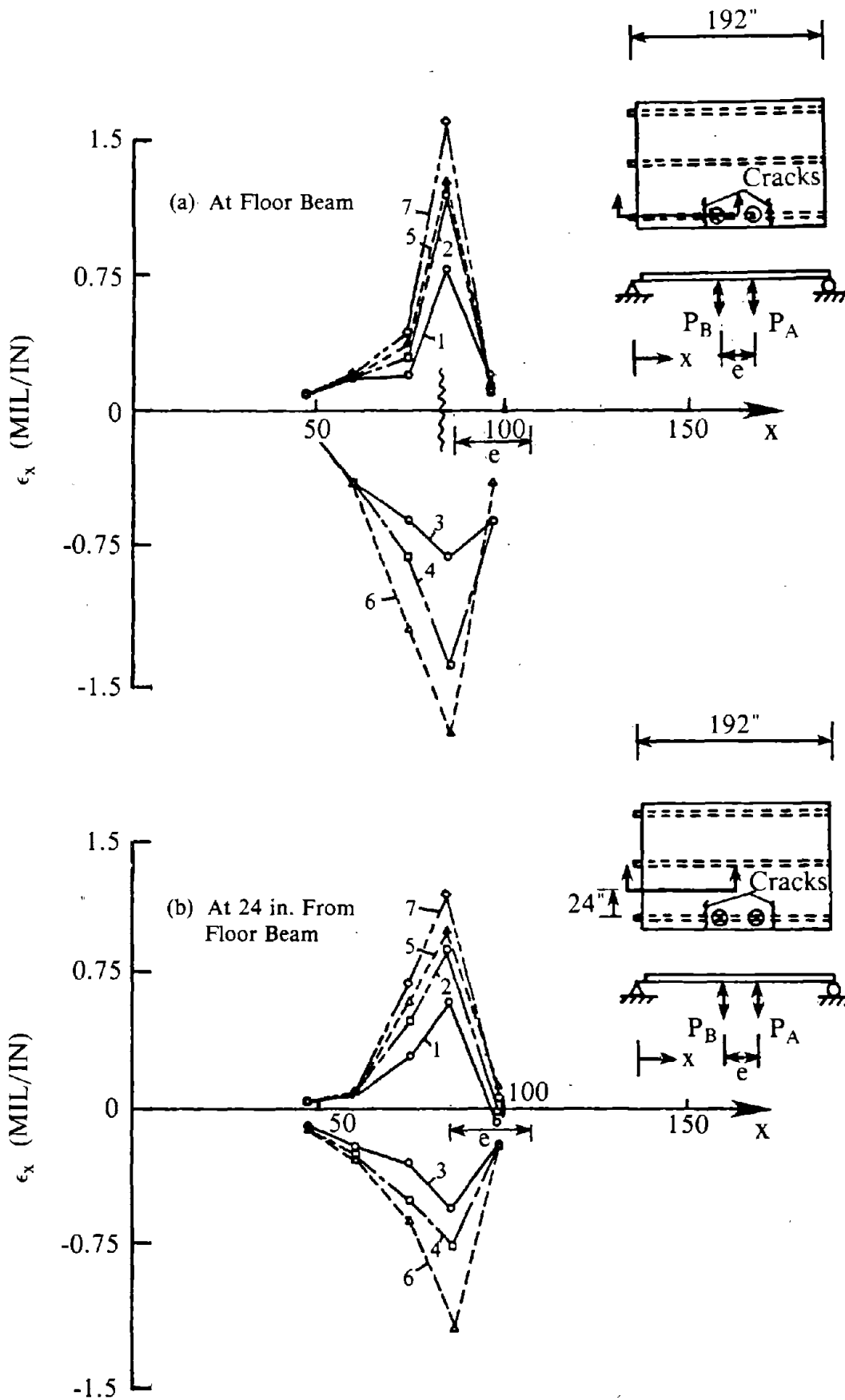
Fig. 4.51    Longitudinal Strain $\epsilon_x$ on Top Surface of Floor Slab
Along Sections Parallel to Floor Beam, Specimen A1.
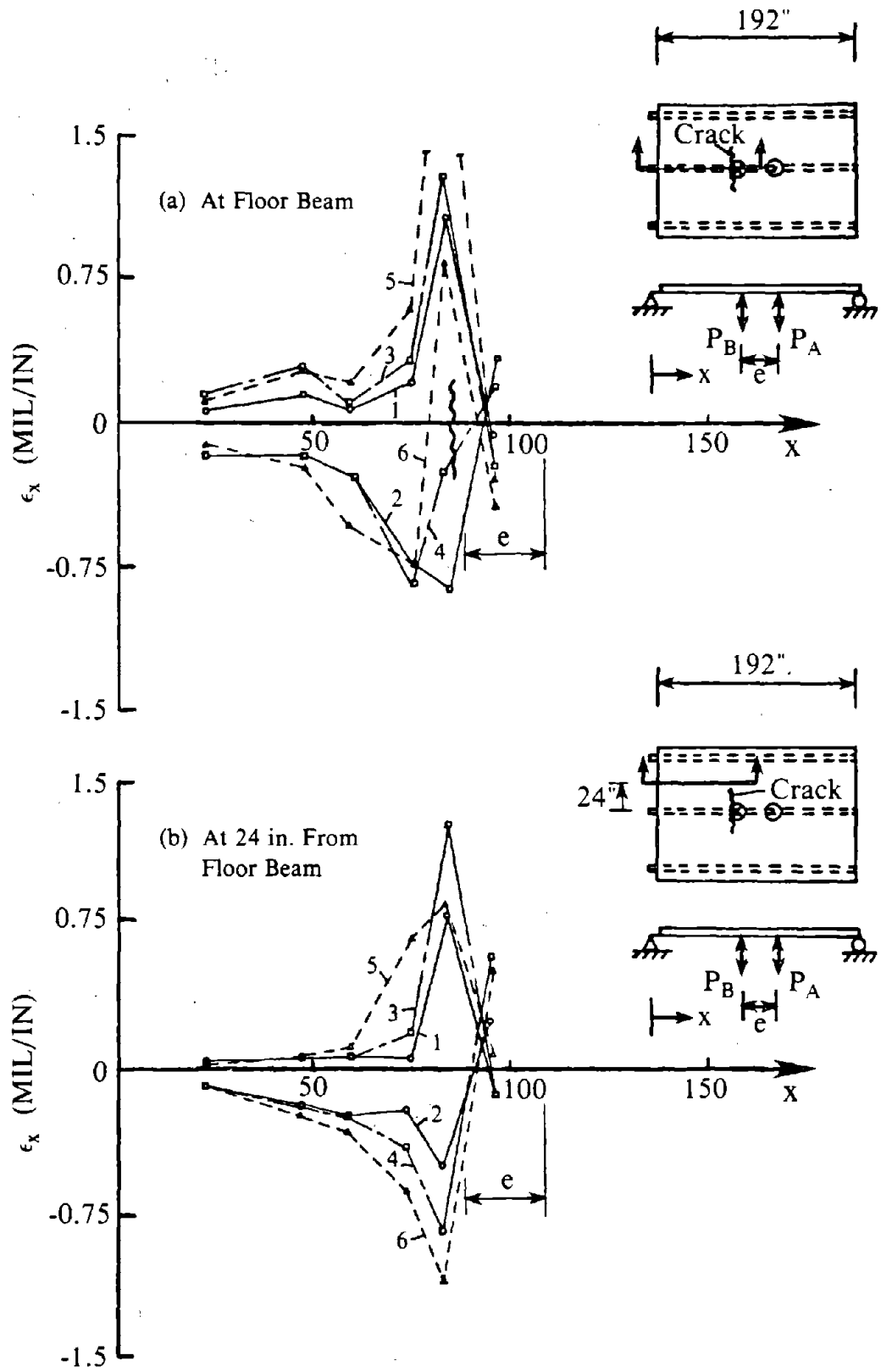
Fig. 4.52    Longitudinal Strain $\epsilon_x$ on Top Surface of Floor Slab
Along Sections Parallel to Floor Beam, Specimen B1.
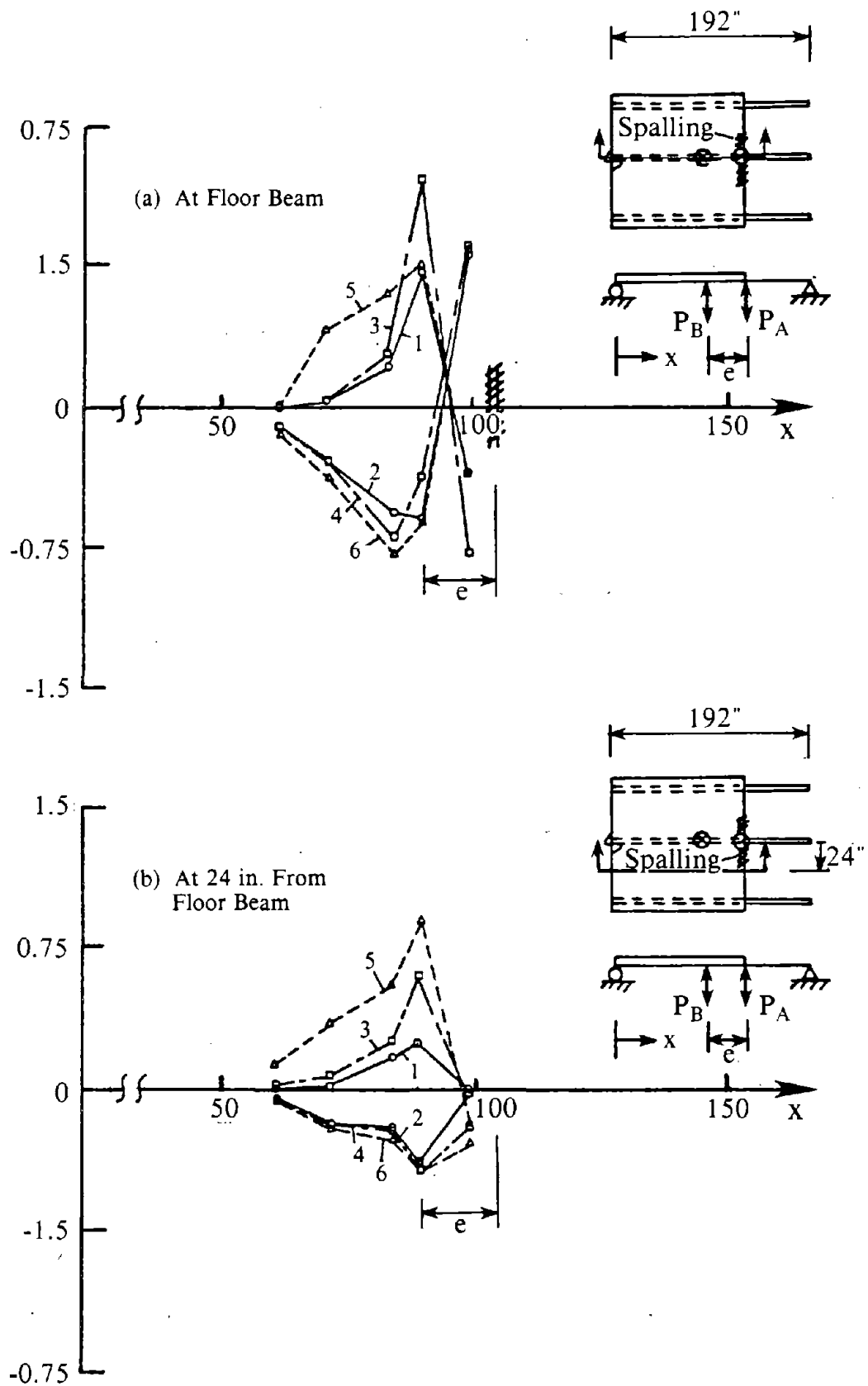
Fig. 4.53    Longitudinal Strain $\epsilon_x$ on Top Surface of Floor Slab
Along Sections Parallel to Floor Beam, Specimen B2.

(a) Inside the Link

(b) Outside the Link, At 18 in. From End of Link

(c) Outside the Link, At 53 in. From End of Link
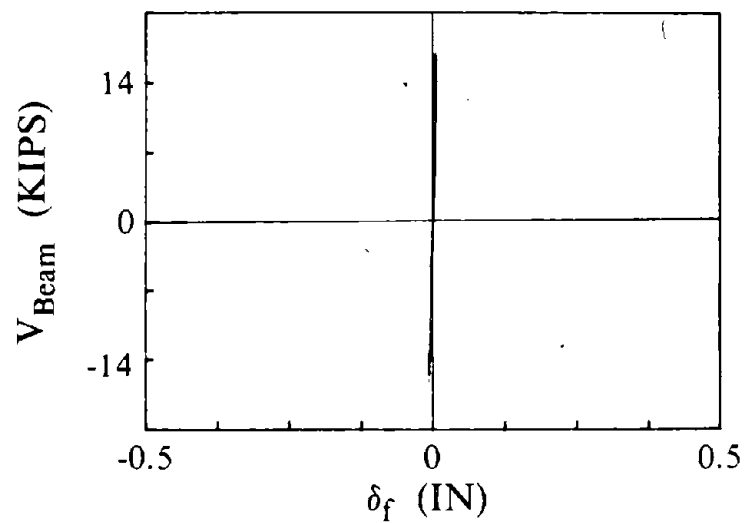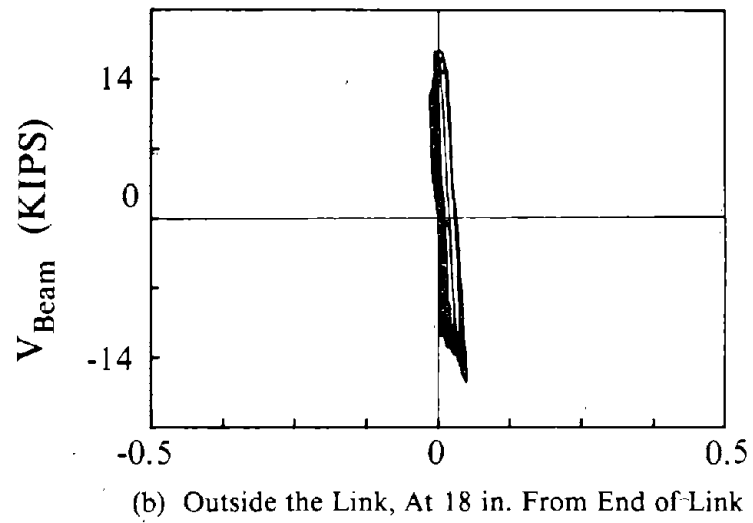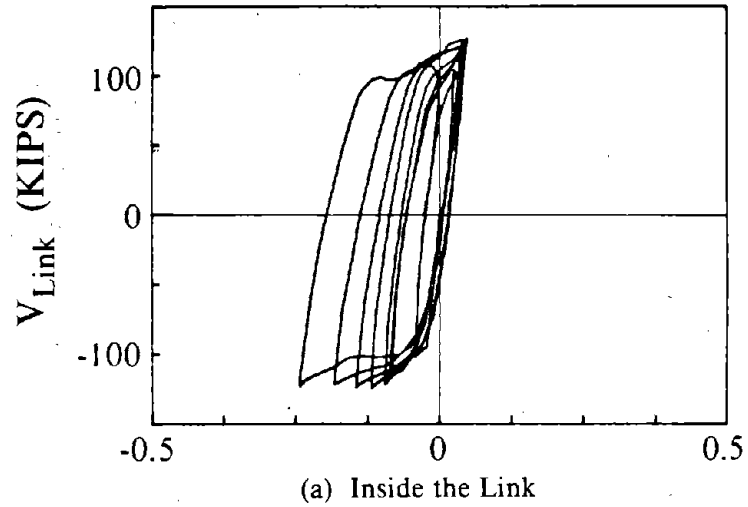
Fig. 4.54    Shear Force-Beam to Concrete Slip Relationship, Specimen B1.
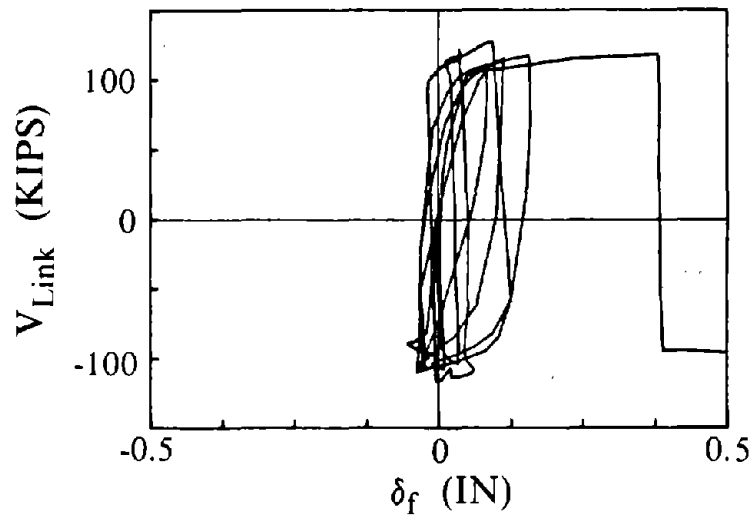
(a) Inside the Link
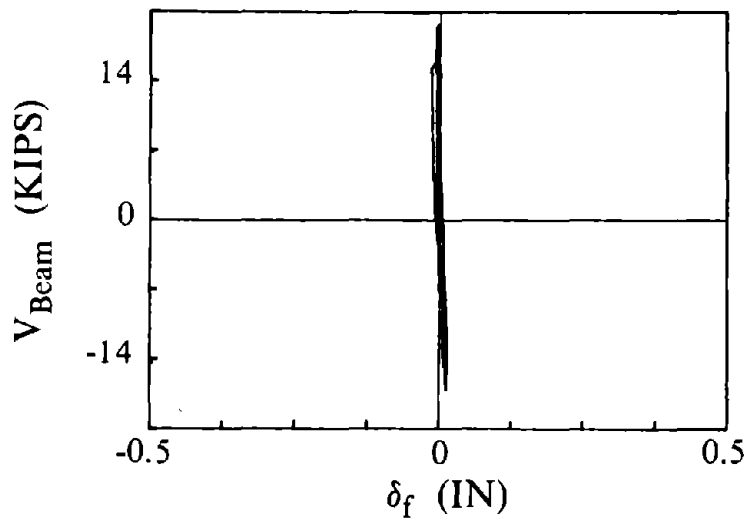


(b) Outside the Link, At 18 in. From End of Link

Fig. 4.55    Shear Force-Beam to Concrete Slip Relationship, Specimen A1.
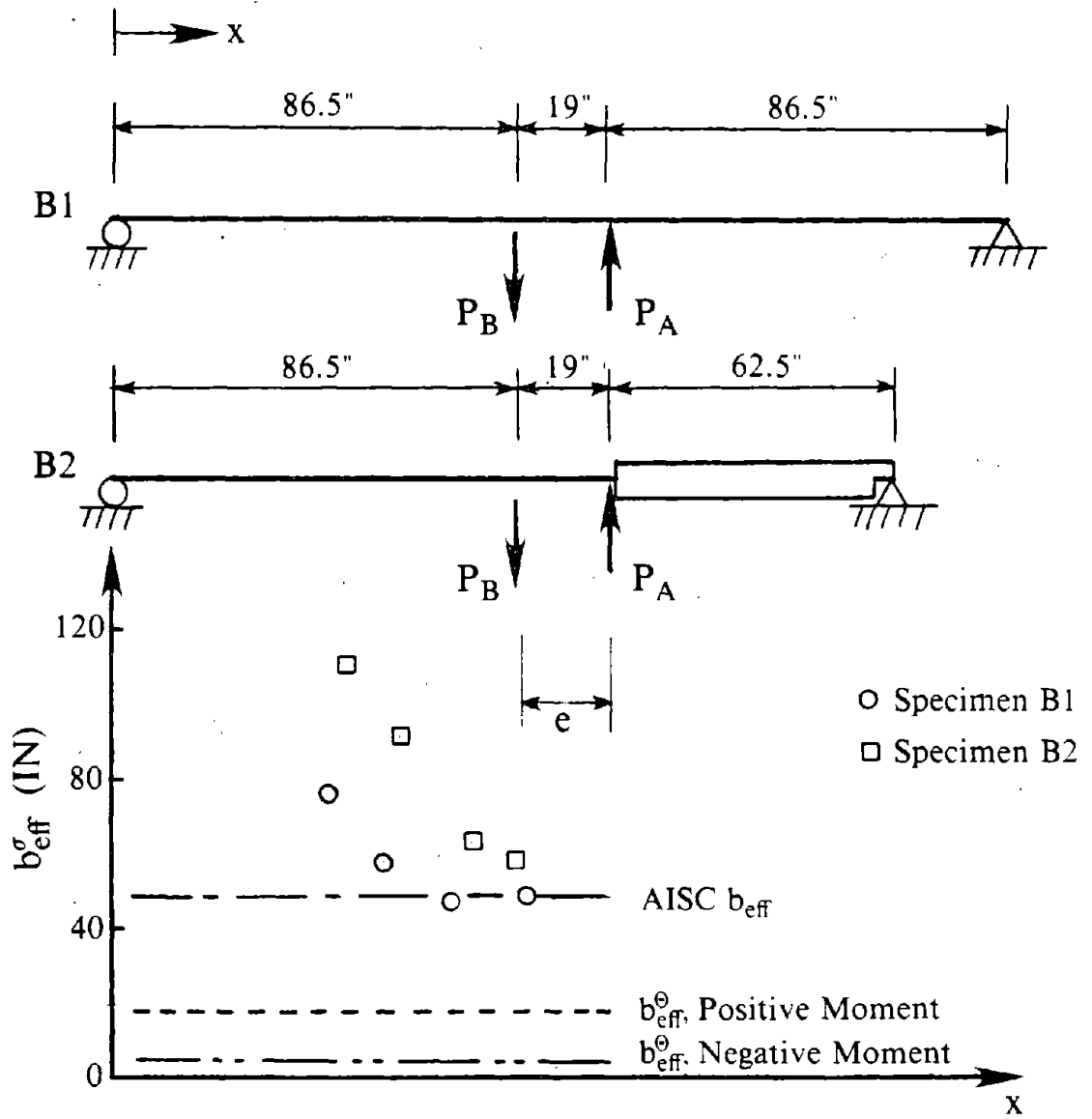
Fig. 4.56    Effective Slab Width, Specimens B1 and B2.
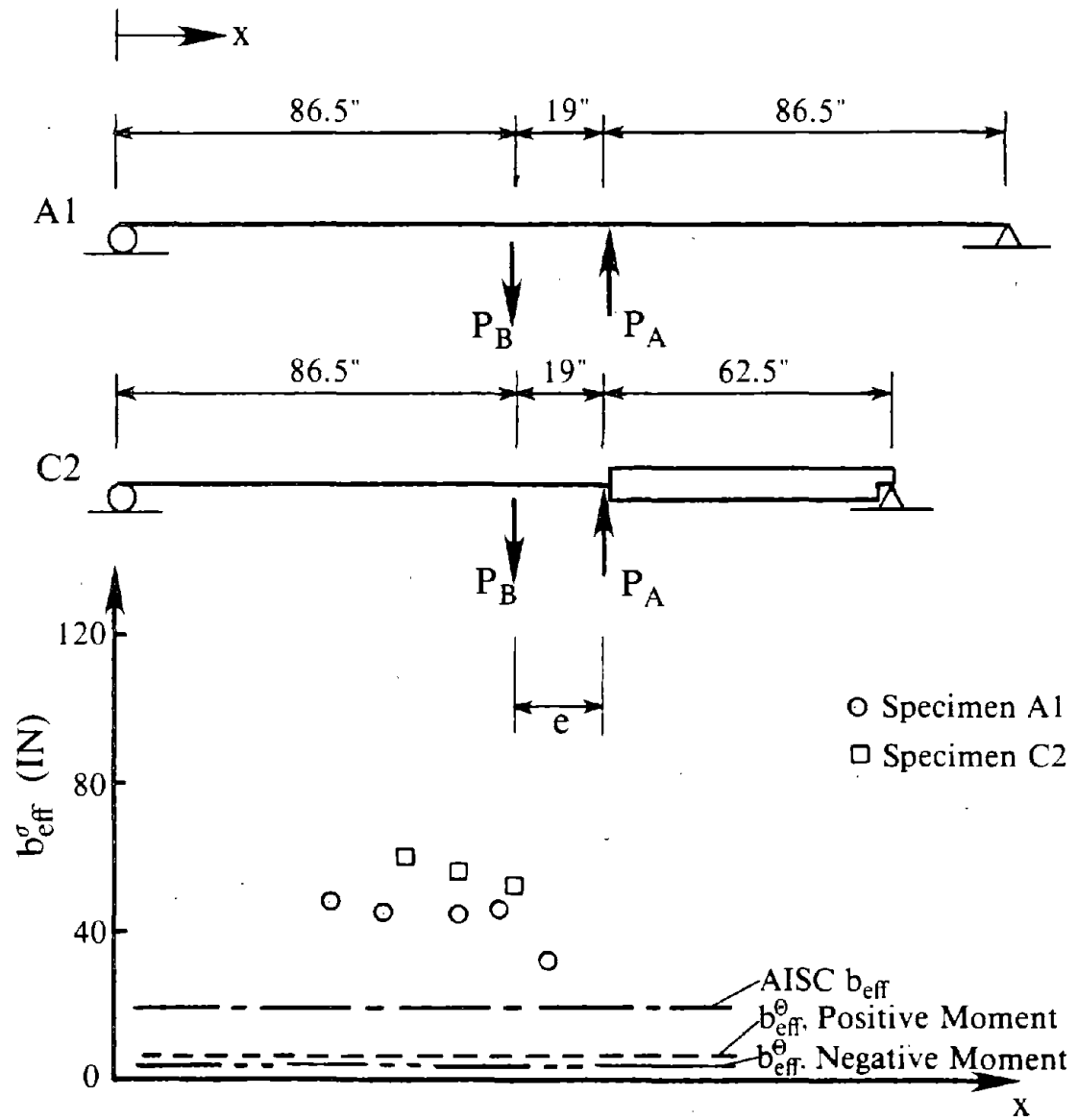
Fig. 4.57    Effective Slab Width, Specimens A1 and C2.

262



(a) Test Setup



$$\Theta_s = \frac{\Delta_A}{L^*}$$

$$\Theta_{ch} = \Theta^* + \Theta_s$$

$$\frac{M}{\Theta_{ch}} = K^+ \approx \frac{3EI_{eff}}{L^*}$$
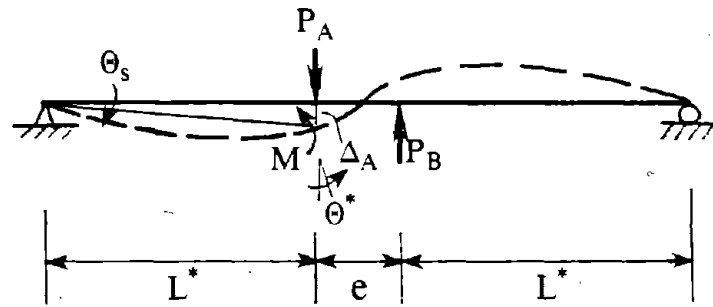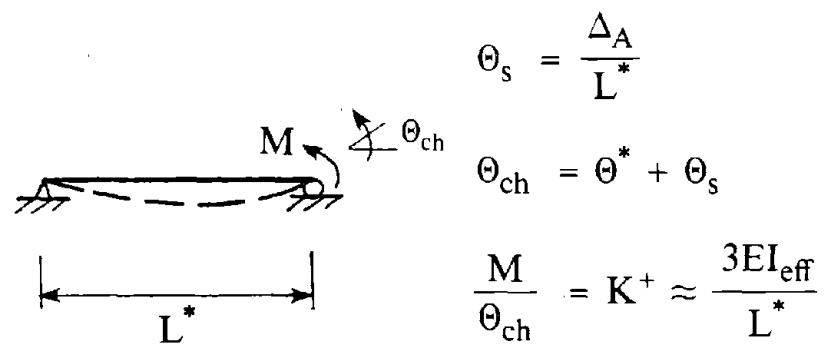
(b) Deformation of the Floor Beam Outside the Link

Fig. 4.58    Determination of Rotational Stiffness $K^+$ of Floor Beam Outside the Link.
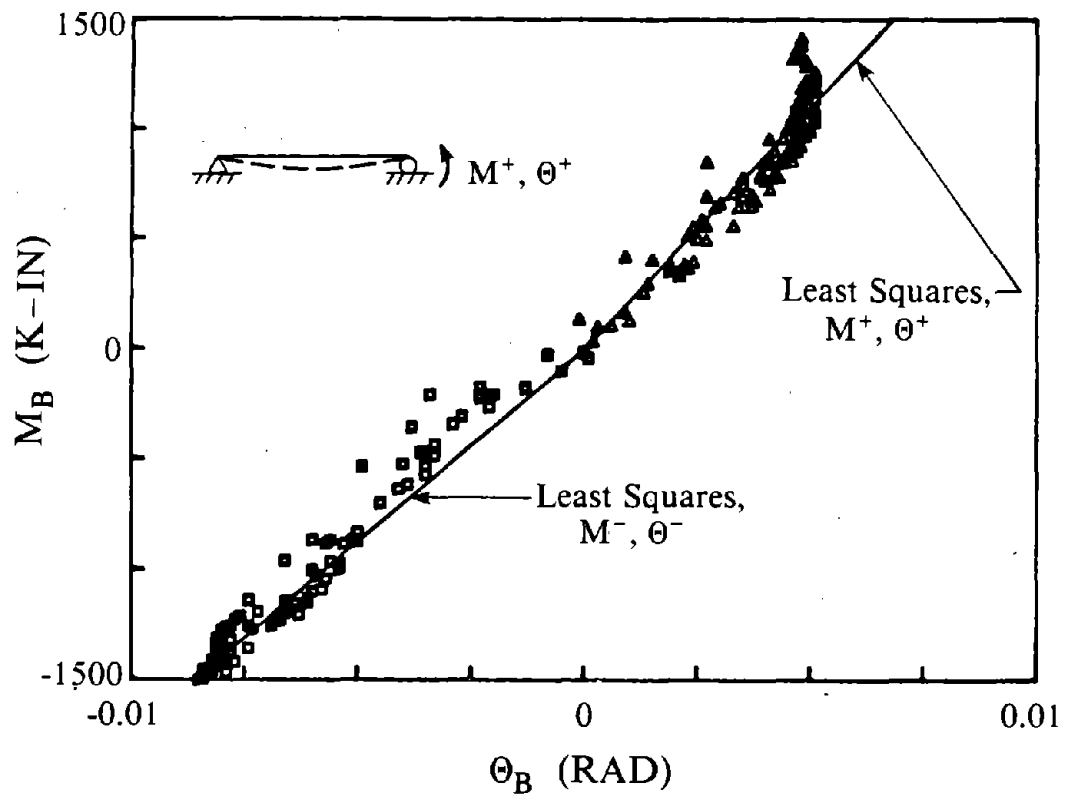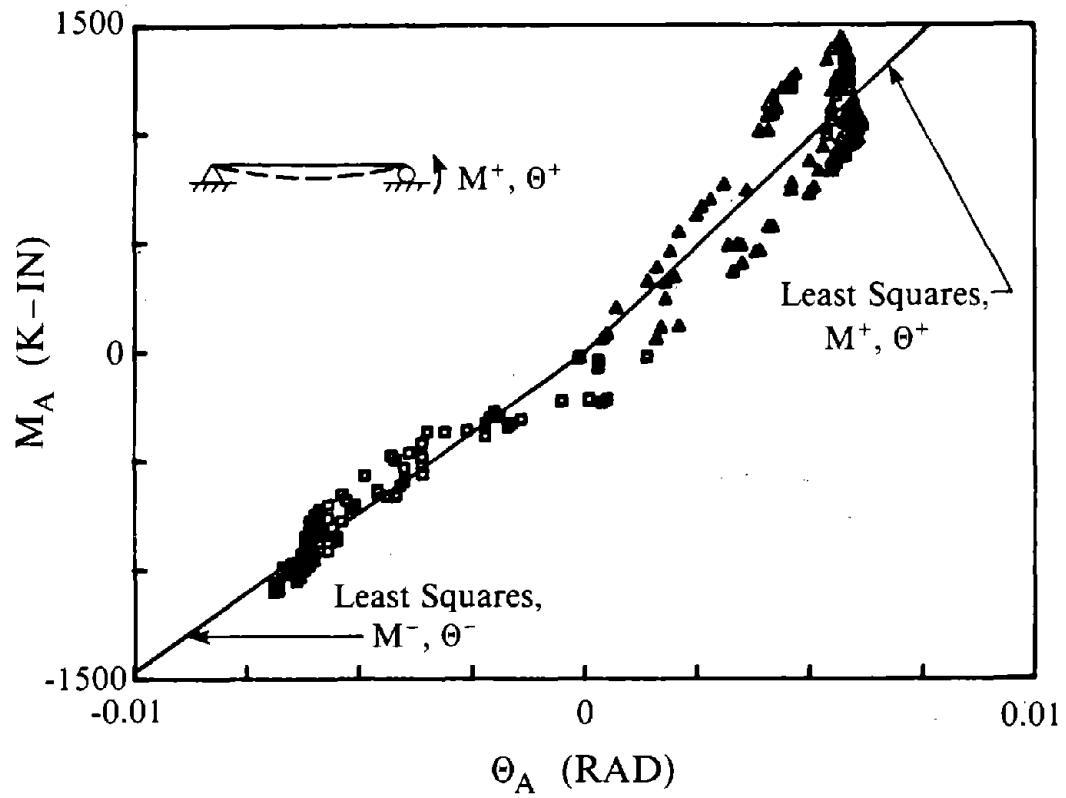
Fig. 4.59    Moment-Rotation Relationship of Floor Beam Outside the Link, Specimen A1.
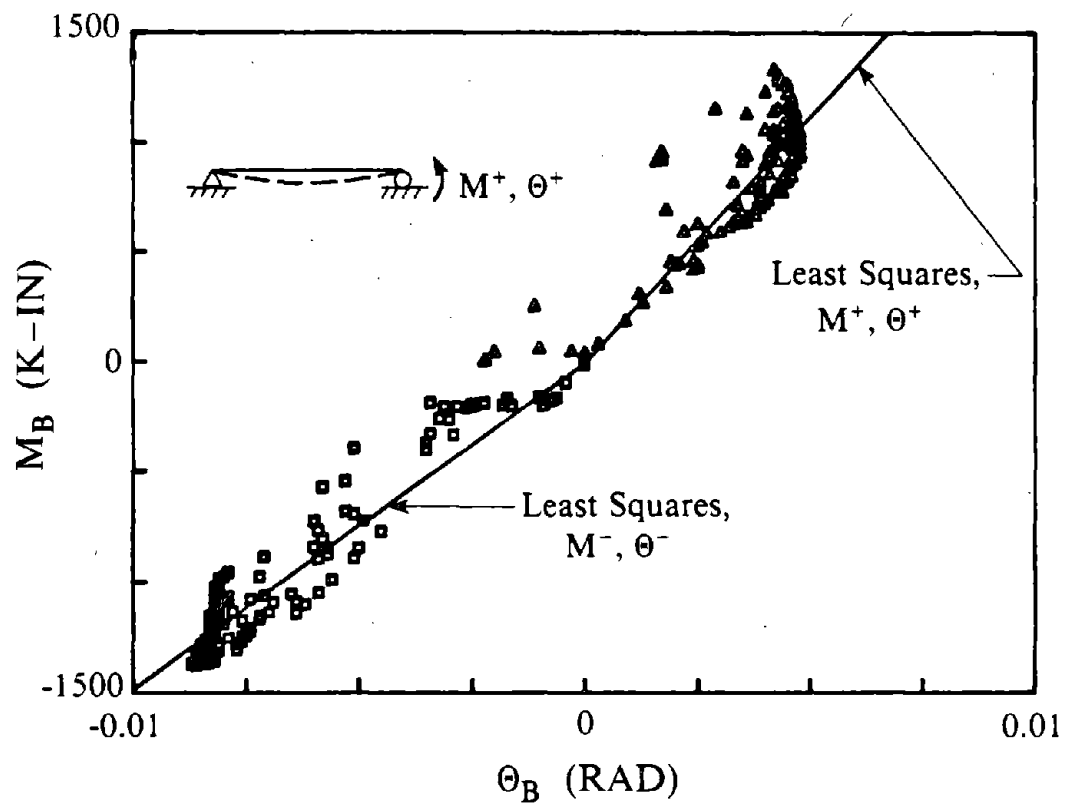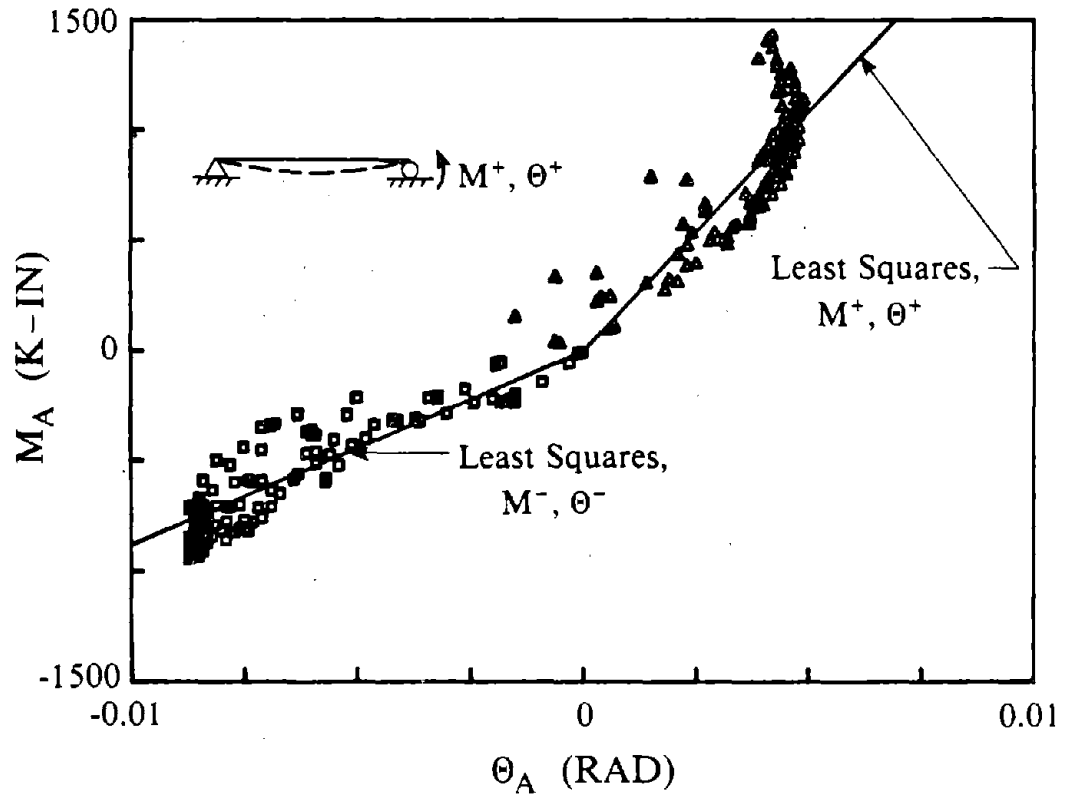
Fig. 4.60    Moment-Rotation Relationship of Floor Beam Outside the Link, Specimen B1.
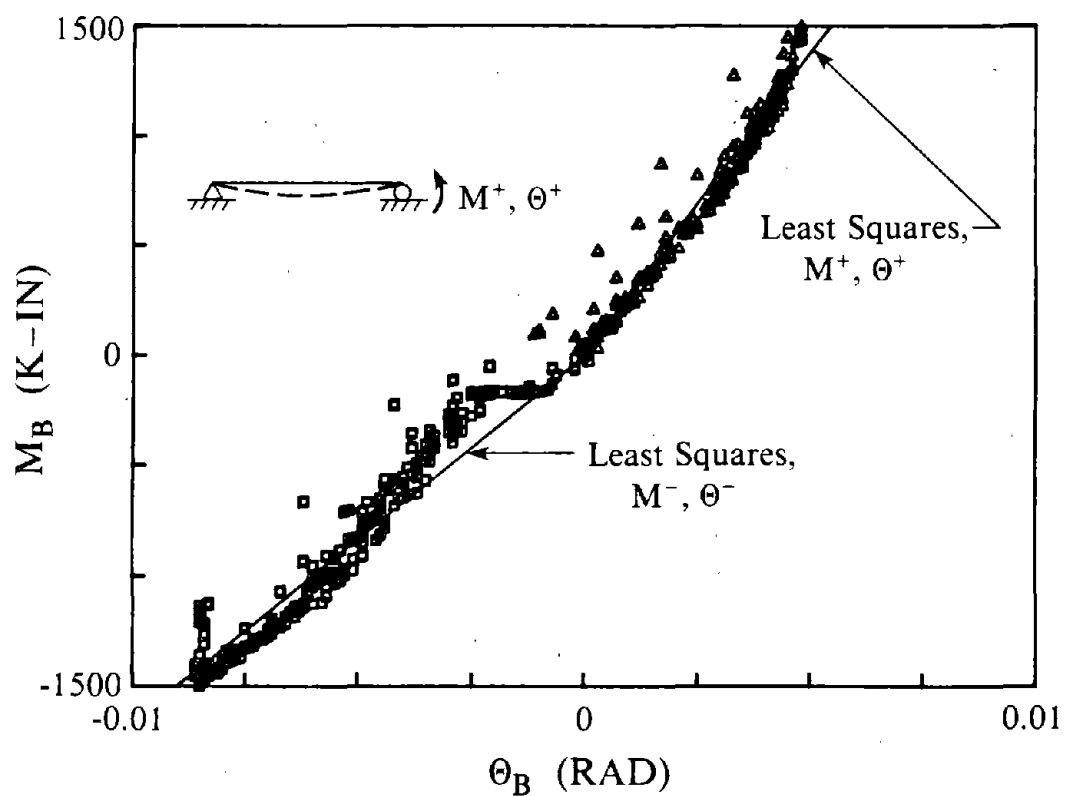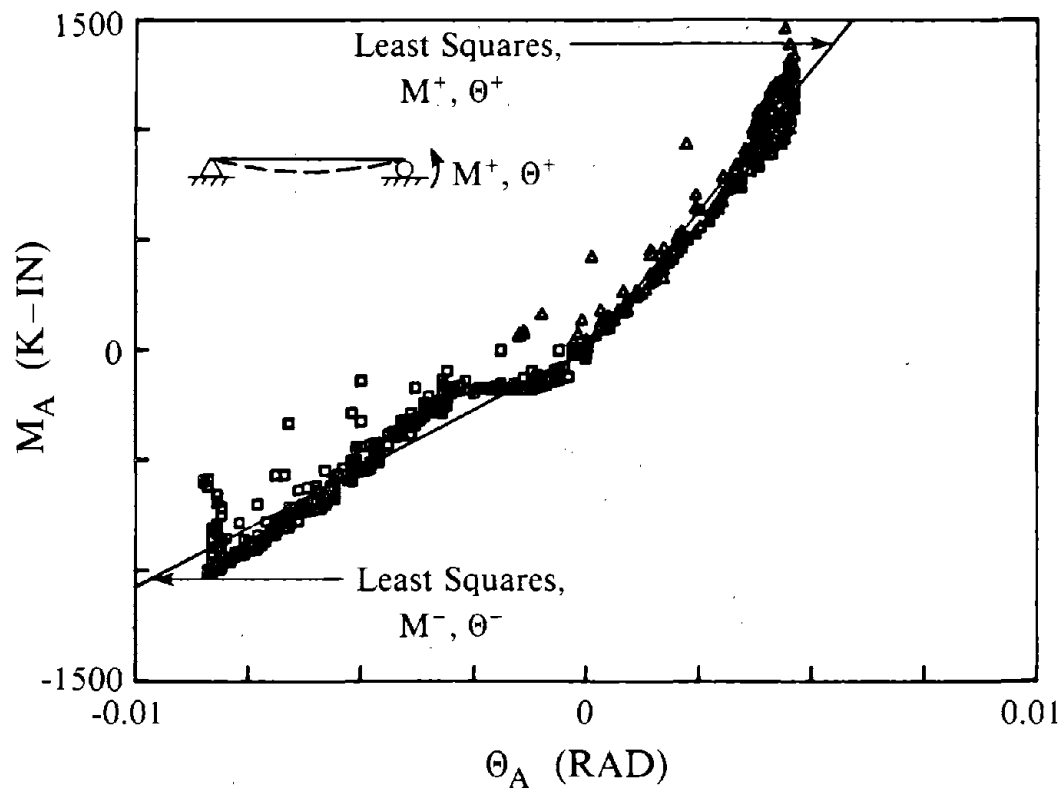
Fig. 4.61    Moment-Rotation Relationship of Floor Beam Outside the Link, Specimen C1.
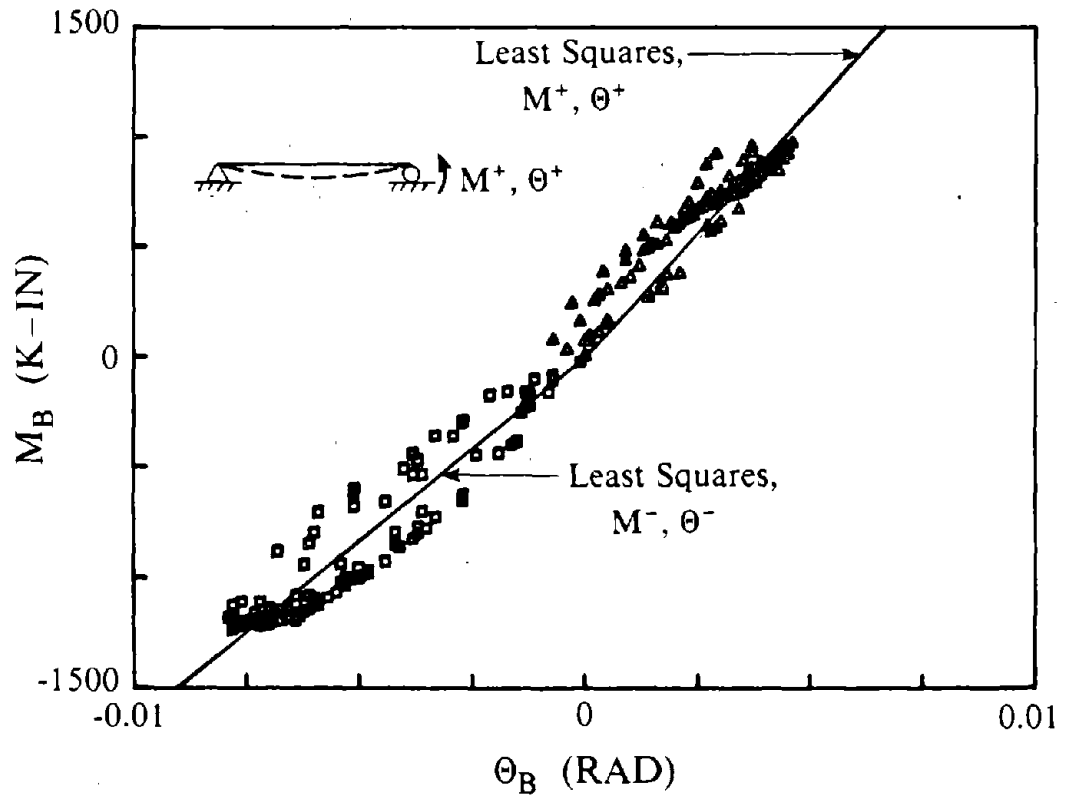
Fig. 4.62     Moment-Rotation Relationship of Floor Beam Outside the Link, Specimen A2.
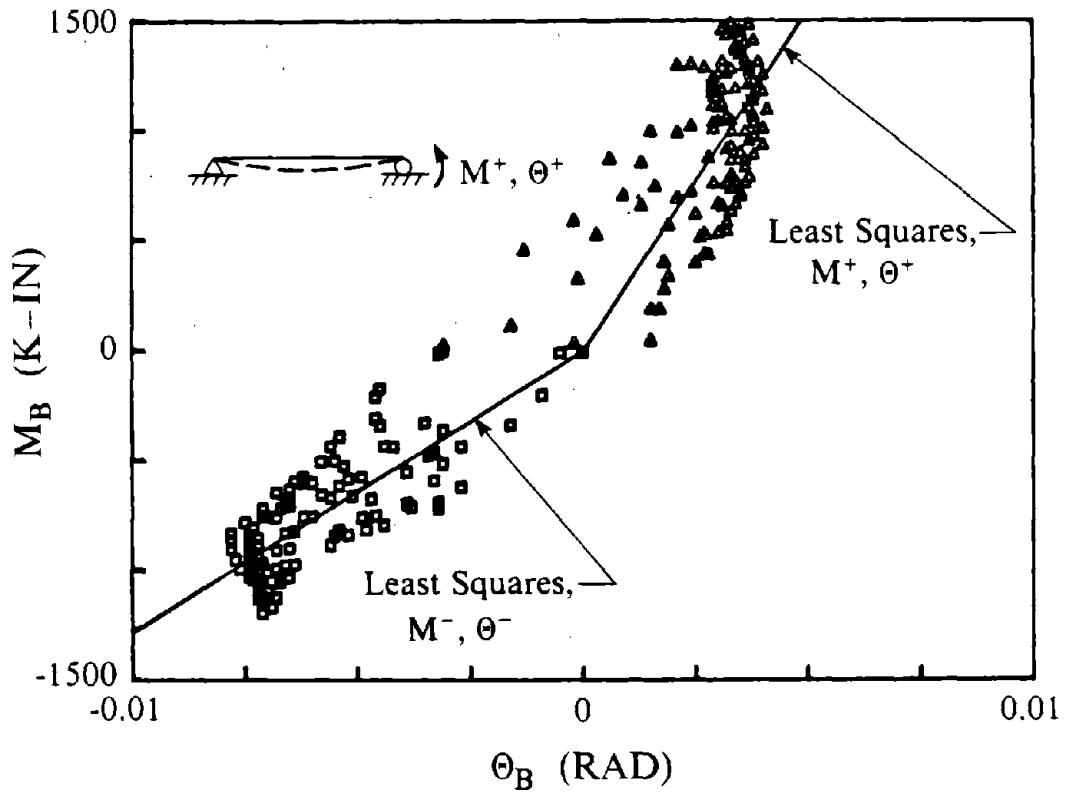


Fig. 4.63     Moment-Rotation Relationship of Floor Beam Outside the Link, Specimen B2.
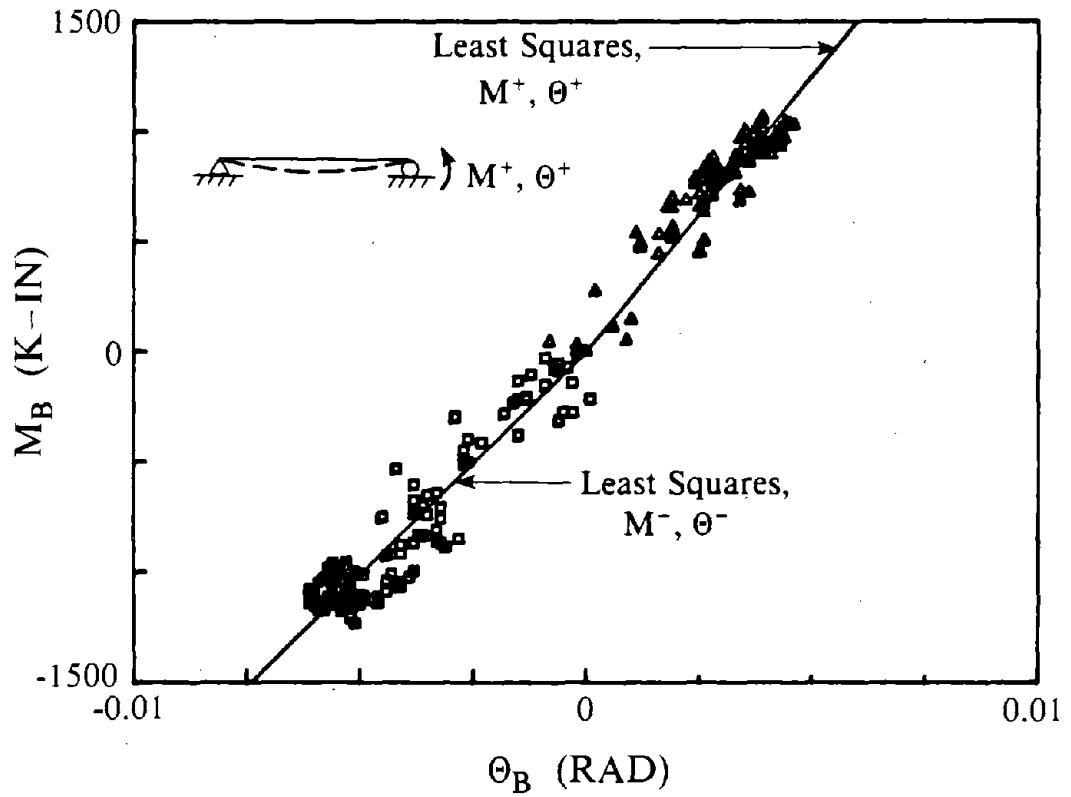
Fig. 4.64    Moment-Rotation Relationship of Floor Beam Outside the Link, Specimen C2.
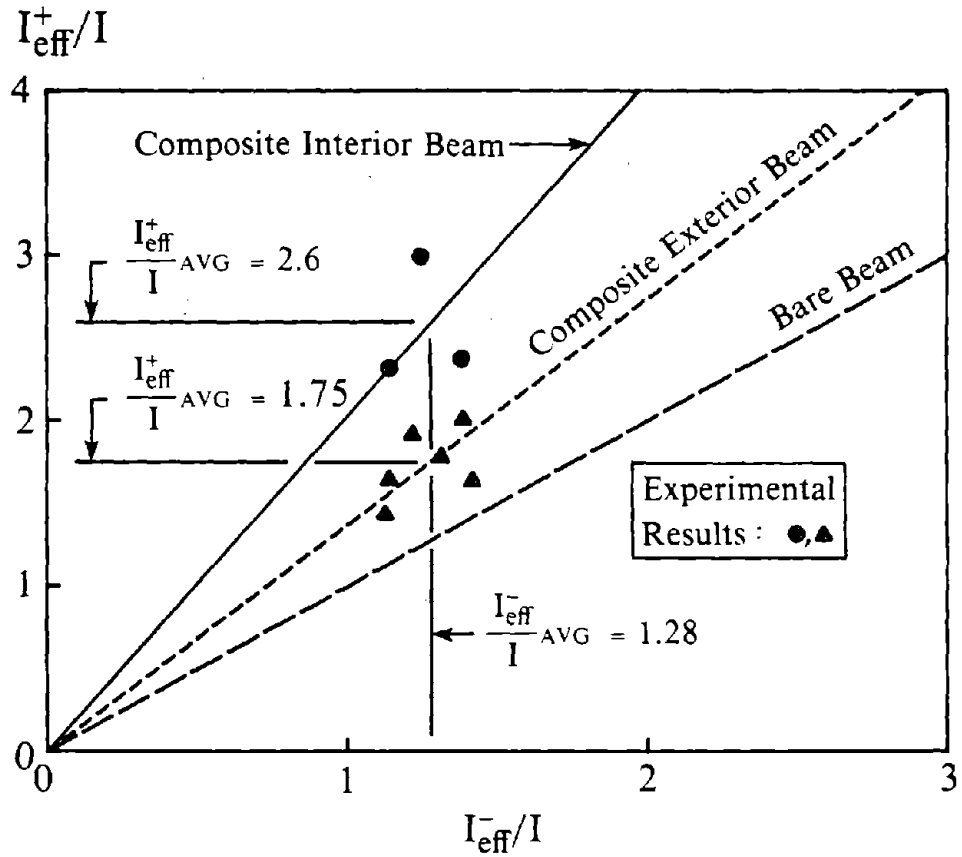
Fig. 4.65    Measured Effective Moment of Inertia for Composite Beams.
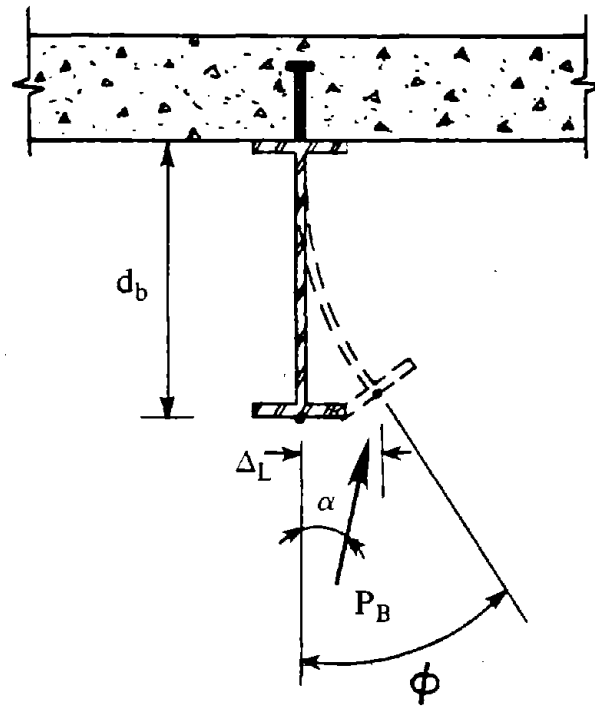
(a) Lateral Movement
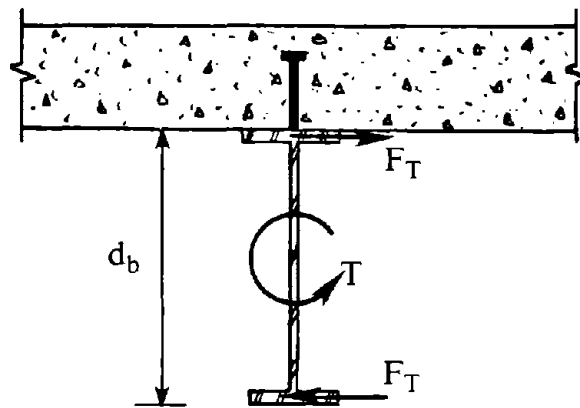


$$F_T = \frac{d_b P_B \sin\alpha + \Delta_L P_B \cos\alpha}{d_b}$$

(b) Restoring Flange Force $F_T$

Fig. 4.66  Lateral-Torsional Buckling of Composite Beam Resulting in
(a) Lateral Movement, Requiring (b) Restoring Flange Force $F_T$.
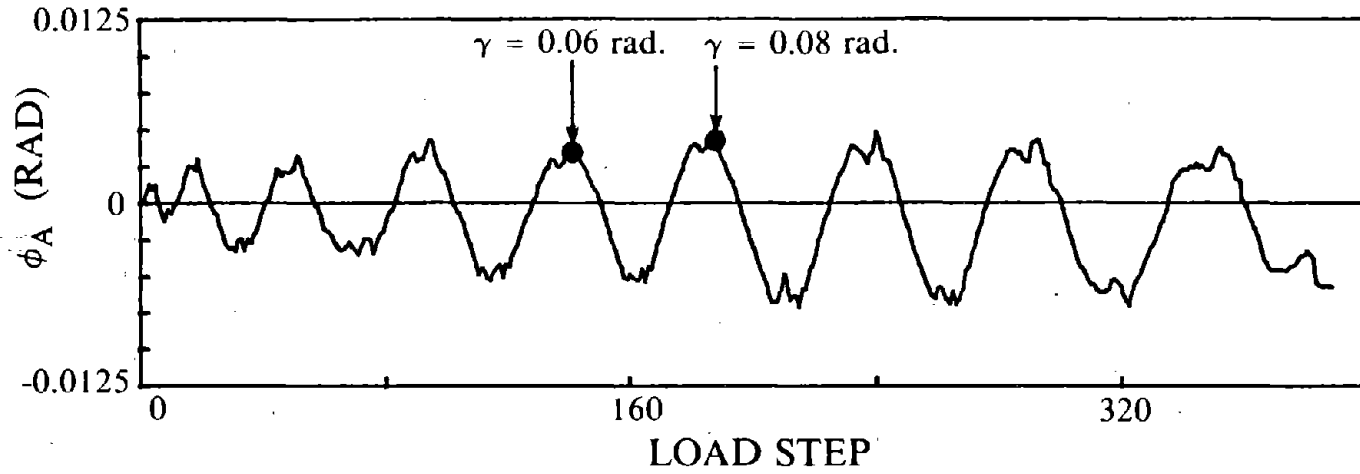
(a) End A
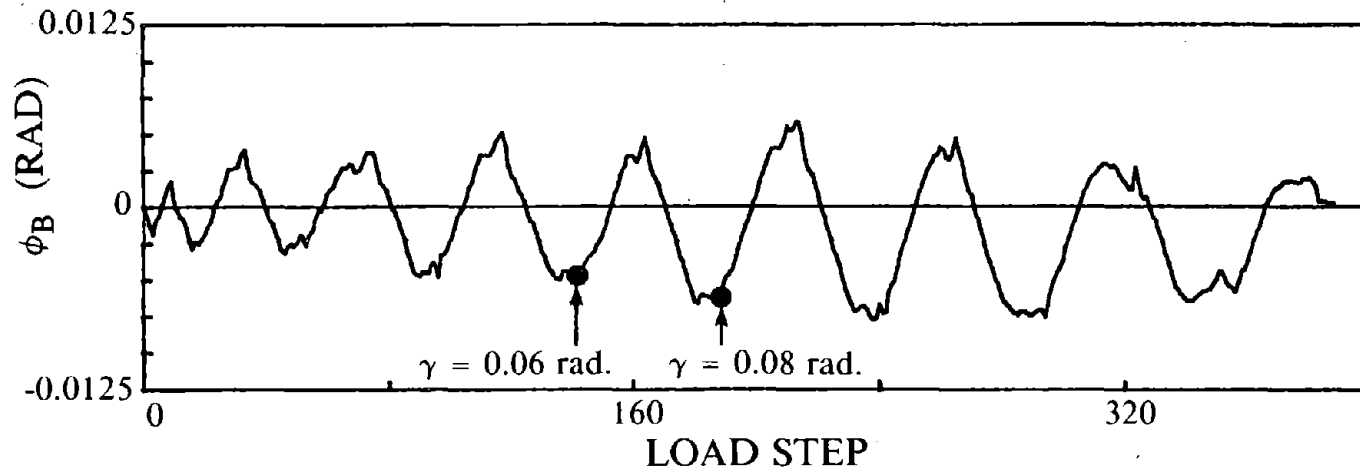
(b) End B

Fig. 4.67    Cross Sectional Twist Developed at Ends of Link, Specimen D1.
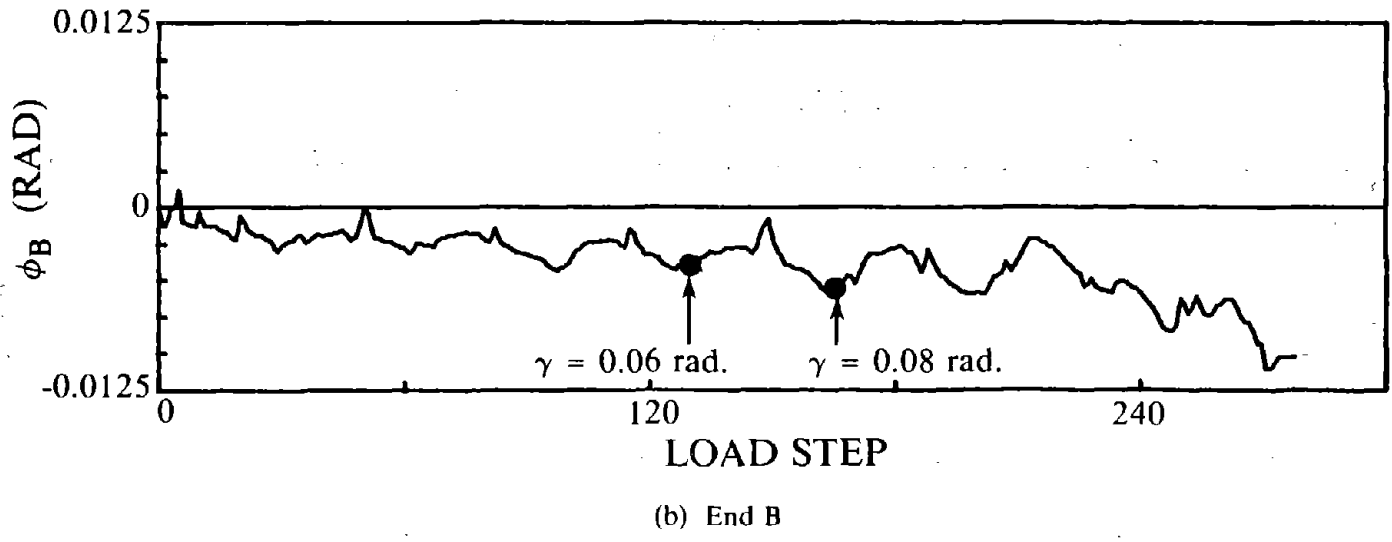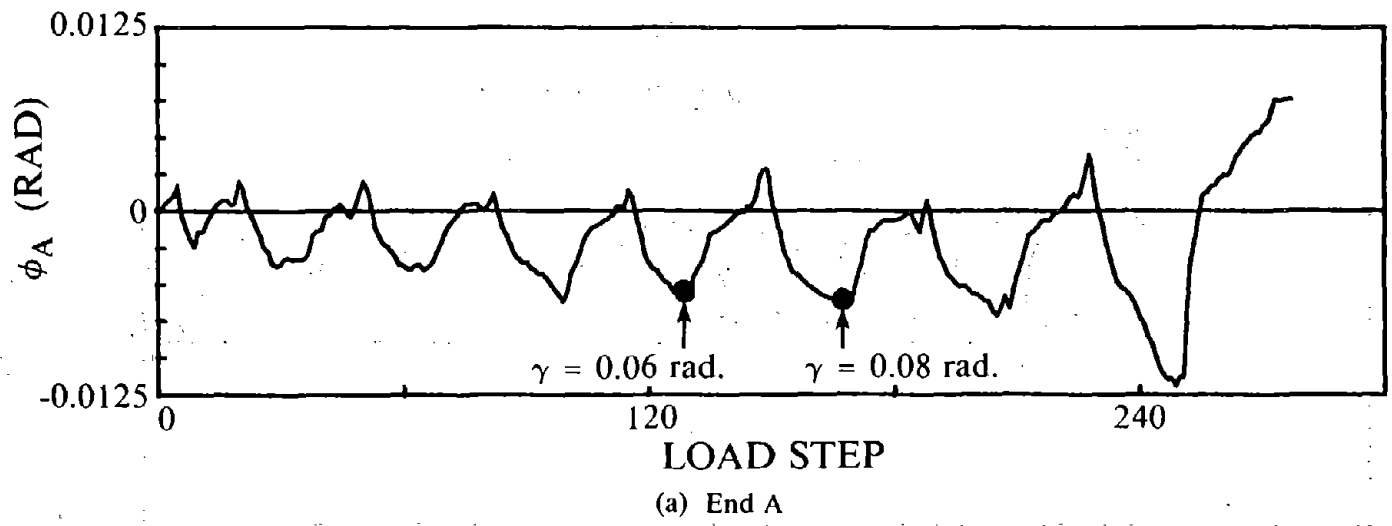
Fig. 4.68    Cross Sectional Twist Developed at Ends of Link, Specimen D2.
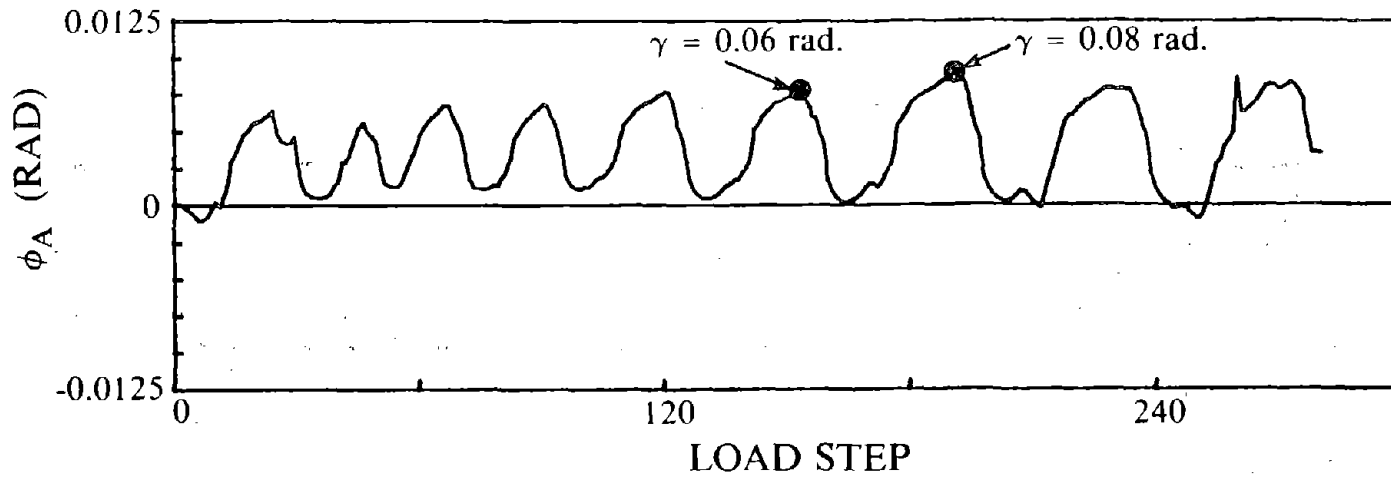
(a) End A
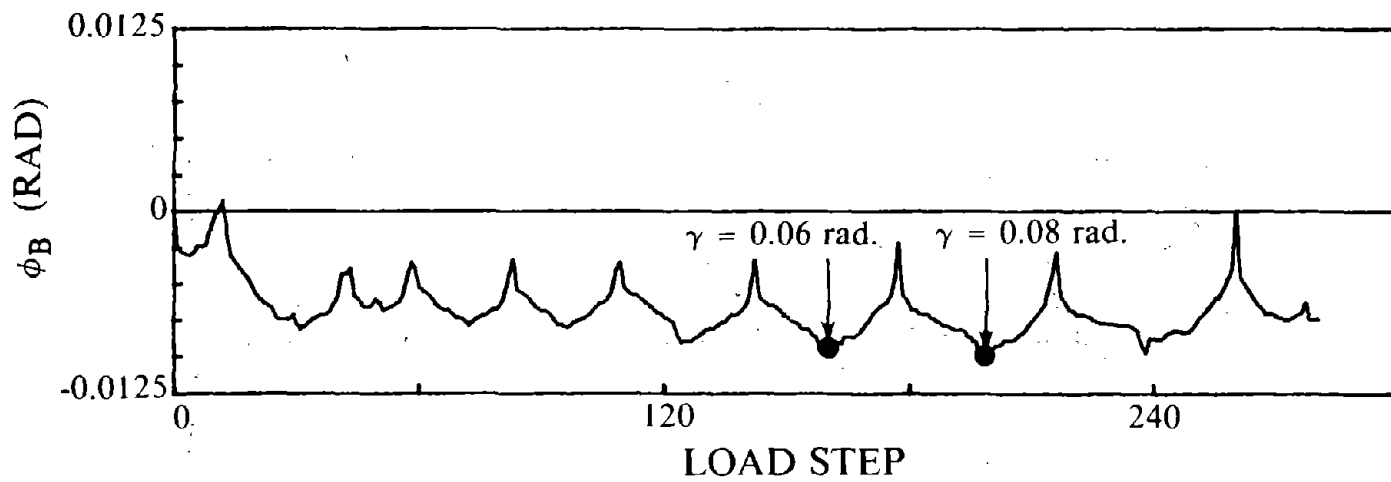
(b) End B

Fig. 4.69    Cross Sectional Twist Developed at Ends of Link, Specimen C2.
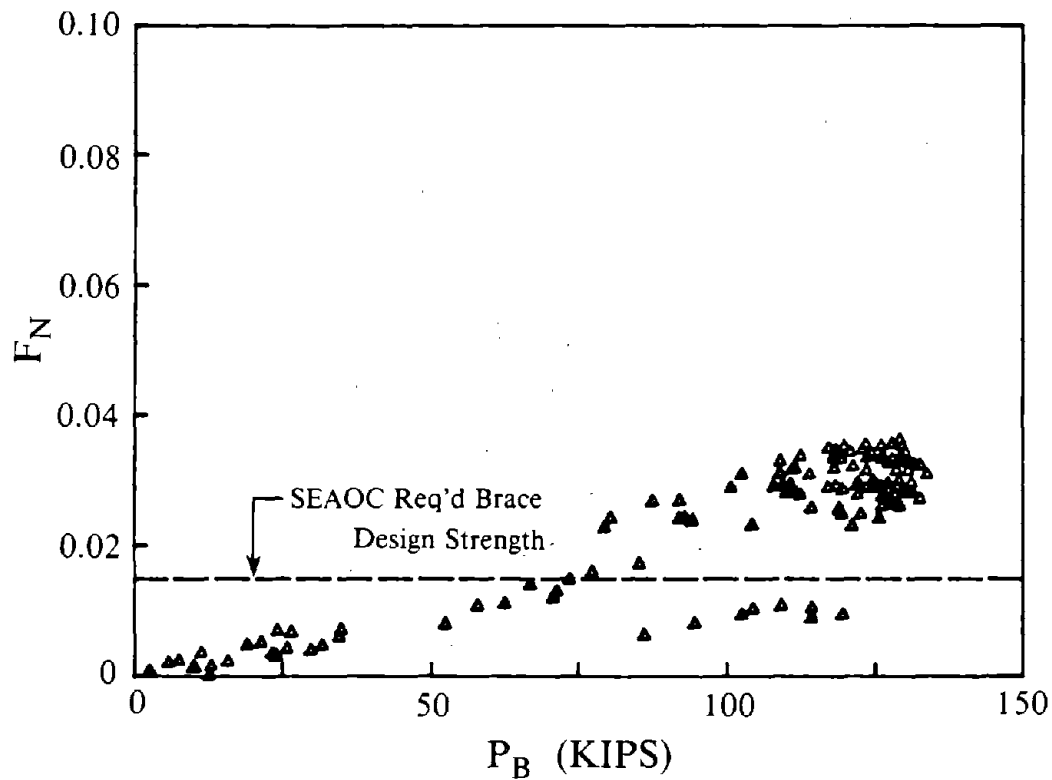
Fig. 4.70    Flange Force Ratio $F_N$ Developed at Link End B, Specimen C2.
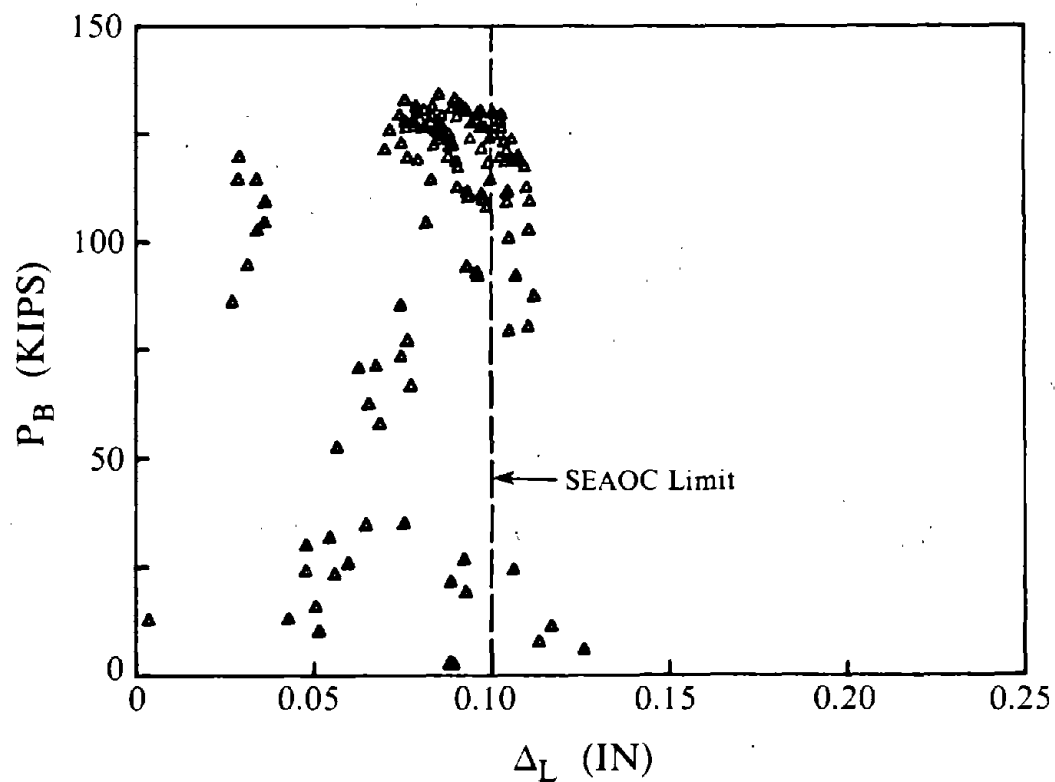


Fig. 4.71    Lateral Movement of Compression Flange at Link End B, Specimen C2.
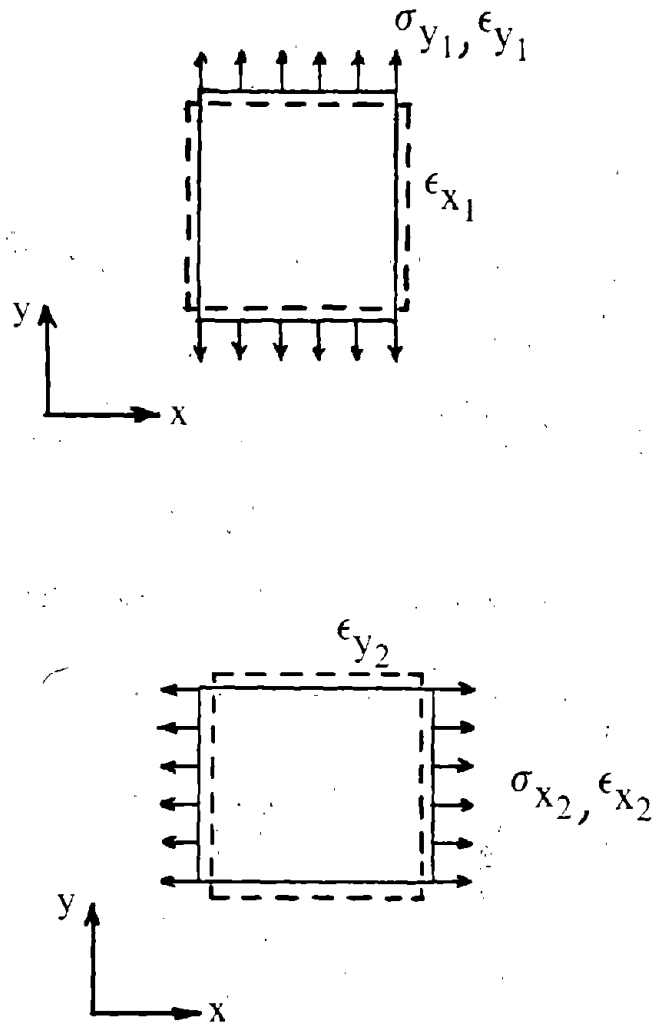
Fig. 5.1    Application of Betti's Reciprocal Theorem to Plane Stress Conditions.

$$@ x = L, \begin{cases} w = 0 \\ m_x = 0 \\ \sigma_x = 0 \\ \sigma_{xy} = 0 \end{cases}$$

@ y = $^-$b, $\omega$ = 0      @ y = b, $\omega$ = 0

$$@x = 0, \begin{cases} w = 0 \\ m_x = 0 \\ \sigma_x = 0 \\ \sigma_{xy} = 0 \end{cases} \qquad @y = 0, \begin{cases} v = 0 \\ \text{Beam-Slab Equilibrium} \\ \text{Beam-Slab Compatibility} \end{cases}$$

x,u
y,v

z,w

2b
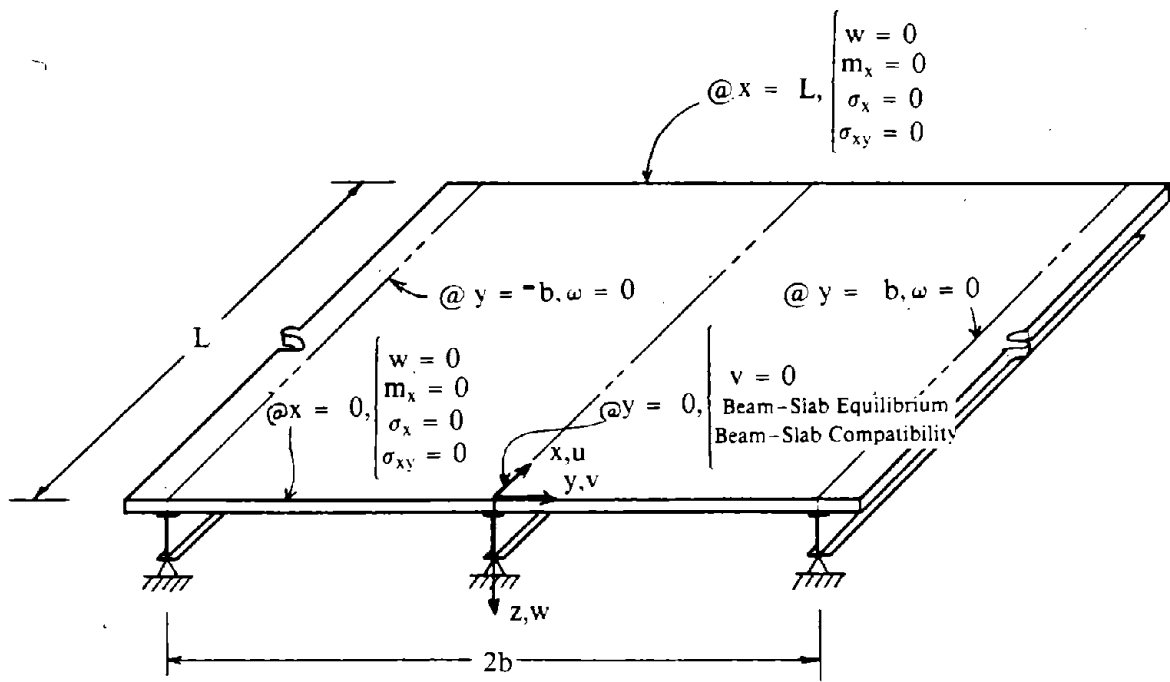
Fig. 5.2      Boundary Conditions for an Interior Composite Beam With Simple End Supports.

$$@ x = L, \begin{cases} w = 0 \\ m_x = 0 \\ \sigma_x = 0 \\ \sigma_{xy} = 0 \end{cases}$$

$$@ y = 0, \begin{cases} \sigma_y = 0 \\ m_y = 0 \\ \text{Beam-Slab Equilibrium} \\ \text{Beam-Slab Compatibility} \end{cases}$$

$$@ x = 0, \begin{cases} w = 0 \\ m_x = 0 \\ \sigma_x = 0 \\ \sigma_{xy} = 0 \end{cases}$$

x,u
y,v

z,w
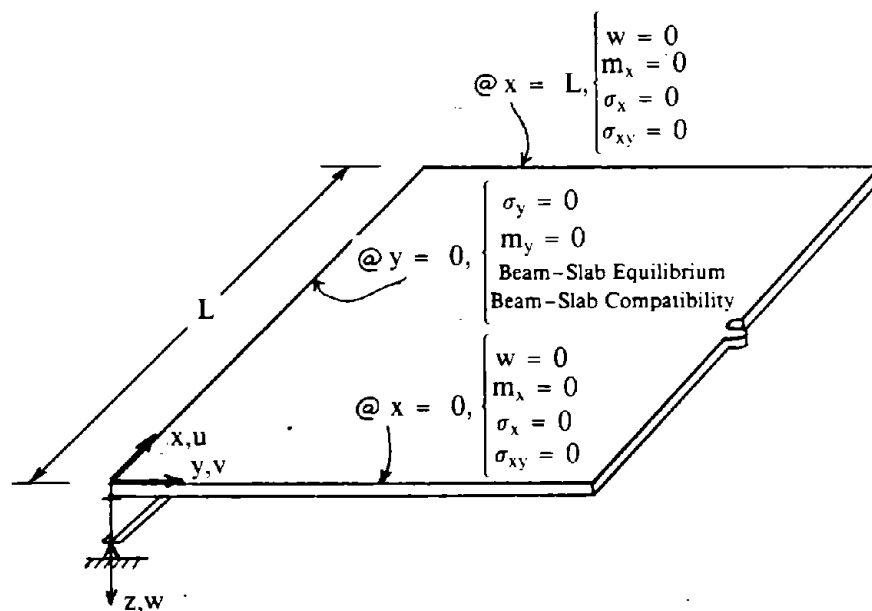
Fig. 5.3      Boundary Conditions for an Exterior Composite Beam With Simple End Supports.

276
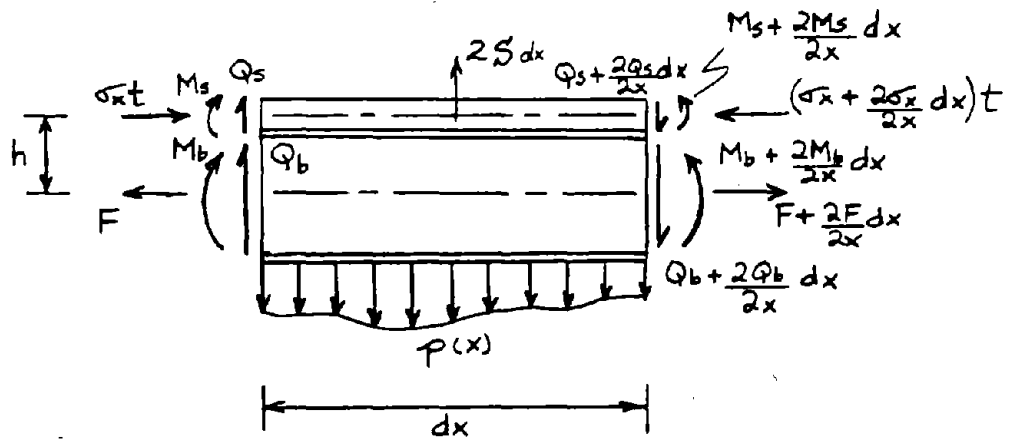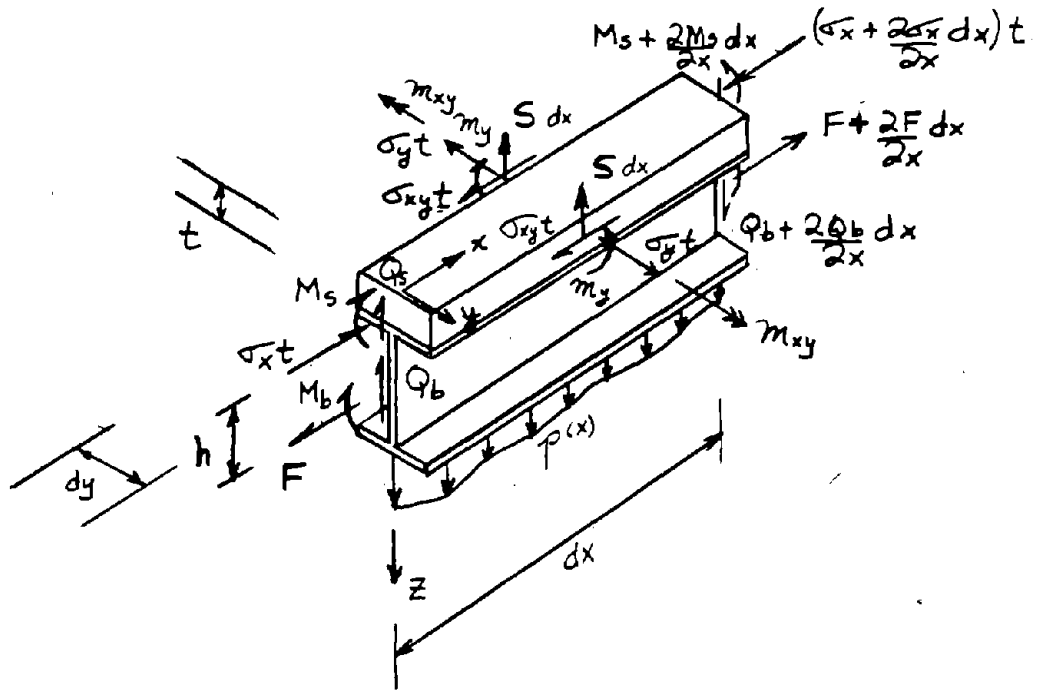


Fig. 5.4    Free Body Diagram at the Beam-Floor Slab Juncture for an Interior Composite Beam Model.
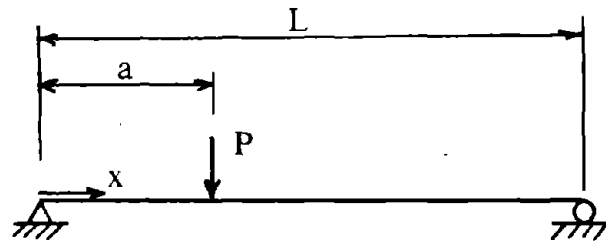
Fig. 5.5     Concentrated Force P Acting on Beam.
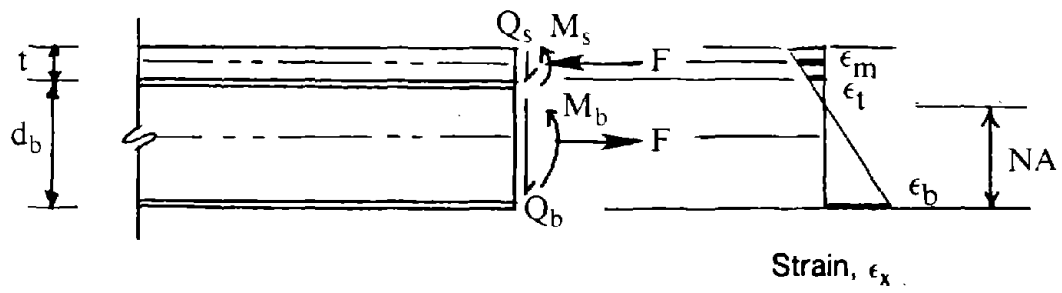


Fig. 5.6     Curvature at Beam-Slab Juncture.

278
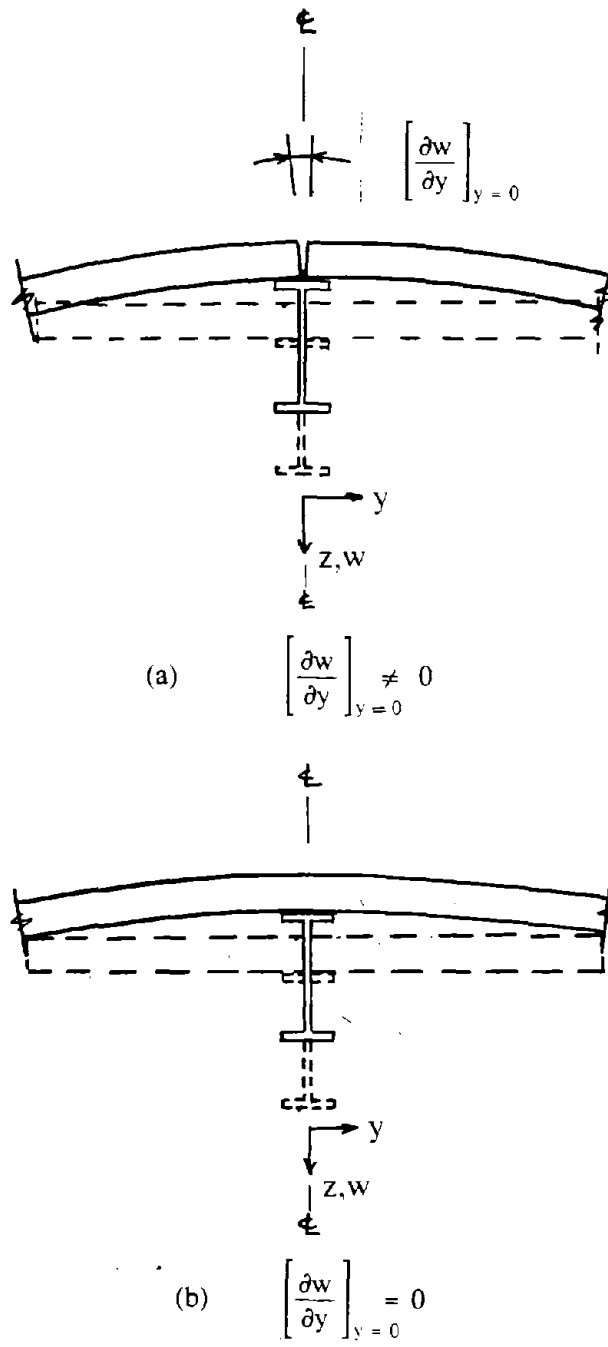


Fig. 5.7    Conditions of Floor Slab Above Beam for
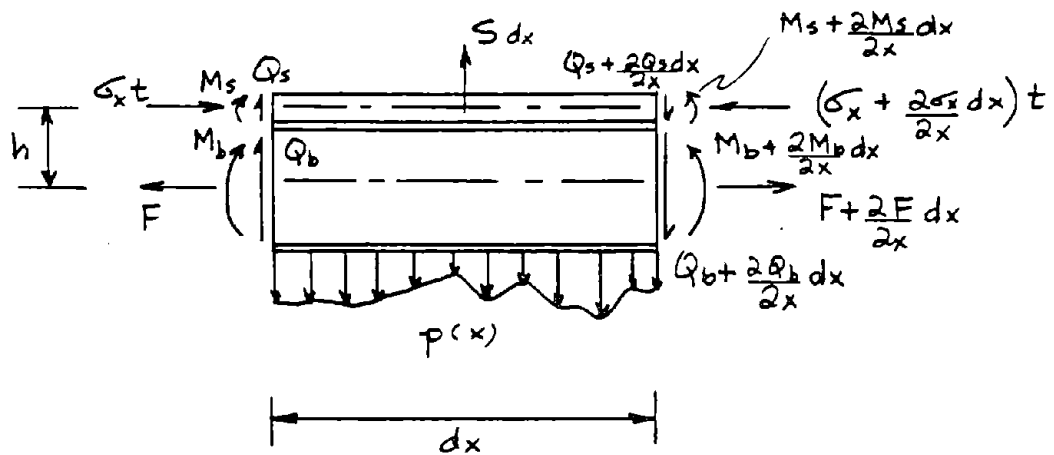(a) Nonzero Slope, and (b) Zero Slope.
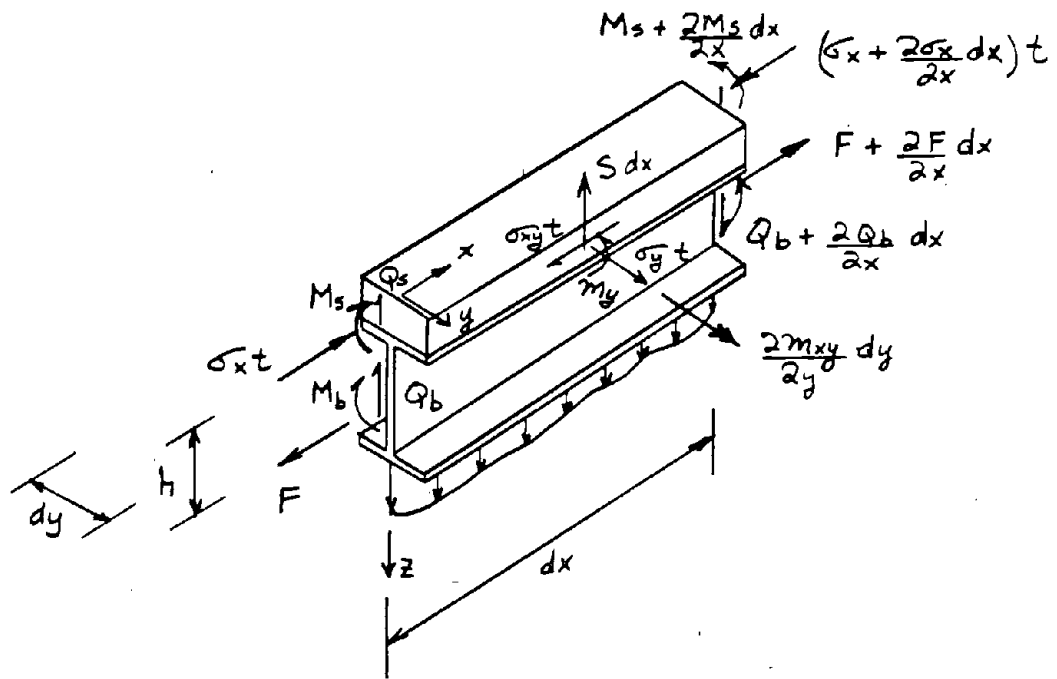
$M_s + \frac{\partial M_s}{\partial x} dx$

$\left(\sigma_x + \frac{\partial \sigma_x}{\partial x} dx\right) t$

$F + \frac{\partial F}{\partial x} dx$

$S\, dx$

$\sigma_{xy} t$

$Q_b + \frac{\partial Q_b}{\partial x} dx$

$x$

$\sigma_y t$

$\sigma_y t$

$Q_s$

$M_s$

$m_y$

$y$

$\sigma_x t$

$\frac{\partial m_{xy}}{\partial y} dy$

$M_b$

$Q_b$

$h$

$F$

$dy$

$z$

$dx$

$S\, dx$

$M_s + \frac{\partial M_s}{\partial x} dx$

$\sigma_x t$

$M_s$

$Q_s$

$Q_s + \frac{\partial Q_s}{\partial x} dx$

$\left(\sigma_x + \frac{\partial \sigma_x}{\partial x} dx\right) t$

$h$

$M_b$

$Q_b$

$M_b + \frac{\partial M_b}{\partial x} dx$

$F$

$F + \frac{\partial F}{\partial x} dx$

$Q_b + \frac{\partial Q_b}{\partial x} dx$

$p(x)$

$dx$

Fig. 5.8    Free Body Diagram at the Beam-Floor Slab Juncture for an Exterior Composite Beam Model.
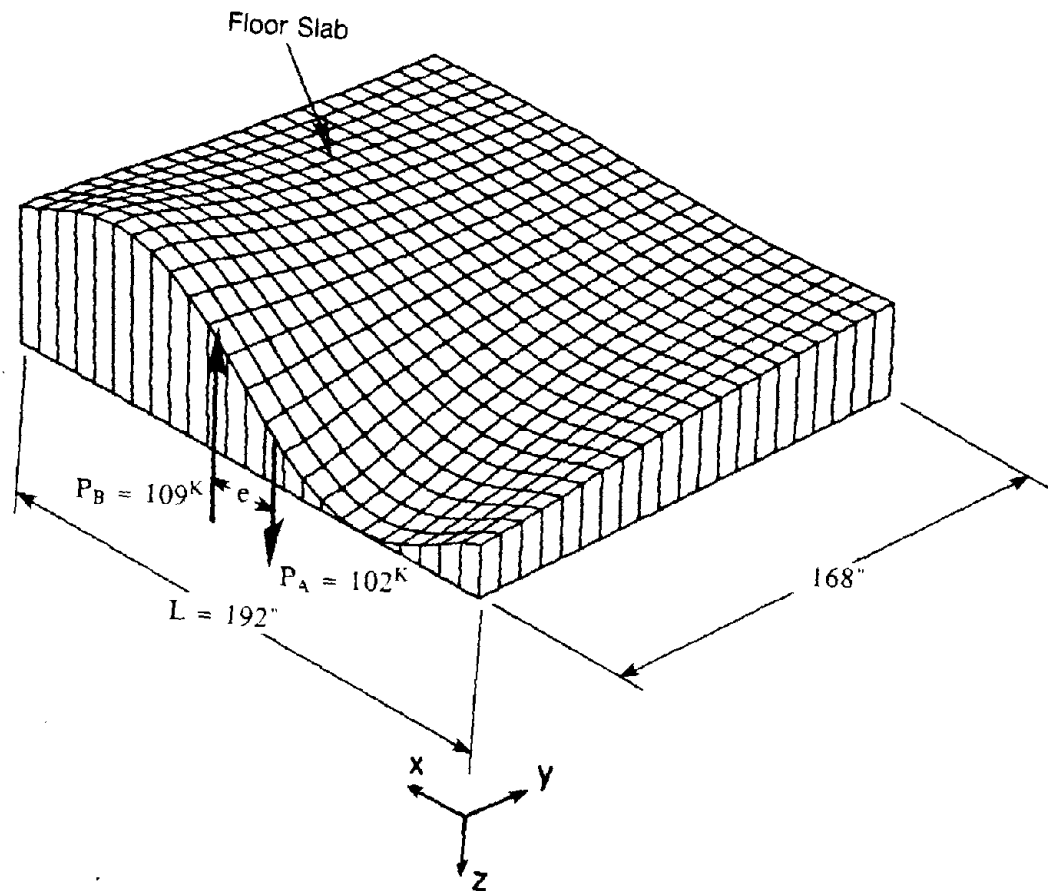
Fig. 5.9    Exaggerated Vertical Floor Slab Displacements for Exterior
Composite Beam Model of Specimen A1 at Initial Yielding.
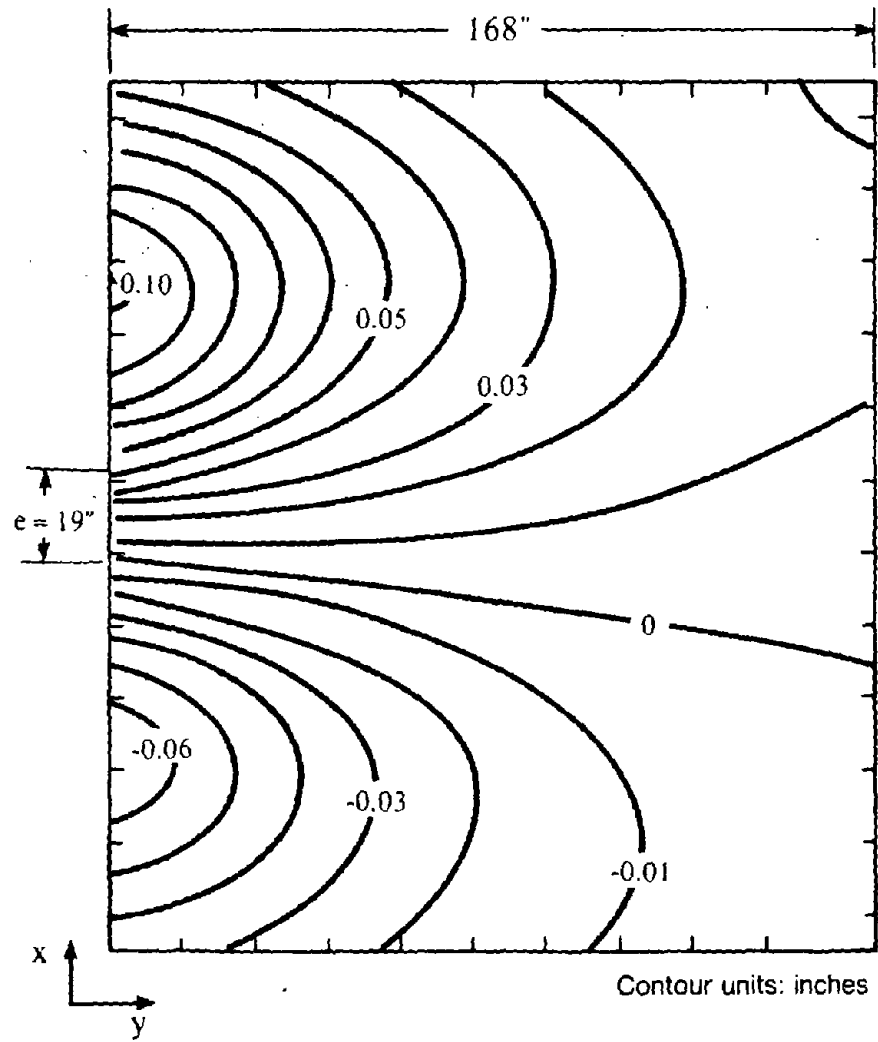
Fig. 5.10    Vertical Floor Slab Displacement Contours for Exterior
             Composite Beam Model of Specimen A1 at Initial Yielding.
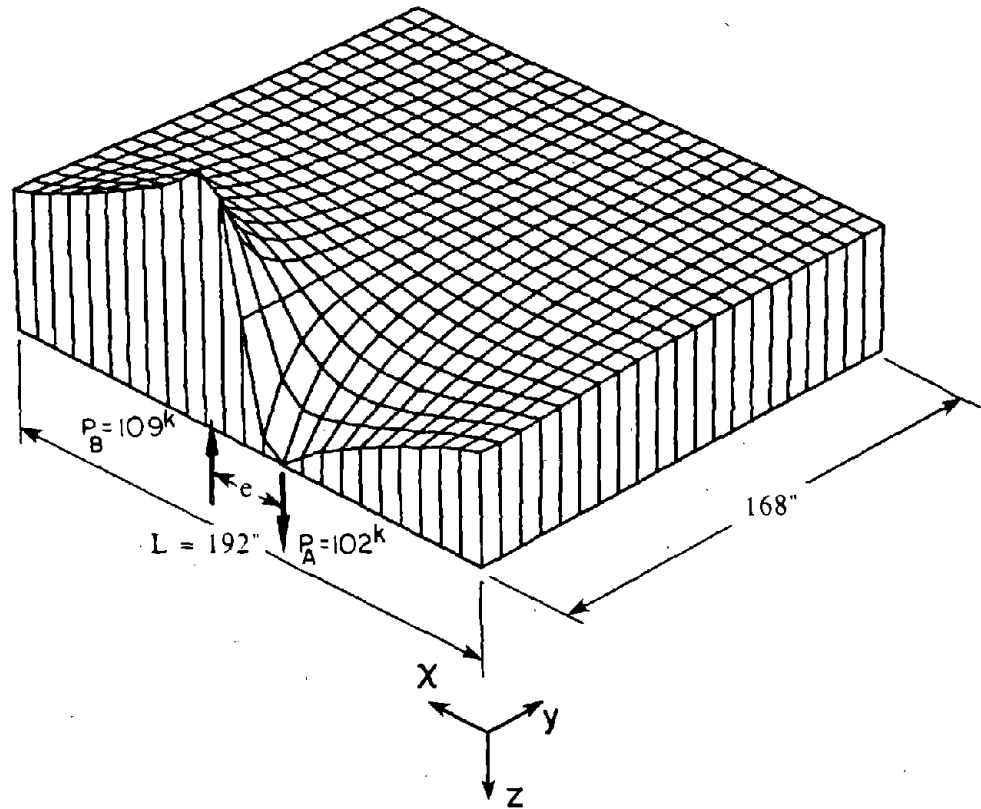
Fig. 5.11    Exaggerated Floor Slab Normal Stress $\sigma_x$ for Exterior Composite Beam Model of Specimen A1 at Initial Yielding.
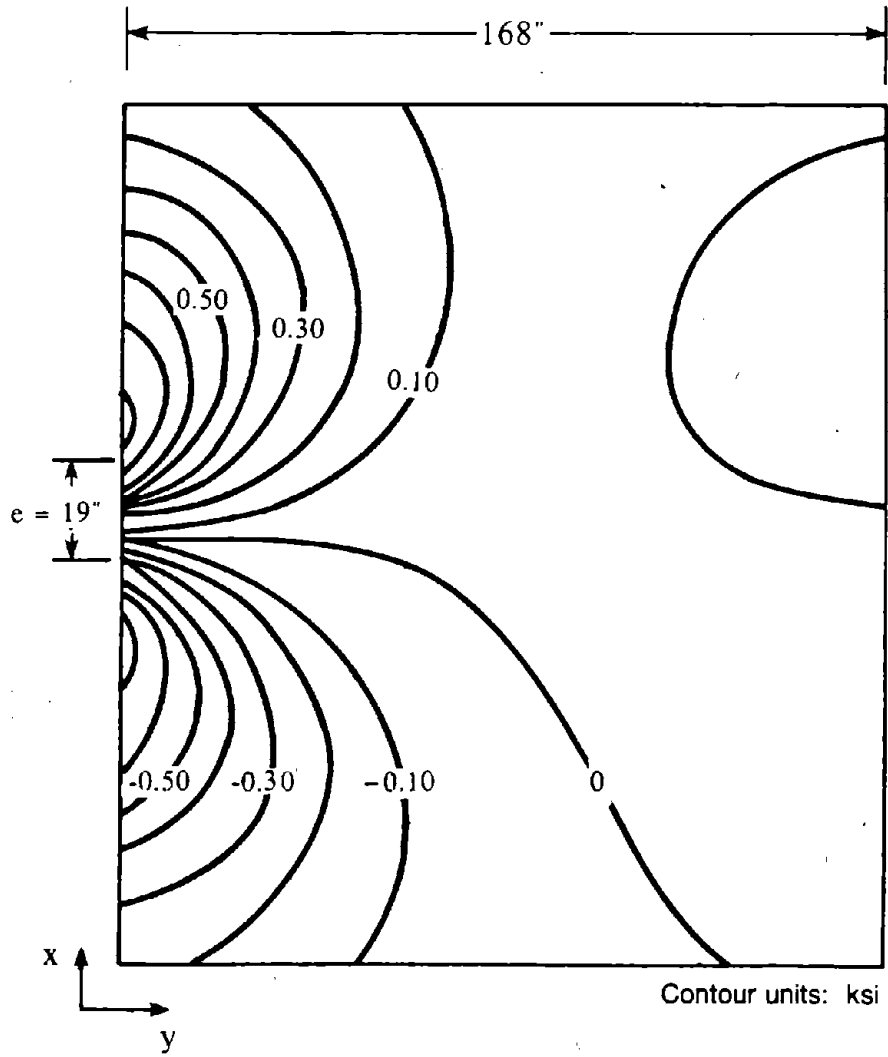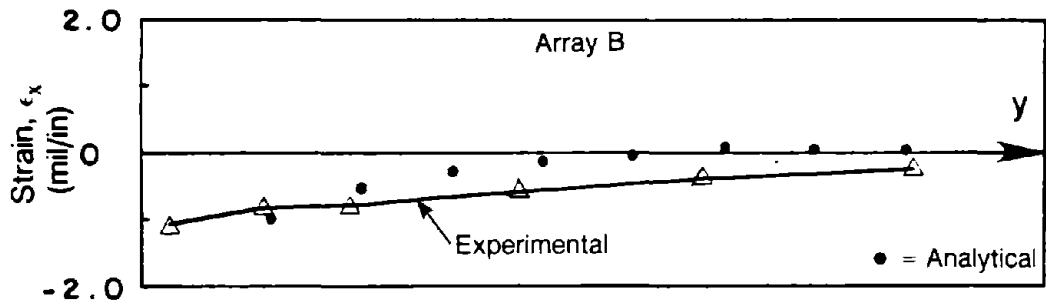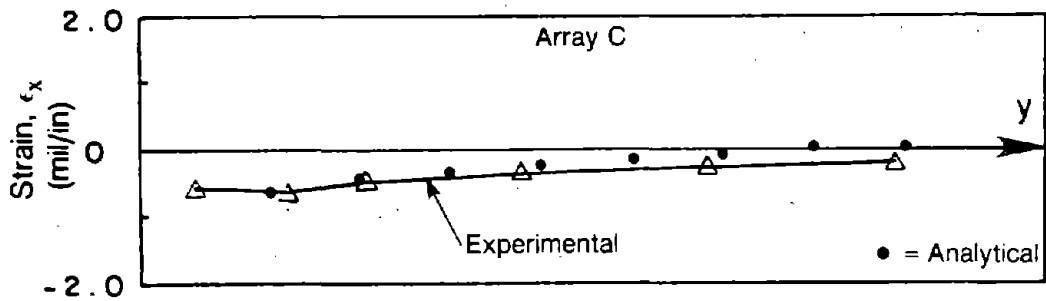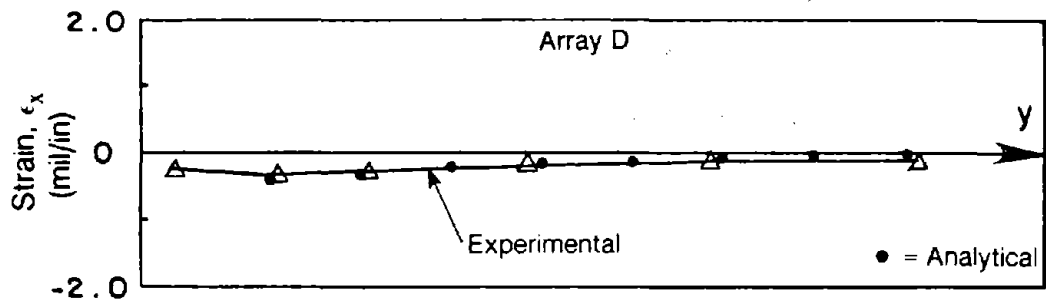
Fig. 5.12  Floor Slab Normal Stress $\sigma_x$ Contours for Exterior
Composite Beam Model of Specimen A1 at Initial Yielding.

(a) Transverse Section at 4.25 in. From Link End

(b) Transverse Section at 13.38 in. From Link End

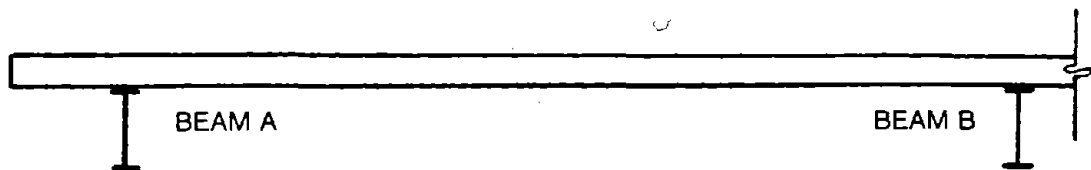(c) Transverse Section at 28.25 in. From Link End

Fig. 5.13    Comparison of Floor Slab Longitudinal Strain $\epsilon_x$ for Exterior Composite Beam Model and Specimen A1 During Cycle 1 at $\gamma = -0.02$ rad.
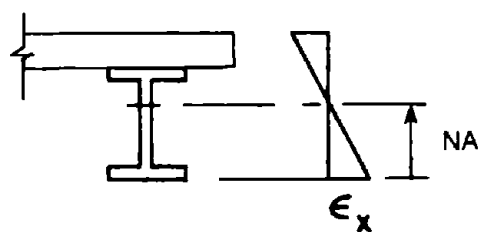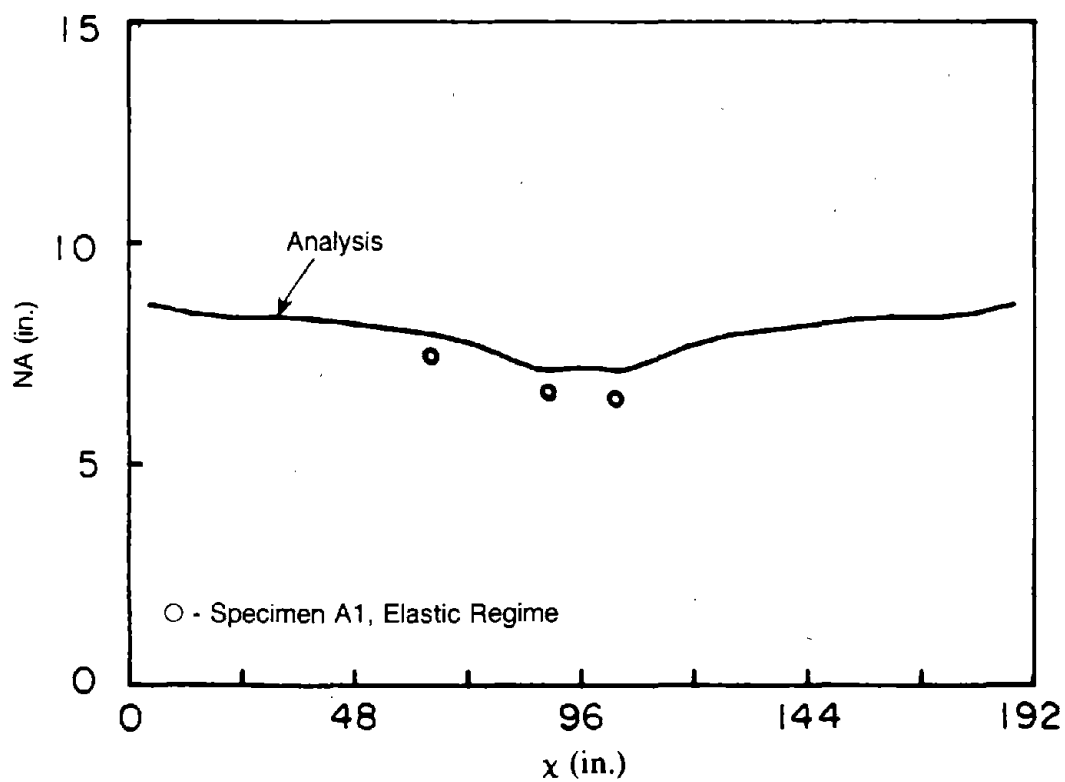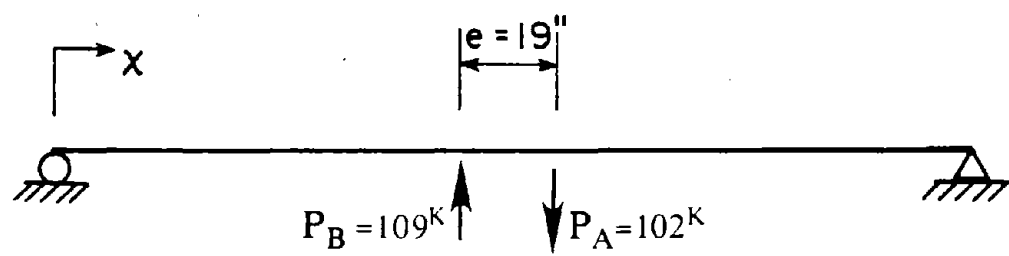
285



Fig. 5.14    Comparison of Neutral Axis Location Along Beam for Exterior
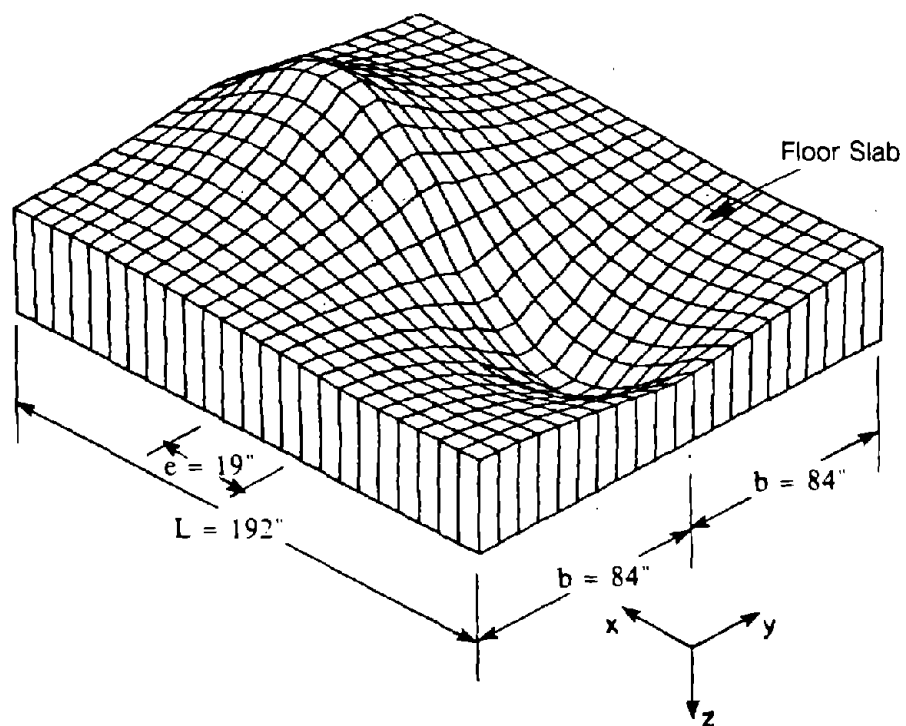Composite Beam Model and Specimen A1.

Fig. 5.15    Exaggerated Vertical Floor Slab Displacements for Interior
Composite Beam Model of Specimen B1 With Equal
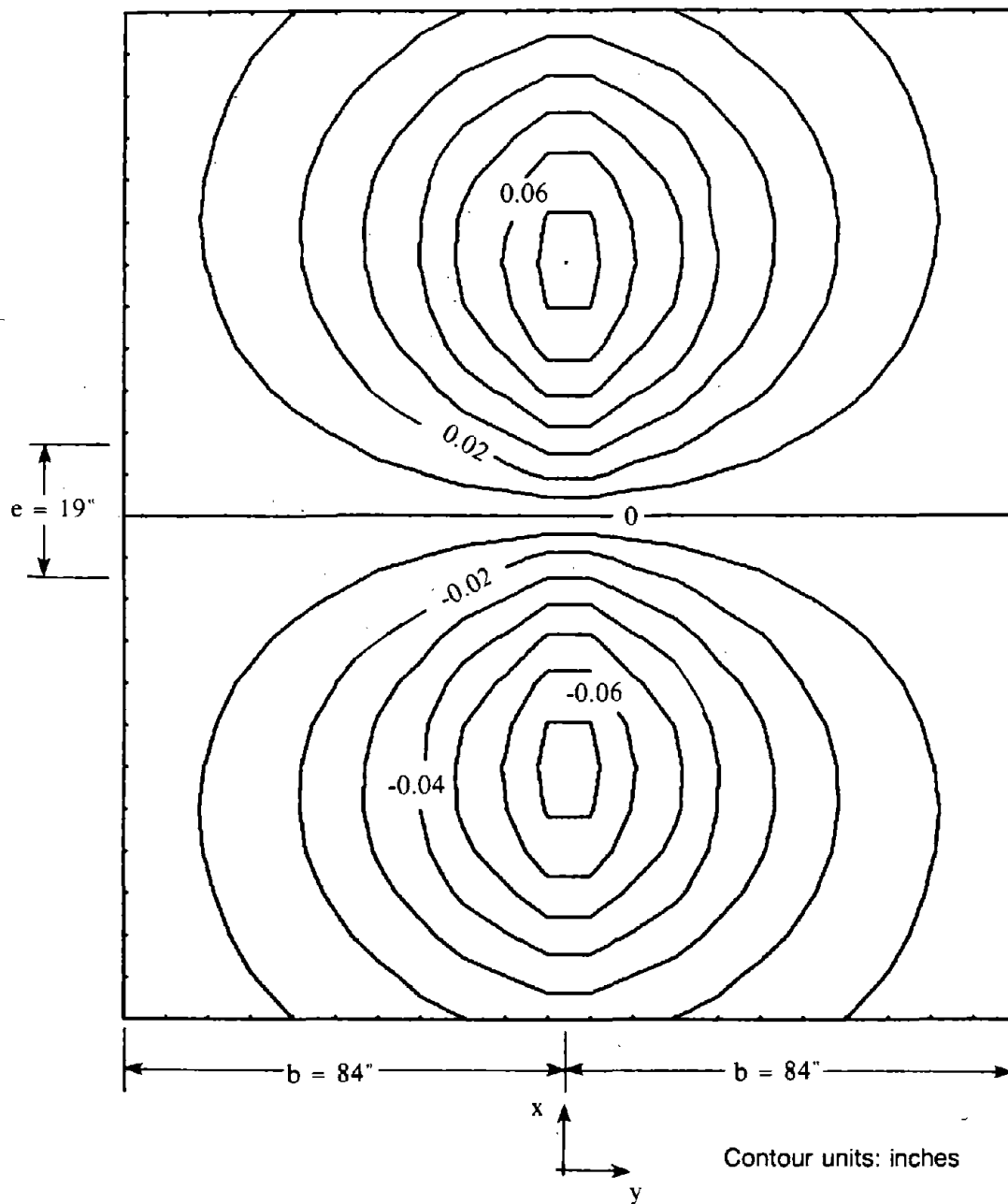Loads of 110 kips.

Fig. 5.16    Vertical Floor Slab Displacement Contours for Interior Composite
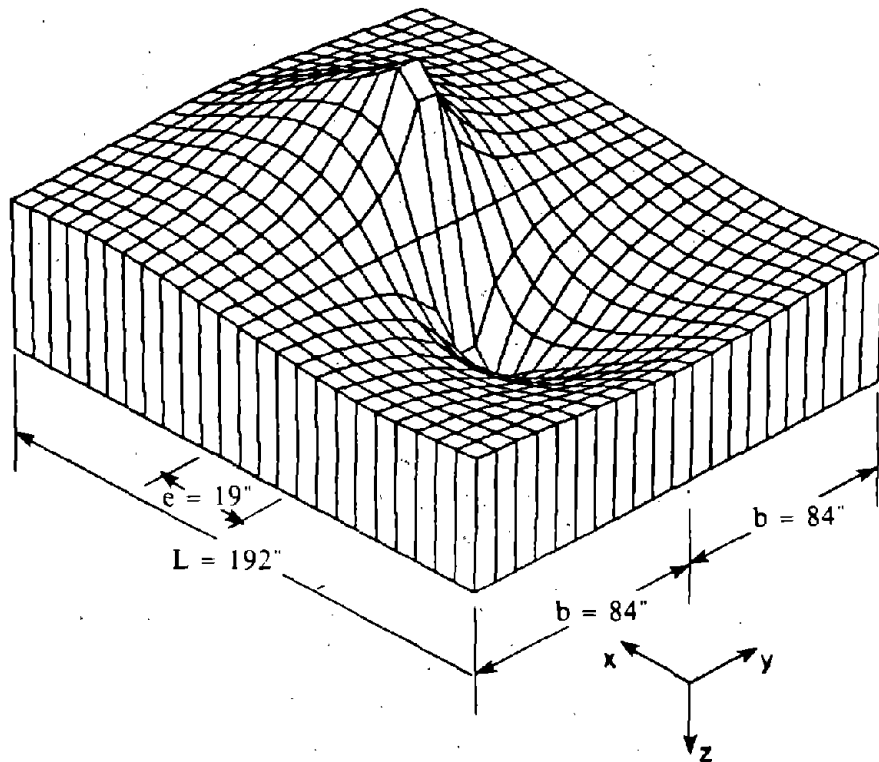Beam Model of Specimen B1 With Equal Loads of 110 kips.

Fig. 5.17    Exaggerated Floor Slab Normal Stress $\sigma_x$ for Interior
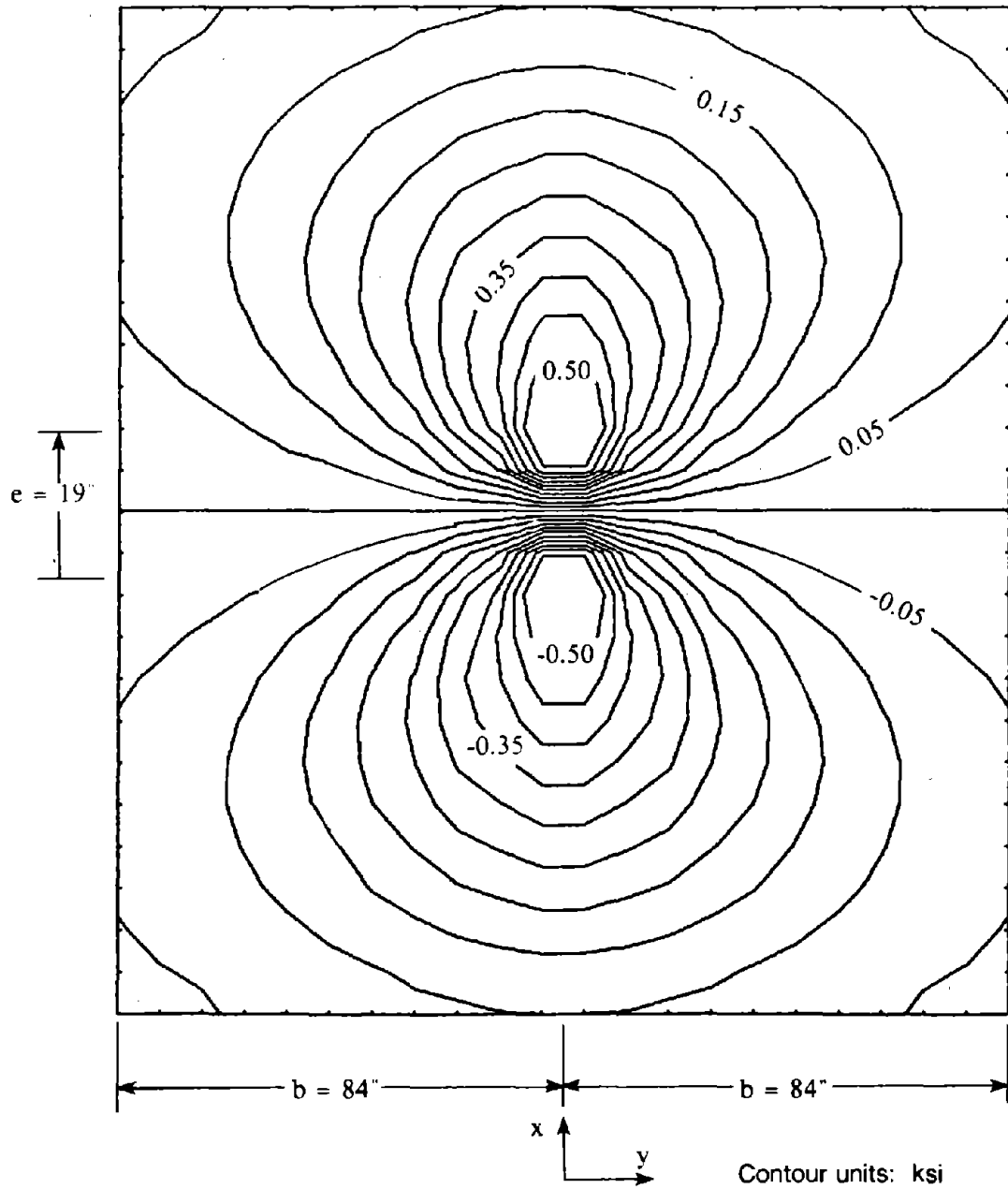Composite Beam Model of Specimen B1 With Equal
Loads of 110 kips.

Fig. 5.18    Floor Slab Normal Stress $\sigma_x$ Contours for Interior
Composite Beam Model of Specimen B1 With Equal
Loads of 110 kips.
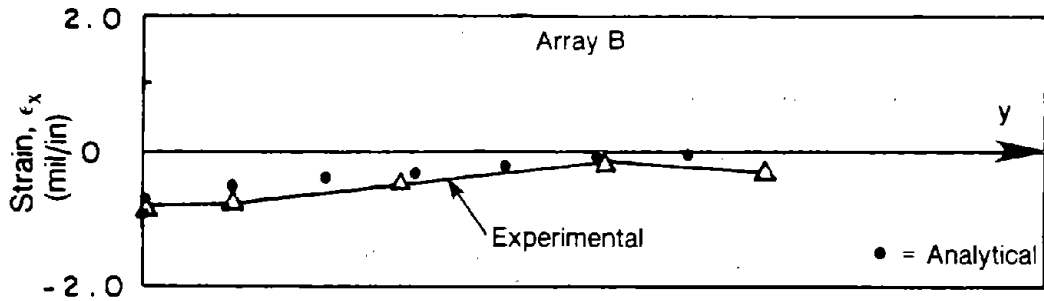
(a)  Transverse Section at 4.25 in. From Link End
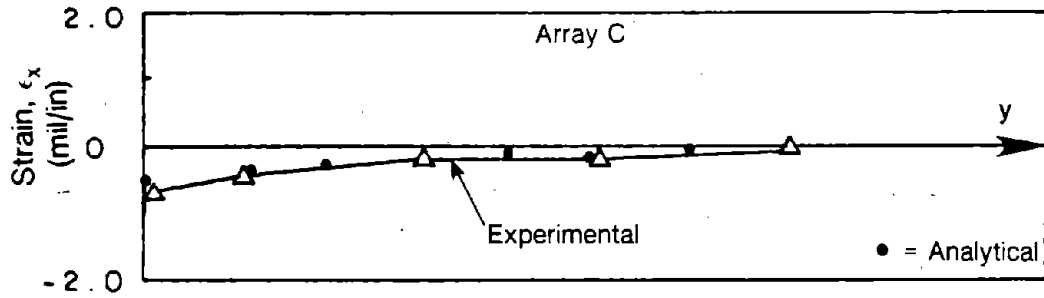
(b)  Transverse Section at 13.38 in. From Link End
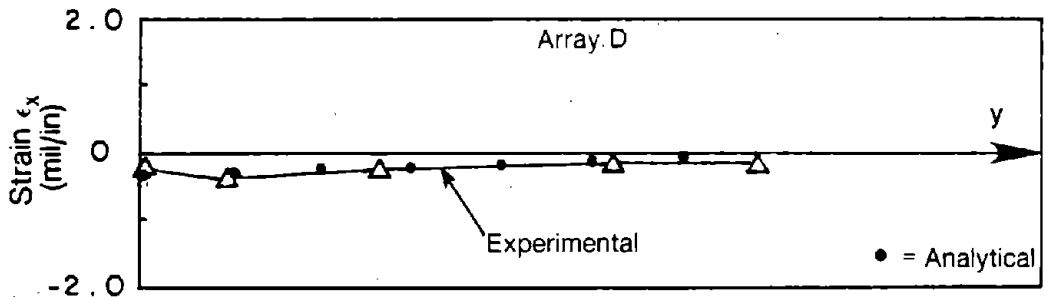
(c)  Transverse Section at 28.25 in. From Link End
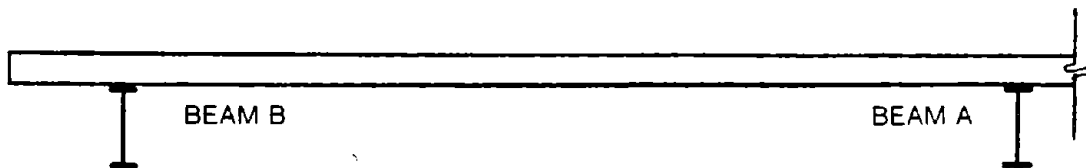
Fig. 5.19     Comparison of Floor Slab Longitudinal Strain $\epsilon_x$ for Interior
Composite Beam Model and Specimen B1 During Cycle 1 at
$\gamma$ = -0.02 rad.
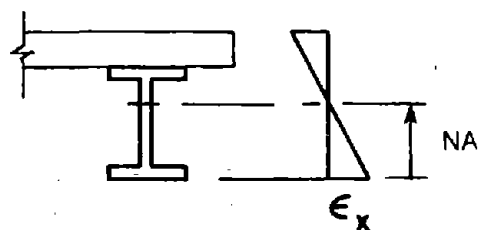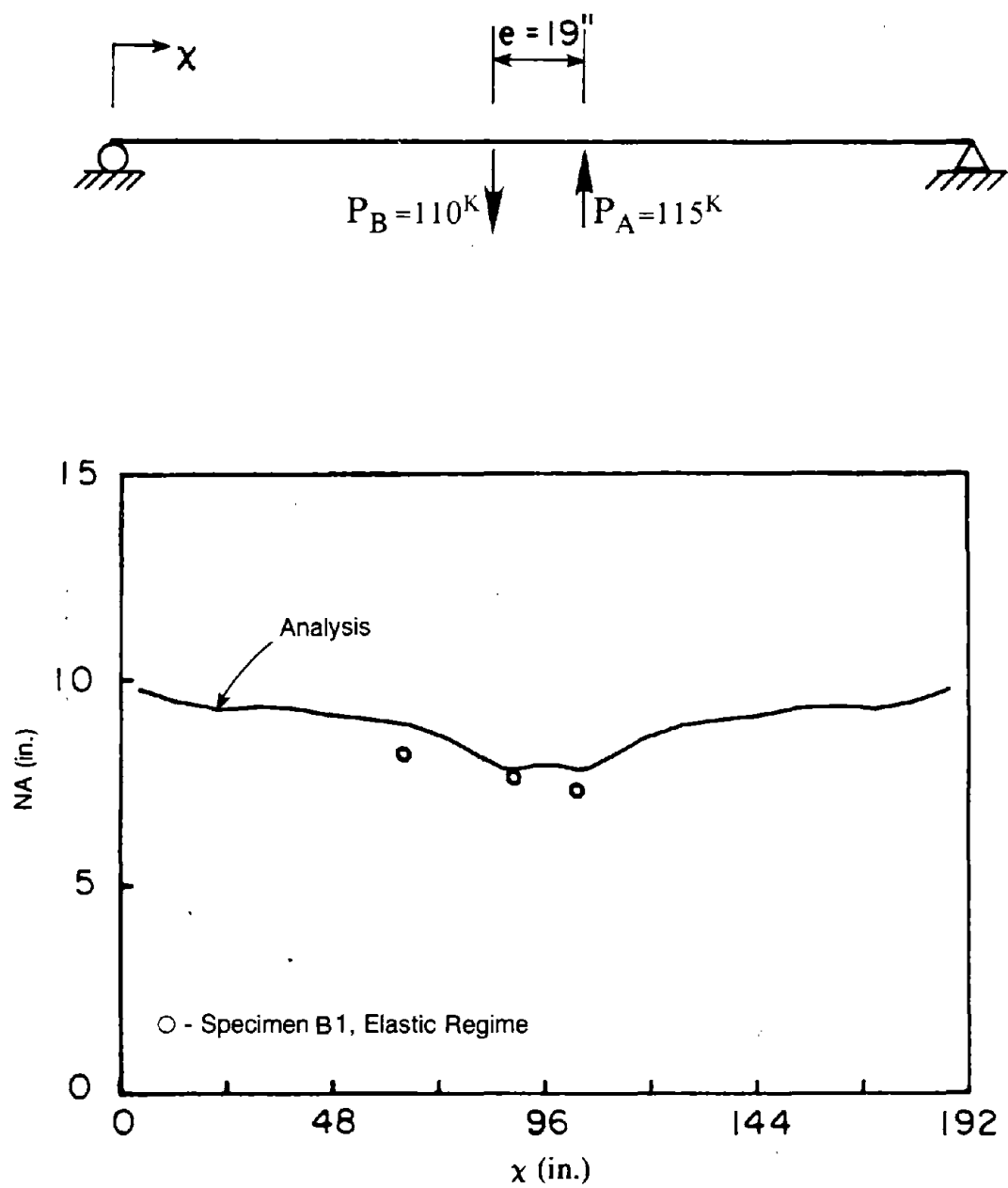
Fig. 5.20     Comparison of Neutral Axis Location Along Beam for Interior
              Composite Beam Model and Specimen B1.
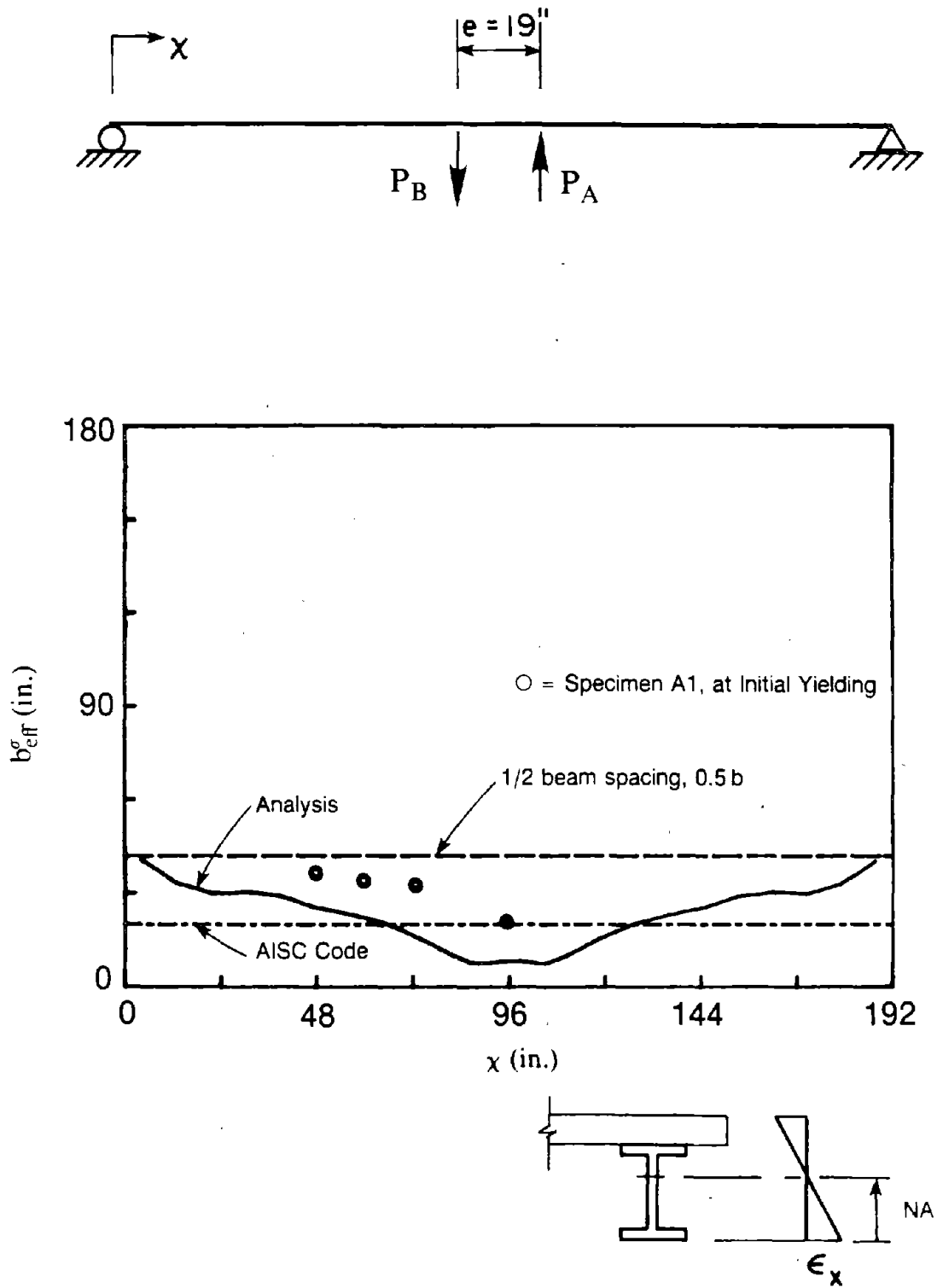
Fig. 5.21      Comparison of Effective Slab Width for Exterior
Composite Beam Model and Specimen A1.
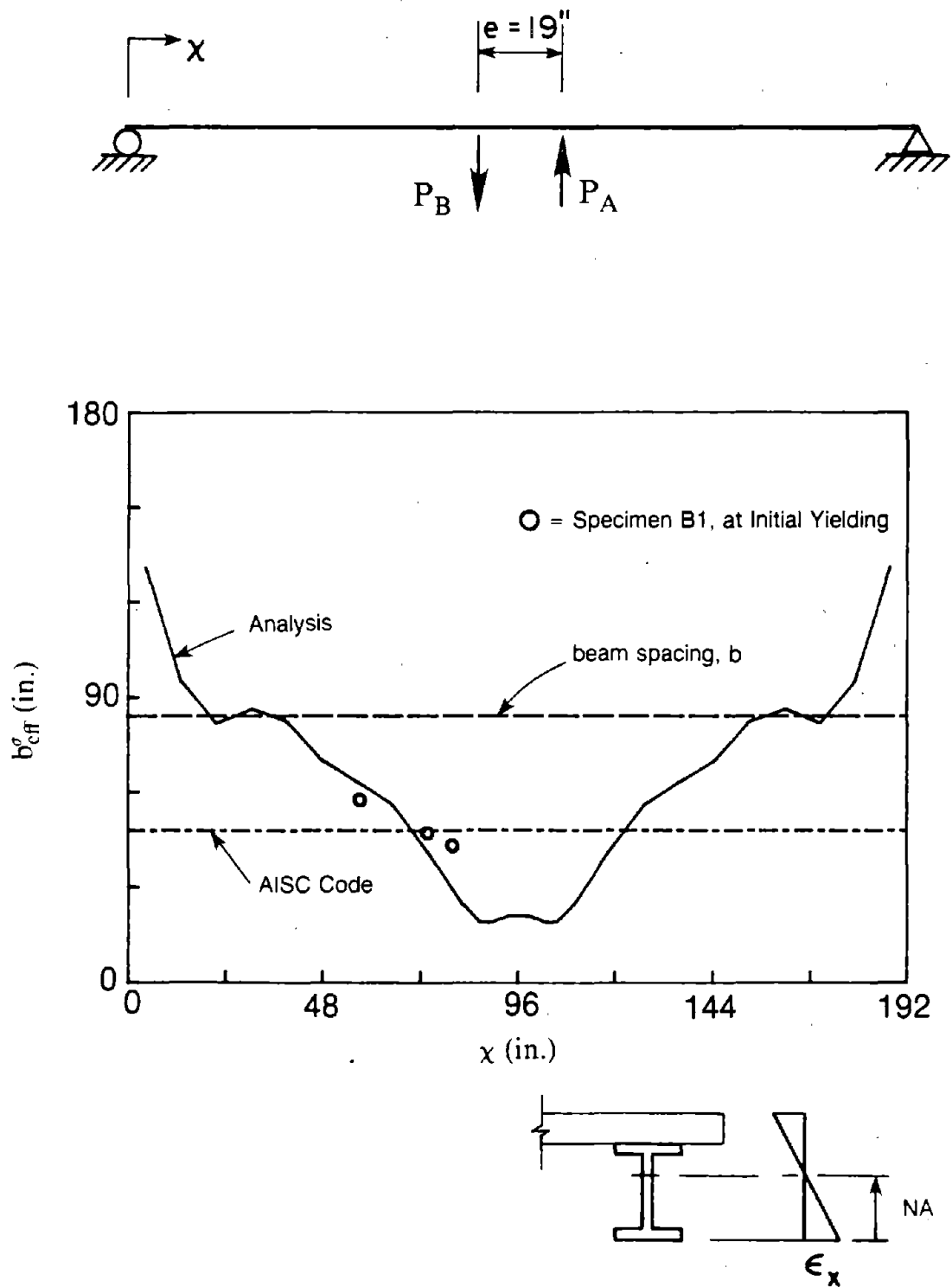
Fig. 5.22   Comparison of Effective Slab Width for Interior
Composite Beam Model and Specimen B1.

294
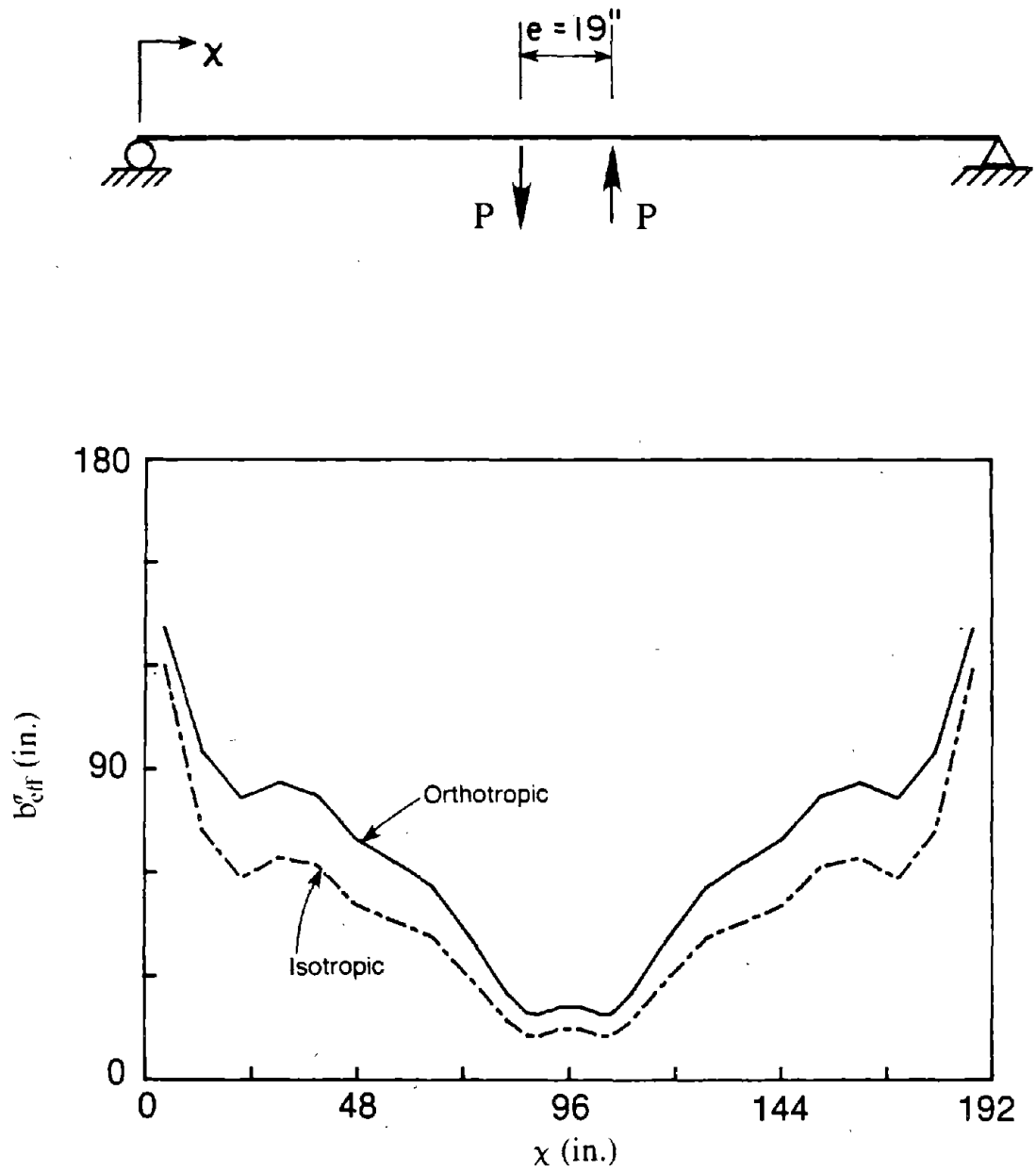


Fig. 5.23   Effective Slab Width for Interior Composite Beam Models With
Orthotropic and Isotropic Floor Slabs, EBF Brace Force Simulation.
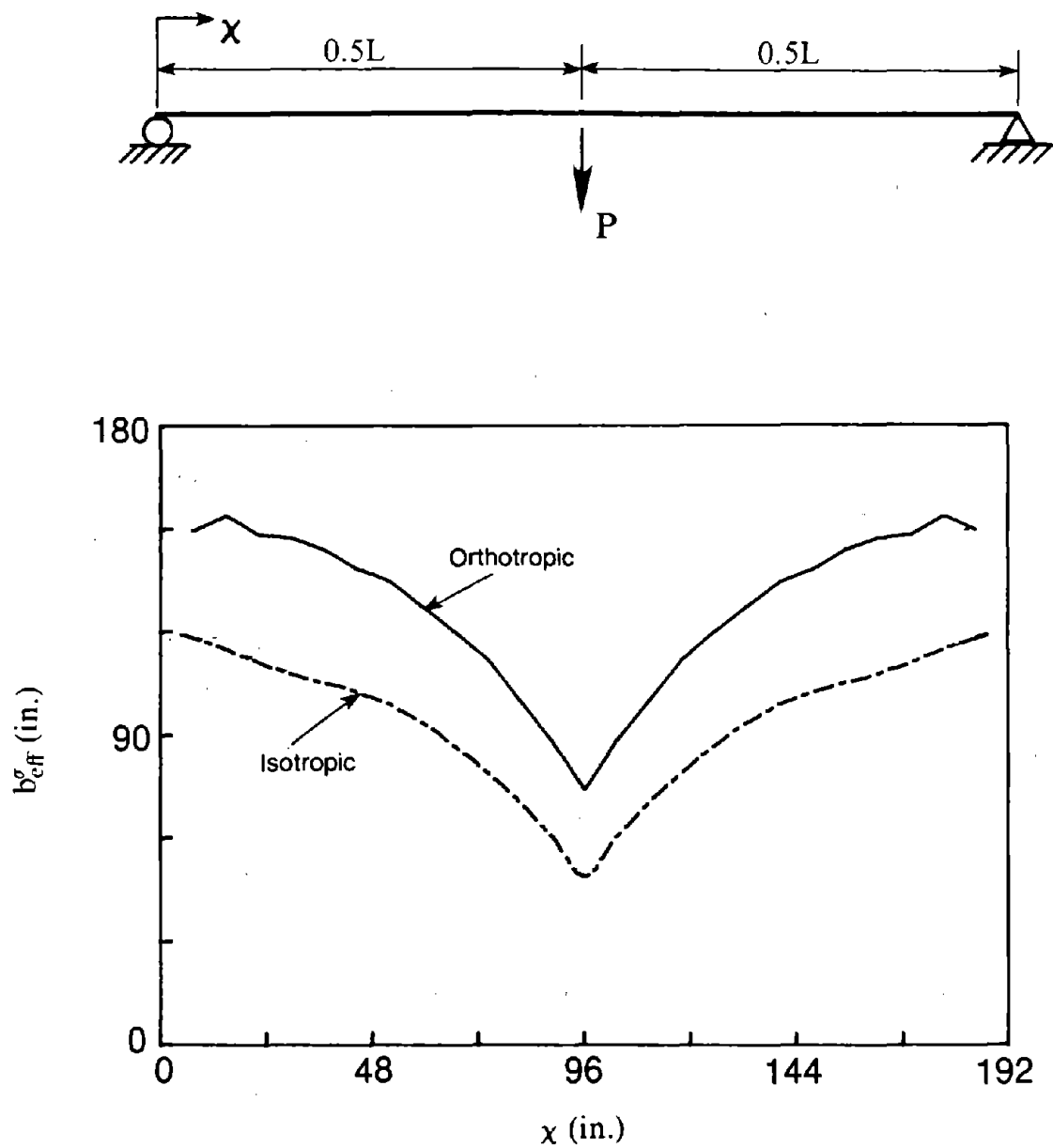
Fig. 5.24    Effective Slab Width for Interior Composite Beam Models With
Orthotropic and Isotropic Floor Slabs, Concentrated Load at Midspan.
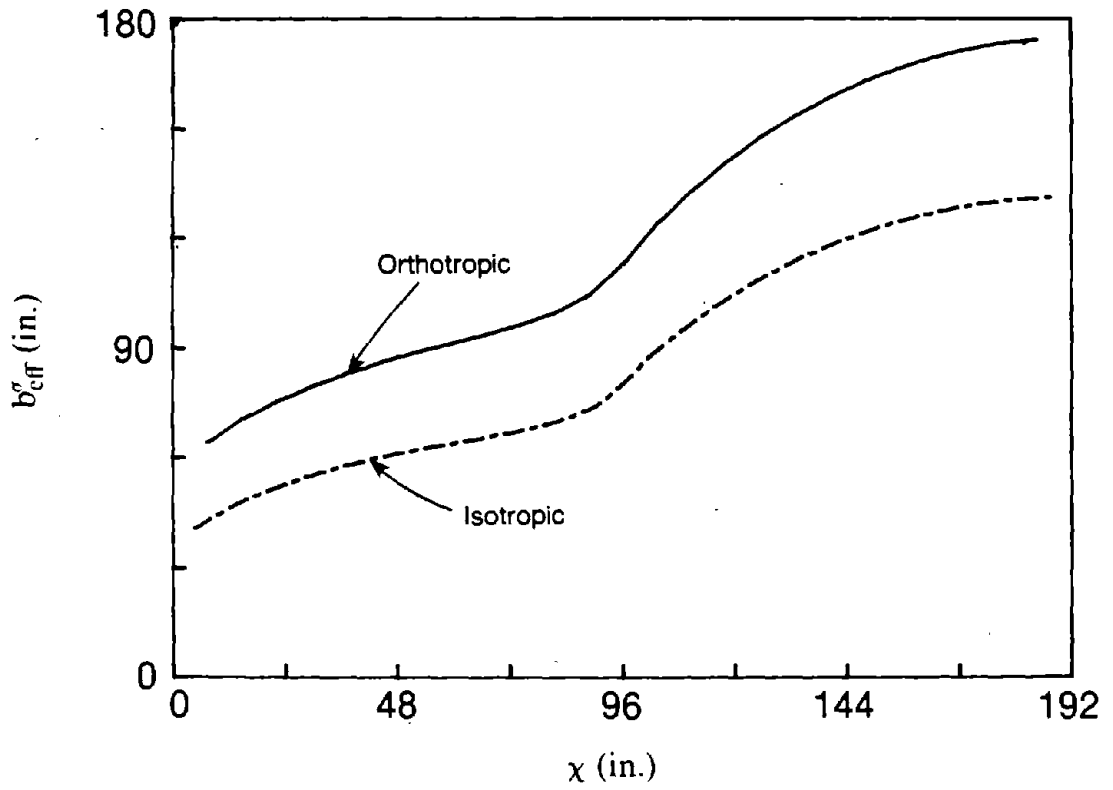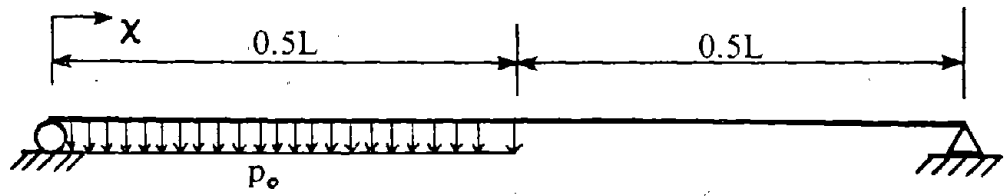
Fig. 5.25    Effective Slab Width for Interior Composite Beam Models With Orthotropic and Isotropic Floor Slabs, Distributed Load Along Floor Beam.
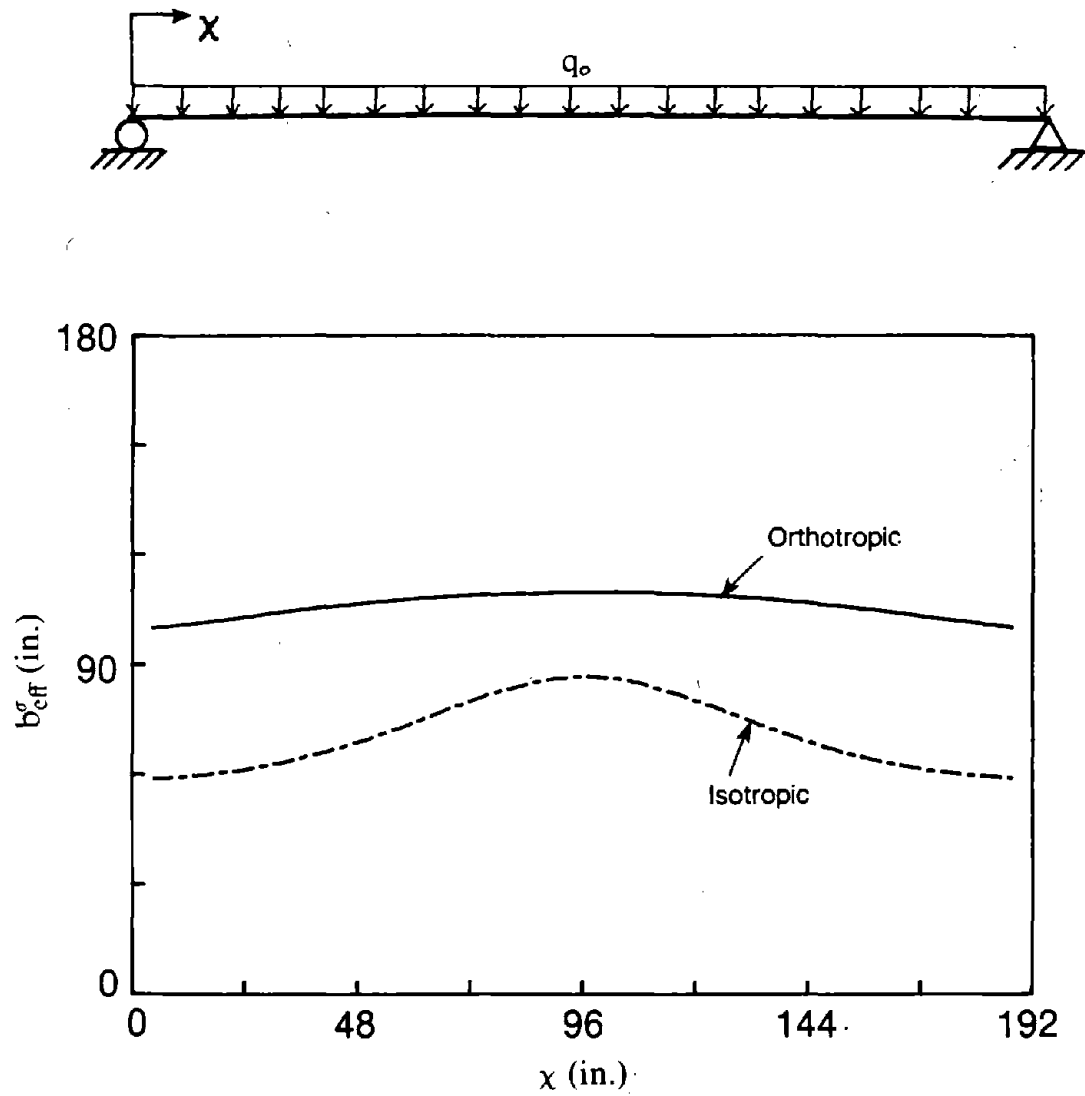
Fig. 5.26    Effective Slab Width for Interior Composite Beam Models With
Orthotropic and Isotropic Floor Slabs, Uniform Dead Load.
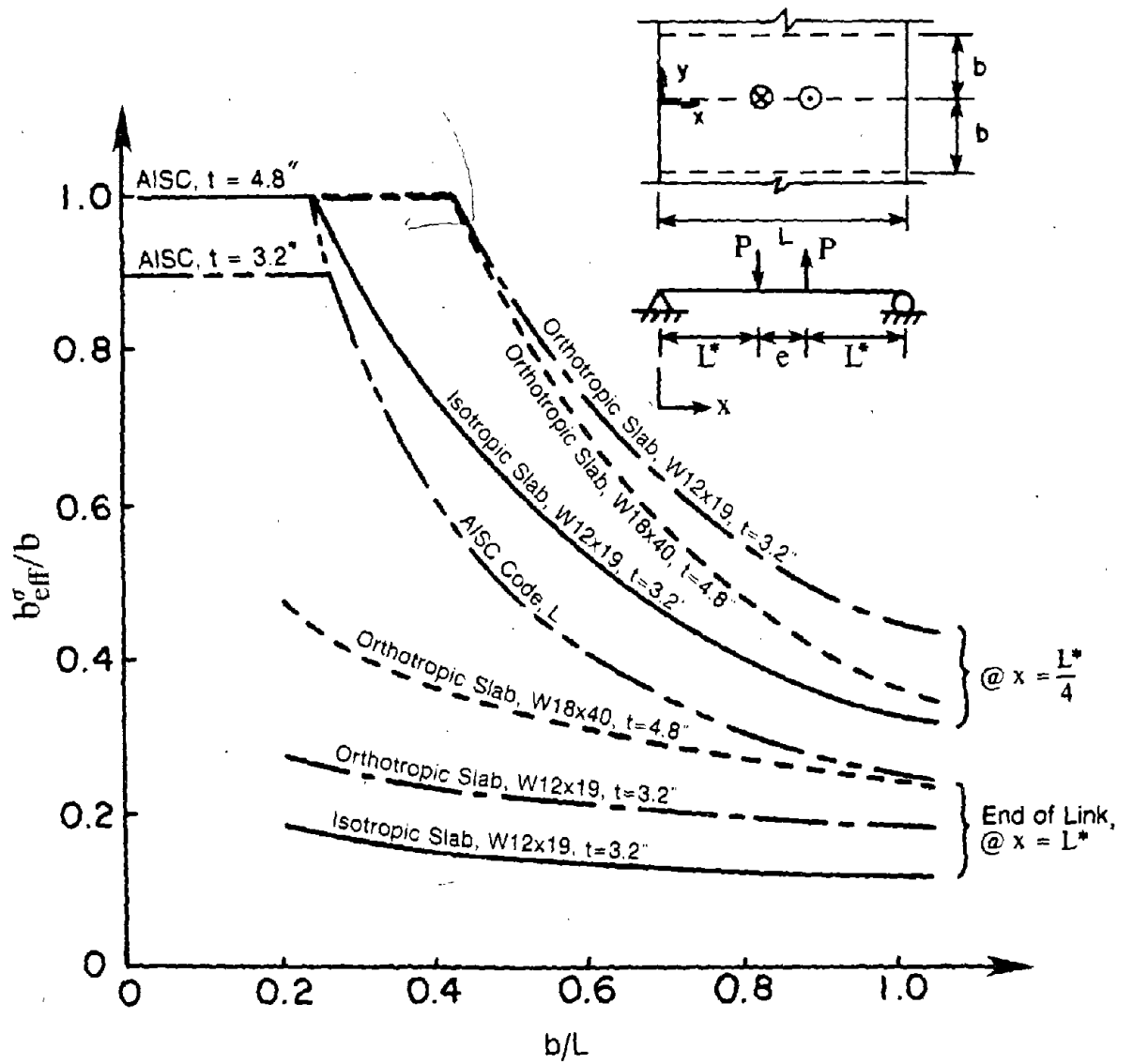
Fig. 5.27    Variation of Effective Slab Width With Slab Aspect Ratio for Interior
Composite Beam Model.
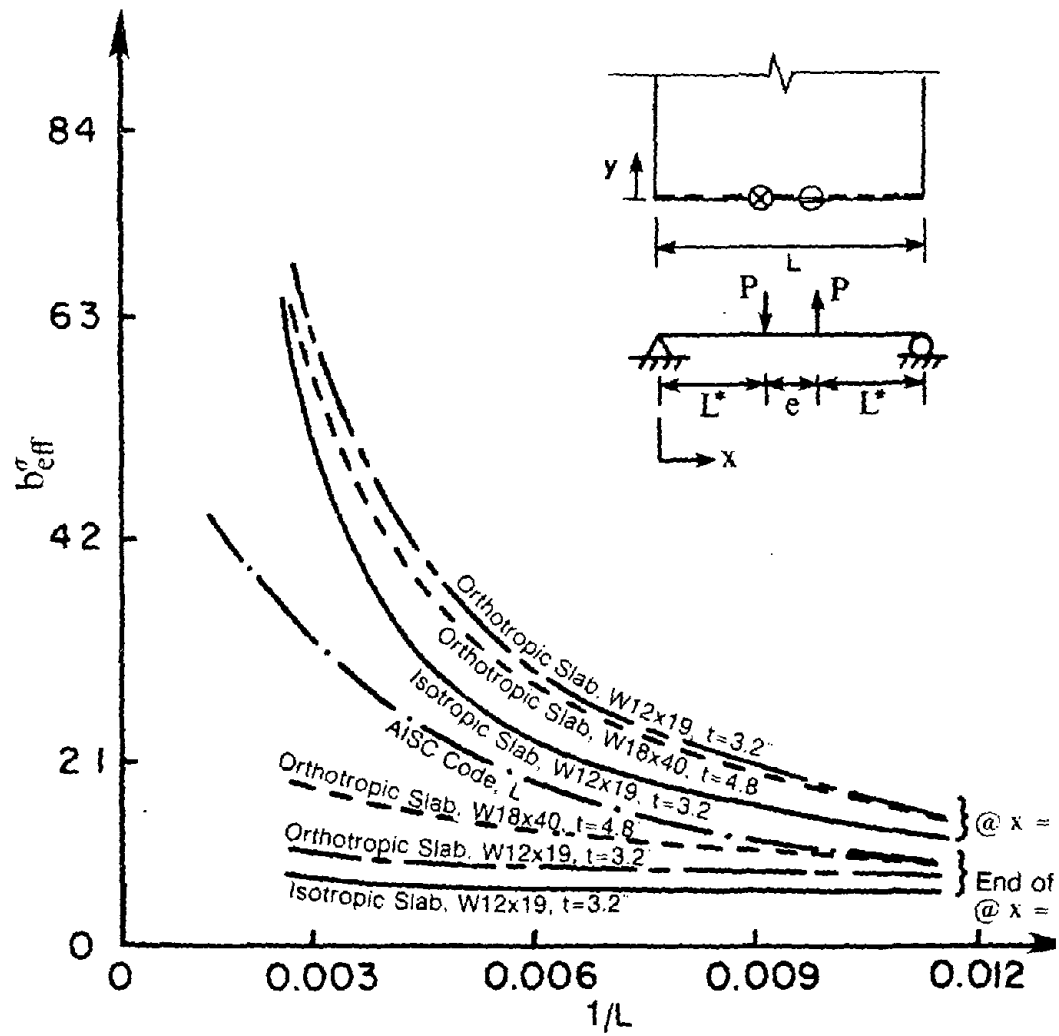
Fig. 5.28    Variation of Effective Slab Width With Beam Span for Exterior
Composite Beam Model.
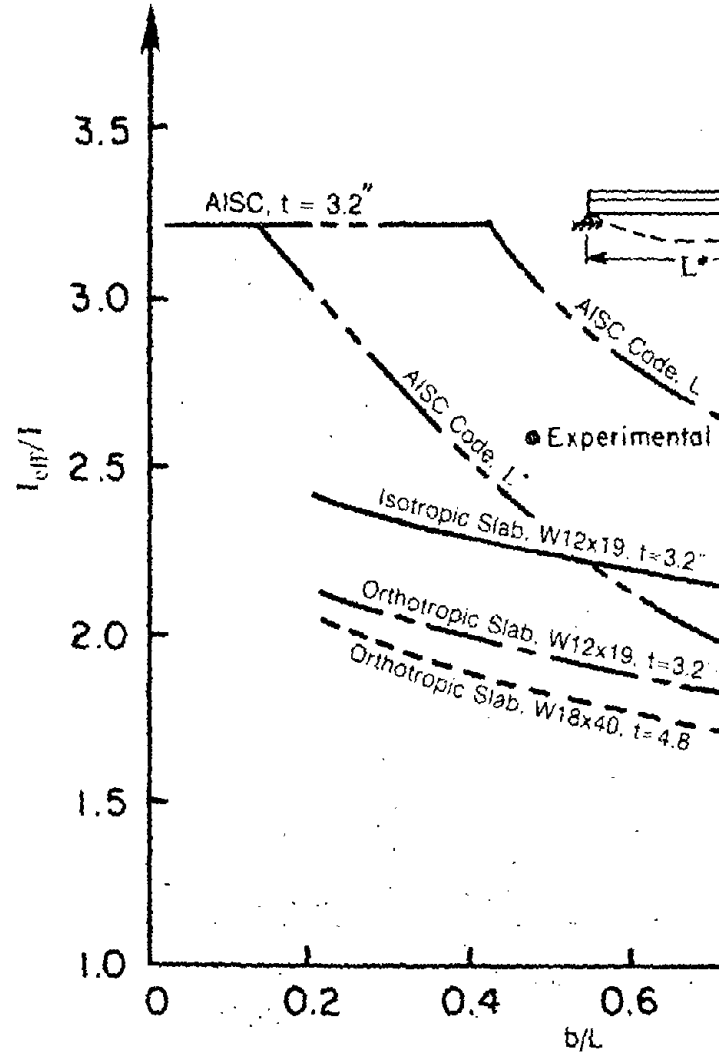
Fig. 5.29    Effective Moment of Inertia of Interior C[...]
Outside the Link as a Function of Slab A[...]
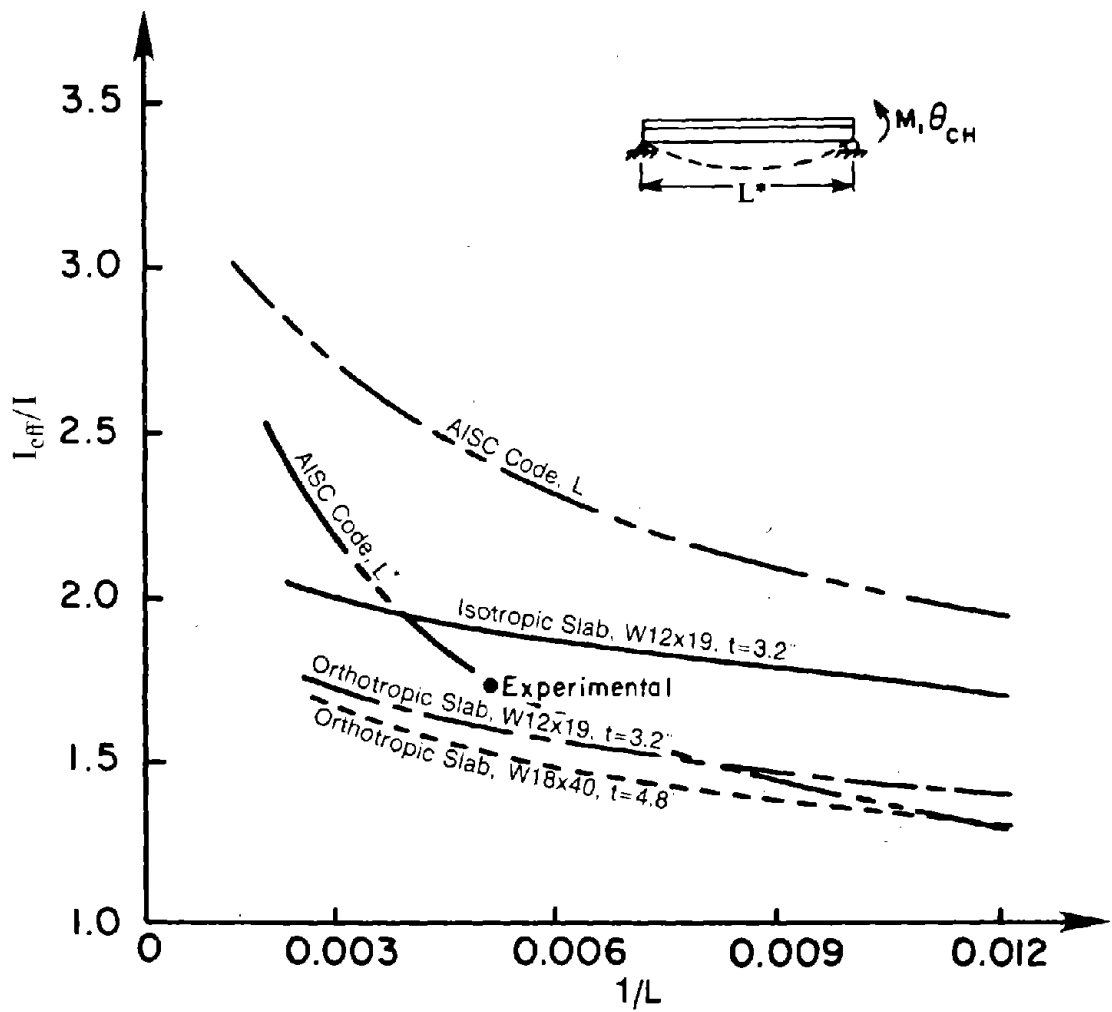
Fig. 5.30    Effective Moment of Inertia of Exterior Composite Beam Model
Outside the Link as a Function of Beam Span.
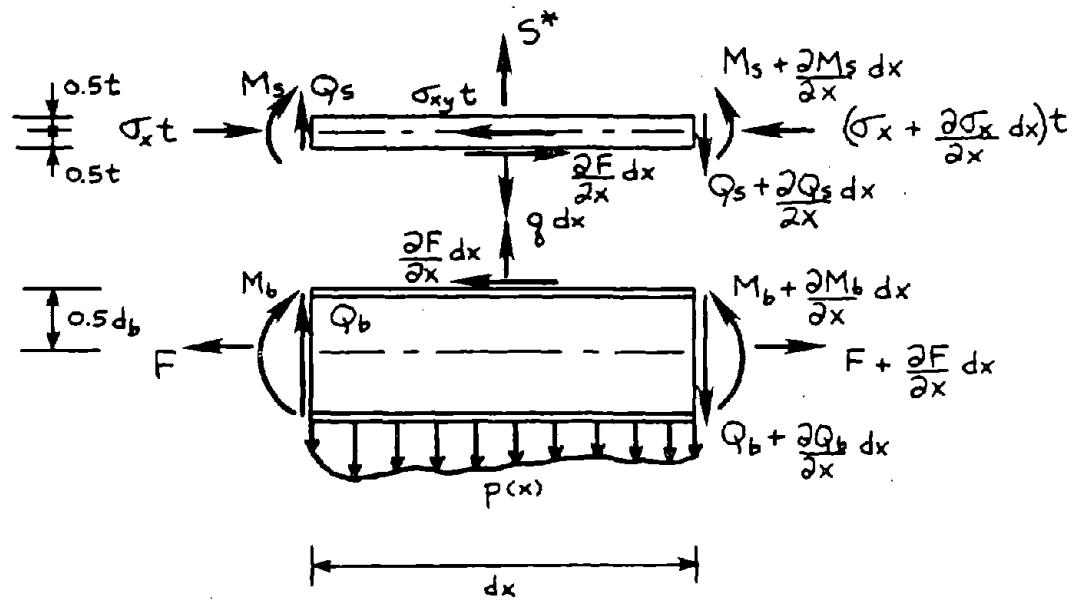
Fig. 5.31    Free Body Diagrams of Beam and Floor Slab to Determine Shear Force $Q_b$.
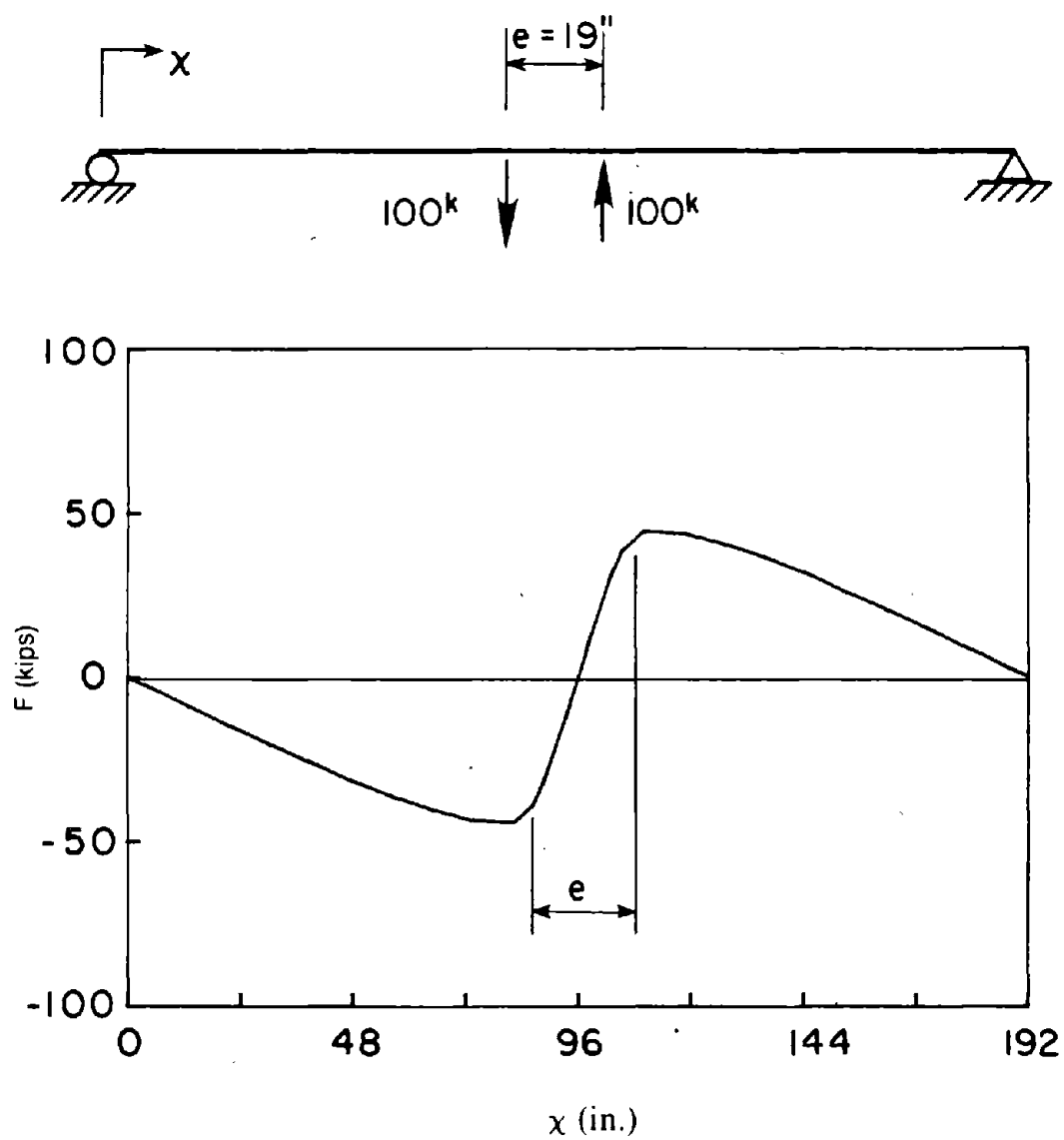
Fig. 5.32    Axial Force Developed in Floor Slab and Beam Along Interior
Composite Beam Model of Specimen B1.
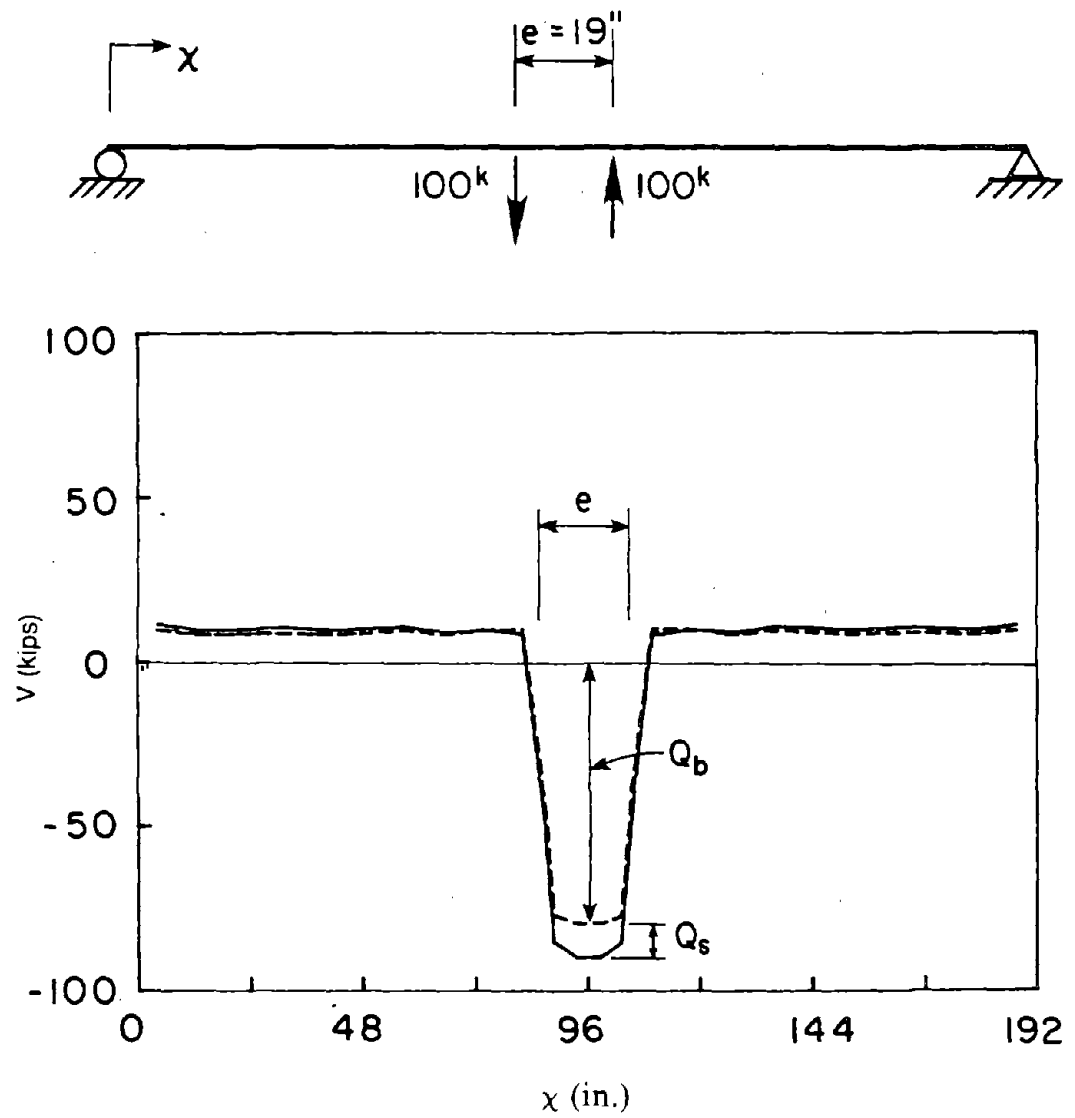
Fig. 5.33    Shear Force Developed in Beam and Floor Slab of the Interior
Composite Beam Model of Specimen B1.
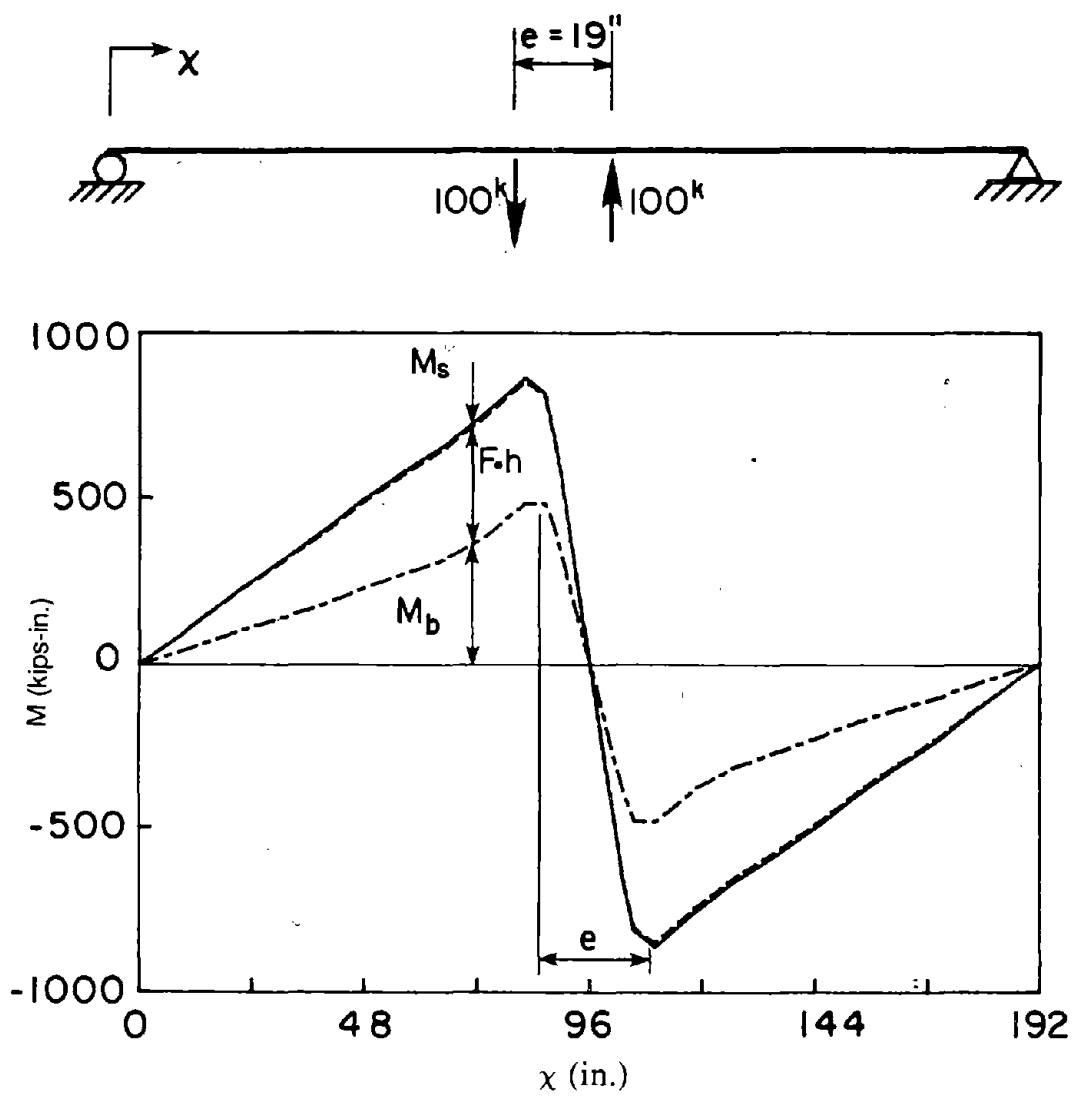
Fig. 5.34    Moment Developed in Interior Composite Beam Model of Specimen B1.
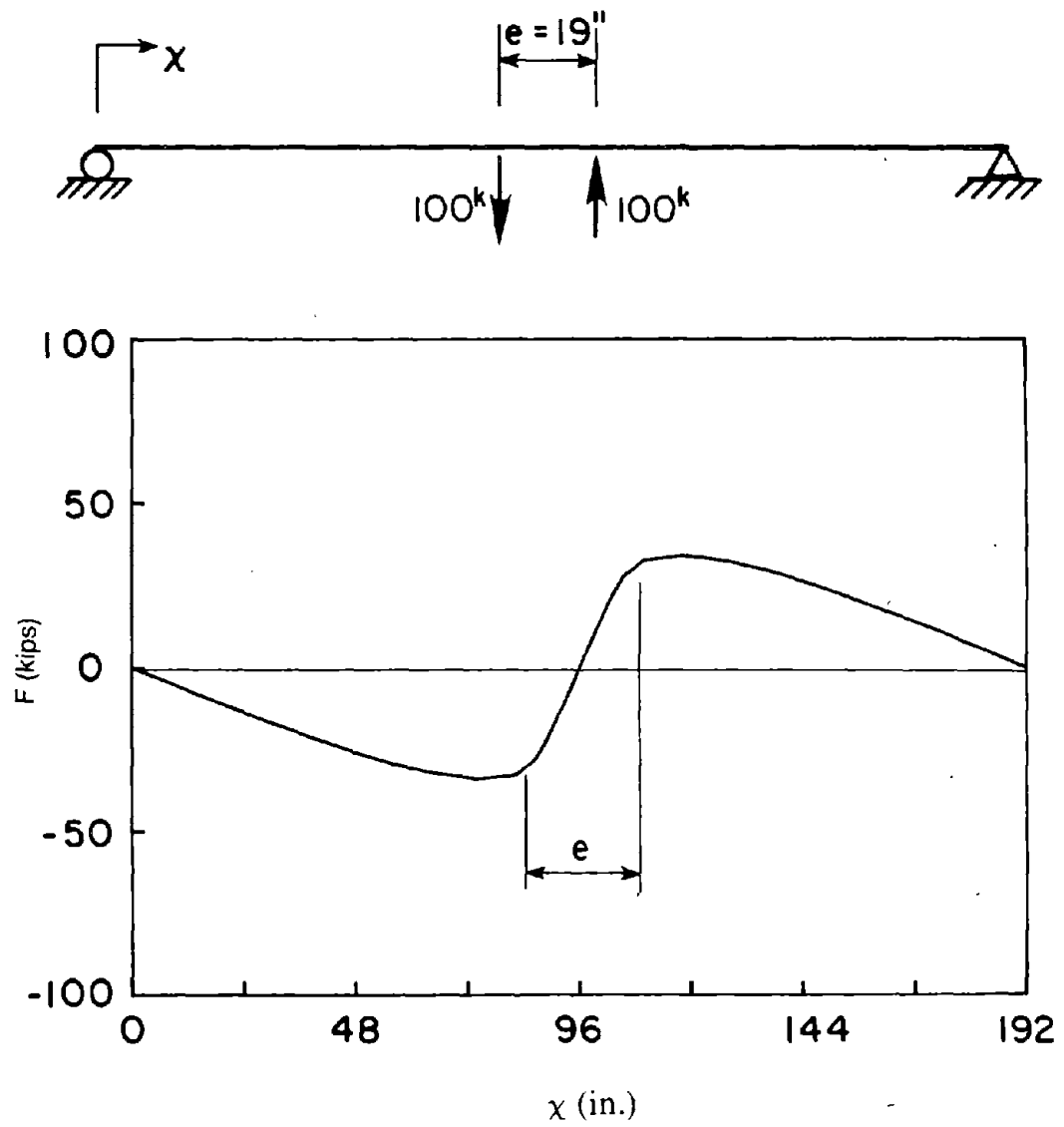
Fig. 5.35    Axial Force Developed in Floor Slab and Beam Along Exterior
Composite Beam Model of Specimen A1.
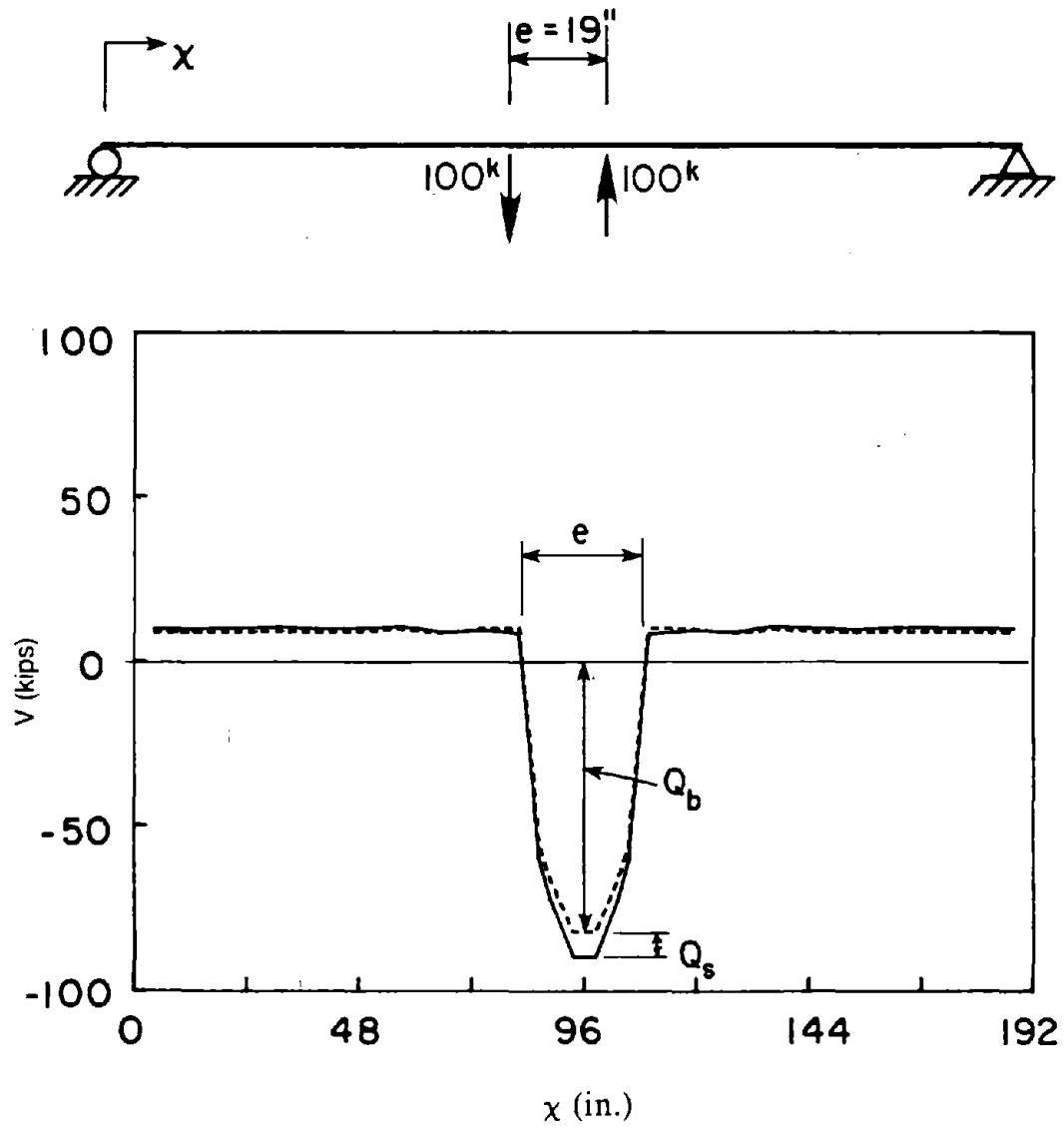
Fig. 5.36    Shear Force Developed in Beam and Floor Slab of the Exterior
Composite Beam Model of Specimen A1.
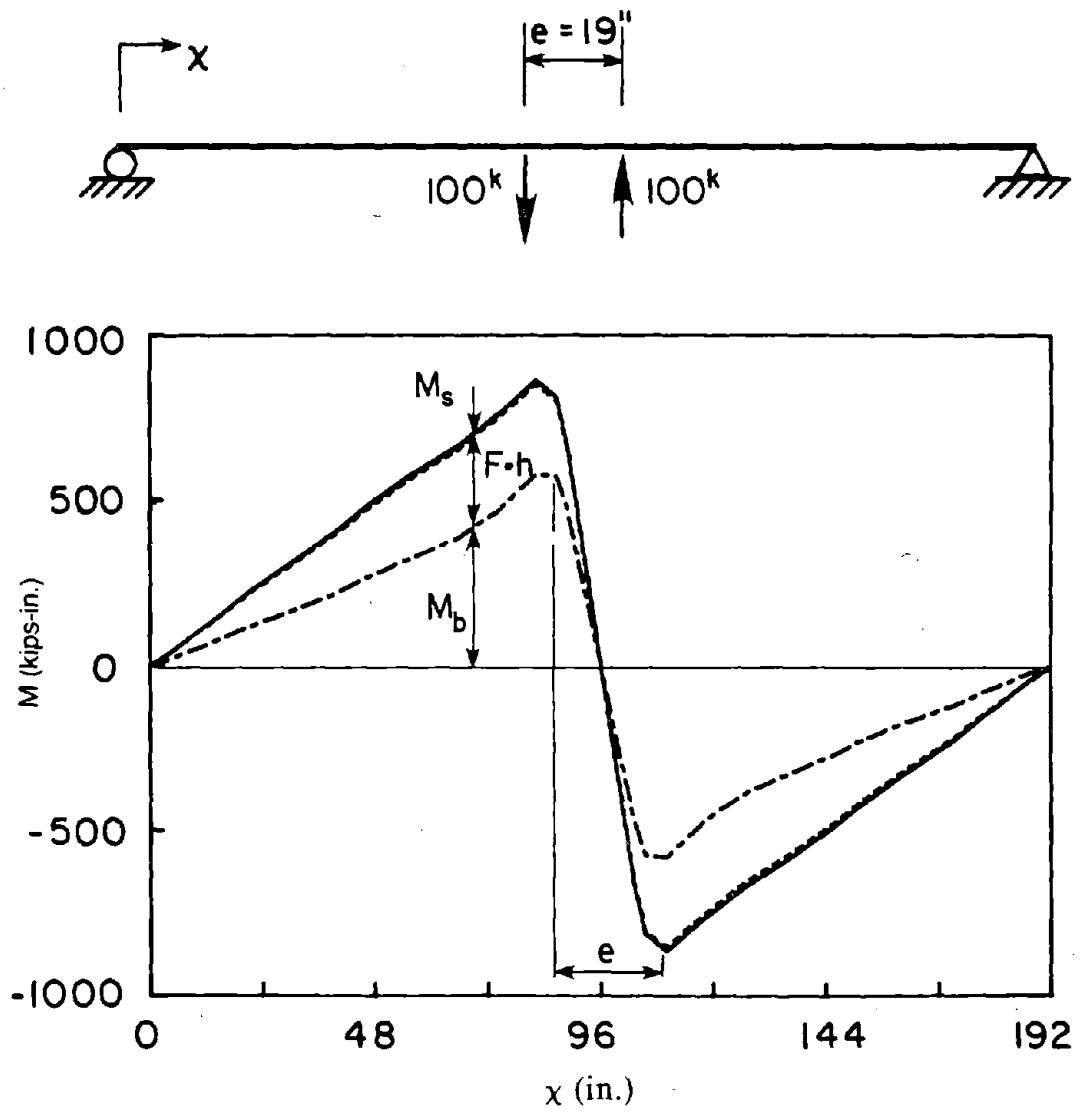
Fig. 5.37    Moment Developed in Exterior Composite Beam Model of Specimen A1.
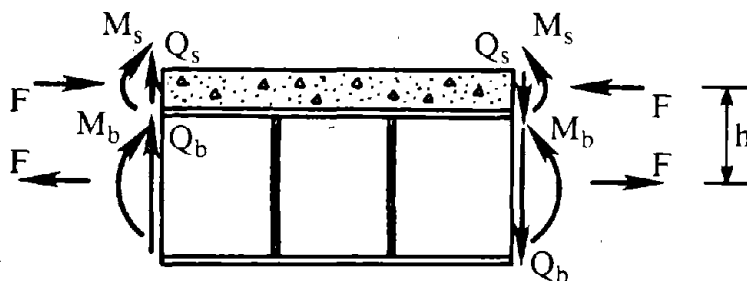
$$V = Q_b + Q_s$$

$$M = M_b + M_s + F \bullet h$$

| MODEL | SHEAR | | MOMENT | | | AXIAL FORCE | |
|---|---|---|---|---|---|---|---|
| | $\dfrac{Q_b}{V}$ | $\dfrac{Q_s}{V}$ | $\dfrac{M_b}{M}$ | $\dfrac{M_s}{M}$ | $\dfrac{F \bullet h}{M}$ | $\dfrac{F^{max}_{LINK}}{A\sigma_y}$ | $\dfrac{F^{max}_{b}}{A\sigma_y}$ |
| [1] | [2] | [3] | [4] | [5] | [6] | [7] | [8] |
| Bare Beam | 1.0 | 0 | 1.0 | 0 | 0 | 0 | 0 |
| Exterior Comp. | 0.92 | 0.08 | 0.67 | 0.01 | 0.32 | 0.11 | 0.17 |
| Interior Comp. | 0.88 | 0.12 | 0.56 | 0.01 | 0.43 | 0.15 | 0.22 |

$$A = 5.57 \text{ in.}^2, \text{ W12x19}$$

Fig. 5.38     Summary of Forces Developed in Link and Maximum Axial Force
Outside the Link for Analyses of Experimental Specimens.
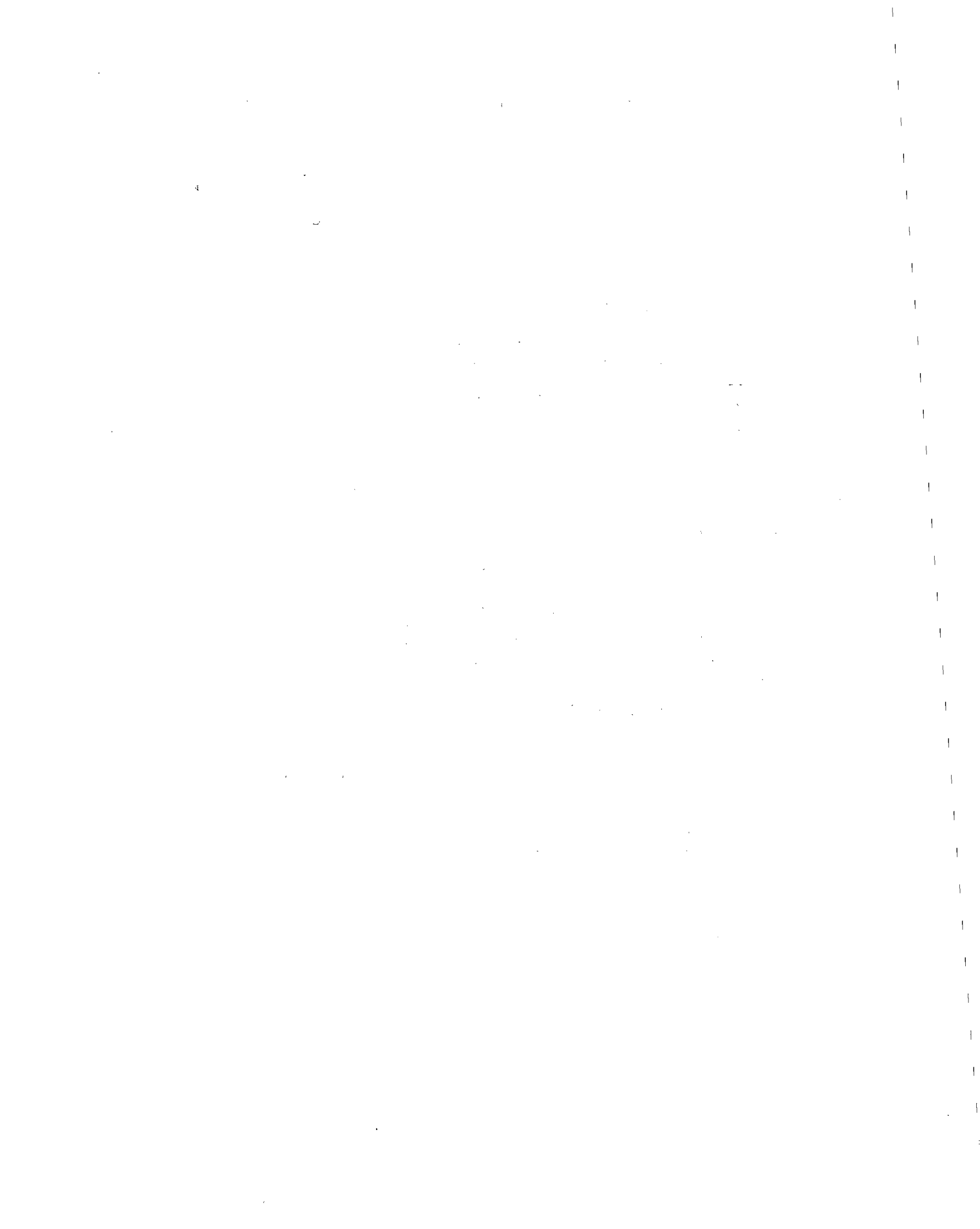
## EARTHQUAKE ENGINEERING RESEARCH CENTER REPORT SERIES

EERC reports are available from the National Information Service for Earthquake Engineering(NISEE) and from the National Technical Information Service(NTIS). Numbers in parentheses are Accession Numbers assigned by the National Technical Information Service; these are followed by a price code. Contact NTIS, 5285 Port Royal Road, Springfield Virginia, 22161 for more information. Reports without Accession Numbers were not available from NTIS at the time of printing. For a current complete list of EERC reports (from EERC 67-1) and availablity information, please contact University of California, EERC, NISEE, 1301 South 46th Street, Richmond, California 94804.

UCB/EERC-80/01 "Earthquake Response of Concrete Gravity Dams Including Hydrodynamic and Foundation Interaction Effects," by Chopra, A.K., Chakrabarti, P. and Gupta, S., January 1980, (AD-A087297)A10.

UCB/EERC-80/02 "Rocking Response of Rigid Blocks to Earthquakes," by Yim, C.S., Chopra, A.K. and Penzien, J., January 1980, (PB80 166 002)A04.

UCB/EERC-80/03 "Optimum Inelastic Design of Seismic-Resistant Reinforced Concrete Frame Structures," by Zagajeski, S.W. and Bertero, V.V., January 1980, (PB80 164 635)A06.

UCB/EERC-80/04 "Effects of Amount and Arrangement of Wall-Panel Reinforcement on Hysteretic Behavior of Reinforced Concrete Walls," by Iliya, R. and Bertero, V.V., February 1980, (PB81 122 525)A09.

UCB/EERC-80/05 "Shaking Table Research on Concrete Dam Models," by Niwa, A. and Clough, R.W., September 1980, (PB81 122 368)A06.

UCB/EERC-80/06 "The Design of Steel Energy-Absorbing Restrainers and their Incorporation into Nuclear Power Plants for Enhanced Safety (Vol 1a): Piping with Energy Absorbing Restrainers: Parameter Study on Small Systems," by Powell, G.H., Oughourlian, C. and Simons, J., June 1980.

UCB/EERC-80/07 "Inelastic Torsional Response of Structures Subjected to Earthquake Ground Motions," by Yamazaki, Y., April 1980, (PB81 122 327)A08.

UCB/EERC-80/08 "Study of X-Braced Steel Frame Structures under Earthquake Simulation," by Ghanaat, Y., April 1980, (PB81 122 335)A11.

UCB/EERC-80/09 "Hybrid Modelling of Soil-Structure Interaction," by Gupta, S., Lin, T.W. and Penzien, J., May 1980, (PB81 122 319)A07.

UCB/EERC-80/10 "General Applicability of a Nonlinear Model of a One Story Steel Frame," by Sveinsson, B.I. and McNiven, H.D., May 1980, (PB81 124 877)A06.

UCB/EERC-80/11 "A Green-Function Method for Wave Interaction with a Submerged Body," by Kioka, W., April 1980, (PB81 122 269)A07.

UCB/EERC-80/12 "Hydrodynamic Pressure and Added Mass for Axisymmetric Bodies.," by Nilrat, F., May 1980, (PB81 122 343)A08.

UCB/EERC-80/13 "Treatment of Non-Linear Drag Forces Acting on Offshore Platforms," by Dao, B.V. and Penzien, J., May 1980, (PB81 153 413)A07.

UCB/EERC-80/14 "2D Plane/Axisymmetric Solid Element (Type 3-Elastic or Elastic-Perfectly Plastic) for the ANSR-II Program," by Mondkar, D.P. and Powell, G.H., July 1980, (PB81 122 350)A03.

UCB/EERC-80/15 "A Response Spectrum Method for Random Vibrations," by Der Kiureghian, A., June 1981, (PB81 122 301)A03.

UCB/EERC-80/16 "Cyclic Inelastic Buckling of Tubular Steel Braces," by Zayas, V.A., Popov, E.P. and Martin, S.A., June 1981, (PB81 124 885)A10.

UCB/EERC-80/17 "Dynamic Response of Simple Arch Dams Including Hydrodynamic Interaction," by Porter, C.S. and Chopra, A.K., July 1981, (PB81 124 000)A13.

UCB/EERC-80/18 "Experimental Testing of a Friction Damped Aseismic Base Isolation System with Fail-Safe Characteristics," by Kelly, J.M., Beucke, K.E. and Skinner, M.S., July 1980, (PB81 148 595)A04.

UCB/EERC-80/19 "The Design of Steel Emergy-Absorbing Restrainers and their Incorporation into Nuclear Power Plants for Enhanced Safety (Vol.1B): Stochastic Seismic Analyses of Nuclear Power Plant Structures and Piping Systems Subjected to Multiple Supported Excitations," by Lee, M.C. and Penzien, J., June 1980, (PB82 201 872)A08.

UCB/EERC-80/20 "The Design of Steel Energy-Absorbing Restrainers and their Incorporation into Nuclear Power Plants for Enhanced Safety (Vol 1C): Numerical Method for Dynamic Substructure Analysis," by Dickens, J.M. and Wilson, E.L., June 1980.

UCB/EERC-80/21 "The Design of Steel Energy-Absorbing Restrainers and their Incorporation into Nuclear Power Plants for Enhanced Safety (Vol 2): Development and Testing of Restraints for Nuclear Piping Systems," by Kelly, J.M. and Skinner, M.S., June 1980.

UCB/EERC-80/22 "3D Solid Element (Type 4-Elastic or Elastic-Perfectly-Plastic) for the ANSR-II Program," by Mondkar, D.P. and Powell, G.H., July 1980, (PB81 123 242)A03.

UCB/EERC-80/23 "Gap-Friction Element (Type 5) for the Ansr-II Program," by Mondkar, D.P. and Powell, G.H., July 1980, (PB81 122 285)A03.

UCB/EERC-80/24 "U-Bar Restraint Element (Type 11) for the ANSR-II Program," by Oughourlian, C. and Powell, G.H., July 1980, (PB81 122 293)A03.

UCB/EERC-80/25 "Testing of a Natural Rubber Base Isolation System by an Explosively Simulated Earthquake," by Kelly, J.M., August 1980, (PB81 201 360)A04.

UCB/EERC-80/26 "Input Identification from Structural Vibrational Response," by Hu, Y., August 1980, (PB81 152 308)A05.

UCB/EERC-80/27 "Cyclic Inelastic Behavior of Steel Offshore Structures," by Zayas, V.A., Mahin, S.A. and Popov, E.P., August 1980, (PB81 196 180)A15.

UCB/EERC-80/28 "Shaking Table Testing of a Reinforced Concrete Frame with Biaxial Response," by Oliva, M.G., October 1980, (PB81 154 304)A10.

UCB/EERC-80/29 "Dynamic Properties of a Twelve-Story Prefabricated Panel Building," by Bouwkamp, J.G., Kollegger, J.P. and Stephen, R.M., October 1980, (PB82 138 777)A07.

UCB/EERC-80/30 "Dynamic Properties of an Eight-Story Prefabricated Panel Building," by Bouwkamp, J.G., Kollegger, J.P. and Stephen, R.M., October 1980, (PB81 200 313)A05.

UCB/EERC-80/31 "Predictive Dynamic Response of Panel Type Structures under Earthquakes," by Kollegger, J.P. and Bouwkamp, J.G., October 1980, (PB81 152 316)A04.

312

UCB/EERC-80/32  "The Design of Steel Energy-Absorbing Restrainers and their Incorporation into Nuclear Power Plants for Enhanced Safety (Vol 3): Testing of Commercial Steels in Low-Cycle Torsional Fatique," by Spanner, P., Parker, E.R., Jongewaard, E. and Dory, M., 1980.

UCB/EERC-80/33  "The Design of Steel Energy-Absorbing Restrainers and their Incorporation into Nuclear Power Plants for Enhanced Safety (Vol 4): Shaking Table Tests of Piping Systems with Energy-Absorbing Restrainers," by Stiemer, S.F. and Godden, W.G., September 1980, (PB82 201 880)A05.

UCB/EERC-80/34  "The Design of Steel Energy-Absorbing Restrainers and their Incorporation into Nuclear Power Plants for Enhanced Safety (Vol 5): Summary Report," by Spencer, P., 1980.

UCB/EERC-80/35  "Experimental Testing of an Energy-Absorbing Base Isolation System," by Kelly, J.M., Skinner, M.S. and Beucke, K.E., October 1980, (PB81 154 072)A04.

UCB/EERC-80/36  "Simulating and Analyzing Artificial Non-Stationary Earth Ground Motions," by Nau, R.F., Oliver, R.M. and Pister, K.S., October 1980, (PB81 153 397)A04.

UCB/EERC-80/37  "Earthquake Engineering at Berkeley - 1980," by , September 1980, (PB81 205 674)A09.

UCB/EERC-80/38  "Inelastic Seismic Analysis of Large Panel Buildings," by Schricker, V. and Powell, G.H., September 1980, (PB81 154 338)A13.

UCB/EERC-80/39  "Dynamic Response of Embankment, Concrete-Gavity and Arch Dams Including Hydrodynamic Interation," by Hall, J.F. and Chopra, A.K., October 1980, (PB81 152 324)A11.

UCB/EERC-80/40  "Inelastic Buckling of Steel Struts under Cyclic Load Reversal.," by Black, R.G. , Wenger, W.A. and Popov, E.P., October 1980, (PB81 154 312)A08.

UCB/EERC-80/41  "Influence of Site Characteristics on Buildings Damage during the October 3,1974 Lima Earthquake," by Repetto, P., Arango, I. and Seed, H.B., September 1980, (PB81 161 739)A05.

UCB/EERC-80/42  "Evaluation of a Shaking Table Test Program on Response Behavior of a Two Story Reinforced Concrete Frame," by Blondet, J.M., Clough, R.W. and Mahin, S.A., December 1980, (PB82 196 544)A11.

UCB/EERC-80/43  "Modelling of Soil-Structure Interaction by Finite and Infinite Elements," by Medina, F., December 1980, (PB81 229 270)A04.


UCB/EERC-81/01  "Control of Seismic Response of Piping Systems and Other Structures by Base Isolation," by Kelly, J.M., January 1981, (PB81 200 735)A05.

UCB/EERC-81/02  "OPTNSR- An Interactive Software System for Optimal Design of Statically and Dynamically Loaded Structures with Nonlinear Response," by Bhatti, M.A., Ciampi, V. and Pister, K.S., January 1981, (PB81 218 851)A09.

UCB/EERC-81/03  "Analysis of Local Variations in Free Field Seismic Ground Motions," by Chen, J.-C., Lysmer, J. and Seed, H.B., January 1981, (AD-A099508)A13.

UCB/EERC-81/04  "Inelastic Structural Modeling of Braced Offshore Platforms for Seismic Loading. ," by Zayas, V.A., Shing, P.-S.B., Mahin, S.A. and Popov, E.P., January 1981, (PB82 138 777)A07.

UCB/EERC-81/05  "Dynamic Response of Light Equipment in Structures," by Der Kiureghian, A., Sackman, J.L. and Nour-Omid, B., April 1981, (PB81 218 497)A04.

UCB/EERC-81/06  "Preliminary Experimental Investigation of a Broad Base Liquid Storage Tank," by Bouwkamp, J.G., Kollegger, J.P. and Stephen, R.M., May 1981, (PB82 140 385)A03.

UCB/EERC-81/07  "The Seismic Resistant Design of Reinforced Concrete Coupled Structural Walls," by Aktan, A.E. and Bertero, V.V., June 1981, (PB82 113 358)A11.

UCB/EERC-81/08  "Unassigned," by Unassigned, 1981.

UCB/EERC-81/09  "Experimental Behavior of a Spatial Piping System with Steel Energy Absorbers Subjected to a Simulated Differential Seismic Input," by Stiemer, S.F., Godden, W.G. and Kelly, J.M., July 1981, (PB82 201 898)A04.

UCB/EERC-81/10  "Evaluation of Seismic Design Provisions for Masonry in the United States," by Sveinsson, B.I., Mayes, R.L. and McNiven, H.D., August 1981, (PB82 166 075)A08.

UCB/EERC-81/11  "Two-Dimensional Hybrid Modelling of Soil-Structure Interaction," by Tzong, T.-J., Gupta, S. and Penzien, J., August 1981, (PB82 142 118)A04.

UCB/EERC-81/12  "Studies on Effects of Infills in Seismic Resistant R/C Construction," by Brokken, S. and Bertero, V.V., October 1981, (PB82 166 190)A09.

UCB/EERC-81/13  "Linear Models to Predict the Nonlinear Seismic Behavior of a One-Story Steel Frame," by Valdimarsson, H., Shah, A.H. and McNiven, H.D., September 1981, (PB82 138 793)A07.

UCB/EERC-81/14  "TLUSH: A Computer Program for the Three-Dimensional Dynamic Analysis of Earth Dams," by Kagawa, T., Mejia, L.H., Seed, H.B. and Lysmer, J., September 1981, (PB82 139 940)A06.

UCB/EERC-81/15  "Three Dimensional Dynamic Response Analysis of Earth Dams," by Mejia, L.H. and Seed, H.B., September 1981, (PB82 137 274)A12.

UCB/EERC-81/16  "Experimental Study of Lead and Elastomeric Dampers for Base Isolation Systems," by Kelly, J.M. and Hodder, S.B., October 1981, (PB82 166 182)A05.

UCB/EERC-81/17  "The Influence of Base Isolation on the Seismic Response of Light Secondary Equipment," by Kelly, J.M., April 1981, (PB82 255 266)A04.

UCB/EERC-81/18  "Studies on Evaluation of Shaking Table Response Analysis Procedures," by Blondet, J. Marcial, November 1981, (PB82 197 278)A10.

UCB/EERC-81/19  "DELIGHT.STRUCT: A Computer-Aided Design Environment for Structural Engineering. ," by Balling, R.J., Pister, K.S. and Polak, E., December 1981, (PB82 218 496)A07.

UCB/EERC-81/20  "Optimal Design of Seismic-Resistant Planar Steel Frames," by Balling, R.J., Ciampi, V. and Pister, K.S., December 1981, (PB82 220 179)A07.

UCB/EERC-82/01 "Dynamic Behavior of Ground for Seismic Analysis of Lifeline Systems," by Sato, T. and Der Kiureghian, A., January 1982, (PB82 218 926)A05.

UCB/EERC-82/02 "Shaking Table Tests of a Tubular Steel Frame Model," by Ghanaat, Y. and Clough, R.W., January 1982, (PB82 220 161)A07.

UCB/EERC-82/03 "Behavior of a Piping System under Seismic Excitation: Experimental Investigations of a Spatial Piping System supported by Mechanical Shock Arrestors," by Schneider, S., Lee, H.-M. and Godden, W. G., May 1982, (PB83 172 544)A09.

UCB/EERC-82/04 "New Approaches for the Dynamic Analysis of Large Structural Systems," by Wilson, E.L., June 1982, (PB83 148 080)A05.

UCB/EERC-82/05 "Model Study of Effects of Damage on the Vibration Properties of Steel Offshore Platforms," by Shahrivar, F. and Bouwkamp, J.G., June 1982, (PB83 148 742)A10.

UCB/EERC-82/06 "States of the Art and Pratice in the Optimum Seismic Design and Analytical Response Prediction of R/C Frame Wall Structures," by Aktan, A.E. and Bertero, V.V., July 1982, (PB83 147 736)A05.

UCB/EERC-82/07 "Further Study of the Earthquake Response of a Broad Cylindrical Liquid-Storage Tank Model," by Manos, G.C. and Clough, R.W., July 1982, (PB83 147 744)A11.

UCB/EERC-82/08 "An Evaluation of the Design and Analytical Seismic Response of a Seven Story Reinforced Concrete Frame," by Charney, F.A. and Bertero, V.V., July 1982, (PB83 157 628)A09.

UCB/EERC-82/09 "Fluid-Structure Interactions: Added Mass Computations for Incompressible Fluid, ," by Kuo, J.S.-H., August 1982, (PB83 156 281)A07.

UCB/EERC-82/10 "Joint-Opening Nonlinear Mechanism: Interface Smeared Crack Model," by Kuo, J.S.-H., August 1982, (PB83 149 195)A05.

UCB/EERC-82/11 "Dynamic Response Analysis of Techi Dam," by Clough, R.W., Stephen, R.M. and Kuo, J.S.-H., August 1982, (PB83 147 496)A06.

UCB/EERC-82/12 "Prediction of the Seismic Response of R/C Frame-Coupled Wall Structures," by Aktan, A.E., Bertero, V.V. and Piazzo, M., August 1982, (PB83 149 203)A09.

UCB/EERC-82/13 "Preliminary Report on the Smart 1 Strong Motion Array in Taiwan," by Bolt, B.A. , Loh, C.H., Penzien, J. and Tsai, Y.B., August 1982, (PB83 159 400)A10.

UCB/EERC-82/14 "Shaking-Table Studies of an Eccentrically X-Braced Steel Structure," by Yang, M.S., September 1982, (PB83 260 778)A12.

UCB/EERC-82/15 "The Performance of Stairways in Earthquakes," by Roha, C., Axley, J.W. and Bertero, V.V., September 1982, (PB83 157 693)A07.

UCB/EERC-82/16 "The Behavior of Submerged Multiple Bodies in Earthquakes," by Liao, W.-G., September 1982, (PB83 158 709)A07.

UCB/EERC-82/17 "Effects of Concrete Types and Loading Conditions on Local Bond-Slip Relationships," by Cowell, A.D., Popov, E.P. and Bertero, V.V., September 1982, (PB83 153 577)A04.

UCB/EERC-82/18 "Mechanical Behavior of Shear Wall Vertical Boundary Members: An Experimental Investigation," by Wagner, M.T. and Bertero, V.V., October 1982, (PB83 159 764)A05.

UCB/EERC-82/19 "Experimental Studies of Multi-support Seismic Loading on Piping Systems," by Kelly, J.M. and Cowell, A.D., November 1982.

UCB/EERC-82/20 "Generalized Plastic Hinge Concepts for 3D Beam-Column Elements," by Chen, P. F.-S. and Powell, G.H., November 1982, (PB83 247 981)A13.

UCB/EERC-82/21 "ANSR-II: General Computer Program for Nonlinear Structural Analysis," by Oughourlian, C.V. and Powell, G.H., November 1982, (PB83 251 330)A12.

UCB/EERC-82/22 "Solution Strategies for Statically Loaded Nonlinear Structures," by Simons, J.W. and Powell, G.H., November 1982, (PB83 197 970)A06.

UCB/EERC-82/23 "Analytical Model of Deformed Bar Anchorages under Generalized Excitations," by Ciampi, V., Eligehausen, R., Bertero, V.V. and Popov, E.P., November 1982, (PB83 169 532)A06.

UCB/EERC-82/24 "A Mathematical Model for the Response of Masonry Walls to Dynamic Excitations," by Sucuoglu, H., Mengi, Y. and McNiven, H.D., November 1982, (PB83 169 011)A07.

UCB/EERC-82/25 "Earthquake Response Considerations of Broad Liquid Storage Tanks," by Cambra, F.J., November 1982, (PB83 251 215)A09.

UCB/EERC-82/26 "Computational Models for Cyclic Plasticity, Rate Dependence and Creep," by Mosaddad, B. and Powell, G.H., November 1982, (PB83 245 829)A08.

UCB/EERC-82/27 "Inelastic Analysis of Piping and Tubular Structures," by Mahasuverachai, M. and Powell, G.H., November 1982, (PB83 249 987)A07.


UCB/EERC-83/01 "The Economic Feasibility of Seismic Rehabilitation of Buildings by Base Isolation," by Kelly, J.M., January 1983, (PB83 197 988)A05.

UCB/EERC-83/02 "Seismic Moment Connections for Moment-Resisting Steel Frames.," by Popov, E.P., January 1983, (PB83 195 412)A04.

UCB/EERC-83/03 "Design of Links and Beam-to-Column Connections for Eccentrically Braced Steel Frames," by Popov, E.P. and Malley, J.O., January 1983, (PB83 194 811)A04.

UCB/EERC-83/04 "Numerical Techniques for the Evaluation of Soil-Structure Interaction Effects in the Time Domain," by Bayo, E. and Wilson, E.L., February 1983, (PB83 245 605)A09.

UCB/EERC-83/05 "A Transducer for Measuring the Internal Forces in the Columns of a Frame-Wall Reinforced Concrete Structure," by Sause, R. and Bertero, V.V., May 1983, (PB84 119 494)A06.

UCB/EERC-83/06 "Dynamic Interactions Between Floating Ice and Offshore Structures," by Croteau, P., May 1983, (PB84 119 486)A16.

UCB/EERC-83/07 "Dynamic Analysis of Multiply Tuned and Arbitrarily Supported Secondary Systems, ," by Igusa, T. and Der Kiureghian, A., July 1983, (PB84 118 272)A11.

UCB/EERC-83/08 "A Laboratory Study of Submerged Multi-body Systems in Earthquakes," by Ansari, G.R., June 1983, (PB83 261 842)A17.

UCB/EERC-83/09 "Effects of Transient Foundation Uplift on Earthquake Response of Structures," by Yim, C.-S. and Chopra, A.K., June 1983, (PB83 261 396)A07.

314

UCB/EERC-83/10  "Optimal Design of Friction-Braced Frames under Seismic Loading," by Austin, M.A. and Pister, K.S., June 1983. (PB84 119 288)A06.

UCB/EERC-83/11  "Shaking Table Study of Single-Story Masonry Houses: Dynamic Performance under Three Component Seismic Input and Recommendations," by Manos, G.C., Clough, R.W. and Mayes, R.L., July 1983, (UCB/EERC-83/11)A08.

UCB/EERC-83/12  "Experimental Error Propagation in Pseudodynamic Testing," by Shiing, P.B. and Mahin, S.A., June 1983, (PB84 119 270)A09.

UCB/EERC-83/13  "Experimental and Analytical Predictions of the Mechanical Characteristics of a 1/5-scale Model of a 7-story R/C Frame-Wall Building Structure," by Aktan, A.E., Bertero, V.V., Chowdhury, A.A. and Nagashima, T., June 1983, (PB84 119 213)A07.

UCB/EERC-83/14  "Shaking Table Tests of Large-Panel Precast Concrete Building System Assemblages," by Oliva, M.G. and Clough, R.W., June 1983, (PB86 110 210/AS)A11.

UCB/EERC-83/15  "Seismic Behavior of Active Beam Links in Eccentrically Braced Frames," by Hjelmstad, K.D. and Popov, E.P., July 1983, (PB84 119 676)A09.

UCB/EERC-83/16  "System Identification of Structures with Joint Rotation," by Dimsdale, J.S., July 1983, (PB84 192 210)A06.

UCB/EERC-83/17  "Construction of Inelastic Response Spectra for Single-Degree-of-Freedom Systems," by Mahin, S. and Lin, J., June 1983, (PB84 208 834)A05.

UCB/EERC-83/18  "Interactive Computer Analysis Methods for Predicting the Inelastic Cyclic Behaviour of Structural Sections," by Kaba, S. and Mahin, S., July 1983, (PB84 192 012)A06.

UCB/EERC-83/19  "Effects of Bond Deterioration on Hysteretic Behavior of Reinforced Concrete Joints," by Filippou, F.C., Popov, E.P. and Bertero, V.V., August 1983, (PB84 192 020)A10.

UCB/EERC-83/20  "Analytical and Experimental Correlation of Large-Panel Precast Building System Performance," by Oliva, M.G., Clough, R.W., Velkov, M. and Gavrilovic, P., November 1983.

UCB/EERC-83/21  "Mechanical Characteristics of Materials Used in a 1/5 Scale Model of a 7-Story Reinforced Concrete Test Structure," by Bertero, V.V., Aktan, A.E., Harris, H.G. and Chowdhury, A.A., October 1983, (PB84 193 697)A05.

UCB/EERC-83/22  "Hybrid Modelling of Soil-Structure Interaction in Layered Media," by Tzong, T.-J. and Penzien, J., October 1983, (PB84 192 178)A08.

UCB/EERC-83/23  "Local Bond Stress-Slip Relationships of Deformed Bars under Generalized Excitations," by Eligehausen, R., Popov, E.P. and Bertero, V.V., October 1983, (PB84 192 848)A09.

UCB/EERC-83/24  "Design Considerations for Shear Links in Eccentrically Braced Frames," by Malley, J.O. and Popov, E.P., November 1983, (PB84 192 186)A07.

UCB/EERC-84/01  "Pseudodynamic Test Method for Seismic Performance Evaluation: Theory and Implementation," by Shing, P.-S. B. and Mahin, S.A., January 1984, (PB84 190 644)A08.

UCB/EERC-84/02  "Dynamic Response Behavior of Kiang Hong Dian Dam," by Clough, R.W., Chang, K.-T., Chen, H.-Q. and Stephen, R.M., April 1984, (PB84 209 402)A08.

UCB/EERC-84/03  "Refined Modelling of Reinforced Concrete Columns for Seismic Analysis," by Kaba, S.A. and Mahin, S.A., April 1984, (PB84 234 384)A06.

UCB/EERC-84/04  "A New Floor Response Spectrum Method for Seismic Analysis of Multiply Supported Secondary Systems," by Asfura, A. and Der Kiureghian, A., June 1984, (PB84 239 417)A06.

UCB/EERC-84/05  "Earthquake Simulation Tests and Associated Studies of a 1/5th-scale Model of a 7-Story R/C Frame-Wall Test Structure," by Bertero, V.V., Aktan, A.E., Charney, F.A. and Sause, R., June 1984, (PB84 239 409)A09.

UCB/EERC-84/06  "R/C Structural Walls: Seismic Design for Shear," by Aktan, A.E. and Bertero, V.V., 1984.

UCB/EERC-84/07  "Behavior of Interior and Exterior Flat-Plate Connections subjected to Inelastic Load Reversals," by Zee, H.L. and Moehle, J.P., August 1984, (PB86 117 629/AS)A07.

UCB/EERC-84/08  "Experimental Study of the Seismic Behavior of a Two-Story Flat-Plate Structure. ," by Moehle, J.P. and Diebold, J.W., August 1984, (PB86 122 553/AS)A12.

UCB/EERC-84/09  "Phenomenological Modeling of Steel Braces under Cyclic Loading," by Ikeda, K., Mahin, S.A. and Dermitzakis, S.N., May 1984, (PB86 132 198/AS)A08.

UCB/EERC-84/10  "Earthquake Analysis and Response of Concrete Gravity Dams," by Fenves, G. and Chopra, A.K., August 1984, (PB85 193 902/AS)A11.

UCB/EERC-84/11  "EAGD-84: A Computer Program for Earthquake Analysis of Concrete Gravity Dams," by Fenves, G. and Chopra, A.K., August 1984, (PB85 193 613/AS)A05.

UCB/EERC-84/12  "A Refined Physical Theory Model for Predicting the Seismic Behavior of Braced Steel Frames," by Ikeda, K. and Mahin, S.A., July 1984, (PB85 191 450/AS)A09.

UCB/EERC-84/13  "Earthquake Engineering Research at Berkeley - 1984," by , August 1984, (PB85 197 341/AS)A10.

UCB/EERC-84/14  "Moduli and Damping Factors for Dynamic Analyses of Cohesionless Soils," by Seed, H.B., Wong, R.T., Idriss, I.M. and Tokimatsu, K., September 1984, (PB85 191 468/AS)A04.

UCB/EERC-84/15  "The Influence of SPT Procedures in Soil Liquefaction Resistance Evaluations," by Seed, H.B., Tokimatsu, K., Harder, L.F. and Chung, R.M., October 1984, (PB85 191 732/AS)A04.

UCB/EERC-84/16  "Simplified Procedures for the Evaluation of Settlements in Sands Due to Earthquake Shaking," by Tokimatsu, K. and Seed, H.B., October 1984, (PB85 197 887/AS)A03.

UCB/EERC-84/17  "Evaluation of Energy Absorption Characteristics of Bridges under Seismic Conditions," by Imbsen, R.A. and Penzien, J., November 1984.

UCB/EERC-84/18  "Structure-Foundation Interactions under Dynamic Loads," by Liu, W.D. and Penzien, J., November 1984, (PB87 124 889/AS)A11.

UCB/EERC-84/19    "Seismic Modelling of Deep Foundations," by Chen, C.-H. and Penzien, J., November 1984, (PB87 124 798/AS)A07.

UCB/EERC-84/20    "Dynamic Response Behavior of Quan Shui Dam," by Clough, R.W., Chang, K.-T., Chen, H.-Q., Stephen, R.M., Ghanaat, Y. and Qi, J.-H., November 1984, (PB86 115177/AS)A07.

UCB/EERC-85/01    "Simplified Methods of Analysis for Earthquake Resistant Design of Buildings," by Cruz, E.F. and Chopra, A.K., February 1985, (PB86 112299/AS)A12.

UCB/EERC-85/02    "Estimation of Seismic Wave Coherency and Rupture Velocity using the SMART 1 Strong-Motion Array Recordings," by Abrahamson, N.A., March 1985, (PB86 214 343)A07.

UCB/EERC-85/03    "Dynamic Properties of a Thirty Story Condominium Tower Building," by Stephen, R.M., Wilson, E.L. and Stander, N., April 1985, (PB86 118965/AS)A06.

UCB/EERC-85/04    "Development of Substructuring Techniques for On-Line Computer Controlled Seismic Performance Testing," by Dermitzakis, S. and Mahin, S., February 1985, (PB86 132941/AS)A08.

UCB/EERC-85/05    "A Simple Model for Reinforcing Bar Anchorages under Cyclic Excitations," by Filippou, F.C., March 1985, (PB86 112 919/AS)A05.

UCB/EERC-85/06    "Racking Behavior of Wood-framed Gypsum Panels under Dynamic Load," by Oliva, M.G., June 1985.

UCB/EERC-85/07    "Earthquake Analysis and Response of Concrete Arch Dams," by Fok, K.-L. and Chopra, A.K., June 1985, (PB86 139672/AS)A10.

UCB/EERC-85/08    "Effect of Inelastic Behavior on the Analysis and Design of Earthquake Resistant Structures," by Lin, J.P. and Mahin, S.A., June 1985, (PB86 135340/AS)A08.

UCB/EERC-85/09    "Earthquake Simulator Testing of a Base-Isolated Bridge Deck," by Kelly, J.M., Buckle, I.G. and Tsai, H.-C., January 1986, (PB87 124 152/AS)A06.

UCB/EERC-85/10    "Simplified Analysis for Earthquake Resistant Design of Concrete Gravity Dams," by Fenves, G. and Chopra, A.K., June 1986, (PB87 124 160/AS)A08.

UCB/EERC-85/11    "Dynamic Interaction Effects in Arch Dams," by Clough, R.W., Chang, K.-T., Chen, H.-Q. and Ghanaat, Y., October 1985, (PB86 135027/AS)A05.

UCB/EERC-85/12    "Dynamic Response of Long Valley Dam in the Mammoth Lake Earthquake Series of May 25-27, 1980," by Lai, S. and Seed, H.B., November 1985, (PB86 142304/AS)A05.

UCB/EERC-85/13    "A Methodology for Computer-Aided Design of Earthquake-Resistant Steel Structures," by Austin, M.A., Pister, K.S. and Mahin, S.A., December 1985, (PB86 159480/AS)A10 .

UCB/EERC-85/14    "Response of Tension-Leg Platforms to Vertical Seismic Excitations," by Liou, G.-S., Penzien, J. and Yeung, R.W., December 1985, (PB87 124 871/AS)A08.

UCB/EERC-85/15    "Cyclic Loading Tests of Masonry Single Piers: Volume 4 - Additional Tests with Height to Width Ratio of 1," by Sveinsson, B., McNiven, H.D. and Sucuoghu, H., December 1985.

UCB/EERC-85/16    "An Experimental Program for Studying the Dynamic Response of a Steel Frame with a Variety of Infill Partitions," by Yanev, B. and McNiven, H.D., December 1985.

UCB/EERC-86/01    "A Study of Seismically Resistant Eccentrically Braced Steel Frame Systems," by Kasai, K. and Popov, E.P., January 1986, (PB87 124 178/AS)A14.

UCB/EERC-86/02    "Design Problems in Soil Liquefaction," by Seed, H.B., February 1986, (PB87 124 186/AS)A03.

UCB/EERC-86/03    "Implications of Recent Earthquakes and Research on Earthquake-Resistant Design and Construction of Buildings," by Bertero, V.V., March 1986, (PB87 124 194/AS)A05.

UCB/EERC-86/04    "The Use of Load Dependent Vectors for Dynamic and Earthquake Analyses," by Leger, P., Wilson, E.L. and Clough, R.W., March 1986, (PB87 124 202/AS)A12.

UCB/EERC-86/05    "Two Beam-To-Column Web Connections," by Tsai, K.-C. and Popov, E.P., April 1986 , (PB87 124 301/AS)A04.

UCB/EERC-86/06    "Determination of Penetration Resistance for Coarse-Grained Soils using the Becker Hammer Drill," by Harder, L.F. and Seed, H.B., May 1986, (PB87 124 210/AS)A07.

UCB/EERC-86/07    "A Mathematical Model for Predicting the Nonlinear Response of Unreinforced Masonry Walls to In-Plane Earthquake Excitations," by Mengi, Y. and McNiven, H.D., May 1986, (PB87 124 780/AS)A06.

UCB/EERC-86/08    "The 19 September 1985 Mexico Earthquake: Building Behavior," by Bertero, V.V., July 1986.

UCB/EERC-86/09    "EACD-3D: A Computer Program for Three-Dimensional Earthquake Analysis of Concrete Dams," by Fok, K.-L., Hall, J.F. and Chopra, A.K., July 1986, (PB87 124 228/AS)A08.

UCB/EERC-86/10    "Earthquake Simulation Tests and Associated Studies of a 0.3-Scale Model of a Six-Story Concentrically Braced Steel Structure," by Uang, C.-M. and Bertero, V.V., December 1986.

UCB/EERC-86/11    "Mechanical Characteristics of Base Isolation Bearings for a Bridge Deck Model Test," by Kelly, J.M., Buckle, I.G. and Koh, C.-G., 1987.

UCB/EERC-86/12    "Modelling of Dynamic Response of Elastomeric Isolation Bearings," by Koh, C.-G. and Kelly, J.M., 1987.

UCB/EERC-87/01    "FPS Earthquake Resisting System: Experimental Report," by Zayas, V.A., Low, S.S. and Mahin, S.A., June 1987.

UCB/EERC-87/02    "Earthquake Simulator Tests and Associated Studies of a 0.3-Scale Model of a Six-Story Eccentrically Braced Steel Structure," by Whittaker, A., Uang, C.-M. and Bertero, V.V., July 1987.

UCB/EERC-87/03    "A Displacement Control and Uplift Restraint Device for Base-Isolated Structures," by Kelly, J.M., Griffith, M.C. and Aiken, I.G., April 1987.

316

UCB/EERC-87/04    "Earthquake Simulator Testing of a Combined Sliding Bearing and Rubber Bearing Isolation System," by Kelly, J.M. and Chalhoub, M.S., 1987.

UCB/EERC-87/05    "Three-Dimensional Inelastic Analysis of Reinforced Concrete Frame-Wall Structures," by Moazzami, S. and Bertero, V.V., May 1987.

UCB/EERC-87/06    "Experiments on Eccentrically Braced Frames With Composite Floors," by Ricles, J. and Popov, E., June 1987.

UCB/EERC-87/07    "Dynamic Analysis of Seismically Resistant Eccentrically Braced Frames," by Ricles, J. and Popov, E., June 1987.